THE PETROGENESIS OF PYROXENITES CONTAINING OCTAHEDRAL GRAPHITE AND ASSOCIATED MAFIC AND ULTRAMAFIC ROCKS OF THE BENI BOUSERA PERIDOTITE MASSIF, N. MOROCCO.

DAVID GRAHAM PEARSON

Submitted in fulfilment of the requirements

for the degree of Doctor of Philosophy

Department of Earth Sciences

The University of Leeds, U.K.

December 1989

BRITISH LIBRARY

IMAGING SERVICES NORTH

Boston Spa, Wetherby
West Yorkshire, LS23 7BQ
www.bl.uk

Contains

Overlays and underlays

TO MY PARENTS FOR 24 YEARS OF CONSTANT
SUPPORT AND ENCOURAGEMENT

CONTENTS

CHAPTER 3

THE OCCURRENCE OF GRAPHITE IN THE BENI BOUSERA PERIDOTITE MASSIF

CHAPTER 4

MINERAL CHEMISTRY OF THE PERIDOTITES AND PYROXENITES

CHAPTER 5

MAJOR AND TRACE ELEMENT GEOCHEMISTRY.

CHAPTER 6

RADIOGENIC ISOTOPE SYSTEMATICS

ACKNOWLEDGMENTS

I would like to express my graditude to the following people for their contribution towards this project:

My supervisors, Dr. Gareth Davies and Dr. Pete Nixon, deserve my immense thanks for giving me the best supervision anyone could wish for. Neither refused me a second of their time, both were always willing to listen to my ideas and heroically battled with my literary efforts, latterly from the other side of the Atlantic in Gareth's case. In addition to geological aspects, Pete gave me excellent tuition in making a "burro" go where you want it to go and acquiring contraband whisky in the middle of nowhere. Gareth's help in the laboratory was invaluable and his patience with my grammatical ability, or lack of it, was amazing.

Steve Reddy provided crucial field assistance during my second visit to Morocco. Without complaint he carried ridiculous loads of rock over 10 miles back to base whilst cheerfully suffering from a severe dose of the Moroccan "trots". He survived the rigours of Tetuan at "rush hour" and offered useful (if not physically impossible) advice to a prayer caller around 3 O'clock one morning. I have greatly benefitted from his help, friendship and advice over the last 3 years.

Thanks and several pints of beer go to Rod Green whose knowledge and experience in the lab proved as valuable as his sense of humour in seeing me through. I sincerely appreciated his help in the lab and derisory comments on the dart board. Eric Condliffe provided microprobe tuition and I benefitted greatly from discussions and advice from him on many occasions.

Tom Oddy and Dennis Pickles spent many hours helping me with the finer points of mineral separation and explaining obscure army jokes, thanks. I am grateful to Phil Guise and Dave Rex who performed the Ar-Ar and K-Ar analyses, Phil also managed to keep the two mass specs running despite the best efforts of the post-graduates and other users! Alan Grey provided expert assistance with XRF analyses. In addition I would like to thank the remainder of the technical staff at Leeds for all their help over the past three years.

Marge Wilson wrestled with several rough and ready versions of chapters and tried in vain to disuade me from using the ubiquitous "however". Her time spent reviewing chapters and discussing Beni Bousera is greatly appreciated. I am also grateful to Bob Cliff for numerous useful discussions and use of the Leeds isotope facilities.

Dave Chaffey generously made available his plotting programs, proof read some of the chapters and provided useful discussions on isotope geochemistry. His wife Sally drafted Appendix 2. The " I'm only going for one " club members: Steve, Simon and Neil together with Keith and Pete provided excellent drinking company on several notable occasions. Pete Bishop also proof read some of the chapters.

In Morocco, I thank members of the Ministere de l'Energie et des Mines for permission to work in the Beni Bousera area. Throughout my stay at Amter the hospitallity and enthusiasm of the two Mohammeds was unceasing. They introduced me to the delights of sardines for breakfast, lunch and dinner and tried, unsuccessfully, to persuade me that rancid goats' milk is good for you.

Peter Greenwood aided by Mike Fowler patiently taught me the intricacies of oxygen isotope analysis and ran several of the samples for me at short notice.

Dave Mattey introduced me to carbon isotope analysis and together with Stuart Boyd gave me the benefit of their opinions about the carbon isotope data.

Judith Milledge and Guy Cooper provided X-ray crystallography guidance, provided me with numerous diamonds to burn in the Edinburgh furnaces and showed me hospitallity during my visits to U.C.L.

I thank Dr Nobu Shimizu for analysing several specimens using the M.I.T. ion microprobe and allowing me to use the data in this thesis. Dr Jill Dill Pasteris made numerous Raman spectroscopic measurements of Beni Bousera graphite and kindly gave permission to use some of the results in Chapter 3.

My brother Richard wrote the Fortran computer program to generate multistage Pb isotope data.

I would like to thank my parents for all their help, encouragement and support throughout my education and for giving me and the rest of their off-spring such a good start in life.

Jonathan and Margaret Jackson patiently put up with my nocturnal habits and untidyness for several weeks and showed me substantial generosity during the completion of this thesis.

Finally, I would like to thank my wife, Samantha for her help in creating this thesis. She enduringly typed hundreds of pages of my deplorable hand writing, corrected mistakes, drew diagrams, proof read manuscripts and performed numerous other monotonous tasks that were vital in finishing this project in addition to doing a full time job of her own. Sam gave me all the love and support (financial, mental and physical) that I needed to get me through and I am eternally grateful to her.

This project was carried out under the tenure of a NERC post graduate studentship, financed by NERC, my wife and Mr and Mrs R. Pearson.

ABBREVIATIONS

LITHOLOGICAL GROUPS

GGP	Graphite garnet clinopyroxenite
GP	Garnet clinopyroxenite
WEB	Websterite
Cr-WEB	Chrome-diopside websterite
OPXITE	Orthopyroxenite
CPXITE	Clinopyroxenite
GTWEB	Garnet websterite
SPLHRZ	Spinel lherzolite
GTITE	Garnetite
GTLHZ	Garnet lherzolite
CORP/CP	Corundum pyroxenite

PHYSICAL PARAMETERS

A	Amperes
cm	Centimeters
C	celsius
g	gram
mg	milligram
ng	nanogram
pg	picogram
µg	microgram
K	kelvin
kb	kilobar
kg	kilogram
km	kilometre
kv	kilovolt
M	Molar
GPa	Giga pascals
V	Volts

MINERALOGICAL ABBREVIATIONS

Al	Almandine
An	Anorthite
CPX	Clinopyroxenite
Di	Diopside
En	Enstatite
Fo	Fosterite
Fs	Ferrosilite
Gros	Grossular
GT	Garnet
Hy	Hypersthene
Jd	Jadeite
Ne	Nepheline
OPX	Orthopyroxene
Plag	Plagioclase feldspar
Py	Pyrope
Qtz	Quartz
Ts	Tschermaks molecule
Uv	Uvarovite
Wo	Wollastonite

GENERAL

ID	Isotope dilution
MORB	Mid Ocean Ridge Basalt
NHRL	Northern Hemisphere Reference Line
OIB	Ocean Island Basalt
SBQD	Sub-Boiled quartz distilled
SEM	Scanning Electron Microscopy
XRF	X-Ray fluorescence spectrometer
CHUR	Chondritic Uniform Reservoir
CMAS	CaO-MgO-Al_2O_3-SiO_2
EDS	Energy dispersive spectrometry
fO_2	Oxygen fugacity
Ga	Giga years i.e. 10^9
HREE	Heavy Rare Earth Elements
K_D	distribution coefficient
LREE	Light Rare Earth Elements
MREE	Middle Rare Earth Elements
Ma	Million years
P	Pressure
REE	Rare Earth Elements
T	Temperature
WDS	Wave length dispersive spectrometry

P-Type Diamonds: Diamonds containing peridotite suite inclusions, ie. pyrope rich garnet, enstatite, chrome diopside, and Fo rich olivine.

E-Type Diamonds: Diamonds containing eclogite suite inclusions, ie. pyrope-almandine garnet and omphacitic CPX.

ABSTRACT

The Beni Bousera peridotite massif, N. Morocco, contains pyroxenite layers of varied mineralogy, including graphitic garnet clinopyroxenite (GGP) layers. The graphite in these rocks occurs as octahedral multi-crystalline aggregates and other forms of cubic symmetry. Scanning electron microscopy and X-ray diffraction studies indicate that the graphite aggregates represent *graphitized diamonds*. Minor Na in coexisting garnets confirms an origin in the diamond stability field. However, other mineral chemical data from the peridotites and pyroxenites indicate major sub-solidus re-equilibration of the silicate assemblages. Major and trace element analyses indicate the peridotites are residues of partial melting (5-30 %) in the spinel and possibly garnet stability fields. Some peridotites have suffered Fe and/or LREE enrichment. The pyroxenite suite crystallized as veins/dikes in the peridotites and shows fractionation trends controlled by OPX, CPX, garnet and possibly spinel. The LREE depleted nature of the pyroxenite suite, combined with their highly variable incompatible element contents which do not correlate with fractionation indices such as Mg No., preclude their derivation from the host peridotites and require a chemically heterogeneous source/sources. Positive and negative Eu anomalies in the pyroxenites suggest their derivation from a low pressure precursor.

Sr, Pb and Nd isotope analyses of the peridotites reveal large magnitude, small scale (sub-km) heterogeneities. Pyroxenites show even greater isotopic diversity and a decoupling of trace element-isotope systematics which indicate a recent melting event. Sr, Pb and Nd isotopes indicate both peridotites and pyroxenites have experienced complex, long term evolution. The extreme isotopic diversity of the pyroxenites, with Pb isotope compositions that plot *both* to the left and right of the geochron, with high $\Delta 7/4$ and $\Delta 8/4$ values, are consistent with their derivation as melts of subducted oceanic crust plus less than 1% sediment, over 1 Ga ago. This interpretation is supported by pronounced oxygen isotope variability ($\delta^{18}O$ = +4.9 to +9.3 ‰) suggesting the oceanic crustal source/s were hydrothermally altered before subduction. Hydrothermal alteration augmented Sr and Pb isotopic heterogeneity in the pyroxenites. If the isotopically light graphite in the GGP ($\delta^{13}C$ = -17 to -27 ‰) represents the carbon isotopic composition of the precursor diamonds, the original diamonds may have formed from subducted crustal (kerogenous?) carbon.

A model is proposed invoking subduction of hydrothermally altered oceanic crust and lithosphere, together with minor amounts of sediment (<1%) into the asthenosphere over 1 Ga ago. The subducted oceanic slab descended to the 670km seismic discontinuity and "ponded" to form a megalith. Thermal equilibration of this megalith induced diapirism into the asthenosphere. Melting during ascent may have formed the pyroxenite layers and refertilized some of the peridotites. Asthenospheric upwelling during a major Neogene extensional event initiated emplacement of pyroxenite veined peridotitic mantle into the N. African crust. Recent, small degree partial melting during ascent into the crust decoupled parent-daughter isotope systematics in the pyroxenites and peridotites. Graphitization of diamond in the GGP may also have occurred at this time.

Pyroxenites containing graphitized diamonds in an orogenic peridotite massif provide evidence in support of a non-volcanic source for diamonds of unexplained provenance which occur in, or close to, major tectonic collision zones.

CHAPTER 1

INTRODUCTION

1:1 The Mantle Sample.

Current knowledge of the chemical and physical composition of the asthenospheric and lithospheric mantle is based mainly on fragments of mantle emplaced into the crust by two distinct mechanisms.

1) Xenolithic mantle fragments entrained accidentally during eruptions of kimberlites and other "deep seated" volcanics (see review by Nixon 1987).

2) Ultramafic/mafic massifs emplaced tectonically into the crust, usually at collision zones.

The latter group vary in size from less than $1m^2$ to over 1000 km^2 in outcrop and are advantageous in two ways for studying mantle geodynamics compared with xenolith samples. One is that tectonically emplaced massifs have not been subjected to major chemical interactions with magmas during their ascent. Interaction with the transporting magma may seriously affect the trace element and isotopic composition of xenolith samples, thus complicating any primary mantle geochemical signatures in the xenoliths. Secondly, the larger dimensions of peridotite massifs allow *in situ* observation of lithological relationships and chemical heterogeneity in the mantle. Trace element and isotope data on rocks from peridotite massifs are sparse, possibly due to the low levels of daughter isotopes in their constituent lithologies and the often altered nature of the samples. Hence, comparatively little information regarding mantle geochemistry has been gained from this important group of mantle samples.

1:2 Varieties of tectonically emplaced ultramafic massifs.

Hitherto, it has been common practice to devide tectonically emplaced peridotite massifs into two subgroups (Thayer 1960, Green 1967), the Lherzolite Group (also known as orogenic "root zone" or "high temperature" peridotite) and the Harzburgite Group (also known as ophiolitic or "low temperature" peridotites). Both groups were collectively named "alpine-type peridotites" by Thayer (1960). This general term has now become common usage and has lead to much confusion in the literature, especially when comparing geochemical signatures of peridotite massifs eg. Bonatti et al (1986). The distinction between peridotites which are part of ophiolite associations and those which clearly have no ophiolitic affinity is crucial in classifying them. Lherzolitic and harzburgitic are misleading because lherzolite massifs can contain significant areas of harzburgite and vice-versa. The high and low temperature nomenclature is similarly misleading because the temperatures recorded by mineral thermometry depend on the amount of re-equilibration the peridotites experienced during emplacement. This can vary widely in each sub-type.

It is proposed here that any tectonically emplaced peridotite massif associated with other rocks of the ophiolite suite or showing ophiolitic affinities should be called "ophiolitic peridotite massifs".

Other peridotite massifs with no ophiolite connection or associated ophiolite lithologies which are tectonically emplaced into continental crust should be called "orogenic peridotites". This nomenclature will be used throughout this study, it is suggested that the collective term, "alpine-type peridotite" should be discontinued.

The orogenic peridotite subtype is exemplified by the peridotite massifs of the western Mediterranean and western Alps such as Beni Bousera (N.Morocco), Ronda and Ojen (S.Spain), Lherz (S.W.France), Alpe Arami and Lanzo (N.Italy). These "orogenic" peridotite massifs are composed of garnet, spinel or plagioclase peridotites, or all three, as in Ronda (Oblata 1980) and contain varying amounts of pyroxenite layers, some of which usually contain garnet. In contrast, ophiolitic peridotite massifs, typified by Troodos (Cyprus), and Semail (Oman) are commonly composed of only spinel-facies peridotites which are harzburgitic. Pyroxenite layers are less conspicuous in ophiolitic peridotites and do not generally contain garnet.

1:3 Objectives of this study.

The Beni Bousera peridotite massif (N.Morocco) is composed predominantly of peridotite with varying proportions of pyroxenites (Milliard 1959, Kornprobst 1969). Two garnet clinopyroxenite layers within the massif were found to contain graphite aggregates showing octahedral and other forms of cubic symmetry by Slodkevich (1980 a) who interpreted the graphite aggregates as graphitized diamonds.

The primary objectives of this study are to further investigate the origin of the graphite aggregates and their host rocks and to determine their relationship to the pyroxenite suite and the host peridotite. Verification of the graphite aggregates as pseudomorphs after diamond could contribute towards our understanding of the origin of certain diamond deposits where no known volcanic source exists (Nixon et al 1986). This study may also provide new information to advance conceptual models of diamond genesis in the mantle.

The geochemical objectives of this study include an investigation of effects of secondary alteration on the trace element and isotope systematics of the peridotites and pyroxenites. Once the effects of secondary alteration can be removed from a sample, meaningful isotopic data can be obtained which will constrain the origin of the rocks.

The origin of pyroxenite layers in peridotite massifs is currently unresolved. Some authors suggest that the pyroxenites are melts, or cumulates from melts, of the surrounding peridotites (Kornprobst 1969 & 1974, Dickey 1970, Bodinier et al 1987, Suen and Frey 1987). Limited isotopic data obtained by other workers suggests that the pyroxenites are not genetically related to their host peridotites and may be the remnants of subducted oceanic crust (Polve and Allegre 1980, Nixon et al 1986, Hamelin and Allegre 1988). Support for a subducted oceanic crustal origin for the pyroxenites is provided by numerical analysis of the structures expected from convective mixing and diffusion in the asthenosphere (Allegre and Turcotte 1986, Kellogg and Turcotte 1987). The aim of this study is to obtain an extensive radiogenic and stable isotope data base for the peridotites and pyroxenites from a single massif and to discern the degree of chemical and physical interaction between the two lithologies. Such a data base will allow more stringent constraints to be placed on the origin of the peridotites and pyroxenites which may be applied to similar rocks from other peridotite massifs.

Isotopic and trace element heterogeneity in present day oceanic magmatism may be explained by

"marble cake" mantle type models (Allegre and Turcotte 1986, Prinzhofer et al 1989), in which isotopic and trace element heterogeneity is generated by melting varying proportions of pyroxenites to peridotites in the asthenospheric mantle. Analysis of the stable and radiogenic isotope characteristics and trace element contents of the Beni Bousera pyroxenite suite will afford better constraints on "marble cake mantle" models.

1:4 Methodology.

Petrographic observations and field relations are discussed in Chapter 2 to elucidate the mode of emplacement of the massif and the origin of the complex structures seen in the pyroxenites. Physical relationships between pyroxenite margins and the surrounding peridotite are also examined to try to elucidate the origin of the pyroxenites. High resolution scanning electron microscopy and X-ray crystallography are used in Chapter 3 to determine the nature and origin of the graphite aggregates in the pyroxenites. Mineral chemical data constrain conditions of equilibration in the peridotites and pyroxenites and document chemical interaction between the two lithologies (Chapter 4). Major and trace element analyses of a large suite of peridotites and pyroxenites are presented in Chapter 5. These data are used to estimate the degree of melt depletion experienced by the peridotites and to determine the type of melting processes operating in the mantle. Major and trace element data ~~is~~ are also used to investigate the origin of the pyroxenite layers. Further constraints on the origin of the pyroxenites and peridotites are provided by radiogenic and stable isotopes in Chapters 6 & 7. Radiogenic isotope data allow the timing of pyroxenite generation to be assessed. Chapter 8 attempts to provide a summary of the petrogenetic evolution of the peridotites and pyroxenites and discusses some of the implications of the data obtained.

CHAPTER 2

THE BENI BOUSERA MASSIF:

FIELD RELATIONS AND PETROLOGY

2:1 Occurrence and Regional Setting

2:1.1 Location

The Beni Bousera peridotite massif is situated in the Rif Mountains of North Morocco, 60km S. E. of Tetuan on the N.E. Mediterranean coast (Fig. 2.1). The peridotite massif and associated high grade metamorphic suite are ovoid in outcrop with the long axis trending NW/SE. The N.E. extremity of the massif outcrops on the beach at Amasihene and continues into the Alboran Sea (Fig. 2.2). The massif covers an area of approximately 75 km^2 rising from sea level to 1174m at the summit of Jebel Karbous.

2:1.2 Regional Geology

Structurally the Internal Zone of the Rif (Fig. 2.1) is dominated by nappes and thrust sheets with S. W. transport directions (Kornprobst 1974). The region forms part of the arcuate Betico-Rifeo-Kabylean orogenic belt which dominates Western Mediterranean tectonics (Ricou 1986). This orogenic belt is thought to be the result of collision between the N. African plate and the Iberian and Alboran blocks during the Alpine Orogeny (Loomis 1975, Bourrouilh and Gorsline 1979, Ricou 1986). A detailed description of the geology of this orogenic zone is provided by Bourrouilh and Gorsline (1979). The orogenic belt extends from the Balearic Islands, and continues to form the Betic Cordillera of S. Spain, and the Straits of Gibralter. From Gibralter the zone forms successively the Moroccan Rif, the Algerian and Tunisian Coastal Atlas and the Siculo-Calabrian Arc (Fig. 2.3). Platt (1989) discusses the geological evolution of this complex orogenic zone, and his proposed model will be discussed in Chapter 8 in terms of the evolution of the Beni Bousera massif.

A series of ultramafic bodies of varying extent outcrop in the Betico-Rifean belt, the largest of which are the Ronda massif of S. Spain and Beni Bousera . The smaller massifs include Ojen (S. Spain), Ras Bougaroun (N. Algeria) and a small outcrop at Ceuta (N. Morocco), see Figure 2.1. A series of minor ultramafic "lenses" outcrop in close proximity to the coast between Beni Bousera and the highly serpentinised Ceuta outcrop (Dickey 1970, Kornprobst 1974).

Gravity data compiled by Bonini et al (1973) demonstrate two coastal gravity high zones along the Moroccan and Spanish margins of the Alboran Sea. The gravity high zones show steep gravity gradients and closures of upto 110 mgal which coincide closely to the surface outcrop of Beni Bousera and Ronda respectively. The magnitude of these coastal gravity highs, in combination with their steep gravity gradients led Bonini et al (1973) to conclude that the steeply dipping density discontinuities required by the data probably extend to the mantle and hence support the theory of diapiric intrusion of ultramafic rock from the mantle (Loomis 1975). However, the data could be consistent with a stack of thrusted ultramafic sheets but the magnitude of the gravity highs and the steep gradients make this possibility unlikey.

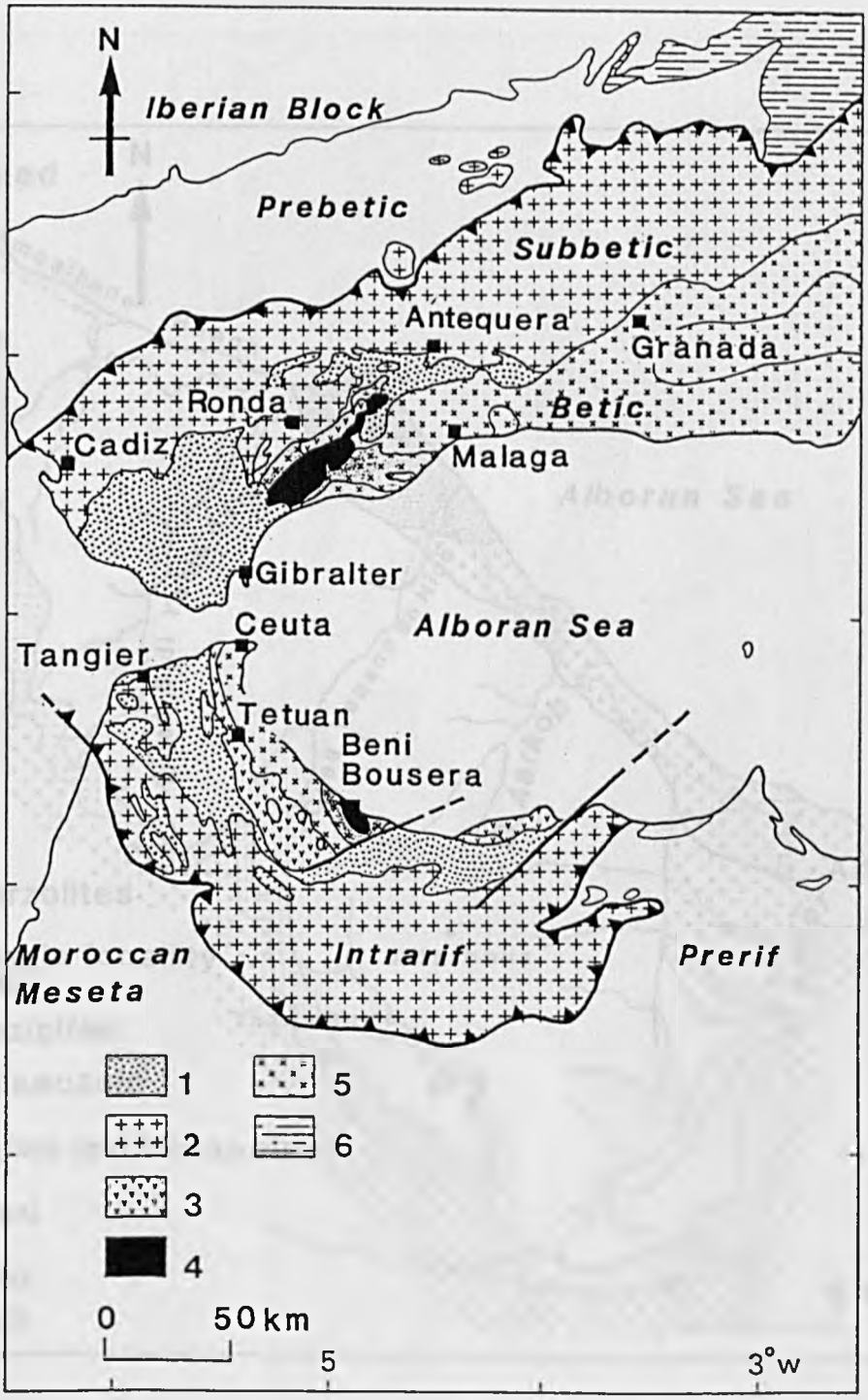

Figure 2.1. Regional geological map of the western Mediterranean area, after Bonini et al (1973). Key to legend: (1) Cretaceous and Tertiary flysch. (2) Mesozoic, Subbetic deep water carbonates and volcanics. (3) Drosdale, Mesozoic and Tertiary epicontinental series. (4) Peridotite bodies, including the Ceuta outcrop. (5) Ghomaride/Malaguide sequence of late Paleozoic clastics. Shaded area within this outcrop represents the Sebtide (Morocco) or Alpujarride sequence (S.Spain) which contains the Filali unit. (6) Late Cenozoic cover of the Prebetic zone and meseta.

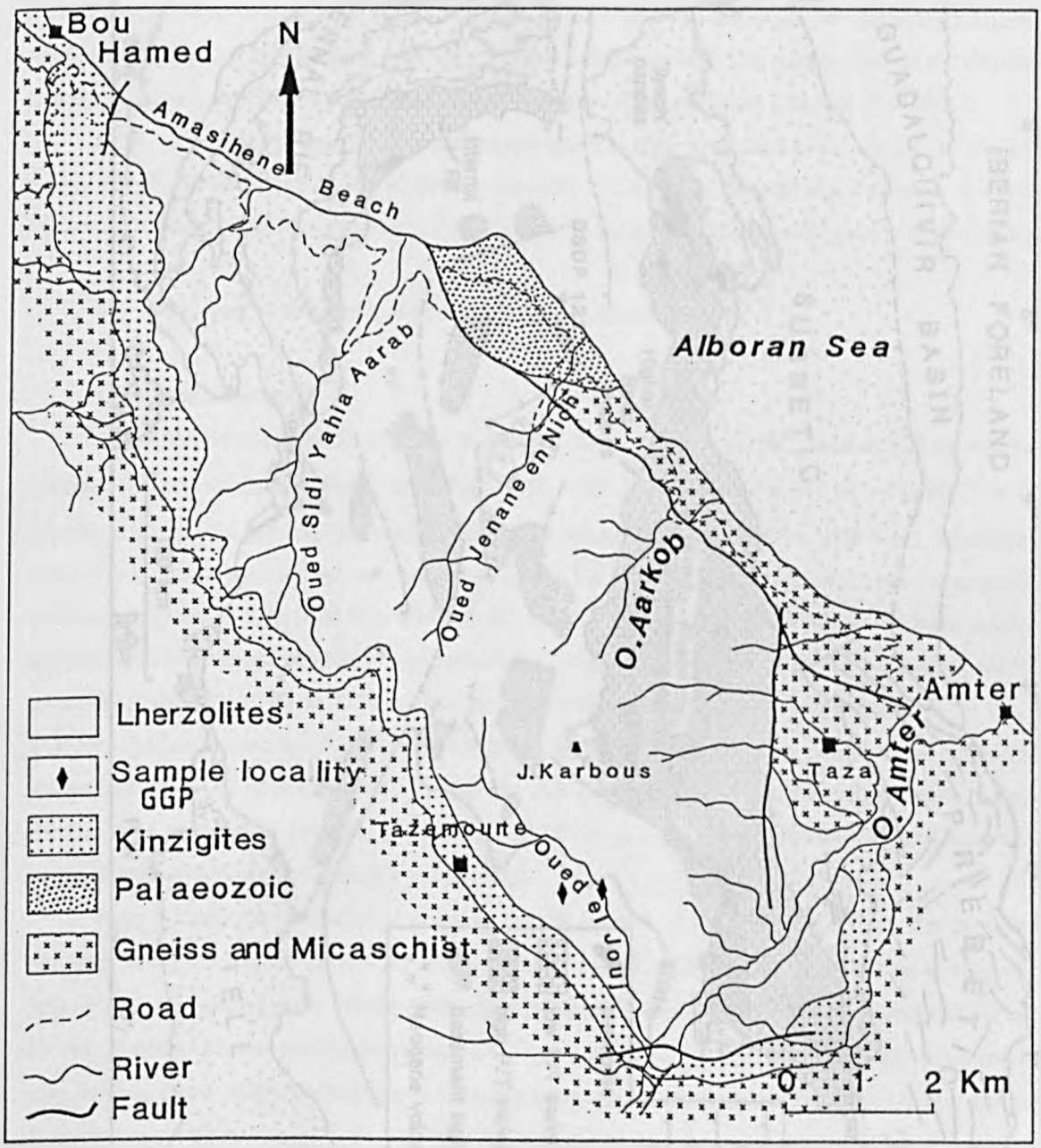

Figure 2.2. Generallized geological map of the Beni Bousera massif indicating the location of the two graphite bearing pyroxenites.

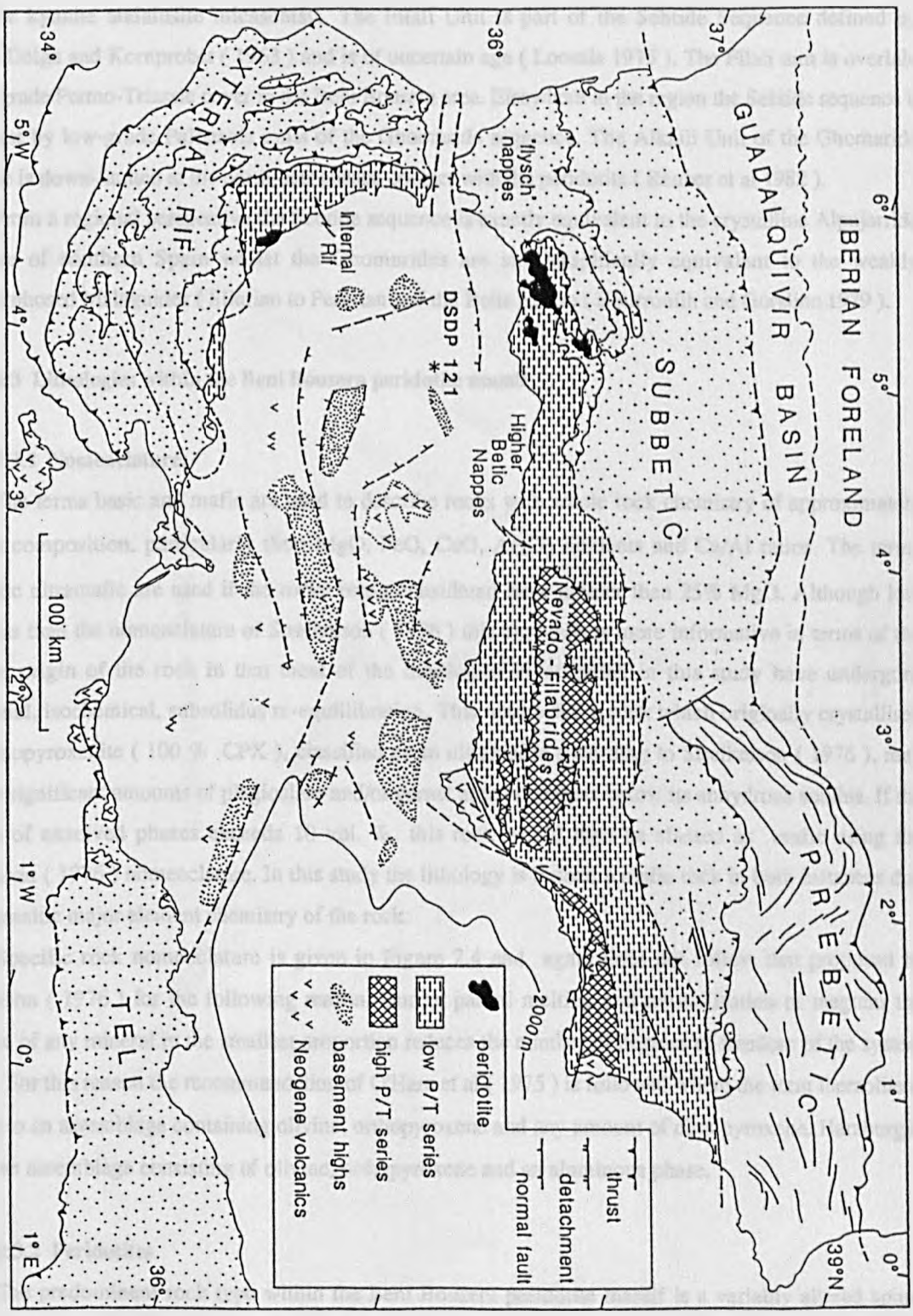

Figure 2.3. Tectonic map of the Alboran Sea and surrounding mountain chains. Low P/T series: unmetamorphosed and low to intermediate P/T rocks of the Internal Rif and Higher Betic nappes (Alpujarride/Sebtide and Malaguide/Ghomaride sequences). High P/T series: glaucophane schist, eclogite and high-P amphibolite facies rocks of the Nevado-Filabride complex. (After Platt and Vissers, 1989).

2:2 Stratigraphy

The Beni Bousera peridotite massif is in contact with the Filali gneisses (Fig. 2.1). The gneisses are garnet-sillimanite granulites at the point of contact, grading outwards into garnet kyanite gneisses and staurolite kyanite andalusite micaschists. The Filali Unit is part of the Sebtide Sequence defined by Durand-Delga and Kornprobst (1963) and is of uncertain age (Loomis 1975). The Filali unit is overlain by low-grade Permo-Triassic cover in the Beni Bousera area. Elsewhere in the region the Sebtide sequence is overthrust by low-grade Paleozoic units of the Ghomaride sequence. The Alkaili Unit of the Ghomaride sequence is down-faulted at the north-east coastal contact with the peridotite (Reuber et al 1982).

From a regional perspective the Sebtide sequence is exactly equivalent to the crystalline Alpujarride sequence of southern Spain whilst the Ghomarides are stratigraphically equivalent to the weakly metamorphosed Malaguides (Silurian to Permian) of the Betic region (Bourrouilh and Gorsline 1979).

2:3 Lithologies within the Beni Bousera peridotite massif

2:3.1 Nomenclature:

The terms basic and mafic are used to describe rocks with whole rock chemistry of approximately basaltic composition, particularly their MgO, FeO, CaO, Al_2O_3 contents and Ca/Al ratios. The terms ultrabasic ultramafic are used if the rocks being considered have greater than 25% MgO. Although less rigo rous than the nomenclature of Streikeison (1976) this approach is more informative in terms of the ultimate origin of the rock in that most of the lithologies investigated in this study have undergone substantial, isochemical, subsolidus re-equlilibration. This means that a rock which originally crystallised as a clinopyroxenite (100 % CPX), classified as an ultramafite according to Streikeison (1976), may exsolve significant amounts of plagioclase and/or garnet at temperatures below its anhydrous solidus. If the amount of exsolved phases exceeds 10 vol. % this rock would then be classed as mafic using the Streikeison (1976) nomenclature. In this study the lithology is termed a mafic rock in both instances due to the basaltic major element chemistry of the rock.

Specific rock nomenclature is given in Figure 2.4 and again does not follow that proposed by Streikeison (1976) for the following reason. During partial melting and crystallisation of magmas the presence of any mineral in the smallest proportion reduces the number of degrees of freedom of the system by one. For this reason the recommendation of O'Hara et al (1975) is followed where the term lherzolite is applied to an assemblage containing olivine, orthopyroxene and any amount of clinopyroxene. Harzburgite is thus an assemblage consisting of olivine, orthopyroxene and an aluminous phase.

2:3.2 Peridotites

The predominant rock type within the Beni Bousera peridotite massif is a variably altered spinel lherzolite. Harzburgites are extremely rare, where they do occur they are commonly highly serpentinized. Garnet lherzolite and garnet spinel lherzolite also occur as small <0.5km^2 "lenses" . Reuber et al (1982) stated all outcrops of this lithology are found close to the margin of the massif, however, a small (100m^2) outcrop of garnet lherzolite was dicovered in the north of the massif at least 1km from the margin . Reuber et al (1982) describe these rock types as garnet bearing dunites, however in the field they can be seen to contain apple green Cr-diopside, pink pyrope rich garnet and bastitized orthopyroxene porphyroclasts set in

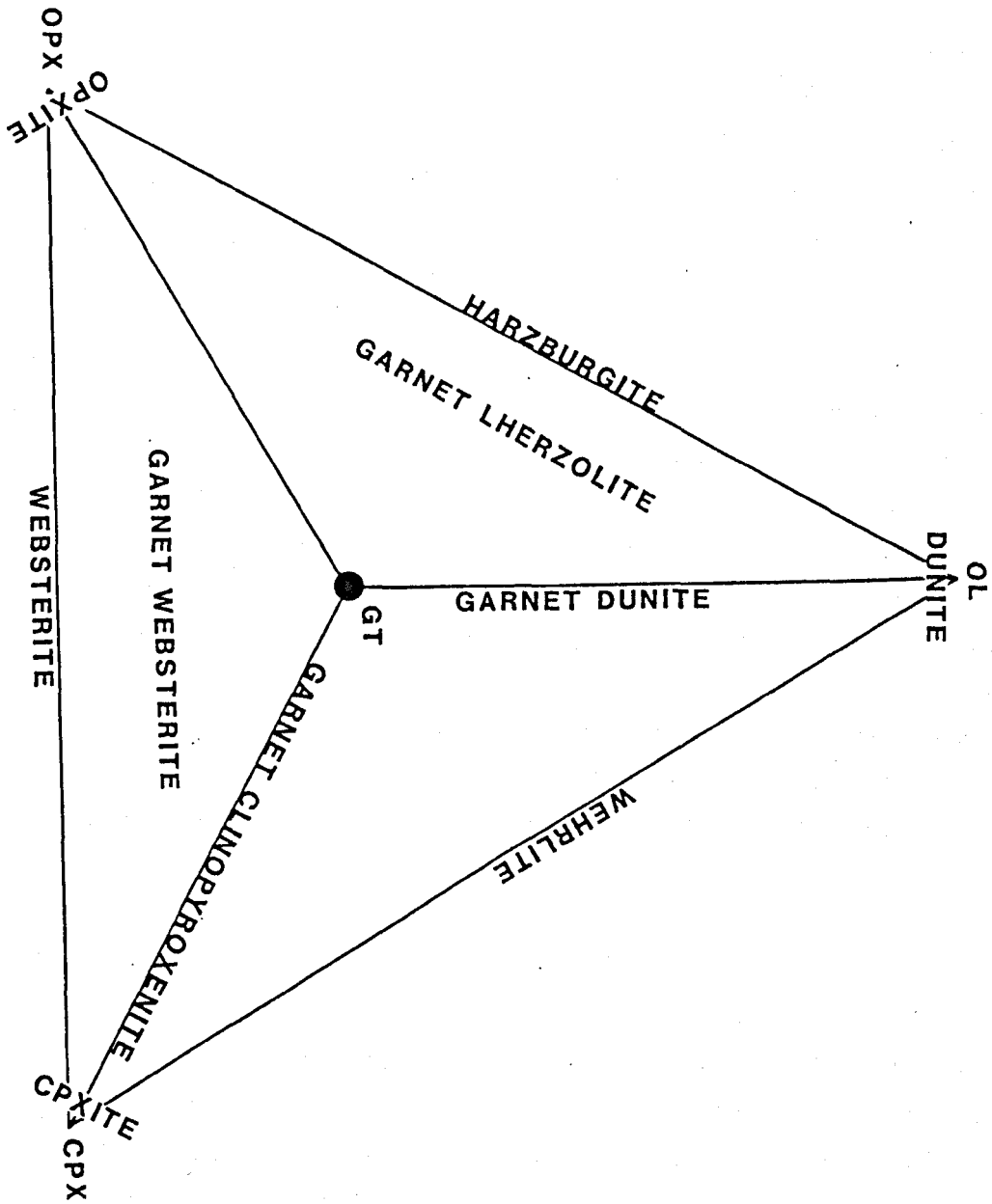

Figure 2.4. Nomencalture of garnetiferous ultramafic rocks. Substitution of spinel for garnet yields spinel lherzolites and spinel pyroxenites etc.

a finer grained sheared matrix of olivine. The origin of these rocks and garnet lherzolites found within the Ronda massif remains controversial and the problem will be addressed in this and subsequent chapters. Dunitic lenses are reported to occur by Kornprobst (1969 and 1974) and Reuber et al (1982), however no convincing samples were encountered in situ or as float during this investigation.

Reuber et al (1982) state that the CPX content of the lherzolites decreases towards the margin of the massif, the lithologies becoming harzburgitic (these authors use harzburgite to denote a peridotite with less than 5% CPX) and eventually dunitic towards the margin. This observation is not supported by the findings of this study, fresh, unaltered lherzolites with up to 15% CPX outcrop in the bed of the Oued el Jouj well within the Reuber et al (1982) zone of harzburgites.

The spinel lherzolites and harzburgites are mineralogically and texturally variable. The CPX content of the lherzolites varies from ~ 2 to 15 vol.%. The coarse grain size of these rocks makes modal estimation difficult. Point counting is extremely time consuming and requires 4 to 5 thin sections per samples, even then the method may still be subject to subtle modal variations in mineralogy. Any petrographic modes referred to subsequently are calculated from XRF bulk rock and microprobe mineral analyses, using a least squares program.

2:3.3 Spinel Lherzolites

Spinel lherzolites are the predominant rock type within the massif and along with other lithologies are variably serpentinised. The freshest specimens are generally found in the bottom of river valleys/wadis, notably the Oued el Jouj, which continuously uncover fresh rocks, indicating that recent weathering contributes significantly to the friability of specimens found on the valley sides. Where fresh the spinel lherzolites appear as rounded grey-brown outcrops (depending on the degree of oxidation) with green chrome-diopside porphyroclasts being noticable. In many areas eg. S.E. of the Oued Amter peridotites are extremely serpentinised, outcrops appearing light yellow to white with light brown islands of less weathered rock. Coarse veins of serpentine (antigorite) with crystals upto 4cm long cross cut the altered peridotite which contains loca lised concentrations of magnesite. Spinel harzburgites are rare, occurring sparodically, often in highly sepentinized areas or as "patches" up to 20m thick which show gradational contacts over several metres to the surrounding lherzolites.

2:3.3a General Textures

Spinel lherzolite and harzburgite textures vary considerably from relatively unstrained tabular aggregates to porphyroclastic/mosaic textures (terminology proposed by Harte 1977). Porphyroclastic textures are typical of most orogenic peridotites and spinel facies lherzolite xenoliths (Mercier 1985) although considerable variation in deformational intensity occurs in some orogenic peridotite bodies. Textural relationships in many samples are obscured due to the disruption of olivine and to a lesser extent pyroxenes by serpentinite veinlets.

2:3.3b Olivine:

Olivine forms between 60-90 % of the spinel peridotites, occurring as both a porphyroclastic and neoblastic phase. Olivine porphyroclasts up to 5mm long generally occur as an aggregate of fresh olivine pools in optical continuity, divided by small scale (0.1mm wide) serpentine veins. Each small pool of olivine may show undulose extinction due to deformation of the olivine lattice by crystal plastic processes at high temperature (Mercier 1985). Olivine porphyroclasts frequently contain kink bands with linear

boundaries (Fig 2.5a). Areas within the kink bands are usually devoid of undulose extinction or may contain further sub-grain concentrations. Kink band boundaries are always at a high angle or perpendicular to the flattening plane which complies with the observations of Nicolas et al (1971) for other orogenic peridotite massifs. Kinking is commonly developed in minerals for which only one slip system is available, inhomogeneous translation gliding taking place when the large porphyroclastic grains are unfavourably orientated for multiple slip (Wenk 1985). Undulose extinction is the result of bending of the crystal lattice without the development of slip. Strain intensity may vary considerably in individual spinel peridotites eg. narrow 3-4 cm bands of highly elongate olivine are found with sutured grain boundaries and high kink band boundary densities whilst some areas may be almost granular. Some olivines contain inclusions of pink-brown euhedral to subhedral spinel. These grains may have been incorporated during olivine recrystallisation (see discussion below).

2:3.3c Orthopyroxene (OPX):

Colourless enstatite occurs as porphyroclasts (upto 8mm) and neoblasts (sub.mm). Porphyroclasts are often subhedral with slightly irregular margins. Most porphyroclastic OPX display fine scale (<0.1mm) exsolution lamellae of Ca-rich pyroxene parallel to {100} which do not persist to the very edge of the grains, probably due to grain margin re-equilibration. Porphyroclasts display irregular extinction due to the presence of kink band boundaries and more irregular sub-grain boundaries. In some peridotites, elongated OPX define a fabric which is parallel to the stretching lineation. Pyroxenes are much more resistant than olivines to crystal-plastic deformation and therefore to polygonisation and recrystallisation. It is extremely difficult for pyroxenes to recrystallise or flow under normal upper mantle conditions when isolated in a much weaker olivine matrix (Mercier 1985). Original preferred orientation may be weakened by bodily rotation of pyroxene porphyroclasts. Asymmetrical fabrics commonly observed in orogenic peridotite massifs are due to strong plastic deformation in the simple shear regime during emplacement and not due to steady state flow in the upper mantle. The fabric defined by large (> 2.5 cm) porphyroclasts of OPX observed by Reuber et al (1982) was probably produced in this way.

Bleb-like exsolution of Ca-rich pyroxene is observed in many sections, often associated with more regular exsolution lamellae intersecting it at acute angles. The lamellar exsolution is frequently kinked and folded perpendicular to its length. However, kinking parallel to their length may have initially promoted exsolution. Fine scale (<0.1 mm) variable birefringence exsolution lamellae parallel to {100} in some OPX porphyroclasts may represent saussuritised plagioclase (anorthite?) exsolution lamellae. Such lamellae have been reported in enstatites from the spinel peridotites of the Ronda massif of southern Spain (Obata 1980). Small (sub. mm) spinels and olivines are sometimes included in the margin of OPX porphyroclasts. A similar texture developed within the Trinity peridotite is thought to be due to incongruent melting of pyroxene to olivine, spinel and melt (Dick 1977). The superimposition of deformational features on recrystallised grains suggests melting synchronous with deformation (possibly taking place during diapiric upwelling). Similar textural relationships have also been noted in the Ronda peridotite, S. Spain (Obata 1980).

OPX neoblasts are optically clear and colourless with limited cleavage development and rarely contain exsolution lamellae. OPX neoblasts and porphyroclasts contain locally abundant fluid inclusions (~10 microns) which form trains across grain boundaries but generally do not continue into the olivine rich matrix. This observation suggests that deformation/recrystallisation were approximately synchronous with the fluid infiltration, the greater facility of olivine to recrystallise via dislocation climb and glide precluding

Figure 2.5. All scale bars 1mm. (a) Kink bands in olivine porphyroclast in spinel lherzolite, XPL. (b) Irregular spinels in spinel lherzolite, PPL. (c) Olivine grain size reduction in peridotite at peridotite/pyroxenite contact. All grains in view are olivine. (d) Lamellar OPX and "bleb-like" garnet-plagioclase exsolution in CPX porphyroclast from GGP sample GP143, XPL. (e) Close up of garnet exsolution showing fine grained kelyphite alteration around garnet exsolution. XPL (f) Partially kelyphitized garnet in GP sample GP87M showing concave margins of unreacted garnet.

d
p
a
b
f
c

preservation of most fluid inclusions. OPX porphyroclasts commonly occur bastitised in hand specimen and in thin section are observed to be partly or totally pseudomorphed by antigorite. Chlorite and talc are also observed as alteration products of OPX along cleavage planes. Clinopyroxene exsolution lamellae are sometimes altered to brown amphibole, probably resulting from late stage, crustally derived fluid infiltration.

2:3.3d Clinopyroxene (CPX):

Bright green chrome diopside visible in hand specimen ranges from 0% in harzburgites to approximately 15% in the most fertile lherzolites although its abundance often varies over a decimetre scale. CPX grain size is continuous from <0.1mm to 4mm and the distinction between porphyroclast and neoblast is not always clear. CPX porphyroclasts are subhedral to anhedral and contain closely spaced exsolution lamellae of orthopyroxene parallel to {100} which do not continue to the crystal margins. As noted for the OPX porphyroclasts some CPX grains contain two sets of exsolution lamellae in different orientations. These lamellae are often severely kinked or folded. CPX porphyroclasts contain coarse subgrains, dynamic recrystallisation at their margins having created a polygonal network of exsolution free CPX neoblasts. Generally, neoblastic CPX occurs close to or adjacent CPX and OPX porphyroclasts or as aggregates of up to 10 crystals which probably represent a disrupted paleoblast.

Many CPX porphyroclasts contain several parallel trains of fluid inclusions of varying crystallographic orientations, usually slightly oblique to the foliation in the peridotite. CPX sometimes contains inclusions of spinel and olivine. Chloritic alteration affects crystal margins and cleavage planes.

2:3.3e Spinel:

The predominant aluminous phase in the spinel peridotites is a dark brown chrome spinel, locally, darker green varieties occur. Spinel may be equal to, or exceed CPX abundance in some sections, forming up to 8% vol. maximum. Spinel crystals vary in size (0.1 to 2mm), their form varying from small equant euhedra to elongate poikilitic anhedra with irregular boundaries (Fig 2.5b). Large grains are frequently elongated parallel to the peridotite fabric and may define a mineral lineation . In thin section, spinel in the harzburgites tends to be darker reddish brown. Spinels are found together with olivine as inclusions within OPX, see above, or as isolated interstitial or intergranular grains, somtimes adjacent to CPX or OPX porphyroclasts. Concurring with the observations of Dick (1977), the origin of all the isolated spinel grains in the matrix of the spinel peridotites cannot be explained via an origin due to exsolution from pyroxene or by breakdown of garnet. The interstitial spinel associated with pyroxenes may have formed due to the incongruent melting of pyroxene. Euhedral spinels within lherzolites, concentrated at triple junctions may be the product of crystallisation from a melt due to inefficient melt extraction (Dick 1977). This observation would require the last melting event experienced by the lherzolites to have taken place in the spinel stability field.

Spinels are not observed to be reacting with pyroxene to form plagioclase and olivine presumably because sub-solidus re-equilibration was slow compared to the cooling/uplift rate. OPX-CPX -spinel clusters are rare in the spinel peridotites but where present may represent the isochemical breakdown of garnet and olivine from a primary garnet lherzolite assemblage re-equilibrating in the spinel lherzolite stability field. The scarcity of these features may be due to disruption of the clusters during high strain rates experienced during the emplacement of the massif.

2:3.3f Sulphide Mineralogy:

Cu-Ni-Fe sulphides coexist with the silicate mineralogy of the spinel peridotites and occur in two parageneses: 1, As inclusions (droplets) totally enclosed by silicates. 2, as coarser anhedral crystals and aggregates up to 500 μm in the interstices of the primary silicate phases. Sulphides are more common in the lherzolites than the harzburgites but never exceed more than 0.2% vol. The occurrence of sulphide inclusions in the primary silicates and in interstices of the peridotites is thought to represent an early immiscible sulphide melt trapped either within silicates or at their layer boundaries during high temperature recrystallization in the upper mantle (Lorand 1985).

Sulphide inclusions in silicates: Sulphide inclusions in host olivine and pyroxene are rounded anhedral droplets up to 40μm across or occur as trains of globules along sealed fracture planes (Lorand 1985). Pentlandite predominates and coexists with pyrrhotite, chalcopyrite and bornite.

Interstitial sulphides: Sulphide phases occur randomly disseminated throughout the peridotites at the grain boundaries of the primary silicates or in close association with serpentine veins. The interstitial assemblage consists of makinawite, pentlandite, pyrrhotite and chalcopyrite

2:3.3g Serpentinization:

All the peridotites within the Beni Bousera peridotite massif are variably serpentinized, some outcrops being extremely fresh whilst others are up to 70% serpentinized (Lorand 1985). Serpentine occurs in two main forms: a, As late stage serpentine veins invading fractures, shear and joint planes, sometimes appearing green due to weathering of associated magnetite and b, As a pseudomorphic network of crystals, the mesh texture described by Wicks and Whittaker (1977) ie. finely crystalline, mainly lizardite (Milliard 1959) with some fine opaques (magnetite ?) in the cenre of the veins. Serpentine is the most common alteration product of olivine. The serpentine veinlets within olivine form an interlocking /interpenetrating texture composed of elongate blades and plates with trains of magnetite euhedra (< 10 μm) concentrated along the central portion of the serpentine vein. This magnetite is a product of Fe release during serpentinization. Veins of brown iddingsite and possibly bowlingite also pervade olivine locally as secondary (late stage) alteration products.

2:3.3h Summary

The spinel peridotites from Beni Bousera contain lithologies varying from relatively fertile CPX rich, spinel lherzolites to scarcer, olivine-OPX rich spinel harzburgites. Petrographic study of spinel peridotites from Beni Bousera has revealed abundant evidence of sub-solidus re-equilibration and high temperature crystal plastic deformation at some stage during their evolution. Sub-solidus re-equilibration processes such as exsolution may have been promoted by stress during plastic deformation as suggested by Dick (1977). Both CPX and OPX usually deform through {100} [001] slip with simultaneous formation of exsolution lamellae due to syntectonic cooling. The formation of these lamellae further accomodate slip at the host/lamellae interface (Mercier 1985) and illustrate the interaction between phase equlibration and deformation processes. The severe folding and kinking of exsolution lamellae in OPX and CPX also suggests that significant deformation occurred after chemical sub-solidus equlibration. Thus the silicate mineralogy of orogenic ultramafic massifs records a response to increasing deviatoric stress as temperature decreases during their emplacement (Mercier 1985). Evidence from sheared OPX in orogenic peridotite massifs indicate that strain superimposed on originally granoblastic textures may reach 1000% or more. The

degree of development of porphyroclasic textures within orogenic peridotites is a function of the stress-strain rate-temperature history of the rocks (Mercier 1985). Strong cooling concurrent with shearing produces emplacement fabric preferred orientations through extensive intragranular flow; this is observed in the Beni Bousera peridotites.

2:3.4 Pyroxenites

2:3.4a Field relationships and occurrence

A variety of pyroxenite layers is found within the pridotites, varying from mafic to ultramafic in composition. Pyroxenite layers have been reported from other orogenic peridotite massifs eg. Lherz (Conquere, 1977), Ronda (Dickey, 1970), Baldissero (Etienne, 1971) and Balmuccia (Lensch, 1971). An idealised section illustrating the main pyroxenite layer variation and zonation is illustrated in Figure 2. 6 which summarises some of the structural features shown by the pyroxenite layers.

The pyroxenite layers occur as lenses or, more commonly, parallel sided layers in the host peridotites. The layers vary in thickness from sub-cm to almost 3m thick. Layers less than 0.5m thick generally occur as approximately parallel sided bodies (Fig 2.7a-d) which may be traced via sparodic outcrops for several tens of metres. Thicker pyroxenite layers (>0.5m) most frequently occur as lensoid masses upto 4m in lateral extent. The rugged topography of the region inhibits determination of the precise form and continuity of most pyroxenite layers

The most common pyroxenite layers thickness is between 1 and 5 cm. (Fig 2.8) with a sharp fall in frequency of layers over 20cm thick. This data set may underestimate the abundance of layers less than 20cm thick and particularly those less than 5cm which are much more difficult to find in the field. Additionally, the thinner layers are generally non-garnetiferous, making them more susceptible to alteration and hence less conspicuous. The general decrease in layer frequency with increasing thickness (Figure 2.8) varifies the thickness vs abundance measurements made by Allegre and Turcotte (1986). Websterites and layers transitional between websterites and orthopyroxenites are the most common lithological type. In contrast garnet pyroxenite and garnet clinopyroxenite are the most abundant lithologies in layers over 20cm. thick.

The volumetric fraction of the massif occup ied by the pyroxenite layers is difficult to estimate due to their heterogeneous spatial distribution and discontinuous outcrop. The measured section in Appendix 2 was taken through approximately 175m of sequence in the well exposed valley floor of the lower section of the Oued el Jouj. The sequence contains a high density of pyroxenite layers compared to other parts of the massif and displays the full variation of lithologies and structural style found within the Beni Bousera massif. The presence of high angle faulting with variable displacements, complicated measurement of the section. The total exposed section length is calculated to be 174.6 metres of which pyroxenites comprise 16.6 metres ie. approximately 9.5% by thickness of the total section. Locally, the pyroxenite layers form over 90% of the thickness of the outcrop (Appendix 2), however, there are also significant sections which are 100% peridotite. Extensive fieldwork throughout the massif indicates that the Oued el Jouj section that was measured in Appendix 2 is probably anomalously rich in pyroxenite layers compared to other areas. A realistic estimate of the percent thickness occu pied by the pyroxenite layers averaged over the whole massif seems to be between 1 and 3 % based on estimates from other measured sections. This is in good agreement with the calculations of Allegre and Turcotte (1986) and Kornprobst (1969) and with estimates from other orogenic peridotite massifs eg. 1.5 vol.% for Lanzo (Bodinier et al 1987).

Figure 2.6. BENI BOUSERA MAFIC LAYER VARIATION

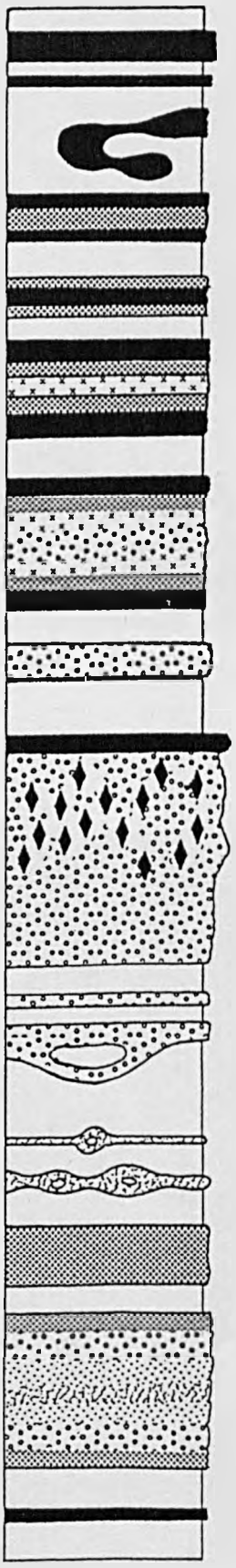

MINERALOGY	ROCK TYPE
OPX(CPX,SP)	ORTHOPYROXENITE
OPX,CPX(SP)	WEBSTERITE
OPX,CPX,GT(SP)	GARNET WEBSTERITE
CPX,GT(OPX)	GARNET CLINOPYROXENITE
CPX,GT	GARNET CLINOPYROXENITE
OPX	
CPX,GT,GRAPH,(OPX)	GRAPHITIC GARNET CLINOPYROXENITE
CPX,GT	
OI,OPX,CPX,GT	GARNET CLINOPYROXENITE ENCLOSING GARNET LHERZOLITE
CPX(GT)	THINNED (GARNET) CLINOPYROXENITE
CPX,OPX	WEBSTERITE
CPX,COR, CPX,GT,COR	CORUNDUM CLINOPYROXENITE CORUNDUM GARNET CLINOPYROXENITE

Figure 2.7. Parallel sided Al-augite pyroxenite layers of varying thickness illustrating how the layers are aligned parallel to each other. Top left is from Amasihene beach, remainder from Oued el Jouj.

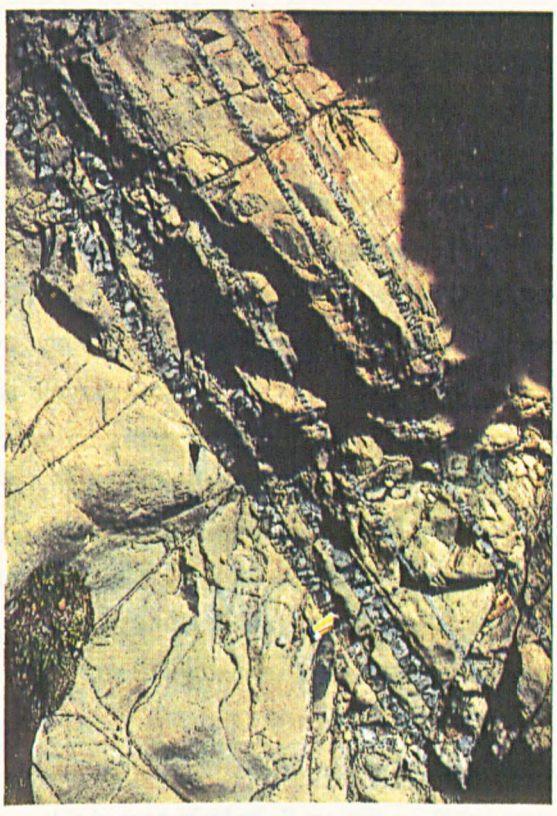

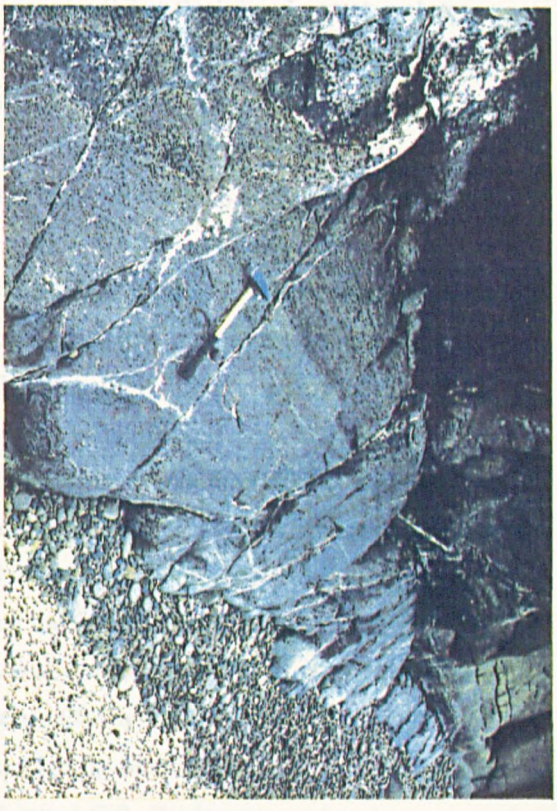

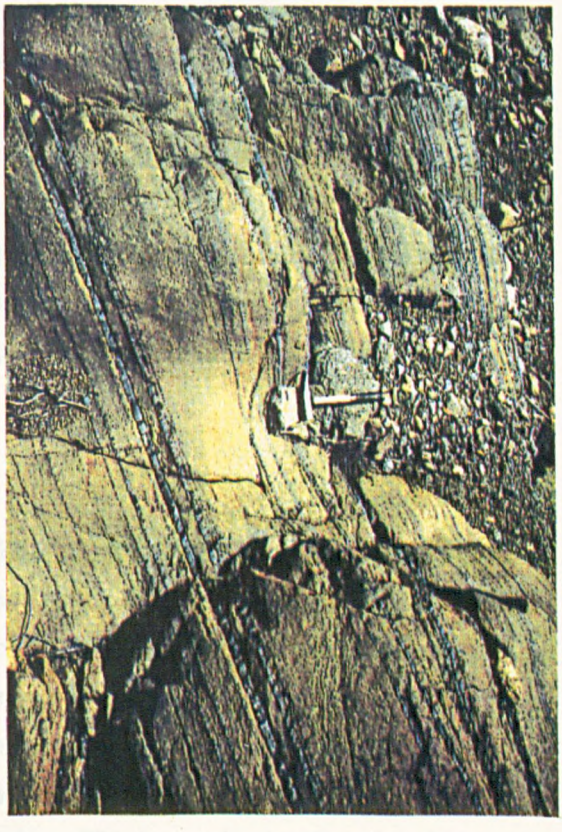

Reuber et al (1982) noted that garnet clinopyroxenites become common in the "peripheral" zone of the massif. Thin, highly strained garnet clinopyroxenites are certainly abundant in the south west margin of the massif, however, relatively thick garnet clinopyroxenite layers (> 0.3 m thick) and garnet websterite layers occur in abundance well away from the margin of the massif, eg. close to the summit of Jebel Karbous and in the slopes west of the tributary flowing into the Oued Amter adjacent to Inoualine (see specimen locality map, Fig.5.1). Large loose blocks of garnet clinopyroxenite also occur ubiquitously across the massif even though *in situ* exposures are rare. Some of these blocks undoubtedly represent eroded fragments of outcrops further up the valley.

Two distinct types of pyroxenite layers are descernible in the field; pyroxenites containing grey/pink Al-rich augite (Fig. 2.7) as the CPX and a scarce group of pyroxenite layers containing green chrome-diopsides (Fig. 2.9). The two groups are classified as the Al-augite pyroxenites and the Cr-pyroxenite group following the nomenclature adopted by Wilshire and Shervais (1975) for peridotite/pyroxenite xenoliths in alkali basalts and "pyroxenites" in orogenic peridotite massifs. The Cr-pyroxenite group are scarce and was only found as layers over 1cm thick in a complexly zoned, lens like body in the Oued el Jouj (see Appendix 2 and Fig. 2.9). Sub-cm. "veins" of clinopyroxenite/websterite belonging to the Cr-pyroxenite group also occur which crosscut the foliation in the peridotite at high angles and cross-cut other pyroxenite layers. Dickey termed the Al-augite group layers in the Ronda massif "magmatic layers" and the Cr-pyroxenite layers "tectonic layers". Dickey (1970) and Obata (1980) also noted the marked abundance of Al-augite group layers compared to the much scarcer Cr-pyroxenite layers however, this is not typical of all massifs eg. Balmuccia and Lanzo (G.R. Davies pers. comm.).

The varied pyroxenite lithologies form individual, monolithological layers, or may constitute parts of zoned, composite layers (Figure 2.6) where one lithology grades into another, often symmetrically with varying modal abundanc es of minerals. The normal zonation sequence has orthopyroxenite or websterite at the periphery of the layer and grades towards the centre through the sequence websterite-clinopyroxenite-garnet clinopyroxenite. A comprehensive summary of the pyroxenite layer mineralogy is presented in Table 2.1. The pyroxenite layers occur either in groups which may be clusters of over 30 layers or as isolated individual layers (Fig. 2.7). It is usually the thicker (>20cm) garnet clinopyroxenite layers that outcrop as isolated unzoned layers or in small clusters (2 to 5) of relatively thick layers.

Where pyroxenite layers outcrop in groups they are approximately parallel sided, parallel to each other, and parallel to the fabric in the peridotites (Fig.2.7) . Clusters of parallel sided sub-decimetre layers equally spaced from each other frequently occur in the Oued el Jouj section where pyroxenite layers may locally occupy over 50% of the total outcrop thickness.

2:3.4b Peridotite/Pyroxenite layer relationships

Contacts between pyroxenite layers and peridotites are lithologically sharp and non-gradational. Layer boundaries are always parallel or sub-parallel to any foliation developed in the host peridotites (with the exception of sub-cm late Cr-diopside veins). Layer boundaries are generally linear, however, small rounded apophyses locally penetrate the peridotite suggesting intrusion by a magma and hence an igneous origin for the layers. The linearity of layer boundaries is probably the result of layer parallel shearing due to high strain developed at rheological discontinuities ie. peridotite/pyroxenite layer boundaries. Occasionally garnets become elongate and sheared out towards the edge of a layer. This is associated with a marked fabric developing within the peridotite immediately adjacent to that layer. Deformation intensity in the peridotites

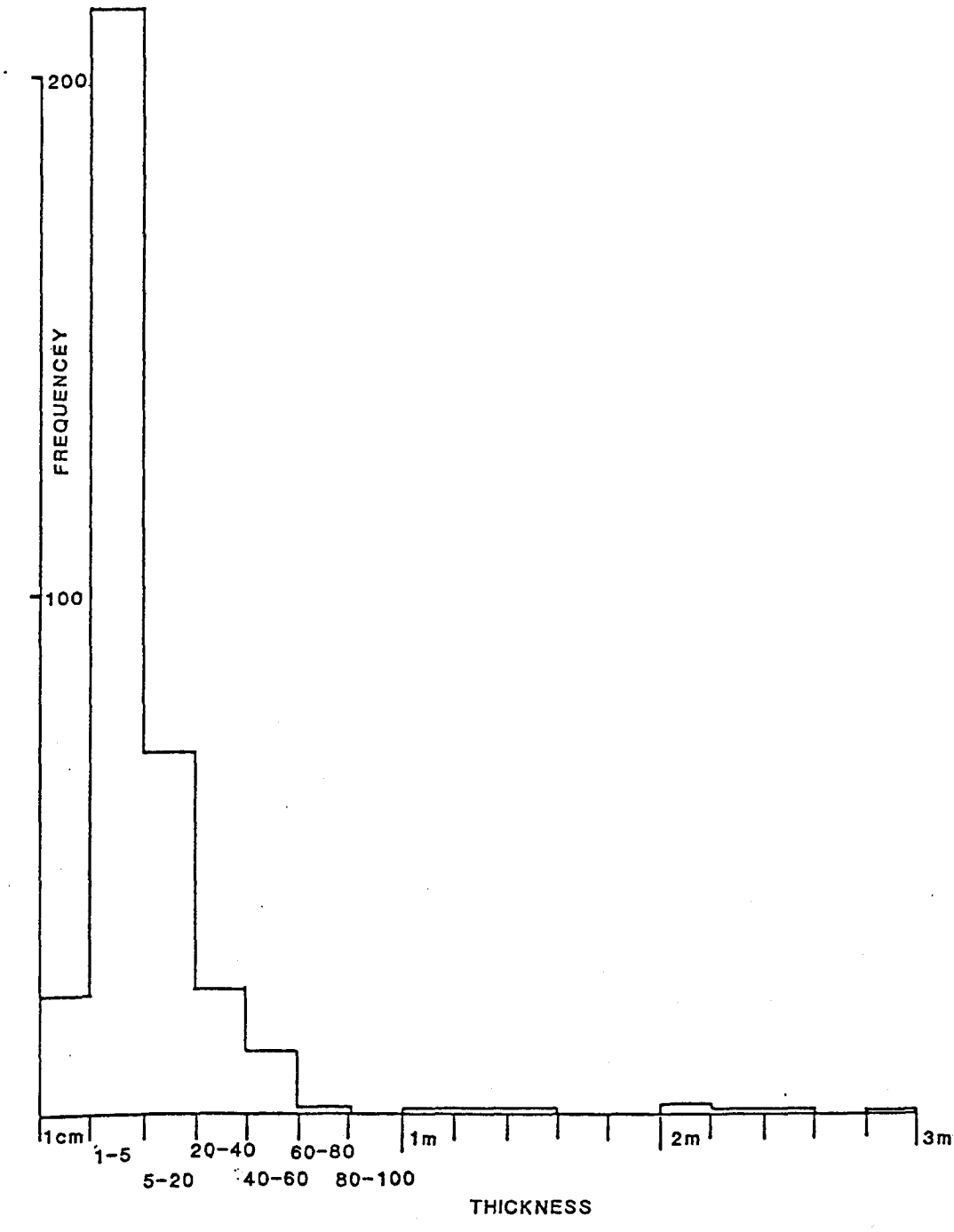

Figure 2.8. Histogram of thickness of pyroxenite layers vs frequency of occurrence.

Figure 2.9. Cr-pyroxenite outcrops. Note; irregular, brownish bastitized OPX in B and disharmonic, open folds in C. All outcrops Oued el Jouj.

A
B
C
D

GROUP	LITHOLOGY	PORPHYROCLAST MINERALOGY Modal %	TEXTURE	THICKNESS RANGE & AV. cm	OCCURRENCE / RELATIONS
Al - AUGITE PYROXENITE	ORTHOPYROXENITE OPXITE	OPX 90-100 CPX 0-10 +/- SP	GRANULAR/ PORPHYRO.	<1 TO 20 AV. 3	INDIVIDUAL LAYERS OR AT MARGINS OF ZONED LAYERS
	CLINOPYROXENITE CPXITE	CPX 70-90 OPX 10-30 +/- SP	GRANULAR/ PORPHYRO.	<1 TO 20 AV. 5	INDIVIDUAL LAYERS OR PARTS OF ZONED LAYERS
	WEBSTERITE WEB	CPX 50-70 OPX 30-50 +/- SP	GRANULAR/ PORPHYRO.	<1 TO 80 AV. 5-20	INDIVIDUAL LAYERS OR MARGINS OF GP AND GGP
	GARNET WEBSTERITE GT WEB	CPX 50-60 OPX 10-40 GT 5-20 +/- SP	GRANULAR/ PORPHYRO/ FLUIDAL	1 TO 20 AV. 5	PREDOMINANTELY PARTS OF ZONED LAYERS (CENTRES)
	GARNET CLINOPYROXENITE GP GRAPHITE GARNET CLINOPYROXENITE GGP	CPX 55-65 GT 35-45 GRAPH 0-15	PORPHYRO./ FLUIDAL	5 TO 260 AV. 20 200-260 AV. 230	PREDOMINANTELY INDIVIDUAL LAYERS OR CENTRES OF ZONED LAYERS. GGP ARE SLIGHTLY ZONED.
	CORUNDUM GARNET PYROXENITE CORP	CPX GT +/- SP		LOOSE BLOCKS	RELATIONSHIPS NOT KNOWN
	GARNETITE GTITE	GT 90-100 CPX 0-10	GRANULAR		ALWAYS PART OF A GP LAYER
Cr-PYROXENITES	Cr-WEBSTERITE WEB	OPX 60-70 CPX 40-30 +/- SP	GRANULAR	< 1 TO 15 AV. 3	INDIVIDUAL LAYERS , RARELY ZONED
	WEHRLITE WER	OL 60-80 CPX 20-40	GRANULAR	1 TO 20 AV. 3	INDIVIDUAL LAYERS RARELY ZONED

Table 2.1. Petrographical summary of Beni Bousera pyroxenites.

increases towards the pyroxenite layer margin, olivines becoming highly elongate with high width/length ratios and high densities of sub-grain boundaries and kink band boundaries. Olivine grain size is also greatly reduced (<0.1mm) and grains are predominantly recrystallised as neoblasts (Fig. 2.5c). A small weathering cavity up to 1cm deep commonly develops at peridotite/pyroxenite layer contacts which may be due to the increased susceptiblity to weathering of the finer grained deformed olvines at the peridotite margins.

Towards the margins of the pyroxenite layers the peridotite often becomes harzburgitic and then dunitic at the contact ie CPX and then OPX show a marked decrease in abundancey towards a pyroxenite layer. This indicates that the peridotite margins may have melted due to infiltration of the pyroxenite host magma.. Coarse brown spinel (>0.3mm) often becomes concentrated at pyroxenite layer margins. The irregular, anhedral form of these spinels does not suggest they are early formed cumulate crystals. Pyroxenes at the margins of the pyroxenite layers become slighlty flattened and contain coarse subgrains but do not appear to have experienced the same intensity of deformation as the peridotite margins. Locally, lobes of mechanically intermixed olivine and CPX occur at peridotite/pyroxenite contacts together with irregular pink-brown spinel.

In the peridotites, olivine porphyroclasts contain well defined kink band boundaries at a high angle (up to 70°) to the the strike of the pyroxenite layers; this effect persists up to 5cm away from the layer margins. Where OPX and less frequently CPX occur in the peridotites close to the layer margins they are granulated and fractured.

Kornprobst (1969) and Dickey (1970) made special reference to the harburgitic/dunitic nature of the peridotites at layer margins. Dickey states that the most fertile lherzolites are obtained from areas where pyroxenite layers are scarce or absent. This evidence was used to support the hypothesis that the pyroxenite layers were derived from the host peridotite by partial fusion leaving behind a residue of depleted harzburgite/dunite. Fertile, CPX-rich lherzolite was found intimately interlayered with pyroxenite layers in many areas of the Beni Bousera peridotites in this study, particularly in the Oued el Jouj section which contains a high abundance of pyroxenites. Additionally there is no correlation between the thickness of pyroxenite layers and the size of their "depletion halos", the zone of olivine rich peridotite tending to be no greater than 10cm wide even adjacent to layers of over 2m in thickness. These observations do not support the conclusion that the pyroxenites are derived from the surrounding peridotites by partial melting.

No evidence of grain size reduction due to chilling is observed at the pyroxenite layers margins as the pyroxenite magmas were probably introduced into the host peridotites at high temperature within the mantle. Several Al augite group pyroxenite layers develop pale to bright green Cr-rich pyroxenes at their margins on one or both sides of a layer. This may be the mineralogical expression of major element equlibration between the intruding pyroxenitic magma and the host lherzolite.

2:3.5 Al-Augite Pyroxenite Group

2:3.5a Graphite garnet clinopyroxenites (GGP)

Garnet clinopyroxenite (GP) layers form a high proportion of the pyroxenite layer population in the section of the Oued el Jouj immediately east of Tazemourte I and II. Graphite occurring as octahedra and other forms of cubic symmetry within GP layers were first described by Slodkevich (1980a). Slodkevich (1980a&b) reported graphite octahedra in four GP layers near the south west margin of the massif. Extensive field work in this area lead to the discovery of only two separate GP layers which contained

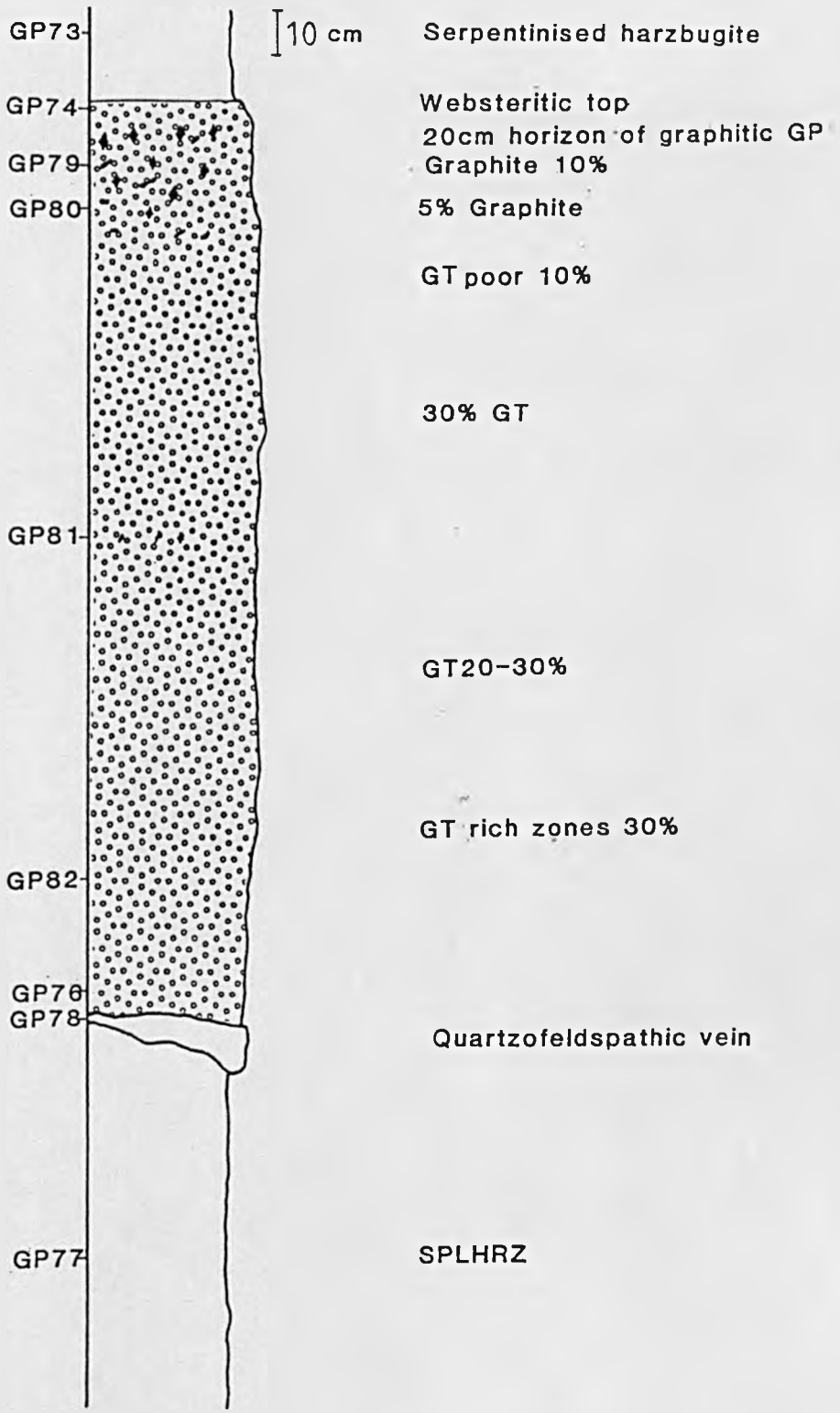

Figure 2.10. Measured section of GGP layer, Tazemourte track.

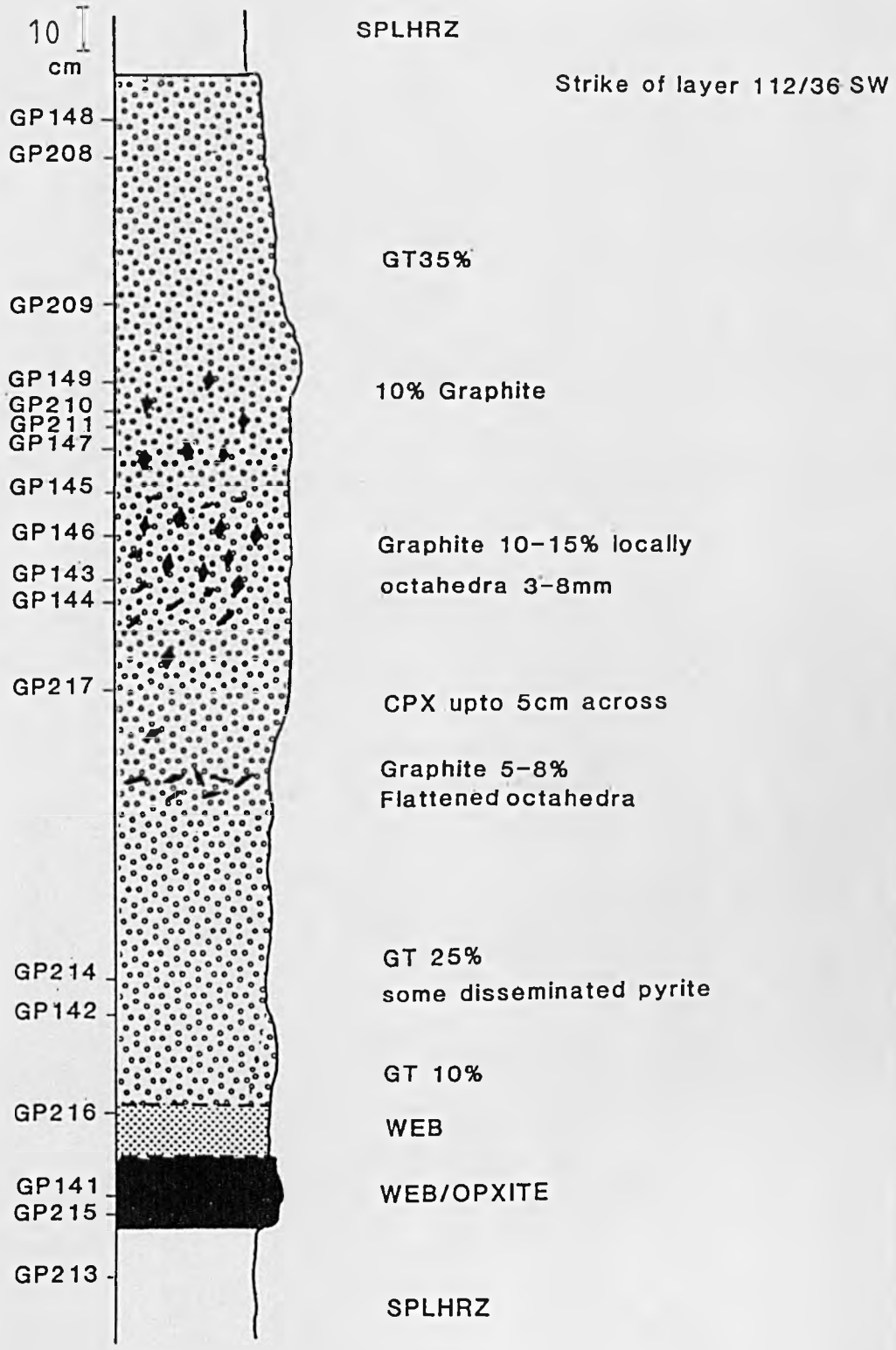

Figure 2.11. Measured section of GGP layer, Oued el Jouj stream section.

graphite (see Chapter 3). Both outcrops are located in the Tazemourte area. One 2 metre thick graphitic garnet clinopyroxenite (GGP) layer outcrops on the path leading east down to the Oued el Jouj from Tazemourte I . The graphite in this layer is concentrated towards its upper margin (Fig. 2.10), octahedra and flattened octahedra occurring predominantly in the upper 30cm of the layer ("upper" is used in the sense of up relative to ground level as no way up indicators are present in the pyroxenite layers). The second GGP layer outcrops in the western bank of the Oued el Jouj east of Tazemourte I (Fig. 2.11) and has graphite concentrated in the centre of the layer, up to 15vol.% in places with octahedral forms becoming more sheared and flattened towards the lower middle of the layer (Fig. 2.11). This layer is approximately 2.6 metres thick and is one of the thickest pyroxenite layers in the massif. The layer also outcrops in the stream bed of the Oued el Jouj. The GGP layer outcropping in the Oued el Jouj is adjacent to another very thick (2.5m) garnet clinopyroxenite layer in which no graphite has been detected. This layer is 1 metre away from the GGP layer (Appendix 2) and is mineralogically identical to the GGP layer but has no graphite. The GGP layer is extremely coarse grained with CPX up to 4cm in its upper-middle and lower-middle zones. This contrasts with the locally fine grained nature of the adjacent GP layer (CPX down to 0.1mm) which may be due to more intense plastic deformation in the non-graphitic layer suggesting high strain gradients.

The graphite appears as rounded, amorphous masses on weathered, eroded surfaces but takes the form of sharp-edged octahedra on freshly broken surfaces (Chapter 3). The GGP contain orange pyrope-almandine garnet and dark sodic augite porphyroclasts which generally constitute 95% by volume of the layers. CPX is the dominant phase, always over 50 vol.% . Plagioclase neoblasts (2-8%) sulphides (1% pyrite/pyrrhotite) and varying amounts of graphite (0-15%) comprise the remainder of the rock. Obata (1980) notes that some garnet pyroxenite layers in the Ronda massif contain irregular blebs of graphite but does not supply details of the graphite morphology.

It is unclear whether both separate outcrops of GGP layers are part of the same layer as their dip and strikes are reasonably similar. There is a substantial difference in altitude between the two layer outcrops (over 200 metres) and their along strike dips are not consistent with them being part of the same layer unless faulting has occurred. Evidence of late stage normal faulting exists close to the margin of the massif, however, none of these faults has a throw over 10 metres and there is no evidence for a fairly major fault between the two outcrops. Additionally the upper GGP layer outcropping on the Tazemourte track is not associated with another thick GP layer and has more abundant narrower pyroxenite layers above it. Additionally, the distribution of the graphite in the two layers is different (Fig 2.10 & 2.11).

2:3.5ai CPX:

CPX crystal size within the GGPs varies from 4cm long porphyroclastic grains in parts of GP147 to <0.01mm neoblasts in highly deformed zones within GP83 and GP139. The highly strained thick GP layer is one metre away from GGP layer GP147. The large CPX porphyroclasts are generally subhedral with irregular crystal margins bo-rdered by neoblastic grains. CPX porphyroclasts contain abundant exsolution, most frequently of OPX parallel to {100} of the CPX; these lamellae may be distinguished from narrow mechanical twins in CPX on {100} by the fact that the exsolution lamellae have [001] and (100) in common with the host augite. Exsolution lamellae of OPX have straight extinction compared to the inclined extinction of twin lamellae. Lamellar twins on {100} also extend to the grain boundary of the CPX porphyroclast whereas exsolution lamellae always terminate within a short distance (100 μm) of the grain boundary .

Exsolution and twinning were probably predominatly synchronous with plastic deformation, however, some degree of post exsolution deformation is implied by the frequent bending and kinking of OPX exsolution lamellae. Lamellar OPX may pass logitudinally into exsolved blebs of An-rich plagioclase and garnet (Fig 2.5 d&e). Microdomains of high strain occur in zones within the thicker pyroxenite layers where porphyroclastic augites, exhibiting kinking and undulose extinction due to subgrain boundary formation recrystallise to a fine grained relatively unstrained neoblastic groundmass. The presence of such unstrained neoblasts is consistent with recrystallisation occurring via a dynamic recovery sequence involving crystal-plastic processes (Mercier 1985). Recrystallisation of CPX neoblasts and exsolution of plagioclase occurs at kink band boundaries. The kink band boundaries probably nucleated on the exsolution lamellae due to their facility to allow intracrystalline slip. Acicular inclusions of ilmenite are also present in CPX crystals within the GGP, some crystals exsolving ilmenite {0001} parallel to {100) of the CPX.

2:3.5aii Garnet:

Garnet occurs predominatly as a porphyroclastic phase in the GGP, up to 8mm in diameter, and occurs as exsolved blebs within CPX crystals (see above). Garnets are pink-orange to pale pink in hand specimen but colourless in thin section. Some garnet grains exhibit strain birefringence in cross polars. Crystals vary from relatively equant to elongate in form. Garnets rarely deform significantly or become elongate during deformation within an olivine rich matrix, however, when enclosed in CPX which does not have the tendencey to flow around rigid porphyroclastic phases garnet may become elongate. Alternatively, the garnets could have exsolved from CPX during a deformation event and eventually aggregated to form single elongate grains. It is difficult to decern what proportion of the present garnet population originally exsolved from CPX. Irving (1973) and Wilkinson (1976) observed sub-solidus exsolution of garnet from clinopyroxenes in pyroxenite xenoliths from S.E. Australia and Hawaii respectively. Irving (op.cit.) demonstrated experimentally that the exsolution processes is due to approximately isobaric cooling and stated that the processes could not account for all the garnet in the garnet pyroxenite xenoliths he studied. Wilkinson (1976) also remarked on the minor amount of garnet produced via exsolution from originally subcalcic clinopyroxenites. It thus seems unlikely that more than a few percent of the garnet in the GGP (and GP) layers originated due to exsolution from CPX, ie. the layers originally crystallised as garnet clinopyroxenites.

CPX inclusions appear in many garnet grains as < 100 μm needles displaying high birefringence and inclined extinction. Garnets in GGP layers possess thin kelyphite alteration rims <0.1mm wide in most instances. Kelyphite development in the central GGP is significantly less than in other garnetiferous layers.

2:3.5aiii Plagioclase:

Plagioclase occurs as both an exsolved phase in CPX porphyroclasts and as sub mm interstitial anhedral grains in the matrix. The latter probably also originated via exsolution.

Garnet and CPX also occur as inclusions within graphite octahedra. In thin section they appear mostly as irregular anhedra however these minerals were observed to possess facets parallel to the octahedra {111} and {100} directions in thin section by Slodkevich (1982). CPX crystals within the graphite are optically identical to host rock CPX and contain OPX exsolution lamellae parallel to {100} and some exsolved blebs of plagioclase. CPX inclusions within the graphite frequently contain coarse sub-grain boundaries. Further morphological and crystallographic details of the inclusions within the graphite

octahedra are given in Chapter 3.

GGP textures are mainly porphyroclastic. A weak fabric is defined in some parts of the GGP layers by elongate garnets. Where textures are strongly porphyroclastic to mosaic, garnets form the dominant porphyroclast phase (up to 8mm long) whilst some residual CPX porphyroclasts have neoblastic margins. Graphite aggregates in the more intensely deformed parts of the GGP layers are strongly sheared and highly elongate with marked kinking evident in reflected light. Linear trains of fluid inclusions (<10 μm) cross cut CPX porphyroclasts but are commonly absent in neoblastic phases indicating a relatively deep origin for the fluids, probably pre/syn plastic deformation.

2:3.5b Garnet Clinopyroxenites +/- spinel (GP)

Layers of this lithology vary in thickness from sub-cm to 2.5 m thick and are frequently unzoned . Garnet Clinopyroxenite also occurs within the centre of some zoned layers (Figure 2.6). Mineralogical and petrographical details of this lithology are very similar to the GGP layers with pyroxenes and garnets being optically identical. One difference however is in the degree of kelyphyitisation around garnets (Fig. 2.5f). This alteration feature around garnets in some GP layers eg GP 87, is seen to increase markedly towards the layer margin. Many garnets at the extreme margins of the layers are completely replaced by a fibrous radiating intergrowth of OPX, plag and spinel. Minor brown amphibole also occurs at the margins of some kelyphite aureoles although it cross cuts the "fabric" of the intergrowth and may be a product of hydrous alteration of the fine grained pyroxene in the intergrowth. Kelyphite rims are abruptly terminated, possibly being sheared off at layer contacts with the peridotite suggesting garnet breakdown occurred prior to the last deformation event.

Modal abundances of garnet and CPX vary non- systematically across a layer and do not show any classical cumulate relationships or indicate any "way up" directions. Locally, garnet concentrations may reach up to 60% by volume in outcrop. A large, approximately 1 cubic metre, loose block was found close to the mouth of the Oued Sidi Yahai Aarab which contained a 3 to 4 cm thick layer of almost pure garnet which graded into the host garnet clinopyroxenite on either side of the zone (GP239). Such a rock type is termed a garnetite and contains over 90% garnet (Table 2.1). This garnetite segregation consists of elongate multi-crystalline aggregates of garnet including blebs of fine grained polycrystalline CPX (< 0.3mm) which display 120° triple junction grain boundary relationships. The garnet shows no signs of kelyphitic alteration. Larger porphyroclastic CPX grains in the GP lithology bordering the garnetite layer are intensely deformed with high densities of sub-grain boundaries and a strong flattening fabric parallel to the trend of the garnetite band. The origin of this garnetite zone within a GP layer is obscure. It may be the product of fractional crystallisation of garnet producing a garnet rich cumulate. Although typical cumulate textures in the other pyroxenite layers are absent, their original existence may have been obscured by subsolidus recrystallization and plastic deformation.

The CPX crystals in unzoned GP layers generally possessabundant OPX exsolution lamellae and blebs of exsolved plagioclase. GP37, a GP layer from the summit of Jebel Karbous, displays little exsolution in the CPX and may not have re-equilibrated to the same extent as other GP layers. Inclusions of rutile in garnet, recorded by Kornprobst (1969), have not been observed. Minor late brown amphibole distributed along CPX grain boundaries and occassional cross cutting serpentinite veins are the main alteration features of the GP layers.

Textures in the GP layers vary from granular eg. GP37 to fluidal mosaic, GP139. The highly deformed, fluidal mosaic textured specimen GP139 was taken from the centre of a 2.5m thick layer and

Figure 2.12 a&b. Cm to sub-cm thinned garnet clinopyroxenite layers in spinel peridotite, Tazemourte. (c) Al-augite pyroxenite showing "blotches" of flattened, kelyphitized garnet, Oued el Jouj. (d) Apparent layering in peridotite, Amasihene beach, due to variable serpentinization parallel to peridotite foliation.

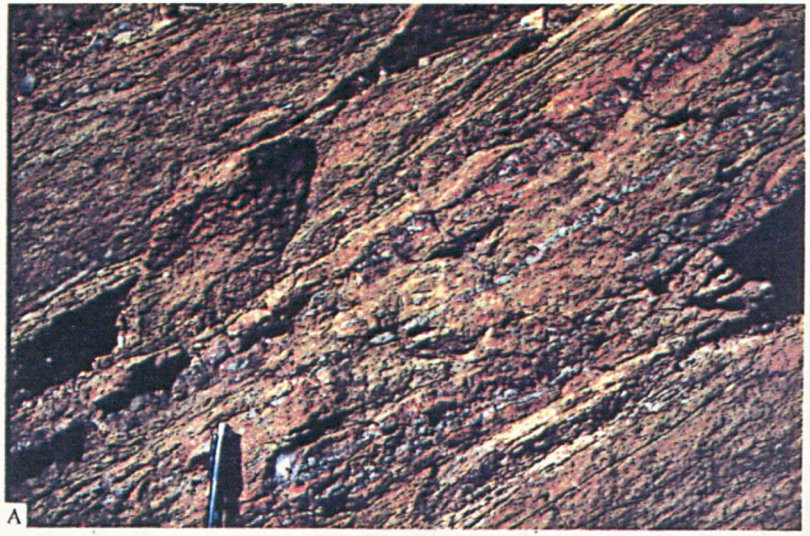

A

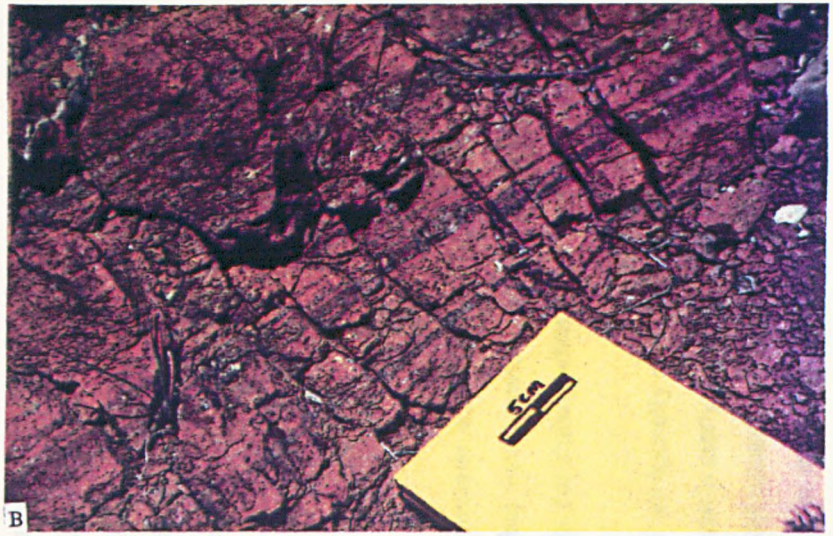

B

C

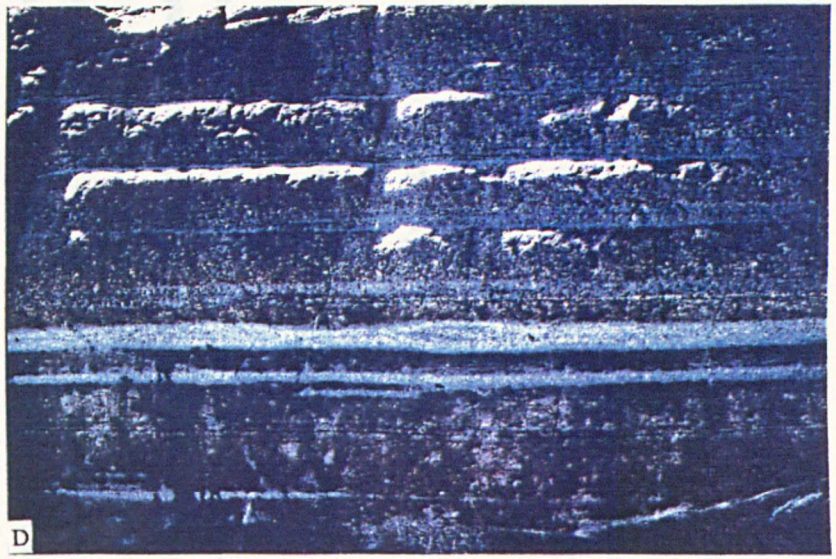

D

supports the occurrence of fine scale (1 to 10cm wide) zones of intense plastic deformation, not necessarily located at layer margins. The elongate garnet and CPX porphyroclasts in this sample define a foliation plane approximately parallel to the layer strike.

Garnet clinopyroxenites with little garnet (<10%) occur in highly stretched GP layers where thin, 1cm thick, clinopyroxenite layers pass laterally into areas occupied by a single large (>1cm) partly kelyphitised garnet porphyroclast (Fig 2.12 a&b). These layers are probably intermediate stages in the formation of garnet peridotites.

2:3.5c Garnet Websterites (GT WEB)

This lithology most commonly occurs in the centre of zoned layers as sub-decimetre parallel sided bands, however, a few individual thin (<10cm) monofacies layers were also observed in the Oued el Jouj section (Appendix 2). Garnet is often completely kelyphitised, occa sionally retaining central fragments of the original grain. CPX crystals, 1 to 3 cm, contain exsolution lamellae of OPX and OPX grains exsolve CPX lamellae. Textures are generally coarse granular to slightly porphyroclastic.

2:3.5d Corundum Pyroxenites (CORP)

Corundum bearing garnet clinopyroxenites and corundum clinopyroxenites have been described from the Beni Bousera massif by Kornprobst et al (1982 and 1987). This lithology is found mainly as loose blocks within the northern part of the massif but their *in situ* occurrence in the peridotite massif has recently been confirmed (J. Kornprobst pers.comm.). No samples of this lithology were discovered during this study. Their general zonation and layering is depicted in Figure 2.6 which is constructed from Kornprobst et al (1987b).

The following petrological description of the corundum pyroxenites is taken from Kornprobst et al (1982): All corundum bearing variants occur in mineralogically zoned layers and exhibit sharp compositional variations over a centimetre scale. Corundum appears as small ruby-coloured euhedra in hand specimen. Pink garnet is low in modal abundance , cm sized CPX being the most abundant phase. CPX porphyroclasts have exsolved garnet, corundum, spinel, saphirrine and plagioclase. Coronitisation of the corundum is common, alteration halos consisting of spinel +plagioclase and spinel+saphirrine assemblages. The presence of garnet in the plagioclase/spinel coronas were interpreted as a result of the reaction:

$$CPX + Cor = GT + Plag. + Spinel$$

2:3.5e Websterites +/- spinel (WEB)

Websterites probably constitute the most abundant pyroxenite layer lithology from Beni Bousera. Mono-facies layers are generally between 1 and 50 cm thick, but most commonly 1 to 5 cm. This lithology generally forms the outer layers of mineralogically zoned layers, particularly when garnet clinopyroxenite is at the centre.

Textures are generally granular to porphyroclastic. CPX are optically colourless and display frequent mechanical twinning and exsolution of OPX along {100}, garnet is rarely observed as an exsolving phase. OPX are slightly pleochroic enstatites with exsolved CPX and occassional plagioclase lamellae. In both CPX and OPX, exsolution lamellae do not continue to the margin of the crystals and indicate re-equilibration at the crystal margins. Pyroxenes often become elongate and flattened towards the edges of a layer. Irregular dark green pleonaste spinel occurs in the matrix along with anhedral plagioclase and late

brown amphibole or phlogopitic mica. Kornprobst (1969) recorded rutile inclusions in CPX porphyroclasts, however none were observed during this study.

OPX occupies less than 50 vol.% of the websterite layers. Minor sulphide phases also occur but are less abundant than in the GP layers. The margins of thick websterite layers sometimes develop the green Cr-rich CPX found at the margins of the GP layers. This Cr-rich CPX is probably the result of major element re-equilibration between pyroxenite layer and the Cr-rich peridotite (see Chapter 4)

2:3.5f Clinopyroxenite (CPXITE)

Clinopyroxenites occur mainly as monofacies layers less than 20cm thick. They are composed of ~90 % CPX which is usually coarse grained (>1cm.). CPX compositions were originally sub-calcic but have exsolved abundant OPX lamellae parallel to {100} and blebs of plagioclase and garnet. OPX constitutes up to 10% of the rock. Textures are mildly porphyroclastic with some kinking and folding of exsolution lamellae. Minor brown pleochroic secondary amphibole is observed in most sections.

2:3.5g Orthopyroxenite (OPXITE)

Orthopyroxenites are generally coarse grained (>1cm) granular to slightly porphyroclastic lithologies consisting of over 90% OPX, with additional CPX and spinel. This lithology frequently comprises the outer margins of zoned layers, usually being highly altered, or exists as monofacies layers in the host peridotite. The highly altered nature of this lithology causes it to appear as brown/green coarse friable aggregates in outcrop.

OPX in the layers are colourless to pink-green pleochroic enstatites and contain abundant CPX exsolution lamellae and blebs of garnet. Crystal margins are irregular and fragmented. OPX alters along cleavage planes to serpentine and/or chlorite together with Fe oxides. Spinels within OPXITE layers tend to be dark brown and interstitial, optically resembling those in the peridotites.

2:3.6 Cr-Pyroxenite Group

2:3.6a Websterites (WEB)

Websterites belonging to the Cr-pyroxenite group were only found in abundance in a 3m thick complexly interlayered zone outcropping in the bed of the Oued el Jouj (Appendix 2). This zone is affected by disharmonic folding (Fig. 2.9) which seems to be of tectonic origin (see below). In outcrop the rocks are extremely fresh, their colour being dominated by fresh bright green Cr-rich CPX which distinguishes them from the brown-grey weathering peridotites and the grey Al-augite pyroxenite group.

This lithology and others of the Cr-pyroxenite group are much less deformed than the Al-augite group pyroxenites, textures being mostly coarse granular to tabular. CPX and OPX are locally devoid of exsolution lamellae and often contain trains of fluid inclusions.

2:3.6b Wehrlites

This lithology comprises Cr-rich, diopsidic CPX and olivine with minor (5%) OPX . The rocks are coarse grained (0.3mm to 1 cm), texturally and mineralogically they are very similar to the Cr-Websterites. Some examples contain radially orientated intergrowths of plagioclase and CPX which may be replacing former garnet.

2:3.6c Cr- Clinopyroxenites/websterites

Narrow (1cm or less) parallel sided "veins" of clinopyroxenite consisting of >90% Cr-rich diopside cross cut the main foliation in the peridotites and pyroxenite layers at a high angle. Laterally these veins grade into websterites and usually have large irregular brown spinel concentrated parallel to their margins. CPX within the Cr-websterite (Cr-WEB) veins contain very narrow OPX exsolution lamellae. CPX is of similar grain size (1-2mm) to that in the surrounding lherzolite. Dark brown spinel occurs within the vein as well as at the margins and is optically identical to that in the surrounding peridotites which is finer grained (0.1 to 1mm). Spinel associated with the Cr-WEB veins poikilitically enclose olivine and CPX suggesting late stage crystallization.

There is no grain size reduction at the margin of the vein and there is little deformation in the surrounding peridotites close to the vein margins; some olivine recrystallisation was observed in one section. The undeformed nature of the veins and their cross cutting relationships suggest that these veins were intruded after the main deformation occurred that caused the foliation in the peridotites. This point will be discussed in the structural geology section.

2:3.7 Pyroxenite Summary

The pyroxenite layers that exist in the Beni Bousera peridotite massif may be devided into two groups, the Al-augite pyroxenite group and the Cr-pyroxenite group, on the basis of pyroxene composition. The Cr-pyroxenite group is volumetrically subordinate to the Al-augite group. The Cr-pyroxenites are non-garnetiferous and generally exhibit less deformation and subsolidus re-equilibration than the Al -augite group. The majority of the pyroxenite layers are parallel sided and parallel to each other, with only thin Cr-rich diopside veins exhibiting cross cutting relationships. No layers show any form of chilling relationships towards the peridotites and thus were presumably intruded under high temperature conditions.

Although no classical cumulate textures were found in the pyroxenites, some of their mineralogical zonation eg. a garnetite segregation from a garnet clinopyroxenite, may represent cumulate layering. Recrystallization, plastic deformation and re-equilibration have destroyed most of the original igneous textures in the pyroxenite layers. Minor apophyses were observed on some pyroxenite layer margins indicating that they crystallised from a magma. This magma appears to have induced partial melting in the adjacent peridotites which are dunitic to harzburgitic immediately adjacent to the pyroxenite layers.

The pyroxenite layers must have been intruded into the host peridotites as magmas crystallising from the walls of conduits to produce the concentric mineralogical zonation displayed by some of the layers. These layers subsequently underwent plastic deformation and re-equilibration which obscured any original igneous textures.

Petrographic evidence indicates that deformation of the pyroxenites occurred at high temperature by intracrystalline plasticity and was approximately synchronous with subsolidus re-equilibration. Deformation may have been assisted by the development of exsolution lamellae loca lising intracrystalline gliding. Finally the occurrence of graphite in the form of octahedra and other morphologies in a garnet clinopyroxenite layer has not been reported from any other orogenic peridotite massif and is restricted to 2 garnet clinopyroxenite layers in the Beni Bousera massif.

2:3.8 Garnet, spinel peridotites

Garnet, spinel peridotites occur locally in small <100m^2 patches, often close to the margin of the massif. These garnetiferous peridotites are highly weathered, the freshest specimen obtained being GP24. The rock weathers to a light brown colour and grades into the surrounding spinel lherzolite over a distance of less than a meter. Pink-red pyrope rich garnets stand proud of the weathered surface. Field relationships are highly variable. The garnet peridotites may occur as zones several metres thick or as zones up to 1 metre thick separated by spinel lherzolite in close proximity to thick garnet pyroxenite layers which apparently show little or no disruption/interaction with the surrounding lherzolite. Alternatively the garnet peridotites may occur as sub-metre zones or pods. This type of occurrence is associated with a transition of the spinel lherzolites containing thin parallel sided garnet clinopyroxenite layers to spinel peridotite containing highly stretched and thinned garnet clinopyroxenite layers (Fig. 2.12a &b). Thus the garnet peridotites are perceived as an end product of intimate tectonic mixing between spinel lherzolites and garnet clinopyroxenites (GP). This interpretation is re-enforced by the occurrence of sub.cm bands of clinopyroxenite within spinel peridotite, often one crystal wide, which sparodically contain a single large garnet porphyroclast along their strike. This lithology passes into garnet peridotite.

2:3.8a Texture:

The garnet peridotites are always highly deformed, displaying mosaic to fluidal mosaic textures with large garnet and OPX porphyroclasts in a matrix of granulated olivine. The Beni Bousera garnet pyroxenites are texturally similar to the sheared, high temperature lherzolite xenoliths found within kimberlite pipes (see Nixon, 1973).

2:3.8b Garnet:

Pink-red pyrope rich garnets form up to 10% of the garnet peridotites. These garnets are distinctly different from the the orange pyrope-almandines in the garnet pyroxenites. Most garnets are round, 0.3 to 5mm in diameter and surrounded by kelyphite rims of varying thickness. Some garnets are completely pseudomorphed by kelyphite. Many garnet crystals are surrounded by OPX rich equigranular mosaics or by coarse OPX crystals up to 4mm across. Sub-mm inclusions of olivine, OPX, CPX and brown spinel are found within garnets.

Textural observations led Kornprobst (1966) to propose that the garnets were mechanically derived from pyroxenite layers, suggesting that the garnets were not in equilibrium with the host peridotite. This interpretation was accepted by Dickey (1970) for the Beni Bousera and Ronda garnet peridotites. Whilst field and petrographic observations undoubtedly indicate that most of the garnets were derived from disruption of garnet clinopyroxenite layers, the frequent observation of garnet and olivine in intimate contact with no intervening kelyphite alteration rim and the pyrope rich composition of the garnets suggest that the garnets were in equilibrium with the peridotite mineralogy prior to kelyphitisation. Similar equlibrium relationships were also observed by Obata (1980) for the Ronda garnet peridotites. Obata (1980) stresses the porphyroclastic nature of the garnet, the frequent inclusion of olivine and chromian spinel in garnet and the curved, intimate nature of the garnet olivine grain contacts as evidence that garnet was in equlibrium with olivine at the time of peridotite crystallisation. The growth of the garnets within the garnet peridotite must have occurred in stability field of the garnet, the breakdown of garnet due to kelyphitisation occurring later.

2:.3.8c Olivine:

Olivine comprises upto 80% of the rock occurring as both porphyroclasts (2-4 mm) and neoblasts (0.1mm). The highly altered nature of the garnet peridotites makes observation of olivine textures difficult, however, many recrystallised strain free neoblasts are evident. Fresh pools of olivine within porphyroclasts contain high densities of sub-grain boundaries and kink bands. Olivine also occurs as inclusions within garnets.

2:3.8d OPX:

Orthopyroxene is predominantly a porphyroclastic phase, 2-5mm in length, and is a colourless enstatite. The porphyroclasts often appear concentrated around garnet grains and are frequently basal sections which have fragmented cataclastically rather than deforming by crystal plastic processes. CPX exsolution lamellae parallel to {100} commonly pervade the porphyroclasts and are not continuous to the edges of grains. The deformed recrystallised olivine matrix is seen to flow around the OPX porphyroclasts, some of which contain olivine inclusions.

2:3.8e CPX:

CPX are generally rare in thin section; however, in hand specimen numerous bright green chrome diopside porphyroclasts are evident which are up to 3mm across. CPX contain exsolution lamellae of OPX parallel to {100}. Coarse sub-grain boundaries are evident in all CPX porphyroclasts.

2:3.8f Spinel:

The garnet peridotites contain irregularly shaped (0.2mm) interstitial brown spinels which poikilitically enclose small olivines and therefore crystallised relatively late. The spinel is irregularly distributed throughout the rock, some sections being devoid of it.

2:3.8g Summary

The above field occurrences of garnet peridotite strongly suggest that they are the product of mechanical mixing between spinel lherzolites and garnet clinopyroxenite layers. This origin was proposed by Kornprobst (1966), however he did not note the different appearance of the garnets in the garnet peridotites and GP layers. Kornprobst (op. cit.) suggested that the garnets in the peridotites were identical to those in the GP layers and were introduced by simple mixing. Such an interpretation has also been advanced to explain the origin of similar garnet peridotites within the Ronda massif (Dickey 1970, Fabries 1979). Obata (1980) proposed that the Ronda garnet peridotites are primary in origin and must have equlibrated in the garnet stability field, however he conceeded that some garnet grains within them may have been derived from surrounding disrupted pyroxenite layers. In agreement with Obata (1980) it seems likely that whatever the ultimate origin of the garnets within these rocks, the growth of garnet in both the Beni Bousera and Ronda peridotites must have occurred in the garnet stability field but the garnets are no longer in equilibrium with pyroxenites. From the observations presented above the Beni Bousera probably originated via mixing of spinel lherzolite and garnet clinopyroxenite at high temperature. Post mixing equilibration at mantle temperatures led to the generation of an equilibrium assemblage of garnet peridotite. The name "pseudo-peridotites a grenat" used by Kornprobst (1969,1974) to describe these rocks thus seems unwarranted.

The observation of garnet and olivine in direct contact, with no intervening kelphite alteration rim

whilst the remainder of the garnet is surrounded by such a rim suggests that garnet and olivine were stabily coexisting both prior to and during kelyphitization. The lack of pyroxene associated with most spinel occurrences in the garnet peridotites does not support its origin via breakdown of garnet and therefore the garnet peridotites from Beni Bousera must have equilibrated as 5 phase, garnet, spinel, lherzolites. The none univarient nature of the multi component garnet lherzolite system in P/T space allows the coexistence of garnet and Cr- rich spinel in the lherzolite assemblage over some pressure interval (MacGregor 1970, Obata 1980) thus explaining other examples of spinel-garnet peridotites in orogenic peridotites (Lansier 1971) and nodules from kimberlite pipes (Nixon 1987).

2:3.8h Garnet Breakdown Textures: Kelyphitisation

All garnets within the garnet lherzolites exhibit evidence of breakdown in the form of kelyphitic alteration rims of variable thickness. Such rims are relatively common features of mantle derived garnet bearing xenoliths. Some of the Beni Bousera garnets may be completely kelyphitised leaving behind residual phases which were originally included in the garnet. The kelyphite rims generally contain green spinel,CPX and OPX. Relatively coarse (0.3mm) brown amphibole is rare and always occurs at the edges of the kelyphite structures.

The Kelyphite aureoles exhibit complex fine scale zonation which is approximately concentric, consisting of dark brown, fine grained inner zones, progressing outwards to coarser light yellow/brown outer zones. In detail the structure of the zones is highly complex. Scanning electron microscopy (S.E.M.) reveals at least 4 distinct zones within the kelyphite (Fig. 2.13a). A "zone" may be discontinous around the whole grain and possibly cross-cut by an adjacent zone. A general descrition of the zones is given below:

Zone 1: Optically dark brown, fine-grained 1-10 micron "blebs" consisting of a fine a symplectic intergrowth of contrasting atomic number phases, possibly spinel and pyroxene (Fig. 2.13b) which is radially orientated away from the garnet interface. Patches occur within this zone where the intergrowth is more elongate and traversed by kink/shear zones. This same fine grained inner zone is also present within intragranular fractures in the garnets where it shows no preferred orientation.

Zone 2: Zone 1 passes gradually into a narrow ~30 micron (max.) wide zone of predominantly CPX exhibiting extremely fine (sub-micron) scale intergrowths/exsolution of at least 2 phases. (Fig 2.13a). This zone may pass laterally into flame like intergrowths up to 30 microns long and 10 microns wide which contain the same sub-micron scale intergrowths/exsolution.

Zone 3: Zone 2 grades into irregular flames 20 by 60-80 microns of a high atomic number phase (Fig. 2.13c) which is probably OPX rimmed by a fine layer of a higher atomic number phase, probably spinel. These flames are set in a matrix of homogeneous CPX. Zone 3 is usually the thickest zone in the kelyphite aureols, reaching 100 microns in places.

Zone 4: Grades outwards from zone 3 and appears to be a relatively coarse 2 phases assemblage up to 80 microns across consisting mainly of pyroxene containing many V-shaped or curved, exsolved spinel bodies (Fig. 2.13d). Coarser blocky spinels may be concentrated in this outer margin which are dark green and up to 60 microns across. This green spinel contrasts with the brown spinel in the matrix of the garnet peridotite. Significant lateral textural heterogeneity exists within each zone and some zones may be absent. Residual core garnets may possess concave interfaces with the kelyphite which suggests the garnet breakdown is progressing from outside inwards.

Reid and Dawson (1970) described kelyphite "coronas" around garnets in a garnet peridotite

Figure 2.13. Backscattered S.E.M. images of kelyphite alteration rim around garnet in GTLHZ sample GP24, see text for explanation.

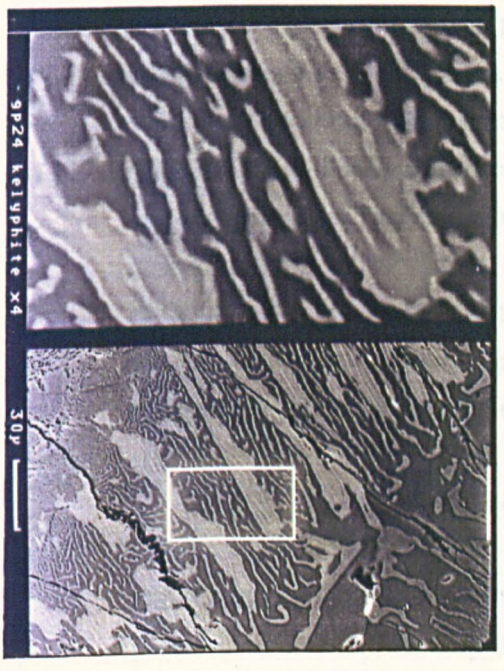
gp24 kelyphite x4
30μ

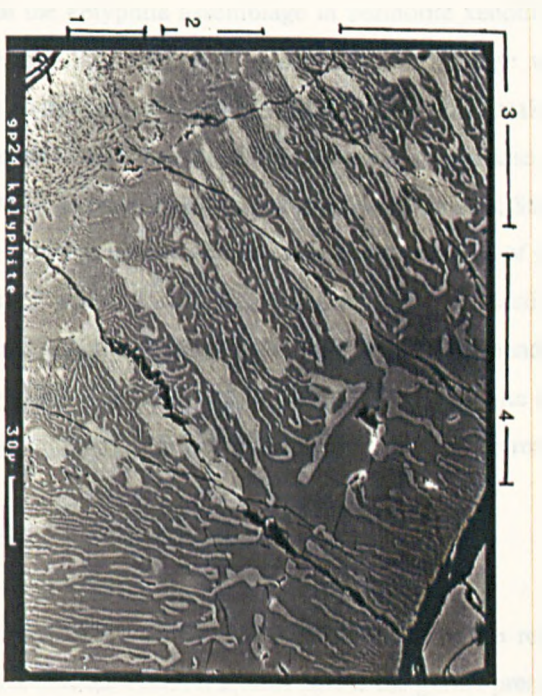
1
2
3
4
gp24 kelyphite
30μ


gp24 kelyphite
30μ

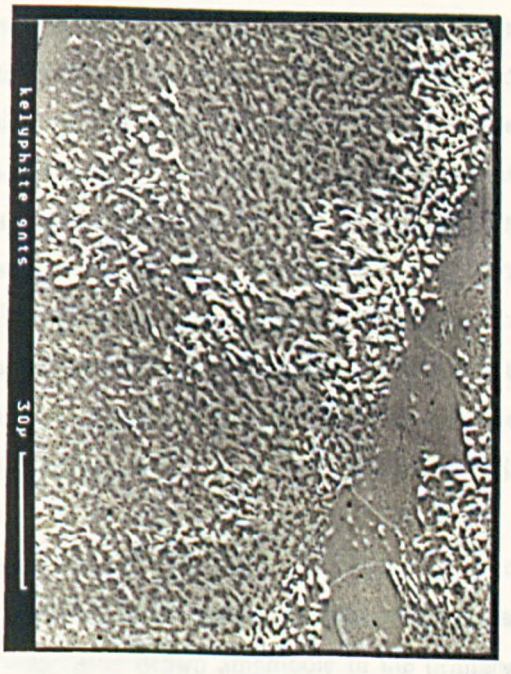
kelyphite gnts
30μ

xenolith from the Lashaine volcano in Tanzania. From transmitted and reflected light optical microscopy these authors devided the kelyphites into 3 zones; a fine grained inner zone grading out to a "feathery aggregate" and finally into a coarse grained thicker outer layer of equant spinel and CPX enclosed by OPX.

Reid and Dawson (1970) sought to explain the kelyphite assemblage in peridotite xenoliths by reaction of garnet with olivine producing anorthite, CPX, OPX and spinel. The assemblage within kelyphite rims in the Beni Bousera garnet peridotites cannot be explained by simple isochemical breakdown of garnet. The lack of sodium in the reactants compared to the products of this reaction (plagioclase is not pure anorthite, and sodium has been detected in the CPX) necessitates the introduction of sodium. Stronger arguments against the kelyphites being produced by a garnet-olivine reaction are; 1, the presence of garnet in intimate contact with olivine, 2, olivine inclusions within garnet displaying no signs of reaction, 3, garnet-olivine contacts with no kelyphite at the contact whilst the remainder of the garnet is surrounded by an extensive kelyphite rim, 4, the presence of kelyphitised garnets within garnet clinopyroxenite layers containing no olivine. Reid and Dawson (1970) also suggested that kelyphitization occurs via the reaction:

$$Ol + OPX + CPX + GT = Ol + {}^{Al}CPX + {}^{Al}OPX + Spinel$$

This reaction is untenable for the Beni Bousera kelyphites as olivine is not present in the reaction products. Additionally, the occurrence of kelyphitic alteration within fractures across the garnet preclude a mineral/mineral reaction. The coarsening outwards of the kelyphite may be the product of thermal equilibration .

Brown amphibole is generally scarce and only found occas ionally in the periphery of the kelyphite aureole, appearing to be of later paragenesis. The scarcity of this mineral and its absence within the kelyphitised fractures indicates that water played a relatively minor role in the development of the kelyphites. The brown amphibole may be a late alteration product of fine grained CPX in the kelyphite aureole.

Hunter and Taylor (1982) described garnet breakdown products of symplectitic spinel, CPX and OPX in the presence of an alkali-rich glass in garnet lherzolites and megacrysts from the Fayette county kimberlite, USA. They noted similarities with other kelyphite occurrences and suggested that incongruent melting of garnet produced the garnet alteration which was subsequently quenched to form the fine-grained complex intergrowths. The fine skeletal morphologies and textural diversity of the products were ascribed to differing nucleation and crystal growth rates due to supercooling. Hunter and Taylor (1982) suggested incongruent melting of garnet to be a common cause of kelyphitisation of garnets from garnet lherzolite and harzburgite xenoliths. This model does not seem to be applicable to the Beni Bousera kelyphite occurrences for two reasons; 1, there is no evidence of other minerals having experienced melting within the garnet peridotites and 2, there is no conceivable mechanism of supercooling of the products. Also the textures developed in the Beni Bousera kelyphites are much more complex than those observed by Hunter and Taylor.

The increase in degree of kelyphitisation of garnets towards the edges of garnet clinopyroxenite layers and the pervasive kelyphitisation of cracks in host garnets strongly implicates fluid infiltration as a major factor in causing garnet instabilty, however the scarcity of brown amphibole in the primary reaction products requires a fluid of low water activity. Further research using transmission electron microscopy to study the complex kelyphite textures and mineralogy are required to resolve the cause of garnet breakdown. The main conclusion to be drawn from the study of the Beni Bousera kelyphite alteration halos

is that similar features commonly described in garnetiferous mantle xenoliths from alkali basalts/kimberlites may not be due to simple low pressure breakdown of the garnet but may initiate due to the presence of a fluid phase in the mantle.

2:3.9 Vein mineralization in the peridotites.

The Beni Bousera peridotites are intruded by Cu-Ni-Fe-Cr-graphite mineralized veins. There are three main types of vein assemblages;

1) The graphite-chromite-Cu-Ni-sulphide assemblage which is altered to hydrated secondary silicates such as garnierite.

2) The graphite-limonite-Cu-carbonate-marcasite-chalcopyrite- annabergite-vermiculite assemblage.

3) The Ni-arsenide-chromite + graphite assemblage.

The Ni-arsenide assemblage is the only assemblage to be studied in detail here. Most of the Ni-arsenide veins are found along the NE border of the peridotite massif. The veins cut the foliation in the peridotite at high angles and are almost vertical. The veins are generally less than 1 m wide and extend for a few tens of meters (Leblanc 1986). The wall rocks of the veins are strongly serpentinised. The vein lode is composed mainly of chromite and a Ni-arsenide (mainly niccolite) with minor pyrrhotite containing cubanite exsolution. The chromite exists in a gangue of amphibolitized OPX (Leblanc 1986). Accessory minerals in the veins are polydimite, Ni-safflorite, Ni-Co rich loellingite, native Cu, native Au, graphite (which may be abundant), bornite, violarite and millerite (Leblanc 1986, Oen and Kieft 1974). The Ni-ores weather to annabergite and garnierite. Native gold is found as inclusions in the niccolite. Chromites contain 35-40% Cr_2O_3 (Leblanc 1986). In addition to gold, economic grades of platinum group elements (PGE) have been reported in the Ni-arsenide veins (Leblanc and Zdenek 1986).

2:3.10 Crustal Rocks:

2:3.10a Kinzigites

The kinzigite gneisses that surround parts of the peridotite massif outcrop in narrow zones up to 400m across. Immediately adjacent to the peridotite contact the graphite bearing kinzigites contain needles of sillimanite and are locally migmatitic. The typical kinzigite assemblage consists of : graphite (upto 10%), K-feldspar, plagioclase, biotite, sillimanite, garnet and quartz with minor rutile. All sections examined were from within ~200m of the peridotite contact and appear in equillibrium with sillimanite. Typical kinzigite outcrops are illustrated in Figure 2.14.

Garnets are rounded to slightly ovoid and vary from 1mm to 15mm across. Garnets contain inclusions of biotite, K-feldspar and quartz and define sigmoidal syntectonic trails within the garnet. Fine mm to sub mm needles of sillimante occur parallel or sub-parallel to the foliation, displaying well formed {110}, {010} and basal {001} sections. Kornprobst (1974) notes that the abundance of sillimanite in the kinzigites decreases markedly away from the contact with the peridotites and may be seen pseudomorphing kyanite in some lithologies. This leads to the conclusion that sillimanite formed from kyanite due to the temperature increase associated with the intrusion of the hot peridotite massif (Kornprobst op. cit.). This heating effect also produced local partial melting leading to the formation of migmatites (Fig. 2.14 b&c).

Figure 2.14. (A) Large garnet porphyroblast with feldspar pressure shadow in kinzigite. (B & C) Migmatitic segregations in kinzigite. (D) Garnet, graphite rich kinzigite.

Figure 2.15. (A) Pegmatitic quartzofeldspathic vein containing large tourmalines cross cutting peridotites. (B & D) weathered serpentinite breccias marking faulted contacts between peridotite and kinzigite, Amasihene beach. (D) contains abundant secondary magnesite. (C) Faulted contact between peridotite and micaschist of the Alkaili unit at Aarkob.

A
B
C
D

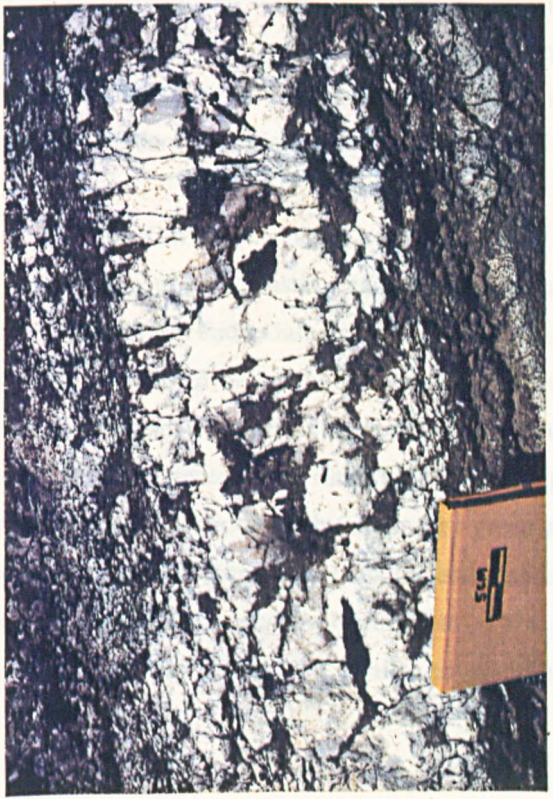

A

B

D

ALTERED PERIDOTITE
STEEPLY
DIPPING
MICASCHIST
MICASCHIST

C

Perthitic K-feldspar is the dominant feldspar, sometimes displaying irregular grain boundaries with the quartz. Minor plagioclase containing antiperthite intergrowths also occur. Graphite normally comprises 0.5 to 1.5% of the rock and occurs as clusters of elongate crystals whose *c* axes are parallel to the foliation. Some graphite has nucleated around the edges of garnets. Graphite only occurs in non-migmatitc, more leucocratic lithologies; the crystals are usually bent and display undulose extinction in reflected light due to sub-grain boundary formation.

2:3.10b Garnet-plagioclase pyroxenites

A variety of granoblastic plagioclase bearing garnet pyroxenites intrude the kinzigites and are found as lenses up to 1.5m thick. Garnets are pink-red to deep-red in hand specimen, 1 to 2mm in diameter and are generally surrounded by kelyphite alteration rims. CPX (2 to 5 mm) is pale pink in thin section and optically resembles titaniferous augite. There is no evidence of OPX exsolution in the CPX. CPX contains inclusions of plagioclase and rutile approximately parallel to the {100} CPX cleavage direction. CPX crystals are often surrounded by secondary green amphibole. Plagioclase laths are up to 0.2mm long, display albite twinning and are labradorite/andesine in composition. The occurrence of scapolite within this lithology has been reported by Kornprobst (1974) but was not found in this study. The textures and mineralogy of these rocks are similar to granulite facies metabasites and they are interpreted as metamorphosed basic dikes.

2:3.10c Quartzofeldspathic Veins

NW-SE striking pegmatitic quartzofeldspathic veins, up to 2m thick, cross cut the peridotites and kinzigites oblique to their foliation. These veins predominatly consist of K-feldspar and plagioclase with lesser quartz, tourmaline and vermiculite. Coarse 1 to 2cm crystals of feldspar comprise 95% of the veins. Tourmalines reach 10cm in length (Fig. 2.15a) and are the black schorlomite variety. Vermiculite occurs at the centre of veins in coarse books or at the margins as disseminated crystals. Where veins cross cut the pyroxenite layers, amphibolitization occurs.

2:4 Structural relationships

2:4.1 Relationships of the peridotite massif to the surrounding crustal rocks.

The contact between the peridotites and surrounding crustal rocks is everywhere faulted or brecciated. A steeply dipping normal fault marks the contact of the peridotite with the Palaezoic Alkaili unit at Aarkob. This fault bifurcates and one arm of it continues to downthrow gneisses and micaschists of the Filali unit against highly serpentinized deformed peridotites (Fig. 2.15c). The fault zone is over 3m wide and consists of brecciated, serpentinized peridotite with abundant magnesite which is faulted against a zone of mylonitized micaschist. The regional foliation in the country rocks steepens markedly towards the peridotites and is sub-vertical at this peridotite contact.

S.E. of Bou Ahmed, the kinzigites are down thrown against peridotites in the N.W. corner of the massif (Fig. 2.1). This fault zone is marked by a weathered serpentinite breccia (Figure 2.15b&d) with abundant secondary carbonates. The normal peridotite/kinzigite contact is a low angle fault bordered by mylonitic peridotite and kinzigite. This fault has been locally steepened by later doming. Small "horses" of peridotite were observed in the kinzigites. The low angle faulted contact is not as heavily serpentinized as the high angle fault contacts.

2:4.2 Evidence of deformation in the peridotite massif.

The existence of a strong foliation is the most obvious evidence of deformation within the spinel and garnet peridotites. The foliation in the peridotites and kinzigites close to their contact is parallel. In thin section the peridotite foliation is defined by flattened OPX porphyroclasts and a prefered orientation of olivine *c* axes. Spinel grains define a stretching lineation lying in the plane of the foliation. Pyroxenite layers are orientated parallel to the foliation in the peridotites. The pyroxenite layers also show evidence of being deformed, most commonly by boudinage which creates well defined pinch-and-swell structures on all scales in the layers (Fig. 2.16). The pyroxenite layers are also tightly to isoclinally folded (Figure 2 .17). Fold hinges are rarely seen, possibly due to intense shearing. More open folds whose hinges are approximately parallel to the tight folds are observed in some areas, particularly in the Cr-pyroxenite rich region of the Oued el Jouj (Fig. 2.9c). Stereographic projection (Fig.2.18) reveals that the pyroxenite layer orientation/peridotite foliation is axial planar to the isoclinal folds. The pyroxenite boudin axes and fold axes are parallel to the stretching lineation in the peridototes and suggest both folding and boudinage are the result of the same deformational event. The straight sided pyroxenite layers may represent the limbs of isoclinal folds which allows the possibility that much of the exposed sequence has been duplicated. Restricted exposure makes this hypothesis impossible to test on a large scale.

The margins of the pyroxenites may have suffered intense layer parallel shearing during isoclinal folding which accounts for the scarcity of apophyses and the truncated nature of some kelyphite rims around garnets at pyroxenite layer margins. The more intense nature of the garnet kelyphitisation at layer margins may encourage greater deformation due to reaction produced grain size reduction.

2:4.3 Mechanism of pyroxenite intrusion into the peridotites and the timing of the deformation

The compositionally zoned nature of the pyroxenite layers, their occasional relict apophyses and the dunitic nature of the peridotites adjacent to them suggest they originated by intrusion of dike-like bodies into peridotites in the mantle. The compositionally zoned nature of the layers may have been produced by a combination of successive injections of magma, reaction with wall rocks and crystal "plating" on the walls of the dikes by flowing magma. This hypothesis raises the question of how and when the pyroxenites acquired their present parallel orientation.

Sleep (1988) considered dike formation in mantle peridotites by the trapping of melt flowing through the host peridotites. The presence of dikes which have crystallized at mantle pressures within orogenic peridotites indicates the mantle's ability to fracture. This is achieved by the presence of a partial fluid pressure (where fluid is equivalent with melt) which enhances fracture formation by reducing the effective stress required to intersect the Griffith failure envelope. Environments of low deviatoric stress and high fluid pressure favour extensional fracturing producing long, fairly straight fractures. Once small veins are initiated they tend to open if the fluid pressure within them exceeds the least principal stress, porous flow into the veins being necessary for them to open (Sleep 1988). The vein may then grow by cycles of inflation and deflation depending on the variation in melt pressure supplied by the surrounding media (Fig.2.19). This method of dike intrusion and growth, in the mantle, will result in dikes orientated perpendicular to a foliation developed in the surrounding peridotites (Sleep 1988). Planar features such as dikes, intruded at high angles to the foliation of peridotites may be gradually re-orientated during continuous rotational plastic flow in the asthenosphere until they are sub-parallel or parallel to the foliation (Nicolas and Jackson 1982). Boudinage and folding of the dikes in the peridotites were ascribed to the heterogeneous

Figure 2.16. (a-c) Pinch-and-swell structures defined by pyroxenite layers in peridotite. (d) Garnetite layering in loose GP block (GP239).

Figure 2.17. (A) Isoclinally folded websterite layer in Oued el Jouj, surrounded by parallel sided pyroxenite layers (the limbs of isoclinal folds ?). (B) Isoclinal folding of websterite, lower hinge sheared out, Oued Sidi Yahia Aarab. (C) Open folding in Cr-pyroxenite layers, Oued el Jouj. (D) Isoclinal fold with attenuated hinge, Oued Sidi Yahia Aarab.

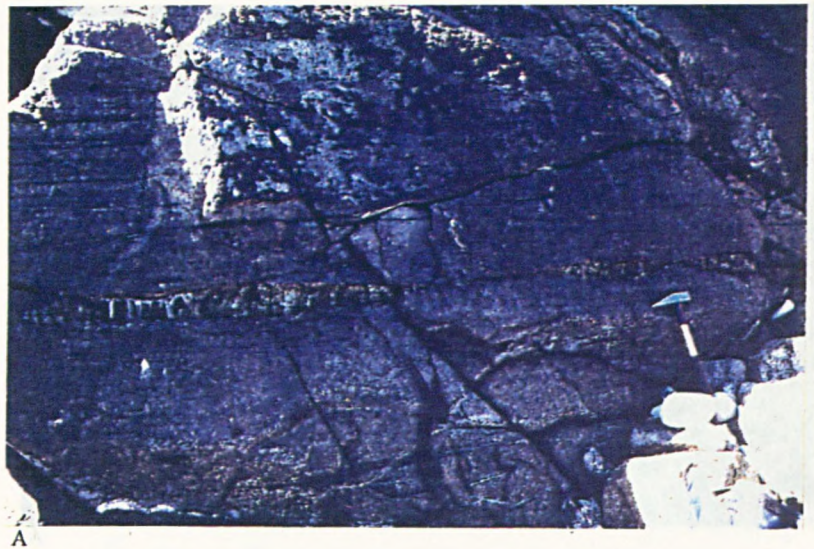

A

B

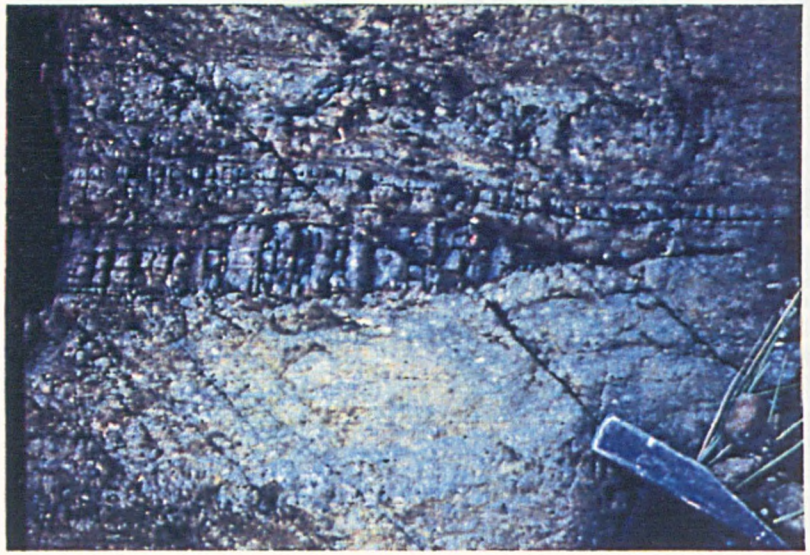

C

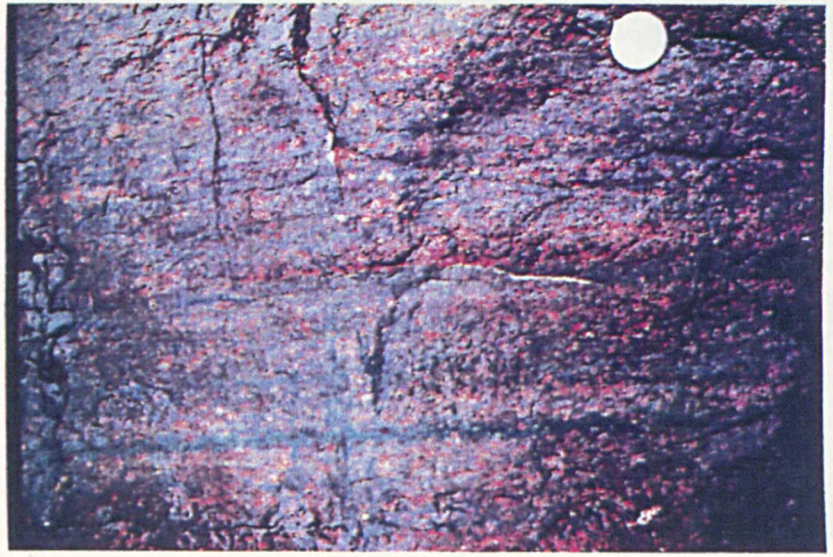

D

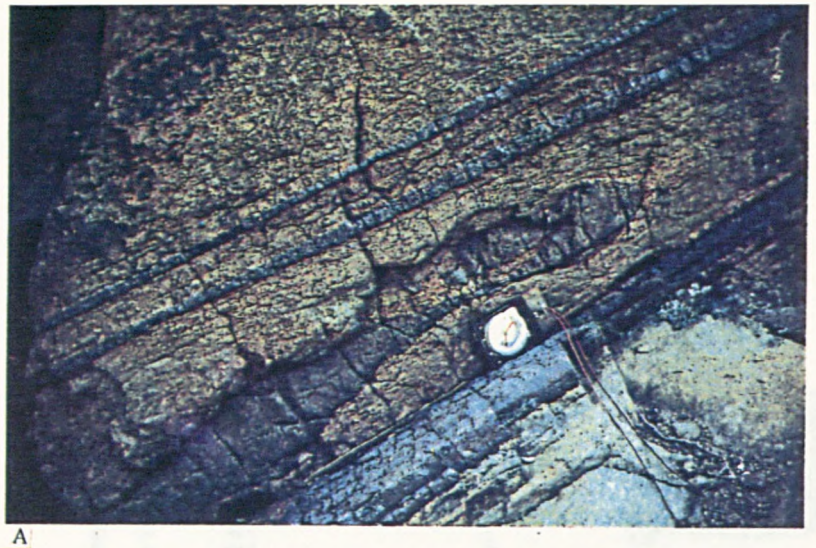

A

B

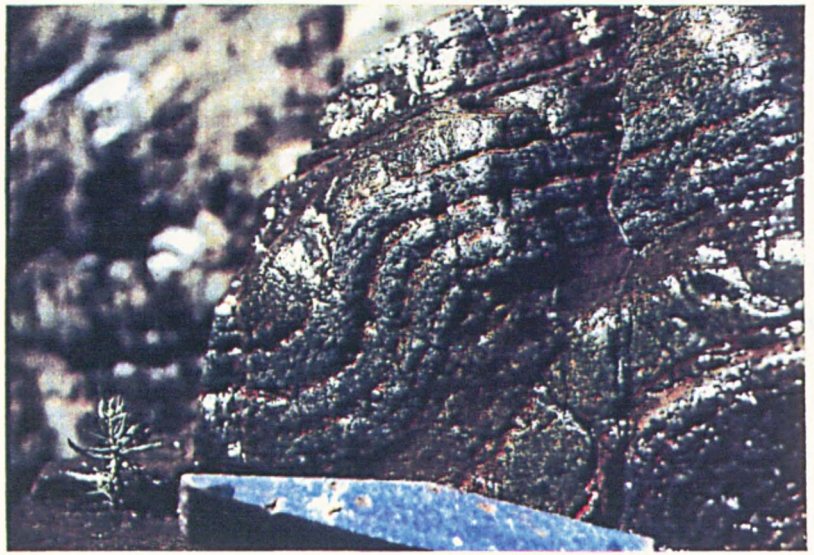

C

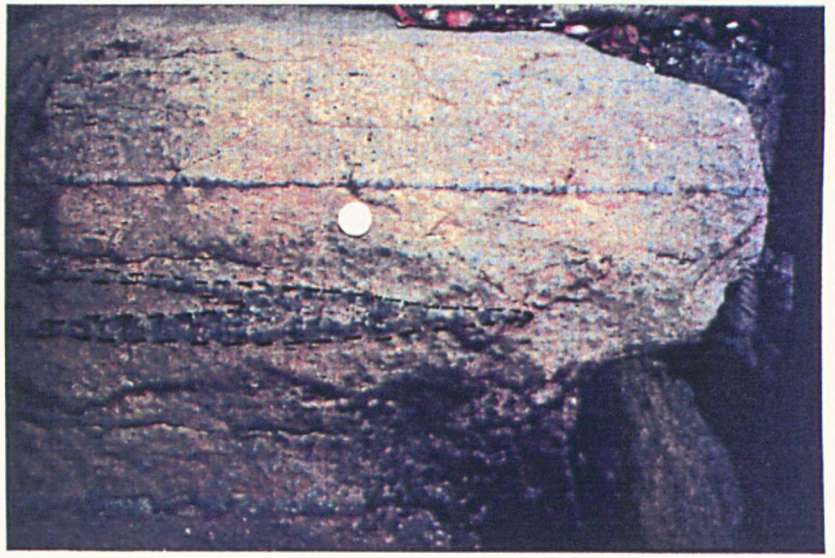

D

Figure 218. Stereographic projection of pyroxenite layer orientation and plunge of folds defined by pyroxenites compared to poles to fabric orientation in kinzigites in the southern Oued el Jouj. (shaded area)

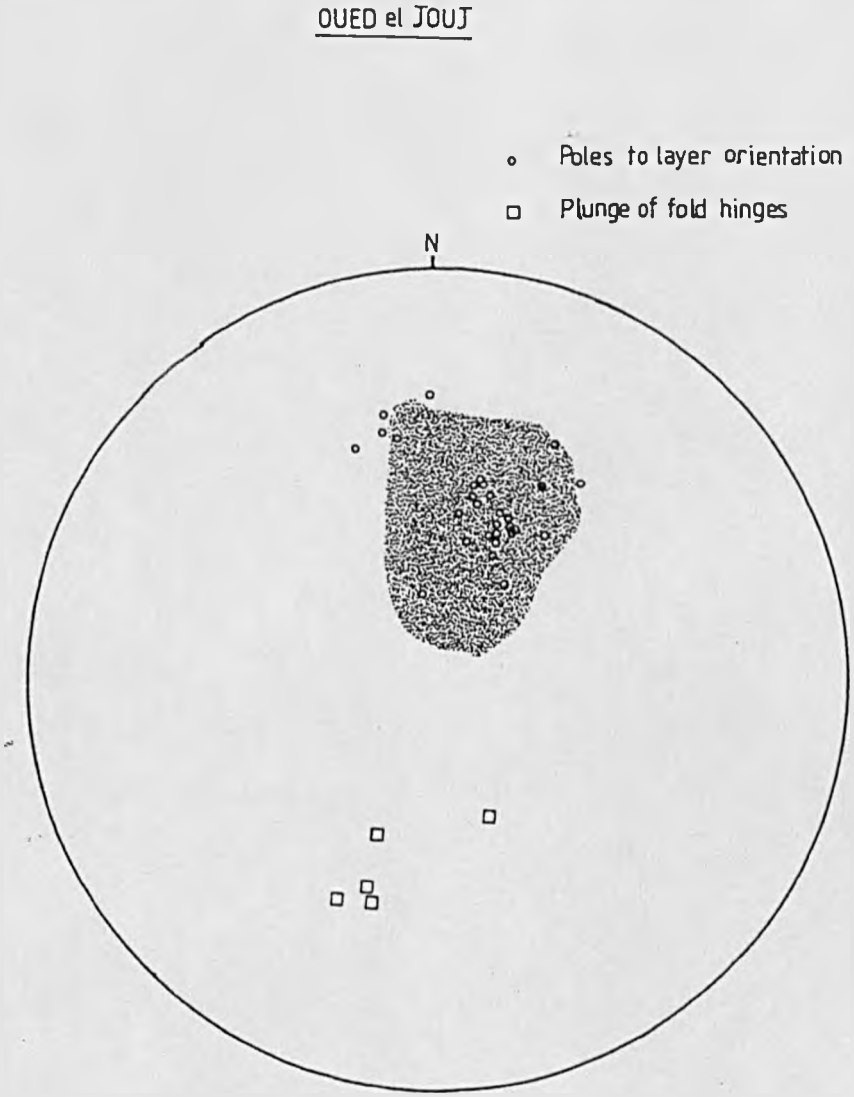

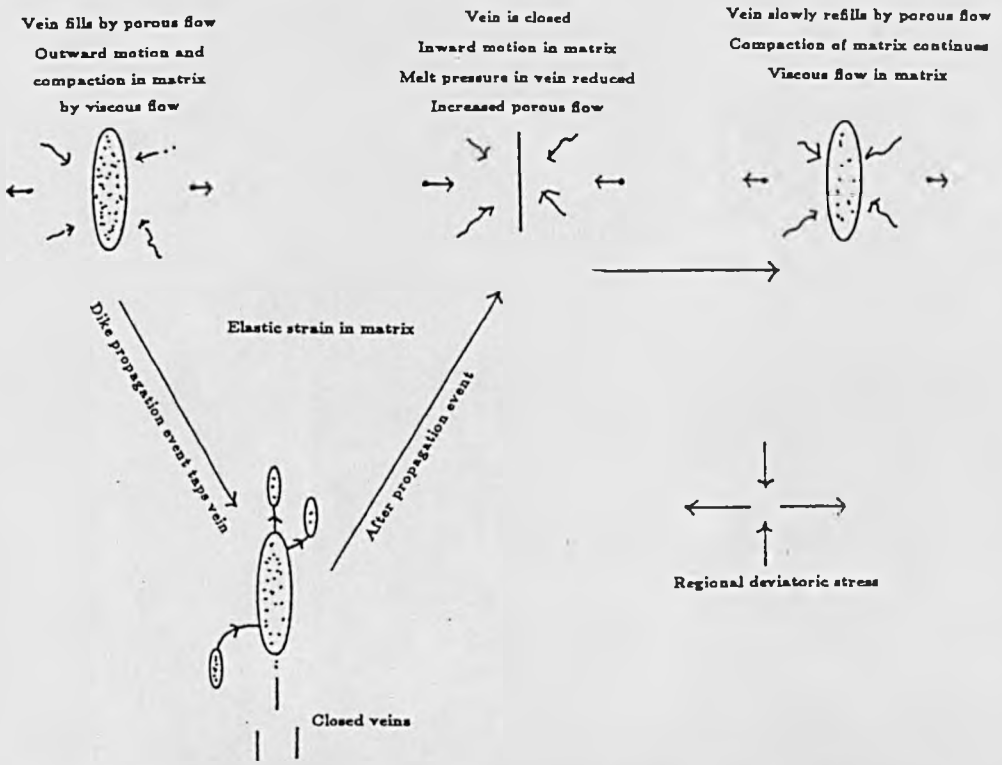

Fig. 2.19 The cycle of inflation and deflation of a vein is shown at the top. The vein fills slowly by porous flow while the matrix compacts (left). Points in the matrix on the sides of the vein move outward (arrows). A dike propagation event involving the vein occurs rapidly (lower left). Material is injected into veins above the dike and tapped from veins after the dike has passed. The net effect is to significantly drain and close the vein (top, center). The matrix on the sides of the vein moves inward when it closes. The reduced pressure in the vein enhances porous flow. The cycle continues with the vein slowly filling (top, right). After Sleep (1988).

nature of the strain regime and the difference in the rheological properties of the respective rock types (Nicolas and Jackson op. cit.). Shear strains could act over a long period in the asthenosphere or could be the products of shearing associated with mantle diapirism and emplacement. The model provides a mechanism whereby large initial angular variations between veins/dikes in the asthenosphere are reduced to very small angles during mantle flow hence producing pyroxenite layers parallel to the foliation except where folded. The axial plane of the isoclinal folds is then parallel to the foliation.

A minimum depth of pyroxenite deformation is provided by the disruption of garnet pyroxenite layers to produce garnet lherzolites. This must have occurred close to the garnet/spinel transition. This early, intense deformation period may have occurred during diapiric upwelling of the peridotite massif. In most areas the foliation in the peridotites is parallel or sub-parallel to that in the kinzigites (Kornprobst 1974). The foliation defined within these two lithologies defines an antiformal dome structure whose long axis trends NNW-SSE and plunges gently SSE. Post emplacement doming probably lead to re-orientation of the peridotite and kinzigite foliations parallel to each other.This late antiformal arching may have resulted from folding in the hanging wall above a major thrust fault which emplaced the peridotite massif and kinzigites into the upper crust. Alternatively the dome may be a result of mantle upwelling beneath the region. Emplacement models for the massif are discussed in the light of geochemical/isotopic data in Chapter 8.

CHAPTER 3

THE OCCURRENCE OF GRAPHITE IN THE BENI BOUSERA PERIDOTITE MASSIF

3:1 Introduction

Graphite occurs in three main parageneses within the Beni Bousera peridotite massif and the surrounding kinzigites:

1, Vein paragenesis: Graphite-Cu-Ni mineralised veins which intrude the peridotites and kinzigites

2, Kinzigite graphite: Disseminated graphite with *c* axes parallel to a gneissic foliation.

3, Graphite in garnet clinopyroxenites: Graphite aggregates displaying cubic symmetry within some garnet clinopyroxenite layers (GGP)

The aim of this chapter is to document each type of graphite occurrence, to examine any possible relationships between them, and to deduce the origin of the unusual cubic graphite aggregates in the GGP layers.

Graphite occurs rarely and as an accessory mineral in terrestrial igneous rocks. Wager and Brown (1968) described graphite coexisting with platinoids and various Cu-Ni-Fe sulphide phases in the Bushveld intrusion, southern Africa. Graphite has also been reported from various other layered intrusions such as Stillwater (Montana), Sulmalkie (Poland) and Skaergaard (Greenland) (see brief review by Slodkevich 1980b). The graphite in all these occurrences appears typically as flakes, hexagonal clusters, massive aggregates and spheroids. Graphite has also been recorded in peridotite and eclogite xenoliths from kimberlite and lamproite pipes (Williams 1932, Robinson et al. 1984, Nixon et al. 1987) and pyroxenite xenoliths in alkali volcanics (Pineau et al. 1987). Graphite from both xenoliths and layered intrusions exhibits euhedral, tabular prism forms between 1 and 4 mm. in diameter, some crystals being rounded and pitted. There is only one known occurrence of graphite from a xenolith occurring in a form with apparent cubic symmetry (P.H. Nixon pers. comm.). The high degree of order shown by graphite from both peridotite and eclogite xenoliths (Pasteris and Pearson unpublished data), its lack of pseudomorphic textures and its coexistence with garnet and even diamond (Robinson et al 1984) suggests crystallization at high temperature and great depth, probably from C-H-O bearing mantle fluids. Graphite is also found in meteorites as cliftonite, often as octahedral and dodecahedral forms; this occurrence will be discussed in section 3:5.

3:2 Vein paragenesis

Graphite occurs together with Cu-Ni sulphides in veins within the peridotite massif (Chapter 2). The veins are of diverse orientation and vary from 10 cm to 1 m in width and may be traced for a few tens of metres along old mine adits. Graphite bearing veins appear to be associated with strongly serpentinised peridotites. Graphite veins are often brecciated and cut by several generations of serpentinite veinlets of

random orientations.

The graphite has been identified by powder camera X-ray methods and found to have a $d_{(0002)}$ spacing of 3.30 Angstroms (*A*.). The precision of this measurement is probably low (> +/- 0.05 *A*) due to the poor powder diffraction photograph obtained for this specimen. Some veins consist of over 90% graphite or contain zones of similar concentration. These "high grade" veins were briefly mined for graphite in 1937 but were subsequently deemed to be uneconomic (Huvelin and Permingeat 1980). Veins containing mainly graphite, but with minor hydrated iron-nickel silicates and oxides such as geothite and garnierite were found adjacent to the Oued el Jouj and to the south of Jbel Zabara ie. in the south-west of the massif, in the same area as the GGPs (Fig. 2.1). In veins where it forms the major constituent, graphite occurs as finely crystalline, irregular stacks of anhedral crystals between 0.1mm to 0.5 µm across. The crystals show very little surface topography but their edges are sub-angular to rounded which may indicate some chemical dissolution by a fluid phase. Aggregates of the crystallites appear as rounded, often mammilatory intergrowths but do not show the zonation of different growth forms observed in the well documented, large scale graphite vein deposits of New Hampshire, U.S.A. and Sri Lanka (Rumble, 1986). Although the graphite veins have gradational margins, no disseminated graphite is seen in the peridotites and pyroxenites adjacent to them.

3:3 Kinzigite Graphite

The garnet sillimanite gneisses (kinzigites) which surround the peridotites contain variable amounts of graphite, usually disseminated and orientated with six-fold axes parallel to the foliation in the gneiss. The crystals are 0.02 to 0.5 mm in diameter and are a mixture of rounded anhedra and sub-rounded subhedra with some stacks of hexagonal plates. Basal {0001} surfaces of the graphite are generally smooth with occasional striations which may form triangular patterns. Graphite only occurs in the sillimanite facies kinzigites close to the margins of the peridotite and is heterogeneously distributed. Bulk chemical analyses, using combustion gas chromatography, demonstrate that the graphite forms between 0 and 15% by volume (this work and Huvelin and Permingeat, 1980), most samples containing around 0.5%. Samples containing the most graphite occur in the migmatitic garnet gneisses adjacent to the peridotite contact and are generally the most garnetiferous horizons in the gneisses. Graphite often occurs as inclusions within garnets in the more mafic horizons. At Hilaouen, where graphite concentrations reach 15%, the kinzigites were exploited for graphite in 1953 (Huvelin & Permingeat 1980).

Powder diffraction reveals a $d_{(0002)}$ value of 3.324 *A* for the kinzigite graphite. Both vein and kinzigite graphite appear fairly well ordered from their powder diffraction patterns, with sharp (112) and (114) reflections. In addition to the sharpness of these two reflections, Grew (1974) suggested that a $d_{(0002)}$ spacing of less than 3.357 *A* was a reliable indicator of well ordered graphite. All the graphite samples from Beni Bousera fall below this value but it is not possible to discriminate between the kinzigite and the mineral ised vein occurrences on this basis. Further detailed discussion on graphite ordering/crystallinity is given in section 3:7 which deals with the Raman spectroscopy of graphites.

Although differences in $d_{(0002)}$ exist between the kinzigite and vein graphite (and graphite in the GGP, see below) it is difficult to interpret the measurements in a rigorous manner, ie. in terms of different original sources and different temperatures of formation. This is in part due to errors inherent in the measurment of the interlayer spacing but also due to the lack of published data to draw upon. Grew

(1974) found that on progressing from biotite to sillimanite zones during regional metamorphism the overall change apparent in the interlayer spacing of the graphite is only a few multiples of analytical precision.

3:4 Graphite in Garnet Clinopyroxenites

3:4.1 Occurrence and field description:

The existence of graphite within certain GP layers was first noted by Milliard (1959) who did not comment on its form or distribution. Slodkevich (1980a) reported the occurrence of polycrystalline aggregates of octahedral graphite within a GP layer in the peridotites (location unstated) from the Beni Bousera massif and interpreted the aggregates to represent octahedral graphite pseudomorphs after diamond. Slodkevich (1980a and b) documented graphite forms with cubic symmetry occurring in 4 GP layers but did not specify the location of the layers. Two GP layers containing cubic forms of graphite were found during field studies in the course of this work. Both layers outcrop in spinel lherzolite to the east of Tazemourte I. One layer outcrops in the bed of the Oued el Jouj G.R. 04512/35128, and the other 200m up the western flank of the Oued el Jouj valley G.R. 04513/35129. Discontinuous outcrops occur at both localities and it is uncertain whether Slodkevich (1980b) refers to each distinct outcrop as a "layer". Loose blocks occur as "float" in coarse (boulder grade) high velocity alluvial deposits in the valley bottom and embeded in soils on the valley sides up to 2km further up stream in the Oued el Jouj valley. Despite extensive search, no other outcrops have been found. The juvenile nature of the stream valley and absence of glaciation in N.Morocco during the past 30ma. suggests that other GGP layers once existed in this area which have been totally eroded. These layers were probably of comparable thickness to the two *in situ* layers as graphite bearing boulders 40x20cm have been found in the upper reaches of the Oued el Jouj valley.

Measured sections of the two GGP layers are presented in Chapter 2. In the layer outcropping on the track up to Tazemourte I, graphite occurs in the upper part of the layer ; "upper" being uphill as no clear way up is consistently descernible from the distribution of silicate phases (Chapter 2). Graphite in the Oued el Jouj GGP layer is concentrated towards the centre of the layer but the graphite is laterally dicontinuous along strike. Locally, graphite concentrations may exceed 15% by volume of the GGP, however, when the total layer is considered this value is less than 1%.

3:4.2 Optical and physical properties of the GGP graphite

In thin section the graphite is opaque, uniaxial and optically negative with blue/green "interference colours" at its edges and along any fractures within it. In reflected light the graphite is pale brown/grey with high bireflectance and extreme anisotropy. Many sections have striations intersecting in trigonal patterns on their polished surface.

Slodkevich (1980b) noted that the physical properties of the graphite from the GGP differ appreciably from "standard" graphite. Its density is of ~2.05 gcm^{-3} is lower than the standard Botogol graphite (2.2 gcm^{-3}) referred to by Slodkevich (1980b), but is similar to cliftonitic graphite (2.12 gcm^{-3}). Botogol graphite is a standard, vein paragenesis graphite. The microhardness of the Beni Bousera core graphite (42.1 $Kgmm^{-2}$) is slightly harder than the coat (36.5 $Kgmm^{-2}$). Both these values are considerably higher than Botogol graphite (7 to 12 $Kgmm^{-2}$, Slodkevich 1980b). Such anomalously hard graphite is characteristic of the graphite produced from graphitized diamonds (Howes 1962).

Reflection spectra for the GGP graphite are comparable to Botogol graphite whilst reflection coefficients slightly exceed the standard values (Slodkevich 1980b).

3:4.3 Graphite Morphology

Where the prefix "cubic" is used in relation to the Beni Bousera graphite forms it implies forms possesing symmetry belonging to the cubic system and does not refer to the specific shape of the aggregates. Graphite in the two pyroxenite layers and in the various "float" specimens occurs in a variety of morphologies usually displaying some degree of cubic symmetry. The following symmetry nomenclature is based on the Haumman-Maugin system with crystal face and form indices following the Miller-Bravais system. Whole graphite aggregates were liberated from the host rock either mechanically or by HF-aluminium chloride dissolution. Forms exhibited by the graphite aggregates belong to the cubic system and are of the hexoctahedral class 4/M32/M whereas naturally occurring graphite belongs to the hexagonal system, dihexagonal-dipyramidal class 6/m2/m2/m. Most graphite occurrences in terrestrial rocks form disseminated scales, laminae, columnar or mammilatory masses. Graphite defining forms of cubic symmetry from the Beni Bousera GGP, consist of tabular graphite crystallites with hexagonal outline possesing excellent pinacoidal {0001} forms and descernable {1010} faces. The overall form of the aggregates have cubic symmetry with particularly well developed {111} forms indicating that the graphite is pseudomorphing a pre-existing mineral of cubic symmetry.

3:4.3a Octahedra: {111}

Graphite aggregates displaying some degree of octahedral morphology are the most common forms in the GGP. Euhedral, sharp-edged octahedra (Fig. 3. 1) displaying the full cubic symmetry $3A_4$, $4A_3$, $6A_2$, 9PC, normals of the form {111} being coincident with the triad axes, are found protruding from broken surfaces of the host GGP. Octahedra protruding from weathered surfaces are more rounded. Some octahedra are flattened normal to the triad or diad axes or sheared parallel to {111}. A variety of octahedral and twinned graphite forms from the GGP are illustrated in Figure 3.2a (after Slodkevich 1980a).

Octahedra vary in size from <1mm to 12mm (edge length). Sharp-edged octahedra have trigonal, flat faces with some minor steps and no apparent rounding of corners or edges. Other octahedra posses {111} faces whose corners and edges are rounded or curvilinear, which may be the result of damage. Scanning electron microscopy (S.E.M.) observations indicate that some octahedra have vertices truncated by a complex intergrowth parallel to {111} (Fig. 3.3b.). This type of truncation was found to be common in a large selection of De Beers "pool" diamonds observed from the collection of Dr. H.J. Milledge, implying that the graphite pseudomorphed the {111} cleavage directions of a pre-existing mineral.

3:4.3b Modified Octahedra: {111} {100} {011}

Graphite octahedra may sometimes possess cube {100} faces of varying development (Fig. 3. 4d). These crystals always have 8 {111} faces but are a distortion of an octahedral polyhedron. An aggregate extracted from sample GP147 had a tetrahexahedroid {011} face on one side (terminology of Robinson 1979) and a cube face terminating its apex ie. the form was a rhombicuboctahedra. This form has been decribed as a growth form in natural diamonds by Machado et al (1982). Unfortunately this specimen disintegrated before photography was possible.

Aggregates also occur which consist of a well developed octahedral form in one half and a rounded, globular mass with no planar features or symmetry in the other. This unusual form has also been observed

Figure 3.1. Upper half of sharp edged graphite octahedron protruding from graphite garnet clinopyroxenite layer, GP147.

Figure 3.2a. Octahedral and twinned forms of graphite extracted from Beni Bousera garnet clinopyroxenites by Slodkevich (1980a).

Figure 3.2b. Radiographs of graphite octahedra from PHN 5730 containing large silicate inclusions. Inclusion in 3.2b1 appears to have cubo-octahedral facets.


1 mm

3.2a

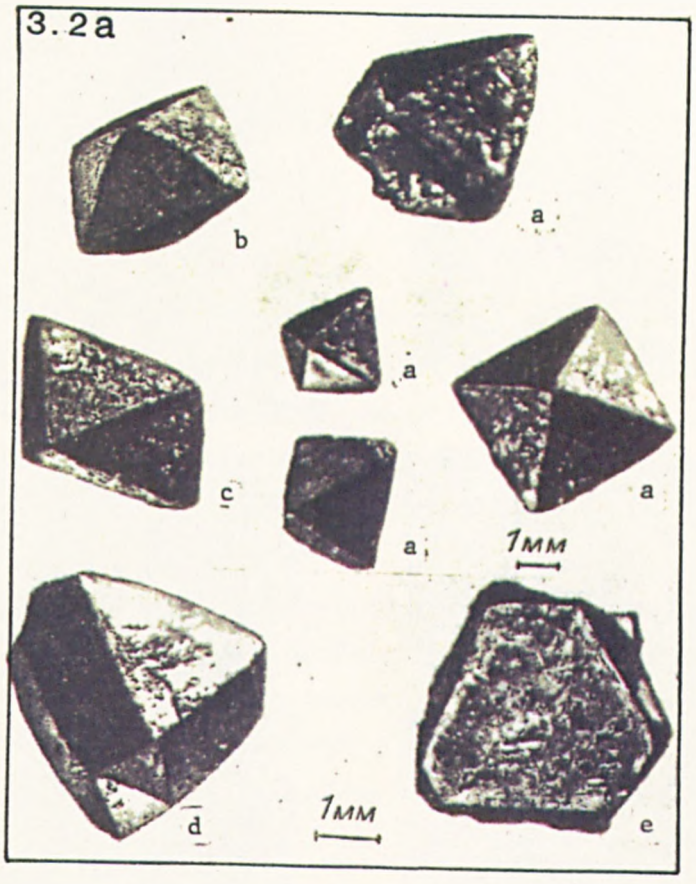

3.2b

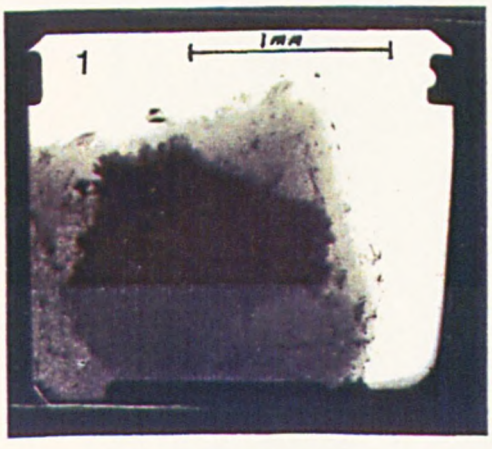

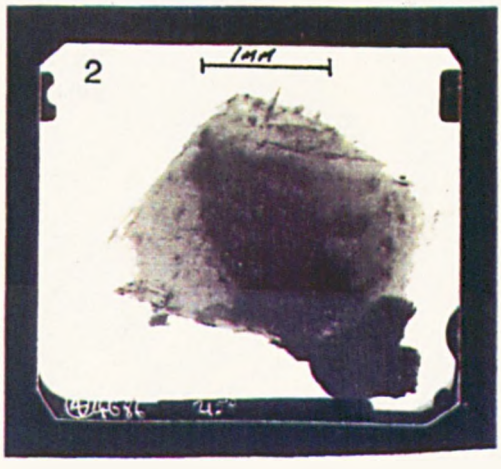

Figure 3.3. A: Sharp edged octahedron from PHN 5734. B: Truncated apex of octahedron revealing {111} cleavage directions, PHN 5734. C: Octahedron showing remnants of coat graphite around peripheries. D: Irregular graphite aggregates from GP147 showing no obvious faces. E: Deformed, irregular graphite from the coat of a coated octahedron (GP147). F: Large coated aggregate from GP75 showing abrupt junction between core and coat graphite.

Figure 3.4. A: Coated octahedron with {111} still visible; GP147. B: Sharp edged octahedron extracted from PHN 5734 with coat remaining around middle of octahedron. Top half of graphite octahedron protruding from broken surface of PHN 5734. Obliquely orientated graphite crystallites are remnants of the coat graphite that surrounded this specimen. D: Deformed upper half of graphite aggregates with cube face. E: Close up of c showing remnant coat graphite with *c* axes oblique or perpendicular to the graphite aggregate.

Figure 3.5. A: Growth steps on the core of a {111} face on an octahedron from GP75. B: Steps on a {111} face of an octahedron from PHN5734. C: Trigonal pits on {111} of GP75. D: Negatively orientated trigonal pits on {111}, PHN5734. E: Faceted CPX inclusion, cube and octahedron faces are parallel to {100} and {111} of the graphite form respectively, right, enlargement of view. F: CPX with cubo-octahedral facets, GP75.

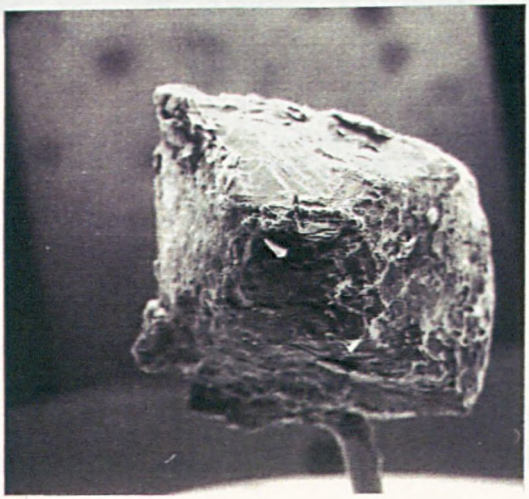

A

B

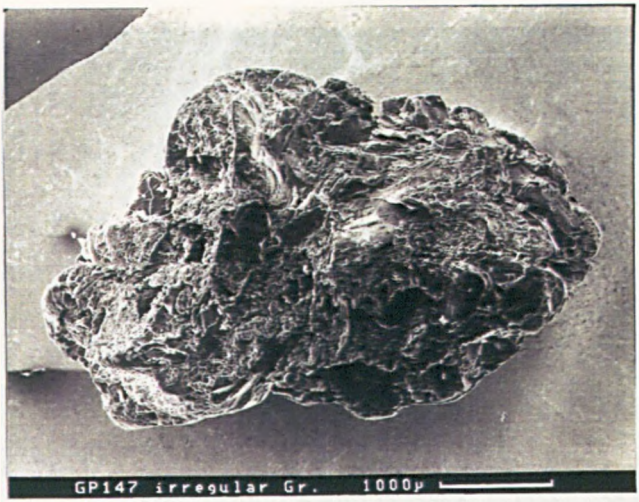

D

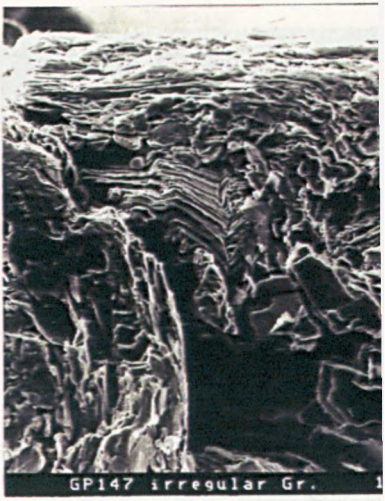

E

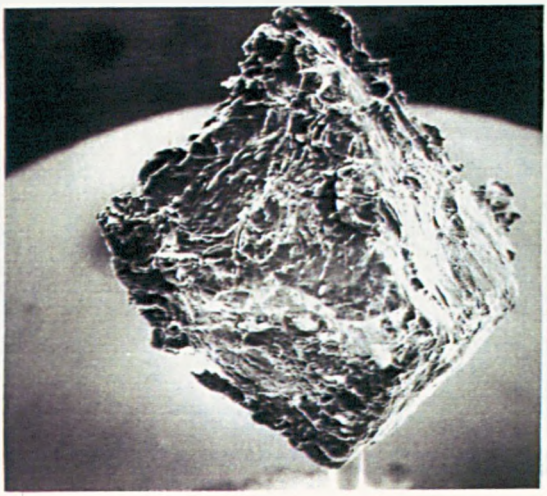

C

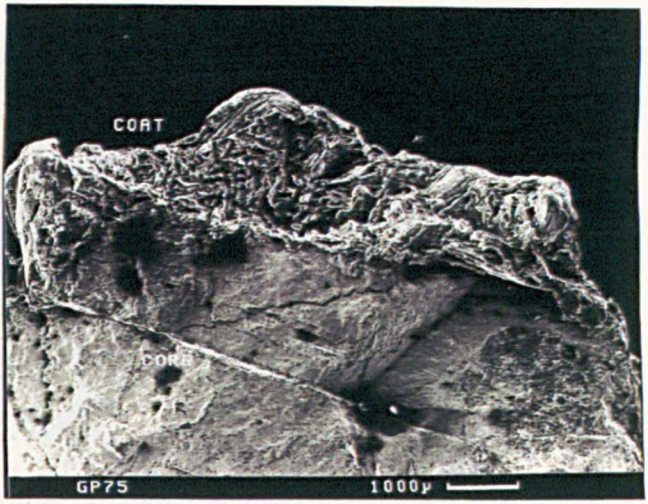

F

3

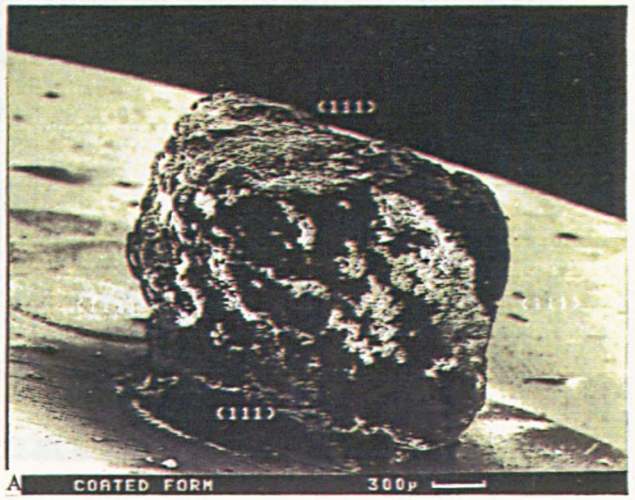
(111)
(111)
(111)
A
COATED FORM
300μ

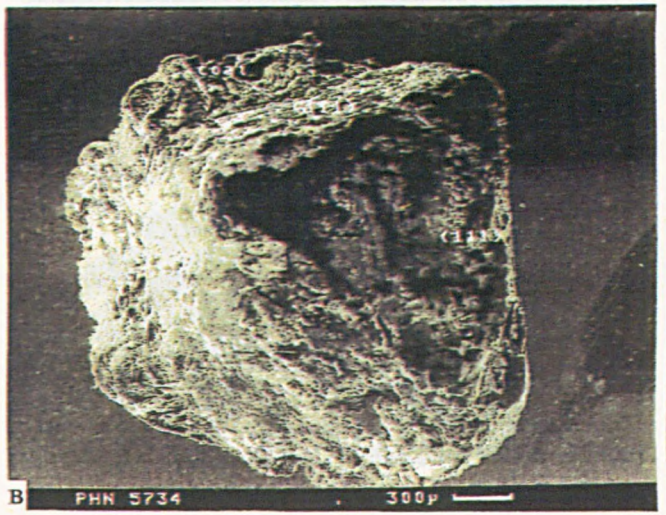
(111)
B
PHN 5734
300μ

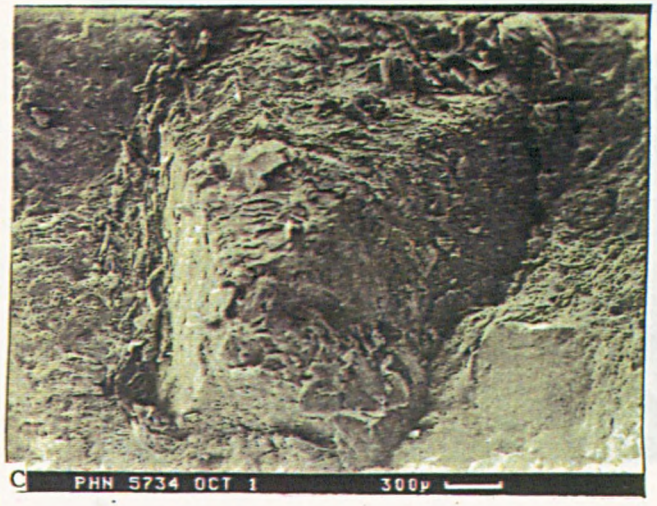
C
PHN 5734 OCT 1
300μ


D
300μ

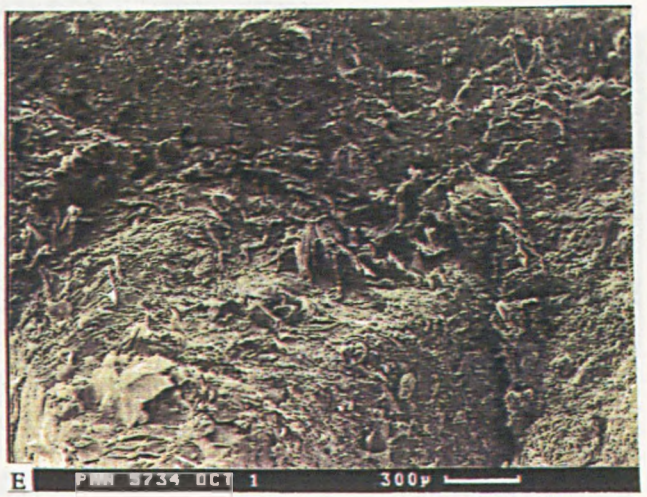
E
PHN 5734 OCT 1
300μ

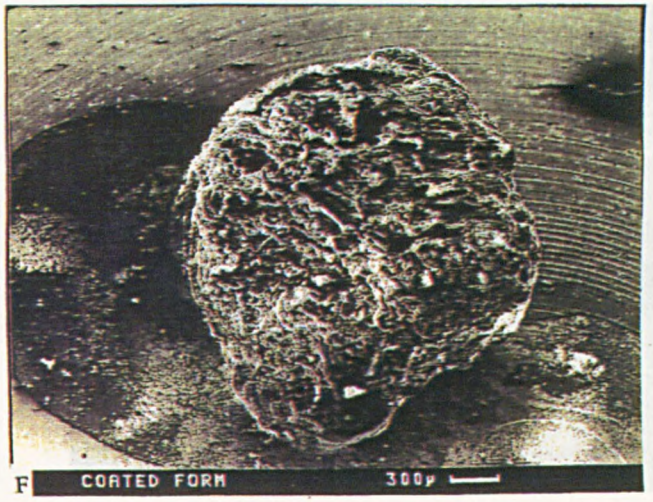
F
COATED FORM
300μ

64


GP 75
100μ

A

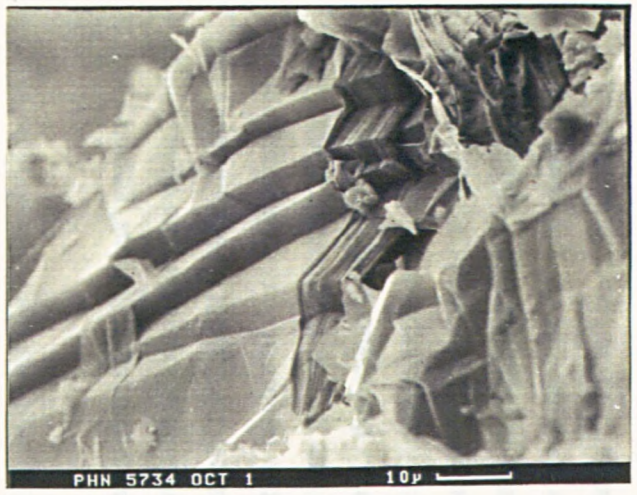
PHN 5734 OCT 1
10μ

B


GP75 internal str.
1000μ

C


(111)
ve TRIGON PHN5734
3μ

D

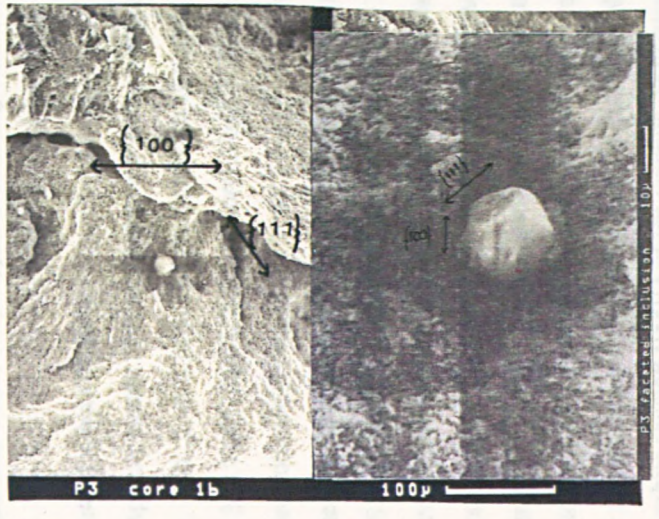
{100}
{111}
P3 core 1b
100μ

E


(111)
GP75 inclusion
10μ

F

in natural diamond specimens (see Orlov 1973).

3:4.3c Twinned Forms:

Flattened triangular aggregates exist in which the two halves of the crystal are related by a twin plane parallel to {111} (Fig 3.2d). These forms are contact twins, twinned according to the the spinel law and are exactly analogous to the macle form exhibited by diamond. The graphite twins have either re-entrant angles or convex angles formed by development of supplementary edges (111) and (111) at the corners. This habit is a growth malformation from octahedral to triangular, platey morphology, a consequence of preferential growth along re-entrant corners due to spinel law twinning (Sunagawa 1984a). Dislocations are orientated in the plane of the twin acting as preferential growth sites. The twinned aggregates do not exceed 3 mm edge length and, as noted by Slodkevich (1980b), have edge/length ratios of betwwen 2.5 and 3, ie. identical to the macle form of diamond. Some contact twins exhibit flattening parallel to the triad axes also occur.

Interpenetration twins, twinned isometric octahedra and twinned, non-uniformly developed, flattened octahedra also occur. These types of twinning also occur in natural diamonds (Orlov 1973).

3:4.3d Coat Graphite:

Approximately 50% of the above graphite forms are surrounded by a coat of "fibrous" graphite (Figs. 3.4a, b, & 3.3f). The coat graphite is typically radially oriented around the core crystal (Figs. 3.3f & 3. 4) and there is a sharp morphological discontinuity between the cores of cubic symmmetry and the more rounded forms of the coats (Fig. 3.3f). On exposing an octahedral form by breaking open a specimen the fibrous coat adheres to the rock substrate, parting from the core crystal along planar {111} faces. S.E.M. secondary electron photographs (Fig. 3.3e) illustrates the irregular, often deformed nature of the coat graphite whose {0001} surfaces are generally highly oblique or perpendicular to {111} of the core graphite or occassionally parallel to {111}. S.E.M. observations also demonstrate that {0001} of the core graphite is approximately parallel to {111} of the octahedra. Slodkevich (1980 b) states that the pinacoidal {0001} faces of the coat graphite are parallel to the {111} faces of the octahedra but this is clearly not generally the case (Fig. 3.f). However, this orientation may result from deformation of the coat graphite causing {0001} of the graphite to become parallel to {111} of the octahedron. One possible interpretation of the re-orientation is that the coat graphite formed first on a rigid diamond substrate and the aggregate suffered plastic shear deformation during graphitization.

Cross polarised reflected light obsevations on polished thin sections of graphite octahedra indicate that they have been deformed at high temperaures. Relatively coarse subgrains in the octahedral core graphite contrast with the irregular crystallites of the coat which contain a high density of kink lamellae which are often bent. The coat graphite is often deformed so that it interdigitates with the surrounding silicate phases. The different deformation styles of coat and core graphite may be a product of a single deformation event, the high mechanical anisotropy of graphite combined with the differing orientation of graphite within the sample producing the observed effects. When the principal deforming stress is applied perpendicular to the {0001} plane of the graphite deformation occurs via dislocation diffusion processes to produce subgrain boundaries. When the principal stress is parallel to {0001} deformation proceeds by dislocation climb and glide to produce kink lamellae (Reynolds, 1968, Jenkins, 1973).

It is difficult to establish the precise morphological variations displayed by the coat graphite as it is commonly left adhering to the host rock when fresh surfaces are exposed. Even when preserved for

examination it is commonly evident that the coat has suffered deformation to some extent due to high temperature crystal-plastic processes or to mechanical extraction of the specimen. Specimens liberated by acid dissolution contain reasonably undisturbed coat graphite. These specimens reveal that the coat transforms the aggregates into ovoid, rounded masses which do not posses crystallographic faces and have irregular surface topography (Fig. 3.4 a and f). In contrast to the study made by Slodkevich (1980a), it was found that not all of the graphite aggregates were surrounded by coats of graphite . The specimen displayed in Figure 3.1 shows no indication of the upper portion having possessed a coat and examination of the junction between the middle of the aggregate and the host rock reveals no evidence either. It is estimated that approximately 50% of the aggregates possessed a coat of graphite. In addition to the above varieties of graphite, flattened, irregular aggregates of graphite are locally abundant (Fig. 3.3d). These forms are of anhedral, sub-rounded outline and do not exhibit any kind of coat/core relationship.

3:4.4 *Summary of graphite morphological characteristics:*

All the regular forms of graphite in the GGP posses cubic symmetry, however, natural graphite crystallises in the hexagonal system, thus the cubic graphite aggregates appear to be pseudomorphs of a cubic mineral. There are a limited number of geologically plausible precursors to the cubic graphite which helps to constrain its origin.

The strongest possibilities for the identity of the cubic mineral are, diamond, and spinel (either magnetite or chromite). The relatively low Cr content of the whole rocks (450 to 1000 ppm) and primary silicate mineralogy, ie. garnet and CPX, together with their low Fe^{3+} contents are not compatible with the GGP originally containing up to 15% of either chromite or magnetite. Furthermore, there is no trace of such a precursor in ashed graphite from the cubic aggregates.

The morphological variations shown by the graphite aggregates have many features in common with natural diamond, especially those originating from eclogite nodules which have not been subjected to high fO_2 conditions of the host kimberlite. Sharp edged octahedra predominate with macles also being locally abundant. The macle edge/length ratio is comparable to that of diamond macles. The only major form of diamond not exhibited by the Beni Bousera aggregates is the tetrahexahedroid (rounded dodecahedra) which is commonly thought to be the result of dissolution of octahedral forms within the kimberlite magma (Orlov 1973, Robinson 1979) or during residence in the mantle (Gurney 1986). There is no evidence to suggest that oxidising fluids comparable to the kimberlite magma have interacted with the Beni Bousera precursor diamonds, thus such dissolution forms would not be expected. The incomplete apical termination of some of the octahedra (Fig. 3. 3b) is commonly observed in natural diamond populations and appears to represent pseudomorphing of the {111} cleavage in the precursor by graphite {0001}. The irregular/anhedral graphite aggregates from the GGP (Fig. 3.3d) resemble forms displayed by carbonado, framesite and polycrystalline aggregates (micro- and phanerocrystalline forms of diamond, Jeynes 1979) and may represent pseudomorphs of such material.

In addition to the morphological similarities between the GGP graphite and diamonds from eclogite xenoliths, the mode of occurrence of the Beni Bousera octahedral graphite in rocks which are of high pressure, upper mantle derivation is compatible with the graphite aggregates representing pseudomorphs after diamond (Slodkevich 1980a,b; Pearson et al. 1989). Slodkevich (1980b) cites the disposition of the graphite octahedra to lower portions of the GGP layers as evidence that the graphite was once diamond, having a density of ~ 3.5 at 50kb which would tend to settle fastest in a magma crystallizing garnet and CPX. Of the two *in situ* GGP layers found in this study, the one outcropping on the track up to

Tazemourte I definitely showed graphite occurring towards one (topographically higher) margin of the layer (Fig. 2.10) whilst the Oued el Jouj layer had a less pronounced bias in the same direction (Fig.2.11). As there are no other consistent indicators of "way-up" in any of the pyroxenites, this criteria is only credible as a way-up indicator if the graphite is definitely after diamond.

S.E.M. observations of the graphite octahedra suface topography features also demonstrate resemblance to diamond. Prominent growth steps are evident on some specimens (Fig. 3.5a&b), comparable to the "growth plates or steps" observed on the faces of diamond, especially those from eclogite xenoliths (Robinson 1984). Despite the coated graphite octahedra showing a certain degree of surface disruption due to mechanical separation of coat from core, triangular patterns and pits are ubiquitous on core {111} surfaces which probably represent the intersection of hexagonal flakes of graphite (Fig. 3.5c). Their apices show no consistent orientation with respect to the apex of the {111} face on the octahedron. In contrast to these features, pronounced trigonal-pyramidal pits have been observed on the {111} faces of two octahedra (Fig.3.5d) which are strikingly similar in internal geometry to the etch pits known as trigons which are common on the surfaces of natural diamonds. The orientation of the trigons is opposite to that of the {111} face of the octahedron and thus analogous to negative trigons on diamonds which are thought to form due to diamond dissolution above 900 °C (Phaal 1962). Dissolution of diamond below 900 °C results in positively oriented trigons.

The above comparisons provide strong evidence that the cubic forms of graphite in the GGP represent graphite pseudomorphs after diamond, the diamonds having undergone the phase change to the lower pressure, higher temperature allotrope of carbon, graphite. This conclusion is consistent with the mantle origin of the GGP and is compatible with the lack of any other precursor mineral. To further substantiate this conclusion single crystal X-ray diffraction studies of the various graphite morphologies in the GGP was undertaken in collaboration with Dr. H.J. Milledge, University College London.

3:4.5 X-ray Diffraction Evidence

The carbonaceous material in the GGP is confirmed as graphite by X-ray powder diffraction, $d_{(0002)}$ for core and coat graphite being 3.352 and 3.354 *A* respectively. The absence of certain lines in the powder diffraction patterns of the graphite is probably due to the lack of total random variation on the specimen wire due to the difficulty experienced in powdering graphite. Well resolved (112) and (114) lines suggest that the graphite from the GGP is well ordered.Laue photographs of the Beni Bousera octahedral graphite reveal sharp, high angle reflections (Fig. 3.6 a&b) with the graphite α doublet well resolved (Milledge and Woods unpublished).

Stereoradiographs of specimen C from PHN 5734 examined by Milledge and Woods (unpublished) revealed the existence of fine grained material having a roughly cruciform shape and lying in a (100) plane in the centre of the octahedron. This feature did not possessfull cubic symmetry, ie the same pattern could not be observed in [010] and [001] directions. Milledge and Woods noted the close correspondence of this pattern with the "central cross" pattern observed in some diamonds utilising topographic techniques (eg. Harrison and Tolansky 1962). The central cross pattern is the surface expected from internal dissolution of diamond at >900 °C (M. Mendelssohn pers. comm.)

The main objective of undertaking single crystal X-ray diffraction studies on the graphite aggregates was to examine the crystallographic orientation graphite crystallites within the octahedra. The nature of any preferred orientation evident could then be compared to that shown by experimentally and naturally

graphitized diamonds. Several graphite aggregates were extracted from the GGP either by chemical dissolution or mechanically. Specimens possessing no coat, or those which retained as little of their coats as possible after mechanical extraction were selected for X-ray study, principally by the Laue method.

Laue photographs of a graphite octahedron (Milledge and Woods unpublished, Fig 3.6 a&b), were taken with the <110> axis of the octahedron vertical and the X-ray beam parallel to the <100> axis. When the specimen is orientated to record the graphite (0002) reflection assuming it is parallel to a particular {111} face, strong preferred orientation is observed (Fig 3.6b and c) due to graphite {0001} planes being parallel to {111} of the octahedron. The actual degree of preferred orientation shown by the specimens is greater than suggested in the Laue photographs as the specimen sizes were in excess of the 2mm in all dimensions, ie. much larger than the diameter of the incident X-ray beam. Figure 3.6c is a copy of a thermal image Laue photograph for another octahedral graphite specimen. This specimen also shows very strong preferred orientation of basal planes of the graphite parallel to {111} of the octahedron. The preferred orientation shown by the Beni Bousera graphite octahedra may be compared to that seen in experimentally graphitized diamonds. Laue photography of a diamond graphitized at 100 kb and 2000°C revealed exactly the same preferred orientation of graphite as that found on the Beni Bousera specimens (Fig. 3.6d) ie. Graphite { 0001 } parallel to {111} of the octahedron. The preferred orientation appar ent in the experimentally graphitized specimen is enhanced due to the small size of specimen used.

A partially coated graphite macle was also studied by the Laue method and found to show only traces of preferred orientation. This may be due in part to the relatively large size of the specimen (4mm) and the presence of residual, misoriented coat graphite. Several other sharp edged graphite octahedra studied did not show any signs of preferred orientation.

X-ray diffraction study of the Beni Bousera graphite aggregates therefore indicates that the crystallographic orientation of the graphite foming some of the aggregates is consistent with that expected for graphitized diamond (Pearson et al 1989) and supports the theory that the aggregates represent graphitized natural diamonds (Slodkevich 1980a,b; Pearson et al 1989). Not all experimentally graphitized diamonds display crystallographic preferred orientation (Lonsdale and Milledge 1964, Evans 1979). Poor preferred orientation is often observed in totally graphitized diamonds (Lonsdale and Milledge 1964, H.J. Milledge pers. comm.). This obsevation may explain the variable intensity of preferred orientation shown by some of the Beni Bousera specimens. If the graphite was pseudomorphic after another pre-existing cubic mineral in the GGP (eg. spinel) then this variable degree of preferred orientation would not necessarily be expected.

Cubic combination forms of graphite have previously been reported from extra-terrestrial material ie. meteorites (Haidinger and Partsch 1846) and have since been reported in fourteen iron meteorites, one enstatite chondrite and one mesosiderite (see review by Okada and Shima 1972). Cliftonite is an aggregate of graphite crystallites occurring in meteorites, typically as cubo-octahedra, octocubohedra, dodecahedra and hexagonal outlines (Brett and Higgins 1969). Urey (1956) has suggested that cliftonite is a pseudomorph after diamond due to the discovery diamonds (as Lonsdaleite) in some meteorites. In contrast to the crystallographic orientation in the Beni Bousera graphite aggregates and graphitized diamonds, X-ray investigation of cliftonite by Grenville-Wells (1952) and Okada and Shima (1972) reveals that the six-fold axes of graphite crystallites are approximately parallel to the <001> and <113> axes of the cubic form. Thus, Grenville-Wells (1952) and Okada and Shima (1972) proposed that cliftonite does not represent graphitized diamond.

Figure 3.6a and b. Laue phototgraphs of Beni Bousera graphite octahedra, after Milledge and Woods (unpublished). c = Thermal image of Laue pattern produced by a sharp edged octahedron form PHN 5734 showing strong preferred orientation of graphite {0001} parallel to {111} of the octahedron. d: Experimentally graphitized diamonds (100 kb and 2000 ^{o}C) showing the same preferred orientation as a, b and c.

X-RAY DIFFRACTION PATTERNS OBTAINED FROM SPECIMEN C

Cu radiation. 30kV. 20mA. Film radius = 3.0 cm.

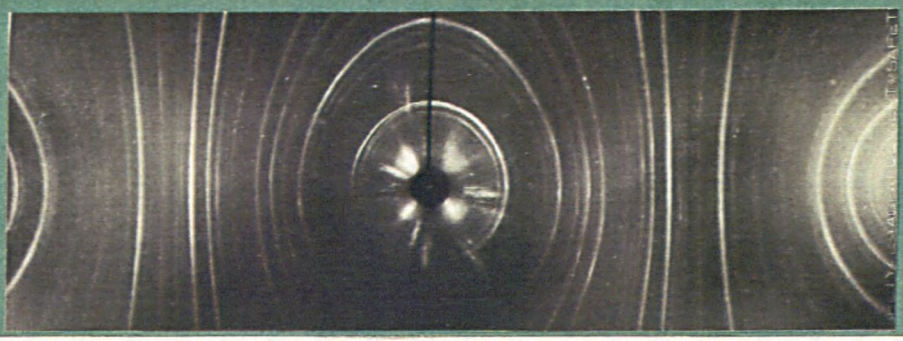

a

Laue pattern, [110]↑, X-rays along [001]. Weak preferred orientation. Note extremely sharp high-angle reflections with α_1, α_2 doublets resolved.

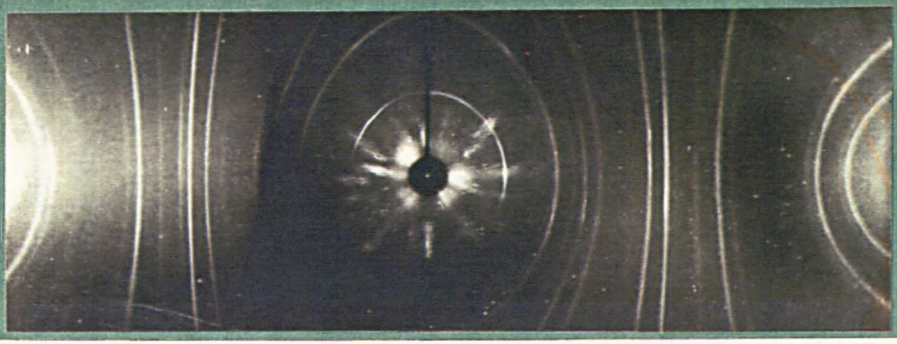

b

Filtered 15° oscillation photograph to pick up (0002) reflexion on the zero layer from graphite plates parallel to an octahedral face. This is orientation to be expected for graphitised diamond.

C

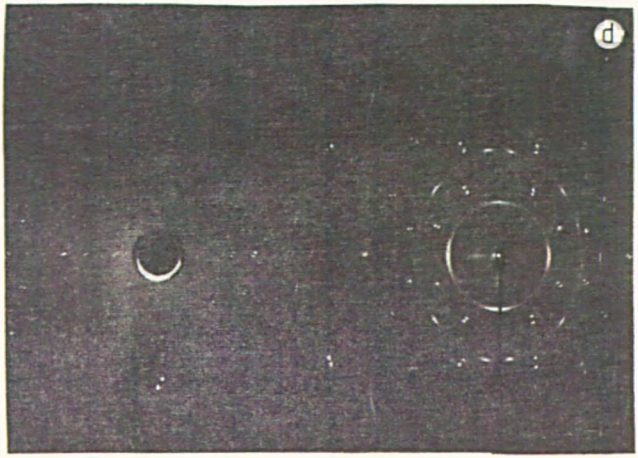

Laue photograph of experimentally graphitized diamond showing the strongly preferred orientation of graphite [0001] parallel to diamond (111) (courtesy of G. Cooper) Cu Kα radiation [110] axis vertical beam along [001].

Cubic pseudomorphs of cliftonitic graphite after cohenite ($(FeNi)_3C$) were synthesized by Brett and Higgins (1969), at atmospheric pressure from carbon bearing Fe-Ni alloys due to the decomposition of cohenite, at 550 °C, to graphite and kamacite. Brett and Higgins (1969) therefore suggested that cliftonite is a pseudomorph of the breakdown of cohenite. Cohenite and cliftonite have been reported from the iron bearing andesitic lavas of Disko Island by Goodrich and Bird (1985), their genesis being ascribed to reduction of the oxygen fugacity of the ascending magma by assimilation of graphite bearing xenoliths. It may be proposed that the Beni Bousera cubic graphite aggregates have a similar origin to cliftonite ie. pseudomorphing cohenite or a similar phase developed either from assimilation of graphitic crustal material during emplacement into the lower crust or during serpentinization. The prevailing oxygen fugacities are often very low during serpentinzation. Serpentinization of the Beni Bousera massif may have caused precipitation of cohenite/ kamacite and its subsequent replacement by graphite. Such a complex origin for the Beni Bousera aggregates has many flaws, particularly with regard to the preservation of the preferred orientation of the graphite in the octahedra. The crystallographic orientation of graphite in the GGP octahedra is inconsistent with it pseudomorphing cohenite/ kamacite. Other problems are the presence of faceted inclusions in the Beni Bousera aggregates (see below), the lack of the full range of forms displayed by cliftonite and no trace of any precursor minerals or associated minerals which always occur with cliftonite eg. kamacite (FeTi), relict cohenite ($(FeNi)_3C$) and shreibersite ($(FeNi)_3P$)

The above discussion illustrates that when cubic aggregates of graphite occur in certain unusual geological circumstances, the crystallographic orientation of the graphite in the aggregates is not that displayed by the Beni Bousera graphite aggregates. The high pressure paragenetic association in the GGP supports the simplest origin of these aggregates as graphite pseudomorphs after diamonds. Table 3.1 summarises some possible precursors for the Beni Bousera graphite aggregates with cubic symmetry and lists reasons for their exclusion from consideration. The lack of physical and chemical evidence for any precursor to the GGP graphite, other than carbon, favours an origin by isochemical, solid state transformation of diamond to graphite (graphitization).

3:5 The graphitization of diamond

The simplest and most plausible explanation for the origin of the Beni Bousera graphite aggregates in certain garnet clinopyroxenite layers is that they are the products of the physical transformation of macro- and microcrystalline diamond to the low-pressure allotrope of carbon, graphite. Consequently it is necessary to elucidate the conditions under which graphitization took place and whether there is any possibility of diamond surviving graphitization either in the Beni Bousera massif or in similar tectonic situations.

Diamond is the thermodynamically unstable allotrope of carbon at the physical conditions occurring at the surface of the Earth. Diamond exists in this environment due to the high activation energy required to initiate the reaction:

$$C_{Diamond} = C_{Graphite}$$

where graphite is the thermodynamically stable form of carbon under normal crustal conditions.

A considerable volume of literature exists concerning the conversion of diamond to graphite, much of which is summarised by Evans (1979). Wagner (1914) reported the discovery of diamonds coated with

POSSIBLE PRECURSOR TO CUBIC GRAPHITE	OCCURRENCE	COMMENTS
COHENITE $(FeNiCo)_3C$	Extra-terrestrial and Sed. contaminated basalt.	Only one known terrestrial occurrence. Crystallographic orientation of graphite incorrect. No evidence of Fe, Ni rich precursor.
OSBORNITE TiN	Extra-terrestrial	No terrestrial occurrence recorded. No evidence for precursor.
SCHREIBERSITE $(Fe_3Ni)_3P$	Extra-terrestrial	No evidence for precursor, incorrect space group.
SPINEL	Terrestrial basic and U. basic rocks.	Bulk rock chemistry not consistent with up to 15% spinel. Would not expect preferred orientation of graphite. Does not explain faceted inclusions.
CUPRITE CuO	Terrestrial, vein/ accessory mineral	No evidence of high concentrations in bulk rock. Does not explain faceted inclusions.
DIAMOND C	Terrestrial and extraterrestrial, kimberlites/ eclogite xenoliths.	Occurrence mineralogically and chemically similar to eclogite. Eclogites can also contain high diamond concentrations. Preferred orientation of graphite correct for graphitized diamond. Transformation is solid state and isochemical.Explains faceted inclusions and coat graphite.

Table 3.1 Possible precursor minerals to the cubic graphite aggregates in the Beni Bousera graphitic garnet clinopyroxenites.

black material from Premier mine, South Africa. The material was chemically identified as graphite. Since then, many partially graphitized diamonds have been found at Premier (Tolansky 1964). Friedel and Ribaud (1924) were the first workers to experimentally graphitize diamond, reporting the development of a black layer on the surface of the diamond when heated to between 1600 to 2100 K. Grenville-Wells (1952) conducted the first detailed study of graphitization and used X-ray methods to reveal the crystallographic orientation of the graphite with respect to the original diamond (the graphite {0001} being parallel to {111} of the octahedron as discussed above). Seal (1958) observed how external graphitization was initiated at discrete nuclei on the diamond surface and found that internal stresses created by internal deformation caused plastic deformation of the diamond.

Howes (1962) heated small (~0.1 ct.) diamonds in a vacuum of less than $5x10^{-6}$ Torr for periods of up to 20hrs at various temperatures. Over this period, graphitization was only detected at temperatures above 2000K after 15 minutes heating. At 2200K small octahedra were found to completely graphitize after 30 minutes. A marked change in the shape of the diamond was observed after graphitization. Graphite formed at the {110} edges of the diamond octahedron more rapidly than on the {111} faces leading to forms with remnant {111} faces surrounded by {110} faces ie a tetrahexahedron. No cube faces were observed to develop. This morphological change accompanying the phase transformation is not always recorded. Experiments carried out by Grenville-Wells (1952), Lonsdale and Milledge (1964) and G.Cooper (unpublished), under vacuum and at 100kb do not reveal such morphological changes. For example, Cooper (unpublished) completely graphitized a sharp-edged octahedral specimen which totally retained its pre-graphitization morphology. Thus the transformation of an octahedron to a tetrahexahedroid is not a consequence of graphitization and is compatible with the absence of {110} faces on the Beni Bousera graphite aggregates.

The work of Seal (1958), Howes (1962) and Evans (1979) indicates that graphitization does not begin uniformly over the entire diamond surface but is initiated at discrete sites of preferential nucleation. Graphite grows from these initial sites to form "three bladed propellor shapes" (Evans 1979), alignment of the three <112> is in the octahedral plane. These nuclei grow by branching until the diamond surface becomes roughened. The *c* axis of this initial graphite is perpendicular to {111} as observed in the X-ray study of Grenville-Wells (1952) and the Beni Bousera graphite aggregates. Individual graphite crystals are approximately 10nm. This result was confirmed by Evans and James (1964) who also found that more extensive graphitization produced graphite crystallites whose *c* axes showed orientations varying within a 30 degree cone perpendicular to {111}. On heating to 2100K, heavy graphitization occurred and the diamond substrate became severely buckled. Selected area diffraction patterns show a wider range of orientations of graphite *c* axes with some crystals oriented along <112> with the *a* axis along <110> of the octahedron. Lonsdale and Milledge (1964) found that on complete conversion of diamond to graphite, the graphite often shows only slight preferred orientation (or none) whilst partial conversion shows very strong preferred orientation of {0001} parallel {111}. In contrast to these early studies Cooper (pers. comm.) found that totally graphitizing diamond at up to 100kb led to graphite aggregates which retained excellent preferred orientation of graphite {0001} parallel to {111} of the octahedron.

From these observations, it appears that when diamonds are graphitized under high pressures, comparable to those prevailing in the upper mantle regions where diamonds are stablized, they tend to retain much of the preferred crystallographic orientation acquired during initial graphitization and retain their primary (often octahedral) form. These observations are compatible with the hypothesis that the Beni Bousera graphite aggregates represent pseudomorphs after diamonds.

The increased dispersion of graphite *c* axes after high degrees of graphitization of diamonds in vacuum is probably due to two main reasons (Evans 1979). The diamond surface becomes roughened and some crystals tend to orient themselves obliquely to the {111} surface. Also, the formation and growth of new graphite at the diamond/graphite interface displaces and exerts force on the earlier formed crystallites causing them to alter their orientation. A lack of confining pressure allows this to occur readily. High confining pressures during graphitization, eg. in the mantle, favour retention of the initial preferred orientation of the graphite as in some of the Beni Bousera graphite aggregates.

In addition to external graphitization, Howes (1962) noted that many diamonds subjected to high temperature under vacuum displayed signs of internal graphitization associated with an increase in internal strain revealed by increased birefringence. The molar volume increase associated with the transformation of diamond to graphite is approximately 55% (associated with a ~ 50% density reduction). This large volume increase would act to inhibit further internal graphitization due the internal pressure created (Howes 1962). The internal graphitization noted by Howes (1962) formed "platelets" in {111} and needles in <110> directions. Evans (1979) proposed that internal graphitization is initiated at internal microcracks or around inclusions where space was available to accomodate the transformation. These observations probably account for the "inclusions of graphite" commonly observed in natural diamonds. The presence of large silicate inclusions within the Beni Bousera graphite would thus promote some degree of internal graphitization (as would the presence of any internal flaws eg. microcracks) in addition to the predominant, external epitaxial transformation.

The volume increase which must have occurred when the Beni Bousera diamonds were graphitized was probably accomodated by crystal plastic deformation mechanisms in the surrounding silicates. Further shearing and associated deformation during ascent of the hot mantle rock body from the diamond stability field would tend to overprint any signs of the early deformation in the surrounding silicates and also deform the graphite aggregates. The presence of sheared and flattened octahedra and macles demonstrates that deformation of the graphite has taken place in the GGP layers.

Slodkevich (1980b) notes radially orientated and concentric ring cracks in garnet around the graphite octahedra and cracking and granulation of adjacent CPX . These cataclastic effects were ascribed by Slodkevich (1980b) to expansion during graphitization of diamond. Such features have not been confirmed in this study. Temperatures must have been high enough during graphitization for any deformation of surrounding silicates to be accomodated via intracrystalline plasticity, hence brittle failure appears unlikely.

3:6 The origin of the graphite coat on the GGP graphite octahedra

An analogy may be drawn between the graphite coat surrounding euhedral core forms and coated diamonds which are surrounded by a fibrous diamond coat of variable thickness (see below). The question of whether the coat graphite was once a diamond coat on the core diamonds is of great significance in determining the origin of this late diamond overgrowth. Gurney (1989) and Boyd et al (1987) have proposed that diamond coats grow as late stage overgrowths in the kimberlite source region prior to eruption. If the Beni Bousera coated graphite aggregates represent graphitized coated diamonds this interpretation cannot be correct as the peridotite massif shows no evidence of interaction with kimberlitic magmas.

difference in crystallographic orientation suggest that the Beni Bousera coated graphite aggregates are graphitized coated diamonds.

The shape assumed by coated diamonds containing regular octahedral cores is a function of the thickness of their coat (Lang 1964). As the coat thickens, sectors of radial growth become more dominant, the diamond aggregate progressively becoming more rounded. The form of a thickly coated diamond may approximate to a sphere (see Orlov 1974). Approximately 50% of the Beni Bousera graphite aggregates are coated, this high proportion is reconcilable with the occurrence of diamond deposits such as in Zaire or Sierra Leone, where high percentages of coated stones are recorded (90 and 50 % respectively, Harris 1987).

Thinly coated diamonds often posses well defined {110}, {100} and {111}faces, forming rhombicuboctahedra (Machado et al. 1982), but no such forms are found in the GGP. For for the Beni Bousera aggregates to be graphitized coated diamonds most of the original stones must have been of the thickly coated forms such as thoseillustrated by Orlov (1973). Grenville-Wells (1952) graphitized coated diamonds under vacuum and found that the coats graphitized at lower temperatures than the cores but did not publish the temperature difference. This author also noted that the Laue spots of the coat became very diffuse on partial graphitization. This result was confirmed by Lonsdale and Milledge (1964) and is compatible with the inferior lattice quality of the coat diamond thus promoting graphitization, especially by internal graphitization. The Beni Bousera coat graphite therefore may have been the first graphite to form, undergoing the phase transformation from diamond to graphite at a lower temperature than the more perfect core diamond. The 1.54 fold volume increase on subsequent graphitization of the core diamond would exert stress on the previously formed coat graphite, explaining the discordant orientation of coat and core graphite. This stress possibly caused the deformation features seen in the coat graphite ie. bending of crystals and generation of slip twins and would have forced the coat graphite against the surrounding silicates forming the observed interdigitating relationship. The presence of subgrain boundaries rather than slip twins in the core graphite is consistent with this applied stress being perpendicular to the {111} faces of the octahedra, ie. perpendicular to the {0001} direction of the core graphite.

It may be argued that the coat graphite represents a later precipitation around the original euhedral core graphite, the coat graphite possibly originating from metasomatic fluids associated with late stage Cu-Ni mineralised graphite veins that cross cut the peridotites. Field evidence argues strongly against an origin of the coat due to hydrothermal precipitation. No signs of any graphite veining are evident at the GGP boundaries or within the layer. Furthermore, there is no evidence of any associated Cu-Ni mineralization in the GGP, ashed graphite of the coat and core being very poor in trace elements with no high values of Cu or Ni (Slodkevich 1980b). A space problem also exists if coat production is to have occuurred later than the cores in solid rock, any dilation to allow extra growth would not have permitted the radially symmetric coat development. Rarely, 1 to 2m thick graphite bearing veins are observed to cross-cut non-graphitic garnet clinopyroxenite layers along joint planes. However, there is no infiltration of graphite into the GP layer from the sides of the vein and no traces of graphite in the GP layer. This evidence argues strongly against any origin of the GGP graphite via late stage metasomatism of C-H-O bearing fluids.

3:7 Raman spectroscopy of the Beni Bousera graphites

3:7.1 Introduction

Tuinstra and Koeinig (1970) used Raman spectroscopy to distinguish degrees of order in carbonaceous material. The degree of order reflects the nature of any carbonaceous precursor and the temperature to which this material has been subjected, either during formation or subsequent metamorphism.

Heat treatment of disordered carbonaceous matter leads to the following changes in crystallographic structure.

1) The structure changes from turbostatic towards graphitic with the appearrance of distinctive graphite *hkl* X-ray lines.

2) The $d_{(0002)}$ spacing of the material decreases from a typical value for turbostatic carbon of 3.44 *A* to 3.354 *A* for pure graphite.

When carbon shows a well developed layer structure in which the atoms are arranged in open hexagons and the layers show some degree of order in the stacking sequence it may justifiably be called graphite (Reynolds 1968). Both first order (1200 to 1700 cm^{-1}) and second order (2400 to 3300 cm^{-1}) Raman bands are utilised in characterizing the degree of crystallinity of carbon (crystallite size) (Tuinstra and Koenig 1970, Nemanich and Solin 1979, Lespade et al 1982). This is because the Raman spectra of graphite is due to in-plane vibrations and hence is a reflection of crystallite size in the crystallographic *a* direction (Wopenka and Pasteris in press). Single crystals of highly ordered graphite have the fewest, best defined Raman bands of all carbonaceous/graphitic material. The ratios of the integrated intensities of certain bands are a function of crystallite size (Tuinstra and Koenig 1970). For crystals greater than 300 *A* in the *a* direction a single first order band (E_{2g2}) exists at 1582 cm^{-1} (+/- 1 cm) which is characteristic of well crystalline graphite (Wopenka and Pasteris in press). For crystals smaller than 300 *A* in the *a* direction additional disorder induced first order bands appear at ~1360 cm^{-1} and 1622 cm^{-1} and the spectra is further modified by the development of a shoulder on the high wave number side of the 1582 cm^{-1} band (J.D.Pasteris pers. comm). The 1622 cm^{-1} and 1582 cm^{-1} bands cannot always be resolved from each other (Wopenka and Pasteris in press). In-plane crystallite size (in the *a* direction) can be derived from the peak intensity ratio (I_{1360}:I_{1600}) by reference to calibration curve relating Raman spectra to X-ray diffraction data (Tuinstra and Koenig 1970).

In well crystallized graphite three groups of "second order overtone bands" exist (see Wopenka and Pasteris in press for details). Raman spectroscopy can be used to measure in-plane crystallite size from ~ 30 *A* to ~ 350 *A*. Temperature controlled experiments on synthetic graphite show rapid increase of in-plane crystallite size from ~ 30 *A* to ~ 350 *A* over a temperature interval of 400 ^{o}C from 1600 to 1200 ^{o}C depending on the prevailing pressure (eg. Kelly 1981). However, Wopenka and Pasteris (in press) noted that a specific degree of crystallinity of graphite is attained at much lower temperature in naturally occurring graphite than for synthetic, highly oriented pyrolitic graphite (HOPG). This observation has previously been noted in X-ray diffraction studies by Grew (1973) and is attributed to catalytic effects of the coexisting silicates and other prevailing geological conditions. The presence of graphite intercalation

compounds (GICs) may further complicate Raman spectra of natural graphites causing shifts in the peak positions and ambiguity in the interpretation of certain disorder induced bands (Wopenka and Pasteris in press). Increased layer ordering in the kinzigite graphite may have been induced by contact metamorphic effects associated with peridotite emplacement (which converted kyanite to sillimanite Komprobst 1974). Much higher temperatures are required experimentally to create highly ordered graphite than those needed in geological environments. This is probably due to a combination of various factors: the absence of silicate and carbonate phases in experiments, which may act as catalysts, the shorter duration of prevailing experimental pressure/temperature conditions, and the absence of a fluid phase (Grew 1974).

3:7.2 Results for Beni Bousera graphite

The Raman spectra of graphite samples from veins, kinzigites and the GGP were obtained by Dr. J.D. Pasteris (University of Washington-in-St.Louis) using 4 to 5 hour scan times. The resulting spectra can be compared to natural graphite spectra obtained from rocks of known metamorphic grade, up to granulite facies, using a data base recently established by Pasteris (pers. comm.). Hence, a relative order of crystallinity can be established for the samples. All the Beni Bousera graphite samples were found to have a high degree of crystallinity with many of the samples being fully ordered graphite (Fig. 3.7) with a prominent 1581 cm^{-1} peak and a total lack of disorder induced peaks. The order of increasing crystallinity is given below:

SAMPLE	LITHOLOGY	EQUIVALENT METAMORPHIC GRADE
GP75 CORE	GGP	Andalusite-sillimanite
GP5	KINZIGITE	Sillimanite-granulite
GP161	KINZIGITE	Granulite
GP9	VEIN	Granulite
GP147 IRREG	GGP	Granulite
GP147 CORE	GGP	Granulite
GP147 COAT	GGP	Granulite

These results indicate that all the Beni Bousera graphite samples have been subjected to temperatures sufficient to produce well crystalline, fully ordered graphite. Spectra from a GGP core-coat graphite pair from sample GP147 were identical. The slight differences in apparent metamorphic grade between some of the spectra may be the result of post-crystallization tectonic deformation of the graphite rather than any temperature of crystallization differences (J. Pasteris, pers. comm.). This is supported by the presence of subgrain boundaries, visible in reflected light, in graphite from the GGP and the kinzigites. Great care was taken during sample preparation to ensure minimal physical damage was inflicted on the samples as this can cause spectral anomalies (J. Pasteris, pers.comm.). Although different carbonaceous precursors will

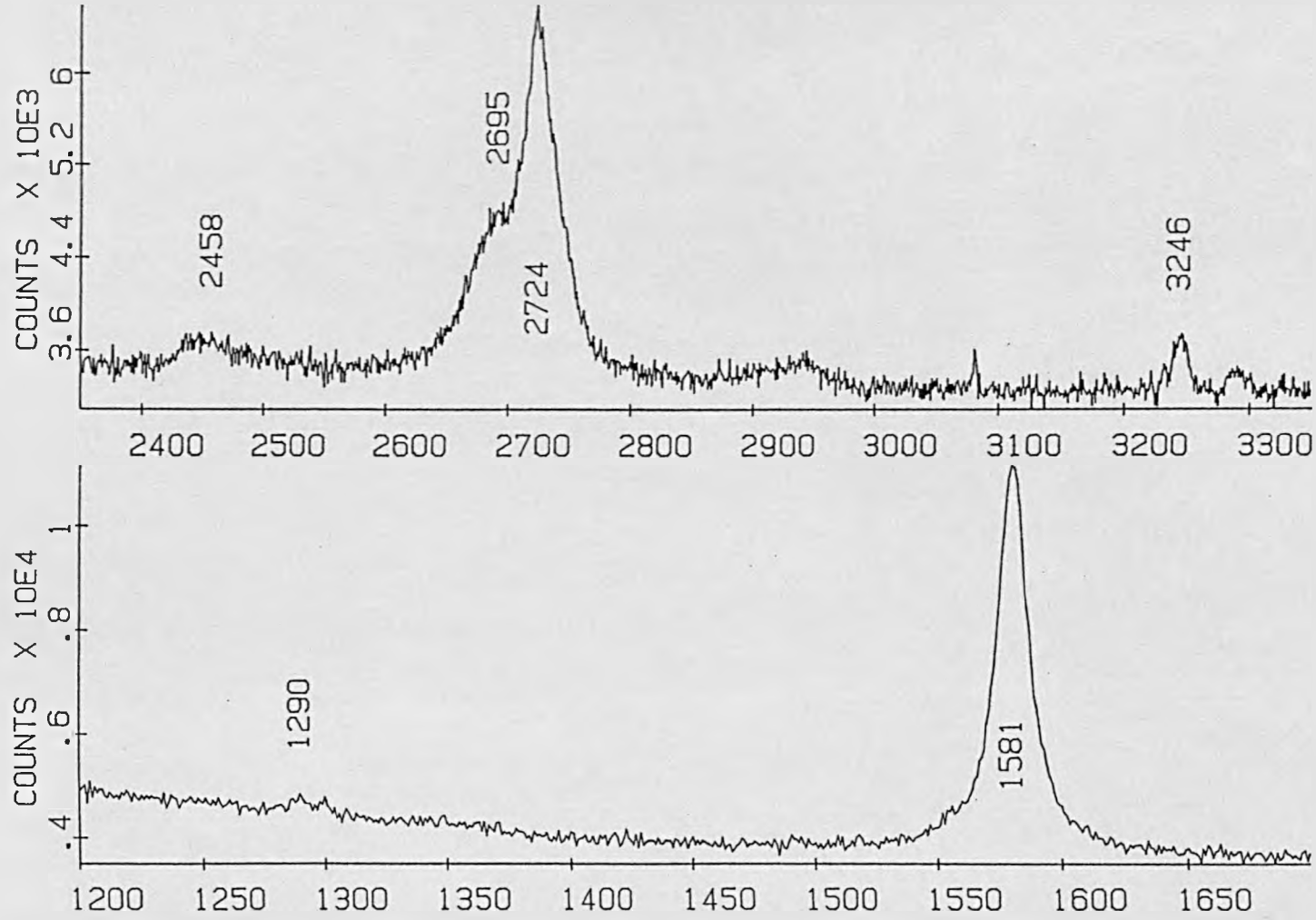

Figure 3.7. Raman spectra of GP147 core showing characteristics of fully ordered graphite. Spectra obtained by a 4 hour scan, lower axis cm^{-1}. (courtesy Dr J.D.Pasteris).

recrystallise to differing extents under the same P/T conditions, a limit is reached at ~ 600 °C and >4kb, where all graphites become fully ordered (Grew 1974) and hence spectrally, virtually indistinguishable.

The main conclusions to be drawn from the Raman spectra of the various Beni Bousera graphite parageneses are as follows:

1, All the graphite appears to have crystallised close to granulite facies conditions, slight variations possibly being due to later tectonic deformation producing spectral deviations.

2, Graphite samples from the vein graphite, kinzigite and GGP are generally spectrally indistinguishable suggesting that either all the graphite originated from similar carbonaceous precursor ,or, more likely, that the samples have been subjected to such high P/T conditions that all spectral information regarding the nature of the precursor carbon has been lost. Raman spectroscopy therefore does not provide useful evidence for or against a genetic link between the three Beni Bousera graphite parageneses.

3, The core and coat graphite from GP147 are spectroscopically identical and do not appear to have crystallized separately.

3:8 Mineral inclusions within the GGP graphite aggregates

3:8.1 General mineralogy

Over 50% of the graphite octahedra have been found to contain mineral inclusions when sectioned. Core graphite contain mineral inclusions of silicates, oxides and sulphides. The 3-dimensional form of such inclusions is difficult to observe due to the opaque nature of graphite but has been studied on octahedra that have been broken open, cut in thin sections or oserved in radiograph images (Fig. 7.2b).

Mineral inclusions of the core consist of: CPX, garnet, ilmenite, and pyrrhotite, some plagioclase is observed as an exsolution product in the CPX. CPX is the predominant inclusion phase, garnet and ilmenite being scarce. Only one garnet inclusion has been found in this study whilst ilmenite was not observed, but is reported by Slodkevich (1980b) . The size of the inclusions vary greatly from 10 μm to 4 mm across and may occupy up to 60% by volume of the octahedral cores.

The coat graphite contains scarce inclusions of pyrrhotite which are locally abundant close to the margin of the coat. This is the only type of mineral inclusion recorded in the coat graphite.

3:8.2 Clinopyroxene:

CPX appears optically colourless under the microscope, containing OPX exsolution lamellae parallel to {100}, some exsolution lamellae are deformed by kink bands. None of the inclusions observed in thin section were in optical continuity with the host rock minerals ruling out the possibility of graphite infiltration and crytallization around the pre-existing host rock mineralogy. Some CPX inclusions show evidence of retrograde breakdown with exsolved plagioclase and spinel along OPX exsolution lamellae. CPX inclusions also contain coarse subgrain boundaries implying crystal plastic deformation took place at mantle temperatures possibly during deformation prior to encapsulation in the diamond, or as a result of internal stresses produced within octahedra during graphitization. Laue photographs reveal the presence of "granulated" CPX within some graphite aggregates which suggest that the mineral inclusion has been disrupted. This feature may be due to extraction by HF dissolution, the porous nature of the graphite allowing the HF to partially dissolve the CPX inclusion.

3:8.3 Garnet:

Slodkevich (1980b) noted the scarcity of garnet inclusions in the graphite aggregates .Only one garnet inclusion was found during this study. The crystals are transparent under the microscope, optically colourless and similar to the host rock garnet. The paucity of garnet inclusions in the graphite aggregates suggests that diamond crytallization occurred for an extended period when only CPX was on the liquidus.

3:8.4 Pyrrhotite:

Pyrrhotite occurs as irregular droplets both on the surfaces and within the CPX inclusions in the graphite, confirming its origin as a primary mineral. Slodkevich (1980b) pointed out that most of the pyrrhotite included in the CPX inclusions occur along the faces of the CPX crytals. Significantly there is no chalcopyrite associated with the pyrrhotite inclusions, chalcopyrite is a scarce secondary mineral in the GGP host rocks. Pyrrhotite is a common inclusion in diamonds and may occur alone without coexisting silicates as part of the sulphide suite of inclusions in natural diamonds (Meyer 1987). Sulphides are a locally abundant inclusion phase in both P- and E-type diamonds suggesting growth in enviro ∩ ments of high fS_2.

3:8.5 Ilmenite:

Slodkevich (1980b) documents the occurrence of sub-rounded, equant ilmenite within the graphite aggregates, close to the surfaces of CPX inclusions. The ilmenite forms crystals up to 0.01mm across and is locally abundant.

3:8.6 Graphite within CPX inclusions:

Some graphite cubes are intergrown or totally included in the CPX inclusions (Slodkevich 1980b). Graphite "inclusions" in CPX were observed in thin secion occasionally in this study. Their exact form in 3 dimensions and whether they represent true inclusions was difficult to establish. The graphite inclusions observed by Slodkevich (1980b) are orientated with {0001} parallel to {100} of the cube form. Slodkevich (1980b) interpreted these intergrowths as also representing pseudomorphs after diamond but did not provide sufficient description of the inclusions for this hypothesis to be examined. Diamond inclusions within diamonds have been reported in the literature eg. Sobolev (1979). If a diamond precursor is sought for the cubic graphite inclusions in CPX reported by Slodkevich (1980b) the change in diamond shape from early formed cubes to predominantly octahedra may reflect a change in the P/T conditions of diamond growth, the octahedral form of diamond generally being regarded as the high temperature growth form. The presence of cubic graphite included in CPX crystals is strong evidence in favour of a primary origin for the carbon in the GGP rather than it being a late stage precipitate from crustal fluids.

3:8.7 Faceting of mineral inclusions:

All the minerals included in the Beni Bousera GGP graphite aggregates have been observed to occur in natural diamonds (Meyer and Tsai 1976, Harris and Gurney 1979, Meyer 1987). No primary minerals have been found in the Beni Bousera graphite aggregates that do not occur as inclusions in natural diamonds. The large size of some inclusions, and more importantly, the large volume of the octahedron they occupy in the graphite (Figure 5.2b) is uncommon in diamonds. This may be due to fragmentation of diamonds containing such large inclusions on reaching low confining pressures near the Earth's surface.

Expansion of the mineral inclusion due to pressure release and possible phase changes/exsolution will create high internal stresses in the diamond which may lead to fragmentation. This is probably the cause of the "explosion" of some diamonds when removed from their confining host rock (P.H. Nixon pers. comm.).

Thin sections through the Beni Bousera graphite aggregates most commonly reveal inclusions with no clearly defined crystallographic faces. However, Slodkevich (1980b) presented drawings of sections through octahedra in which CPX and garnet inclusions exhibit excellent cubo-octahedral facetting such that the cube and octahedral faces of the inclusion are parallel to the cube and octahedral directions of the host octahedron. Good crystal faces on silicate mineral inclusions in the graphite were also observed in this study using SEM. Figure 3.5 e&f show CPX inclusions with cubo-octahedral faceting in the centre of fractured, coated graphite octahedra. The CPX was identified using the E.D.S detector on the SEM. Radiographs also reveal the presence of large faceted inclusions of CPX within graphite aggregates (Fig 3.2b1).Precise interfacial angles have not been measured in this study due to the prohibitively small size of the inclusions.

Inclusions possessing cubo-octahedral faceting in the graphite octahedra exhibit specific orientations with respect to the crystallographic forms of their graphite host. CPX inclusion forms are atypical of normal monoclinic pyroxene habits, being much more equant and displaying cubic symmetry. The principal faces of the CPX inclusion ie {111} and {100} are parallel to the {111} and {100} directions of the host graphite octahedron. This epitaxial relationship where facets aquired by the inclusions take the form of a negative crystal of the host mineral (Meyer and Tsai, 1976, Sobolev et al. 1979) is very characteristic of mono- and polyminerallic inclusions within diamonds. The cubo-octahedral faceting displayed by CPX and garnet inclusions in the Beni Bousera graphite octahedra is thus powerful evidence that the graphite was formerly diamond.

Inclusions within diamond possessing diamond imposed morphologies probably nucleated on growing diamond surfaces (Meyer and Tsai 1976) and hence are of syngenetic origin with respect to the diamond. Unorientated inclusions exhibiting their common habits also occur in the Beni Bousera graphite .These inclusions probably grew prior to diamond growth or encapsulation in a similar manner to unfaceted diamond inclusions (Harris 1968).

3:9 Summary of evidence for the origin of the graphite within the GGP

The evidence in favour of the graphite aggregates in the GGP being pseudomorphs after diamond is summarized below:

1) All morphological forms displayed by the graphite are exhibited by macro- or microcrystalline diamond.

2) X-ray diffraction and SEM evidence indicates that some graphite aggregates retain strong preferred orientation of graphite {0001} parallel to {111} of the octahedra, ie. the same preferred orientation displayed by graphitized diamonds. Other occurrences of cubic graphite aggregates replacing minerals such as kamacite do not show this preferred orientation.

3) Raman spectra of the graphite in the GGP are consistent with graphite crystallization at very high temperatures (>600 ^{o}C).

4) Surface features of the octahedra observed by SEM are analogous to those observed on natural diamonds, including the presence of scarce, negatively oriented trigons.

5, The graphite aggregates contain the same silicate and sulphide inclusion suite as E-type diamonds. The host rock containing the graphite has a re-equilibrated eclogite mineralogy (see Chapter 4). Eclogites are a xenolith type from kimberlites and lamproites sometimes found to contain very high concentrations of diamonds (eg Robinson et al 1979).

6, The cubo-octahedral faceting displayed by some CPX and garnet inclusions in the graphite aggregates, with faces parallel to the same directions in the host octahedron, are a characteristic of mineral inclusions in diamonds.

No evidence has been found in this study to support any alternative origin for the graphite in the GGP. An origin as graphitized diamonds is not contradicted by any available evidence and provides the simplest explanation for the origin of the graphite aggregates.

3:10 Discussion: The origin of the Beni Bousera precursor diamonds

Diamonds may grow metastably during kinetically favourable conditions in P/T conditions far outside their thermodynamic stability field. Eversole (1962) first claimed to have synthesised diamond via decomposition of methane at 0.1 to 1 Torr and 1000 ^{o}C, epitaxially depositing finely crystalline diamond on a pre-existing diamond nuclei. Since these initial experiments other workers eg. Matsumoto et al (1985) have initiated epitaxial diamond growth on diamond surfaces in microwave plasmas in a high temperature methane/hydrogen mixture. These chemical vapour deposition techniques (CVD) generally do not involve diamond nucleation and such growth conditions hardly seem applicable to geological environments, usually requiring microwave or plasma conditions.

Diamonds grown under metastable conditions are characterized by a high frequency of multiply twinned crystals or abundant cubo-octahedral type (Matsumoto 1982) . Metastabily grown diamonds also show large degrees of non-faceted growth (Sunagawa 1984b). The euhedral, sharp edged graphite morphologies of cubic symmetry seen in the GGP layers are characterized by octahedra lacking cube faces and showing no evidence of solution. This suggests that the precursor diamond grew at high temperatures, close to equilibrium conditions. Although synthetic diamonds are thought to grow at higher temperatures than natural diamonds and in different media, the relative P/T relationships of their growth forms are thought to be applicable to natural diamonds (Sunagawa 1984b). Thus, the octahedron is thought to be the most favourable high temperature high pressure form of diamond. The predominance of sharp edged octahedral forms in the GGP argues against a metastable origin for the Beni Bousera precursor diamonds.

If the graphite coat on the GGP graphite aggregates represents graphitized diamond coat and the irregular, anhedral graphite forms were originally framesites or carbonado (see Jeynes 1978 for definition of terminology) we may make inferences about the growth conditions of radially orientated-fibrous and polycrystalline diamond in the mantle. The fibrous growth exhibited by diamond coats suggests that it is the product of rapid crystallization. Boyd et al (1987) found diamond coats to be extremely homogeneous with respect to their carbon isotopic composition. These two observations led Boyd et al (op. cit.) and Gurney (1989) to suggest that diamond coats are the products of rapid crystallization from the host kimberlite melt which entrains pre-existing diamonds as xenocrysts. Such an origin is supported by C and N isotopic data for coated diamonds from kimberlites (Boyd et al 1987).If the Beni Bousera coated graphite aggregates are considered to be graphitized coated diamonds, then the coats of the precursor diamonds could not have precipitated from a kimberlite magma.

Sunagawa (1977 and 1984) discussed the generation of coated and polycrystalline diamond in terms of the relationship between the supersaturation, σ, and the chemical potential difference between solid and

liquid phases, $\Delta\mu/\kappa T$. According to Sunagawa (1984a and b) there are two transitional supersaturations, σ^* and σ^{**} (Figure 3.8) . Above σ^{**}, a high carbon supersaturation, the morphology of new crystals is fibrous to spherulitic, therefore in a system below σ^{**}, if the sytem changes to higher supersaturation conditions, fibrous to spherulitic growth occurs. Below σ^* (a relatively low carbon supersaturation) crystals occur as polyhedra bounded by flat surfaces due to crystal growth being controlled by interface and dislocation kinetics (Sunagawa 1984a & b). This means that monocrystalline diamond octahedra represent crystals grown under relatively low supersaturation ie below σ^*. Consequently polycrystalline diamond aggregates, framesites and carbonado etc. represent diamond growth in abnormally high supersaturation conditions, above σ^{**} (Fig. 3.8).

Coated diamonds are crystals which have undergone changes in environmental conditions during their growth histories either due to changes in local P/T conditions or due to an increase in the effective carbon supersaturation of their growth reservoir. The original presence of graphite resembling diamond grown under high, low and changing conditions of carbon supersaturation in the GGP at Beni Bousera demonstrates a two stage history of diamond growth in these rocks. An intial period of diamond growth took place under conditions of relatively low carbon supersaturation ($< \sigma^*$) in the diamond stability field at high temperatures during which most of the octahedra and macles were formed. This was followed by a period of growth from a reservoir of high supersaturation ($> \sigma^{**}$) which may have been induced by changing the abundances of carbonaceous species in the melt or fluid from which the diamonds were growing. A coating of fibrous diamond was then deposited on the nuclei of earlier formed crytals and polycrystalline, microcrystalline diamond also precipitated. Although none of the petrographical evidence examined so far indicates a likely cause of changing diamond growth conditions it is possible to speculate that the impetus required to alter the physiochemical conditions of diamond growth may have come from the initiation of diapirism in the surrounding mantle which began upward movement of the peridotite massif from within the diamond stability field towards the crust (see Chapter 8).

3:3.11 Comparison of the Beni Bousera graphites in garnet clinopyroxenites with diamonds in eclogite xenoliths:

Diamondiferous eclogites described by Wagner (1914) and Williams (1932) from southern Africa have subsequently been reported from many more kimberlite pipes in southern Africa and also in Siberia (Sobolev 1979). One of the stongest similarities between the GGP and diamondiferous eclogites is the high diamond or original diamond concentration in each rock type and the form of the diamonds contained within them (Table 3.2). Diamonds extracted from eclogite xenoliths differ markedly in terms of their form from diamonds extracted from the kimberlite itself (Robinson 1979). Diamonds from the eclogite xenoliths are predominantly octahedral (the high temperature form). Interpenetration twins and aggregates are also common in diamonds from eclogites (Robinson 1979, Robinson et al 1984). Tetrahexahedra, the dissolution forms of octahedra, are rarely present. This contrasts with the high abundance of tetrahexahedra found in kimberlites. The abundance of sharp-edged octahedra in eclogite xenoliths is thought to be due to the eclogite derived diamonds being protected from dissolution by the oxidising kimberlite magma. The distribution of morphologies in diamondiferous eclogite xenoliths is thus comparable to that seen in the Beni Bousera GGP. (Table 3.2).

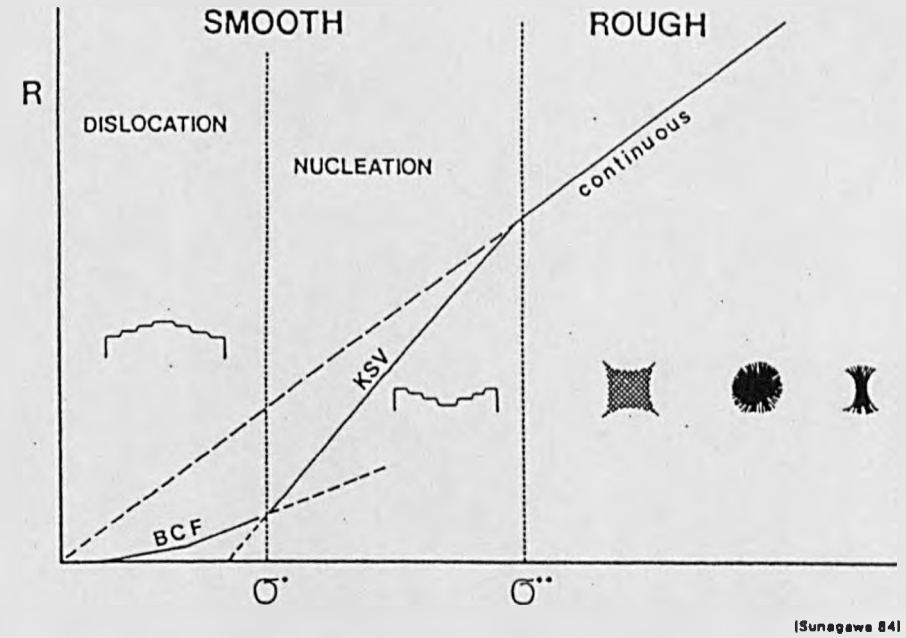

Fig. 3-8 Correlation between diamond growth rates and morphology. Schematic drawing to show different morphologies of diamond crystals depending on growth rate (R) vs supersaturation relation (σ) (from Sungawa 1984).

Table 3.2 Comparison of the diamond grade and relative abundances of diamond morphology in diamondiferous eclogites xenoliths (D.ECLOG), Graphitic garnet clinopyroxenites (GGP) and discrete diamonds from kimberlite pipes.

FORM	GGP	D.ECLOG	KIMB
Sharp-edged octahedra	Common (predom.)	Common (predom.)	variable/scarce
Tetrahexahedroids (+ resorbed forms)	Absent	Rare	Common
Irregular	Rel. common	Rare	Variable
Interpenetration twins and aggregates	Common	Common	Variable
Coated stones	Common/predom?	Non recorded	Highly variable

Significantly, the low fO_2 environments of the eclogites and GGP contain abundant sharp-edged octahedra whereas diamonds exposed to the more oxidized kimberlite contain abundant dissolution forms. Another implication from the abundance of octahedra in the GGP and eclogite environments is that many of the diamonds form at high temperatures, close to the graphite/diamond equilibrium curve at high pressures. This is consistent with eclogite suite inclusions within diamonds generally recording higher temperatures of equilibration than Peridotite suite inclusions and with the occurrence of diamond-graphite eclogites where the graphite is not pseudomorphic after diamond (ie the eclogite crystallized close to the graphite-diamond equilibrium line Robinson et al 1984).

From morphological considerations Sunagawa (1984 a&b) concluded that natural euhedral macrodiamonds grow in fluids or melts ("solution phases") rather than by metamorphic processes from pre-existing carbon. This conclusion is compatible with the precursor diamonds in the GGP originally crystallizing from the same silicate melt that fractionated garnet and CPX, some of which are included in the graphite pseudomorphs. Thus the diamonds would have been an early formed cumulate phase in this magma. Such an origin may now be tested using whole rock and mineral geochemical techniques.

CHAPTER 4

MINERAL CHEMISTRY OF THE PERIDOTITES AND PYROXENITES

4:1 Introduction

Mineral compositions were determined on polished sections using a Jeol JXA-501 electron microprobe utilizing energy dispersive analytical techniques with on line ZAF corrections (see Appendix 4 for operating conditions and analytical precision). Pyroxene end-member calculations follow the procedure of Cawthorne and Collerson (1974) which minimizes the significance of Fe_2O_3 calculations and permits more rigorous comparisons of end-member variations. This recalculation scheme involves allocating Na first with Al to Jd where $Na < Al^{vi}$ as recommended by Thompson (1974). Three or more spot analyses were performed and then averaged. Only analysis totals within the range 99.0 to 100.9 % were accepted providing they produced acceptable stoichiometry. Due to the coarse grained nature of the rocks, three or more thin sctions of each sample were probed to ensure representative coverage. Both the peridotites and pyroxenites have experienced slow, sub-solidus cooling as evidenced by the presence of abundant exsolution lamellae in their pyroxenes. The presence of exsolution complicates interpretation of pyroxene analyses and it is essential to be aware of its effect on compositional data. Unless otherwise specified, pyroxene analyses referred to in this chapter are compositions of the exsolved pyroxene phase. Several workers have attempted to recalculate "primary" pre-exsolution compositions of exsolved pyroxenes from modal analyses of host and exsolved phases eg. Beeson and Jackson (1970), Wilkinson (1974). This approach has several drawbacks, one being the presence of optically invisible, fine exsolution "plates" within the host phase (Campness and Lorimer 1973) which lead to underestimation of the volume of the exsolved phase. Additionally the areal distribution of the exsolved phases is highly dependant on the angle at which the section is cut through the crystal. The Beni Bousera pyroxenite CPX porphyroclasts sometimes contain exsolved blebs of garnet and plagioclase in addition to OPX lamellae. These blebs are discontinuous in three dimensions. Some sections may not intersect such exsolved products thus leading to errors in modal estimation and in the recalculation of the pre-exsolution pyroxene composition. Several approaches are available to tackle this problem; two are discussed in the following sections. The term "primary pyroxene composition" is used by some authors, eg. Conquere (1977), to discuss such recalculated pyroxene compositions. The term "primary" is misleading and should be modified to "pre-exsolution" composition as the pyroxene may have undergone significant cation exchange with surrounding minerals prior to exsolution and as such will not represent the crystallization composition of the mineral.

4:2 Peridotites

4:2.1 Olivine

Representative olivine analyses from the Beni Bousera peridotites are presented in Table 4.1. Individual crystals are chemically homogeneous with no significant core-rim zonation. Despite some serpentine veins cross-cutting individual crystals, most grains have fresh pools of olivine and yield cation totals based on 4 oxygens of between 2.969 and 3.011. Olivine from the spinel lherzolites average 3.001. Olivines from the spinel harzburgites seem to yield consistently above the theoretical 3.000 cation total, averaging 3.007. Silicon per formula unit is similarly variable ranging from 0.992 to 1.003 atoms per formula unit (AFU) in the spinel lherzolites whereas the spinel harzburgites are consistently low, 0.993 to 0.988 AFU. The sum of octahedrally co-ordinated cations in the spinel lherzolites is low ~1.987, however, this site is very close to the theoretical value of 2 in the spinel harzburgites, averaging 2.003. Such analytical discrepancies are minor and will not affect any petrological interpretations based on the analyses.

Most olivines contain negligible amounts of Ti, Al, or Cr although some crystals from the spinel lherzolite GP12 were found to contain upto 0.23wt% Al_2O_3 and 0.1wt% TiO_2. No systematic variation was observed for these values in relation to other oxide components and although these values are above analytical precision they are probably spurious (E. Condliffe pers.comm.). Minor contents of MnO and traces of CaO were found in some olivines, a negative correlation existing between MnO and MgO, with olivines from sample GP12 providing the highest values of MnO and being the poorest in MgO (0.32 % MnO, 46.9 % MgO). Lower MnO values are observed in the more magnesian olivines from the spinel harzburgite GP178 (0.06 % MnO, 50.47 % MgO). Although these values suggest the presence of minor tephorite and even monticellite molecules in the structures their amounts are trivial and it is safe to regard the olivines as mixtures of the binary forsterite - fayalite solid solution series. Forsterite contents of olivines from spinel and garnet peridotites are illustrated in Figure 4.1a. The spinel harzburgites are slightly more magnesian than the lherzolites with forsterite contents averaging Fo 91 whereas the spinel lherzolites show a pronounced mode at Fo 89 with some values as low as Fo 86. This variation is consistent with the more basaltic element depleted nature of the harzburgites (see Chapter 5) and the positive correlation between olivine Fo content and modal percent olivine in the rock (Fig.4.1b). The highly magnesian, relatively constant olivine compositions of both lherzolites and hazburgites are consistent with the peridotites representing fragments of upper mantle rather than forming part of a high pressure, differentiated (or magmatic) layered intrusion as suggested by Mikailov (1975). This is supported by Figure 4.2 which shows that olivines from the Beni Bousera peridotites are richer in MgO at a given Ni content compared to olivines from layered intrusions and basalts, although this plot is not infallible as a descriminant. Probably the best argument against the peridotite massif being a layered mafic intrusion is the high proportion of ultramafic rocks to mafics (> 10:1) in contrast to all large layered intrusions (Wager and Brown 1968).

Olivine compositions in the spinel peridotites are very similar to spinel facies peridotites from other orogenic peridotite massifs, with a modal peak around Fo 90. Olivine from abyssal peridotites tend to be slightly more Mg-rich than orogenic lherzolites. The range of olivine compositions shown by orogenic

Table 4.1. Representative olivine analyses for Beni Bousera peridotites.CR = core analysis, RIM = Rim analysis.

SAMPLE	GP178 HARZ	GP178 HARZ	GP178 HARZ	GP178 HARZ	GP178 HARZ	GP178 HARZ	GP24 GTLHZ	GP24 GTLHZ	GP24 GTLHZ	GP41 SPLHRZ
ANALYSIS	CR	CR	CR	CR	CR	RIM	CR	CR	CR	CR
SiO2	40.94	40.73	40.88	40.79	40.85	40.52	40.53	40.32	40.16	40.22
TiO2	0.00	0.05	0.00	0.00	0.02	0.00	0.00	0.00	0.00	0.01
Al2O3	0.00	0.15	0.00	0.00	0.07	0.00	0.21	0.00	0.29	0.00
Cr2O3	0.00	0.07	0.05	0.08	0.03	0.04	0.00	0.01	0.06	0.02
Fe2+	8.98	9.32	8.69	8.92	9.05	9.29	10.31	10.02	9.82	10.22
MnO	0.25	0.12	0.17	0.17	0.15	0.15	0.21	0.15	0.09	0.17
MgO	50.37	49.89	50.14	50.20	50.21	49.61	49.11	49.44	49.59	48.93
CaO	0.00	0.00	0.01	0.03	0.02	0.06	0.02	0.00	0.04	0.00
NiO	0.28	0.37	0.36	0.36	0.37	0.37	0.42	0.44	0.39	0.42
SUM	100.82	100.70	100.30	100.56	100.77	100.04	100.81	100.09	100.45	99.99
CATS O=4										
Si	0.993	0.991	0.995	0.992	0.992	0.993	0.990	0.985	0.983	0.990
Ti	0.000	0.001	0.000	0.000	0.000	0.000	0.000	0.000	0.000	0.000
Al	0.000	0.004	0.000	0.000	0.002	0.000	0.006	0.000	0.008	0.000
Cr	0.000	0.001	0.001	0.002	0.001	0.001	0.000	0.000	0.001	0.000
Fe2+	0.182	0.190	0.177	0.181	0.184	0.190	0.211	0.206	0.201	0.210
Mn	0.005	0.002	0.004	0.004	0.003	0.003	0.004	0.003	0.002	0.003
Mg	1.821	1.809	1.820	1.820	1.818	1.812	1.788	1.812	0.002	1.796
Ca	0.000	0.000	0.000	0.001	0.001	0.001	0.000	0.000	1.809	0.000
Ni	0.005	0.007	0.007	0.007	0.007	0.007	0.008	0.009	0.001	0.008
SUM	3.007	3.006	3.004	3.007	3.007	3.007	3.007	3.015	3.003	3.009
Mg. No	90.700	90.400	91.000	90.800	90.700	90.400	89.300	89.700	89.900	89.400

SAMPLE	GP12 SPLHRZ	GP12 SPLHRZ	GP12 SPLHRZ	GP12 SPLHRZ	GP89a SPLHRZ	GP89a SPLHRZ	GP89a SPLHRZ	GP89a SPLHRZ	GP89a SPLHRZ
ANALYSIS	CR	CR	CR	RIM	CR	CR	CR	RIM	RIM
SiO2	40.89	40.42	40.48	40.43	39.90	40.72	40.43	40.59	41.13
TiO2	0.06	0.00	0.00	0.07	0.00	0.00	0.09	0.00	0.00
Al2O3	0.10	0.00	0.23	0.13	0.00	0.00	0.01	0.00	0.01
Cr2O3	0.00	1.00	0.05	0.00	0.13	0.06	0.00	0.00	0.00
Fe2+	9.89	9.79	13.15	9.85	10.03	9.69	9.94	9.96	9.72
MnO	0.14	0.14	0.17	0.14	0.09	0.09	0.17	0.12	0.12
MgO	48.93	48.50	46.38	48.72	48.78	48.61	49.20	49.48	49.08
CaO	0.00	0.00	0.00	0.04	0.04	0.00	0.00	0.04	0.01
NiO	0.47	0.31	0.25	0.28	0.40	0.38	0.51	0.36	0.43
SUM	100.49	99.17	100.70	99.66	99.38	99.55	100.36	100.55	100.50
CATS O=4									
Si	0.999	1.000	1.000	0.996	0.988	1.003	0.991	0.992	1.003
Ti	0.001	0.000	0.000	0.001	0.000	0.000	0.002	0.000	0.000
Al	0.003	0.000	0.007	0.004	0.000	0.000	0.000	0.000	0.000
Cr	0.000	0.000	0.001	0.000	0.003	0.001	0.000	0.000	0.000
Fe2+	0.202	0.203	0.272	0.203	0.208	0.199	0.204	0.204	0.198
Mn	0.003	0.003	0.004	0.003	0.002	0.002	0.004	0.002	0.002
Mg	0.782	1.788	1.708	1.788	1.801	1.784	1.797	1.802	1.784
Ca	0.000	0.000	0.000	0.001	0.001	0.000	0.000	0.001	0.000
Ni	0.009	0.006	0.005	0.006	0.008	0.008	0.010	0.007	0.008
SUM	2.999	3.000	2.996	3.001	3.011	2.997	3.007	3.008	2.997
Mg. No	89.700	89.7	86.100	89.700	89.6	89.900	89.700	89.700	89.900

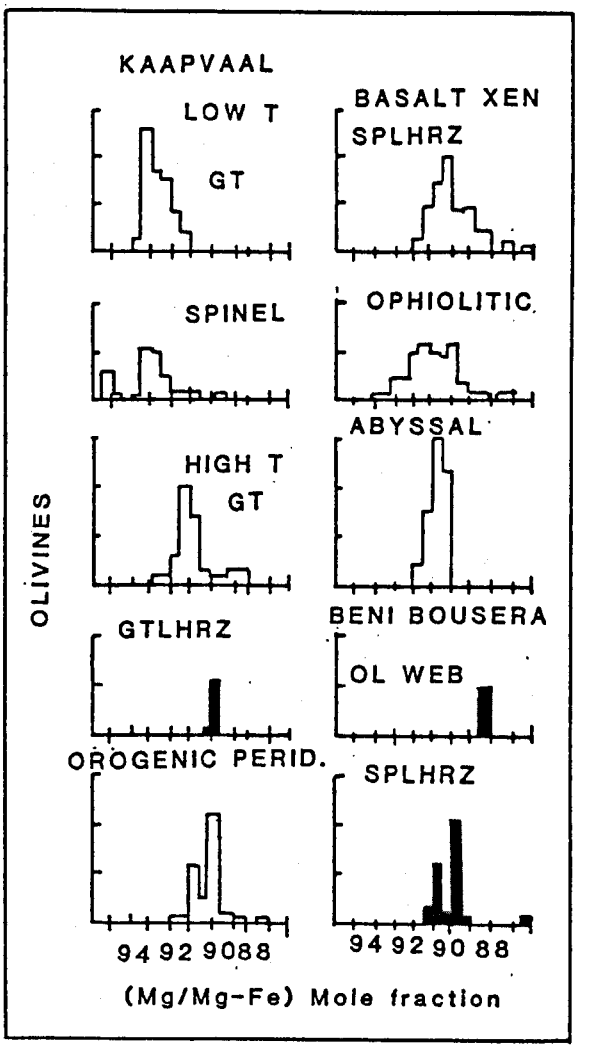

Figure 4.1a 100Mg/(Mg+Fe) values for olivines from Beni Bousera garnet and spinel xenoliths compared to ultramafic xenoliths from volcanic pipes, other orogenic peridotites (Ronda, W.Alps, Zaboragad), ophiolitic peridotites and abyssal peridotites. Also plotted are olivines within the margins of some pyroxenite layers from Beni Bousera.

Kap = Xenoliths from kimberlites on the Kaapvaal craton, S.Africa. Modified after Boyd and Mertzman (1987), additional data from Ernst (1978), Bonatti et al (1986) and Obata (1980).

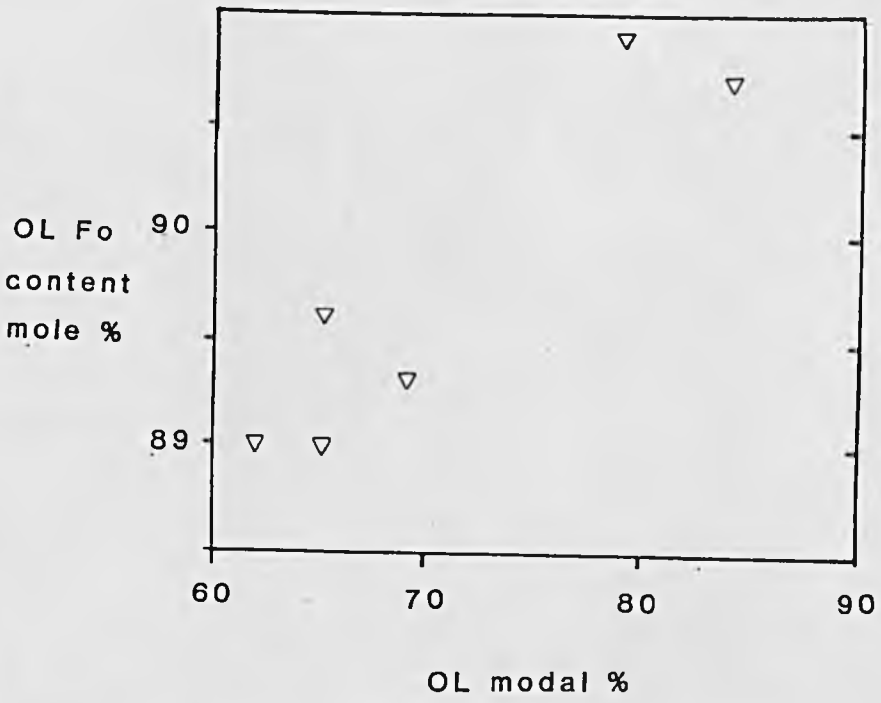

Figure 4.1b. Average olivine Fo content vs calculated modal % olivine in Beni Bousera spinel peridotites.

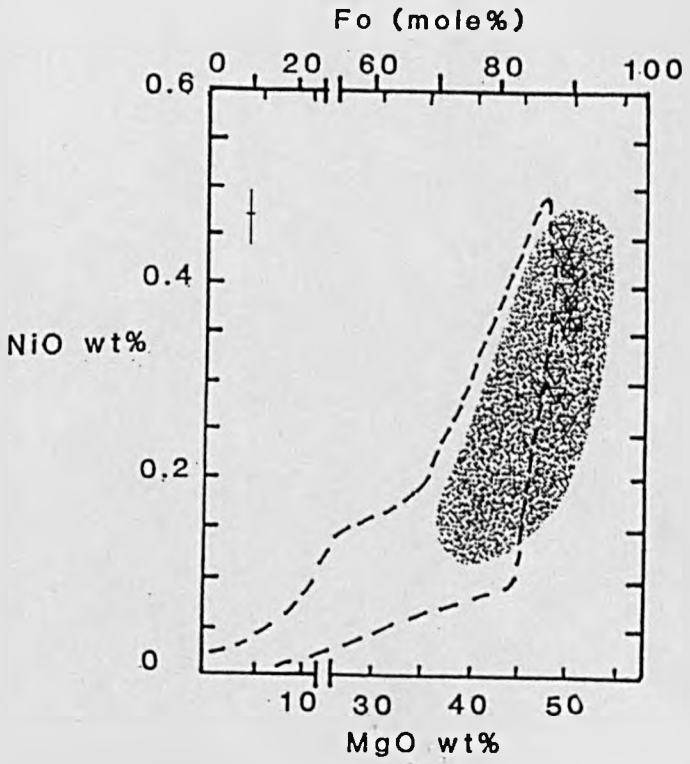

▽ SPLHRZ

▣ GTLHZ

Figure 4.2. NiO vs MgO in olivines from Beni Bousera peridotites compared to olivines from mantle peridotites (shaded) and olivines from basalts and layered intrusions (empty, dashed field). Error bar is typical 2σ analytical error (Modified after Fleet et al 1977).

peridotites is similar to that of spinel peridotite xenoliths from alkali volcanics (Fig.4.1a). Similarities also exist between the Beni Bousera peridotite olivine data and the high temperature xenoliths from the Kaapvaal craton studied by Boyd and Mertzman (1987), Figure 4.1a. These authors suggested an oceanic origin for the high temperture xenoliths.

There is no detectable difference between olivine porphyroclasts and neoblastic olivine, confirming the observation of Obata (1980) that there is no Mg/Fe fractionation during olivine recrystallization. Olivines from the Beni Bousera garnet lherzolites (Fig 4.1a) are compositionally similar to those from the spinel lherzolites and suggest that the olivine has equilibrated with the rest of the rock as no zoning is present.

4:2.2 Orthopyroxene

Orthopyroxenes (OPX) from the spinel lherzolites are characterized by high Mg numbers ~90. Those from the harzburgites being even higher (Mg Nos upto 91.6, Fig 4.3). OPX have upto 89.5% En, 8.4 % Fs and minor Wo components. Cr-Ca Tschermacks molecule makes up the remainder with occasional minor calcium Tschermacks and Ti-Ca-Tschermack molecules (Table 4.2).

Table 4.2 Orthopyroxene end member variation in Beni Bousera spinel peridotites.

END MEMBER	MAX %	MIN %	WIDE BEAM
Fe^{3+}CaTs	1.2	0.0	2.6
CrCaTs	1.1	0.6	0.0
TiCaTs	0.5	0.1	0.5
CaTs	4.8	0.0	1.4
Wo	0.0	0.0	0.0
En	89.0	86.0	87.8
Fs	10.3	7.8	9.7

The OPX from spinel lherzolites have a small range in composition and lie within the field for other orogenic peridotites (Fig 4.3). Al_2O_3 contents (Table 4.3) are variable but typical of those from other mantle derived peridotites such as the Lizard (S.W. England) and Ronda (S. Spain) and are comparable (3.2 to 5.8 wt % Al_2O_3) to OPX derived from mantle derived xenoliths in volcanics (Fig 4.4). The OPX Al_2O_3 values in the Beni Bousera peridototes are much higher than those observed in layered, cumulate peridotite bodies e.g. Bushveld, S. Africa (Fig 4.4). TiO_2 in OPX from the spinel harzburgites is low, ~ 0.08 wt %, compared to that in the spinel lherzolites (0.13 to 0.22 wt % TiO_2). TiO_2 is mainly held as the TiCaTs molecule in the OPX lattice. Cr_2O_3 values of OPX are generally highest in the spinel harzburgites which also contain the most Cr-rich spinels. A relatively good inverse correlation is observed for Al_2O_3 content of OPX against 100 Cr/Cr +Al of spinel (Fig. 4.5) which lies sub-parallel to the increasing partial melting trend obtained from experimental compositions by Jaques and Green (1980).

Table 4.3. Representative OPX porphyroclast data for peridotites.

SAMPLE	GP178 HARZ	GP178 HARZ	GP178 HARZ	GP132(3) SPLHRZ	GP132(3) SPLHRZ	GP89a SPLHRZ	GP89a SPLHRZ	GP89a SPLHRZ	GP12 SPLHRZ	GP24 GTLHZ	GP24 GTLHZ
ANALYSIS	OPX CR	OPX CR	OPX CR	OPX CR	OPX CR	OPX CR	OPX CR	OPX RIM	OPX CR	OPX CR	OPX CR
SiO2	55.68	55.49	55.68	53.85	54.71	53.81	54.38	54.23	54.82	56.22	55.72
TiO2	0.05	0.18	0.07	0.12	0.21	0.21	0.19	0.22	0.10	0.05	0.00
Al2O3	3.75	3.82	3.29	5.26	5.26	5.50	5.08	4.93	4.92	2.99	2.96
Cr2O3	0.74	0.76	0.76	0.34	0.40	0.79	0.56	0.56	0.48	0.06	0.12
Fe3+	0.00	0.00	0.00	0.12	0.00	0.33	0.00	0.00	0.00		
Fe2+	5.70	5.70	5.75	6.63	6.82	6.03	6.79	6.60	6.52	6.55	6.34
MnO	0.18	0.24	0.08	0.10	0.03	0.09	0.15	0.11	0.09	0.09	0.11
MgO	33.31	33.37	33.54	31.97	32.44	32.05	32.27	32.04	31.74	33.93	33.64
Ca	0.68	0.72	0.61	0.57	0.66	0.95	0.48	0.49	0.55	0.28	0.32
NiO	0.06	0.14	0.10	0.07	0.09	0.08	0.03	0.13	0.01	0.09	0.00
SUM		100.43	99.87	99.03	100.62	99.86	99.94	99.30	99.25	100.26	99.21
CATS O=6											
Si	1.917	1.908	1.922	1.882	1.883	1.866	1.884	1.890	1.907	1.934	1.936
Ti	0.001	0.005	0.002	0.003	0.005	0.006	0.005	0.006	0.003	0.001	0.000
Al	0.152	0.155	0.134	0.217	0.213	0.225	0.208	0.202	0.202	0.121	0.121
Cr	0.020	0.021	0.021	0.009	0.011	0.022	0.015	0.015	0.013	0.002	0.003
Fe3+	0.000	0.000	0.000	0.003	0.000	0.009	0.000	0.000	0.000		
Fe2+	0.164	0.164	0.166	0.194	0.196	0.175	0.197	0.192	0.190	0.188	0.184
MnO	1.000	0.007	0.002	0.003	0.001	0.003	0.004	0.003	0.003	0.003	0.003
MgO	1.709	1.710	1.726	1.665	1.664	1.658	1.667	1.665	1.645	1.741	1.742
CaO	0.025	0.026	0.023	0.021	0.024	0.035	0.018	0.018	0.021	0.010	0.012
Ni	0.002	0.004	0.003	0.002	0.002	0.020	0.010	0.040	0.000	0.002	0.000
SUM	3.996	4.000	3.999	4.000	4.000	4.000	3.999	3.996	3.983	4.003	4.002

Figure 4.3. Ca:Mg:Fe: pyroxene quadrilateral atomic proportion plot and coexisting olivine Mg No. for peridotites and pyroxenites. Fields outlined by dashes are CPX and OPX ranges for other orogenic peridotites.

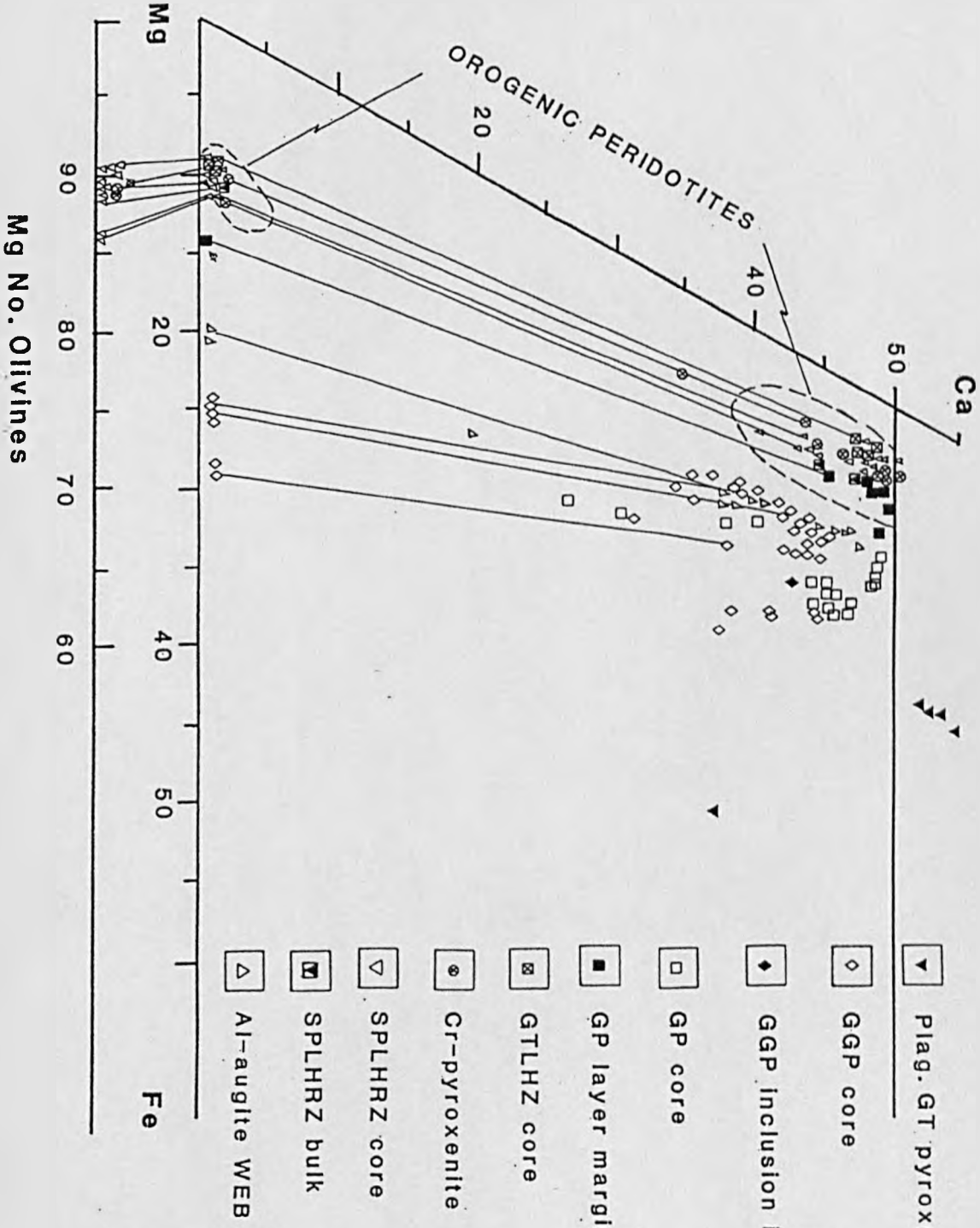

Figure 4.4. Al_2O_3 contents of OPX from Beni Bousera peridotites compared to other orogenic, ophiolitic and xenolithic peridotites. Data from Bonatti et al (1986).

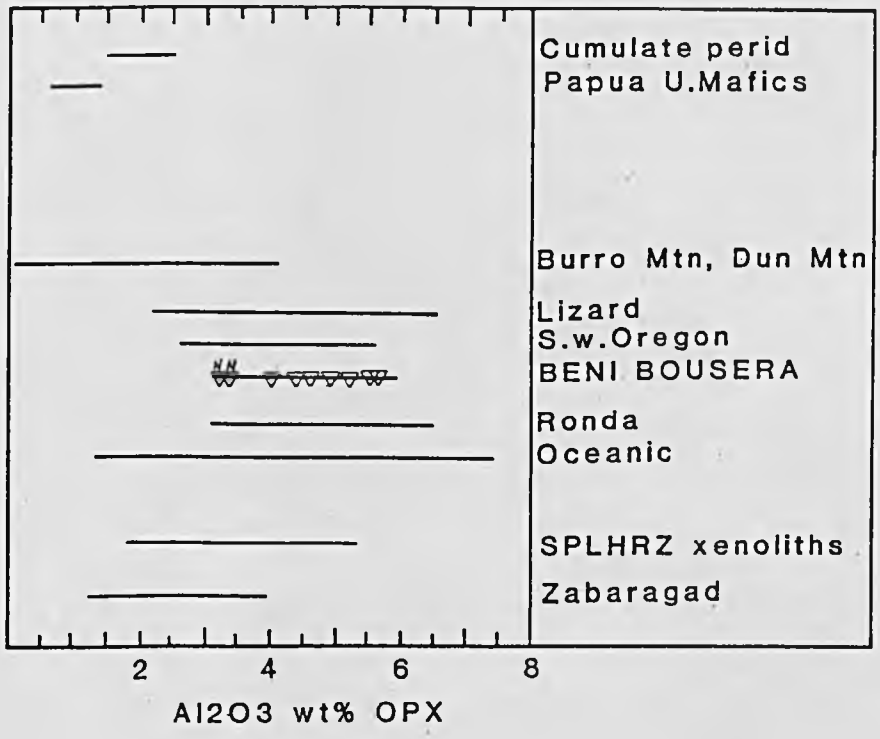

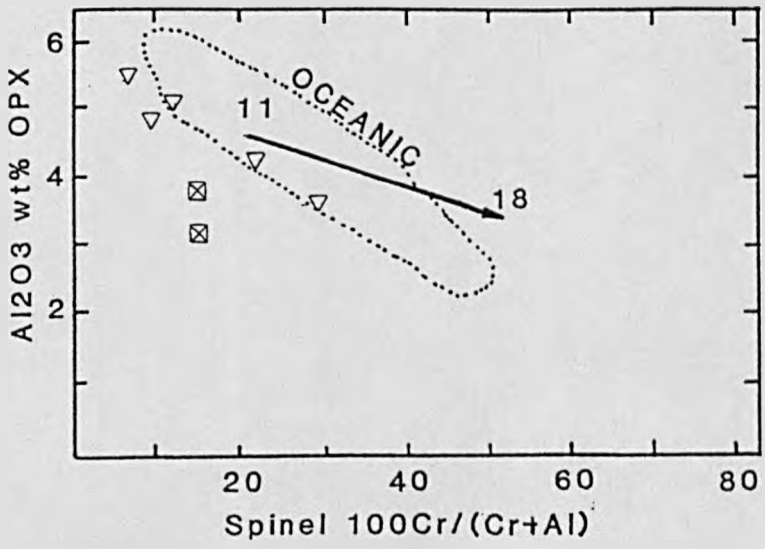

Figure 4.5. Al_2O_3 OPX vs 100Cr/Cr + Al in spinel of Beni Bousera peridotites compared to peridotites dredged from the ocean floor . Arrow marks the trend from 11 to 18 % experimental partial melting of a Tinaquillo peridotite from Jaques and Green (1980). See Fig 4·3 for Symbols

This indicates that the Beni Bousera spinel harzburgites could represent residues from more advanced degrees of partial melting than the lherzolites.

The OPX have low CaO contents, however, the fact that all the OPX porphyroclasts in the spinel lherzolites and harzburgites have exsolved CPX demonstrates that they were saturated with respect to diopside at high temperatures. The presence of exsolved CPX in the OPX of the spinel harzburgites suggests that partial melting cannot have progressed far beyond the four phase field Ol-OPX-CPX and an aluminium phase. Wide beam microprobe analysis of OPX cores indicate the effect of Ca rich pyroxene exsolution, with an increase in Al_2O_3 or CaO being the most notable feature. The bulk OPX composition in Table 4.3 may be taken as an indication of the primary, pre-exsolution composition of the OPX only if the CPX lamellae intersect the (010) surface of the OPX crystal at right angles and show a homogeneous distribution. This homogeneity is seldom the case and such bulk compositions must be taken only as estimates of the OPX pre-exsolution composition. OPX porphyroclast rims and neoblastic crystals are exsolution free and probably record the last stage of re-equilibration of the OPX population. A decrease in the Al_2O_3 content may be observed in spot analysis from core to rim of OPX crystals (Table 4.3). However the Mg/Fe distribution does not appear to show any consistent variation.

4:2.3 Clinopyroxene

CPX in the spinel facies peridotites are typical Cr-rich diopsides, complying with the nomenclature of Morimoto et al (1988), with Cr_2O_3 values up to 1.39 wt %. In terms of the Ca-Mg-Fe pyroxene quadrilateral the compositions are diopsidic to sub-calcic augite (endiopside), Figure 4.3. The CPX are heavily exsolved with high concentrations of OPX lamellae at their centres which do not continue to the very edges of the crystals. Chromium contents are highest in the most basaltic element depleted lherzolites e.g.GP132(3) which also record high Fo contents for olivines (section 4:2.1). CPX from the most fertile spinel lherzolites contain well over 10 % non-quadrilateral components (Table 4.4).

Table 4.4 Non quadrilateral component variation in CPX from spinel lherzolites and comparison of spinel lherzolite CPX chemistry with bulk rock MgO content

SAMPLE	GP12	GP41	GP89a	GP132(3)
BULK ROCK MgO	37.8	38.4	39.64	44.17
Jd %	9.3	16.6	12.2	6.2
TiCaTs %	2.3	0.0	0.0	0.1
CaTs %	7.6	9.6	0.0	3.9
CrCaTs %	1.4	5.1-8.93	0.0	1.9
Al_2O_3 wt %	6.69	7.45	8.28	3.35
Cr_2O_3 wt %	0.94	0.79	0.94	1.39
Na_2O wt %	1.30	2.41	1.73	0.89
TiO_2 wt %	0.84	0.61	0.61	0.0

CPX from lherzolites which depleted in terms of basaltic components have high Cr_2O_3 contents and

lower jadeite, calcium-Tschermaks components and lower Al_2O_3 than more fertlie, MgO poor peridotites (Table 4.4) . The Cr contents of the diopsides from the Beni Bousera periodotites vary from ~ 0.73 wt % in the most CPX-rich lherzolites to 1.34 wt % Cr_2O_3 in the CPX poor lherzolite; GP132(3). The average for the total population is 0.93 wt %. Bulk wet chemical analyses of CPX from Beni Bousera presented by Kornprobst (1969) show a range of Cr_2O_3 contents from 0.44 to 1.15 wt %, thus CPX from the spinel lherzolites may be justifiably called chrome-diopsides. The incorporation of chromium in diopsides arises via a coupled substitution with aluminium to form the kosmochlor (ureyite) $NaCrSi_2O_6$ and calcium-chromium aluminium-Tschermaks molecules $CaCrAlSiO_6$. Chromium has a very high octahedral-site preference energy in CPX compared to nickel (37.7 cf. 20.6 kcal.mol^{-1}), and will therefore tend to have a much larger partition coefficient for M1 and M2 sites in the CPX compared to V, Sc, Ni etc. Hence in mantle peridotites where Ni and Cr are present in approximately equal abundances, Cr is preferentially incorporated into the CPX. Cr/(Cr+Al) vs Mg No. for CPX in the lherzolites (Fig. 4.6) shows a poititve correlation , CPX with high Cr contents and Mg Nos. are from the more olivine rich, CPX poor lherzolites, confirming their greater residual character.

Sodium contents of CPX in the CPX-rich lherzolites are high (up to 2.41 wt.% Na_2O, Table 4.5), those from the CPX-poor lherzolites contain lesser amounts of Na_2O eg. 0.89 wt.% in GP132(3). Comparable CPX Na contents were recorded in the Ronda peridotites, S. Spain, by Obata (1980). The Beni Bousera peridotite CPX define a rough evolutionary trend of increasing Al and decreasing Si which is reflected in a marked enrichment of tetrahedrally co-ordinated Al (Figs. 4.7a & 4.8). Although enrichment of tetrahedrally co-ordinated Al occurs, octahedral Al remains dominant and is distributed between jadeite and CaAlTs molecules in the CPX. Spinel lherzolite CPX have generally lower Al contents than CPX from the more Al-rich pyroxenite layers.

There is a slight decrease from core to rim in Al_2O_3 content (0.24 wt % difference) and a consistent decrease in the Na_2O content from core to rim in CPX porphyroclasts (Table 4.5). This style of zonation is the same as that observed in CPX porphyroclasts and neoblasts in spinel and plagioclase lherzolites from the Ronda massif and is due to sub-solidus re-equilibration. The coupled decrease in Al and Na from core to rim results in slight decrease in jadeite component of the rim CPX.

TiO_2 contents of CPX from the lherzolites range from below detection limit in the CPX poor lherzolite GP132(3) (Table 4.5) to 0.84 wt % in the CPX rich lherzolite, GP13. The increase in CPX TiO_2 content may be correlated with a decrease in Fo content of the co-existing olivine. The TiO_2 contents of the CPX from the Beni Bousera peridotites are comparable to those observed in CPX from the spinel lherzolites of Zabargad by Benatti et al (1986).

The pre-exsolution CPX compositions (Table 4.5) are focus ed broad beam analyses with a beam diameter of 50μm. The slightly high total may be due to local surface aberations on the specimen over such a large integrated area. The MgO and Al_2O_3 and Na_2O contents of the pre-exsolution or bulk CPX composition are noticably higher than the exsolved core compositions. Such compositional differences result from the high P/T conditions experienced by the pre-exsolution CPX. This is supported by the more sub-calcic composition of the bulk CPX (Wo = 29.5) which reflects increased OPX solid solution at higher temperatures. The more sub-calcic composition of the bulk CPX analysis is evident on a pyroxene quadrilateral plot (Fig. 4.3). This pre-exsolution composition must only be viewed as an approximation

Table 4.5. Representative CPX porphyroclast data for lherzolites, . left table gives bulk compositions for OPX and CPX from peridotites. B.B. = broad beam microprobe analysis. WC = wet chemical analysis from Kornprobst (1969).

SAMPLE	GP12 SPLHRZ	GP12 SPLHRZ	GP13 SPLHRZ	GP41 SPLHRZ	GP41 SPLHRZ	GP41 SPLHRZ	GP41 SPLHRZ	GP89a SPLHRZ	GP132(3) SPLHRZ	GP132(3) SPLHRZ	GP24 GTLHZ	GP24 GTLHZ
ANALYSIS	CPX CR	CPX CR	CPX CR	CPX CR	CPX CR	CPX CR	CPX RIM	CPX CR	CPX CR	CPX CR	CPX CR	CPX CR
SIO2	51.62	52.19	54.12	51.53	51.84	51.52	51.42	51.32	53.89	53.75	53.59	53.29
TIO2	0.56	0.63	0.23	0.74	0.58	0.65	0.62	0.84	0.05	0.21	0.55	0.37
AI2O3	7.77	7.60	6.27	8.13	7.58	7.55	7.36	6.69	3.35	3.83	5.00	4.57
Cr2O3	0.95	1.04	0.67	0.89	0.75	0.93	0.80	0.94	1.34	0.91	0.66	0.75
Fe3+	0.00	0.00	0.00	0.48	0.56	0.00	1.27	0.00	0.00	1.39	0.79	0.77
Fe2+	2.45	2.36	5.47	2.35	3.05	2.76	1.46	3.43	1.91	0.65	1.35	1.42
MnO	0.17	0.00	0.18	0.13	0.14	0.05	0.00	0.12	0.08	0.08	0.23	0.07
MgO	14.07	13.90	29.21	14.29	16.49	14.01	14.27	15.18	15.74	16.03	15.39	15.49
CaO	20.67	20.36	3.98	20.03	17.41	19.93	20.14	19.24	23.64	21.88	21.32	21.01
Na2O	1.50	1.76	0.00	1.85	1.65	1.87	1.98	1.30	0.89	1.54	1.77	1.72
K2O	0.04	0.03	0.07	0.00	0.00	0.00	0.04	0.00	0.00	0.00	0.00	0.00
NI	0.12	0.17	0.04	0.09	0.00	0.00	0.05	0.03	0.00	0.00	0.00	0.00
SUM	99.93	100.02	100.23	100.51	100.05	99.26	99.41	99.10	100.89	100.26	100.65	99.51
CATS O=6												
SI	1.868	1.883	1.876	1.853	1.863	1.875	1.867	1.874	1.940	1.935	1.921	1.931
TI	0.015	0.017	0.006	0.020	0.016	0.018	0.017	0.023	0.001	0.006	0.015	0.010
AI	0.331	0.323	0.256	0.345	0.321	0.324	0.315	0.288	0.143	0.163	0.211	0.195
Cr	0.027	0.030	0.018	0.025	0.021	0.027	0.023	0.027	0.038	0.026	0.019	0.021
Fe3+	0.000	0.000	0.000	0.013	0.015	0.000	0.035	0.000	0.000	0.038	0.021	0.021
Fe2+	0.074	0.071	0.159	0.071	0.092	0.084	0.044	0.105	0.038	0.020	0.040	0.043
Mn	0.005	0.000	0.005	0.004	0.004	0.002	0.000	0.004	0.002	0.002	0.007	0.002
Mg	0.759	0.747	1.509	0.766	0.883	0.760	0.773	0.826	0.845	0.860	0.823	0.837
Ca	0.801	0.787	0.148	0.772	0.670	0.777	0.784	0.753	0.912	0.844	0.819	0.818
Na	0.106	0.123	0.000	0.129	0.115	0.132	0.139	0.092	0.062	0.107	0.123	0.121
K	0.002	0.001	0.003	0.000	0.000	0.000	0.002	0.000	0.000	0.000	0.000	0.000
NI	0.004	0.005	0.001	0.003	0.000	0.000	0.001	0.001	0.000	0.000	0.000	0.000
SUM	3.992	3.986	3.982	4.000	4.000	3.998	4.000	3.992	4.000	4.000	4.000	4.000

SAMPLE	GP41 CPX	GP41 CPX	GP89a CPX	GP89a OPX	M6-128 CPX	M6-128 OPX	OPX
ANALYSIS	B.B	B.B	B.B	B.B	WC	WC	
SIO2	51.84	52.12	51.32	55.03	51.76	51.77	
TIO2	0.58	0.62	0.84	0.21	0.16	0	
AI2O3	7.58	8.06	6.69	3.65	4.99	5.93	
Cr2O3	0.75	0.9	0.94	0.32	0.92	0.32	
Fe3+	0.56			1.64	1.8	1.49	
Fe2+	3.05	3.33	3.43	5.28	1.59	5.17	
MnO	0.14	0.1	0.12	0.11	0.15	0.16	
MgO	16.49	15.16	15.18	32.61	16.55	33.83	
CaO	17.41	19.06	19.24	1.2	20.76	1.87	
Na2O	1.65	2.17	1.3	0.16	1.34	0.04	
NIO	0	0	0.03	0.07	0	0	
SUM	100.05	101.52	99.1	100.27	100.7	100.31	

SAMPLE	PAIR	ln KD	Y	SP/Cr	T K	T C
GP 178	C-C	1.5297	0.284		974	701
GP 178	C-C	1.4646	0.3036		1017	744
GP 178	C-C	1.5792	0.3173		986	713
GP 178	C-C	1.2288	0.2201		1035	762
GP132(3)	C-C	1.4371	0.2414		967	694
GP132(3)	R-R	1.3911	0.2259		970	697
GP89a	C-C	1.0348	0.1389		1040	767
GP89a	C-C	1.0256	0.0981		991	718
GP89a	C-C	0.9752	0.1073		1033	760
GP 41	C-C	0.9574	0.0852		1013	740
GP12	C-C	1.0072	0.1022		1007	734
GP12	R-R	1.127	0.0935		931	658

Table 4.7. Spinel olivine geothermometry in spinel peridotites using the formulation of Fabries (1989). C-C = core-core pair, R-R = rim-rim pair.

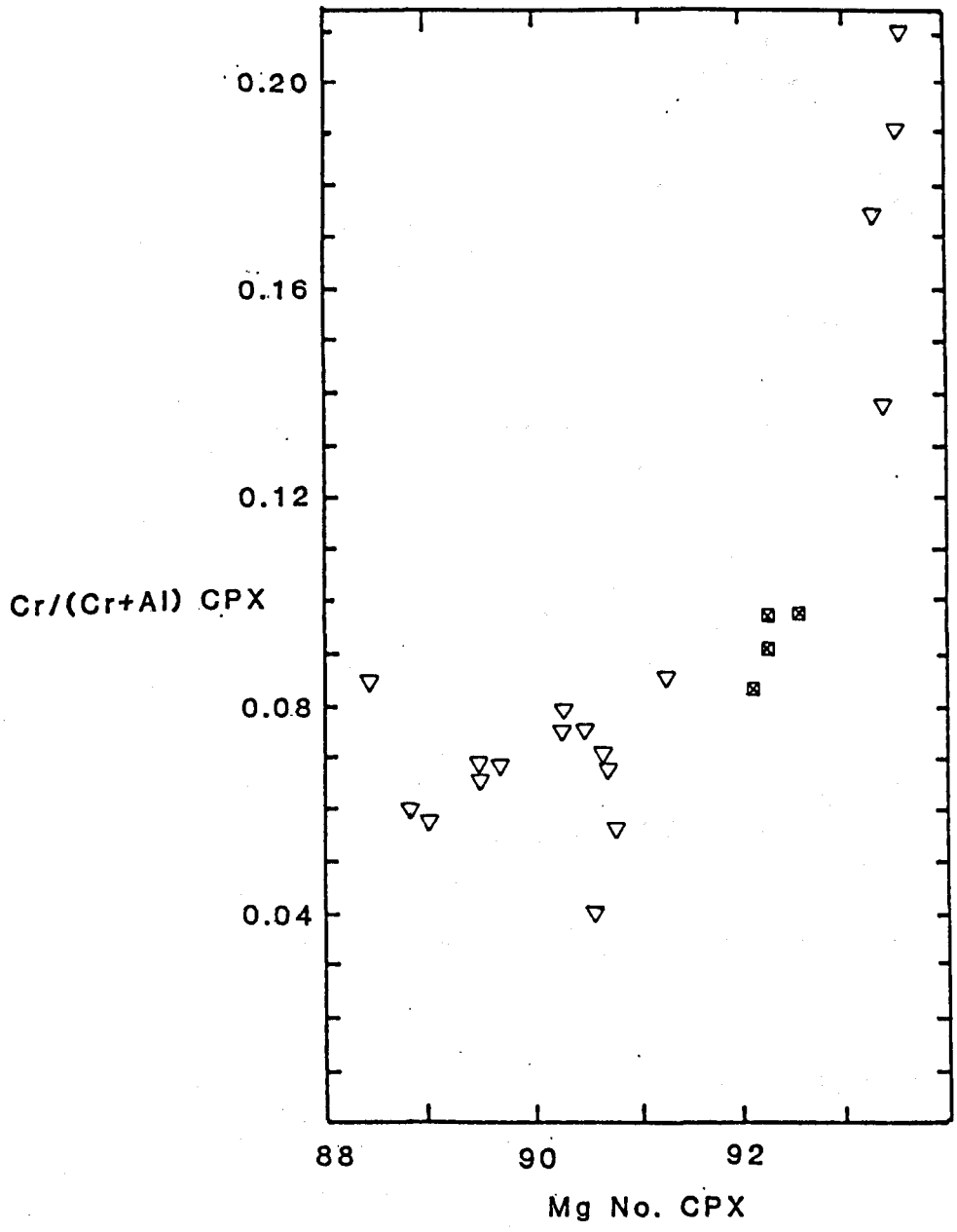

Figure 4.6. CPX (Cr/Cr + Al) vs Mg No. of CPX in Beni Bousera peridotites. Symbols as in Fig. 4.3.

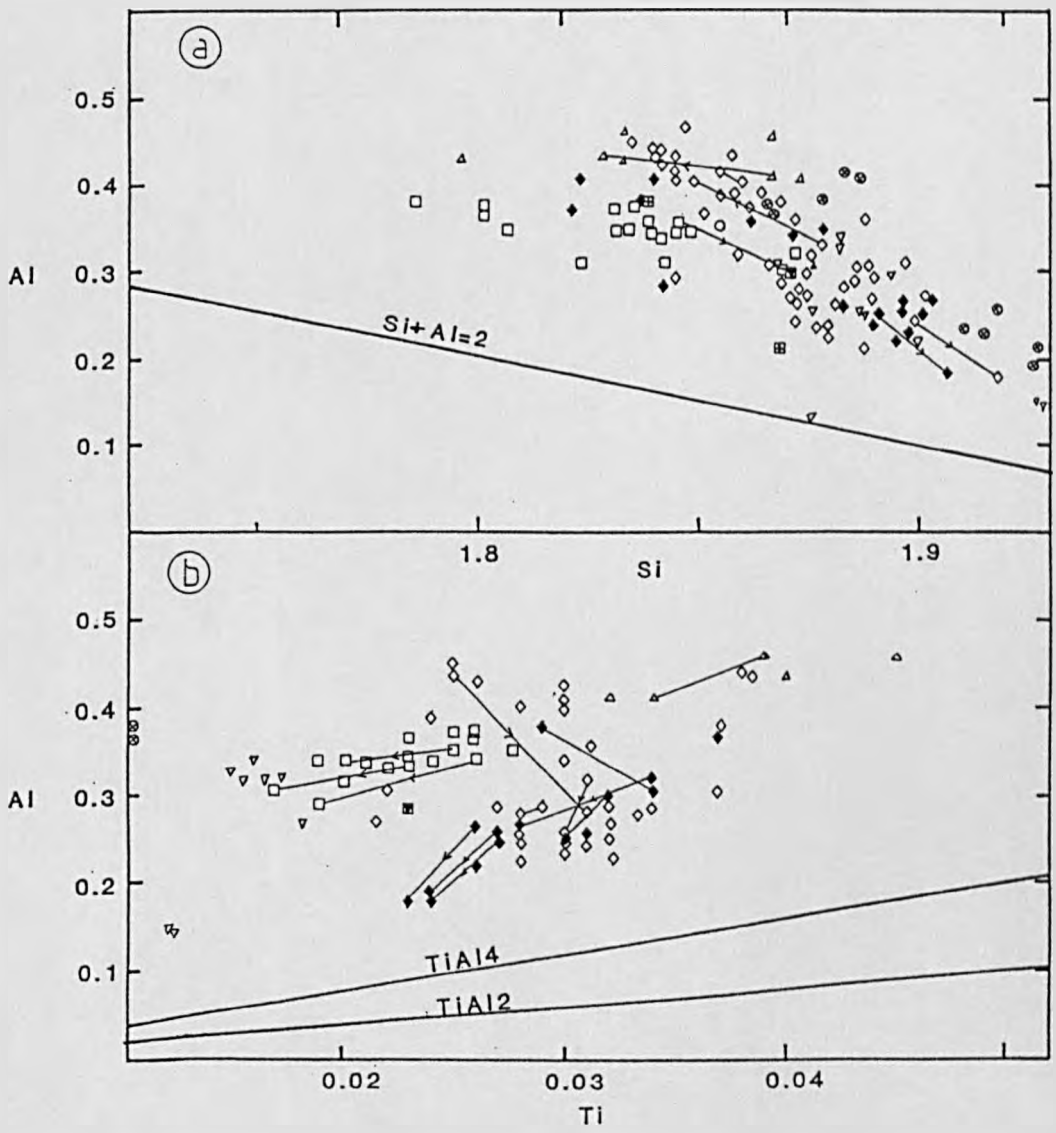

Figure 4.7a. Al vs Si (cation proportions) for CPX from peridotites and pyroxenites. Arrows on core-rim pairs always point towards the rim composition. Symbols as in Fig. 4.3 except square with horizontal cross = Bulk CPX from GP layer.

Figure 4.7b. Al vs Ti (cation proportions) for CPX from peridotites and pyroxenites.

Figure 4.9. (Na + Al^{iv}) vs (Al^{vi} + 2Ti + Cr) in CPX plot for Beni Bousera peridotites and pyroxenites. Dashed field outlines CPX from ridge basalts (Schweitzer et al 1979).

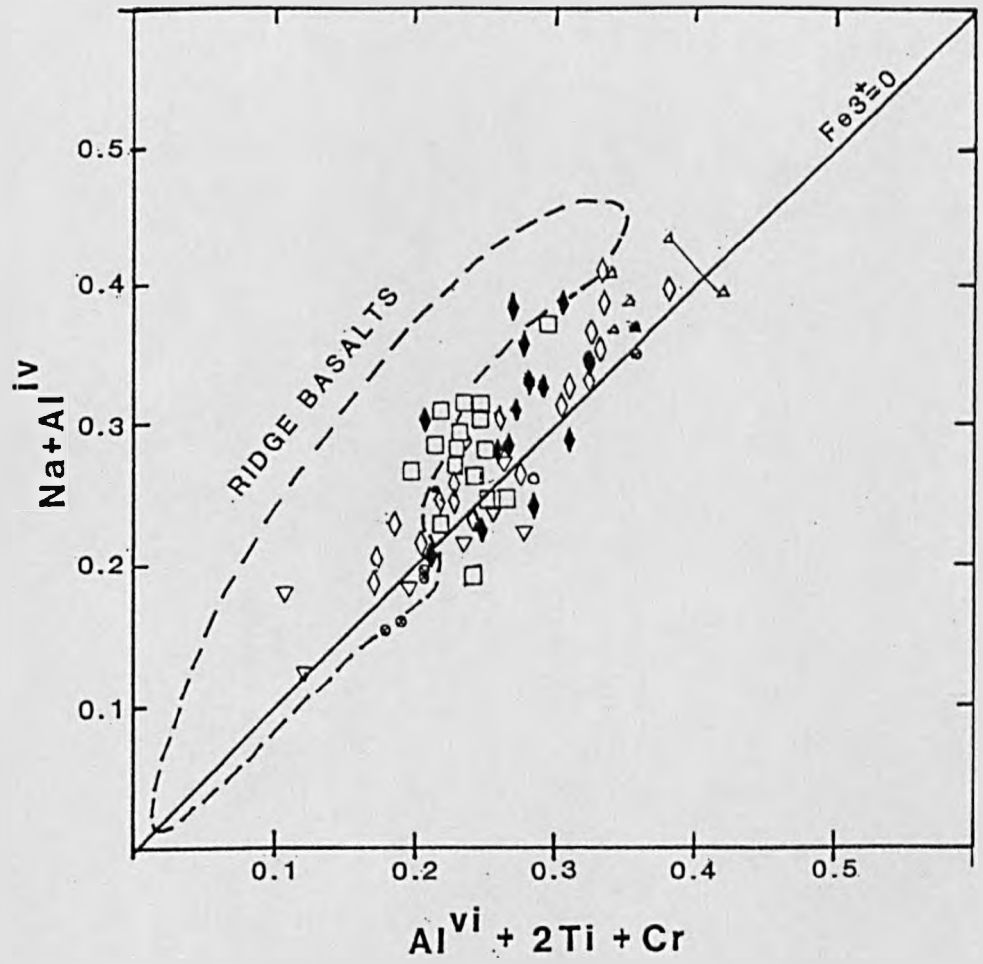

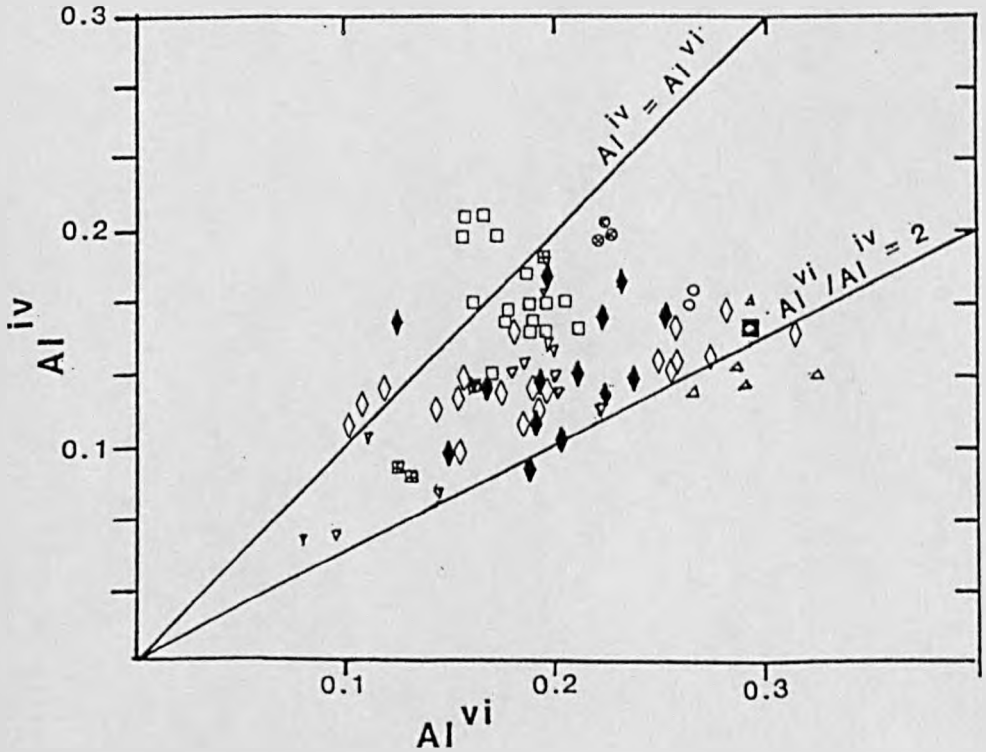

Figure 4.8. Al^{iv} vs Al^{vi} cation proportion plot for CPX from peridotites and pyroxenites.

Figure 4.10. Al_2O_3 ranges of CPX porphyroclasts from Beni Bousera spinel peridotites compared with cumulative peridotites and orogenic and ophiolitic peridotites.

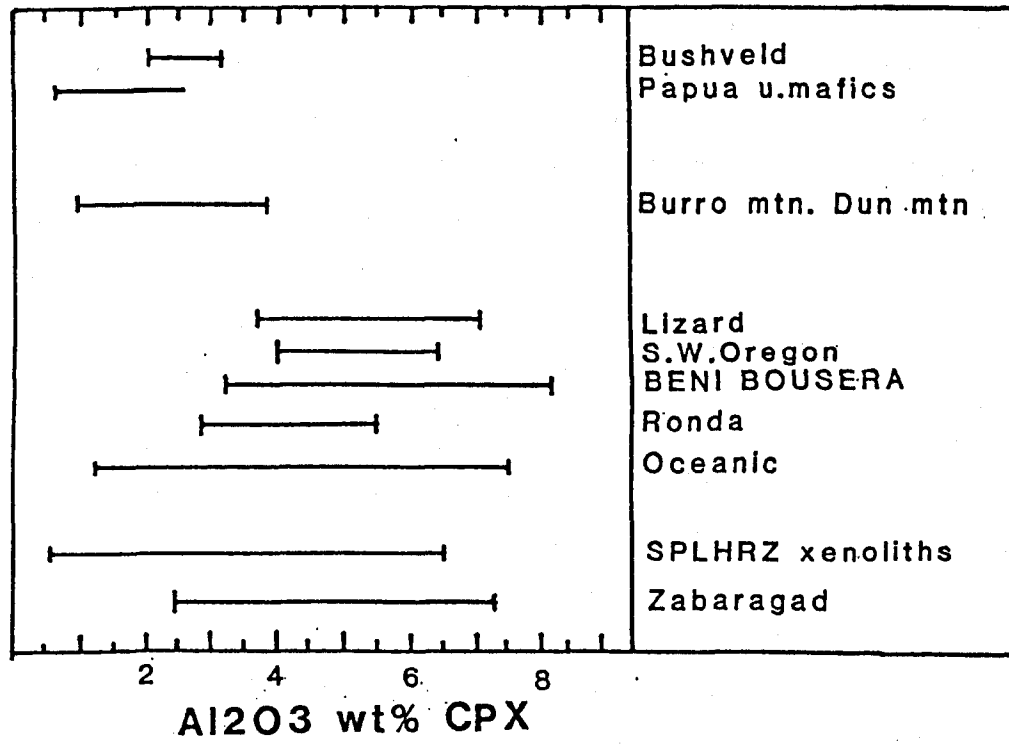

due to inherent errors in the analysis due to the presence of inclusions, the irregular distribution of OPX exsolution lamellae and the likelyhood of the crystal not being sectioned normal to (100). .

The ferric iron content of clinopyroxenes may be infered from a charge balance plot for the M2 site (Figure 4.9). Charge imbalances are calculated relative to a pyroxene of charge-balanced composition i.e. with 100 % quadrilateral components (Schweitzer, et al 1979). Substitution of Na for Ca in the pyroxene M2 site or Al for Si in the tetrahedral sites induces a charge deficiency relative to the ideal quadrilateral composition. Coupled substitution of high valance cations e.g. Al^{3+}, Cr^{3+}, Fe^{3+} or Ti^{4+} in the octahedral sites creates charge excess. In Figure 4.9 lateral displacement of points to the left of the Fe^{3+}=0 line indicates the amount of ferric iron present. The representative CPX plotted from spinel lherzolites indicate very little Fe^{3+} present, most clustering around the Fe^{3+} =0 line. All the CPX data plotted on this diagram have lower Fe^{3+} contents than most CPX from oceanic ridge tholeiites and alkalic basalts, implying lower fO_2 conditions prevailed during the genesis of the Beni Bousera rocks.

The spinel lherzolites display a wide range of Al_2O_3 contents in their CPX (Table 4.5), ranging from 3.35 to 8.13 wt % for exsolved core compositions (Figure 4.10). The bulk analysis from GP89a contains 8.28 wt % Al_2O_3. There is also a negative correlation between the Al_2O_3 content of CPX and the Fo content of the coexisting olivine, i.e. the more fertile rocks have more aluminium rich, MgO poor mineral compositions. The wide variation in the Al_2O_3 contents of both OPX and CPX in the Beni Bousera spinel lherzolites indicates the danger in using the Al_2O_3 contents of pyroxenes as indicators of temperature or pressure in spinel facies lherzolites.

4:2.4 Spinel.

Cr-rich spinel (Table 4.6) is a ubiquitous aluminous phase in peridotites. Spinel is extremely sensitive to bulk composition changes due to petrogenetic processes affecting the host rock and hence is a good petrogenetic indicator (Dick and Fisher 1984). During fractional crystallization or partial melting Cr and Mg are partitioned into the solid residue and Al is partitioned strongly into the melt. On an atomic proportion plot of (100 Cr/Cr + Al) vs (100 Mg/Mg + Fe^{2+}), Figure 4.11, the Beni Bousera data define a relatively narrow linear sub-vertical trend which is sub-parallel to the vector labelled " increasing partial melting ". The spinels from harzburgite GP178 have the highest 100Cr/Cr + Al values of ~30 whilst the CPX rich lherzolites have very low 100Cr/Cr+Al values which plot at the lower end of the field labelled "Orogenic and ophiolitic lherzolites ". This field encompasses other orogenic peridotites and includes the ophiolitic ultramafic complexes e.g. the Papuan Ultramafics and the peridotites from the Samail ophiolite. The CPX poor lherzolites from Beni Bousera plot at an intermediate position on Fig.4.14, between the CPX rich lherzolites and harzburgite and confirm the progressively "depleted" character of the lherzolite-harzburgite suite. The trend defined by the Beni Bousera peridotites is very similar to that of the Ronda peridotites.

Although some inconsistencies exist, spinel rim compositions are generally less Cr rich than cores (Fig.4.11). All the Beni Bousera and Ronda data plot well away from the field occupied by spinels from stratiform basic /ultrabasic intrusions which supports the theory that the peridotites represent fragments of upper mantle.

Table 4.6. Representative spinel analyses for peridotites and spinels from margins of pyroxenite layers.

SAMPLE	GP12 SPLHRZ	GP12 SPLHRZ	GP12 SPLHRZ	GP12 SPLHRZ	GP12 SPLHRZ	GP89a SPLHRZ	GP89a SPLHRZ	GP89a SPLHRZ	GP89a SPLHRZ	GP89a SPLHRZ	GP89a SPLHRZ	GP178 HARZ	GP178 HARZ	GP178 HARZ	GP178 HARZ	GP178 HARZ
ANALYSIS	CR	CR	CR	RIM	RIM	CR	CR	CR	CR	RIM	RIM	CR	CR	CR	CR	CR
SiO2	0.12	0.63	0.32	0.35	0.13	0.14	0.00	0.01	0.12	0.35	0.12	0.46	0.32	0.56	0.33	0.41
TiO2	0.00	0.00	0.12	0.06	0.07	0.18	0.08	0.07	0.00	0.06	0.06	0.20	0.10	0.10	0.12	0.09
Al2O3	58.15	58.00	58.12	58.09	56.52	53.69	53.76	56.44	56.86	51.14	55.03	42.22	39.67	42.88	40.99	38.89
V3	0.11	0.19	0.09	0.10	0.05	0.00	0.16	0.08	0.20	0.07	0.14	0.14	0.24	0.20	0.24	0.36
Cr2O3	9.17	9.10	9.28	9.03	9.79	13.34	13.32	10.37	9.59	16.16	11.31	26.82	28.11	25.97	26.70	28.73
Fe3+	1.14	0.00	0.64	1.11	1.31	2.00	2.65	2.30	2.30	1.90	2.14	0.00	1.45	0.00	0.47	0.94
Fe2+	12.14	13.42	11.69	11.79	12.51	11.78	10.87	10.56	10.57	12.00	11.05	14.16	13.87	13.88	13.12	14.62
MnO	0.18	0.04	0.08	0.18	0.14	0.16	0.12	0.00	0.23	0.12	0.05	0.19	0.22	0.42	0.58	0.50
MgO	18.63	18.44	19.18	19.11	17.82	18.51	19.10	19.43	19.28	18.36	19.07	16.38	15.88	16.57	16.12	15.18
CaO	0.07	0.00	0.01	0.02	0.06	0.07	0.01	0.00	0.00	0.02	0.06	0.06	0.05	0.05	0.02	0.01
NiO	0.31	0.30	0.51	0.41	0.47	0.41	0.26	0.50	0.58	0.33	0.27	0.01	0.08	0.12	0.20	0.09
ZnO	0.21	0.31	0.29	0.23	0.55	0.33	0.27	0.23	0.30	0.43	0.20	0.27	0.40	0.07	0.15	0.49
SUM	100.23	100.51	100.36	100.48	99.41	100.61	100.59	99.99	100.04	100.94	99.49	100.91	100.39	100.83	99.04	100.30
CATS O=4																
Si	0.003	0.016	0.008	0.009	0.003	0.004	0.000	0.000	0.003	0.009	0.003	0.013	0.009	0.015	0.009	0.012
Ti	0.000	0.000	0.002	0.001	0.001	0.004	0.002	0.001	0.000	0.001	0.001	0.004	0.002	0.002	0.002	0.002
Al	1.781	1.776	1.774	1.772	1.760	1.668	1.665	1.736	1.734	1.600	1.710	1.377	1.316	1.394	1.365	1.300
V3	0.002	0.004	0.002	0.002	0.001	0.000	0.003	0.002	0.004	0.002	0.003	0.003	0.005	0.004	0.005	0.008
Cr	0.188	0.187	0.190	0.185	0.205	0.278	0.277	0.214	0.198	0.339	0.236	0.587	0.626	0.567	0.596	0.645
Fe3+	0.022	0.000	0.012	0.022	0.026	0.040	0.052	0.045	0.045	0.038	0.042	0.000	0.031	0.000	0.010	0.020
Fe3+	0.264	0.291	0.253	0.225	0.276	0.260	0.239	0.231	0.230	0.266	0.244	0.328	0.327	0.320	0.310	0.347
Mn	0.004	0.001	0.002	0.004	0.003	0.003	0.003	0.000	0.005	0.003	0.001	0.005	0.005	0.010	0.014	0.012
Mg	0.722	0.713	0.740	0.737	0.702	0.727	0.748	0.756	0.749	0.726	0.749	0.678	0.666	0.681	0.679	0.642
Ca	0.002	0.000	0.000	0.001	0.002	0.002	0.000	0.000	0.000	0.000	0.002	0.002	0.002	0.002	0.001	0.000
Ni	0.006	0.006	0.011	0.009	0.010	0.009	0.006	0.010	0.012	0.007	0.006	0.000	0.002	0.003	0.005	0.002
Zn	0.004	0.006	0.006	0.004	0.011	0.006	0.005	0.004	0.006	0.008	0.004	0.006	0.008	0.001	0.003	0.010
SUM	3.000	3.000	3.000	3.000	3.000	3.000	3.000	3.000	3.000	3.000	3.000	3.000	3.000	3.000	3.000	3.000

SAMPLE	GP132(1) WEB	GP132(1) WEB	GP132(1) WEB	GP132(1) WEB	GP132(1) WEB	GP41 SPLHRZ	GP41 SPLHRZ	GP24 GTLHZ	GP24 GTLHZ	GP24 GTLHZ	GP24 GTLHZ	GP38 WEB	GP38 WEB	GP31 WEB	GP31 WEB
ANALYSIS	CR	CR	CR	RIM	RIM	CR	CR	CR	CR	CR	RIM	CR	CR	CR	CR
SiO2	0.39	0.90	0.00	0.10	0.18	0.26	0.00	0.16	0.28	0.12	0.32	0.00	0.00	0.00	0.00
TiO2	0.03	0.14	0.12	0.17	0.00	0.09	0.06	0.00	0.17	0.00	0.00	0.07	0.04	0.04	0.19
Al2O3	52.82	50.39	51.41	48.76	52.70	58.87	59.57	62.99	47.88	53.81	63.28	59.23	60.18	62.58	62.74
V3	0.04	0.03	0.04	0.00	0.12	0.05	0.11	0.07	0.15	0.15	0.00	0.00	0.01	0.06	0.00
Cr2O3	16.80	18.12	18.55	20.85	16.97	8.26	8.16	5.57	19.95	14.76	6.02	2.42	1.52	3.73	3.81
Fe3+	0.00	0.00	0.63	0.57	0.62	1.02	1.59	0.51	1.29	0.58	0.00	4.43	4.00	3.00	2.81
Fe2+	11.12	10.20	9.83	10.38	9.65	10.80	10.03	9.38	11.25	10.58	9.86	18.22	18.32	8.11	8.64
MnO	0.13	0.15	0.00	0.05	0.02	0.06	0.15	0.05	0.22	0.03	0.03	0.16	0.21	0.00	0.09
MgO	19.10	19.45	19.86	19.26	19.98	19.85	20.03	21.10	18.38	19.19	21.03	14.72	14.50	21.71	21.51
CaO	0.00	0.03	0.00	0.00	0.09	0.06	0.07	0.00	0.03	0.00	0.00	0.02	0.00	0.05	0.00
NiO	0.15	0.28	0.30	0.12	0.33	0.23	0.36	0.50	0.32	0.37	0.27	0.43	0.48	0.28	0.04
ZnO	0.17	0.00	0.00	0.21	0.27	0.07	0.27	0.07	0.20	0.33	0.01	0.00	0.16	0.21	0.12
SUM	100.76	99.69	100.75	100.47	100.92	99.62	100.11	100.40	100.11	99.93	100.83	99.70	99.41	99.77	100.34
CATS O=4															
Si	0.010	0.024	0.000	0.003	0.005	0.007	0.000	0.040	0.008	0.003	0.008	0.000	0.000	0.000	0.000
Ti	0.001	0.003	0.002	0.003	0.000	0.002	0.001	0.000	0.003	0.000	0.000	0.001	0.001	0.001	0.004
Al	1.635	1.578	1.595	1.535	1.625	1.794	1.798	1.871	1.523	1.672	1.870	1.857	1.887	1.865	1.864
V3	0.001	0.001	0.001	0.000	0.003	0.001	0.002	0.002	0.003	0.003	0.000	0.000	0.000	0.001	0.000
Cr	0.349	0.381	0.386	0.441	0.351	0.169	0.166	0.111	0.426	0.308	0.119	0.051	0.032	0.075	0.076
Fe2+	0.000	0.000	0.013	0.011	0.012	0.020	0.031	0.010	0.026	0.011	0.000	0.089	0.080	0.057	0.053
Fe3+	0.244	0.227	0.216	0.232	0.211	0.233	0.216	0.198	0.254	0.233	0.207	0.405	0.407	0.171	0.182
Mn	0.003	0.003	0.000	0.001	0.000	0.001	0.003	0.001	0.005	0.001	0.001	0.004	0.005	0.000	0.002
Mg	0.748	0.770	0.779	0.767	0.779	0.765	0.768	0.792	0.739	0.754	0.786	0.584	0.575	0.819	0.808
Ca	0.000	0.001	0.000	0.000	0.003	0.002	0.002	0.000	0.001	0.000	0.000	0.001	0.000	0.001	0.000
Ni	0.003	0.006	0.006	0.003	0.007	0.005	0.007	0.010	0.007	0.008	0.005	0.009	0.010	0.006	0.009
Zn	0.003	0.000	0.000	0.004	0.005	0.001	0.005	0.001	0.004	0.006	0.000	0.000	0.003	0.004	0.002
SUM	2.997	2.993	3.000	3.000	3.000	3.000	3.000	3.000	3.000	3.000	2.997	3.000	3.000	3.000	3.000

Figure 4.11 (100Cr/Cr + Al) vs (100Mg/Mg + Fe^{2+}) of spinels from Beni Bousera peridotites, websterites (circles with crosses) and spinels at the edges of pyroxenite layers (filled circles). Fields indicated for orogenic and ophiolitic mantle peridotites and stratiform or layered basic/ultrabasic intrusions. Shaded area is trend for Ronda peridotites. (Symbols - Fig 4.3)

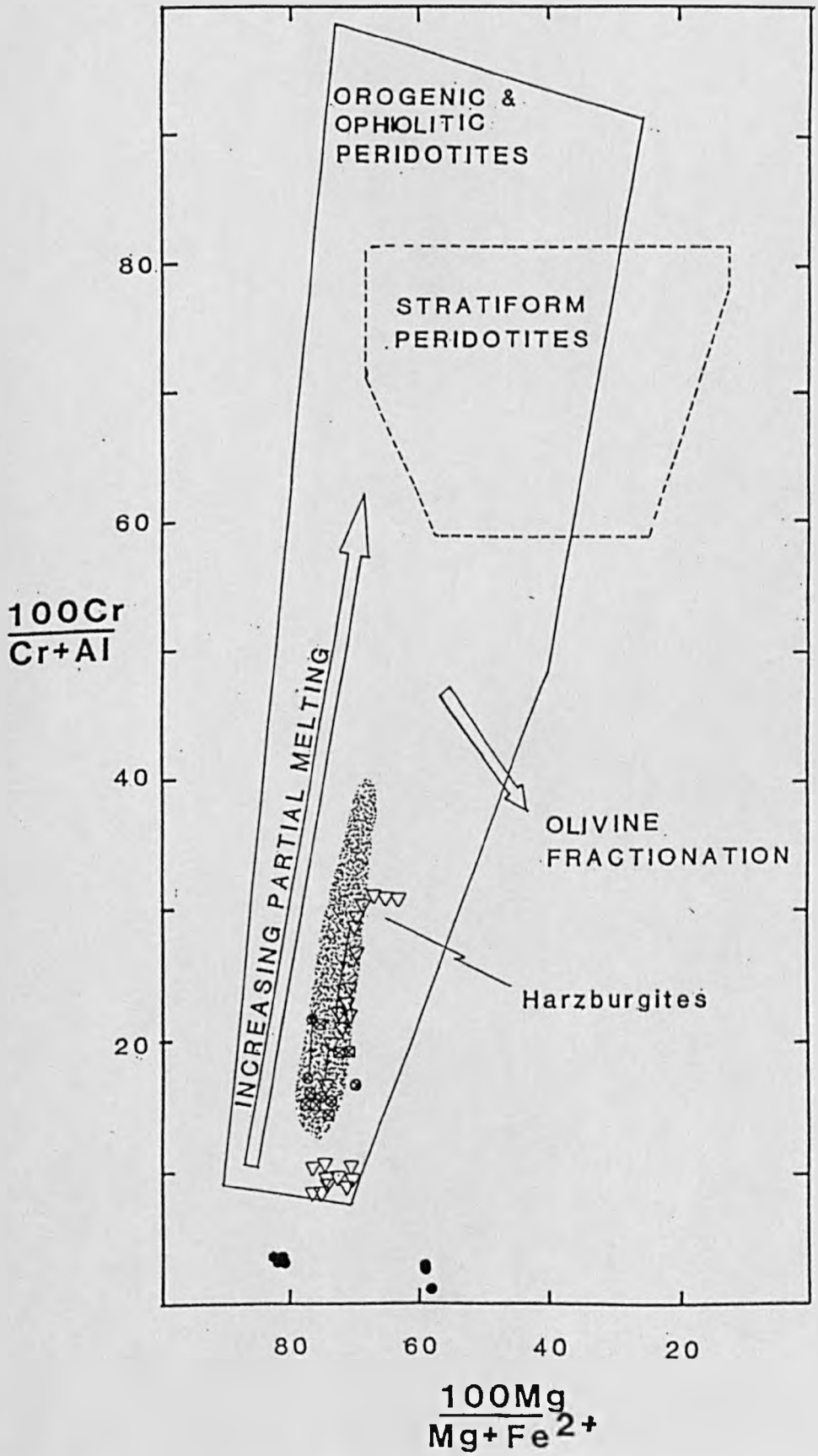

Spinels from the spinel lherzolites have low TiO_2 contents, < 0.2 wt %, which is typical for spinels from orogenic peridotites. TiO_2 contents of greater than ~ 0.4 wt % are only found in spinels from dunites and massive chromites from ultrabasic ophiolite sections which formed as early precipitates from a magma (Auge and Roberts 1982). Layered or "Stratiform" peridotite bodies commonly contain spinel with TiO_2 > 1 wt % e.g. Bushveld (Wager and Brown 1968), emphasizing the mantle origin of the Beni Bousera peridotites.

4:2.5 Spinel zonation

The larger >30 μm irregular spinels within the lherzolites and harzburgites are frequently zoned, especially with respect to Cr, Al and Mg. Figure 4.12 is a traverse through a spinel grain in the spinel harzburgite GP178 in 10 μm steps over the 150 μm width of the grain. The rim one side of the grain is enriched in Al and Mg and depleted in Cr and Fe^{2+} relative to the core with Ti showing no consistent zonation.The opposite side of the grain shows virtually no enrichment or depletion relative to the core but shows variable enrichment/depletion in Cr, Al and Fe around the rim. In another grain the core of the spinel is relatively constant at ~ 26 wt % Cr_2O_3 whereas various spots around the rim have between 20 to 28 wt % Cr_2O_3. This grain is surrounded on all sides by olivine and thus this effect cannot be due to differential element partitioning between the Cr-rich spinel and different phases in contact with the grain at different places. One explanation for such complex zonation is that the grain has been subject to irregular partial dissolution. A more likely explanation is that the zonation is due to stress induced chemical segregation of the type recently reported by Ozawa (1989). Ozawa (op.cit.) observed chemical segregation of Al and Cr in elongate grains of Cr-rich spinel for the Miyamori peridotite massif in Japan. Further study led Ozawa (op.cit.) to find multi-polar Al-Cr zoning in spinels from the Horoman peridotite. Spinels elongated parallel to the foliation of the peridotite showed enrichment of Al parallel to the mineral lineation and corresponding depletion in Al but enrichment in Cr perpendicular to the mineral lineation.

Muli-polar Al-Cr zoning is thus characterized by;

1, A maximum concentration of Al and minimal concentration of Cr at the extremeties of the long axis of the crystal;

2, A minimum concentration of Al and maximum concentration of Cr at the extremeties of the short axis of the crystal;

3, An intermediate concentration of Al + Cr at the core of the crystal.

Ozawa (1989) proposed this type of stress induced chemical zonation was due to a combination of; cation transport through the spinel lattice (Nabarro-Herring creep) and oxygen transport along interfaces (Coble creep).

The unusual nature of the zonation in the spinel grains from the deformed harzburgite GP178 from

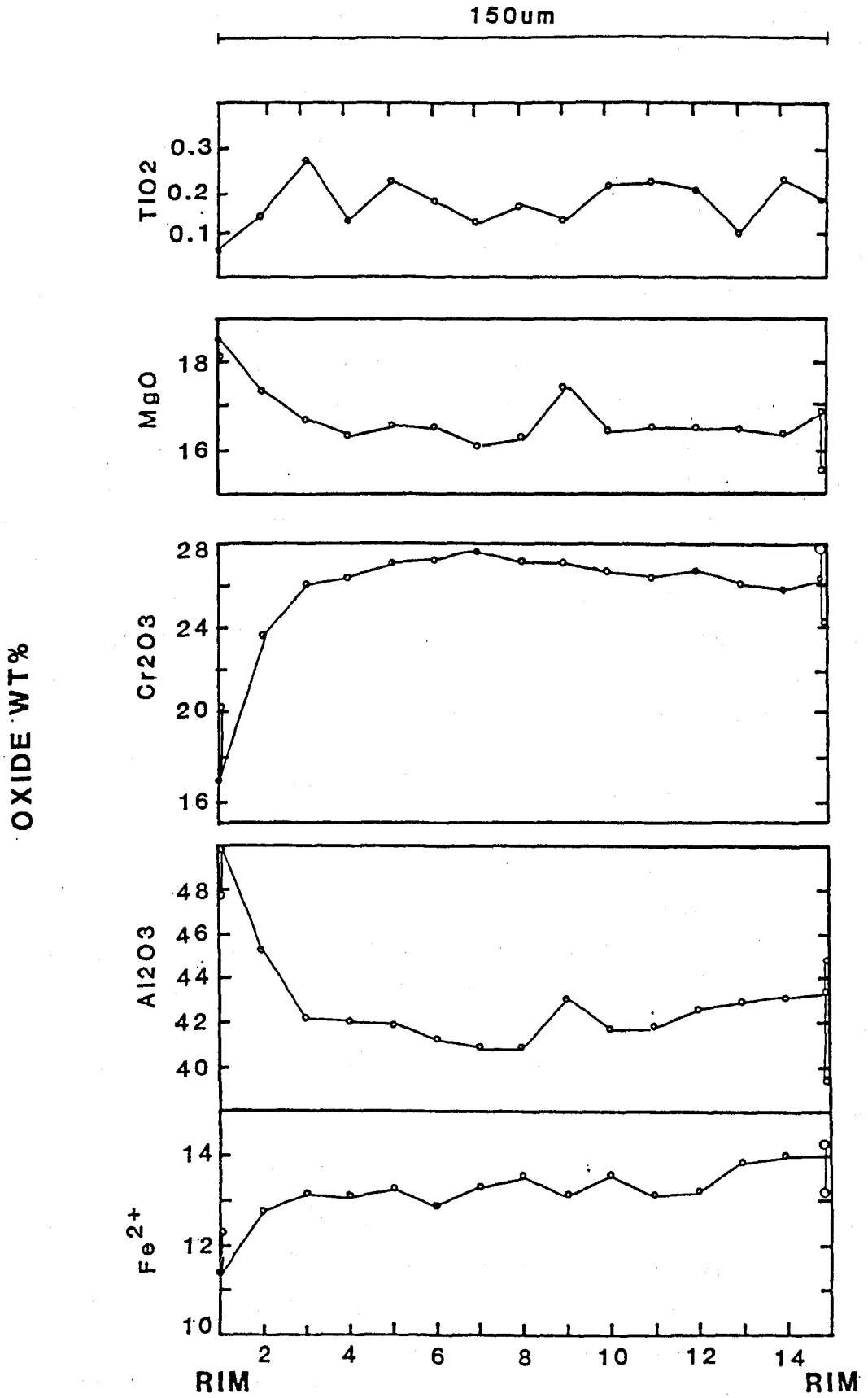

Figure 4.12. Oxide wt % variation across a 150 μm traverse of a Cr-spinel grain from harzburgite GP178. Steps are every 10 μm.

Beni Bousera is roughly analogous to the stress-induced zonation observed by Ozawa (op.cit). The Beni Bousera peridotites have suffered very similar high temperature deformation mechanisms (intra-crystalline plasticity) to the peridotites studied by Ozawa (op.cit.). The slightly non-polar nature of the zoning in the GP178 spinel crystal is probably due to the oblique orientation of the polished thin section. A more detailed micro-probe study of spinels from the Beni Bousera peridotites should be undertaken in order to confirm this theory.

4:2.6 Sulphides.

The mineral chemistry of the Cu-Ni-Fe sulphides in the Beni Bousera peridotites has been extensively studied by Lorand (1985). Compositional variations of the Cu-Ni-Fe-S minerals are quite similar at Beni Bousera and Ronda, especially in pentlandite which covers the entire field of solid solution for Co-poor pentlandites. The occurrence of sulphide phases within the peridotites was discussed in Chapter 2. The majority of the sulphide analyses discussed below are taken from the work of Lorand (1985).

1) Sulphide inclusions within silicate grains:- Lorand (op.cit) found that Cu sulphide inclusions within primary silicates in the peridotites were close to stoichiometry while pentlandite inclusions had the lowest Fe/Ni ratio and lowest Co contents of the pentlandites studied. Pyrrhotite inclusions containing up to % wt% Ni are monoclinic.

2) Intergranular assemblages:- The intergranular pentlandites contain more Fe and Cu than the pentlandite inclusions, with lower Fe/Ni ratios (Fig 4.19). The pentlandite from GP41 contains 2.62 wt % Cu. This is unusual and may be the effect of a finely intergrown Cu sulphide phase. The intergranular pentlandites adjacent to serpentine veinlets are markedly enriched in Fe (up to 42 wt %) and have very low Fe/Ni ratios. Lorand (op.cit.) found the intergranular pyrrhotite to be Ni-free suggesting a lower temperature of equilibration (< 200 °C) than the sulphide inclusions in the silicates. The sulphide composition adjacent some serpentine veins approaches troilite (Lorand op.cit.).

Lorand (op.cit.) suggests the marked differences between the inclusion and intergranular pentlandite phases is due to partitioning of Fe and Co from silicates into pentlandite. It is possible that the chemistry of the intergranular pentlandites in close contact with serpentine has been controlled by a serpentine producing reaction. The strong Fe and Co enrichment observed may have been produced by selective leaching of Ni from pentlandite by aqueous fluids during serpentinization (possibly being transported as a nickel carbonyl). Although the lack of sympathetic variation of Fe and Co does not favour the hypothesis it is an effective process by which to produce the very late Ni mineralized graphite veins which are also associated with hydrated nickel serpentines such as garnietite in Beni Bousera.

4:2.7 Re-equilibration conditions/geothermometry

Orogenic peridotite massifs are probably emplaced into the crust via a combination of diapirism and late thrusting (Kornprobst and Veilzuf, 1984). The relatively slow ascent of the peridotite massif through the mantle into the crust produces slow cooling rates which cannot freeze mineral-mineral chemical equilibria at the same rate as volcanic entrainment and eruption. This results in continual sub-solidus re-equilibration between phases, until the intermineral blocking temperature for the element in question is reached. Consequently, pressure and temperature estimates acquired by mineral thermobarometry

are always sub-solidus equilibration temperatures and do not reflect the source P/T conditions experienced by the rocks. Application of mineral thermobarometry to orogenic peridotites and ophiolite complex must consider the effects of sub-solidus exsolution within pyroxenes. High strain rate deformation related to emplacement and synchronous cooling invariably results in stress/strain related exsolution features in pyroxenes. This is due to the destabilization of the lattice and simultaneous migration of Ca into and out of unstable zones which produces exsolution (Mercier 1985). Analysis of exsolved phases will yield the most recent condition of subsolidus equilibrium whereas an estimate of the pre-exsolution composition of the phases will give approximate near solidus P/T conditions. Both approaches will be attempted in this section.

Obtaining meaningful pressure estimates from spinel facies peridotites is extremely difficult. In contrast to the results of MacGregor (1974), Presnall (1976), found that for the CMAS system in the spinel lherzolite stability field, the Al_2O_3 isopleths of enstatite have gentle, negative dT/dP slopes. Only when entering the garnet lherzolite stability field are the enstatite Al_2O_3 isopleths more steeply negative to provide a good geobarometer. This finding was confirmed by Obata (1976) who found that even in the simple Mg-Al-Si system, the univariant reaction lines curve significantly hence, linear extrapolation of high temperature experimental data to low temperatures is invalid. For the Beni Bousera spinel peridotite suite the Al content of both ortho- and clinopyroxenes appear to be functions of the bulk rock Al content. Application of the MacGregor (1974) barometer to the exsolved composition of enstatites in peridotites 1 km apart along the Oued el Jouj, produces pressures of ~6 and 15 kb respectively for an assumed equilibration temperature of 900 ^{o}C. There is no field evidence to suggest that deformation has juxtaposed rocks of such differing equilibration pressures, suggesting that these pressure estimates are erroneous. Francis (1987) concludes "geobarometers for the spinel lherzolite stability field are highly suspect and it is presently impossible to confidently determine possible depth relationships of spinel lherzolite xenoliths".

There are also many examples of disagreement of temperatures calculated by different mineral thermometers for spinel facies peridotites. Wilshire and Jackson (1975) revealed the shortcomings of several geothermometer and barometer formulations for pyroxenes from both xenoliths and orogenic peridotites. These disrepancies may be due to several of the reasons given below;

1, Inadequate calibration of geothermometers at low temperatures for natural complex systems;

2, The kinetics of intercrystalline cationic exchange during thermal events. Diffusion rates of cations in minerals depend on both the elements and minerals involved, different mineral pairs approach equilibrium to a different extent during a thermal event.

3, When applied to rocks which have undergone continuous cooling , a thermometer, based on minerals in which the diffusion rates of the components involved are high, may give lower temperatures than one based on minerals with components having lower diffusion rates.

To successfully apply mineral thermobarometers based on equilibrium thermodynamic theory it is essential to establish chemical equilibrium (homogeneity) on the scale of study. Detailed mineral chemical studies on peridotites have shown that mineral heterogeneity is a common feature (e.g. Obata 1980). The approach adopted here is to look at temperature variations in relation to crystal size and crystal generation i.e. to investigate possible isothermal stages by core-core pairs from large crystals (probably

porphyroclasts) and rim-rim pairs in relation to the conditions recorded by recrystallized neoblastic phases.

A detailed study by Ozawa (1983) found that the olivine-spinel geothermometer of Fabries (1979) was the most reliable thermometer in terms of consistency of results for natural spinel peridotites. This geothermometer is useful for 2 main reasons;

1, Neither phase is normally subject to extensive sub-solidus exsolution under spinel facies conditions.

2, Olivine-spinel geothermometry is based on the simple Mg^{2+}-Fe^{2+} exchange reaction and does not require complex solution models for site ordering.

Pyroxene thermometry based on cation mixing parameters was not used to determine the equilibration conditions of the exsolved pyroxene mineralogy due to the probable non-ideality of pyroxene solid-solution below 900 C and the steep limb of the solvus below this temperature (Wells 1977). Most two pyroxene formulations are based on empirical curve fitting using an arbitarily chosen form of functions and thus extrapolations outside the range 900 to 1400 ^{o}C are suspect (Mori 1977).

4:2.8 Spinel-olivine geothermometry.

In the following thermobarometry sections, solid solutions are represented as X*i*, the fraction of atoms *i* per site in phase *j* or per site *j*, (M1 or M2) for pyroxenes. Cation symbols (e.g. Ca,Mg etc) are used for raw total atomic values per structural formulae. This work will be based upon the spinel-olivine geothermometry of Fabries (1979). The formulation of Roeder et al (1979) is not used as the free energy values for the end-member spinels are not known accurately and temperatures given by this formulation seem suspect for spinels of fairly low (Cr/Cr + Al) common in lherzolite rocks (Fabries 1979, Ozawa 1983).

The Mg-Fe^{2+} exchange equilibrium between olivine and spinel may be described by:

$$Kd = (\gamma_{ol}\, Mg_2SiO_4)^{1/2} (\gamma_{sp}\, FeAl_2O_4) / (\gamma_{ol}\, Fe_2SiO_4) (\gamma_{sp}\, MgAl_2O_4)$$

where γ is the activity coefficient, ol= olivine and sp= spinel.

As the Fe^{3+} contents of spinel from lherzolites are generally small the concentration of trivalent ions in the tetrahedral sites of the spinel structure should be low (Fabries 1979). Mixing in each structural site should be ideal for solid solutions in the synthetic series: $MgCr_2O_4$ -$MgAl_2O_4$, $FeCr_2O_4$-$MgCr_2O_4$ and $FeAl_2O_4$-$MgAl_2O_4$. Thus the spinel may be regarded as a (Mg,Fe)(Al,Cr)$_2O_4$ multi-site solid solution (Fabries 1979) in which the distribution of ions on each individual sublattice is random.

From these considerations Fabries (1979) derived the following thermometric equation:

$$T(^{o}K) = 4250\, \gamma^{Sp}Cr + 1343 / \ln K_D^{o} + 1.825\gamma^{Sp},Cr + 0.571$$

where: $K_D^{o} = X^{ol}Mg.\ X^{sp}Fe\ /\ X^{ol}Fe.\ X^{sp}Mg$ and $\gamma^{Sp}Cr = Cr/Cr+Al+Fe^{3+}$

Olivine is regarded as an essentially Mg-Fe^{2+} binary solution, virtually all Fe being bivalent over the compositional range of peridotite olivines. Accurate analysis of spinel is required to obtain accurate Fe^{3+}:Fe^{2+} estimates from stoichiometric considerations. As Fe^{3+} is generally low in the samples studied

Figure 4.13. Log of spinel/olivine partition coefficient for Fe/Mg vs Cr (Cr + Al + Fe^{3+}) in spinel from Beni Bousera spinel peridotites. Diagonal lines are isotherms calculated after the method of Fabries (1979). Open triangles are Core-Core pairs, half filled triangles are rim-rim pairs. Dashed field outlines data from the Finero peridotite (N.Italy).

Figure 4.14. Histograms of spinel-olivine equilibration temperatures for Beni Bousera, other orogenic and ophiolitic peridotites and spinel lherzolites xenoliths from alkali basalts. All temperatures estimated using the formulation of Fabries (1979).

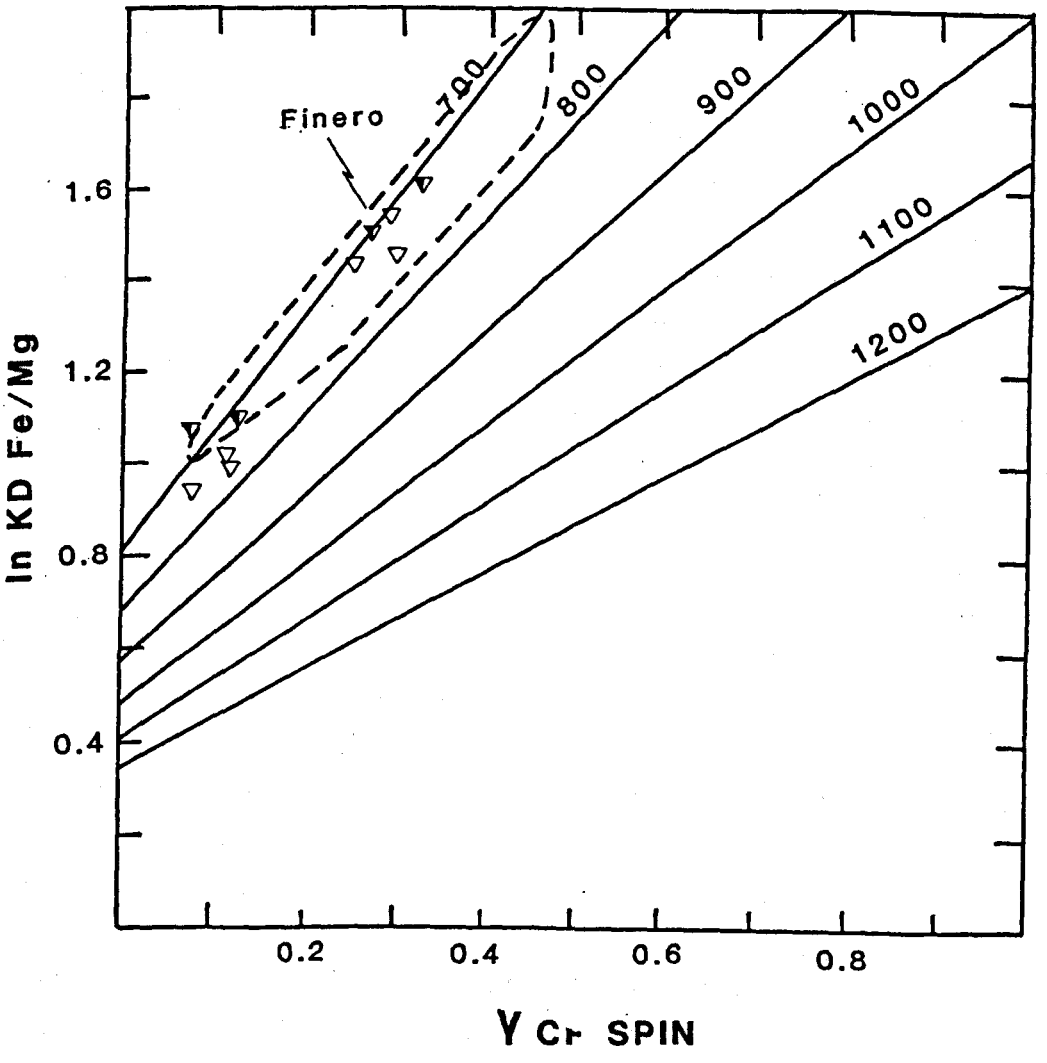

▽ Core-Core pairs

▼ Rim Rim pairs

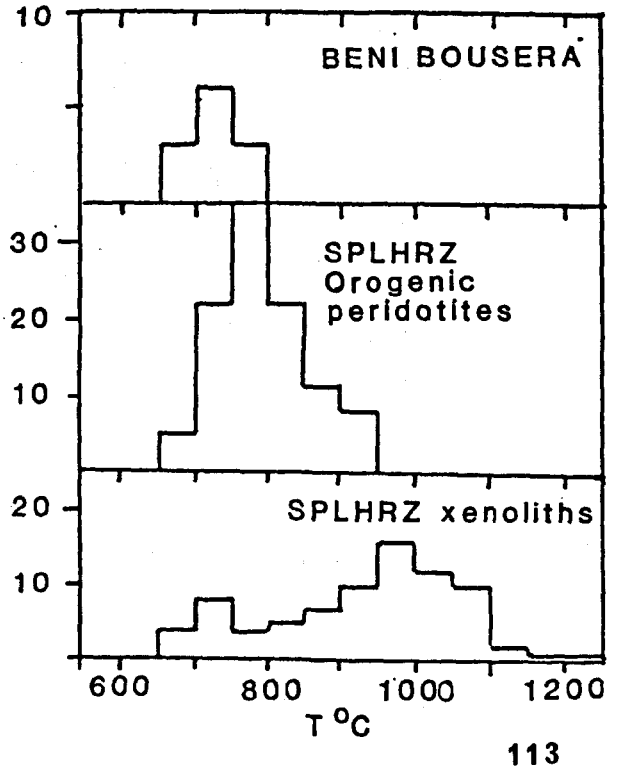

the distribution coefficient Kd is less sensitive to errors in Fe^{3+} than other Fe/Mg partition coefficients, espicially those involving clinopyroxene (Fabries 1979). The typical uncertainty due to analytical errors of Mg and Fe^{2+} in spinel and olivine and Cr, Al and Fe^{3+} in spinel are typically +/- 50 °C (Fabries 1979).

The spinel-olivine geothermometer was applied to core-core and rim-rim pairs of spinel from spinel harzburgites and CPX rich and CPX poor spinel lherzolites, the results are summarized in Table 4.7. The samples in Table 4.7 display a range of equilibration temperatures from 658 °C to 767 °C; the two lowest temperatures being recorded by rim-rim pairs , although a rim-rim pair from GP178 records a temperature of 762 °C. This irregularity in rim temperatures may be a function of element partioning during deformation enhanced chemical segregation in the spinels. Small grains of spinel, <30 μm, together with olivine neoblasts, <100 μm, yield temperatures within the observed range for larger grains. A plot of spinel/olivine Fe/Mg partition coefficient versus γCr of the spinel shows a roughly linear isothermal relationship for both cores and rims at ~ 700 and 750 °C (Fig.4.13). The equilibration temperatures recorded by the spinel-olivine pairs of spinel peridotites from Beni Bousera are just to the lower end of the range recorded for a compilation of other ultramafic complexes by Fabries (1979) and similar to the range recorded by Finero spinel peridotites (Fig.4.13). Ultramafic complexes generally record lower spinel-olivine equilibration temperatures than peridotite xenoliths in alkali basalts (Fig. 4.14) which must in part be due to the rapid uplift and quenching of mineral equilibria in the xenolith peridotites.

The temperatures recorded by either core-core or rim-rim pairs from any single rock from the Beni Bousera spinel lherzolites are probably within error of each other; if the error for the method is assumed to be around 50 °C (Fabries 1979). Data for a core-core pair from GP178 was also applied to the Roeder et al (1979) formulation of the spinel-olivine geothermometer which resulted in an equilibration temperature 50 °C higher than the method of Fabries (1979). However, the Roeder et al (1979) formulation is thought to be suspect for spinels with such low (Cr/ Cr + Al) ratios.

Estimates of re-equilibration temperatures from exsolved pyroxenes using the technique of Lindsley and Anderson (1983) yield temperatures between 600 °C and 900 °C for CPX but the technique does not give as consistent results as spinel-olivine thermometry.

Comparison of the spinel-olivine geothermometer with other thermometers based on element partitioning led Fabries (1979) to suggest that differential diffusion and recrystallization rates cause large equilibration temperature ranges for various mineral geothermometers when applied to ultramafic massifs. Fabries (1979) noted that geothermometers based on the Ca contents of CPX or Al partitioning between pyroxenes and coexisting minerals yield the highest temperature estimates whilst geothermometers based on Fe/Mg distribution in pairs involving garnet or spinel are sensitive to the late stages of cooling and frequently record the lowest re-equilibration temperatures. The very low, relatively uniform temperatures ~700 °C recorded by many spinel peridotites from ultramafic massifs studied by Fabries (1979) indicate that spinel-olivine mineral thermometry records an elemental exchange blocking temperature and does not necessarily imply any discrete isothermal/isobaric event experienced by these rocks.

4:2.9 Pyroxene thermometry

Pre-exsolution pyroxene compositions from spinel lherzolites were obtained either by employing a wide-beam "raster scan " using a focussed beam on the microprobe or by using the bulk compositions

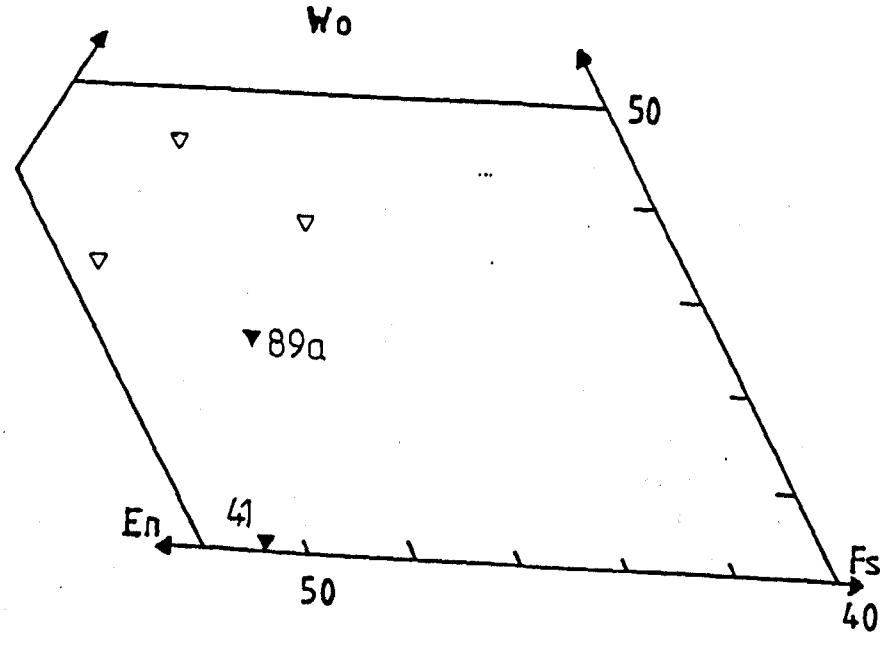

Figure 4.15. Portion of Wo:En:Fs pyroxene quadrilateral showing broad beam "bulk" analyses (open triangles) of CPX from spinel peridotites.

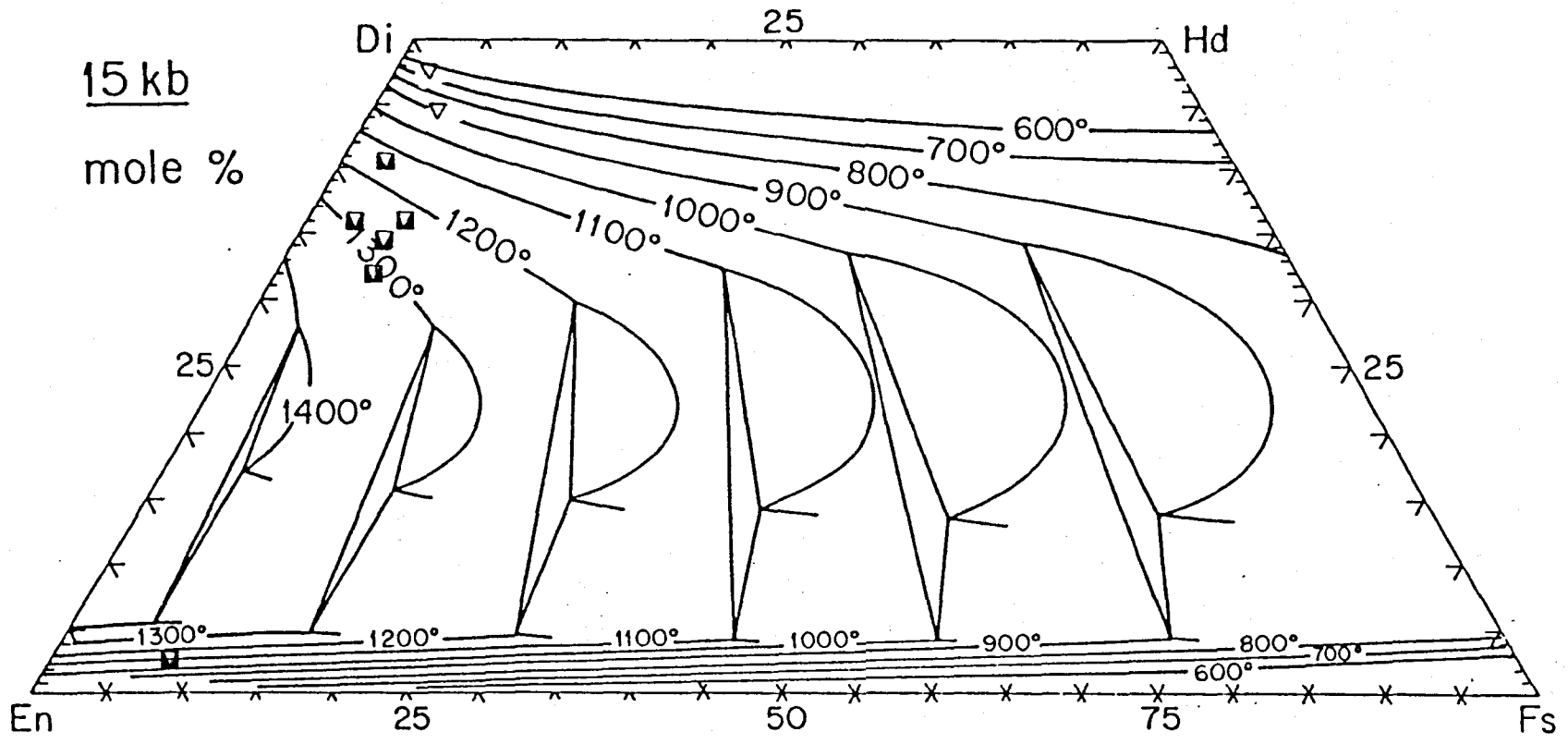

Figure 4.16. Broad beam microprobe and wet chemical analyses of CPX from spinel lherzolites plotted on the Lindsley and Anderson (1983) graphical pyroxene geothermometer. Symbols as in Fig. 4.15.

obtained by wet-chemical analyses by Kornprost (1969) which should give a more realistic estimate of bulk CPX composition prior to exsolution. Comparison of broad beam analyses and bulk wet chemical CPX analyses are given in Table 4.5. Figure 4.15 indicates that the reconstituted or bulk CPX compositions were sub-calcic, one sample from GP41 having as little as 40 mole % Wo in terms of quadrilateral components. The broad beam analyses give cation totals which are up to 0.6 % too high or too low indicating the relatively inaccurate nature of the analyses. Such inaccurate analyses cannot be used to apply CPX cation exchange mineral thermometers to these rocks. Application of the Boyd (1973) thermometer to these compositions would yield temperatures between 1050 and 1200 °C for the most subcalcic compositions. However, the pyroxenes from the Beni Bousera spinel lherzolites are distinctly more aluminous than those from Kimberlite nodules (> 1.5 wt %) , thus lack of consideration of the effect of Al on the diopside-enstatite solvus may yield serious errors which are difficult to estimate.

Lindsley and Anderson (1983) experimentally determined Ca-Mg-Fe pyroxene phase relations at 800-1200 °C between one atmosphere and 15 kb which were combined with calculated phase equilibria for the Di-En and Hd-Fs joins to produce a graphical thermometer applicable to a wide variety of rocks. The thermometer was applied to the bulk CPX compositions. The results gave temperatures between 1120 and 1315 °C at an assumed pressure of 15 kb (Fig. 4.16). This pressure is in the middle of the spinel stability field. There is no evidence of large scale re-equilibration of plagioclase in any of the peridotites studied. Only the bulk OPX analysis in one of the samples yields comparable temperatures to the bulk CPX using this method (~1100 °C compared to 1060 °C). This difference in bulk OPX and CPX equilibration temperatures probably reflects the poor error on Ca determinations at low concentrations in OPX.

The broad beam analyses in Table 4.5 are more sub-calcic than the wet chemical data of Kornprost (1969) when the compositions are recalculated via the projection scheme of Lindsley and Anderson (1983). The larger apparent Fe^{3+} content of the wet chemical analyses causes it to have a high Wo component and thus yields the lowest of the bulk CPX temperatures ~ 1100 °C (Fig 4.16). High Fe^{3+} in the wet chemical analysis could be due to analysis of an impure CPX separate. The effect of selecting the lower equilibration pressure of 10 kb, on the edge of the spinel stability field, results in temperature differences that are well within the error of the graphical thermometry method.

Having derived an estimate of the bulk composition of the original pre-exsolution CPX from various spinel lherzolites and from this an estimate of the equilibration temperature recorded by this composition, we must now interpret the significance of this "pre-exsolution equilibration condition". The interpretation of the bulk CPX equilibration temperatures is dependent on the pressure of equilibration. Although a pressure of 15kb was assumed for the purpose of the thermometry projections in figure 4.23, it is difficult to imagine a distinct isobaric equilibration stage for the peridotites which are likely to have experienced if they were emplaced into the crust via diapirism. The slowly cooled nature of the rocks (as suggested by the pyroxene exsolution) indicates that the pre-exsolution equilibration temperatures obtained from bulk pyroxene analyses are unlikely to represent an igneous crystallization temperature. The temperature derived from the bulk pyroxene analyses can only be safely interpreted as a metamorphic re-equilibration temperature of a CPX saturated with OPX at the assumed pressure. For the three broad beam analyses it appears that the CPX could have equilibrated between 1230 and 1130 °C whilst at 15kb pressure during

slow ascent upwards. The estimate of ~1120 °C for the M6-128 bulk CPX composition of Kornprobst (1969) is probably too low and may be the result of poor analysis. The higher temperature estimates obtained from the broad beam probe analyses are close to or just greater than the solidus temperature of peridotite M6-128, determined experimentally by Kornprobst (1970) at 15 kb. The bulk CPX temperature estimates thus appear to record solidus or close to solidus temperature conditions at 15kb. From these observations it appears that the broad beam analyses of CPX crystals exhibiting subsolidus exsolution features can give an indication of the near-solidus bulk CPX composition and equilibration temperature at a given pressure.

4:2.10 Summary

The mineral chemistry of the spinel facies peridotites from Beni Bousera reveals a clear correlation between modal mineralogy (CPX content) and mineral composition indicating that the harzburgite-lherzolite suite represents a series of residues variably depleted in basaltic components, with the CPX absent harzburgites being the most depleted residues. Although the harzburgites contain no discrete diopside, most contain Ca-rich enstatite saturated, or very nearly saturated, in diopside at the end of melting. This places them very close to the boundary of the four phase and three phase fields during melting and requires that these harzburgites are the residues of around 25 % partial melting (Dick and Fisher 1984). It thus appears that the diopside-out phase boundary between residual peridotites with and without diopside provides an effective barrier beyond which partial melting has rarely proceeded in the Beni Bousera and Ronda peridotites. This is also a common feature in abyssal peridotites (Dick and Fisher op. cit.). This phase boundary is probably a thermal devide or a cusp in the peridotite melting curve with a steep rise in temperature or heat input required to produce further partial melting. The mineral chemistry of the peridotites is very similar to that of other orogenic peridotites which in turn show similarities to oceanic "abyssal" peridotites and spinel peridotite xenoliths from basaltic volcanics. Estimation of bulk CPX analyses from broad beam microprobe analyses of exsolved crystals record equlibration conditions close to the peridotite solidus, ~1250 °C at 15kb.

4:3 Pyroxenite mineral chemistry

4:3.1 Non-garnetiferous pyroxenites

The two groups of non-garnetiferous pyroxenites, Cr-pyroxenites and the Al-augite group will be discussed together in this section. Two Cr-pyroxenites and one Al-augite pyroxenite were analysed in detail. Of the two Cr-pyroxenites, GP132(1) represents a websterite/Cr-diopside vein which obliquely cross-cuts the foliation in the peridotites whilst GP101 is from a 30 cm thick bright green websterite layer within a zone containing abundent Cr-pyroxenites in the Oued el Jouj wadi (see measured section , Appendix 2 for exact location).

4:3.1.a Clinopyroxenes.

CPX from the Cr-pyroxenites appears bright green in hand specimen and resemble the Cr-diopside from the host peridotites whereas CPX from the Al-augite pyroxenites appear dark greyish. A distinction

Table 4.8 Representative analyses of CPX and OPX from non-garnetiferous pyroxenites.

SAMPLE	PHN 5732 CPX1 CORE	PHN 5732 CPX2 CORE	PHN 5732 CPX5 CORE	PHN 5732 CPX5 RIM	GP101a CPX3 CORE	GP101a CPX4 CORE	GP132(1) CPX1 CORE	GP132(1) CPX2 CORE	GP132(1) CPX2 RIM
SIO2	51.10	52.20	49.79	50.28	52.84	52.51	52.87	53.44	53.25
TIO2	1.40	1.26	1.94	1.48	0.27	0.19	0.20	0.20	0.20
AI2O3	11.00	9.93	10.13	10.25	9.96	9.57	5.37	5.50	4.68
Cr2O3	0.30	0.18	0.27	0.23	0.40	0.43	1.04	1.02	0.77
Fe Total	4.51	4.92	6.09	4.45	2.50	2.67	2.42	3.22	1.92
MnO	0.21	0.33	0.29	0.27	0.10	0.02	0.01	0.01	0.12
MgO	11.68	13.30	13.89	11.83	13.33	13.48	16.97	19.16	16.10
CaO	16.62	14.99	14.58	17.49	18.13	19.36	19.63	15.46	21.71
Na2O	3.94	3.46	3.13	3.14	2.78	2.63	0.94	1.16	0.86
TOTAL	100.76	100.67	100.11	99.43	100.32	100.86	99.52	99.17	99.61

SAMPLE	PHN5732	PHN5732	M5-103	GP101a	GP101a	GP132(1)	GP132(1)	GP132(1)
TYPE	AL-Augite	Al-Augite	Al-Augite	Cr-Pyroxenite	Cr-Pyroxenite	Cr-Pyroxenite	Cr-Pyroxenite	Cr-Pyroxenite
SIO2	53.49	53.28	53.03	53.93	53.55	55.57	55.66	55.40
TIO2	0.57	0.23		0.16	0.06	0.20	0.09	0.12
AI2O3	3.40	3.70	4.23	5.14	6.30	4.42	3.99	4.68
Cr2O3	0.11	0.16	0.12	0.20	0.30	0.85	0.74	0.79
Fe Total	12.82	12.93	7.92	7.24	7.74	5.45	5.59	5.65
MnO	0.46	0.33	0.11	0.19	0.13	0.11	0.13	0.14
MgO	29.05	28.18	32.25	32.53	31.96	33.03	32.92	32.79
CaO	0.47	0.45	1.05	0.61	0.42	0.65	0.65	0.71
Na2O	0.04	0.00	0.01	0.05	0.14	0.24	0.18	0.10
TOTAL	100.41	99.27	99.35	100.04	100.61	100.52	99.95	100.37

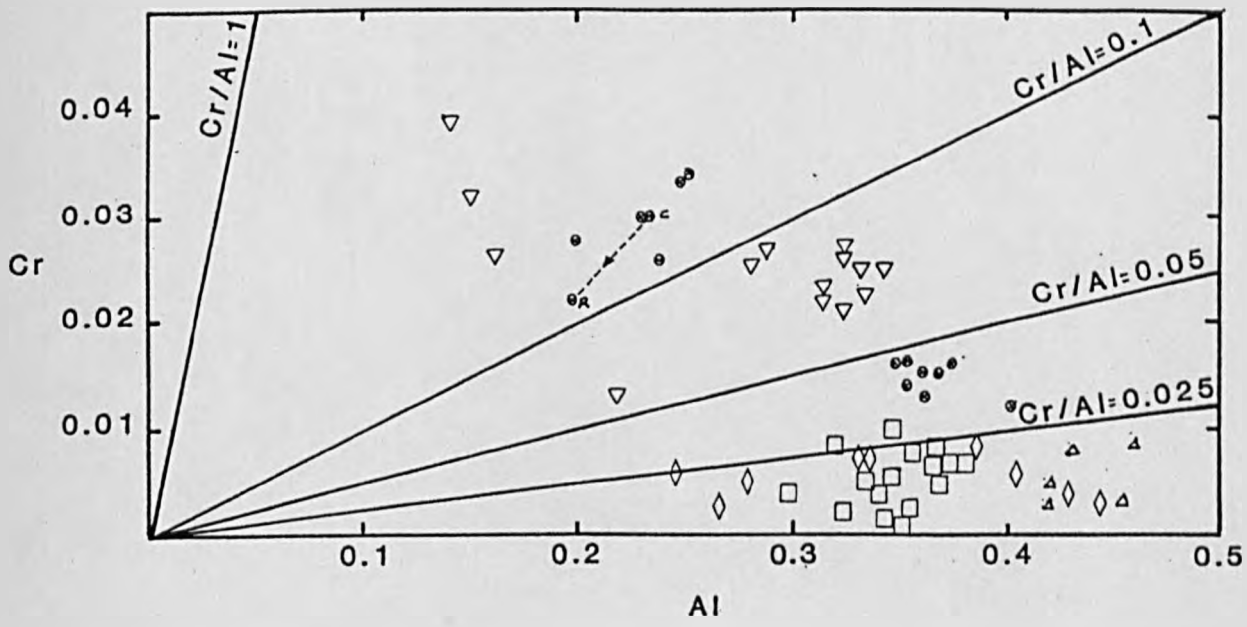

Figure 4.17. Cr vs Al cation proportion plot of CPX from different pyroxenite lithologies. Symbols as in Figure 4.3 Cr-pyroxenites are circles with crosses, Al-augite pyroxenites are open triangles pointing up.

Figure 4.18 Ternary CaTs, Jd, En end member plot , symbols as in Fig. 4.3.

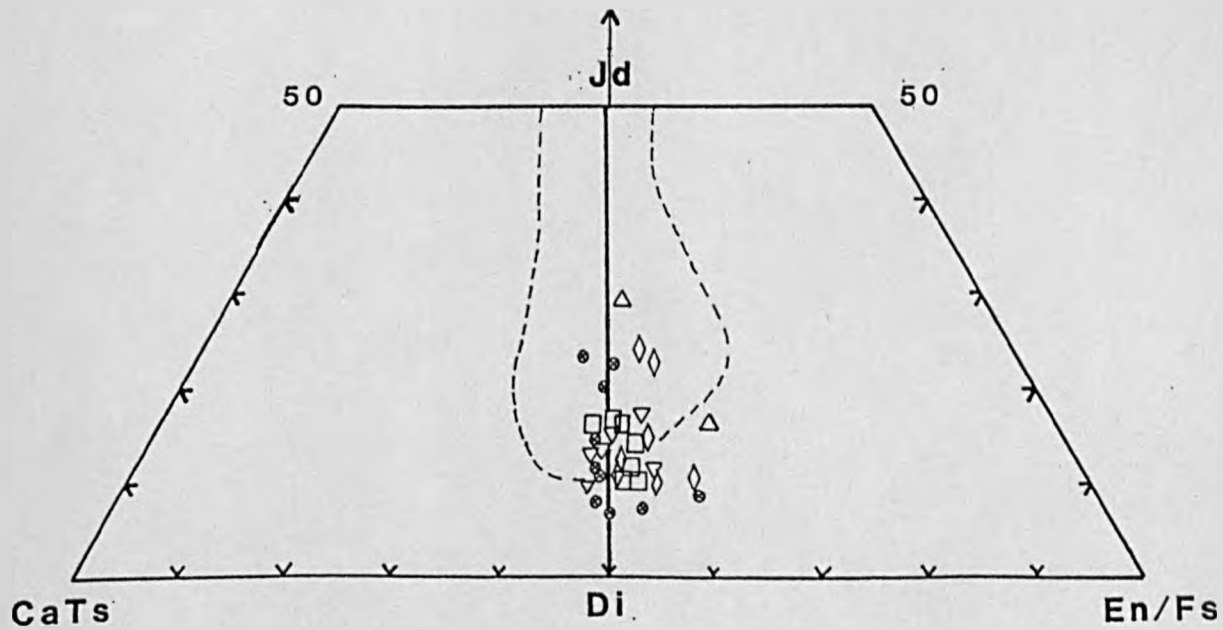

may be drawn between the two groups on the basis of their Cr contents (Table 4.8). A plot of Cr vs Al (Figure 4.17) illustrates the distinctly higher Cr contents of the Cr-pyroxenites, especially the vein sample GP132(1) which has CPX with higher Cr/Al ratios than most of the lherzolite CPX (Cr/Al > 0.1). Cr/Al ratios of GP101 are markedly lower (<0.05) due to the highly aluminous nature of the CPX, however, the Cr/Al values remain higher than any Al-augite pyroxenites (average Cr/Al < 0.025) indicating that the lithological division is valid.

CPX from the Al-augite pyroxenite, PHN5732, which is a websterite, are generally more jadeititic than CPX from the Cr pyroxenites (upto 27 mol % Jd compared to 23 % Jd ,see Figure 4.18) and are generally more Mg and Ca rich; some analyses from the Al-augite pyroxenite are distinctly subcalcic (Fig. 4.3). The non-garnetiferous Al-augite pyroxenites are richer in Mg than the garnetiferous Al-augite pyroxenites (Fig. 4.3).

Table 4.8 shows the distinct difference in CPX chemistry between GP101 and GP132(1). The vein pyroxenite CPX are richer in Cr_2O_3 and MgO and poorer in Al_2O_3 and Na_2O which is reflected in the much lower jadeite component of the vein Cr-pyroxenites. These differences and the higher Na_2O and Al_2O_3 content of the Al-augite pyroxenite are evident in Figure 4.19. Core-rim zonation in PHN5732 is irregular, with rims often slightly richer in Na_2O and Al_2O_3 than cores (Fig 4.19). This contrasts with the more usual core-rim decrease in Na_2O and Al_2O_3 due to lower temperature/pressure re-equilibration.

The Al-augite CPX from PHN5732 are considerably more Na rich and generally more aluminous than the high pressure sub-calcic augite clinopyroxenites reviewed by Wilkinson (1976,1974) from the E. Australian fold belt volcanics (Fig. 4.19). In addition to having high Al_2O_3 contents the Al-augite CPX have large proportions of octahedrally coordinated aluminium (Fig 4.7a and 4.8) such that $Al^{vi} >> Al^{iv}$. CPX from the Cr-pyroxenite, GP101, are also very aluminous (Table 4.8 and Fig 4.7a) with considerable excess of Al^{vi} which leads to high jadeite contents and up to 10 mole % CaAl-Tschermaks components. Al contents of GP132(1) are of the same order as the lherzolite CPX. Ti contents of the Cr pyroxenite group are very low (> 0.001 cation units) in most cases, in contrast to most CPX of the non gernetiferous Al-augite pyroxenites (Fig. 4.7b). Calculated Fe^{3+} contents of CPX from Cr-pyroxenites are close to zero. CPX from the Al-augite pyroxenites show slightly more scatter about the $Fe^{3+}=0$ line in Figure 4.9.

The jadeite and Ca-Tschermak's components of the non-garnetiferous and garnetiferous pyroxenites are plotted in Figure 4.20 which indicates the predominance of Jd over CaTs in all the pyroxenites. The dominance of Jd in the Beni Bousera pyroxenites contrasts with the CaTs rich nature of CPX from the crustal granulites within the garnet-sillimanite gneisses. The diagonal line on Fig 4.20 from 23% Jd to 25 % CaTs is taken from Thompson (1974) and divides his selection of pyroxenes which coexist with garnet (above the line) from those that do not (below). This relationship for the Beni Bousera pyroxenites is clearly not straightforward. CPX plotting below the line in Fig 4.20 may have exsolved significant garnet, although CPX from GP101, the Cr-pyroxenite which does not show any evidence of being in equilibrium with garnet plot above this line. In a study of experimentally synthesised CPX from magmas of widely varying bulk composition Thompson (1974) found that in runs that crystallized with garnet on the liquidus, the Na and Al contents of the pyroxenes increased with increasing pressure and temperature and consequently their Jd and CaTs components increased with increasing pressure (see Fig 4.20). Although

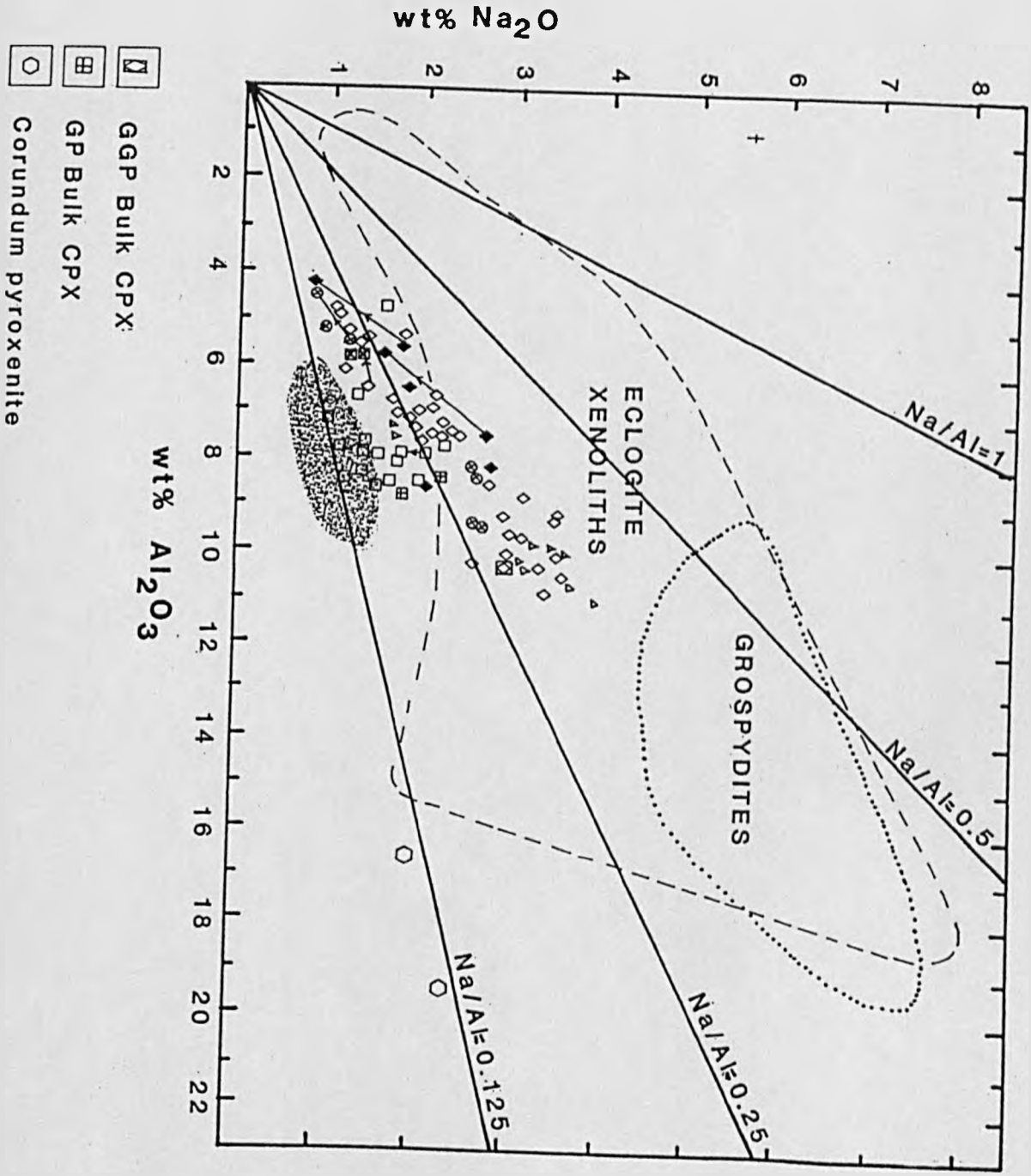

Figure 4.19. Na_2O vs Al_2O_3 of CPXs from Beni Bousera pyroxenites. Symbols as in Fig. 4.3 but hexagon is CPX from corundum pyroxenite (Kornprobst et al 1982). Shaded field is for CPX from garnet pyroxenite xenoliths from E.Australia described by Wilkinson (1976). Open dashed field encompasses CPX from diamondiferous eclogite xenoliths and E-type diamond inclusions (Reid et al 1976, Sobolev 1979). Dotted open field is for CPX from grospydite xenoliths (Sobolev 1979).

such trends were discernible, Thompson (1974) concluded that the most important factor controlling pyroxene compositions precipitated over a broad range of pressure and temperature is the composition of the melt from which they crystallized. The low pressure liquidus pyroxenes showed very little jadeite but a wide range of CaTs component. Considering the different chemistries of the Cr- and Al-augite pyroxenes it is difficult to decipher any discrete P/T information from the differing position they occupy on Figure 4.20. Analyses from the two different Cr-pyroxenites do seem to define a combined trend of increasing Jd and increasing CaTs components ,with a steep slope. This is consistent with the positive correlation observed by Thompson (1974) for increasing pressure and temperatures. Considering the similarity of the two Cr-pyroxenite lithologies (Cr-rich websterites), the higher Jd and CaTs component of CPX from GP101 (22 and 10 mol % respectively) may be taken as indicating that GP101 equilibrated at significantly higher pressures and temperatures than the websterite vein, GP132 (1) . As CPX from the Cr-pyroxenites show little evidence of exsolution, their composition may represent CPX that have undergone less physical re-equilibration than the Al-augites. Alternatively the Cr pyroxenite trend is consistent with that found by Thompson (1974) for isobaric cooling at constant pressure in the absence of garnet. In this case Jd and CaTs components both rise with falling temperature.

The non-garnetiferous Al-augite pyroxenite, PHN5732, plots at the top of the sub vertical trend of all CPX from both garnetiferous and non-garnetiferous Al-augite pyroxenites (Fig.4.20). This trend of increasing Jd component and slightly decreasing CaTs component is consistent with that found by Thompson (1974) for isobaric cooling in the presence of garnet. A similar trend was also noted by O'Hara (1969) from a sub-solidus experimental study of natural garnet-CPX pairs.

4:3.1b Orthopyroxenes.

Analyses of the OPX from non-garnetiferous websterites are presented in Table 4 8. .The analyses are for exsolved OPX core compositions of OPX porphyroclasts. The OPX from Cr-pyroxenite show little evidence of CPX exsolution. The difference between the Cr- and Al-augite pyroxenites is again apparent from the Cr content of their OPX. OPX from the Al-augite series have Cr_2O_3 contents of ~ 0.1 to 0.16 wt % whereas OPX from Cr-pyroxenites contain upto 0.85 wt % Cr_2O_3. OPX from Cr-pyroxenites are also significantly richer in MgO than the Al-augite series OPX (Fig. 4.3).

In contrast to relationships shown by CPX, OPX from Cr-pyroxenites are generally richer in Al_2O_3 contents (Table 4.8) compared to those from Al-augite pyroxenites. The enhanced Al_2O_3 contents of the Cr-pyroxenite OPX are illustrated in Figure 4.21. In almost all the OPX, tetrahedrally co-ordinated Al exceeds octahedral Al (Fig.4.21). Several Cr-pyroxenite OPX analyses plot close to the 1:1 line on Figure 4.21 whilst bulk analyses for an OPX from an orthopyroxenite and from a websterite taken from Kornprost (1969) also have $Al^{vi} \sim Al^{iv}$ and higher Al contents than exsolved porphyroclast cores. This indicates that the Al-poor nature of the OPX from the Al-augite websterite is due to sub-solidus exsolution of CPX whereas the Cr-pyroxenite OPX do not exhibit CPX exsolution. CaO contents of OPX from both lithological groups are low (0.3 to 0.6 %); the Al-augite pyroxenite OPX containing the lowest values due to CPX exsolution. The bulk analysis from a websterite taken from Kornprobst (1969) gives the highest CaO content (1.05 % CaO) confirming saturation of the host OPX in Ca-rich pyroxene.

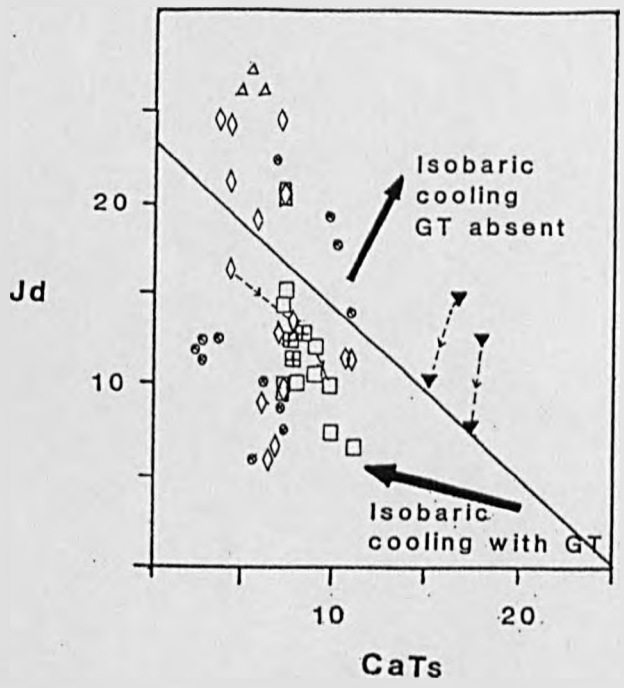

Figure 4.20. Jd vs CaTs component of Beni Bousera pyroxenite CPX. Arrows on lines joining core-rim pairs point to rim compositions. Large arrows are for isobaric cooling with garnet (sub horizontal) and isobaric cooling without garnet (sub vertical), the arrows are taken from trends proposed by Thompson (1974). Symbols as in Fig. 4.3. Thin diagonal line devides Thompson's (1974) selection of CPX coexisting with garnet (above line) from CPX without garnet (below line).

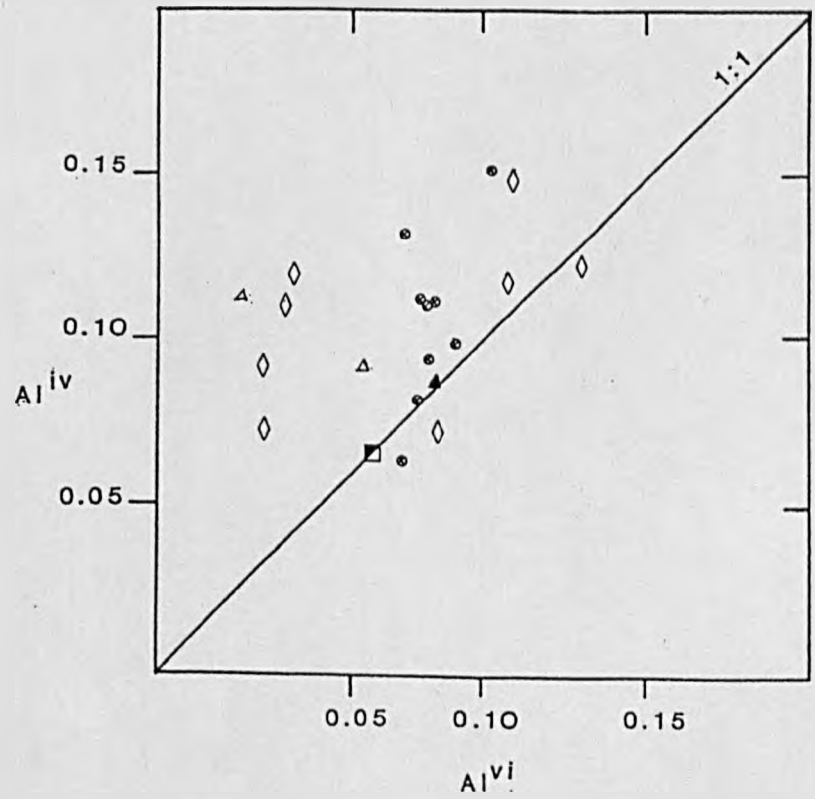

Figure 4.21. Al^{iv} vs Al^{vi} in OPX from Beni Bousera pyroxenites. Half filled square is bulk OPX from an orthopyroxenite and filled triangle is bulk OPX from Al-augite websterite analysed by Kornprobst (1969). GGP symbols are for exsolved OPX lamellae in CPX porphyroclasts.

4:3.2 Garnet pyroxenites.

Garnet pyroxenites from Beni Bousera include garnet websterites, garnet clinopyroxenites and zoned garnet clinopyroxenites containing "zones"of over 90 % garnet i.e. garnetite (see Chapter 2). All garnetiferous pyroxenites belong to the Al-augite pyroxenite series. In terms of mineral chemistry this study has concentrated on graphite bearing garnet clinopyroxenites and garnet clinopyroxenites. A single garnetite zone has been analysed and one garnet websterite.

4:3.3 Graphitic and non-graphitic garnet clinopyroxenites.

All garnet pyroxenites show varying degrees of sub-solidus exsolution and recrystallization. Thus the majority of the mineral chemical data presented in this section refers to composition of exsolved, recrystallized porphyroclasts.

4:3.3a Clinopyroxenes.

The core compositions of CPX porphyroclasts in this section represent the exsolved CPX host composition after exsolution of varying amounts of OPX ,garnet and plagioclase. Due to a combination of the presence of wide, often irregularly distributed OPX exsolution lamellae, and the sporadic appearance of exsolved blebs of garnet and plagioclase, broad beam micro-probe analyses of CPX porphyroclasts did not give a good quantitative estimate of the primary or "unmixed" compositions of the constituent CPX. Bulk compositions for CPX from non-graphitic garnet clinopyroxenites were obtained by wet chemical methods by Kornprobst (1969). These analyses represent the best estimate of primary CPX compositions providing that ex-grain exsolution/diffusion has not occurred.

Bulk compositions of CPX from the graphitic garnet clinopyroxenites were estimated by mass balance calculations using a least squares mixing routine to estimate the percentage of exsolved phases. The largest error invoved in this procedure is in the estimation of the proportion of exsolved phases relative to the host crystal as the original bulk composition of the crystal is not known.The most sub-calcic bulk analyses of a CPX from a garnet pyroxenite was taken as the end member from which to estimate the mixing proportions. Although this composition is more magnesium rich than many of the exsolved CPX compositions from the GGP, it plots close to the tie line between exsolved composition of Ca-rich and Ca-poor pyroxenes from GP147. The compositions of the exsolved OPX , garnet, plagioclase and host CPX from a porphyroclast from GP147 were used as mixing components. The subcalcic CPX analysis from garnet clinopyroxenite M5-101 of Kornprobst (1969) used as a "target" bulk composition. The result of the least-squares modelling for this set of data are presented below as Table 4.9. The sum of squares of the residuals is relatively high (>3) and this remains high even if crude modelling of only Al_2O_3 ,SiO_2 ,MgO,CaO and Na_2O is used.

Table 4.9 Least squares residual modelling of bulk CPX composition, normalised to 100%.

	M5-101	CALCULATED	DIFFERENCE
SiO_2	50.79	51.44	-0.65
TiO_2	1.02	0.77	+0.25
Al_2O_3	8.92	8.21	+0.71
Fe Total	9.43	10.49	-1.06
MnO	0.14	0.39	-0.25
MgO	15.16	13.92	+1.24
Cao	12.75	12.95	-0.2
Na_2O	1.79	1.82	-0.03
MODAL %			
CPX		66	
OPX		20	
PLAG		7	
GT		7	

Various exsolved CPX host compositions were combined in the above proportions with exsolved garnet, plagioclase and OPX compositions (see Tables 4.10 & 4.11) from CPX porphyroclasts in the GGP to produce bulk "pre-exsolution" composition. Using exsolved CPX host compositions with high Al_2O_3 and high Na_2O (~10 and 3 wt % respectively) tends to produce analyses which are very sub-calcic (Figure 4.28) but do not yield good stoichiometry when cation proportions are calculated on the basis of 6 oxygens due to Al_2O_3 being unrealistically high. The calculated bulk CPX composition for the GGP sample GP147 is given in Table 4.12 . It is a subcalcic sodic-augite composition with 9.48 % Al_2O_3 and 2.13 % Na_2O, plotting at 36 % wollastonite on the quaderateral diagram of Figure 4.22. Despite being more Fe rich than most analyses of CPX from the GP and GGP, several "exsolved" spot analyses are more subcalcic. This may be due to accidental inclusions of OPX lamellae in the probe spot or to heterogeneous domains of unexsolved CPX within the exsolved host. These subcalcic spot compositions are also marked by high Al_2O_3 and Na_2O contents and may be unexsolved CPX. Bulk wide beam CPX analyses from the GGP (Fig. 4.22) are generally more subcalcic and more Fe rich than exsolved CPX porphyroclast cores. The calculated bulk CPX analyses are the most Fe rich and not as subcalcic as the broad beam analyses (Table 4.12). This is because the broad beam analyses do not include any noticeable plagioclase or garnet thus they are more subcalcic and Fe poor. Broad beam analyses including exsolved garnet and plagioclase proved impractical due to the coarseness of the garnet/plagioclase blebs compared to the total beam area which grossly over estimated their volumetric importance and did not yield satisfactory CPX totals or stoichiometry. Thus the broad beam probe analyses are not a true representation of the pre-exsolution composition.

Table 4.10. Representative CPX analyses for GP and GGP layers.

SAMPLE	GP81 GGP	GP81 GGP	GP81 GGP	GP81 GGP	GP81 GGP	GP81 GGP	GP 147 GGP	GP 147 GGP	GP 147 GGP	GP 147 GGP	GP 147 GGP	GP 143 GGP
ANALYSIS	CR	CR	CR	CR	CR	CR	CR	CR	CR	RIM	RIM	CR
SiO2	51.11	51.02	51.38	51.57	51.49	51.48	50.93	51.46	50.94	51.27	51.34	51.11
TiO2	0.72	0.60	0.54	0.53	0.51	0.64	1.02	1.14	1.03	1.08	0.72	1.41
Al2O3	0.19	7.27	5.17	5.57	5.09	5.16	5.30	7.48	6.20	6.09	7.72	9.48
Cr2O3	0.00	0.08	0.11	0.10	0.02	0.00	0.24	0.17	0.25	0.18	0.17	0.21
Fe3+	9.44	1.73	0.33	0.85		1.76						2.30
Fe2+	0.01	8.17	10.54	9.03	11.34	7.23	5.42	5.98	7.53	5.98	7.55	4.09
Mn	11.66	0.32	0.19	0.05	0.15	0.18	0.19	0.21	0.11	0.22	0.28	0.11
Mg	16.92	12.48	13.87	12.97	13.16	12.46	14.02	13.34	15.95	13.90	14.69	11.95
Ca	2.02	17.10	17.36	18.03	16.39	19.35	21.22	18.00	16.01	19.76	14.94	16.33
Na	0.00	1.92	0.91	1.46	1.23	1.66	1.24	2.16	1.24	1.32	2.03	3.42
K	0.02	0.00	0.00	0.03	0.00	0.01	0.05	0.05	0.03	0.00	0.04	0.05
Ni	0.00	0.00	0.00	0.00	0.03	0.00	0.00	0.03	0.07	0.00	0.00	0.00
Sum	99.58	100.69	100.40	100.18	99.41	99.94	99.62	100.03	99.35	99.82	99.47	100.46
CATS O=6												
Si	1.891	1.869	1.899	1.904	1.921	1.905	1.879	1.876	1.872	1.881	1.878	1.846
Ti	0.020	0.016	0.015	0.015	0.014	0.018	0.028	0.031	0.028	0.030	0.020	0.038
Al	0.326	0.314	0.225	0.242	0.224	0.225	0.230	0.321	0.269	0.264	0.333	0.404
Cr	0.005	0.002	0.003	0.003	0.001	0.000	0.007	0.005	0.007	0.005	0.005	0.006
Fe3+	0.000	0.048	0.009	0.024		0.049						0.062
Fe2+	0.292	0.250	0.326	0.279	0.354	0.224	0.167	0.182	0.231	0.183	0.231	0.123
Mn	0.000	0.010	0.006	0.002	0.005	0.006	0.006	0.007	0.003	0.007	0.009	0.003
Mg	0.643	0.682	0.765	0.714	0.732	0.687	0.771	0.725	0.874	0.760	0.801	0.643
Ca	0.671	0.671	0.688	0.713	0.655	0.767	0.839	0.703	0.630	0.777	0.585	0.632
Na	0.145	0.136	0.065	0.104	0.089	0.119	0.089	0.152	0.089	0.094	0.144	0.239
K	0.001	0.000	0.000	0.001	0.000	0.000	0.002	0.002	0.001	0.000	0.002	0.002
Ni	0.001	0.000	0.000	0.000	0.001	0.000	0.000	0.001	0.002	0.000	0.000	0.000
Sum	3.995	4.000	4.000	4.000	3.997	4.000	4.019	4.007	4.007	4.001	4.007	4.000

SAMPLE	GP 143 GGP	GP37 GP	GP37 GP	GP37 GP	GP37 GP
ANALYSIS	CR	CR	CR	CR	RIM
SiO2	51.08	50.03	49.68	50.16	50.12
TiO2	1.32	0.94	0.75	0.70	0.71
Al2O3	8.66	8.02	7.87	8.01	7.89
Cr2O3	0.22	0.05	0.16	0.17	0.10
Fe3+	1.50	2.99	1.08	2.05	1.32
Fe2+	5.56	5.32	6.80	5.09	6.05
Mn	0.19	0.17	0.23	0.12	0.02
Mg	12.91	12.03	11.65	12.06	12.41
Ca	16.12	18.97	19.56	20.23	20.26
Na	2.80	2.02	1.54	1.71	1.36
K	0.01	0.02	0.00	0.00	0.05
Ni	0.03	0.00	0.09	0.08	0.00
Sum	100.41	100.55	99.41	100.37	100.29
CATS O=6					
Si	1.852	1.831	1.845	1.838	1.839
Ti	0.036	0.026	0.021	0.019	0.020
Al	0.370	0.346	0.344	0.346	0.341
Cr	0.006	0.001	0.005	0.005	0.003
Fe3+	0.041	0.082	0.030	0.056	0.036
Fe2+	0.169	0.163	0.211	0.156	0.186
Mn	0.006	0.005	0.007	0.004	0.001
Mg	0.698	0.657	0.645	0.659	0.679
Ca	0.626	0.744	0.778	0.794	0.797
Na	0.197	0.143	0.111	0.122	0.097
K	0.000	0.001	0.000	0.000	0.002
Ni	0.001	0.000	0.003	0.002	0.000
Sum	4.002	4.000	4.000	4.000	4.000

GP37 GP RIM	GP87B GP CR	GP87B GP CR	GP87B GP CR	GP87T GP CR
50.24	51.47	51.22	50.36	50.22
0.78	0.62	0.71	1.13	0.74
7.61	6.41	6.43	7.82	8.08
0.08	0.39	0.34	0.23	0.43
3.66	0.75	3.34	0.88	4.03
4.11	3.64	1.42	3.12	0.24
0.06	0.14	0.20	0.19	0.07
12.05	13.73	14.29	13.65	14.99
20.23	20.95	20.73	21.51	19.79
1.98	1.50	1.72	1.28	1.80
0.00	0.01	0.00	0.00	0.00
0.01	0.02	0.26	0.08	0.02
100.81	99.62	100.66	100.25	100.41
1.834	1.882	1.854	1.831	1.810
0.021	0.017	0.019	0.031	0.020
0.327	0.276	0.274	0.335	0.343
0.002	0.011	0.010	0.006	0.012
0.101	0.021	0.091	0.024	0.109
0.125	0.111	0.043	0.095	0.007
0.002	0.004	0.006	0.006	0.002
0.656	0.749	0.771	0.740	0.806
0.791	0.821	0.804	0.838	0.764
0.140	0.106	0.121	0.090	0.125
0.000	0.000	0.000	0.000	0.000
0.000	0.001	0.008	0.002	0.001
4.000	4.000	4.000	4.000	4.000

GP/GGP CPX

SAMPLE	GP87T GP	GP151 GTWEB	GP151 GTWEB	PHN5730 GGP	PHN5730 GGP
ANALYSIS	RIM	CR	CR	GR INCLN CR	GR INCLN CR
SiO2	50.02	51.73	50.87	51.46	51.82
TiO2	0.64	0.20	0.35	1.09	1.00
Al2O3	7.04	7.10	7.65	5.69	5.94
Cr2O3	0.52	0.27	0.18	0.22	0.08
Fe3+	3.75	1.02	1.85		
Fe2+	0.00	3.28	2.60	8.49	8.37
Mn	0.11	0.03	0.01	0.32	0.19
Mg	14.67	13.45	13.27	13.91	13.77
Ca	21.21	21.42	21.43	17.24	17.19
Na	1.52	1.61	1.60	1.98	1.97
K	0.00	0.00	0.00	0.06	0.07
Ni	0.12	0.10	0.03	0.00	0.06
Sum	99.60	100.04	99.82	100.45	100.46
CATS O=6					
Si	1.824	1.881	1.855	1.890	1.897
Ti	0.018	0.006	0.009	0.030	0.028
Al	0.302	0.304	0.328	0.246	0.256
Cr	0.015	0.008	0.005	0.006	0.002
Fe3+	0.103	0.028	0.051		
Fe2+	0.000	0.100	0.079	0.261	0.256
Mn	0.003	0.001	0.000	0.010	0.006
Mg	0.798	0.729	0.721	0.761	0.752
Ca	0.829	0.827	0.837	0.678	0.675
Na	0.108	0.113	0.113	0.141	0.140
K	0.000	0.000	0.000	0.003	0.003
Ni	0.003	0.003	0.001	0.000	0.002
Sum	4.002	4.000	4.000	4.026	4.017

PHN5730 GGP GR INCLN CR	PHN5730 GGP GR INCLN CR	PHN5730 GGP GR INCLN CR	PHN5730 GGP GR INCLN RIM
52.06	50.76	50.96	51.82
0.99	1.06	1.04	0.85
5.81	9.29	9.62	4.26
0.14	0.16	0.21	0.31
7.41	6.81	6.87	6.88
0.33	0.27	0.25	0.31
13.16	12.25	11.97	13.59
19.03	16.80	17.13	21.05
1.88	2.43	2.93	0.85
0.05	0.05	0.00	0.00
0.00	0.09	0.00	0.00
100.86	99.98	100.98	99.43
1.900	1.853	1.845	1.907
0.027	0.029	0.028	0.024
0.250	0.400	0.410	0.187
0.004	0.005	0.006	0.009
0.226	0.208	0.208	0.214
0.010	0.008	0.008	0.010
0.716	0.666	0.646	0.752
0.744	0.657	0.664	0.838
0.133	0.172	0.205	0.061
0.002	0.002	0.000	0.000
0.000	0.003	0.000	0.000
4.013	4.003	4.021	4.002

SAMPLE	PHN5730 GGP	PHN5730 GGP	PHN5730 GGP
ANALYSIS	GR INCLN RIM	CR	CR
SiO2	51.52	51.80	51.08
TiO2	0.81	1.22	1.18
Al2O3	4.14	6.52	9.85
Cr2O3	0.29	0.18	0.11
Fe3+			
Fe2+	6.71	7.05	6.75
Mn	0.20	0.17	0.14
Mg	13.45	13.48	11.46
Ca	20.68	18.84	17.58
Na	1.32	1.47	2.78
K	0.00	0.00	0.04
Ni	0.01	0.04	0.00
Sum	99.12	100.78	100.96
CATS O=6			
Si	1.918	1.884	1.848
Ti	0.023	0.033	0.032
Al	0.182	0.280	0.420
Cr	0.008	0.005	0.003
Fe3+			
Fe2+	0.209	0.214	0.204
Mn	0.006	0.005	0.004
Mg	0.746	0.731	0.618
Ca	0.825	0.734	0.682
Na	0.095	0.104	0.195
K	0.000	0.000	0.002
Ni	0.000	0.001	0.000
Sum	4.012	3.992	4.007

GP/GGP CPX

PHN5730 GGP CR	PHN5730 GGP RIM	PHN5730 GGP CR	PHN5731 GGP CR	PHN5731 GGP CR
50.96	50.88	50.04	50.28	50.20
1.04	1.09	1.36	0.92	0.92
9.62	7.15	10.25	10.29	10.43
0.21	0.15	0.11	0.09	0.08
			2.06	2.99
6.87	6.93	6.05	6.05	4.80
0.25	0.12	0.18	0.21	0.25
11.97	12.77	10.80	10.64	10.47
17.13	18.30	17.66	15.80	15.98
2.93	2.44	2.62	3.30	3.59
0.00	0.00	0.05	0.03	0.00
0.00	0.00	0.00	0.07	0.00
100.98	99.82	99.12	99.75	99.71
1.845	1.872	1.840	1.841	1.835
0.028	0.030	0.038	0.025	0.025
0.410	0.310	0.444	0.444	0.450
0.006	0.004	0.003	0.003	0.002
			0.057	0.082
0.208	0.213	0.186	0.185	0.147
0.008	0.004	0.006	0.007	0.008
0.646	0.700	0.592	0.581	0.571
0.664	0.721	0.696	0.620	0.626
0.205	0.174	0.187	0.234	0.254
0.000	0.000	0.002	0.002	0.000
0.000	0.000	0.000	0.002	0.000
4.021	4.028	3.993	4.000	4.000

GP/GGP CPX

SAMPLE	PHN5731 GGP	PHN5731 GGP	PHN5731 GGP	PHN5731 GGP	PHN5731 GGP	PHN5731 GGP	PHN5731 GGP	PHN5731 GGP
ANALYSIS	RIM	RIM	GR INCLN CR	GR INCLN CR	GR INCLN CR	GR INCLN CR	RIM	RIM
SiO2	51.05	50.61	50.75	51.19	51.39	51.94	51.92	50.61
TiO2	0.89	1.11	1.05	1.17	1.15	1.09	1.07	1.11
Al2O3	9.22	9.12	9.01	7.01	8.26	8.15	6.29	9.12
Cr2O3	0.04	0.00	0.04	0.12	0.14	0.20	0.05	0.00
Fe3+	1.49	0.68	3.12	1.05	2.09	1.60	0.00	0.68
Fe2+	8.21	5.96	5.64	6.60	6.43	6.58	7.16	5.96
Mn	0.17	0.31	0.21	0.21	0.23	0.13	0.30	0.31
Mg	12.41	10.97	12.69	12.32	12.47	12.65	12.65	10.97
Ca	13.87	18.16	15.38	17.00	15.93	15.42	17.88	18.16
Na	2.93	2.66	2.87	2.50	2.84	3.02	1.98	2.66
K	0.00	0.03	0.00	0.03	0.00	0.00	0.04	0.03
Ni	0.00	0.00	0.16	0.00	0.02	0.05	0.03	0.00
Sum	100.28	99.61	100.92	99.21	100.94	100.83	99.38	99.61
CATS O=6								
Si	1.860	1.858	1.837	1.889	1.862	1.878	1.913	1.858
Ti	0.024	0.031	0.029	0.032	0.031	0.030	0.030	0.031
Al	0.396	0.394	0.384	0.305	0.353	0.347	0.273	0.394
Cr	0.001	0.000	0.001	0.004	0.004	0.006	0.002	0.000
Fe3+	0.041	0.019	0.085	0.029	0.057	0.044	0.000	0.019
Fe2+	0.250	0.183	0.171	0.204	0.195	0.199	0.221	0.183
Mn	0.005	0.010	0.006	0.006	0.007	0.004	0.009	0.010
Mg	0.674	0.600	0.685	0.678	0.673	0.682	0.695	0.600
Ca	0.542	0.714	0.597	0.672	0.618	0.598	0.706	0.714
Na	0.207	0.190	0.201	0.179	0.199	0.212	0.142	0.190
K	0.000	0.001	0.000	0.001	0.000	0.000	0.002	0.001
Ni	0.000	0.000	0.005	0.000	0.000	0.002	0.001	0.000
Sum	4.000	4.000	4.000	4.000	4.000	4.000	3.992	4.000

Table 4.11. Exsolved garnet, OPX and plagioclase compositions from CPX porphyroclasts in the GGP.

SAMPLE	GP147	GP147	GP147	GP147
MIN.	GT EX.	GT EX.	GT EX.	GT EX.
SIO2	39.9	39.57	39.65	39.33
TIO2	0.19	0.13	0.23	0.06
Al2O3	23.02	22.85	22.94	22.58
Cr2O3	0.14	0.17	0.18	0.14
Fe3+	0.06	0.23	0.06	0.37
Fe2+	19.44	19.12	19.47	19.6
MnO	0.94	0.9	1.24	1.08
MgO	12.53	12.49	12.09	11.82
CaO	4.58	4.71	4.79	4.82
SUM	100.82	100.19	100.65	99.78
CATS. O = 12				
SI	2.962	2.956	2.956	2.963
TI	0.011	0.007	0.013	0.003
AI	2.015	2.013	2.017	2.005
Cr	0.008	0.01	0.01	0.008
Fe3+	0.004	0.013	0.004	1.234
Fe2+	1.207	1.195	1.214	0.069
Mn	0.059	0.057	0.078	1.326
Mg	1.386	1.391	1.343	0.389
Ca	0.364	0.377	0.383	8.019
SUM	8.015	8.02	8.017	

SAMPLE	PHN5731	PHN5731	PHN5731	GP147	GP147
MIN.	OPX EX	OPX EX.	OPX EX.	OPX EX.	OPX EX.
SIO2	52.68	50.72	50.65	51.75	52.14
TIO2	0.23	0.22	0.11	0.24	0.25
Al2O3	3.84	6.02	6.04	4.12	5.18
Cr2O3	0.18	0.08	0.05	0.01	0
Fe3+	0	0	3.39	1.16	0
Fe2+	18.44	20.84	17.21	16.72	16.97
MnO	0.3	0.37	0.42	0.36	0.31
MgO	22.48	21.01	21047	24.84	24.59
CaO	1.96	0.59	0.54	0.57	0.56
Na2O	0.38	0.07	0.83	0	0.01
SUM	100.48	99.92	100.7	99.77	100.1
CATS. O = 6					
SI	1.923	1.875	1.85	1.888	1.889
TI	0.006	0.006	0.003	0.007	0.007
AI	0.165	0.263	0.26	0.177	0.221
Cr	0.005	0.002	0.002	0	0
Fe3+	0	0	0.093	0.032	0
Fe2+	0.563	0.644	0.526	0.51	0.514
Mn	0.009	0.012	0.013	0.011	0.009
Mg	1.223	1.158	1.169	1.352	1.329
Ca	0.76	0.023	0.021	0.021	0.022
Na	0.0027	0.005	0.059	0	0.001
SUM	3.999	3.989	3.997	4.001	3.994

SAMPLE	PHN5731	PHN5731	PHN5731	PHN5731	PHN5731
MIN.	PLAG. EX.	PLAG. EX.	PLAG. EX.	PLAG. EX.	PLAG. EX.
SIO2	61.52	61.01	57.17	59.35	61.93
TIO2	0.05	0.08	0.03	0.11	0
Al2O3	23.88	24.13	25.37	25.56	23.95
Fe Total	0.44	0.45	1.25	0.22	0.37
MnO	0	0.01	0	0	0
MgO	0.005	0.06	1.33	0	0.01
CaO	5.58	5.76	8.12	7.21	5.5
Na20	8.53	8.49	5.91	7.35	8.88
K	0.03	0	0.38	0	0.04
Ba	0.03	0	0.06	0.06	0
SUM	100.7	99.99	99.63	99.86	100.69
CATS. O=8					
SI	2.732	2.714	2.579	2.65	2.735
TI	0.002	0.003	0.001	0.004	0
AI	1.25	1.265	1.349	1.345	1.247
Fe	0.015	0.015	0.042	0.007	0.12
Mn	0	0.001	0	0	0
Mg	0	0.004	0.089	0	0.001
Ca	0.266	0.275	0.393	0.345	0.26
Na	0.735	0.732	0.517	0.636	0.761
K	0.002	0	0.022	0	0.002
Ba	0.001	0	0.001	0.001	0
SUM	5.002	5.009	4.993	4.989	5.017

TABLE 4.12 BULK CPX DATA

1 SAMPLE	GP147 GGP	GP147 GGP	GP147 GGP	GP147 GGP	M5-101 GP	M6-79 GP	GP37 GP
2 ANALYSIS	WIDE BEAM	CALCULATED	WIDE BEAM	EXSOLVED	WET CHEM.	WET CHEM.	WIDE BEAM
3							
4 SiO2	51.30	50.31	50.73	51.46	50.60	50.02	49.96
5 TiO2	0.72	0.80	0.91	1.14	1.02	0.52	0.91
6 Al2O3	6.49	10.31	6.48	7.48	8.89	4.88	8.13
7 FeTOTAL	9.89	9.83	8.83	5.98	9.39	10.54	8.11
8 Cr2O3	0.07	0.09	0.14	0.17	0.18	0.55	0.05
9 MnO	0.35	0.24	0.31	0.21	0.14	0.08	0.00
10 MgO	17.80	11.67	16.28	13.34	15.10	14.33	12.13
11 CaO	11.83	13.60	14.01	18.00	12.70	17.24	19.48
12 Na2O	1.22	2.92	1.45	2.16	1.78	1.58	1.89
13							
14 CATIONS							
15 Si	1.872	1.849	1.864	1.876	1.838	1.868	1.824
16 Ti	0.020	0.022	0.025	0.031	0.028	0.013	0.025
17 Al	0.279	0.447	0.281	0.321	0.382	0.216	0.350
18 Fe 3+	0.022		0.039		0.052	0.034	0.086
19 Fe 2+	0.277	0.302	0.228	0.182	0.225	0.292	0.153
20 Cr	0.002	0.003	0.004	0.005	0.007	0.016	0.002
21 Mn	0.011	0.008	0.010	0.007	0.004	0.002	0.000
22 Mg	0.968	0.639	0.892	0.725	0.919	0.799	0.660
23 Ca	0.462	0.536	0.552	0.703	0.493	0.689	0.762
24 Na	0.086	0.204	0.103	0.152	0.127	0.114	0.134
25 END							
26 Jd	8.6	20.2					
27 Fe3CaTS	1.2	0.1					
28 TiCaTs	2.0	2.2					
29 CaTs	7.65	9.8					
30 Wo	17.7	20.5					
31 En	48.4	31.7					
32 Fs	14.4	15.4					

Porphyroclast core compositions of the GGP CPX appear to be more "evolved" in terms of their chemistry than CPX from the GP. GGP CPX have significantly higher TiO_2, Al_2O_3 and Na_2O (Table 4.10). Considering the spatial proximity of the GGP and GP these differences cannot reflect differences in depth of crystallization but probably result from the fact that the GGP precipitated from a more evolved magma composition than the GP. However, some of the differences in Na_2O and Al_2O_3 contents may be due to the heterogeneous and incomplete exsolution in CPX.

Table 4.13 Comparison of GGP and GP exsolved pyroxene compositions. Oxide variation is wt %.

	GGP	GP
TiO_2	1.45 - 0.88	0.96 - 0.67
Al_2O_3	10.25 - 5.73	8.65 - 7.08
Cr_2O_3	0.31 - 0.05	0.33 - 0.02
MnO	0.34 - 0.19	0.21 - 0.02
Na_2O	3.49 - 1.24	2.16 - 0.98

CPX inclusions within graphite octahedra in the GGP are included within the compositional range summarized in Table 13 and listed in Table 4.10. There is no compositional distinction between CPX in the host GGP and the inclusions within the graphite octahedra (Figure 4.23). Exsolution of OPX, garnet and plagioclase from the CPX inclusions within the graphite result in them following the same chemical equilibration trends as the host rock CPX, i.e. low Cr/Al ratio, high Ti, Al and Na contents.

Most of the exsolved CPX core compositions from the GP and GGP lithologies contain excess octahedral aluminium but with the GGP containing significantly greater Al^{vi} (up to 2x tetrahedral Al) than the GP (Al^{vi}/Al^{iv}~1), Figure 4.7a & 4.8. Al^{vi} generally increases with pressure in CPX (Thompson 1974). This is verified by the more Al^{vi} rich nature of the bulk wet chemical CPX analyses from Kornprobst (1969) and the calculated bulk GGP CPX compositions which approximate to higher P/T pre-exsolution compositions. Thompson (1974) also found that Al^{vi} contents in CPX increase with increasing Al_2O_3 content of the parent magma. It is unlikely that the closely associated GGP and GP crystallized under greatly different pressure conditions, thus the greater Al^{vi} component in the GGP CPX is probably due to higher Al_2O_3 in the parental liquid. These results support the findings of Thompson (1974), that bulk liquid composition is one of the strongest controls on CPX chemistry. The GGP CPX also contain slightly higher Fe^{3+} than the GP, and peridotite CPX, however Fe^{3+} contents are towards the lower range of Fe^{3+} in ridge basalts (Figure 4.9). Some CPX appear to contain slight difficiencies of Fe^{3+} (Figure 4.9) indicating that other cations are required to fill the M1 sites. The sodic, aluminous

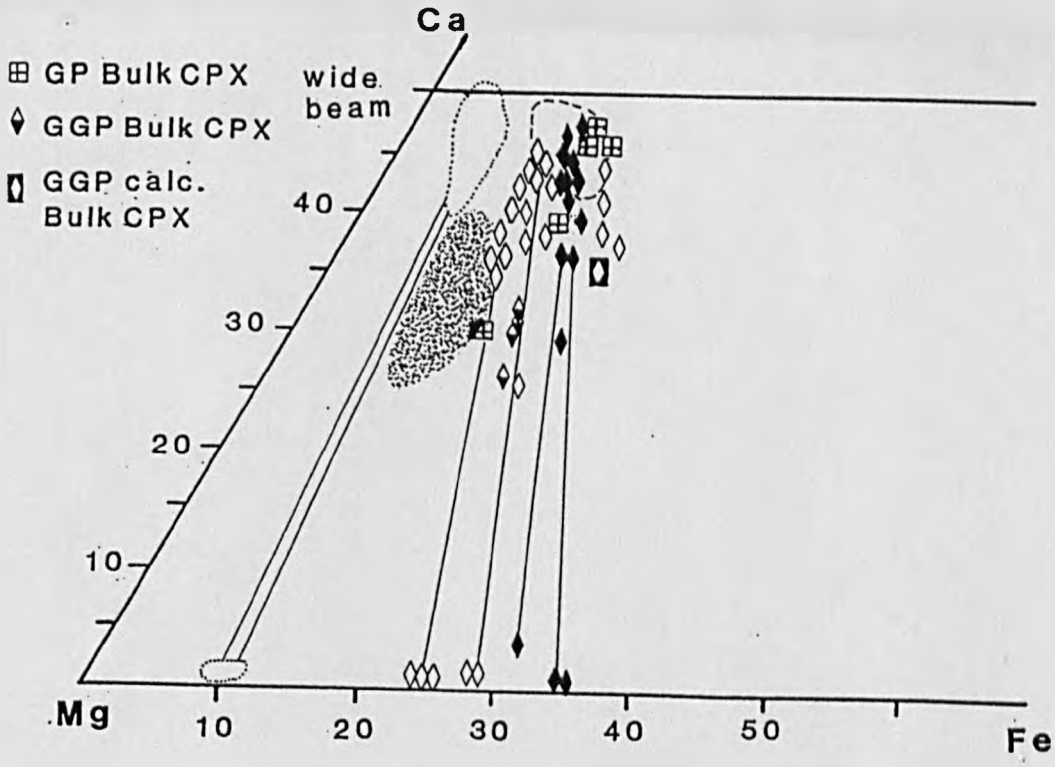

Figure 4.22. Ca:Mg:Fe pyroxene quadrilateral plot for garnetiferous pyroxenites. Symbols for bulk and broad beam analyses indicated on diagram. Shaded field represents compositions of sub-calcic CPX from garnet pyroxenite xenoliths analysed by Wilkinson (1976). Dotted open fields is region occupied by peridotite CPX. Tie lines join coexisting CPX and exsolved OPX lamellae.

Figure 4.23. Na_2O contents of CPX from host GGP and CPX inclusions within graphite octahedra. Range for CPX inclusions in E-type diamonds and CPX from diamondiferous eclogites indicated for comparison.

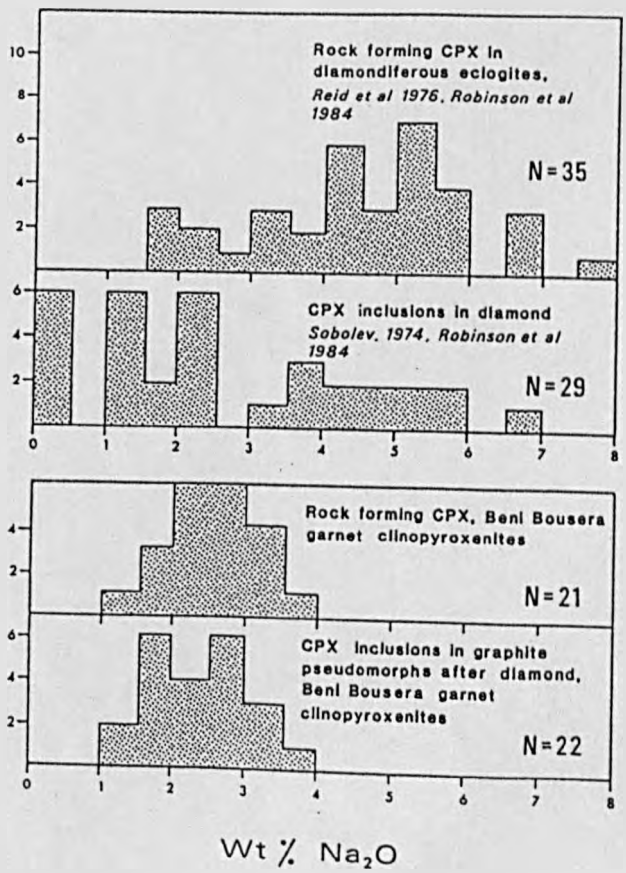

nature of the GGP CPX is illustrated in Figure 4.19. Most of the GGP CPX and graphite inclusion CPX have Na/Al >0.25 whilst exsolved CPX in the GP have Na/Al <0.25. Bulk, pre-exsolution compositions of the GP CPX are more comparable with those of the GGP.

Figure 4.24 shows the extent of Ca and Na occupancy of the M2 site of CPX from all types of pyroxenites from Beni Bousera. Departure below the dashed line (Na + Ca = 1) in Fig.4.24 is a reflection of the presence of additional cations in M2 such as Mn ,Fe^{2+} and Mg. The relatively high Mn contents of the GGP CPX and some GP CPX cause substantial lateral displacement below the line as this divalent cation substitutes for Ca^{2+}. The total absence of points plotting above the line indicates that there is no Na or Ca in the M1 sites. Points plotting slightly above the line usually indicate poor analytical quality. None of the Beni Bousera pyroxenites contain CPX that may be described as omphacites as most show significant departure from Na - Ca solid solution (Figure 4.24). This contrasts with CPX in eclogites from Western Alpine peridotite massifs which contain high Na omphacites showing considerable Na-Ca solid solution towards chloromelan ite. Also shown for comparison in Figure 4.24 is the field for CPX from a selection of eclogite xenoliths from Kimberlite pipes which range from omphacite -chloromelanite solid solution to sodic augite composition with high "other" M2 components. Core-rim variation indicates the decreasing Na contents but increasing Ca in M2 from core to rim of both GGP and GP CPX (Fig. 4.24). This variation is consistent with the core-rim trend of decreasing Jd but increasing CaTs components (Figure 4.20). The decreasing Na content from core to rim of CPX in GGP and GP is correlated with decreasing total Al and Al^{vi} content (Fig. 4.8 + 4.19).

Garnet pyroxenite xenoliths of similar mineralogy to the Beni Bousera pyroxenites are found in alkali basalts in some areas eg. Hawaii (Beeson and Jackson 1970) and E. Australia (Wilkinson 1976). These garnet pyroxenite xenoliths have been equated with garnetiferous pyroxenite layers found in orogenic peridotite massifs (Wilshire and Shervais 1975, Wilkinson 1976). It is therefore of interest to compare the mineral chemistry of these garnet pyroxenite xenoliths to the Beni Bousera garnetiferous pyroxenites. The exsolved CPX from GP are slightly more sodic and bulk CPX composition are considerably more sodic than the subcalcic bulk CPX compositions from garnet pyroxenite xenoliths analysed by Wilkinson (1976). CPX from the GGP are more sodic and aluminous than the garnet clinopyroxenite xenoliths and plot into the field occupied by eclogite xenoliths and eclogite suite inclusions in diamond. These two compositional fields are very large and extend to highly sodic and aluminous compositions (Fig. 4.23).

Some of the less exsolved (less re-equilibrated) CPX compositions from inclusions within the graphite and the host GGP are similar to E-type diamond inclusion and diamondiferous eclogite CPX (Fig.4.19 and 4.25). CPX from the Beni Bousera GGP plot in the less Na_2O rich end of the range of E-type diamond inclusions and eclogite CPX compositions. Two CPX compositions from a corundum bearing garnet pyroxenite analysed by Kornprobst et al (1982) are also plotted in Figure 4.19. These CPX are highly aluminous (upto 19 % Al_2O_3) but are considerably poorer in sodium than grospydite xenoliths (many of which are corundum bearing) from Kimberlite pipes. CPX from the Al-augite group pyroxenites are more Mn rich than the Cr-pyroxenites from Beni Bousera (Fig. 4.26) and more MnO rich than any subcalcic CPX from garnet pyroxenite xenoliths from alkali basalts. The only mantle derived CPX with comparable MnO contents are those from eclogite xenoliths and contain E-type diamond inclusions analysed by Deines et al 1987 (Fig. 4.26). Deines et al (op.cit) make particular note of the

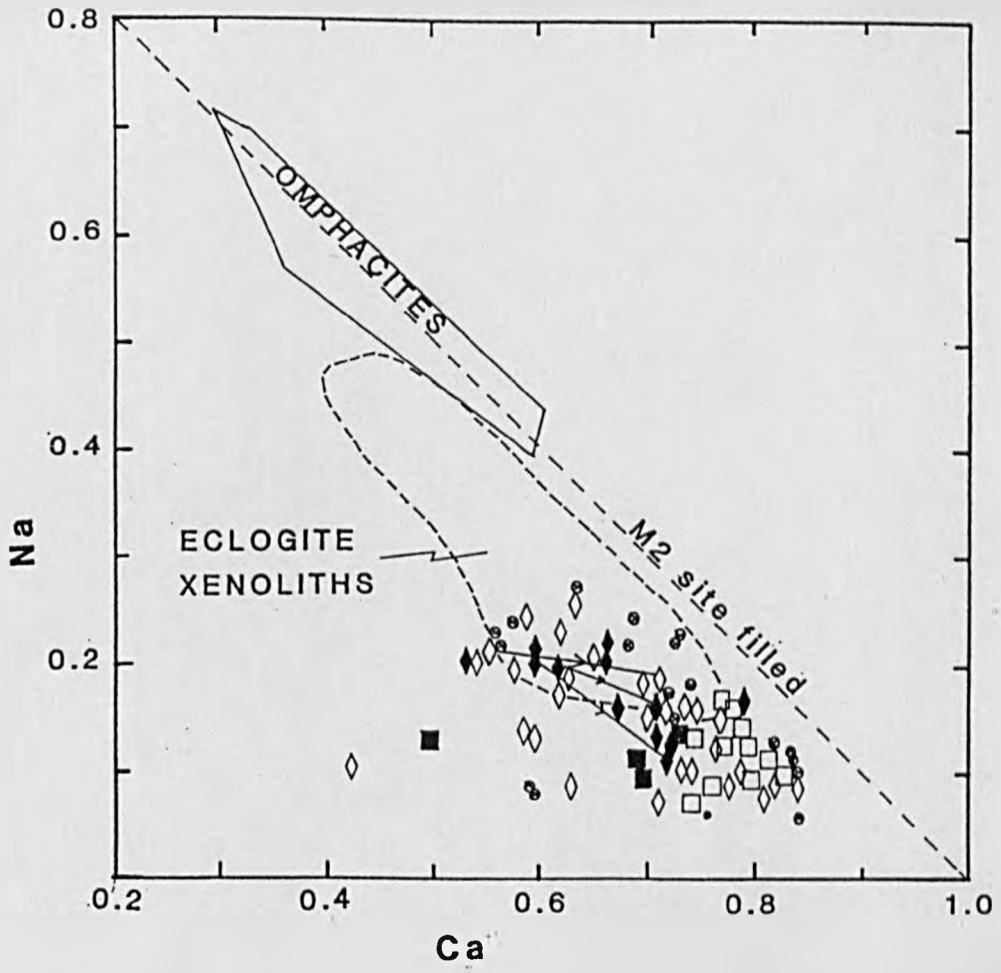

Figure 4.24. Na vs Ca cation proportions for CPX from Beni Bousera pyroxenites compared to CPX from eclogite xenoliths (dashed field) and omphacites from W.Alpine eclogite pods (Data from Ernst 1978 and Robinson et al 1984).

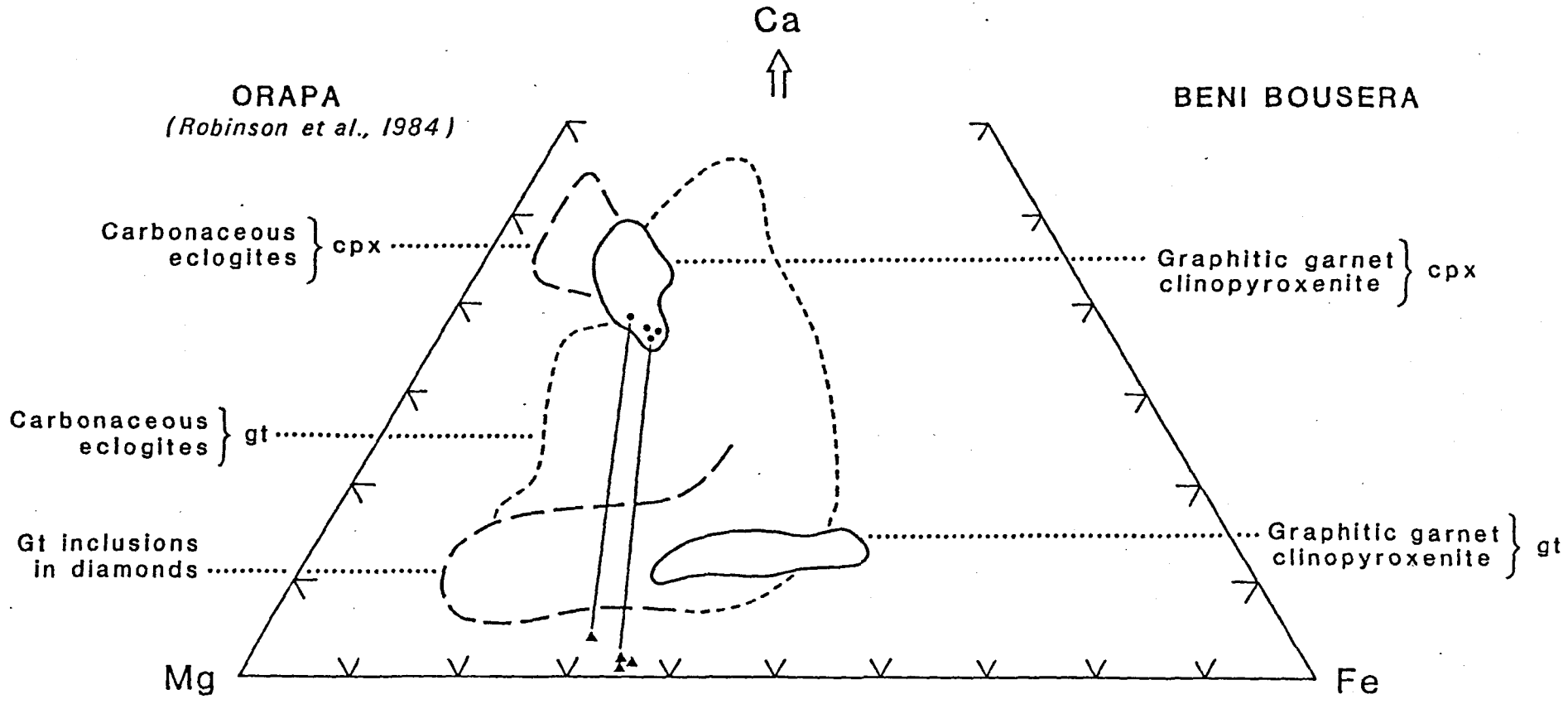

Figure 4.25. Ca:Mg:Fe quadrilateral plot of CPX and garnet from Beni Bousera GGP compared to CPX and garnet from Orapa carbonaceous (graphitic and diamondiferous) eclogite xenoliths and eclogite suite inclusions in diamonds. Representative CPX exsolved OPX tie lines indicated.

Figure 4.26. MnO vs FeO in CPX from Beni Bousera pyroxenites compared to the Type I (open field) and Type II (shaded field) E-type diamond inclusions from Roberts Victor analysed by Deines et al 1987.

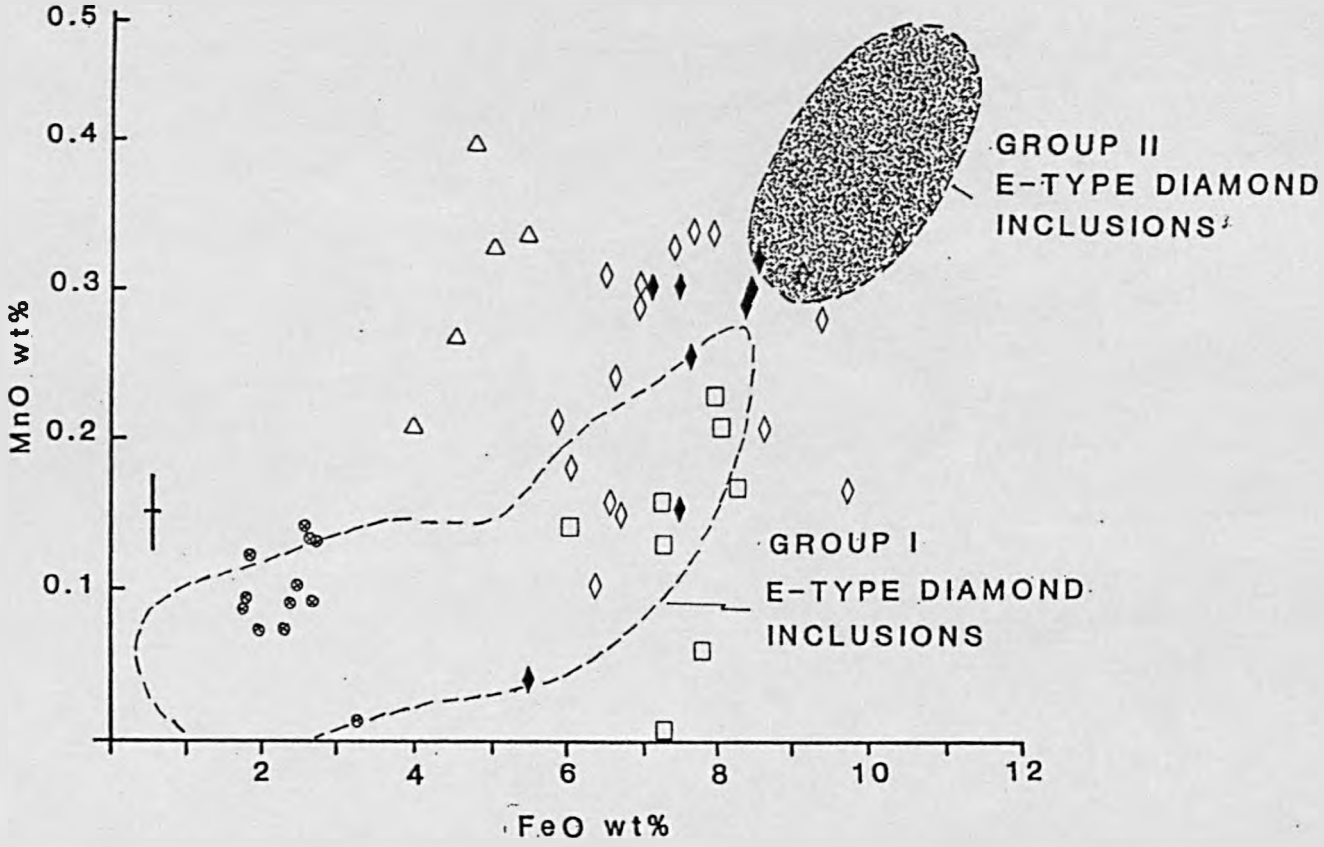

so called type II inclusions which are enriched in Al_2O_3, FeO and MnO but do not explain their different chemistry. CPX from the GGP host rocks and from inclusions within graphite are the most enriched in terms of MnO and FeO of the Beni Bousera suite, some plotting in the lower range of the Deines et al (1987) group II inclusions. This supports the suggestion that the GGP represent the most evolved members of the Al-augite pyroxenite suite and strengthens the similarities between the GGP and diamondiferous eclogites (see Chapter 2).

The GGP CPX contain the highest Jd component of the garnetiferous pyroxenites CPX (Fig. 4.20). The data follow a trend of increasing Jd and deceasing CaTs's components, consistent with isobaric cooling in equilibrium with garnet. Core-rim variation for GGP and GP show an opposite trend of decreasing Jd and increasing CaTs components. The core-rim zonation trend (Fig. 4.20) may indicate CPX re-equilibration (in the presence of garnet) in an environment of decreasing pressure and temperature as the CPX exsolves plagioclase.

4:3.3b Exsolution products in the CPX.

The composition of OPX lamellae exsolved from CPX porphyroclasts in GGP are presented in Table 4.11. Tie lines to co-existing CPX hosts are shown in Figure 4.22 & 4.25. Fs contents of the OPX lamellae vary from 23 to 35 %, the more Fe rich lamellae exsolving from Fe rich hosts suggesting that the GGP precipitated from an evolving magma. Al_2O_3 contents vary from 2.63 to 6.04 wt % with OPX from PHN 5730 having the highest Al_2O_3 contents and most Fe-rich compositions. Some OPX from PHN 5730 also contain a slight excess of Al^{vi} whilst OPX lamellae from the other GGP are deficient in Al^{vi} (Figure 4.21). The low Al_2O_3 contents of the OPX lamellae are lower than most of the spinel peridotite OPX core compositions even though the GGP crystallized from liquids considerably richer in Al_2O_3. This indicates the OPX lamellae in the GGP CPX exsolved at low temperatures and pressures.

Exsolved plagioclase "blebs" in CPX (Table 4.11) contain between 25 and 44 % anorthite component with cores between 5-10 % richer in anorthite than the rims. The variation in exsolved plagioclase core compositions suggest variable, incomplete exsolution. Plagiolcase neoblasts occur sporadically around the rims of the CPX porphyroclasts and are chemically similar to the exsolved plagioclase. The plagioclase neoblast may represent plagioclase exsolved from CPX margins which have undergone dynamic recrystallization.

Garnet exsolved from CPX porphyroclasts are slightly more Ca (grossular) rich than porphyroclastic garnets, but are significantly lower in Py content (Figure 4.27). In summary, exsolution of garnet, plagioclase and OPX from the CPX porphyroclasts indicates a regime of decreasing temperature and pressure during the sub-solidus evolution of the pyroxenites. The variably deformed nature of many exsolution lamellae suggest that cooling and depressurization was synchronous with plastic deformation.

4:3.3c Garnet.

Garnets from the garnetiferous pyroxenites (Table 4.14) are pyrope-almandines with grossular contents between 10 and 15 %, a summary of end member variatioin for different lithologies is given in Table 4.15. Both GGP and GP garnets exhibit a considerable range of pyrope-almandine solid solution with a large degree of overlap. GP garnets are slightly more pyrope rich , up to 59 % Py, compared to

Table 4.14. Representative garnet compositions from GP, GGP, and GTLHZ.

SAMPLE	GP24 GTLHZ	GP24 GTLHZ	GP24 GTLHZ	GP24 GTLHZ	GP24 GTLHZ	GP24 GTLHZ	GP24 GTLHZ	PHN 5730 GGP	PHN5730 GGP	PHN5730 GGP	PHN5730 GGP	PHN5730 GGP	PHN5730 GGP
ANALYSES	CR	CR	CR	CR	RIM	RIM	CR	CR	CR	CR	CR	CR	RIM
SIO2	41.62	42.16	41.83	42.04	42.03	42.28	41.62	40.51	40.19	41.00	40.52	40.39	39.67
TIO2	0.24	0.27	0.32	0.21	0.20	0.23	0.24	0.31	0.28	0.23	0.21	0.21	0.18
AI2O3	22.87	23.33	22.98	22.97	23.33	23.34	22.87	22.59	22.57	22.42	22.66	22.30	22.10
Cr2O3	1.53	1.42	1.20	0.91	1.32	1.25	1.53	0.17	0.13	0.04	0.14	0.14	0.18
Fe3+	0.33	0.03	0.00	0.44	0.29	0.10	0.33	0.00	0.00	0.00	0.00	0.31	0.54
Fe2+	7.34	7.78	7.57	6.82	7.19	7.84	7.34	17.28	16.90	17.60	18.38	17.84	19.47
Mn	0.36	0.30	0.31	0.24	0.39	0.26	0.36	0.57	0.65	0.60	0.78	0.72	1.10
Mg	20.50	20.54	20.25	20.94	20.77	20.54	20.50	13.45	13.41	13.34	12.82	12.97	11.33
Ca	4.99	5.03	4.90	4.77	5.13	5.00	4.99	5.14	5.02	5.45	5.05	5.09	5.40
SUM	99.79	100.86	99.36	99.33	100.65	100.84	99.79	100.03	99.15	100.67	100.58	99.97	99.97
CATS O=12													
SI	2.963	2.968	2.984	2.989	2.962	2.975	2.963	2.999	2.998	3.019	3.000	3.004	2.987
TI	0.013	0.014	0.017	0.011	0.011	0.012	0.013	0.018	0.016	0.013	0.012	0.012	0.010
AI	1.920	1.937	1.933	1.925	1.939	1.937	1.920	1.972	1.985	1.947	1.977	1.956	1.962
Cr	0.086	0.079	0.068	0.051	0.073	0.070	0.086	0.010	0.007	0.002	0.008	0.008	0.010
Fe3+	0.018	0.002	0.000	0.023	0.015	0.005	0.018	0.000	0.000	0.000	0.000	0.017	0.031
Fe2+	0.437	0.458	0.452	0.405	0.424	0.461	0.437	1.070	1.054	1.084	1.137	0.110	1.226
Mn	0.022	0.018	0.019	0.014	0.023	0.016	0.022	0.036	0.041	0.037	0.049	0.046	0.070
Mg	2.175	2.155	2.152	2.218	2.181	2.154	2.175	1.484	1.490	1.464	1.414	1.437	1.271
Ca	0.381	0.379	0.374	0.364	0.388	0.377	0.381	0.408	0.401	0.430	0.400	0.405	0.436
SUM	8.014	8.010	7.999	8.001	8.015	8.008	8.014	7.995	7.992	7.995	7.997	8.000	8.003

SAMPLE	PHN5731 GGP	PHN5731 GGP	PHN5731 GGP	PHN5731 GGP	PHN5731 GGP	PHN5731 GGP	PHN5731 GGP	PHN5731 GGP	PHN5731 GGP	PHN5731 GGP	PHN5731 GGP	PHN5731 GGP	PHN5731 GGP
ANALYSES	CR	CR	CR	CR	CR	CR	RIM	RIM	RIM	RIM	CR	CR	RIM
SIO2	39.88	39.97	40.48	39.82	40.50	40.42	39.52	39.66	39.44	40.05	40.65	40.06	40.31
TIO2	0.17	0.27	0.20	0.31	0.21	0.09	0.05	0.14	0.15	0.22	0.32	0.30	0.23
AI2O3	22.08	22.23	22.70	22.00	22.28	22.66	22.10	22.01	22.12	22.28	22.25	22.29	22.37
Cr2O3	0.08	0.14	0.13	0.19	0.12	0.13	0.12	0.23	0.03	0.18	0.08	0.12	0.05
Fe3+	0.59	0.00	0.00	0.00	0.00	0.00	0.29	0.00	0.24	0.00	0.00	0.52	0.00
Fe2+	19.74	19.90	19.58	19.60	19.18	19.24	20.60	21.31	21.64	20.31	19.23	18.73	19.62
Mn	0.72	0.74	0.73	0.60	0.45	0.66	0.94	0.88	1.22	0.66	0.61	0.54	0.65
Mg	11.86	11.69	12.09	11.85	12.11	12.28	10.52	10.25	9.86	11.77	12.08	12.52	12.07
Ca	4.79	4.88	4.98	4.82	5.17	5.13	5.47	5.37	5.28	4.66	5.22	5.08	5.05
SUM	99.91	99.81	100.89	99.18	100.01	100.60	99.60	99.86	99.98	100.12	100.44	100.15	100.35
CATS O=12													
SI	2.996	3.003	3.001	3.006	3.021	3.001	2.998	3.006	2.996	3.002	3.022	2.987	3.006
TI	0.010	0.015	0.011	0.017	0.120	0.005	0.003	0.008	0.009	0.013	0.018	0.017	0.013
AI	1.956	1.970	1.984	1.959	1.960	1.984	1.976	1.967	1.981	1.969	1.950	1.960	1.967
Cr	0.005	0.008	0.007	0.022	0.007	0.007	0.007	0.014	0.002	0.011	0.004	0.007	0.003
Fe3+	0.034	0.000	0.000	0.000	0.000	0.000	0.017	0.000	0.014	0.000	0.000	0.029	0.000
Fe2+	1.240	1.250	1.214	1.237	1.196	1.195	1.306	1.351	1.374	1.273	1.196	1.168	1.224
Mn	0.046	0.047	0.046	0.038	0.028	0.041	0.061	0.056	0.079	0.042	0.038	0.034	0.041
Mg	1.328	1.309	1.336	1.334	1.346	1.358	1.189	1.158	1.116	1.314	1.339	1.392	1.341
Ca	0.385	0.393	0.395	0.390	0.413	0.408	0.444	0.436	0.429	0.374	0.416	0.406	0.403
SUM	7.999	7.994	7.994	7.993	7.985	8.000	8.001	7.997	7.999	7.997	7.984	8.000	7.998

SAMPLE	GP81 GGP	GP81 GGP	GP147 GGP	GP147 GGP	GP147 GGP	GP147 GGP	GP147 GGP	GP147 GGP	GP147 GGP	GP147 GGP	GP239 GTITE	GP239 GTITE	GP239 GTITE	GP239 GTITE
ANALYSES	CR	CR	CR	CR	CR	CR	CR	CR	RIM	RIM	CR	CR	CR	RIM
SiO2	39.72	39.70	39.99	41.10	40.70	40.70	40.51	40.91	41.09	39.69	40.44	40.11	40.35	40.61
TiO2	0.19	0.19	0.10	0.26	0.13	0.27	0.40	0.16	0.04	0.18	0.14	0.07	0.02	0.18
Al2O3	21.98	22.31	22.36	22.49	22.66	22.05	22.20	22.44	22.56	22.14	23.10	22.29	22.44	22.79
Cr2O3	0.05	0.08	0.15	0.07	0.02	0.15	0.22	0.23	0.06	0.13	0.12	0.09	0.04	0.12
Fe3+	0.79	0.57	0.98	0.70	1.21	0.86	0.77	0.87	0.85	0.63	0.06	0.46	0.36	0.15
Fe2+	20.66	21.56	16.43	16.26	14.90	15.05	15.85	15.61	15.91	19.39	16.86	16.60	16.31	17.27
Mn	0.60	0.60	0.94	0.87	0.79	0.70	0.86	0.84	0.98	2.01	0.48	0.55	0.56	0.52
Mg	10.81	10.64	13.89	14.61	15.59	15.22	14.48	15.05	14.53	11.38	13.19	13.07	13.26	13.10
Ca	5.58	5.32	4.94	4.52	4.55	4.29	4.69	4.48	4.89	4.77	6.27	5.88	5.96	5.85
SUM	100.37	100.97	99.77	100.87	100.56	99.29	99.99	100.59	100.90	100.30	100.66	99.12	99.31	100.6
CATS O=12														
Si	2.990	2.978	2.972	3.005	2.973	3.008	2.990	2.993	3.003	2.984	2.977	3.000	3.005	2.994
Ti	0.011	0.012	0.006	0.014	0.007	0.015	0.022	0.009	0.002	0.010	0.008	0.004	0.001	0.010
Al	1.951	1.973	1.959	1.938	1.952	0.921	1.932	1.936	1.994	1.962	2.005	1.965	1.971	1.981
Cr	0.003	0.005	0.009	0.004	0.001	0.009	0.013	0.014	0.004	0.008	0.007	0.005	0.003	0.007
Fe3+	0.045	0.032	0.055	0.038	0.067	0.048	0.043	0.048	0.047	0.036	0.003	0.026	0.020	0.008
Fe2+	1.301	1.352	1.021	0.994	0.910	0.930	0.978	0.955	0.972	1.219	1.038	1.038	1.016	1.065
Mn	0.038	0.038	0.059	0.054	0.049	0.044	0.054	0.052	0.060	0.128	0.030	0.035	0.036	0.033
Mg	1.212	1.190	1.539	1.591	1.697	1.676	1.593	1.642	1.538	1.274	1.447	1.456	1.471	1.440
Ca	0.450	0.427	0.393	0.354	0.356	0.340	0.371	0.351	0.383	0.384	0.495	0.471	0.476	0.462
SUM	8.001	8.007	8.013	7.992	8.012	7.990	7.996	8.000	7.999	8.005	8.009	8.000	7.999	8.000

SAMPLE	GP37 GP	GP37 GP	GP37 GP	GP37 GP	GP37 GP	GP37 GP	GP87B GP	GP87B GP	GP87B GP	GP87M GP	GP87M GP	GP87M GP	GP151 GTWEB	GP151 GTWEB
ANALYSES	CR	CR	CR	CR	RIM	RIM	CR	CR	CR	CR	CR	CR	CR	CR
SiO2	40.13	39.71	39.93	40.32	39.76	39.70	42.01	42.04	41.30	40.51	40.59	40.65	41.77	42.65
TiO2	0.17	0.19	0.16	0.12	0.08	0.25	0.11	0.05	0.11	0.24	0.24	0.36	0.19	0.13
Al2O3	22.44	22.41	22.43	22.45	22.15	22.37	22.99	23.28	22.94	22.77	22.78	22.35	23.00	23.21
Cr2O3	0.19	0.24	0.14	0.05	0.15	0.13	0.50	0.50	0.25	0.25	0.18	0.35	0.19	0.18
Fe3+	0.73	0.96	0.84	0.63	0.98	0.83	0.72	0.46	0.58	1.01	0.66	0.89	0.95	0.73
Fe2+	18.13	17.90	18.68	18.66	18.33	17.93	10.01	10.26	10.15	12.75	13.48	12.86	8.89	9.00
Mn	0.45	0.39	0.49	0.37	0.44	0.42	0.37	0.35	0.36	0.44	0.38	0.30	0.34	0.28
Mg	12.04	12.10	11.83	11.90	11.78	12.12	18.67	18.63	18.21	15.98	15.59	15.69	19.14	19.47
Ca	6.62	6.75	6.38	6.37	6.50	6.51	5.22	5.22	5.17	6.05	5.84	6.12	5.35	5.25
SUM	100.91	100.65	100.89	100.87	100.16	100.27	100.59	100.80	99.07	99.99	99.73	99.58	99.82	100.82
CATS O=12														
Si	2.976	2.955	2.970	2.992	2.977	2.963	2.995	2.991	2.990	2.957	2.973	2.979	2.988	3.016
Ti	0.009	0.011	0.009	0.006	0.004	0.014	0.006	0.003	0.006	0.013	0.013	0.020	0.010	0.007
Al	1.963	1.966	1.966	1.964	1.955	1.969	1.932	1.953	1.958	1.960	1.967	1.932	1.940	1.934
Cr	0.011	0.014	0.008	0.003	0.009	0.008	0.028	0.028	0.014	0.014	0.011	0.020	0.011	0.010
Fe3+	0.041	0.054	0.047	0.035	0.055	0.047	0.038	0.025	0.032	0.055	0.036	0.049	0.051	0.039
Fe2+	1.124	1.114	1.162	1.158	1.147	1.119	0.597	0.610	0.615	0.778	0.826	0.788	0.532	0.531
Mn	0.028	0.025	0.031	0.023	0.028	0.027	0.023	0.021	0.022	0.027	0.023	0.019	0.021	0.017
Mg	1.331	1.342	1.311	1.315	1.314	1.347	1.983	1.975	1.965	1.738	1.701	1.714	2.040	2.052
Ca	0.526	0.538	0.509	0.506	0.521	0.520	0.398	0.398	0.401	0.473	0.458	0.481	0.410	0.398
SUM	8.009	8.018	8.012	8.003	8.011	8.013	8.001	8.005	8.003	8.016	8.009	8.002	8.003	8.005

GGP garnets (57 % Py) which are consequently more almandine rich (up to 49 % Al). Grossular contents are similar for both groups . GGP garnets are consistently richer in spessartine component, reaching upto 4.3 % whilst the GP garnets contain only upto 2.6 %. The high MnO content of the GGP garnets (over 1.5 wt %) is compatible with the high MnO values of their CPX. Values comparable to those found in the GGP garnets were recorded by Deines et al (1987) from their group II E-type diamond inclusions. Such values are not recorded by other mantle derived garnets.

Table 4.15 . Garnet end member variation in GGP and GP. Py = Pyrope, Al = Almandine, Gr = Grossular, Sp = Spessartine, An = Andradite, Uv = Uvarovite,

	GGP	GP
Py	57.0 - 34.6	59.3 - 42.0
Al	48.9 - 30.6	41.5 - 24.1
Gr	14.6 - 8.6	15.1 - 8.5
Sp	4.3 - 0.0	2.6 - 0.0
An	3.1 - 0.0	2.9 - 0.0

Uv < 1%

The range of pyrope contents of garnets from all the garnetiferous pyroxenites spreads from almost the group C eclogite field of Coleman et al (1965) across group B and into group A (a range of over 55 % Py) indicating that the garnets probably precipitated as cumulates from evolving liquids. Garnet Ca:Mg:Fe variation (Figure 4.27) shows that garnets from the garnet-plagioclase pyroxenites (granulites) within the kinzigites contain up to 40 % grossular component.

Garnets from the GGP and GP (Figure 4.25) plot within the large field of garnets in carbonaceous eclogites from Orapa (Robinson 1984) but extend to more Fe-rich compositions. The most Fe-rich garnets co-exist with the most Fe-rich CPX. The intersecting nature of some GP and GGP garnet-CPX tie lines suggest that they did not crystallize from the same evolving liquid but probably several of similar bulk composition. Garnets from the garnetite layer, GP 239, (Figure 4.27) plot towards the Mg-rich end of the range for the GP suggesting relatively early crystallisatioin. Detailed garnet core-rim relationships (Figure 4.27) indicate that rim compositions have equilibrated to more Fe rich compositions with little change in Ca content. The magnitude of core-rim variations is frequently over 15 mole % Py indicating substantial re-equilibration at lower temperatures.

Inclusions of garnet within the octahedral graphite aggregates in the GGP are of similar composition to the host rock garnets (Figure 4.27). The inclusion data presented in Figure 4.27 are from Slodkevich (1980 b). The one garnet inclusion in the graphite octahedra found in this study was used for ion-probing and is not now am enable for microprobing. A plot of CaO wt % vs Cr_2O_3 wt % (Fig. 4.28) is effective at discriminating between P-type and E-type diamond inclusions; P-type diamond inclusions having considerably higher Cr_2O_3 and lower CaO contents than E-type inclusions. Garnets from the GGP and GP

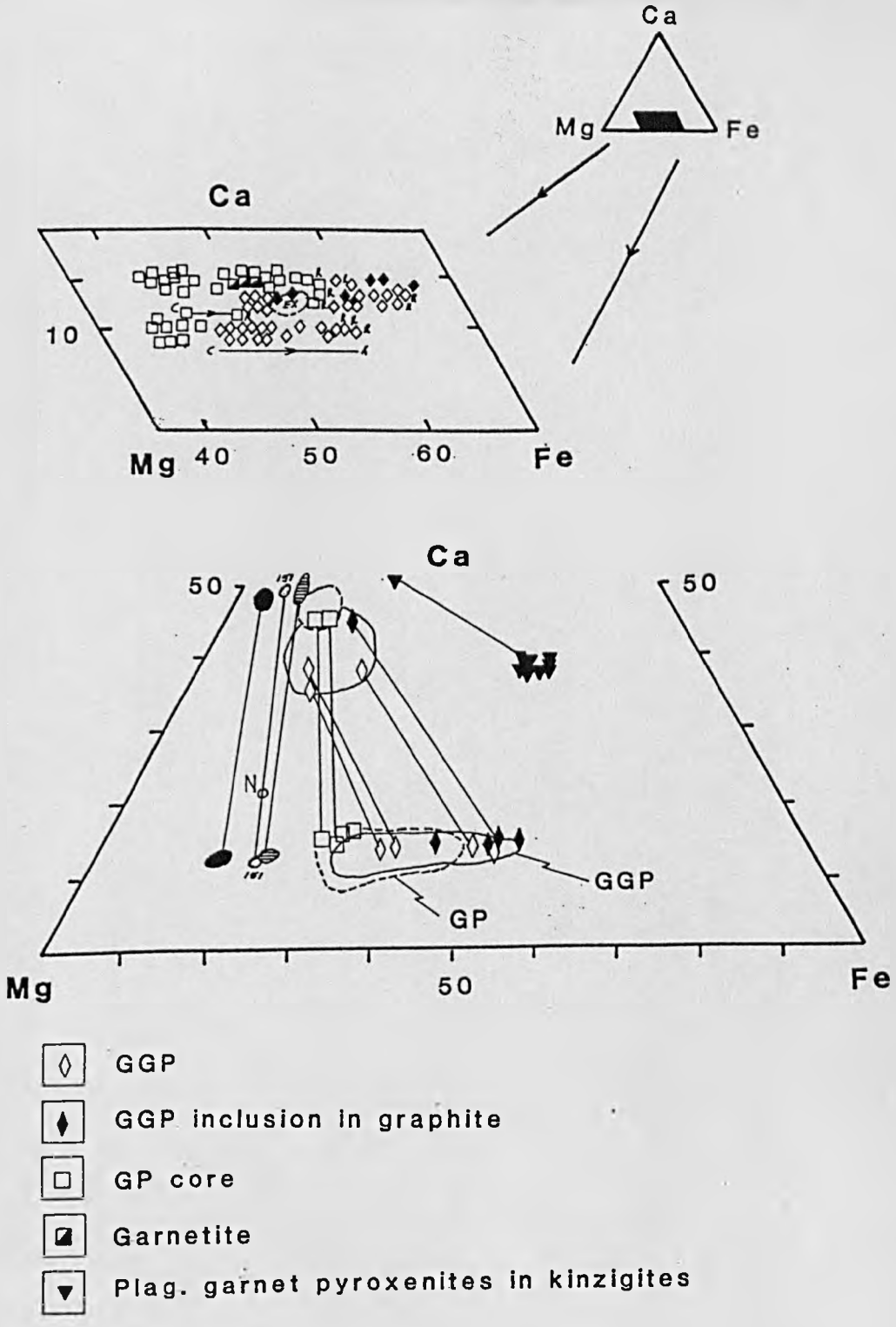

Figure 4.27. Ca:Mg:Fe garnet-CPX relationships and garnet compositions for GGP, GP and crustal plagioclase garnet pyroxenites. Solid field for garnet spinel lherzolites, horizontally lined field is for CPX-garnets at GP layer margins. Field labelled 151 is for 1 cm thick garnet websterite layer GP151.

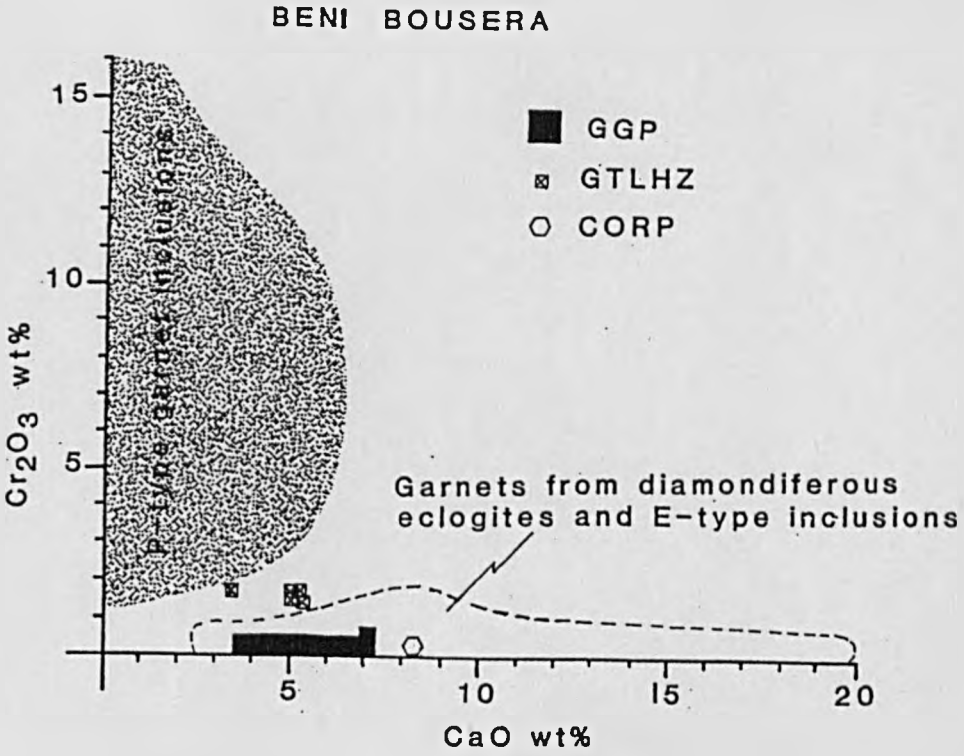

Figure 4.28. Cr_2O_3 vs CaO for Beni Bousera garnets from pyroxenites and peridotites. GGP garnets and GP garnets lie in the low Cr_2O_3 field of garnets from diamondiferous eclogites and E-type diamond inclusions (dashed field). Shaded field is for peridotite suite (P-type) garnet inclusions. Data from Reid et al (1976) and Sobolev (1979).

also contain low Cr_2O_3 but have CaO contents between 4 to 6 wt %, plotting in the middle of the E-type diamond field (Fig. 4.28). The garnet from the corundum bearing pyroxenite described by Kornprobst et al (1982) has a higher CaO content than any of the other garnet pyroxenites from Beni Bousera (~ 8.5 wt %) but is not as calcic as most garnets in corundum-bearing grospydite xenoliths from Kimberlite pipes. Garnets from the Beni Bousera pyroxenites are distinct from garnet lherzolite garnets found in the massif which contain significantly higher Cr_2O_3.

Garnet core-rim variations (Fig.4.27) indicate that some large porphyroclasts show large increases in Fe^{2+} towards their rims. Garnet rim compositions are identical to those of small < 100 μm grains of neoblastic garnet, whilst many rim compositions from both GP and GGP lithologies are more Fe-rich than garnet exsolved from CPX porphyroclasts. Elemental variation across a large garnet porphyroclast from PHN 5730 was studied by analysing points at 30 μm intervals (Figure 4.29). The strong Fe enrichment at the rim is only evident on one side of the crystal which is accompanied by a corresponding decrease in MgO. The core of the garnet has a generally higher Cr_2O_3 content than the rim (Fig.4.29). The chemical variation across the crystal represents a diffusion gradient towards the outer margin in response to lower temperature and pressure re-equilibration in contact with CPX. The lack of significant chemical variation on one margin of the garnet is difficult to explain. This margin is also surrounded by CPX and hence the inter mineral cation exchange should be identical. One possibility is that a very small Fe-rich phase was originally present between the garnet and CPX margins although this was not visible using backscattered S.E.M.

4:3.3d The occurrence of sodium in garnets from the GGP

Garnets from eclogite xenoliths bearing diamonds or those found as inclusions within diamonds, often contain sodium in minor amounts (0.03 to 0.25 wt% Na_2O, Sobolev and Lavrent'ev 1971, Reid et al 1976, Robinson et al 1984) or more rarely up to 1.03 wt% (Moore and Gurney 1985). The presence of sodium in garnet is thus taken to be a consequence of a high pressure origin of those garnets. Exploratory tests were made using manual, wave length dispersive analyses on the microprobe at Leeds using 100 second count times on the Na peak position and two 50 second background counts. This was done with an accelerating voltage of 20kv and a beam current of 20 nA. Specimens GP143 and GP147 contained Na significantly above "background" levels but the precise amount was not quantifiable due to excessive background "noise". Similar analyses on garnets from crustally derived rocks did not indicate Na to be present above background. GP143 was analysed at the Open University (O.U.) by Dr. A.Tindle using a Cameca microprobe. Sodium was counted for 30 seconds and the background for 30 seconds. Sodium values of three analyses range from 0.03 to 0.05 wt% Na_2O. The detection limit using the O.U. instrument is generally 0.02 wt% (A.Tindle pers.comm.), two of the analyses are distinctly above this detection limit. GP147 garnets were analysed at Edinburgh University by Dr. P.Hill using a Cameca Cambex microprobe with minimum count times of 60 seconds for sodium with an accelerating voltage of 20Kv and a beam current of 19mA. Sodium contents of two garnets traversed varied from 0.019 to 0.055 wt % Na_2O with the average of 40 analyses being 0.036 wt % Na_2O with a standard deviation of 0.010 wt%.

In summary, three different wavelength dispersive microprobe instruments indicate that sodium is

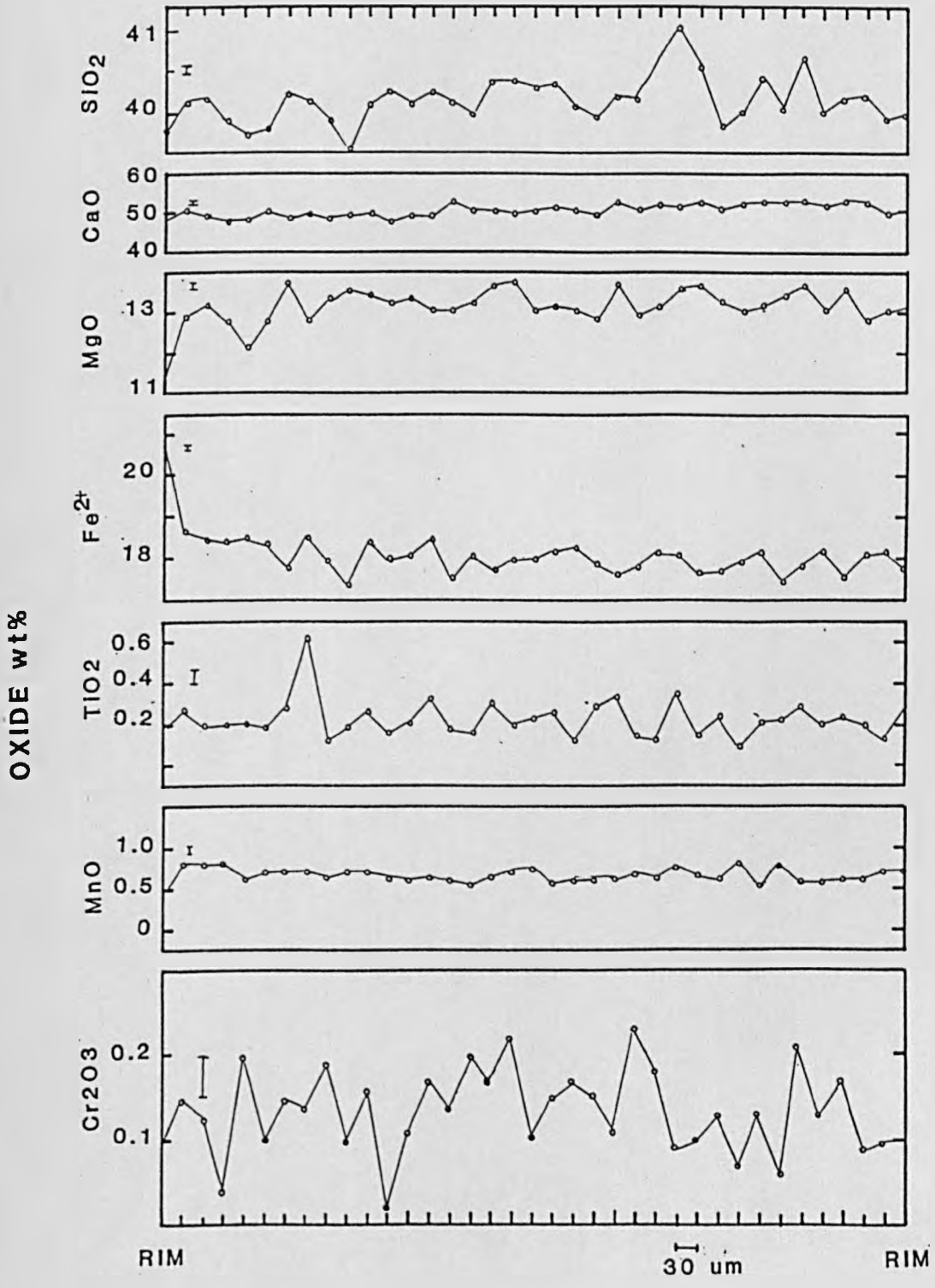

Figure 4.29. Wt % oxide variations across a garnet porphyroclast from GGP sample PHN5730. Steps are 30 μm intervals.

present in the garnets from some GGP at amounts significantly above background levels. Slodkevich (1980 b) also reports garnet analyses containing Na_2O varying between zero and 0.20 wt % with two garnet inclusions in graphite octahedra having 0.14 and 0.10 wt % respectively, analytical conditions are not specified. Such high Na values were not detected in this study.

Sobolev and Lavrent'ev (1971) suggested that the presence of Na in garnet from eclogites is a response to high pressure (> 40 kb) and proposed that Na enters the garnet structure according to the equation:

$$Ca^{viii} + Al^{vi} = Na^{viii} + Si^{vi}$$

requiring some Si to be present in octahedral coordination. No clear correlations were observed between Na and Si in the GGP garnets. Thompson (1975) proposed a coupled substitution between Na-P and Ca-Si on the basis of finding P_2O_5 levels of upto 0.57 wt % in garnets synthesized from anhydrous basaltic melts at 45 kb. Thompson (1975) suggested that the Na-P couple in garnet would be enhanced at high pressure due to the sum of their atomic radii being less than Ca + Si. Bishop et al (1976) explained the presence of Na in garnets by the substitution suggested by Thompson (1975) and a Ca + Al = Na + Ti coupled substitution. Na may alternatively be included in garnet via CPX solid-solution in the garnet structure with increasing pressure (Kato, 1986, Ringwood, 1982). Moore and Gurney (1985) found sodium levels of over 1 wt % Na_2O in eclogite garnet inclusions in diamonds. This sodium was accompanied by significantly higher SiO_2 values (up to 47 wt %) and low Al_2O_3 values (11.3 wt %). Such marked excesses in SiO_2 are not obvious in the GGP garnets as their Na_2O contents are considerably lower. However, the Na seen in the GGP garnets may originate from the orignal CPX solution in the garnet which becomes significant at pressures in the diamond stability field.

All these garnet substitutions are thought to take place at high pressures (> 40 kb), approaching the diamond stability field. In order for them to be evaluated properly a much more detailed study is necessary on garnets from both GP and GGP samples to deduce why some garnets seem to preserve this high pressure signature and others do not. The presence of detectable Na in garnets from some GGP therefore confirms that these rocks have at some time in their past experienced pressures of over 40 kb, as indicated by the presence of graphite pseudomorphs after diamond.

4:3.3e Sulphides

Sulphides analysed from the GP and GGP are found as discrete octahedra at triple junctions between CPX and garnet or as inclusions within the graphite octahedra. Chemically both groups are very similar, consisting of Ni-poor pyrite and pyrrhotite (Fig 4.30). One pyrrhotite inclusion within a graphite octahedron (occuring on the face of a CPX inclusion) contains ~2 wt% Ni. No complex intergrowth of these two phases is evident. The pyrrhotites plot close to, or in, the monosulphide solution stability field at 1000 °C (Fig 4.30). Secondary, irregular chalcopyrite is relatively common along serpentinized fractures in the GGP.

Pyrrhotite is a common inclusion in both P and E type diamonds whereas pyrite occurs to a lesser extent (Meyer 1987). The composition of pyrite and pyrrhotite from the GGP are similar to the low Ni

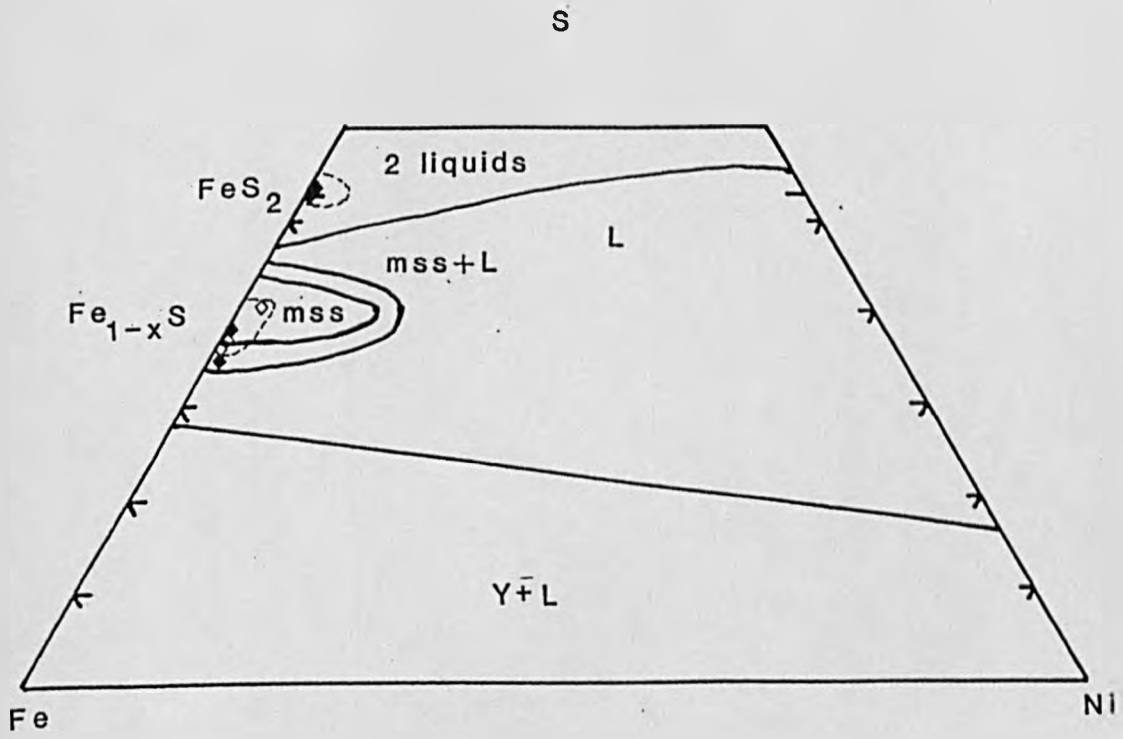

Figure 4.30. Sulphide compositions of Beni Bousera GGP (open diamonds) and sulphide inclusions within graphite aggregates (solid diamonds) compared with sulphide inclusions in diamonds (dashed field). Stability relations at 1000 ^{o}C are indicated (Data from Tsai et al 1979).

sulphides found as inclusions in diamonds (Fig.4.30). The presence of sulphides, most commonly pyrrhotite, on the surfaces of CPX inclusions within the graphite octahedra is a common physical relationship seen in natural diamonds. Tsai et al (1979) noted that in most diamonds, sulphides occur as assemblages such as pyrrhotite + pentlandite +/- chalcopyrite or pentlandite + magnetite +/- pyrrhotite +/- pyrite, which reflect sub-soildus re-equilibration from a single monosulphide solid solution (MSS). No pentlandite has been found in the graphite octahedra in the GGP. Sulphides re-equilibrate easily with decreasing temperature (Lorand 1985), however, the effect of pressure on the stability fields of sub-solidus sulphide phases is not known. Meyer (1987) concludes that during entrapment by diamond, the coexisting sulphide phases consist of a single MSS. On falling temperature a Ca-rich phase exsolves leaving a Ni-rich monosulphide with a pyrrhotite structure which eventually re-equilibrates to pentlandite and pyrrhotite. There does not appear to have been an Ni-Ca rich MSS precurser to the sulphide phases in the GGP, the sulphides probably evolved from a Fe-Ni monosulphide.

4:3.3f Ilmenite.

Picroilmenite (Mg rich ilmenite) was identified as an inclusion in the graphite octahedra, occurring at the surfaces of CPX inclusions within the graphite. No ilmentite was analysed during this study but Slodkevich (1980 b) analysed ilmenite occurring as inclusions in the graphite aggregates and in the "groundmass" of the GGP. No significant SiO_2 is found in the analyses, the inclusion ilmenite being richer in TiO_2 (56 wt %) than the host GGP (53 wt %) and having a lower Mg/Fe ratio. This implies ilmenite may have been crystallizing for a significant period before it was incorporated into the precursor diamond in the GGP. Ilmenite is relatively rare as an inclusion in diamond (Meyer 1987), however the Mg-rich ilmenites included in the GGP graphite octahedra and host GGP are chemically comparable to Mg rich ilmenites (picroilmenites) included in diamond and other ilmenites associated with kimberlites. Ilmenite was also observed exsolving from a CPX porphyroclast in a GP layer by Kornprobst 1969 although no compositional data was reported.

4:3.3g Equilibration conditions: Geothermobarometry

Geothermobarometric calculations on minerals from the GP and GGP are limited due to their essentially bimineralic nature. OPX occurs only as exsolution lamellae in CPX. The three phase assemblage GT-CPX-OPX occuring as exsolved products from primary CPX may be used to infer minimum pressures of sub-solidus re-equilibration. The Harley (1984) geobarometer which relates Al contents of M1 sites in OPX coexisting with garnet to pressure was applied to the exsolved pyroxenes. The formulation of Harley (1984) was modified slightly in that Al contents in M1 were calculated as:

$$[\ Al^{total} - (\ Cr+Fe^{3+}+2Ti-Na\ )\ ]/2$$

as recommended by Carswell and Gibb (1987). Pressures derived using this barometer ranged from 8.8 to 12 kb depending on the OPX analysis used. These equlibration pressures only apply to the fine grained exsolved phases in the CPX and as such are minimum estimates. Doubt must be cast on the validity of the pressures calculated using this method due to the widely varying Al_2O_3 contents of the OPX exsolution

lamellae analysed in the CPX. The range of pressures may reflect incomplete equi libration between late-formed lamellae and the host CPX, or fine scale CPX lamellae within exsolved OPX. In cases where the OPX lamellae were extremely thin, the microprobe beam probably interacted with the underlying host CPX.

The presence of corundum in garnet clinopyroxenites as described by Kornprobst (1982) may be used as an indicator of P/T conditions. Gasparik (1984) calculated P-X phase relationships of the assemblage CPX-garnet-corundum at 900, 1100 and 1300 °C in the system CaO-Mg-Al_2O_3-SiO_2. For the garnet composition given by Kornprobst et al (1982), ~ 22 % Grossular, garnet and corundum are in equilibrium with CaTs rich CPX in this system between ~ 16 to 22 kb at 900 to 1300 °C. At lower pressures the corundum breaks down due to reaction with CPX to give garnet, anorthite and spinel.

At lower temperatures the CaTs component in garnet becomes unstable and undergoes the reaction

GT + Corundum = CPX + Anorthite + Gehlenite.

Kornprobst et al (1982) observed breakdown of corundum crystals in the corundum pyroxenites to intergrowths of garnet, plagioclase and spinel. Hence some lower pressure re-equilibration has also taken place in the corundum pyroxenites, initiating the reaction

CPX + Corundum = GT + Plag + Spinel

Considering primary crystallization conditions, the most significant pressure indicator in the pyroxenite suite is the presence of octahedral graphite pseudomorphs after diamond. The lack of morphological evidence suggesting that the diamonds grew metastabily requires that at least the GGP have experienced conditions within the diamond stability field. This requirement is supported by the presence of small but significant sodium contents in some GGP garnets. Pre-exsolution equlibration conditions will be considered in more detail later.

The extent of mineralogical re-equilibration with decreasing temperature and thus the effective blocking temperature for a given cation exchange reaction depends mainly on the cation diffusivity in the slowest diffusing phase (garnet for the Fe-Mg exchange thermometers used here). Harley (1984) has pointed out that even if inter-phase cation exchange ceases at the closure temperature of the garnet (T^{GT}°C), intraphase diffusion could continue in other coexisting phases to eradicate rimward compositional zoning. A consequence of this is that temperatures obtained for adjacent rim pairs would not correspond to T^{GT}°C or minimum temperature conditions, but would be artificial temperatures. Effective closure temperature conditions for exchange equilibria can also vary with varying texture and reaction mechanisms. If the pyroxenes from the GP and GGP ceased to exsolve pyroxene lamellae from an initially homogeneous grain at ~ 700-800 °C and subseqeuntly experienced garnet exsolution (a net transfer reaction) at temperatures less than the bulk grain closure temperature (T^{CPX}°C), the newly nucleated pyroxene grains would be forced to approach compositions demanded by the lower temperature (Harley 1989). Conventional cation exchange geothermometers such as garnet-CPX Fe-Mg thermometers may at best only be considered as guides to the post-peak crystallization/metamorphic temperatures of

slowly cooled, exsolved, crystalline rocks.

Equilibration temperatures for the garnetiferous pyroxenites were calculated using thermometers based on Fe^{2+}-Mg^{2+} exchange between garnet and CPX. The most reliable calibrations of this thermometer according to recent reviews by Carswell and Gibb (1987) and Finnerty and Boyd (1984) are those proposed by Ellis and Green (1979) and Powell (1985). These two formulations were used together with a more recent re-evaluation of existing experimental data by Krogh (1988). Carswell and Gibb (1987) found that the formulation of Ellis and Green (1979) reproduced experimentally determined temperatures for synthetic and natural systems more closely at temperatures above 1200 °C whereas the formulation of Powell (1985) yields temperatures which are lower than Ellis and Green (1979) and closer to the experimentally determined values below 1200 °C. The Krogh (1988) formulation has not been reviewed in detail for high temperature mantle rocks.

Carswell and Gibb (1987) noted that despite uncertainty concerning the presence of Fe^{3+} in phases crystallized during some experimental studies, temperatures calculated assuming $Fe^{2+} = Fe_{Total}$ are, in the vast majority of cases for mantle rocks, closer to experimentally determined temperatures than those calculated using Fe^{3+} contents determined on the basis of stoichiometric charge balance. It must be noted that the presence of Fe^{3+}, particularly in CPX, produces slight overestimates in temperature if Fe^{2+} is assumed to equal Fe_{Total}, as in this study. Although Luth et al (1989) found that Fe^{3+} contents of up 12 % caused overestimation of some geothermometers by up to 200 °C when applied to garnet peridotites, the more iron-rich nature of garnets from the Beni Bousera pyroxenites significantly decreases this error. More complex formulations of the garnet-CPX geothermometer employing Margules parameters to calculate CPX site mixing e.g. Ganguly (1979) were found by Carswell and Gibb (1987) to overestimate temperatures by up to 100 °C at 1200 °C.

Consideration of mineral stability in the garnet pyroxenites leads to the assumption that the mineral core compositions equilibrated at close to 20 kb. For comparative purposes this value is also used to calculate rim temperatures.

The following formulations were used to obtain temperatures from the garnet pyroxenites:

Ellis & Green (1979): T = °K, P = kb

$$T = 3104\ X^{Gt}_{Ca} + 3030 + 10.86P\ /\ \ln Kd + 1.9034$$

Powell (1985):

$$T = 2790 + 10P + 3140\ X^{Gt}_{Ca}\ /\ 1.735 + \ln Kd$$

Krogh (1988):

$$T = -6173\ (X^{Gt}_{Ca})^2 + 6731\ X^{Gt}_{Ca} + 1879 + 10P\ /\ \ln Kd + 1.393$$

Where: $Kd = (Fe^{2+}/Mg^{2+})^{GT} / (Fe^{2+}/Mg^{2+})^{CPX}$ and $X^{Gt}_{Ca} = Ca / (Ca+Mg+Mn+Fe^{2+})$

Error estimation based on 4-8 % error on the Fe determination in CPX for the chosen thermometers produces "maximum" errors of +/- 50 °C.

Assessment of the relative errors involved in assuming $Fe^{2+} = Fe_{Total}$ for this suite of rocks produced temperature over estimates which ranged from +20 ° C to a worst case of +55 °C with an an estimated average of ~ +35 ° C, thus the maximum worst case error in assuming $Fe^{2+} = Fe_{total}$ is 55 °C which is equal to average propagated analytical error for most calculations. Utilization of Fe^{3+}/Fe^{2+} ratios determined by wet chemical analyses from Kornprobst (1969) gave an overestimate of 50 °C for the data listed by this author, however, the stoichiometry of some of the analyses are poor and doubt exists about the quality of these Fe^{3+}/Fe^{2+} determinations (which ultimately depend on the quality of the bulk mineral seperates analysed).

Assessment of the three different formulations used (Table 4.16) reveals that the Ellis and Green (1979) thermometer (E+G '79) consistently yields temperature estimates 10 to 15 °C higher than Powell (1985) (P' 85) at values of $X^{Gt}_{Ca} < 1.5$ for both core and rim calculations, whereas Krogh (1988) (K' 88) gives temperatures of between 20 to 60 °C lower than P'85 at low values of X^{Gt}_{Ca} . At higher values of X^{Gt}_{Ca} , E+G '79 gives comparable results to P'85 whereas K'88 gives temperatures equal to or 10-40 °C lower or higher than P'85. K'88 also seems to give the largest range of temperatures over the entire range of core-core compositions at 20 kb (389 °C, compared with 293 °C and 274 °C for P'85 and E+G '79 respectively) . K'88 also gives the greatest temperature range when appied to the CPX bulk compositions at varying pressures K'88 gives a range of 120 °C over the interval 20-40 kb whereas P'85 and E+G '79 give ranges of less than or equal to 100 ° C.

From this appraisal of the different garnet-CPX geothometers, E+G '79 and P'85 are deemed more reliable mineral thermometers than K'88 for the Beni Bousera garnet pyroxenites suite. Carswell and Gibb (1987) preferred the P'85 formulation from E+G '79 at temperatures below 1200 °C as it yields results closer to experimentally determined temperatures. As most of the equilibrium temperatures determined from the garnet pyroxenites are below 1200 °C, the P'85 formulation was adopted in this study to aid relative comparison of the samples. It should be noted however that Carswell and Gibb (1987) preferred E+G '79 above 1200 °C. Of the Beni Bousera specimens yielding temperatures above this value the E+G '79 formulation gives the lowest temperature range over a spread of bulk compositions and generally yields the lower equilibrium temperatures. However, to maintain a uniform approach the formulation P'85 is used above 1200 °C (Figure 4.31). The effect of different equilibration pressures on P'85 is to increase the equilibration temperature by approximately 50 °C for every 10 kb pressure increase and vice-versa.

In the following discussion the temperatures refered to were obtained from mineral core compositions from the central regions of pyroxenite layers unless otherwise stated. Comparison of the different pyroxenite groups using P'85 reveals that the corundum bearing pyroxenite analysed by Kornprobst et al (1982) yields a higher equilibration temperature at 20 kb (1229 °C) than the average core pairs of either GP or GGP (Table 4.16 and 4.17), only one pair yields a higher temperature (1250 °C). The most striking conclusion from the geothermometry is that the GGP have equilibrated on average 90 °C cooler than the GP (even allowing for the much lower population of GP mineral pairs analysed). A much steeper temperature gradient is apparent between core and rim pairs in the GP pairs. This variation

Table 4.16. GT/CPX thermometry of pyroxenite layers and GTLHZ using the formulation of Powell (1985), assuming a pressure of 20kb.

SAMPLE/MIN	C/R	Mg. No GT.	Na CPX,M2	X Ca, Gt	Kd	ln Kd	T E&G 79	T P'85	T K'88
1 GP147 2/6	C	0.63	0.172	0.113	2.043	0.7144	1102	1093	1038
2 GP147 4/6	C	0.63	0.239	0.113	2.056	0.7206	1098	1089	1034
3 GP147 XPD/XPC	C*	0.40	0.198	0.117	2.056	0.7206	1102	1093	1043
4 GP147 XPB/XPE	C*	0.61	0.249	0.116	1.995	0.6907	1117	1109	1060
5 GP147 BULK/XPA	C	0.61	0.204	0.116	1.328	0.2834	1376	1389	1384
6 GP147 BULK/6	C	0.63	0.204	0.113	1.251	0.2242	1413	1435	1435
7 GP147 EX	LAM	0.53	0.135	0.125	2.868	1.0538	945	940	882
8 GP147 4/11	R	0.51	0.094	0.126	5.212	1.6510	750	727	657
9 GP147 4/1	R	0.41	0.094	0.128	2.904	1.0659	954	938	882
10 PHN5730 1/8	C	0.58	0.104	0.136	2.463	0.9014	1035	1023	983
11 PHN5730 6/20	R	0.52	0.154	0.134	3.062	1.1189	939	922	870
12 GP83 2/5	C	0.47	0.136	0.139	2.495	0.9144	1032	1020	981
13 PHN5731 3/2	C			0.130	2.932	1.0758	953	936	882
14 PHN5731 44/3	C			0.137	2.375	0.8649	1053	1042	1004
15 PHN5731 44/9	C			0.137	2.125	0.7540	1109	1101	1071
16 PHN5731 3/31	C			0.129	2.304	0.8350	1059	1048	1004
17 PHN5731 58/4	C			0.139	2.279	0.8240	1077	1067	1034
18 PHN5731 32/10	R			0.126	3.543	1.2651	876	856	792
19 PHN5731 52/66	R			0.140	3.204	1.1644	927	910	861
20 PHN5731 10/8	R			0.148	3.596	1.2797	994	873	826
21 SLOD. 106/1/106/18	C	0.59	0.097	0.125	2.457	0.8988	1024	1011	959
22									
23 CORP CPX/GT	C	0.76	0.161	0.215	2.027	0.7065	1227	1229	1271
24 GP37 4/3	C	0.53	0.143	0.175	2.328	0.8450	1106	1099	1098
25 GP37 10/8	C	0.53	0.111	0.167	2.428	0.8871	1076	1067	1055
26 GP37 9/9	R	0.44	0.159	0.156	3.812	1.3382	878	859	817
27 GP87M 3/5	C	0.68	0.095	0.151	1.714	0.5386	1248	1250	1256
28 GP87M 2/2	C	0.66	0.091	0.139	1.833	0.6058	1178	1192	1177
29 GP87B 4/6	C	0.76	0.066	0.132	1.763	0.5667	1207	1205	1185
30 GP87B 3/5	C	0.76	0.091	0.128	2.007	0.6968	1114	1122	1086
31 GP37 3/11	R	0.51	0.097	0.161	3.843	1.3463	879	860	822
32									
33 GP24 4/8	C	0.82	0.121	0.126	2.655	0.9765	990	975	920
34 GP24 3/1	C	0.82	0.110	0.126	2.625	0.9651	995	981	927
35 GP24 2/5	C	0.84	0.119	0.124	2.677	0.9847	984	970	913

occurs at relatively constant X^{Gt}_{Ca} (Fig. 4.31) and is compatible with isobaric cooling at relatively constant X^{Gt}_{Ca}.

Table 4.17 . Comparison of average equilibration temperatures of garnet pyroxenites from Beni Bousera using the formulation of Powell (1985) assuming an equlibration pressure of 20kb. COPR = Corundum bearing pyroxenite analysed by Kornprobst et al (1982).

LITHOLOGY	AVERAGE CORE-CORE °C	AVERAGE RIM-RIM °C
GGP	1062	907 *
GP	1152	860
CORP	1229	

* Excludes high MnO pair which gives 727 °C.

Equilibration temperatures calculated using the GGP bulk CPX compositions, assuming they were in equilibrium with the most Mg rich cores of garnets from the same rock, yield much higher temperatures, 1389 to 1435 °C at 20 kb. However, the pre-exsolution CPX compositions were probably in equilibrium with garnet at higher pressures than 20 kb. If an equilibration pressure of 30 kb is assumed temperatures of 1438 to 1486 °C are obtained. These temperatures are of the same magnitude of those estimated for pre-exsolution CPX compositions in pyroxenites from the Ariege orogenic peridotite massif (S.W. France) by Conquere (1977). The inadequate accuracy of the wide beam CPX analyses from the GGP is demonstrated by the fact that they yield temperatures of only 1140 °C at 30 kb which is very close to the exsolved CPX core garnet equilibration temperatures at 30 kb.

The higher temperatures recorded by the GP compared to the GGP are surprising considering their major element chemical similarity. The corundum pyroxenite has higher X^{Gt}_{Ca} values and higher Jd content in its CPX than CPX from GP or GGP groups. These differences may be a reflection of the highly variable degrees of re-equilibration and exsolution these rocks have experienced. This is supported by the much lesser degree of exsolution in CPX from the GP samples studied eg. GP87 and GP37 which would lead to lower Kd values and hence higher equilibration temperatures.

In addition to core-rim variation highlighting the effect of differing degrees of re-equilibration on the temperatures obtained via geothermometry , the two core pairs from the outer margin of GP 87 yield equilibration temperatures 60 °C lower than those obtained from the middle of this layer . This could be a reflection of a palaeo-temperature gradient existing due to emplacement of hot magma into cooler peridotites. Considering the increased deformation and recrystallization that is common at layer margins (Chapter 2), this temperature gradient is probably a response to more intense, deformation-induced, re-crystallization and deformation at layer margins. More detailed work on pyroxenite layers is needed to fully substantiate this.

Application of Fe-Mg exchange geothermometers to the garnet pyroxenites does not reveal

Figure 4.31. Plot of $\ln K_D$ vs X_{Ca} in GT for CPX-Gt pairs from garnet bearing pyroxenites and garnet lherzolites. Isotherms are calculated using the formulation of Powell (1985) at an assumed pressure of 20 kb.

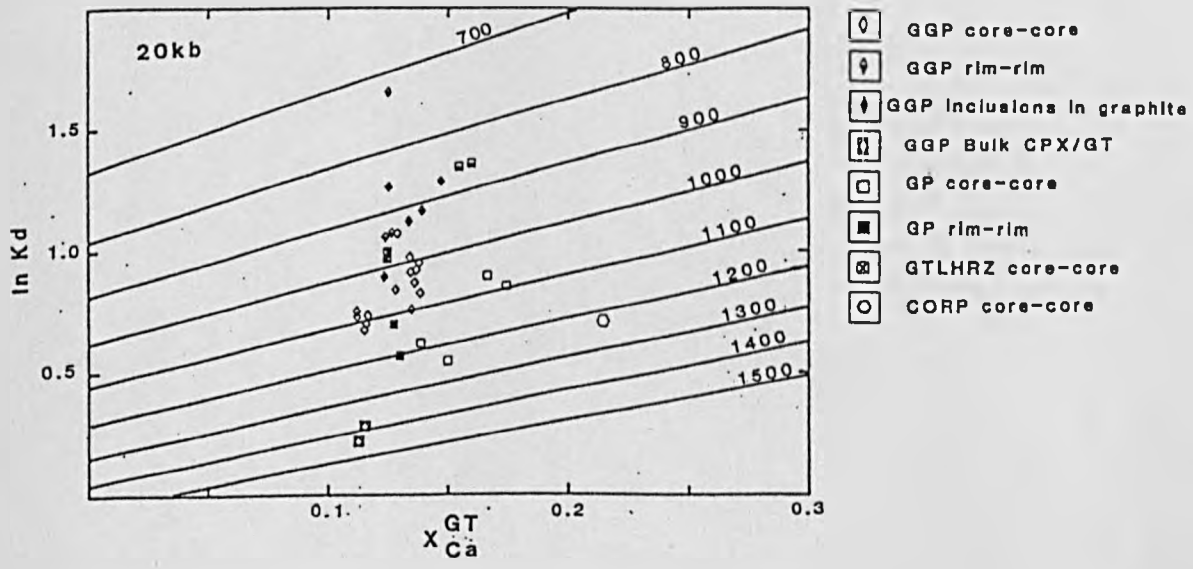

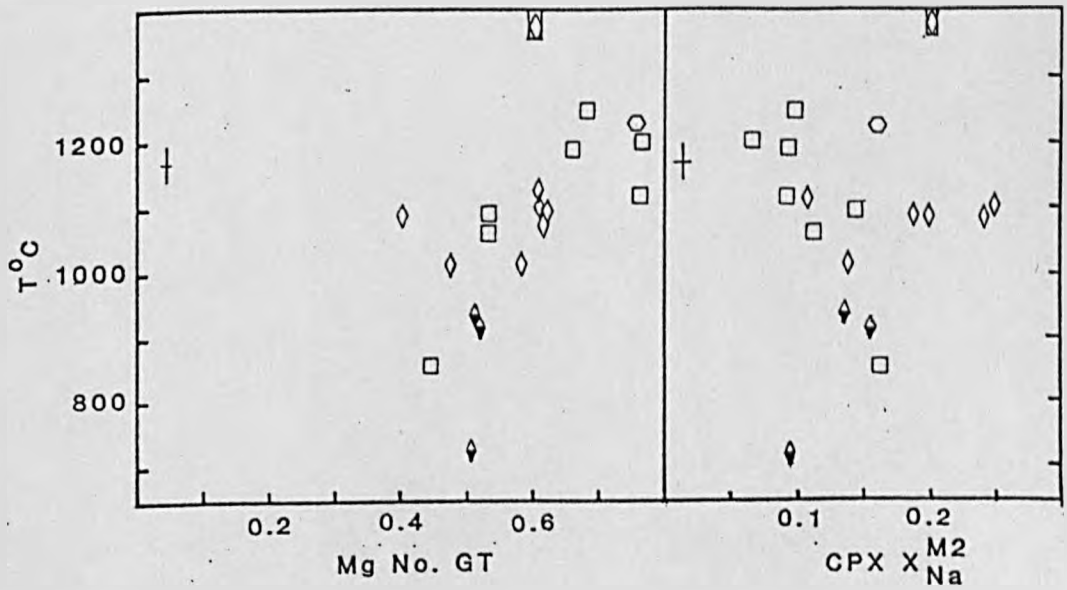

Figure 4.32. GT-CPX equilibration temperature vs Mg No. of garnet and $X^{M2}Na$ of CPX from garnetiferous pyroxenites. Temperatures calculated using Powell (1985).

information concerning the primary crystallization conditions of these mafic layers but records the influence of variable exsolution and re-equilibration on Fe-Mg exchange between garnet and CPX. Application to calculated pre-exsolution CPX composition indicates that the original CPX are of high temperature origin (> 1350 ^{o}C).

There is no correlation between equilibration temperatures and Mg number of the garnet or $X^{M2}Na$ in CPX (Figure 4.32) indicating that the P'85 thermometer is not adversely influenced by Jd content of the CPX. Fe-Mg garnet-CPX exchange geothermometers are subject to large errors at very high Jd contents (Jd > 60 %, Koons 1984). Krogh (1988) found that where (Na + Ca)CPX << 1, the Fe-Mg distribution in the system is affected. This is confirmed by the very low rim equilibration temperature obtained from a CPX from GP147 which has much a higher $X^{CPX}Mn$ content and lower $X^{M2}Na$ content than other CPX (Table 4.1). A positive correlation exists between the Mg number of garnet and both Kd and temperature (Figure 4.32). The dependance of Kd on garnet Mg number was suggested by Pattison and Newton (1987) but was not confirmed by Krogh (1988), however, Krogh (1988) studied garnets with Mg numbers generally < 0.5 whereas in this study the positive correlation between Kd and garnet Mg No. is displayed by garnets with Mg Nos. above 0.5.

4:3.3h SUMMARY.

On the basis of mineral chemical relationships the GP and GGP appear to represent a fractionation series, the rocks having originally crystallized from magma batches of similar compositions which have undergone CPX, garnet and probably OPX fractionation (this will be discussed in Chapter 5). The generally more Fe-rich mineral chemistry of the GGP together with the higher TiO_2 and MnO contents of their CPX suggest they are the most evolved rocks of the suite. The mineral chemistry of the GGP, including their calculated bulk CPX compositions, are similar to the mineral chemistry of carbonaceous and non-carbonaceous eclogite xenoliths from Kimberlite pipes. GGP CPX are more Na_2O,Al_2O_3 and MnO rich and MgO poor compared to mineralogically similar garnet pyroxenite and subcalcic clinopyroxenite xenoliths from alkali basalts (Wilkinson 1976).

All minerals observed as inclusions in graphite octahedra also occur as inclusions in natural diamonds. The mineral chemistry of inclusions in the Beni Bousera graphite overlaps the large range shown by E-type inclusions in diamonds although the Beni Bousera graphite inclusions have undoubtedly undergone more re-equilibration. This evidence supports the conclusion in Chapter 3 that the graphite aggregates within the GGP represent graphitized diamonds.

The combined effects of incomplete exsolution and recrystallization have caused varying degrees of re-equilibration in the silicate mineralogy of the pyroxenite suite. Extensive sub-solidus re-equilibration precludes determination of the pressure/temperature conditions of crystallisation in all the pyroxenites. Small but significant amounts of Na present in some garnets within the GGP support the hypothesis that these rocks have resided in the diamond stability field for a significant period of time before uplift and emplacement in the continental crust. The high pre-exsolution temperatures recorded by recalculated bulk CPX compositions (> 1400 ^{o}C @ 30 kb) places the GGP well within the *graphite* stability field at high pressures and hence may record prevalent P/T conditions during graphitization of the precursor diamonds. A summary of the P/T evolution of the whole peridotite massif will be presented in Chapter 8 when other

geochemical data have been considered.

4:4 Garnet-spinel lherzolites.

4:4.1 Introduction

The field relations between thinned GP layers and spinel lherzolites and their coincidence with the occurrence of outcrops of garnet-spinel lherzolite, discussed in Chapter 2, indicate that the garnet lherzolites are probably the product of mixing and high pressure/temperature equilibration (between GP layers and spinel lherzolite). To stabilize garnet lherzolite this mixing must have occurred close to, or in, the garnet lherzolite stability field. It is possible that the two lithologies were mixed via physical shearing, close to the upper limit of the spinel lherzolite field. The increased stability of pyrope garnet in CMAS systems of higher bulk CaO content (MacGregor 1970) may have encouraged the stabilization of the garnet, spinel lherzolite.

4:4.2 Olivine.

Mg/(Mg + Fe) values for the garnet lherzolites (Figure 4.1) range from 89.5 to 90.5 and lie within the mode of the spinel lherzolites and to the low Mg/Mg + Fe range of olivines from fertile garnet lherzolite xenoliths from kimberlite pipes.

4:4.3 OPX.

OPX porphyroclasts from garnet lherzolites (Table 4.3) are magnesian, En 89.4-89.5 (Figure 4.3) with low CaO contents (0.47 wt % maximum) and Al_2O_3 contents that lie within the range of OPX from spinel lherzolites and harzburgites (2.96-4.35 wt %). However, a plot of Al_2O_3 (wt %) in OPX vs 100 Cr / Cr + Al in spinel (Fig. 4.5) reveals that the garnet lherzolite OPX are low in Al_2O_3 compared to spinel lherzolites and even spinel harzburgites. This may be due to the presence of garnet which along with spinel will preferentially incorporate Al.

4:4.4 CPX.

CPX from the garnet, spinel lherzolites are diopsides (Fig.4.3) with over 47.5 % Wo component and 4 % Fs (Table 4.5). CPX contain between 4.4 and 5.5 wt % Al_2O_3 and upto 1.8 wt % Na_2O producing Jd contents of upto 12 % with minor (~ 3 %) CaTs and TiCaTs components (~1.5 %).
Cr / (Cr + Al) ratios are slightly lower than expected for CPX Mg Nos of over 92.

4:4.5 Garnet.

Garnet compositions (Table 4.14) are pyrope rich (upto 77 % Py), plotting at the most Mg rich compositions in Figure 4.27 and showing little compositional spread. Chemical variation in terms of garnet end-members is: Py $_{77.4\text{-}71.5}$; Gr $_{9.2\text{-}2.8}$; Al $_{12.5\text{-}15.1}$; Uv $_{2.5\text{-}4.9}$. The cores of the garnets are generally slightly more Mg rich than the rims which are affected by secondary kelyphite. Cr_2O_3 contents

in garnet cores reach up to 1.7 wt % (5 % uvarovite). These garnets are comparable to garnets from fertile garnet lherzolite xenoliths from kimberlite pipes (Nixon 1973). Pyrope contents of 70-80 % and low Cr_2O_3 (1-2 %) contents are charcteristic of garnets from garnet peridotite bodies occuring in gneiss complexes such as those described by Ernst (1978) which also contain eclogite bodies. Pyrope rich garnets in the garnet, spinel lherzolites are similar in composition to the Mg rich garnets occuring at the margins of garnet pyroxenite layers, eg GP 87B or very thin GP layers (see Fig. 4.27) which contain garnets that have partially equilibrated with the surrounding more Mg rich spinel lherzolites. The parallel CPX-garnet tie lines for the narrow GP layer GP151 and the layer margin of GP87B indicate that the garnet compositions are intermediate products of recrystallization and chemical re-equilibration of the pyroxenite layers with the surrounding spinel lherzolites. Neoblastic garnet from the narrow GP layer , GP 151, are slightly less Mg rich but considerably more Cr rich, plotting on the garnet-CPX tie line towards CPX (Fig. 4.27). This mineralogical evidence supports the view that the Beni Bousera garnet lherzolites represent the products of intense shearing and chemical re-equilibration between garnet clinopyroxenites and spinel lherzolites.The problem of physical and chemical re-equilibration of pyroxenite layers with the peridotites will be addressed in the next section.

4:4.6 Spinel.

Spinels from the garnet lherzolites are relatively Cr rich compared to most of the spinel lherzolites (Table 4.6); 100 Cr/Cr + Al ratios varying between 14 and 22. Although parallel to the trend of partial melting on Figure 4.11, the trend may be interpreted in terms of decreasing (Cr /Cr + Al) and decreasing (Mg / Mg + Fe) due to mixing and equilibration of spinel lherzolite with Cr-poor, Fe-rich garnet clinopyroxenite.

4:4.7 Equilibration conditions.

The presence of kelyphite rims around all of the garnets in the lherzolites means that it is only possible to determine core-core mineral equilibration temperatures for the garnet, spinel lherzolites. Assuming garnet core and exsolved CPX core composition were once in equilibrium at a pressure of 20 kb (see section 4:3.3f), the garnet-CPX geothermometer of Powell (1985) was applied to microprobe analyses of these two phases. The results of three core pairs are presented in Table 4.16. The three temperatures derived from the Powell (1985) formulation are within error of each other and have an average of 975 °C (Figure 4.31). This temperature is at the low end of the range defined by garnet-bearing pyroxenites. In Chapter 2 it was noted that the garnet lherzolites display highly sheared textures involving intense re-crystallization of olivine and probably CPX. This indicates that re-crystallization at lower temperatures has significantly affected the mineral pairs. The much smaller size of the CPX grains analysed compared to the garnet suggest they may be neoblastic and thus not in equilibrium with the garnet core compositions. Therefore, equilibration temperatures derived from the highly deformed garnet lherzolites must be viewed with extreme caution considering the assumptions involved in their calculation.

The garnet-OPX geobarometer of Harley (1984) was applied to garnet core-exsolved OPX porphyroclast core compositions to estimate an equilibration pressure for the garnet lherzolites, assuming the approximate 1000 °C equilibration temperature calculated above. Pressures calculated varied from 16.3 kb to 19 kb, the upper value being recorded by a garnet core in equilibrium with the least aluminous OPX

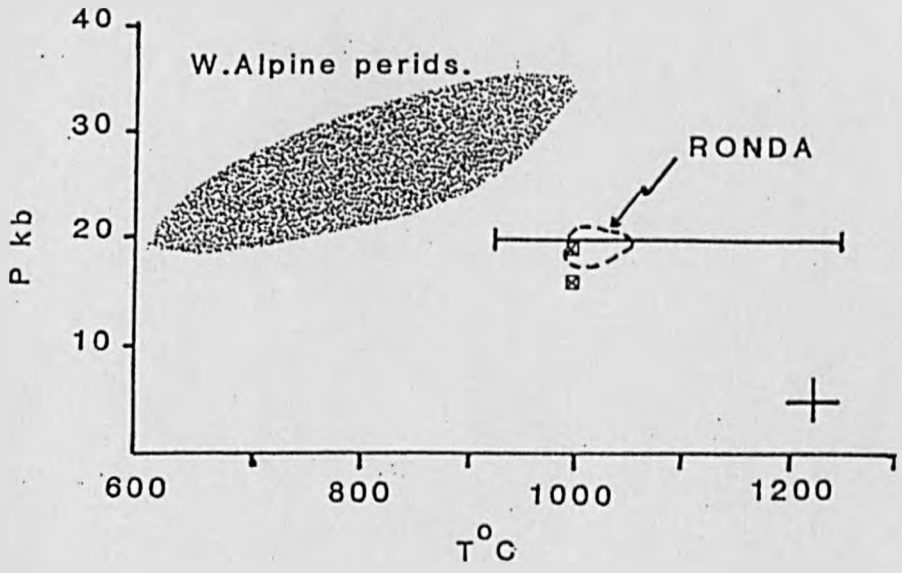

Figure 4.33. Sub-solidus P/T equilibration estimates for Beni Bousera garnet pyroxenites (solid line) and garnet lherzolites (squares with diagonal crosses) compared to equilibration conditions for Ronda garnet peridotites (dashed open field) and W.Alpine orogenic peridotites (shaded area). Estimated error bar shown. Equilibration temperatures for Beni Bousera pyroxenites all at assumed pressures of 20 kb.

porphyroclast. None of these values are within the stability field of "normal" garnet lherzolites at 1000 °C. However, 19 kb is consistent with the 20 kb equilibration pressure estimate derived from the corundum bearing garnet clinopyroxenites. This pressure may be the equilibration pressure of the garnet-spinel lherzolites before garnet breakdown (kelyphitization). The possibility of incomplete exsolution in the OPX-porphyroclasts, indicated by variable Al_2O_3 contents of OPX 's from the same rock, place large errors on the calculated equilibration pressures using garnet-OPX barometry. Estimated pressures are also dependant on calculated equilibration temperatures due to the *dP/dT* slope of the garnet-OPX geobarometer. Harley (1984) states that even use of the most reliable geothermometers for garnet-peridotites and pyroxenites (the garnet-CPX Fe-Mg exchange thermometers) with accuracies of +/- 50 °C result in errors of +/- 2 kb in the pressure estimation before analytical precision and compositional heterogeneity are considered. Total errors on estimated equilibration pressures are probably reater than +/-4 kb.

The sub-solidus equilibration pressures calculated for the Beni Bousera garnet peridotites using the method of Harley (1984) are comparable to those calculated for the garnet peridotites of the Ronda massif (S.Spain) for exsolved OPX-garnet compositions by Harley (1984). The Ronda pressures range from 15 to 21 kb at between 900 and 1000 °C. The lower pressures were calculated using lower temperature estimates derived from two pyroxene thermometry. Both the Ronda and Beni Bousera garnet peridotites have equilibrated at much higher temperatures but lower pressures than other orogenic and Norwegian garnet-peridotite bodies studied by Harley (1984) which have commonly equilibrated above 20 kb (upto 35 kb) and below 900 °C (average ~ 780 °C), Figure 4.33. This indicates the Beni Bousera and Ronda peridotite massifs were emplaced under very similar, high geothermal gradients and is consistent with the close spatial and tectonic relationships between the two massifs.. The high prevailing geothermal gradients during emplacement (uprise) of the Beni Bousera massifs would favour graphitization of any pre-existing diamond in the GGP and indicates that both Beni Bousera and Ronda peridotite bodies may have originated from hot upwelling "diapiric" mantle, which was subsequently emplaced into the crust by faulting as suggested by Kornprobst and Vielzuf (1984).

4:5 Pyroxenite layer/peridotite interaction.

Field and petrographical observations discussed in Chapter 2 indicate that the mafic layers and host peridotite have undergone chemical and physical interaction. Peridotites immediately adjacent to the mafic layers are depleted in CPX and spinel and, sometimes OPX, at the contact of the layers, appearing as harzburgite or dunites, whilst the margins of the mafic layers are enriched in spinel. The spinel occurs as elongate, irregular, olive green crystals poikilitically enclosing small OPX neoblasts. In hand specimen, the CPX within many Al-augite pyroxenite layers change from pink/greys at the layer centre to distinctly green at the layer margins which resemble the Cr-diopsides in the peridotites. This variation is also evident in terms of mineral chemistry. CPX from garnet-bearing pyroxenites are notably richer in Cr_2O_3 at the margin of a layer compared to its centre eg. CPX from GP87T have average Cr_2O_3 contents of 0.76wt% compared to 0.22wt% in CPX from the centre of the layer. This variation is illustrated in Figure 4.34 which is a detailed traverse across the edge of a websterite layer. Cr_2O_3 almost doubles passing from 1.2cm in from the layer margin to the peridotite contact. In terms of pyroxene quadrilateral components (Fig. 4.35) the layer margin CPX from both the top and base of GP87 trend towards the more Ca-Mg-rich

Figure 4.34. Oxide wt % variation in CPX at the margin of a websterite layer versus distance in mm from peridotite contact.

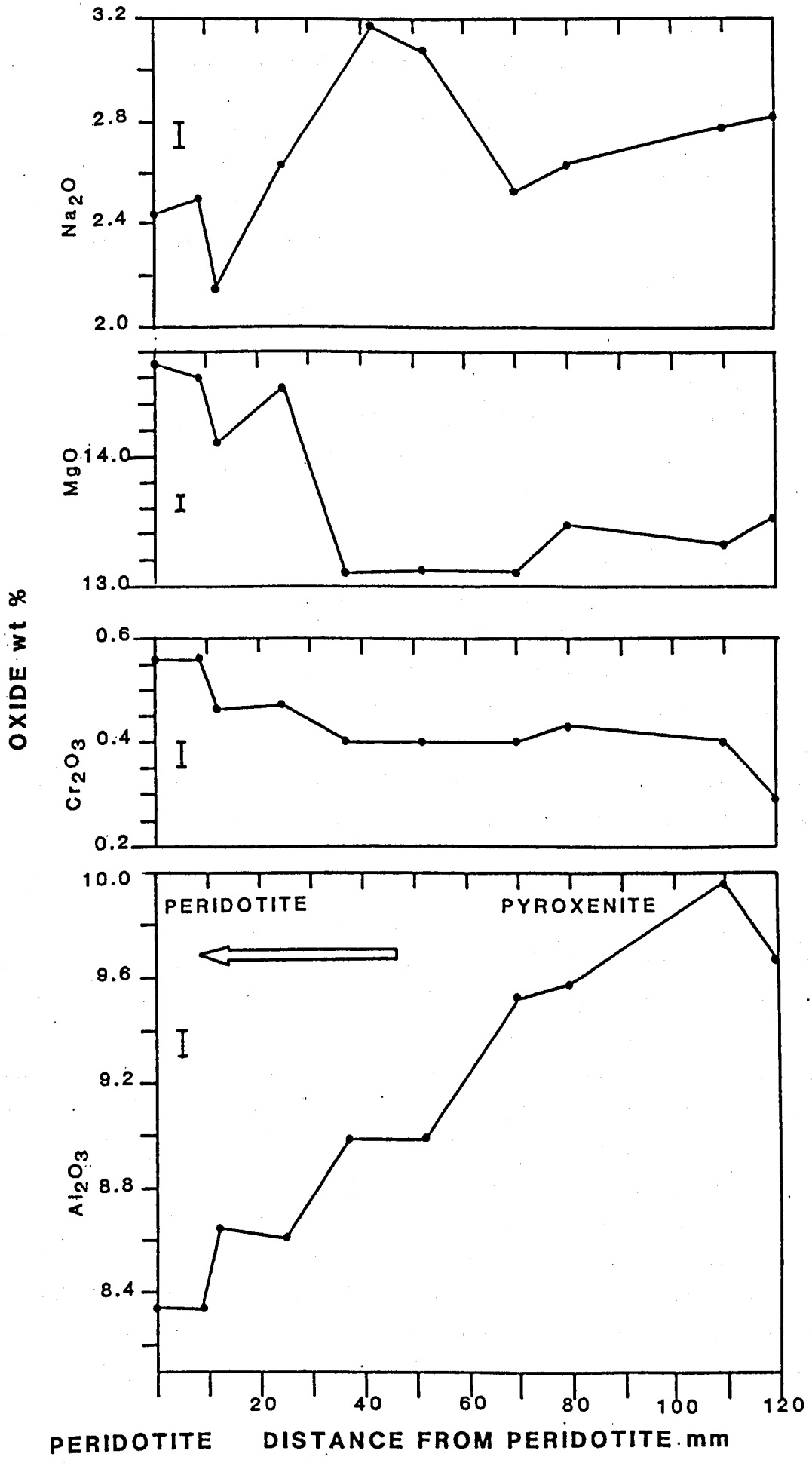

compositions of the spinel and garnet lherzolite CPX. Garnets from the margin of GP87 also become considerably more pyrope rich within 1cm of the pyroxenite/peridotite contact, following the trend to more Mg-rich compositions of the CPX. CPX from the highly sheared and thinned GP layer GP151 (~1cm thick) plot very close to, or in, the lherzolite CPX field in Figure 4.27, whilst garnets from this thin layer are even more pyrope rich than the margins of GP87 (upto 67% Py). It therefore appears that as the thickness of the pyroxenite layers decreases, major element re-equilibration of the pyroxenite with the surrounding peridotite becomes more complete. Pyroxenite layers 1cm or less in thickness have almost completely re-equilibrated with the surrounding peridotite.

The traverse across the margin of GP 101 websterite also illustrates how MgO becomes enriched in CPX at the layer boundary whilst Na_2O and Al_2O_3 record significant decreases. The relative elemental increases and decreases are in accord with apparent diffusion gradients between Mg, Cr rich peridotites and Na_2O,Al_2O_3 rich pyroxenites. Spinels at the margin of the pyroxenites are considerably poorer in Cr_2O_3 than spinels from either garnet or spinel lherzolites (Figure 4.11). Those from the websterite, GP 31 are slightly more Cr-rich (5 % Cr_2O_3) and considerably more Mg rich than spinels from the margin of GP layer GP38 (Figure 4.11). This variation could be a result of garnet and CPX fractionation decreasing Cr and Mg in the GP parent liquid.

The spinels at the pyroxenite layer margins are very irregular and appear texturally to be very late. These spinels are also associated with olivines which interdigitate with pyroxenes at layer margins. The more Cr, Mg-rich spinels which occur at the layer boundary and for several mm into the pyroxenite layer could the product of incongruent melting of pyroxene during intrusion of the pyroxenite layer. Equilibration temperatures calculated using bulk CPX compositions from the GGP layer indicate that at 30 kb the GGP layers would be as hot as 1480-1530 °C which is on or above the experimentally determined peridotite solidus of Kornprobst (1970). Intrusion of such hot magma into lherzolite (garnet bearing at 30 kb), which is also close to its solidus, would induce melting of the low melting component of the immediately adjacent lherzolite. Thus CPX and garnet would melt and the resulting liquid would be free to infiltrate the intruding pyroxenite. Melting of peridotite close to pyroxenite layer margins would explain the locally dunitic to harzburgite compositions and would explain the small extent of the "depletion halo". Olivine produced by incongruent melting of pyroxene would not have the high Fo contents expected of harzburgite/dunitic residues but would probably have Fo contents below or equal to those of the surrounding olivine in the undepleted lherzolite due to buffering of the residual olivine composition at near-solidus temperatures. Slightly lower Fo contents in olivines close to pyroxenite layer margins are in fact observed (Figure 4.36). Olivines within the margins of certain pyroxenites may represent xenocrysts which have been tectonically disrupted from the surrounding lherzolites or may be the product of incongruent melting of OPX. The Fo content of these olivines is lower (<88.5 %) than that of olivines in the dunitic/harzburgitic margins of the peridotites. Lower Fo contents of these olivines could be due to re-equilibration with a more Fe-rich environment if the crystals were xenocrysts or would be expected if the olivine was the product of OPX melting. A decrease in Fo content of olivines is also apparent in peridotites co-existing with abundant pyroxenite layers. This may be the result of interaction with an Fe-rich melt expelled from the peridotite margins which percolates and interacts with the surrounding sheared lherzolite.

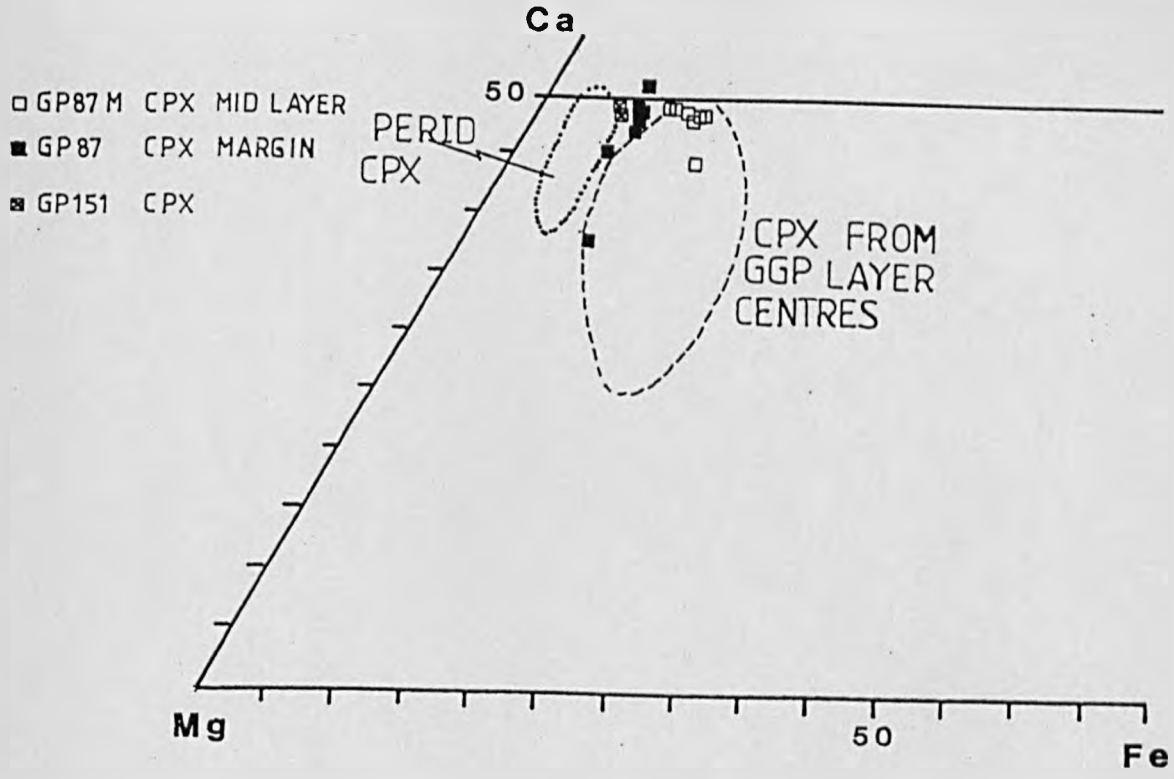

Figure 4.35. CPX Ca:Mg:Fe variation from the centre to margin of GP layer GP87 and in 1 cm thick garnet websterite layer GP151.

Figure 4.36. Olivine Fo contents in peridotites close to pyroxenite layers in pyroxenite layer margins and in peridotites containing sparse or abundant pyroxenites. Comparative data for Lherz and Ronda also shown (Data from Dickey 1970).

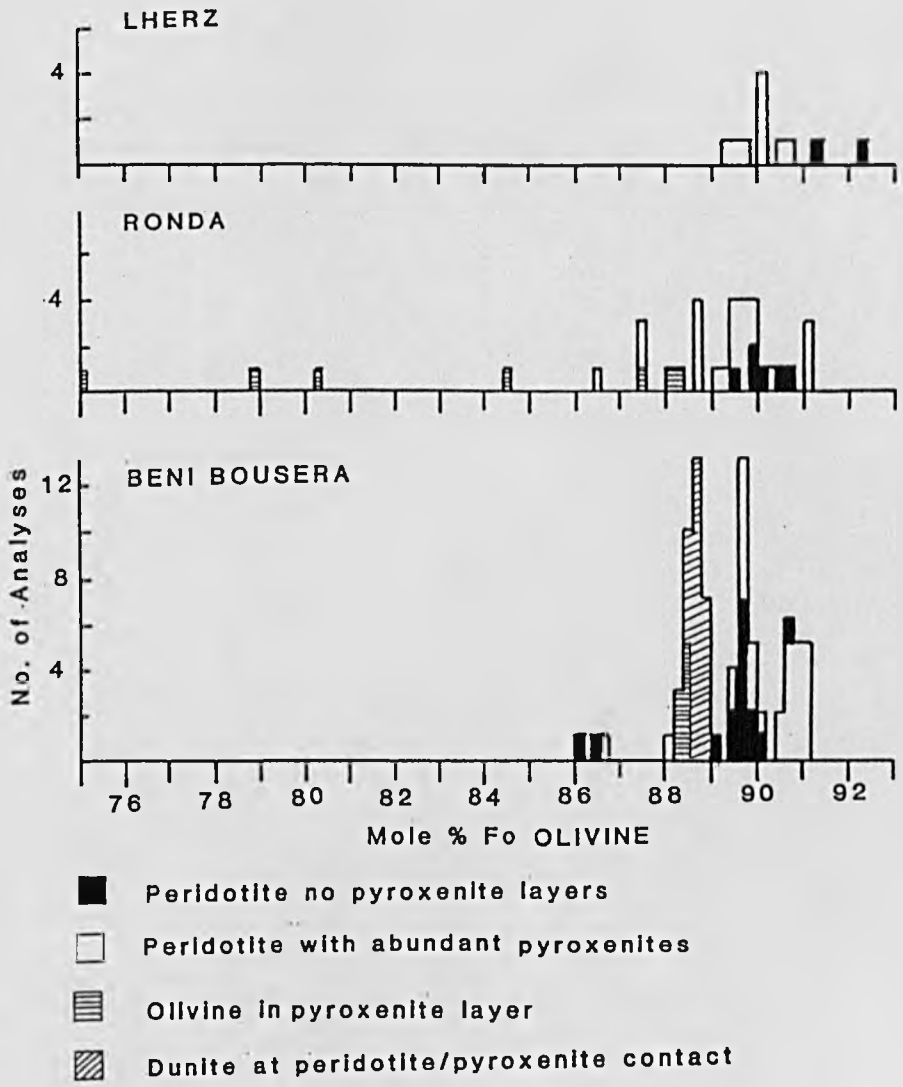

The generally lower Fo contents of olivines in peridotites with abundant pyroxenite layers is not consistent with the suggestion of Michard et al (1982) , that abundant pyroxenites are the product of increased melting in the surrounding lherzolites. Harzburgites with high Fo contents would be a consequence of such a theory.

Although incongruent melting of pyroxene in lherzolites due to infiltration of pyroxenite magma has been invoked to successfully explain the depleted lherzolite/pyroxenite margins in the Trinity peridotite (Quick 198), this theory is problematic when applied to such features in Beni Bousera. Garnet would be expected as the aluminous phase if the layers were intruded into hot peridotite in the diamond stability field or even at 30 kb, however, abundant spinel is often present at the margins of many pyroxenite layers. Additionally, incongruent melting of pyroxene is probably only possible up to pressures of ~ 27 kb in complex systems (Kushiro and Yoder 1974).

A more reasonable model to explain the observed zonation is one in which the host pyroxenite magma depletes the host peridotite of its lowest melting fraction at high pressure i.e. CPX and aluminous phases (spinel and garnet). This is consistent with the observed depletion in modal abundance of CPX and aluminous phases in peridotites immediately adjacent to pyroxenite layers. The incipient melt would be saturated with an aluminous phase which may precipitate in the pyroxenite as liquidus garnet and possibly spinel. Near-liquidus crystallization of CPX may be also be enhanced in preference to olivine. Although garnet is not observed at the margins of many non garnetiferous pyroxenite layers, a myrmekitic fine intergrowth of CPX, OPX and pale green spinel does occur. This assemblage represents the low pressure breakdown products of garnet. Such features are also present at the margins of orthopyroxenite and websterite layers. The larger Cr-poor, Fe-rich olive green spinels at layer margins may also be the products of garnet breakdown. Many poikilitically enclose small OPX and CPX crystals at their margin and may have precipitated from the original melt. The irregular forms of some of these spinels which form continuous or near-continuous networks among pyroxene grains may be due to late stage crystallization from a high pressure melt.

This type of wall rock reaction process may explain the two different spinel populations seen in Figure 4.11 in that the high Fe, low Cr aluminous spinel may be the product of garnet breakdown ,whilst the higher Mg-Cr spinel crystallized from the original melt. The ability of garnet breakdown processes to form coarse, irregular spinels is illustrated in Chapter 2 where kelyphitized garnets show coarser, irregular spinel developing at the periphery of the kelyphite rim. Thus, the depleted dunitic to harzburgitic wall rocks to the pyroxenite layers may be explicable in terms of the loss of the low melting component (CPX and an aluminous phase) during intrusion by hotter pyroxenite magma. The depleted peridotite margins formed channels through which the magma could pass. The symmetrical zonation in the pyroxenite layers probably formed by crystal plating on the walls of the conduits as the magma flowed through them. This is analogous to the mode of formation of pyroxenite dikes in spinel lherzolite xenoliths proposed by Irving (1980).

The pyroxenites are envisaged as the products of crystal plating on the walls of conduits which originally represented dikes in the mantle. Post crystallization tectonic rotation and shearing subsequently created their parallel alignment (see Chapter 2). The extent to which wall rock reaction affects the mineral chemistry of the layer margins can be striking and may contribute to some of the petrological diversity

observed in mantle xenoliths from deeply derived volcanics. The small size of many of the xenoliths and the lack of available field relationships allow the possibility that some Cr-rich eclogites may be the margins of eclogite dikes or layers in the mantle that have equilibrated with the surrounding peridotite. The effect of re-equilibration on < 5cm thick layers may be striking. This is illustrated by the very thin GP layer, GP 151, which contains garnets of enhanced pyrope content and diopsidic CPX as a result of a large degree of equilibration with the surrounding peridotite. The garnet-CPX "segregation" from a peridotite xenolith illustrated on plate 30B of Nixon (1973) may represent a highly equilibrated garnet clinopyroxenite/eclogite layer in peridotite.

CHAPTER 5:

MAJOR AND TRACE ELEMENT GEOCHEMISTRY.

5:1 Sampling and analytical techniques

Twenty seven peridotites and forty eight pyroxenite samples were selected for whole rock geochemical analysis. Sample localities are given in Figure 5.1 and listed in Appendix 1. The sample set is biased to the areas indicated on Figure 5.1 due to the restriction of good exposures of less weathered rocks to the bottom of river valleys/wadis. Peridotites were selected on the basis of being the least serpentinized specimens from a particular area. Twenty five spinel peridotites and three garnet peridotites were sampled at varying distances from pyroxenite layers to evaluate the effects of peridotite-pyroxenite interactions (as discussed by Frey et al 1985 and Bodinier et al 1988). Details of whole-rock sample preparation for peridotites and pyroxenites are discussed in Appendix 3. All powders were prepared from specimens weighing at least 1kg, most were over 2kg. This sample size is considered adequate to obtain representative whole-rock compositions from these coarse-grained rocks. The peridotites are sometimes zoned into pyroxene-rich and pyroxene-poor areas (Chapter 2), a feature which occurs in other orogenic peridotite massifs (Obata and Nagahara 1985). Peridotite sampling avoided such areas. The three garnet lherzolite specimens collected show considerable degrees of serpentinization, loss on ignition being > 5 wt %. Unfortunately, no fresher specimens could be obtained as most outcrops were highly friable.

Ten GGP samples were studied, of which four were loose blocks further upstream than the two GGP layer outcrops. It is probable that these blocks were derived from GGP layers that were either undetected by field studies or, more likely, that they represent the remnants of previously existing GGP layers which have been destroyed by erosion. The four "float" samples were analysed to determine the maximum possible compositional range of the GGP. The "float" specimens are GP25, PHN5730, PHN5734 and PHN5740, all of which probably originate from near the centres of the original GGP layers as none display wall-rock reaction features which characterize the margins of pyroxenite layers. The remainder of the pyroxenite suite consists of twenty three GP layers, twelve websterite layers, two orthopyroxenite layers and one clinopyroxenite/websterite vein cross cutting a lherzolite. The vein sample, GP132(1), is only 1cm thick and was cut out of the surrounding lherzolite with a diamond saw. This process undoubtedly incorporates some of the surrounding lherzolite and thus the bulk composition of this sample is a mixture of a small portion (< 5 wt %) of the lherzolite and the vein. All pyroxenite samples were taken from the centre of layers unless suffixed with a letter. Where samples were collected from various positions across the thickness of a pyroxenite layer the letters T, M or B signifies a sample taken from top, middle or bottom of the layer respectively.

The most common pyroxenite lithology is websterite/orthopyroxenite-websterite, however, the sample set is artificially biased towards garnetiferous compositions. This bias is due to several factors. The garnet bearing layers are generally much less altered than the other lithologies and also tend to form some of the thickest layers in a particular section which are less likely to have suffered sub-solidus re-equilibration with the surrounding peridotites. The widespread orthopyroxenite/websterite lithologies are usually highly

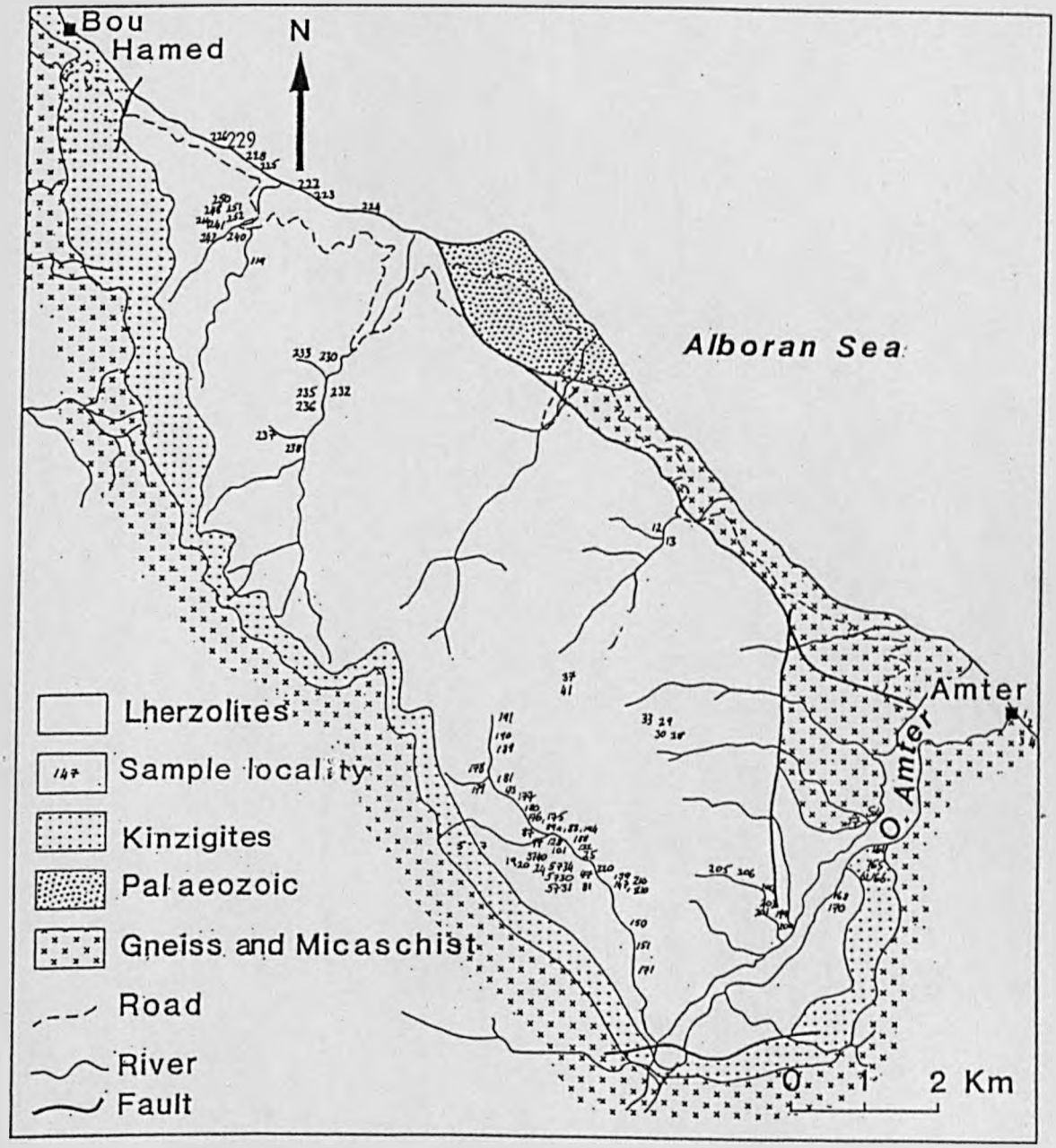

Figure 5.1. Specimen local ity list of samples analysed for whole rock geochemical data.

serpentinized and not suitable for analysis.

Major and trace-element analyses were carried out by X-ray fluorescence, precision being estimated from duplicate analysis of four separate samples of varying chemical composition (see Appendix 4). Rare earth elements (REE) were determined by isotope-dilution analysis following high-pressure bomb dissolution. REE precision was estimated from duplicate analyses of GP147CPX. A detailed discussion of the accuracy and precision of the REE isotope dilution method used and its comparison to other analytical methods is given by Thirwall (1981) and Appendix 4).

5:2 PERIDOTITIES

5:2.1 Analytical data

Throughout the following section the whole rock geochemistry of the Beni Bousera peridotites will be compared to the Ronda peridotites because: A, High quality major and trace element analytical data are available for comparison (Frey et al 1985). B, The Ronda peridotite outcrops within 200 km of Beni Bousera and shows a very similar, steep sided, gravity anomaly. C, The Ronda and Beni Bousera peridotites were emplaced into the continental crust simultaneously and D, The peridotites and pyroxenites are mineralogically and petrographically similar. Major and trace element abundances for both garnet and spinel peridotites are presented in increasing sample number in Table 5.1 which also includes the approximate distance of the peridotite from the nearest pyroxenite layer and the relative abundance of pyroxenites in the immediate vicinity (denoted by H=high ,L=low).

In order to compare major element analyses of the peridotites in Table 5.1 the data were normalized to 100 % after subtracting loss on ignition and converting all measured Fe_2O_3 to FeO. This procedure is based on the assumption that serpentinization is an isochemical process, with only water being added to the system. This assumption has been shown to be a reasonably sound one for serpentinized ophiolites (Coleman 1977) and other orogenic peridotites (Green 1964). The normalized data provide a much better comparison between peridotites containing varying amounts of serpentine as reflected by variable loss on ignition values (Table 5.1) and show a much narrower range of compositions than the hydrated analyses (see Table 5.2). All elemental ratios were subsequently calculated from these normalized values. REE data are presented in Table 5.3.

5:2.2 Major element trends.

The lithological variation from harzburgite to lherzolite (Chapter 2) is evident from the peridotite major element compositions (Table 5.2). MgO contents vary from ~ 47 % to 39.6 wt % for spinel facies peridotites and 36.5 to 39.7 wt % MgO for garnet lherzolites. No spinel facies peridotites were found to be as fertile ,in terms of major elements, as estimates of "primitive" undepleted upper mantle or PUM (Palme and Nickel 1985, Hart and Zindler 1986). The most fertile Beni Bousera spinel peridotite (GP230) is more depleted in basaltic constituents than the most fertile lherzolite from the Ronda massif (Frey et al 1985), Table 5.4 , suggesting that all the samples analysed from Beni Bousera may represent residues after partial melting. A positive correlation is observed between increasing MgO contents and increasing modal olivine and normative olivine content. The MgO contents of olivines also increase with increasing bulk

TABLE 5.1

SAMPLE	GP175	GP178	GP189	GP191	GP220	GP222
LITHOLOGY	SP.LHRZ	SP.HARZ	SP.LHRZ	SP.LHRZ	SP.LHRZ	SP.LHRZ
SiO2	43.64	41.53	44.03	42.25	41.2	42.66
TiO2	0.1	0.05	0.04	0.11	0.02	0.11
Al2O3	2.87	0.88	2.03	2.96	1.51	2.75
Fe Total	8.69	8.77	8.68	8.82	7.93	8.5
MnO	0.14	0.13	0.14	0.14	0.13	0.14
MgO	40.57	45.61	43.38	39.36	41.93	39.12
CaO	2.4	0.81	1.87	2.68	1.35	2.31
Na2O	0.25	0.15	0.1	0.3	0.54	0.29
K2O	0	0	0	0	0.01	0
P2O5	0.02	0.02	0.02	0.01	0.01	0
L.O.I.	2.11	2.71	0.27	2.38	4.78	4.36
Cr	2532	2172	2806	2445	2684	2524
Co	107	129	115	108	112	105
Ni	2183	2517	2353	2190	2363	2133
Cu	9	0	5	14	1	7
Zn	45	44	47	48	43	46
Rb	0	0	0	0	0	0
Sr	4	2	0	7	1	7
Y	0	0	0	1	0	0
Ba	2	0	0	2	0	1
V	53	31	47	56		54
Sc	16	7	11	13		12

GP224 SP.LHRZ	GP229 SP.LHRZ	GP230 SP.LHRZ	GP233 SP.LHRZ	GP238 SP.LHRZ
40.13	40.69	41.99	43.8	43.51
0.13	0.08	0.15	0.15	0.14
1.61	1.67	3.59	3.7	3.32
7.92	8.46	8.49	9.14	9.33
0.13	0.13	0.14	0.15	0.15
38.55	39.85	37048	39.62	40.32
1.29	1.14	2.98	2.98	2.46
0.16	0.11	0.55	0.3	0.31
0	0.02	0	0	0
0.02	0.02	0.02	0.02	0.02
9.45	7.95	5.32	0.7	0.69
2386	2600	2543	2599	2466
109	120	104	105	112
2202	2240	2036	2147	2193
1	0	20	41	11
46	53	51	52	53
0	0	0	0	0
13	4	10	11	11
2	1	3	1	2
0	5	2	2	0
42	37	70	67	61
9	10	17	15	14

TABLE 5.1

SAMPLE	GP240	PHN5733	GP24	GP248	GP250
LITHOLOGY	SP.LHRZ	SP.LHRZ	GTLHZ	GTLHZ	GTLHZ
SiO2	43.24	42.32	42.58	42.94	43.44
TiO2	0.11	0.05	0.15	0.08	0.19
Al2O3	3.03	2.26	3.4	2.52	4.02
Fe Total	8.61	8.67	8.79	8.79	9.24
MnO	0.14	0.14	0.14	0.14	0.15
MgO	39.38	43.41	36.64	36.89	34.26
CaO	2.52	1.83	2.95	1.99	3.15
Na2O	0.49	0.51	0.32	0.43	0.36
K2O	0	0	0	0	0
P2O5	0.02	0.01	0	0	0
L.O.I.	1.57	1.36	5.65	6.14	5.23
Cr	2646	2549	2528	2760	25.17
Co	106		113	114	109
Ni	2207		2083	2371	2046
Cu	14		16	11	23
Zn	49		50	47	52
Rb	0		0	0	0
Sr	4		11	6	13
Y	1		4	1	1
Ba	3		2	2	2
V	57		69	54	74
Sc	13		16	10	16

Table 5.1. Major and trace element data for Beni Bousera peridotites. Total Fe as Fe^{3+}.

SAMPLE	GP12	GP13	GP41	GP88	GP89a	GP89b	GP89c	GP91	GP119	GP132(2)	GP132(3)
LITHOLOGY	SP.LHRZ	SP.LHRZ	SP.LHRZ	SP.LHRZ	SP.LHRZ	SP.LHRZ	SP.LHRZ	SP.LHRZ	SP.LHRZ	SP.LHRZ	SP.LHRZ
SiO2	42.07	41.58	43.01	42.58	43.01	43.28	42.93	40.9	42.26	40.63	41.19
TiO2	0.14	0.13	0.13	0.1	0.15	0.17	0.15	0.02	0.12	0.04	0.03
Al2O3	3.21	3.19	3.32	2.62	2.55	3	2.52	0.67	3.08	1.93	1.23
Fe Total	8.63	8.43	9.27	10.61	9.77	9.29	9.43	8.56	8.67	8.26	8.66
MnO	0.14	0.14	0.15	0.14	0.14	0.14	0.14	0.13	0.14	0.13	0.13
MgO	37.82	36.84	38.44	38.47	39.64	39.21	39.67	43.18	38.5	40.55	44017
CaO	2.63	2.79	2.64	2.43	2.23	2.47	2.03	0.52	2.54	1.57	0.79
Na2O	0.23	0.28	0.18	0.19	0.17	0.18	0.29	0	0.17	0.16	0.45
K2O	0	0	0	0	0	0	0	0	0	0	0.01
P2O5	0.04	0.04	0.04	0.14	0.04	0.04	0.04	0.03	0.04	0.01	0.01
L.O.I.	5.43	7.13	2.54	2.43	1.69	2.29	2.29	5.34	4.35	6.57	4.24
Cr	2572	2569	2680	3071	2889	2822	2825	2997	2641	3076	2117
Co	113	106	111	120	117	110	110	124	109	114	119
Ni	2046	2008	2206	2154	2139	2086	2211	2512	2073	2291	2422
Cu	14	13	16	56	22	11	31	12	12	9	1
Zn	52	46	53	77	67	65	82	51	49	46	44
Rb	0	0	0	0	0	0	0	0	0	0	0
Sr	7	10	11	10	5	14	5	2	5	3	3
Y	2	4	4	1	1	1	2	0	1	0	0
Ba	3	1	0	2	6	4	0	2	0	0	0
V	50	60	63	53	58	58	51	21	58	29	29
Sc	10	15	13	13	10	14	11	8	15	10	10

Table 5.2. Beni Bousera peridotites, recalculated anhydrous major elements. All Fe as FeO. Mole FeO and MgO also tabulated.

SAMPLE	GP12	GP13	GP41	GP88	GP89a	GP89b
LITHOLOGY	SP.LHRZ	SP.LHRZ	SP.LHRZ	SP.LHRZ	SP.LHRZ	SP.LHRZ
SiO2	44.73	44.91	44.69	44.25	44.47	44.69
TiO2	0.15	0.14	0.14	0.10	0.16	0.18
Al2O3	3.41	3.45	3.45	2.72	2.64	3.10
FeO	8.26	8.19	8.67	9.92	9.09	8.63
MnO	0.15	0.15	0.16	0.15	0.14	0.14
MgO	40.21	39.79	39.94	39.98	40.98	40.49
CaO	2.80	3.01	2.74	2.53	2.31	2.55
Na2O	0.24	0.30	0.19	0.20	0.18	0.19
P2O5	0.04	0.04	0.04	0.15	0.04	0.04
Fe mol%	5.90	5.86	6.20	7.10	6.46	6.16
Mg mol%	51.19	50.74	50.93	50.97	51.94	51.46

SAMPLE	GP89c	GP91	GP119	GP132(2)	GP132(3)	GP175
LITHOLOGY	SP.LHRZ	SP.LHRZ	SP.LHRZ	SP.LHRZ	SP.LHRZ	SP.LHRZ
SiO2	44.60	43.91	44.65	43.95	42.99	44.62
TiO2	0.16	0.02	0.13	0.04	0.03	0.10
Al2O3	2.62	0.72	3.25	2.09	1.28	2.93
FeO	8.82	8.27	8.24	8.04	8.13	7.99
MnO	0.15	0.14	0.15	0.14	0.14	0.14
MgO	41.21	46.35	40.68	43.86	46.11	41.48
CaO	2.11	0.56	2.68	1.70	0.82	2.45
Na2O	0.30	0.00	0.18	0.17	0.47	0.26
P2O5	0.04	0.03	0.04	0.01	0.01	0.02
Fe mol%	6.26	5.71	5.87	5.63	5.63	5.67
Mg mol%	52.16	57.06	51.65	54.74	56.91	52.42

SAMPLE	GP178	GP189	GP191	GP220	GP222	GP224
LITHOLOGY	SP.HARZ	SP.LHRZ	SP.LHRZ	SP.LHRZ	SP.LHRZ	SP.LHRZ
SiO2	42.78	44.29	44.13	43.91	44.89	45.02
TiO2	0.05	0.04	0.11	0.02	0.12	0.15
Al2O3	0.91	2.04	3.09	1.61	2.89	1.81
FeO	8.13	7.86	8.29	7.60	8.05	7.99
MnO	0.13	0.14	0.15	0.14	0.15	0.15
MgO	46.99	43.63	41.11	44.68	41.17	43.24
CaO	0.83	1.88	2.80	1.44	2.43	1.45
Na2O	0.15	0.10	0.31	0.58	0.31	0.18
P2O5	0.02	0.02	0.01	0.01	0.00	0.02
Fe mol%	5.60	5.50	5.89	5.30	5.71	5.61
Mg mol%	57.71	54.48	52.07	55.47	52.08	54.08

ANHYDROUS PERIDOTITE DATA

SAMPLE	GP229	GP230	GP233	GP238	GP240	PHN5733
LITHOLOGY	SP.LHRZ	SP.LHRZ	SP.LHRZ	SP.LHRZ	SP.LHRZ	SP.LHRZ
SiO2	44.56	44.42	44.27	44.12	44.73	43.04
TiO2	0.09	0.16	0.15	0.14	0.11	0.05
Al2O3	1.83	3.80	3.74	3.37	3.13	2.30
FeO	8.34	8.08	8.31	8.51	8.01	7.93
MnO	0.14	0.15	0.15	0.15	0.14	0.14
MgO	43.64	39.64	40.04	40.88	40.73	44.15
CaO	1.25	3.15	3.01	2.49	2.61	1.86
Na2O	0.12	0.58	0.30	0.31	0.51	0.52
P2O5	0.02	0.02	0.02	0.02	0.02	0.01
Fe mol%	5.84	5.79	5.95	6.07	5.70	5.55
Mg mol%	54.52	50.63	51.06	51.91	51.67	55.07

SAMPLE	GP24	GP248	GP250
LITHOLOGY	GT.LHRZ	GT.LHRZ	GT.LHRZ
SiO2	45.25	46.21	46.25
TiO2	0.16	0.09	0.20
Al2O3	3.61	2.71	4.02
FeO	8.41	8.51	8.85
MnO	0.15	0.15	0.16
MgO	38.94	39.70	36.48
CaO	3.13	2.14	3.35
Na2O	0.34	0.46	0.38
P2O5	0.01	0.01	0.00
Fe mol%	6.04	6.08	6.46
Mg mol%	49.87	50.56	47.43

Table 5.3. Anhydrous major and trace element data for Beni Bousera pyroxenites. All Fe as FeO.

SAMPLES	GP19	GP20	GP25	GP28	GP30	GP33a	GP33b	GP37	GP47	GP61	GP81	GP87T	GP87M	GP87B
LITHOLOGY	GP	GP	GGP	WEB	WEB	WEB	WEB	GP	GGP	GRAN	GGP	GP	GP	GP
THICKNESS		170	FLOAT	30	30	70	70	50	FLOAT	150	2.5		18	
SiO2	48.76	47.86	46.68	46.32	46.54	49.38	45.82	45.45	48.02	45.85	46.91	46.38	46.34	46.45
TiO2	0.83	0.75	0.79	0.43	0.58	0.73	0.55	0.65	0.84	1.00	0.59	0.57	0.67	0.61
Al2O3	11.26	11.84	13.66	15.73	9.77	10.98	16.38	13.12	12.68	16.26	13.59	14.81	13.66	13.41
Fe Total	11.19	11.17	13.88	5.91	8.33	7.46	8.39	11.82	11.33	9.28	13.81	8.13	9.11	8.40
MnO	0.27	0.27	0.33	0.21	0.16	0.17	0.20	0.22	0.32	0.18	0.30	0.19	0.19	0.18
MgO	14.86	15.55	11.37	20.30	22.97	18.39	15.74	13.30	14.51	7.60	11.07	17.41	14.80	16.98
CaO	11.37	11.98	11.87	10.13	10.53	11.52	11.80	13.86	10.26	18.02	12.13	11.81	14.33	13.03
Na2O	1.38	1.11	1.37	0.92	1.09	1.32	1.07	1.52	1.98	1.70	1.50	0.67	0.86	0.92
K2O	0.04	0.04	0.01	0.03	0.01	0.01	0.00	0.02	0.02	0.02	0.07	0.00	0.00	0.01
P2O5	0.05	0.04	0.04	0.03	0.03	0.04	0.05	0.04	0.04	0.08	0.04	0.04	0.04	0.02
Mg No.	50.74	51.93	38.85	72.71	68.15	65.67	59.27	46.60	49.84	38.84	38.33	62.44	55.76	61.06
Cr	1000	728	458	1978	1942	2134	2130	929	850	460	305	1587	1499	1906
Co	63	63	53	45	67	51	55	66	48	42	59	51	53	51
Ni	522	365	50	686	1012	778	597	364	139	121	79	487	351	402
Cu	57	58	19	103	43	93	105	6	20	71	42	29	21	41
Zn	88	98	94	19	63	47	37	66	77	78	78	52	42	34
Rb	0	1	0	0	0	0	0	0	0	5	1	0	0	0
Sr	4	23	2	44	53	49	45	17	7	109	41	53	38	86
Y	23	23	46	25	15	17	24	18	30	24	45	17	16	9
Ba	27	58	5	7	6	25	3	35	15	5	46	0	7	14
V	233	250	580	236	164	264	233	364	354	256	658	287	253	247
Sc	46	56	76	81	35	63	59	62	57	55	80	115	59	63
Zr	21	9	-	37	20	30	40	8	-	42		33	17	15

PYROXENITE WHOLE ROCKS

SAMPLE	GP97	GP101a	GP125	GP130	GP132(1)	GP137	GP138	GP139
LITHOLOGY	WEB	WEB	WEB	WEB	WEB	OPXITE	GP	GP
THICKNESS	50	10	16	10	0.5	20		250
SiO2	45.95	51.93	46.71	54.09	46.38	53.28	48.30	47.80
TiO2	0.17	0.10	0.18	0.05	0.11	0.44	1.34	0.85
Al2O3	16.68	7.24	15.88	5.87	6.08	4.07	12.42	12.70
Fe Total	6.26	4.22	6.22	6.19	6.10	7.54	10.97	12.46
MnO	0.13	0.12	0.14	0.13	0.14	0.18	0.28	0.28
MgO	14.43	20.75	15.73	31.36	34.44	32.43	14.35	12.67
CaO	13.89	13.73	13.73	2.10	6.19	1.75	10.20	11.38
Na2O	2.57	2.25	1.39	0.21	0.54	0.31	2.07	1.82
K2O	0.02	0.03	0.00	0.00	0.02	0.00	0.01	0.01
P2O5	0.03	0.03	0.02	0.00	0.02	0.00	0.07	0.05
Mg No.	64.12	79.23	66.25	79.72	81.40	76.93	50.36	44.10
Cr	943	3832	923	3562	9775	3568	903	769
Co	51	39	48	79	78		55	58
Ni	349	963	399	1368	1799		188	156
Cu	102	58	145	64	73		32	43
Zn	30	43	30	63	62		79	95
Rb	0	0	0	0	0		0	0
Sr	16	12	77	1	27		40	1
Y	6	3	4	2	2		49	35
Ba	12	7	10	2	0		0	7
V	108	187	124	123	124		352	504
Sc	47	38	44	19	35		57	69
Zr	0	4	0	1	2		89	15

GP140 GP	GP143 GP	GP147 GGP 260	GP148a GGP	GP148b GGP	GP170 WEB FLOAT
48.87	47.63	47.48	48.99	48.52	52.40
0.71	0.83	0.79	0.81	0.88	0.25
12.38	13.04	13.38	12.36	11.88	5.29
10.34	11.87	12.23	11.25	11.04	8.54
0.30	0.38	0.39	0.34	0.35	0.19
15.40	14.97	15.11	14.64	16.80	24.34
10.01	9.54	9.42	9.67	8.88	8.16
1.96	1.70	1.15	1.89	1.60	0.81
0.01	0.01	0.00	0.00	0.02	0.02
0.03	0.03	0.05	0.05	0.04	0.00
53.60	49.44	48.93	50.25	54.15	68.86
819	827	861	946	1017	3234
52	50	53	57	56	66
176	128	138	192	149	715
35	27	24	33	21	12
67	81	80	79	83	59
0		0			0
12		3			11
24	27	30		25	6
9	3	0		11	17
397	379	377		345	404
55	57	58		48	45
23		-			3

PYROXENITE WHOLE ROCKS

SAMPLE	GP183	GP188	GP194M	GP196	GP200	GP204	GP207	GP231
LITHOLOGY	GP	WEB	GP	GP	GP	GP	GP	GP
THICKNESS	25	15	14	10	20	50	30	20
SiO2	47.07	54.44	48.81	47.55	45.62	48.29	46.06	47.41
TiO2	0.48	0.06	0.60	0.83	0.39	0.66	0.34	0.45
Al2O3	13.66	5.68	11.28	10.97	16.21	11.91	15.00	13.74
Fe Total	8.20	6.27	6.90	8.10	9.50	10.80	12.29	10.76
MnO	0.17	0.13	0.17	0.02	0.19	0.19	0.29	0.22
MgO	19.70	31.28	17.73	19.11	12.06	16.55	14.02	15.31
CaO	9.40	1.91	14.03	12.45	14.79	10.39	10.48	10.88
Na2O	1.27	0.21	1.18	0.93	1.22	1.21	1.48	1.22
K2O	0.01	0.00	0.19	0.01	0.00	0.00	0.01	0.00
P2O5	0.04	0.02	0.02	0.03	0.02	0.00	0.03	0.03
Mg No.	65.07	79.47	66.59	64.66	49.60	54.30	46.93	52.47
Cr	1767	3493	3568	2451	645	1234	580	1026
Co	61	78		49	56	66	65	65
Ni	713	1289		543	219	567	194	478
Cu	69	49		12	82	70	37	88
Zn	47	66		32	53	80	53	65
Rb	3			1	0	2	1	2
Sr	65			51	43	38	13	20
Y	16	0		18	13	10	28	14
Ba	4	0		0	14	12	7	0
V		121		242	256	277	380	234
Sc		18		59	58	46	74	53
Zr	27	0		27	5	22	9	16

GP232
WEB
20
48.45
0.50
12.71
6.76
0.18
20.11
10.08
1.17
0.01
0.03
69.78

1470
48
581
39
32
0
40
11
4
188
49
24

PYROXENITE WHOLE ROCKS

SAMPLE	GP234	GP236M	GP237	GP241	GP244	GP251M	GP252	PHN5732	PHN5734	PHN5739
LITHOLOGY	GP	WEB	GP	GP	GP	GP	GP	CPXITE	GGP	GP
THICKNESS	FLOAT	40	30	20	10	40	75	FLOAT	FLOAT	FLOAT
SiO2	48.25	47.57	43.50	46.61	47.30	47.62	46.56	52.52	47.28	47.40
TiO2	0.65	0.34	0.80	0.52	0.43	0.63	0.14	2.03	0.74	0.32
Al2O3	12.84	13.07	15.34	13.77	14.11	13.17	16.60	7.30	12.82	14.14
Fe Total	9.67	8.63	13.01	8.26	6.87	10.64	6.15	5.81	12.61	8.96
MnO	0.20	0.21	0.29	0.17	0.19	0.24	0.14	0.24	0.39	0.17
MgO	18.07	17.47	10.96	19.01	18.90	15.50	13.50	15.89	13.71	15.71
CaO	8.95	11.24	14.60	10.60	11.15	10.60	15.55	13.83	11.17	12.10
Na2O	1.35	1.43	1.47	1.03	1.05	1.57	1.34	2.45	1.26	1.12
K2O	0.00	0.03	0.01	0.00	0.00	0.01	0.00	0.00	0.00	0.04
P2O5	0.02	0.02	0.03	0.03	0.00	0.02	0.02	0.05	0.03	0.04
Mg No.	59.18	61.09	39.52	64.09	68.10	53.04	63.02	67.95	45.75	57.62
Cr	1083	1111	321	1199	2262	823	958			
Co	59	59	55	62	49	63	43			
Ni	527	478	143	605	474	472	245			
Cu	40	49	6	70	51	47	41			
Zn	44	36	56	40	26	56	33			
Rb	0	0	1	1	3	0	2			
Sr	40	24	15	112	49	43	32			
Y	11	17	32	10	13	32	2			
Ba	4	8	0	0	0	0	0			
V	216	283	355	190	355	320	-			
Sc	42	65	69	49	69	55	-			
Zr	28	14	17	22	14	35	1			

SAMPLE	P.U.M. 1	P.U.M. 2	PYROLITE	GP230	R717
SiO2	46.2	46	45.1	44.4	44.97
TiO2	0.23		0.2	0.16	0.17
Al2O3	4.75	4.06	4.6	3.79	3.91
FeO	7.7		7.9	8.08	8.38
MnO	0.13		0.1	0.15	0.13
MgO	35.5	37.8	38.1	39.65	37.97
CaO	4.36	3.27	3.1	3.15	3.51
Na2O	0.4		0.4	0.58	0.31
K2O			0.02	0.01	0.01
Mg. No.	82		83	83	82
Ca/Al	1.24	1.09	0.91	1.12	1.21

Table 5.4. Major element composition of GP230 (the most fertile Beni Bousera peridotite) and Ronda peridotite R717 compared with pyrolite (from Jaques and Green 1980) and estimates of primitive upper mantle (PUM). PUM1 is from Palme and Nickel (1985), PUM2 is from Hart and Zindler (1986). All data anhydrous and Fe = FeO.

Table 5.5. Isotopic dilution REE analyses of Beni Bousera whole rock peridotites and CPX from peridotites.

SAMPLE LITHOLOGY	GP12 SPLHRZ	GP13 SPLHRZ	GP41 SPLHRZ	GP88 SPLHRZ	GP89a SPLHRZ	GP89c SPLHRZ	GP119 SPLHRZ	GP178 SPHARZ	PHN5733 SPLHRZ	GP24 GTLHZ
La		0.198	0.158	0.100	0.933	0.080	0.157	0.092	0.094	0.165
Ce	0.302	0.591	0.583	0.397	1.380	0.292		0.125	0.268	0.406
Nd	0.669	0.632	0.711	0.468	0.588	0.371	0.585	0.097	0.278	0.697
Sm	0.260	0.246	0.290	1.610	0.185	0.169	0.234	0.043	0.103	0.279
Eu	0.108	0.094	0.122	0.063	0.069	0.066	0.097	0.020	0.043	0.088
Gd	0.450	0.350	0.447	0.225	0.240	0.237	0.380		0.178	0.434
Dy		0.533		0.299	0.273	0.285			0.287	0.574
Er		0.341	0.382	0.195	0.181	0.189		0.038	0.195	0.361
Yb	0.337	0.345	0.392	0.205	0.193	0.205	0.326	0.030	0.209	0.363
Lu		0.054		0.033	0.030	0.033			0.033	0.056
(Ce/Yb)n	0.228	0.433	0.378	0.495	1.840	0.362		1.077	0.326	0.285
Sm/Nd	0.388	0.389	0.408	0.408	0.315	0.456	0.400	0.443	0.370	0.400

PERIDOTITE CPX REE

SAMPLE	GP13 CPX	GP24 CPX	GP88 CPX	GP89a CPX	GP119 CPX	GP132(3) CPX	GP189 CPX	GP191 CPX	GP220 CPX	GP222 CPX
La	1.026	1.255	0.899	0.779	1.14	1.87	1.041	0.646	1.338	0.49
Ce	3.523	4.698	3.031	2.941	4.06	4.007	2.26	2.544	4.101	1.381
Nd	4.343	5.109	4.73	3.924	4.727	2.023	1.87	3.462	3.043	3.438
Sm	1.703	1.721	1.692	1.709	1.877	0.739	0.655	1.46	0.887	1.617
Eu	0.712	0.613	0.677	0.678	0.823	0.385	0.267	0.629	0.195	0.7
Gd	2.625		2.26	2.1	2.793		1.161	2.4		2.564
Dy	2.92		2.547	2.461	3.509		1.971			
Er	2.051		1.528	1.546	2.189		1.299	1.837		2.039
Yb	1.814	0.147	1.42	1.396	2.064	1.057	1.246	1.879	0.605	1.853
Lu	0.247		0.212		0.321		0.19			0.274
Sm/Nd	0.392	0.337	0.358	0.436	0.397	0.365	0.35	0.422	0.292	0.471

rock MgO. Small amounts (up to 1.5 %) of magnetite also appear in the C.I.P.W norms of the peridotites which results from the assumption of Fe_2O_3 /FeO = 0.1 for the calculation. Higher Fe_2O_3 ratios would result in more normative magnetite and the possibility of artificially high Hy in the norm due to relative SiO_2 excess as less MgO + FeO is available for mafic silicates (Cox,Bell and Pankhurst 1979).

Major element compositions exhibit several systematic trends when plotted on element-element plots. MgO contents decrease as CaO, Al_2O_3 and TiO_2 increase (Figure 5.2). This trend is also mirrored by decreasing Mg No. (100Mg/Mg +Fe^{2+}) of the peridotites. Na_2O does not show the expected negative correlation with MgO, with several of the more magnesian peridotites possessing anomalously high Na_2O contents. These high Na_2O samples also have anomalous, high, FeO at given MgO contents with a very poor negative correlation between FeO and MgO. These anomalously enriched samples will be discussed in Section 5:2.3.

Several trace elements (Table 5.1) reveal strong correlations with major element abundances, especially MgO (Figure 5.2). Ni in particular shows a strong positive correlation with MgO (Fig 5.3) whilst the incompatible trace elements Sr, Sc, V + Cu show inverse correlations with MgO. Cr is weakly correlated with bulk rock MgO.

The Beni Bousera peridotites have low light REE (LREE) abundances relative to chondrites (Fig 5.4 Table 5.3), most being LREE depleted with Ce ranging from 0.15 to 0.7 X chondritic abundances. Heavy REE (HREE) abundances range from 0.13 to 1.7 X chondrites. Of the samples enriched in FeO and Na_2O only GP89a is anomalously LREE enriched. The spinel harzburgite GP178 with the highest MgO content has the lowest total REE content but is not the most depleted in terms of $(Ce/Yb)_n$.

5:2.3 Implications of the bulk-rock geochemical data.

5:2.3a Major elements

Many of the peridotites analysed were found to contain significant amounts of serpentine minerals. Table 5.1 shows that 11 of the 27 peridotites yield over 3wt.% L.O.I. which is mostly represented by H_2O^+ which is equivalent to the samples containing over 10% serpentine (Frey et al 1985). These fairly heavily serpentinized samples span the entire compositional range of the spinel and garnet peridotites and their major element compositional trends are consistent with those shown by samples containing much lower amounts of serpentine. Na and Ca are the most likely major elements to be affected by serpentinization. The consistent behavior of both Na and Ca in both serpentine rich and poor samples suggests serpentinization had no significant effect on their abundances. These data support the assumption made when normalizing major elements to anhydrous values that serpentinization is approximately isochemical except for the addition of water. Frey et al (1985) also found that serpentinization did not significantly affect major element correlations in peridotites from the Ronda massif. There does not seem to be any correlation between degree of serpentinization and degree of depletion (in terms of major elements). A plot of Ca/Mg (degree of residual character) vs loss on ignition (Fig 5.5) indicates no correlation with the degree of alteration.

Figure 5.2. Major element vs MgO (wt %) variation in Beni Bousera peridotites. Values are anhydrous wt % data from Table 5.2. a = SiO_2 vs MgO. b = Al_2O_3 vs MgO, c = CaO vs MgO, d = FeO vs MgO, e = Na_2O vs MgO, f= TiO_2 vs MgO.

Figure 5.3. Trace element versus MgO variation in Beni Bousera peridotites anhydrous data, MgO is wt %, other elements ppm. a = Ni, b = Cr, c = Co, d = Sc, e = V, f = Cu.

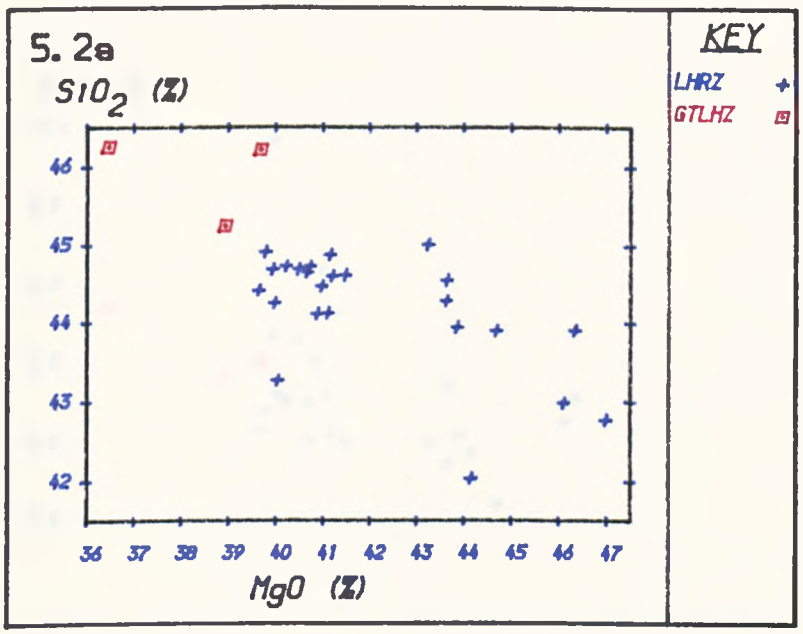
5. 2a
SiO2 (%)
46
45
44
43
42
36 37 38 39 40 41 42 43 44 45 46 47
MgO (%)
KEY
LHRZ
GTLHZ

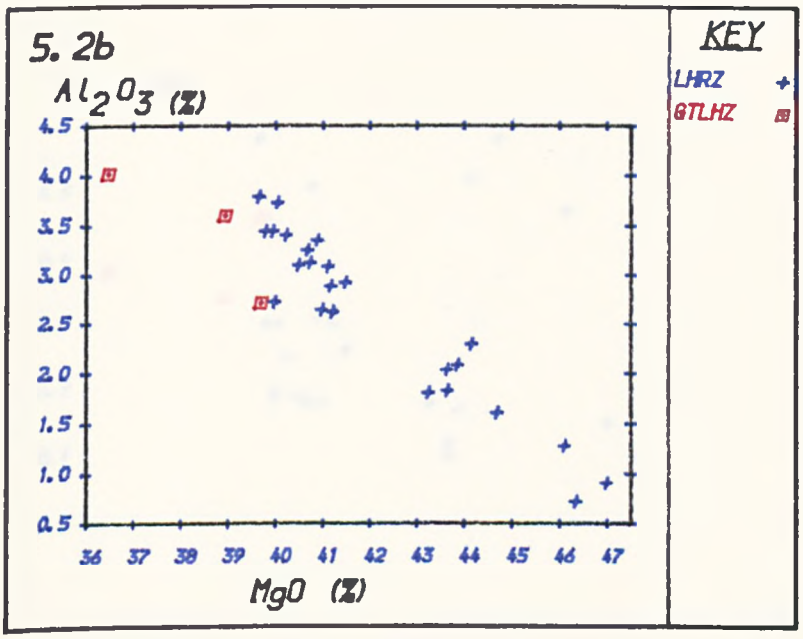
5. 2b
Al2O3 (%)
4.5
4.0
3.5
3.0
2.5
2.0
1.5
1.0
0.5
36 37 38 39 40 41 42 43 44 45 46 47
MgO (%)
KEY
LHRZ
GTLHZ

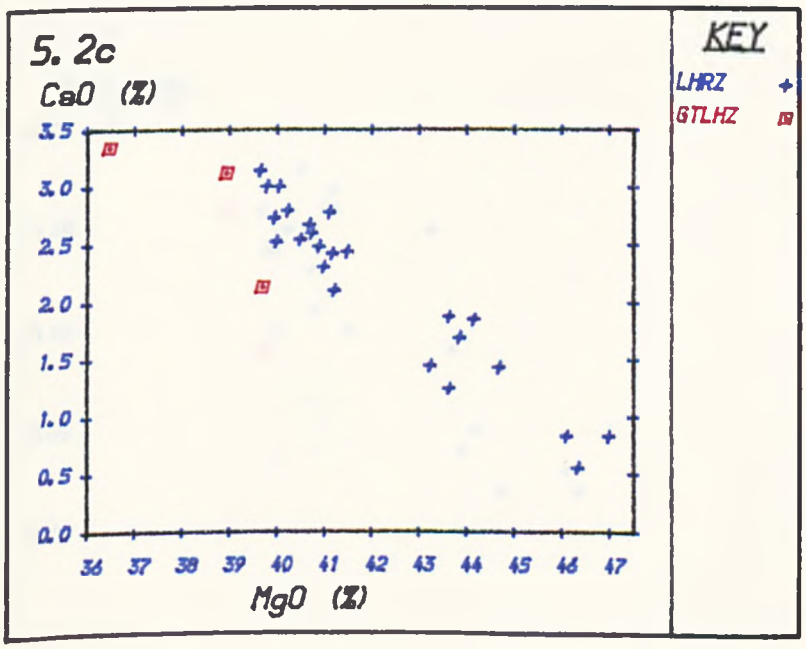
5. 2c
CaO (%)
3.5
3.0
2.5
2.0
1.5
1.0
0.5
0.0
36 37 38 39 40 41 42 43 44 45 46 47
MgO (%)
KEY
LHRZ
GTLHZ

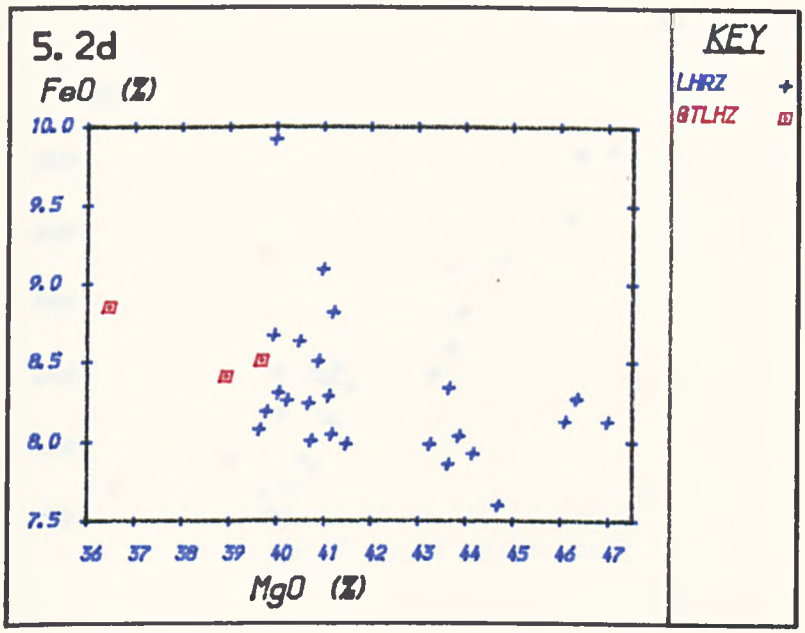
5. 2d
FeO (%)
10.0
9.5
9.0
8.5
8.0
7.5
36 37 38 39 40 41 42 43 44 45 46 47
MgO (%)
KEY
LHRZ
GTLHZ

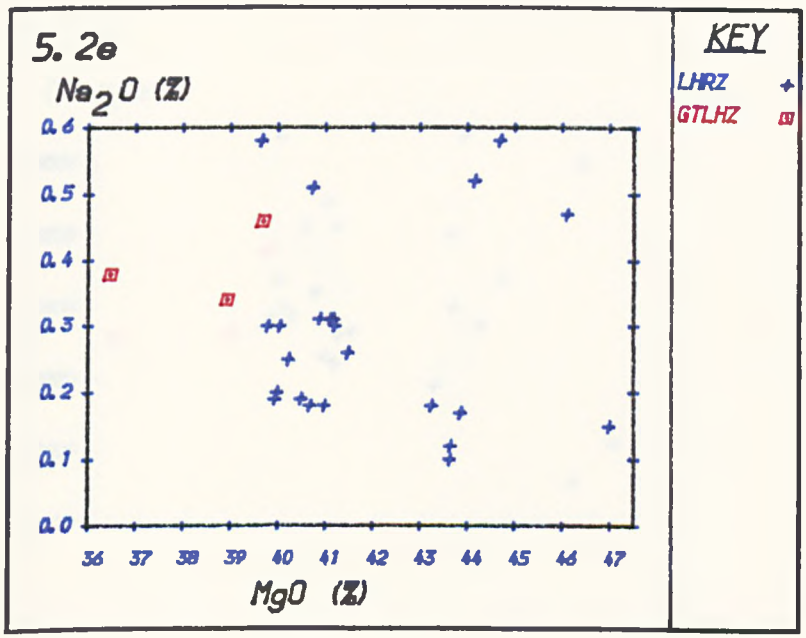
5. 2e
Na2O (%)
0.6
0.5
0.4
0.3
0.2
0.1
0.0
36 37 38 39 40 41 42 43 44 45 46 47
MgO (%)
KEY
LHRZ
GTLHZ

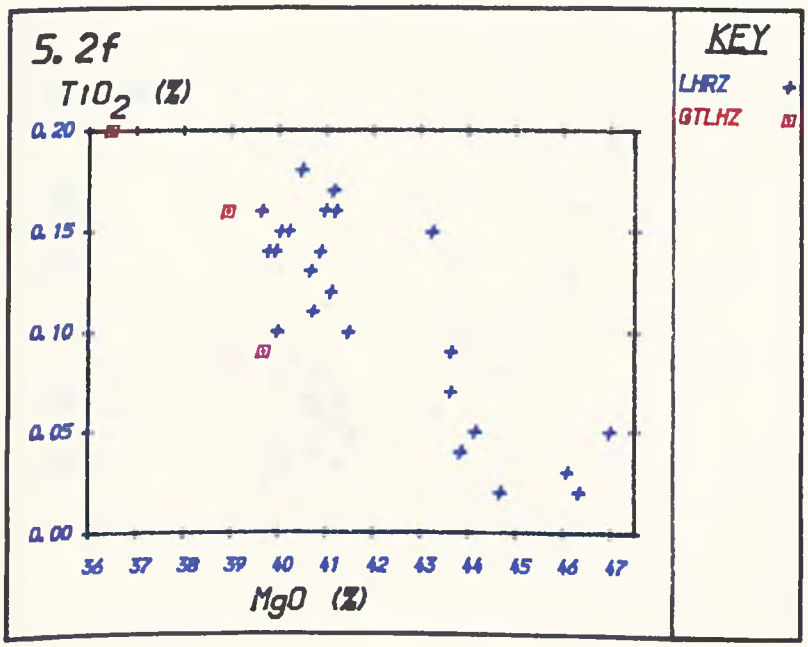
5. 2f
TiO2 (%)
0.20
0.15
0.10
0.05
0.00
36 37 38 39 40 41 42 43 44 45 46 47
MgO (%)
KEY
LHRZ
GTLHZ

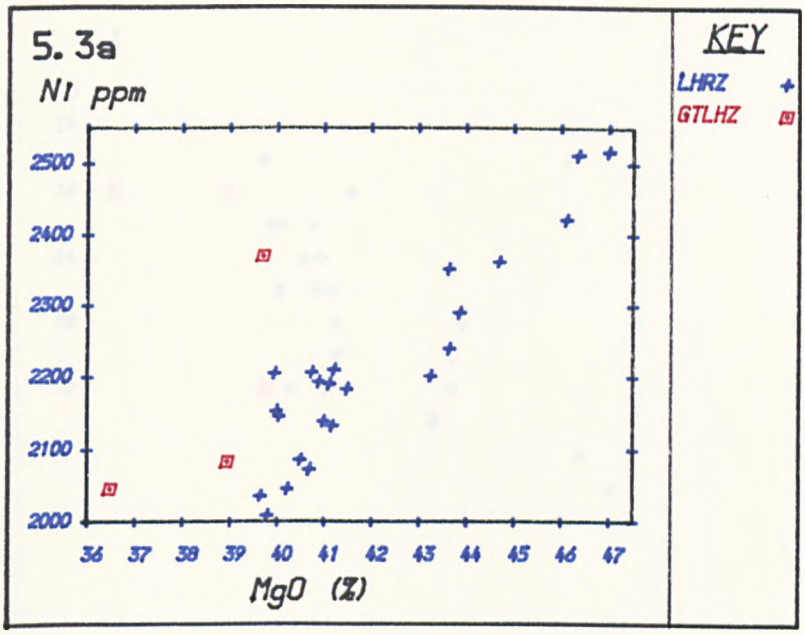
5. 3a
Ni ppm
2500
2400
2300
2200
2100
2000
36 37 38 39 40 41 42 43 44 45 46 47
MgO (%)
KEY
LHRZ
GTLHZ

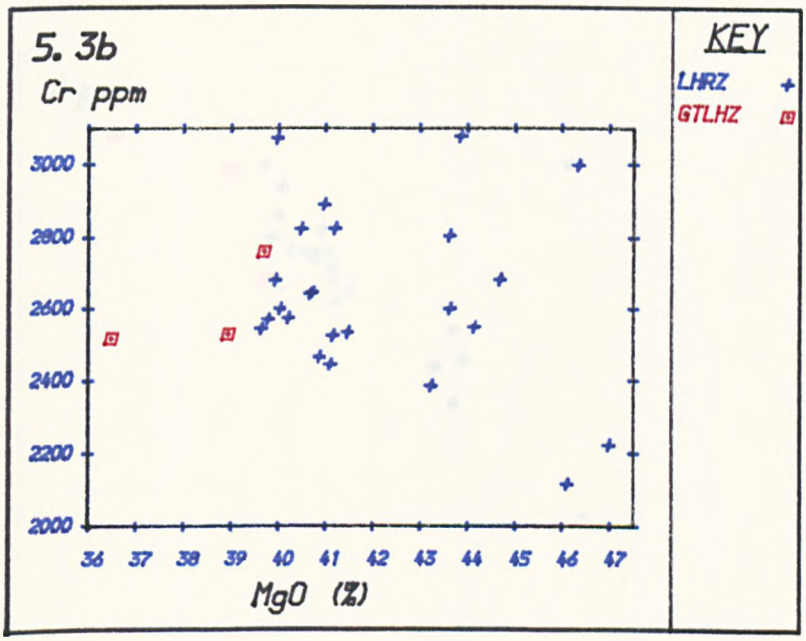
5. 3b
Cr ppm
3000
2800
2600
2400
2200
2000
36 37 38 39 40 41 42 43 44 45 46 47
MgO (%)
KEY
LHRZ
GTLHZ

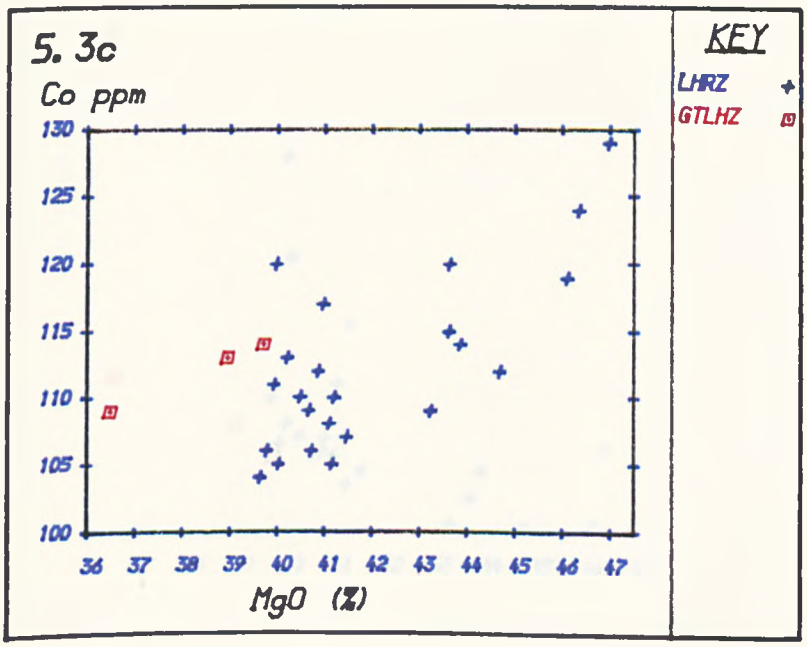
5. 3c
Co ppm
130
125
120
115
110
105
100
36 37 38 39 40 41 42 43 44 45 46 47
MgO (%)
KEY
LHRZ
GTLHZ

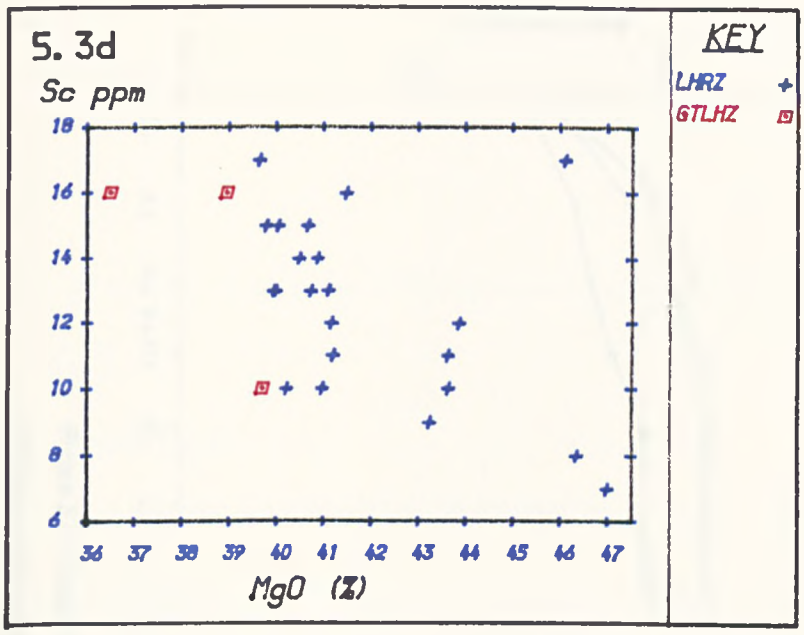
5. 3d
Sc ppm
18
16
14
12
10
8
6
36 37 38 39 40 41 42 43 44 45 46 47
MgO (%)
KEY
LHRZ
GTLHZ

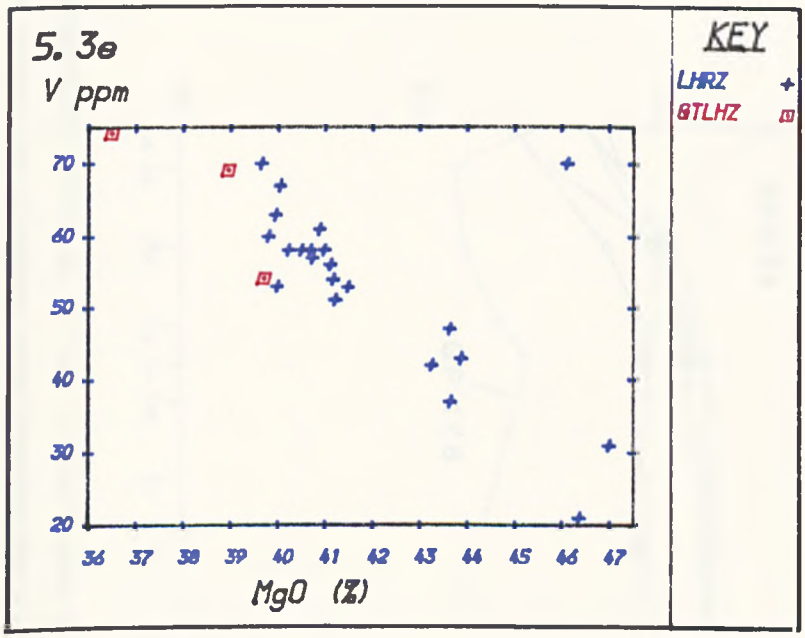
5. 3e
V ppm
70
60
50
40
30
20
36 37 38 39 40 41 42 43 44 45 46 47
MgO (%)
KEY
LHRZ
GTLHZ

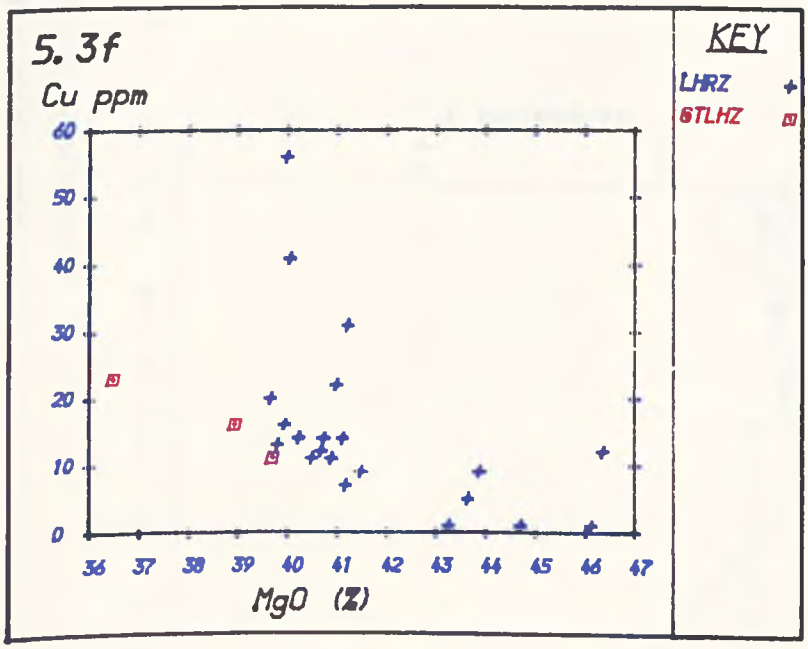
5. 3f
Cu ppm
60
50
40
30
20
10
0
36 37 38 39 40 41 42 43 44 45 46 47
MgO (%)
KEY
LHRZ
GTLHZ

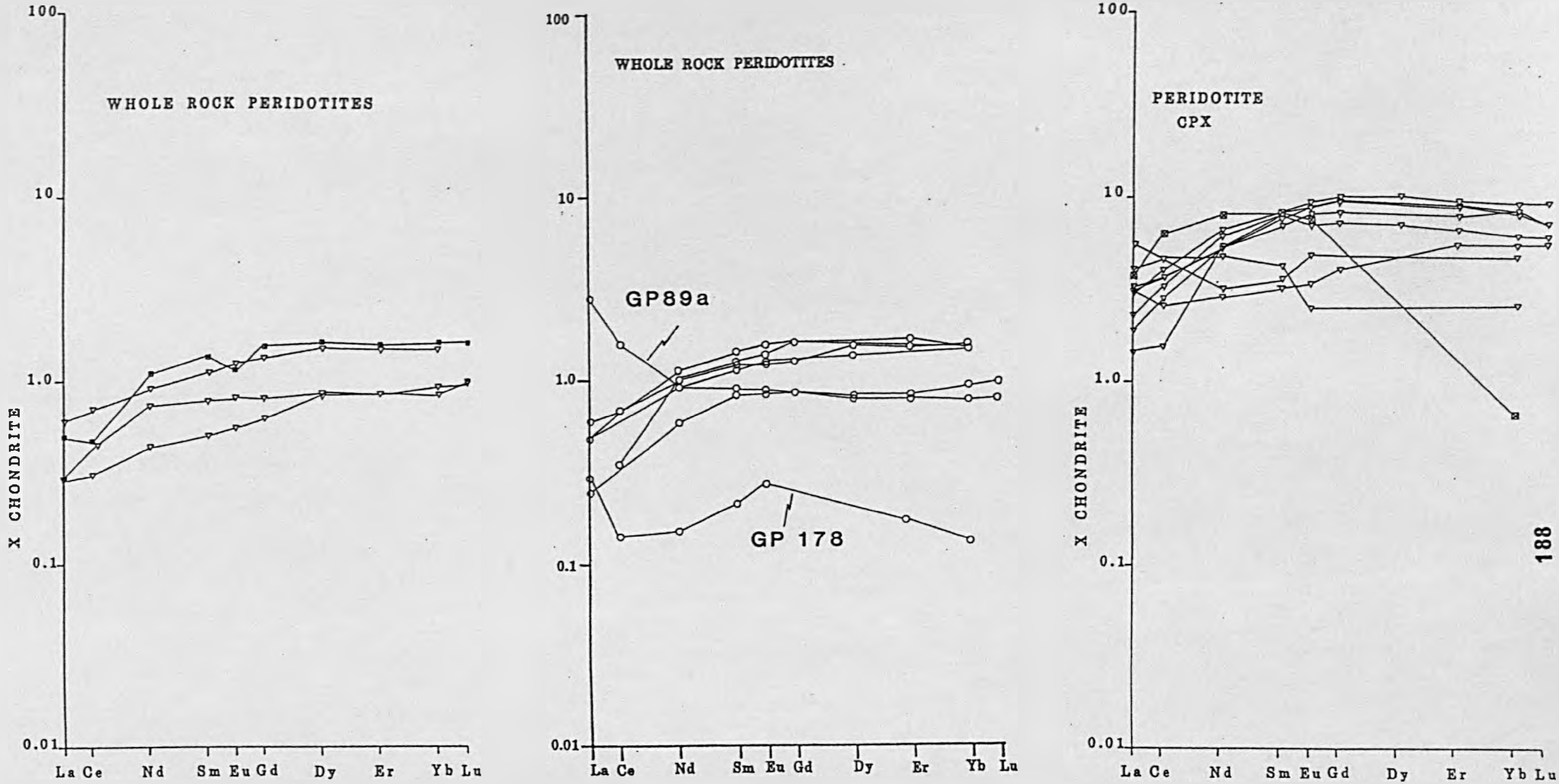

Figure 5.4. Chondrite normalized whole rock REE data for Beni Bousera whole rock peridotites and CPX from lherzolites. Inverted open triangles are spinel peridotites, box with diagonal cross is garnet peridotite GP24.

5.5

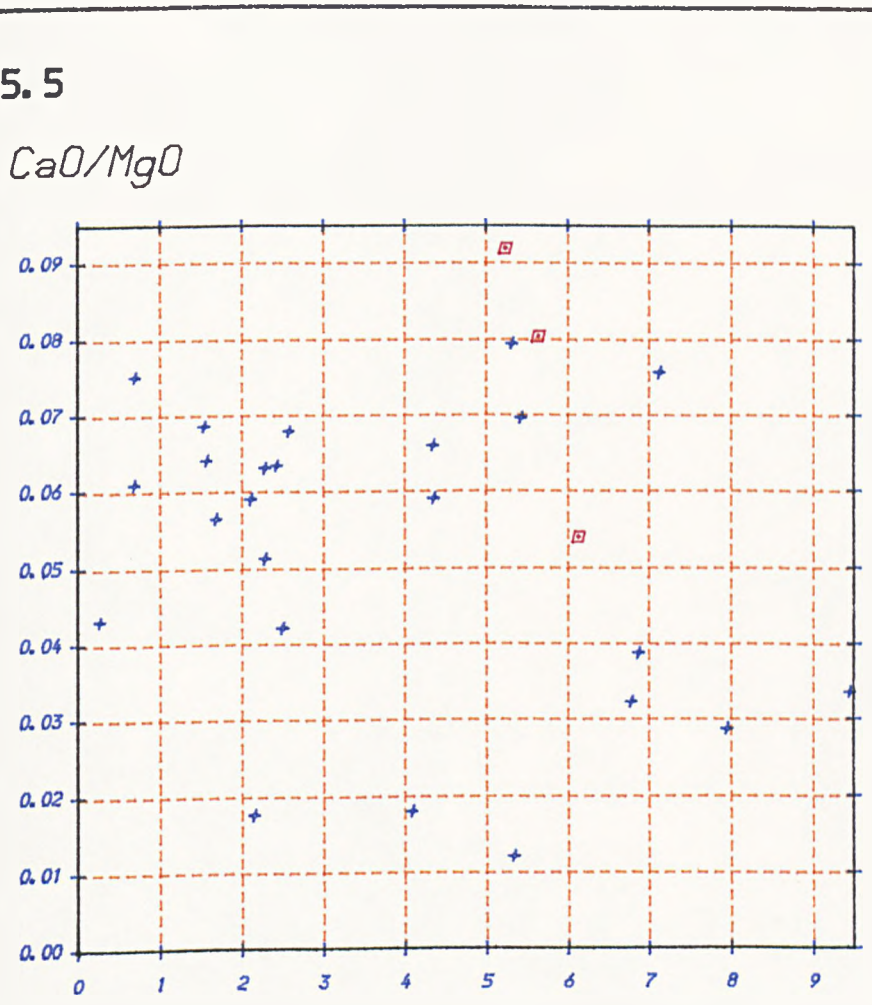
CaO/MgO
0.09
0.08
0.07
0.06
0.05
0.04
0.03
0.02
0.01
0.00
0
1
2
3
4
5
6
7
8
9
Loss on Ign.
KEY
LHRZ
GTLHZ

In order to discuss the major element data for the peridotites it is necessary to discriminate between those samples showing anomalous abundances of Fe + Na and other samples. Frey et al (1985) also noted a Ronda peridotite sample (R131) with anomalously high Fe and TiO_2 content but with anomalous Na_2O which they attributed to complex pyroxenite-peridotite melt interaction during emplacement of the pyroxenite veins. To pick out samples with anomalously high Fe values at a given MgO content (Fig 5.2) a reference line is required which defines a "normal" trend of increasing FeO content with decreasing MgO content in the whole rock. The Fe-Mg "reference line" must be constructed from rocks which are thought to have originated from a similar source and be exposed in a similar tectonic and petrological environment to that of the Beni Bousera peridotites. Samples R717 and R771 from the Ronda peridotite data set of Frey et al (1985) have been selected as end-members to define an "evolution line" in terms of Fe-Mg space. The remaining Ronda peridotites samples, considered by Frey et al (op.cit.) to represent a trend of residues from variable degrees of melt extraction , plot very close to this line within the area marked on Fig 5.6 . This Fe-Mg "reference line" is plotted in Figure 5.6 which is an enlarged FeO vs MgO wt % diagram to highlight samples with anomalously high FeO contents at a given value of MgO. The diagram is designed only to semi-quantitatively illustrate Fe enrichment as it is unlikely that phase equilibria controls would yield melts and residues defining perfectly linear relationships on element-element variation diagrams. Deviations from linearity can also be caused by sampling errors and alteration effects together with analytical uncertainties. The assumption that data points plotting significantly above the MgO-FeO reference line on Figure 5.6 have been enriched in FeO requires a homogeneous source for all the Beni Bousera peridotites; this will be discussed later. Relative FeO enrichment can be quantified by using the parameter ΔFeO (Table 5.6). ΔFeO represents the deviation of a particular peridotite sample in units of wt % FeO for its MgO content relative to the Fe-Mg reference line (Fig. 5.6).

Ideally a sample formed by partial melting and extraction of "basaltic" liquid from a source identical to R717 would have ΔFeO = 0.0 % units. In the Beni Bousera peridotites ΔFeO can be seen to vary from slightly positive to highly positive values (ΔFeO= + 0.01 to + 0.95 wt % units, Table 5.6). The samples most notably enriched in FeO at a given MgO relative to the reference line are, in decreasing order of ΔFeO: GP88 (0.95), GP89a (+0.60), GP91 (+0.53), GP178 (+0.52) GP89b (+0.48), GP132(3) (+0.45). Most "normal" samples plot within an upper or lower limit of ~ 0.25 FeO units either side of the ΔFeO=0 line on Figure 5.6. Although a poor correlation exists between sample proximity to a pyroxenite layer and the magnitude of ΔFeO, the data set is heavily biased by GP88 with a very high ΔFeO (+0.95). Several samples deviate significantly from the expected ΔFeO vs. distance from pyroxenite trend. GP191 and GP119 outcrop close to pyroxenite layers and yet have small ΔFeO values. Sample GP178, the only harzburgite in the suite, has the highest MgO content (47 wt %), is located well over 10m away from the nearest visible pyroxenite layer and yet displays one of the highest ΔFeO values (+0.52). More significantly, all the garnet lherzolite samples occur very close to garnet clinopyroxenite layers and are intermixed with them (see later). The garnet lherzolite samples have low ΔFeO values (within + 0.25) indicating that the high ΔFeO values in the spinel peridotites are not solely due to their proximity to

Figure 5.6. FeO vs MgO wt % diagram. Solid straight line joins Ronda peridotite samples R717 and R771. Dashed line parallel to solid line marks 0.25 wt % FeO variation from this trend. Field enclosed by solid line is total Ronda peridotite FeO-MgO variation. Open triangles are Beni Bousera spinel peridotites, squares with crosses garnet peridotites. The figure illustrates the high FeO nature of some Beni Bousera peridotites.

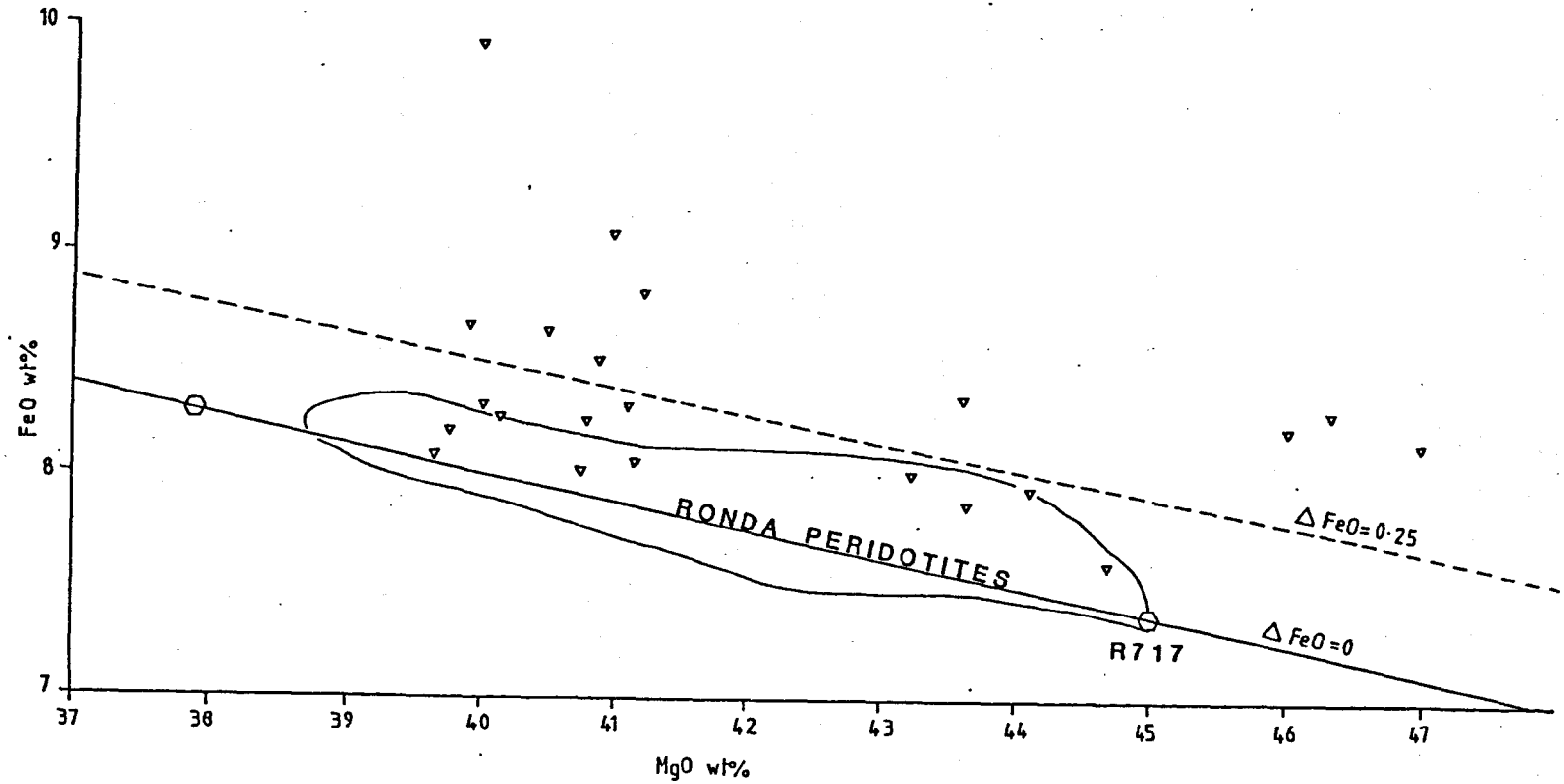

SAMPLE	LOCATION	PROXIM. ML.	DENSITY ML	Δ FeO	(Ce/Yb)n
GP12	Aarkob	>10	0	+ 0.16	0.228
GP13	Aarkob	>10	0	0.08	0.433
GP41	JK	0.5	0.3	0.32	0.378
GP88	OeJ	0.1	0.3	0.95	0.495
GP89a	OeJ	0.1	0.3	0.6	1.84
GP89b	OeJ	0.1	0.3	0.35	
GP89c	OeJ	0.3	0.3	0.48	0.362
GP91	OeJ	0.3	0.3	0.53	
GP119	OeJ	3	0.05	0.16	0.4
GP132(2)	OeJ	0.05	0.05	0.15	
GP132(3)	OeJ	0.1	0.05	0.45	
GP175	OeJ	10	0	0.09	
GP178	OeJ	10	0.05-0	0.52	1.08
GP189	OeJ	10	0	0.16	
GP191	OeJ	1	0.05	0.21	
GP220	OeJ	3	0.3	0.1	
GP222	Am Beach	10	0.05	0.09	
GP224	Am Beach	5	0.05	0.2	
GP229	Am Beach	2	0.1	0.4	
GP230	O. Sidi Y.	10	0	0.01	
GP233	O. Sidi Y.	5	0.05	0.15	
GP238	O. Sidi Y.	10	0	0.31	
GP240	O. Am.	10	0.05	0.04	
PHN5733	F			0.22	0.326
GP24	OeJ	0.1	0.3	0.12	0.285
GP248	O. Am.	1	0.3	0.22	
GP250	O. Am.	1	0.3	0.18	

Table 5.6. Proximity of peridotites to mafic (pyroxenite) layers (PROXIM.M.L.) in meters. Density ML is the fraction of pyroxenites per meter of outcrop in the nearest outcrops of pyroxenites in peridotites, eg. 0.3 = 30 cm of pyroxenites in 1 meter of outcrop. Δ FeO and (Ce/Yb)$_n$ are also listed. Location abbreviations are given in Appendix 1.

pyroxenite layering. Some spinel peridotites with high ΔFeO also have anomalously high sodium contents. However, there is no correlation between FeO content or ΔFeO and Na_2O content. Limited REE data does suggest a general correlation between ΔFeO and degree of LREE enrichment in that samples with high ΔFeO generally have relatively high $(Ce/Yb)_n$. The CPX from peridotite GP132(3) shows a very similar LREE enriched signiture to the CPX from the Cr-websterite which cross-cuts the peridotite.

Samples with high ΔFeO content are not consistently anomalous with respect to any other major element. CaO and Al_2O_3 show coherent negative correlations with MgO (Fig.5.2). TiO_2 also shows a negative correlation with MgOin these samples (Fig.5.2). Of the high ΔFeO samples, only GP89 a, b + c are high in TiO_2. The sample with the highest ΔFeO (GP88) has a low TiO_2 content, whilst the TiO_2 content of the harzburgite GP178 is in keeping with its highly magnesian character.

The lack of a positive correlation between FeO content and TiO_2 content precludes the peridotites having been enriched by Fe-Ti rich fluids as recorded in some peridotite xenoliths, Hawkesworth et al (1984), Nixon and Davies (1987). Two processes seem to be responsible for the complicated major element relationships of the Beni Bousera peridotite samples. One is the interaction of pyroxenite layers with the host peridotite creating high TiO_2 and possibly some FeO enrichment, similar to the effects recorded by composite lherzolite / pyroxenite xenoliths reported by Irving (1980). The expected LREE enrichment of the peridotites which accompanies this process in composite xenoliths is not consistently observed in Beni Bousera, probably because many of the Beni Bousera pyroxenites are much lower in LREE than the pyroxenites analysed by Irving (1980).

The combined effect of pyroxenite melt heterogeneously invading peridotite on variable scales with often random Fe and LREE metasomatism hampers interpretation of the peridotite major element data. It is unlikely that the observed variation is due to variable degrees of partial melting of a heterogeneous source as parallel trends may be expected above and below the Mg-Fe reference line and this is not observed. Also, such a heterogeneous source would not produce the Ti-Fe decoupling seen in some samples. The Beni Bousera peridotites appear to be more variable and show poorer correlations in their major element chemistry than the Ronda peridotites.

Taking into consideration the effects of Fe, Ti and possible Na enrichment it is still possible to interpret samples with the lowest CaO and Al_2O_3 contents and highest MgO contents as residues from the highest degrees of melting of a fertile lherzolite source. This conclusion is in accord with that of Kornprobst (1969, 1974) and workers on other orogenic peridotites e.g. Quick (1981) and Frey et al (1985).

Frey et al (1985) pointed out that the linear arrays defined on oxide vs MgO plots are indicative of two component mixing or unmixing (eg partial melting) processes such that in addition to variable melt depletion, incomplete segregation of partial melts could also generate such arrays. Figure 5.7 is a CMAS projection (of the type outlined by O'Hara, 1968) projected from diopside into C_3A-M-S, the non-FeO enriched samples define a linear trend emanating from the olivine position, i.e. an olivine control line. This trend is analogous to the trend predicted by O'Hara (1968) for the evolution of residues from the melting of

a lherzolitic source. A similar trend was observed for the Ronda peridotites by Frey et al (1985). This trend does not preclude incomplete melt extraction or re-fertilization of a residue with basaltic magma.

Partial melting appears to be the main process producing the linear major element variation trends in the non-FeO enriched peridotites. The possibility that the peridotites represent residues from a uniform degree of melting of either a homogeneous or heterogeneous source are not supported by the experimental melting study of Jaques and Green (1980) who concluded that compositionally invariant melts were not formed over a wide degree of melting. There is no petrological evidence for melt trapping in the Beni Bousera peridotites, hence they are probably not created by incomplete and variable degrees of melt segregation produced by a uniform degree of melting of a homogeneous source. On the contrary, petrological evidence and the major element chemistry of the non-FeO enriched peridotites are consistent with their origin as residues left by complete segregation of magma produced by variable degrees of partial melting of a homogeneous source.

The peridotite suite sampled in this study and by Kornprobst (1969) contain more MgO rich, basaltic element depleted compositions than the sample set analysed by Frey et al (1985). The most "fertile" sample in the Beni Bousera data set in terms of relatively low MgO, high FeO, CaO + Al_2O_3 is GP230. GP230 is still considerably more magnesian (39.65 wt %) than most current estimates of "primitive", undepleted upper mantle (see section 5.4) or the most fertile lherzolite from the Ronda peridotite. The fertile Ronda sample R717 is very similar in terms of MgO, Al_2O_3 and CaO contents to the "Primitive Upper Mantle" (PUM) composition derived by Hart and Zindler (1986) which justifies its use as a constraining end-member on the ΔFeO diagram and in estimating degrees of partial melting from the Beni Bousera samples. REE and the petrological characteristics of R717 do not indicate that it has been re-fertilized by exotic fluids. Figure 5.8 compares the Beni Bousera lherzolite major element compositions and those of other orogenic lherzolites with the estimated PUM composition of Hart & Zindler (1986). On an Mg/Si vs Al/Si diagram (Figure 5.8) the Beni Bousera lherzolites cut across the "geochemical fractionation trend" of Jagoutz et al (1979) in which Mg/Si decreases as Al/Si increases as expected for progressive partial melt extraction. The reasons for this are not clear. Duplicate XRF analyses are well within the range of the Mg/Si and Al/Si spread, even for low values of Al_2O_3, the presence of unusually high (unrepresentative) amounts of Al-rich spinel in these whole rock samples may cause a shift to higher Al/Si values. Additionally, some dispersion may be due to undetected melt enrichment and/or serpentinization effects. The most striking variations in Figure 5.8 are shown by the Ca/Al ratios of the lherzolites. Ca/Al ratios of orogenic lherzolites are generally more variable than spinel lherzolite xenoliths from alkaline volcanics (Nickel and Palme 1985). Several Beni Bousera samples plot below the average chondritic Ca/Al ratio 1.09 defined by Ahrens et al (1969). Two samples, GP132(3) and GP229 have particularly low Ca/Al ratios, 0.87 and 0.92 respectively, which are only equalled by one sample from the Trinity peridotite, these samples are not plotted in Figure 5.8. The anomalously low Ca/Al ratios of these two samples are not correlated with MgO content and may indicate some degree of source heterogeneity or possibly unrepresentative, high amounts of modal spinel in the sample analysed.

No correlation exists between MgO content and Ca/Al ratio for the lherzolites and the harzburgite GP178 (Figure 5.9). GP178 would be expected to have the lowest Ca/Al ratio due to the lack of CPX,

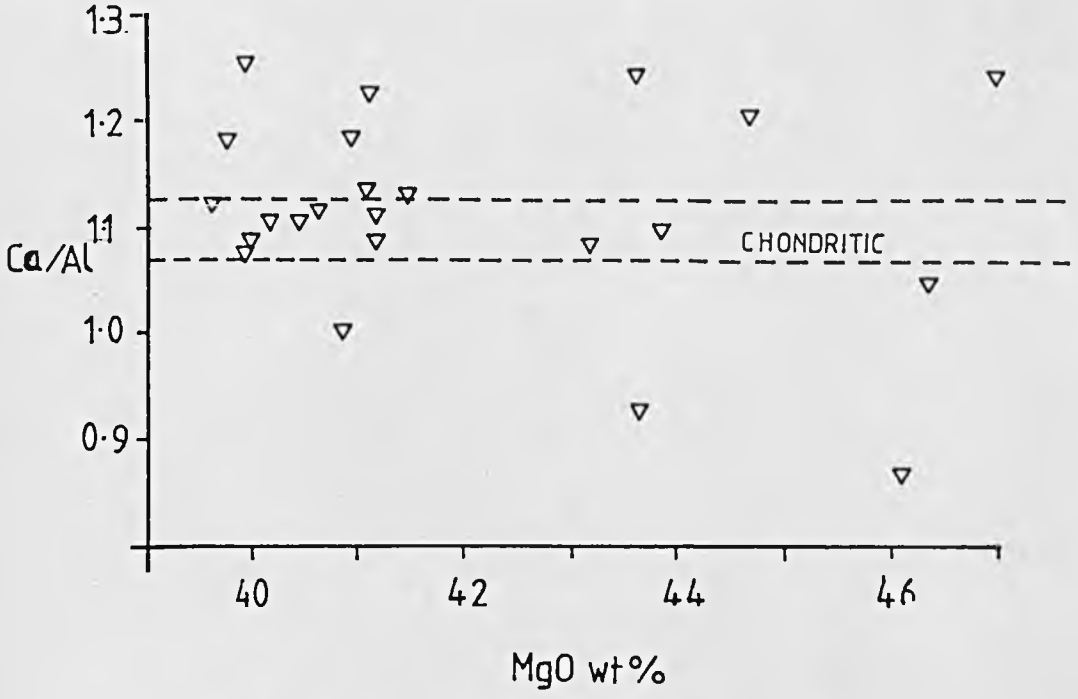

Figure 5.9. Atomic Ca/Al vs MgO wt% of Beni Bousera spinel peridodtite.

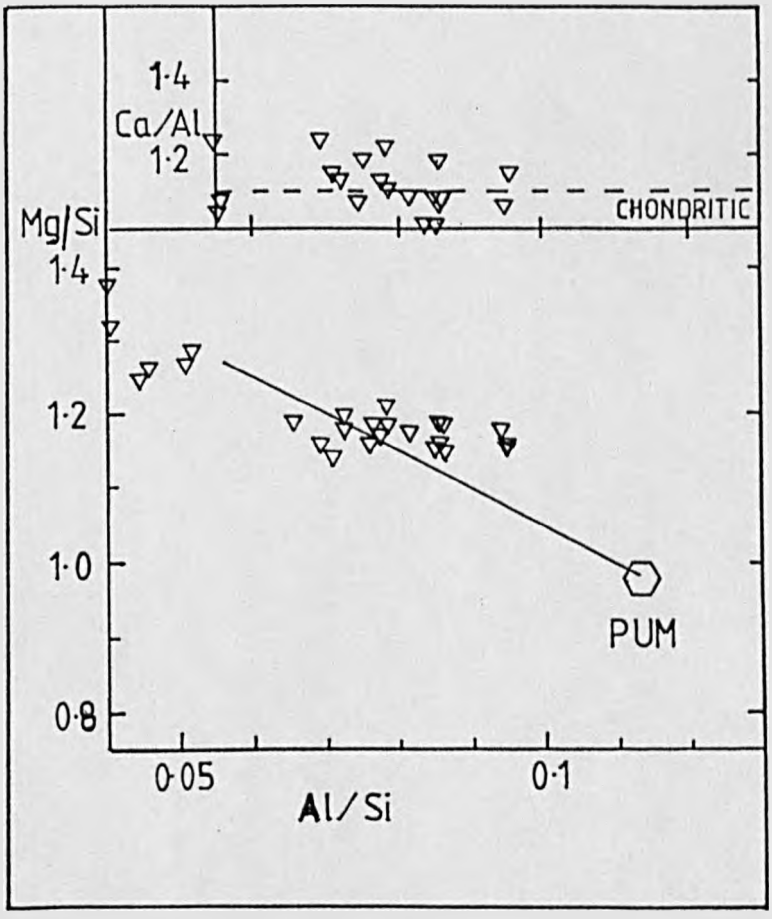

Figure 5.8. Atomic proportions plot of Mg/Si and Ca/Al vs Al/Si showing Beni Bousera spinel peridotites. Diagonal line is " terestrial geochemical fractionation " trend of Jagoutz (1979), indicative of partial melting. PUM composition is from Hart and Zindler (1986). Dashed line is the chondritic Ca/Al ratio defined by Ahrens et al (1969). Low Ca/Al peridotites are not plotted for clarity.

however it posesses one of the highest Ca/Al ratios (1.24). Plots of Ca and Al vs MgO in Figure 5.3 do not suggest any anomalous behaviour of Ca or Al. Some of the scatter in Ca/Al ratios may result from greater analytical uncertainties in measuring low CaO and Al_2O_3 contents but XRF reproducibility (Appendix 4) cannot account for the large spread which is not correlated to Al_2O_3 or CaO abundances. Palme and Nickel (1985) excluded samples with > 42 % MgO from their study to eliminate analytical uncertainties at low CaO an Al_2O_3 abundances. If samples with less than 42 wt % MgO are considered from Beni Bousera the data are still uncorrelated with MgO or Al/Si. Palme and Nickel (1985) noted that the Ca/Al ratio of spinel lherzolite xenoliths is significantly above the chondritic ratio at a given MgO content and found this to be generally true for the 8 orogenic lherzolite massifs they studied. If the terrestrial lherzolite Ca/Al range is a melt depletion array the high Ca/Al ratios of the Beni Bousera peridotites plotted in Figure 5.9 cannot be produced by extraction of common mantle melts which have Ca/Al ratios ~ chondrite (average MORB 1.02, Hart & Zindler 1986). It is possible to produce a high Ca/Al ratio in moderately depleted lherzolite by extraction of a low Ca/Al melt. However, Hart & Zindler (1986) and Palme and Nickel (1985) point out that the global peridotite data set shows no systematic variation of Ca/Al with MgO or any other degree of residual character. This observation is also true for the Beni Bousera lherzolites data (Fig 5.9) but of the samples with < 42 wt % MgO the majority have Ca/Al ratios much closer to chondritic (10 samples Ca/Al between 1.075-1.15) compared to the predominatly higher values recorded by spinel lherzolite xenoliths and massifs studied by Palme & Nickel (1985).

Palme and Nickel (1985) concluded that the upper mantle requires a non-chondritic Ca/Al ratio to explain the differences between Ca/Al ratios in chondrites and terrestial spinel lherzolites, but that the "Bulk Silicate Earth" must have a chondritic Ca/Al ratio overall. They sought to explain the high Ca/Al ratios in spinel lherzolites as being due to removal of 4 % garnet (probably as majorite) from the upper mantle during an early global melting event. Hart & Zindler (1986) emphasize that the Palme & Nickel reconstituted mantle (prior to garnet removal) will have a very high Al/Si ratio (~ 0.13) which cannot be reconciled with a C1 chondrite parent for the Earth or a C3V parent. Hart & Zindler (op.cit.) postulate that the high Ca/Al ratios noted in many spinel lherzolite xenoliths and massifs are an artifact of high, unrepresentative CPX contents of the samples collected for analyses. This proposal is supported to some extent by the present Beni Bousera lherzolite data set. 10 of the samples containing less than 42 wt % MgO have Ca/Al ratios between 1.075 and 1.15 i.e. closer to chondritic values than the Palme & Nickel (1985) data set. Although the Beni Bousera specimens were collected for a variety of geochemical analyses, including radiogenic isotope analyses of their constituent CPX, strenuous efforts were made to collect large samples (> 2 kg) in order to minimize the effect of heterogeneous CPX distribution which is common in orogenic lherzolites (see Chapter 2, Dick and Sinton, 1978, and Obata and Nagahara, 1986). Hart & Zindler (1986) employ a "CPX correction" method to overcome the problem of high (non-chondritic) Ca/Al ratios in their chosen lherzolites. This correction procedure involves subtracting CPX from the major element composition of the sample until the Ca/Al weight ratio is < 1.09 . The method succeeds in reducing the scatter of data on the element ratio plots employed by Hart & Zindler but it is difficult to prove whether the excess CPX problem accounts for all the excess Ca of the high Ca/Al ratios. The excess CPX model cannot, however, account for the high Ca/Al ratios recorded in the harzburgite sample GP178. Those lherzolite samples with very low Ca/Al ratios (e.g. GP238, MgO = 40 %) may be the residues of

extraction of melts with particularly high Ca/Al ratios. Picrites have variable, often high Ca/Al ratios, up to 1.28 (Clarke 1970) which may explain some of the low Ca/Al ratios in residual peridotites. Komatiites can have even higher Ca/Al ratios > 1.3; however, the relatively MgO poor nature of the residue GP238 is not consistent with komatiite extraction.

Recent analyses of fresh peridotites from both orogenic lherzolites (Zabargad; Bonatti et al 1986) and xenoliths (Mongolia; Sun 1987) suggest that the high Ca/Al ratios of spinel peridotites found by Palme & Nickel (1985) and Hart and Zindler (1986) are not as widespread as the latter authors suggest. The Zabargad, Mongolia and Beni Bousera samples are much closer to chondritic values than samples studied previously. Although data presented in this study indicate that "excess" CPX may be responsible for many of the high Ca/Al ratios found in orogenic peridotites we must also question to what extent orogenic peridotites represent unmodified chondritic mantle. The remainder of this chapter and succeeding chapters will indicate that the Beni Bousera peridotites have undergone a very complex geochemical evolution which does not justify a simple melt extraction model from chondritic (PUM) mantle.

5:3 Major Element Modelling of Melt Residues.

In the previous section the Beni Bousera peridotites were interpreted as a suite of residues derived by varying degrees of melting of a compositionally homogeneous source. This hypothesis can be tested by the sort of geochemical modelling technique developed by Hanson and Langmuir (1978). These authors propose that major elements can be numerically modelled in similar ways to trace elements. The major element modelling is constrained by the stoichiometry of the solid phases and knowledge of K_D for $(MgO)_{ol}/(MgO)_{melt}$ and $(FeO)_{ol}/(FeO)_{melt}$ as a function of pressure, temperature and composition. These data can be applied to calculate the MgO and FeO contents of peridotite residues from varying degrees of melting of a uniform source. To utilize such calculations it is necessary to know the composition of the undepleted source peridotite. The data set for the Beni Bousera peridotites presented here, and that published by Kornprobst (1969, 1974) are dominated by relatively MgO rich compositions (anhydrous), with the most fertile candidate, GP230, having 39.7 wt % MgO. GP230 is over 1.5 wt % richer in MgO than the most MgO rich estimate of PUM in Table 5.4 and although it contains comparable amounts of CaO to some PUM estimates, Al_2O_3 is markedly depleted (Table 5.4). Hence, the major element composition of GP230 appears to represent a residue from melt extraction of an even more fertile source mantle. In order to estimate the degree of melt extraction experienced by the various Beni Bousera peridotites and hence calculate the composition of the extracted melt, the most fertile peridotite from the Ronda massif sample (R717) was selected as an undepleted source composition. The justification of using R717, a Ronda sample, to model the Beni Bousera peridotites is given in section 5:1. Additionally, sample R717 is very similar to the PUM estimates of Hart & Zindler (1986) and to "average Pyrolite" (Ringwood 1975), although it does have a slightly high Ca/Al ratio compared to these estimates, it is within the overall PUM "range" of the compilation made in Table 5.4.

Frey et al (1985) used sample R717 as a source composition to perform similar melting calculations for a peridotite suite from Ronda. These authors also noted the higher than chondritic Ca/Al ratio of R717 and pointed out that it is slightly depleted in highly incompatible trace elements such as LREE relative to

most estimates of PUM. Frey et al (1985) surmise that this sample may be the residue from a small degree of partial melting and hence the degrees of partial melting (F values) inferred in the following discussion would be slightly higher for a truly chondritic source. The effect of this discrepancy on the melt calculated using this F estimate is probably within the overall error associated with the calculation of melt compositions. The equations of Hanson and Langmuir (1978) have been used in conjunction with the Mg-Fe partition coefficient data of Grover et al (1980) at 25 kb to calculate a "residue grid" (Fig 5.10) by various degrees of melting of a source composition equivalent to R717 for different temperature. The variation of K_D as a function of P and T documented by Grover et al (1980) differs slightly from that determined by Takahashi and Kushiro (1983), however, the general geometry of the residue field remains the same. From Figure 5.10 it is evident that most of the spinel peridotites, even those with elevated FeO contents, can be explained in terms of representing residues from ~ 5 to 30 % batch melting of the source R717. The range of residues on Figure 5.10 is very similar to that shown by the Ronda suite studied by Frey et al (1985). It is posible that most of the peridotites with high ΔFeO on Figure 5.6 are either residues of a source similar to R717, produced at differing temperatures, or they are residues from various source compositions. The highly anomalous, high ΔFeO sample GP88, is difficult to explain in terms of being a residue of melting except from a highly FeO rich source lherzolite not normally sampled from the mantle. The peridotites with $\Delta FeO < 0.25$ lie within the boundaries formed by 0 to 25 % melting at temperatures between 1400 and ~ 1650 °C at 25 kb on Fig 5.10. The liquidus temperature of a mantle consisting of a four phase lherzolite increases with increasing pressure (e.g.Thompson 1984). This effect, combined with the pressure dependence of K_D causes residues created by melting at higher pressures to plot further to the left on Figure 5.10 and lower pressure residues to plot further to the right. Consequently, the high FeO samples could also represent residues of melting at lower pressures. Whilst the temperatures at which the residues were created may vary with pressure, the extent of melting remains approximately the same (see Fig 4 of Hanson and Langmuir 1978). From Figure 5.10 it is not possible to discern peridotites containing trapped melt as this would indicate a lower extent of partial melting. Figure 5.11 also shows a (shaded) field for peridotite xenoliths from kimberlites plotted by Hanson and Langmuir (1978). Xenolith peridotites are generally poorer in Fe than the Beni Bousera and Ronda peridotites. If the peridotites from kimberlites are derived from a source similar to R717 i.e. pyrolite, they either reflect greater degrees of melting at higher temperatures and pressures than the Beni Bousera peridotites, or they are the residues of continuous melting of more limited extent.

Having semi-quantitatively established the extent of melting which produced the Beni Bousera peridotite suite it is of interest to quantitatively determine the amount and composition of the melts extracted. To determine these parameters the approach of Frey et al (1985) is adopted. A major assumption adopted in this approach is that the peridotite samples represent residues with no trapped/resorbed melt that formed from a compositionally homogeneous source (in terms of major elements). The sample R717 is again adopted as a source for reasons outlined previously, however other source variants are tested. Following Langmuir and Hanson (1980) a mass balance approach is adopted which utilizes the equation:

$$C^O = C^lF + C^R(1-F) \qquad (\text{eqn } 5.1)$$

where C^o = source concentration, C^l = liquid concentration (unknown), C^R = residue concentration F = degree of melting (unknown).

For equilibrium or batch melting C^l is effectively the melt produced in equilibrium with the residues. In all the calculations FeO was taken as Fe total. Assuming that the olivine composition of the residue has not changed during sub-solidus cooling i.e. olivine buffers the Fe/Mg value of the rock, then F , the percent melting can be calculated if the olivine liquid Fe/Mg equilibrium constant (K_D) is known from :

$$F\,(MgO)^l + (1-F)(MgO)^R = (MgO)^o$$

then $$F\,(FeO)^l + (1-F)(FeO)^R = (FeO)^o$$

given that: $$\alpha = (Fe/Mg)^R \sim (Fe/Mg)_{ol}/K_D$$

it follows that: $$F = 1 - \{ (\alpha\,(MgO)^o - (FeO)^o) / (\alpha\,(MgO)^R - (FeO)^R) \} \qquad (eqn\ 5.2)$$

Solving Equation 5.2 for the degree of melting allows equation 5.1 to be solved individually for each major element. The assumption that FeO = Fe_{TOTAL} is based on the observation that Fe^{3+}/Fe^{2+} in mantle melts and residues is generally very low, 0 to 0.1 (Haggerty and Tomkins 1983, Eggler 1983, Frey et al 1985). If a melt were to have a Fe^{3+}/Fe^{2+} ratio of ~ 0.1 the approximation $\alpha = (Fe/Mg)_{ol}/K_D$ causes the degree of melting, F, to be overestimated by 5% of its total value which is within the range of uncertainty of the calculation (Frey et al 1985). The results of calculations of melts derived from the Beni Bousera peridotites using various sources are presented in Table 5.7. For melts derived by batch melting the FeO/MgO ratio in olivine used to calculate α is that of the olivine in equilibrium with the residue at the end of melting. For fractional melting, the olivine composition in equilibrium with the melt varies over the whole melting interval and is the integrated average of the FeO/MgO ratio in the source and in the final residue. The effect of varying FeO/MgO of the olivine on the composition of the equilibrium melt extracted has been investigated in Table 5.7 where melt number 5 was calculated using the average $FeO/MgO_{olivine}$ of the source and residue to calculate α.

Using the fertile Ronda peridotite R717 as a source composition and taking a representative selection of Beni Bousera peridotites of varying MgO contents (GP230, GP13, GP222, GP220, GP189 and GP178) as residues from partial melting of this source it is evident that the selected samples represent residues from ~ 7 to 31 % melting (Table 5.7). As would be expected, the peridotites with the lowest concentrations of CaO, Al_2O_3 and TiO_2 and the highest MgO contents (GP220 and GP178) are residues from the largest amount of melt extraction (26.9 + 30.5 % respectively). Sample GP178 is the only sample chosen which has an anomalously high FeO concentration. Despite this fact the sample still yields a sensible melt composition. If the FeO content of GP178 is reduced so that it lies on the $\Delta FeO = 0$ line of Figure 5.6 and the major element composition renormalized to 100 %, the amount of melt extracted from this rock (using

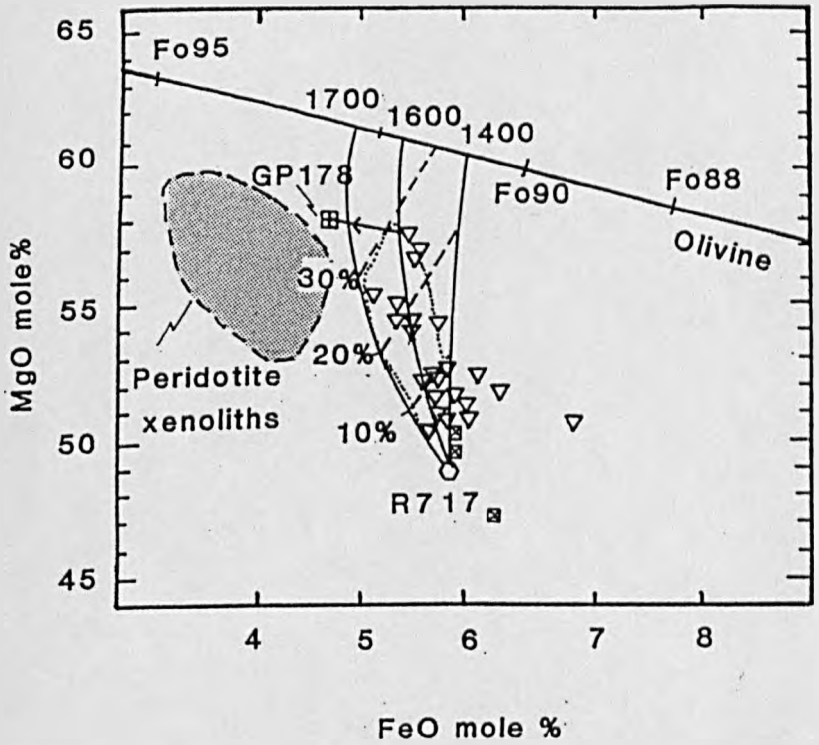

Figure 5.10. Mgo vs FeO (mole %) plot of Beni Bousera peridotites. MgO/FeO melting trends calculated by melting a source equivalent to R717 (a fertile Ronda peridotite from Frey et al 1985) following the procedure of Langmuir and Hanson (1978). Following Frey et al (1985) the olivine K_D of Grover et al (1980) at 25 kb were used. Dashed lines indicate % melting of R717 required to produce present residual composition. Shaded area indicates the field occuppied by peridotite xenoliths from kimberlite pipes. Dotted field within melting grid is the range for Ronda peridotites from Frey et al (1985).

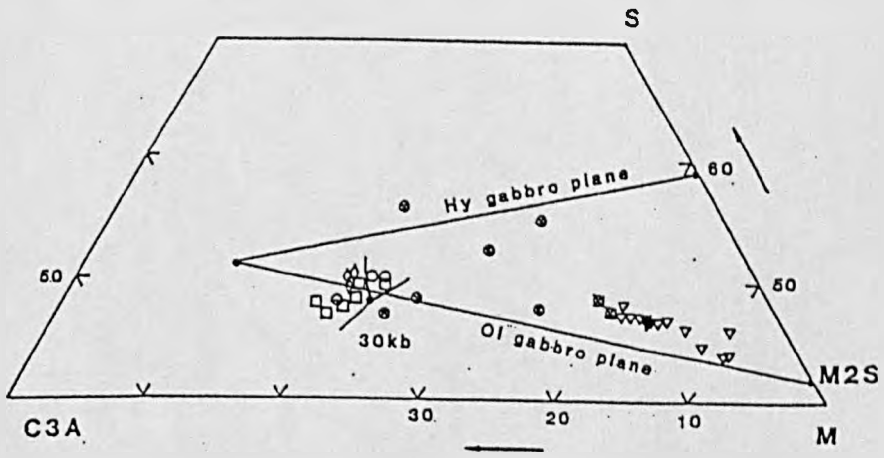

Figure 5.7. CMAS projection from *diopside* into C_3A-M-S (O'Hara 1968). Inverted triangles: spinel peridotites. Squares with crosses: garnet peridotites. For pyroxenite symbols see Figs 5.17, 5.18. The linear trend defined by the peridotites is indicative of residues formed by partial melting of various degrees. Note the most fertile peridotites, the garnet lherzolites, are nearest to high pressure melt compositions indicated by the 30 kb cotectic (from Clarke 1970).

R717 as a source and a K_D of 0.35) increases to 36.1 %, with a corresponding increase in the MgO content of the extracted melt of ~ 2%. The higher degree of melting of GP178 is more compatible with its very MgO rich chemistry. The effect of this renormalization is to move GP178 diagonally up and left on Figure 5.10, i.e. to increase the degree of residual character. If this process were carried out on all the samples plotted in Figure 5.10 they would plot within the "melting-grid" depicted. Samples in Table 5.2 with higher FeO contents than the source R717 are not amenable to this type of mass balance calculation as they yield negative amounts of FeO in the melt. This also happens with Na_2O for samples GP220 and GP230 in Table 5.6 as they have higher Na_2O concentrations than R717, however the remainder of their major element chemistry is compatible with them being residues from this sample.

All the calculated melts in Table 5.7 have Mg Nos. greater than 68, the lower limit required for a "primary magma" derived from the upper mantle by Frey et al (1978); with a range from 72.6 to 78.5. In most cases in Table 5.7 two different melt compositions have been calculated that could be in equilibrium with the same residue composition. These two melts result from different assumed K_D values of 0.35 and 0.3. The main effect of varying this parameter is to reduce the MgO content and Mg No. of the melt by using a lower K_D. The most realistic melt compositions obtained by using $K_D = 0.35$ which is consistent with the high pressure data of Grover et al (1980) and Takahashi and Kushiro (1983) for melting at ~ 25 kb and 1600 ^oC. The effect of varying the source composition was also evaluated in Table 5.7. It may be argued that the most likely source peridotite composition from which the Beni Bousera residue suite was derived was the most fertile lherzolite sampled in the suite i.e. GP230 or GP13. If GP230 were the source composition, the degree of melting for each residue is greatly decreased e.g. by 7 % for GP189 (melts 1 + 2 Table 5.7). Neither GP230 or GP13 are likely contenders for fertile mantle peridotite due to their high MgO contents and low Ca and Al contents compared with current estimates of PUM (see Table 5.4). GP13 is also significantly LREE depleted (see later).

It may be argued however that the Beni Bousera peridotite suite is a product of multiple melting events, the penultimate melting event leaving a homogeneous residue composition similar to GP230 or GP13. This residue then acted as a source for a further, variable degree melting episode which created the observed spectrum of compositions. It is of interest to note that GP230 has a more chondritic Ca/Al ratio than R717 and hence the potential melts produced from this source also have lower, more chondritic Ca/Al ratios than melts produced from R717 (Table 5.7). The effect of chosing a source similar to PUM 2 in Table 5.4 is also to lower the Ca/Al ratio of the melt produced (compare melts 2 + 6, Table 5.7).

The last variable in the model to be considered was the varying FeO/MgO ratio of olivine in the residue. Predictably, the value used depends entirely on the melting model chosen and the effect of this parameter is evaluated in Table 5.7 by varying it whilst retaining a constant K_D and source composition for a melt in equilibrium with a residue of GP189. As expected, choosing the FeO/MgO ratio of the source and residue define the low and high end members in terms of the MgO content of the melt (16.5 to 19.5 % MgO) whilst the averaged value (melt 5) defines an intermediate value. Frey et al (1985) consider that for each source-residue pair the most realistic melt compositions are calculated applying the residual olivine FeO/MgO ratio equal to that in the residual peridotite. The calculated melts in Table 5.7 are of picritic basalt composition, MgO ~ 16-21 % ; SiO_2 45.1-51.8; FeO 9.3-10.9; Al_2O_3 5.2-13.3 % ; CaO 8-12.8 %,

Table 5.7. Calculated equilibrium melts of selected Beni Bousera peridotites derived from various source peridotites including R717 and GP230. Following Frey et al (1985) most melts are calculated assuming an olivine Fe/Mg K_D = 0.35. Listed for comparison are: picrites from Baffin Island (Clarke 1970) and New Georgia (Stanton and Bell 1964), Troodos 1 and 2 are picrites from the Troodos ophiolite listed in Francis (1987). MORB 1 and 2 are possible primary MORB compositions of Elthon (1979) and Green et al (1979) respectively. E1 to 3 are experimentally derived melts at moderate to high pressures (see table) from Jaques and Green (1980), E1 , and Takahashi and Kushiro (1983), E2 and E3.

TABLE 5-7 PERID. MELTS

Column 1	MELT 1	MELT 2	MELT 3	MELT 4	MELT 5	MELT 6	MELT 7	MELT 8
1 SOURCE	GP230	R717	R717	R717	R717	PUM 2	R717 *	R717 *
2 RESIDUE	GP189	GP189	GP189	GP189	GP189	GP189	GP220	GP220
3 % MELT	15.6	22.9	21.1	20.4	21.5	22.9	26.9	24.5
4 Kd	0.35	0.35	0.3	0.35	0.35	0.35	0.35	0.3
5 Ol. Res.	0.18	0.18	0.18	0.218	0.199	0.18	0.18	0.18
6								
7 SiO2	45.1	48.8	49.2	49.4	49.1	51.8	45.7	48.2
8 TiO2	0.81	0.63	0.68	0.70	0.66		0.57	0.63
9 Al2O3	13.3	10.5	11.3	11.6	11.1	10.9	10.2	11.0
10 FeO	9.3	10.0	10.2	10.3	10.2		10.1	10.4
11 MnO	0.14	0.10	0.10	0.10	0.1		0.30	0.30
12 MgO	18.1	19.5	17.4	16.5	17.9	18.2	19.7	17.3
13 CaO	10.0	9.2	9.9	10.3	9.8	8.0	9.1	9.9
14 Na2O	3.2	1.1	1.1	1.1	1.1			
15								
16 100Mg/Mg+Fe	77.7	77.7	75.2	74.1	75.8		77.7	74.8
17 Ca/Al	1.02	1.18	1.18			1.07		
18								
19								
20 SAMPLE	BAFFIN ISL.	E1	E2	E3	MORB 1	MORB 2	TROODOS 1	TROODOS 2
21	1500/30kb	1500/15kb	1400/15kb	1555/30kb				
22 SiO2	46.1	49.6	49.9	47.5	47.8	48.3	52.3	52.4
23 TiO2	0.78	0.2	0.81	1.08	0.59	0.60	0.35	0.3
24 Al2O3	11.0	9.2	13.0	11.9	12.1	13.7	12.9	11.7
25 FeO	10.5	9.3	10.6	9.2	9.0	7.9	8.1	8.4
26 MnO	0.18	0.2	0.25	0.21	0.12	0.12	0.14	0.1
27 MgO	20.1	22.4	14.3	18.7	17.8	16.7	15.7	15.8
28 CaO	9.4	8.5	8.9	8.8	11.2	10.9	9.2	10.7
29 Na2O	1.06	0.5	1.41	2.11	1.31	1.65	0.93	0.7
30								
31 100Mg/Mg+Fe	77	81	71	78	78	79	78	77

MELT 9	MELT 10	MELT 11	MELT 12	MELT 13	MELT 14	MELT 15	MELT 16
R717	R717	R717	R717	R717	R717	R717	GP230
GP13	GP230	GP230	GP222	GP178	GP178	GP178(2)	GP178(2)
8.4	7.9	7.1	14.1	30.5	21.1	36.1	29.9
0.35	0.35	0.30	0.35	0.35	0.3	0.35	0.35
0.202	0.202	0.202	0.184	0.173	0.173	0.171	0.171
49.6	51.4	52.2	48.0	48.8	49.2	48.9	47.3
0.55	0.29	0.3	0.50	0.63	0.68	0.39	0.42
9.8	5.2	5.4	10.7	10.5	11.3	9.4	10.6
10.1	10.6	10.9	10.2	10.0	10.2	10.6	10.4
	0.14	0.13	0.15	0.1	0.1	0.13	0.20
19.8	18.5	16.2	19.5	19.5	17.4	21.6	21.3
9.7	12.8	8.2	10.7	9.2	9.9	8.3	8.6
0.46			0.3	1.1	1.1	0.60	1.59
77.7	75.7	72.6	77.3	77.7	75.2	78.4	78.5
						1.19	1.10

BAS. KOM	N. GEORGIA PICRITE
46.1	48.0
0.4	0.43
8.4	9.7
10.9	10.2
0.22	0.18
23.6	19.7
8.8	9.0
0.84	1.5
	78

Figure 5.11 MgO - oxide (wt%) diagrams for Beni Bousera peridotites and calculated equilibrium melts from a source equivalent to R717 using the Beni Bousera peridotites as residues (Table 5.7). The primary MORB composition of Elthon (1979), the Baffin Island picrite and New Georgia picrite compositions listed in Table 5.7 all plot within the field of calculated equilibrium melts. The vector shown on the MgO vs Al_2O_3 diagram illusrates the effect of mixing spinel lherzolite (GP 220) with garnet clinopyroxene sample GP20, 20 % addition of GP20 marked.

20

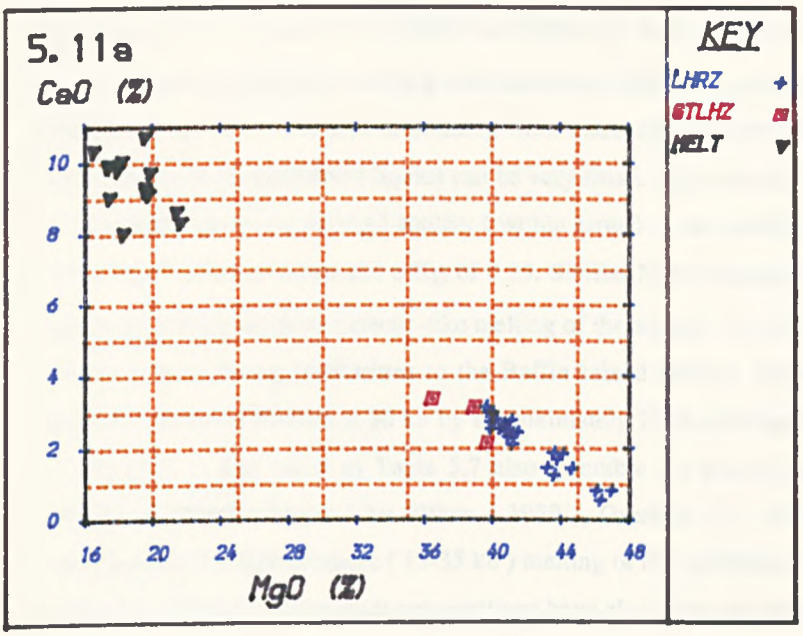
5. 11a
CaO (%)
10
8
6
4
2
0
16
20
24
28
32
36
40
44
48
MgO (%)
KEY
LHRZ
GTLHZ
MELT

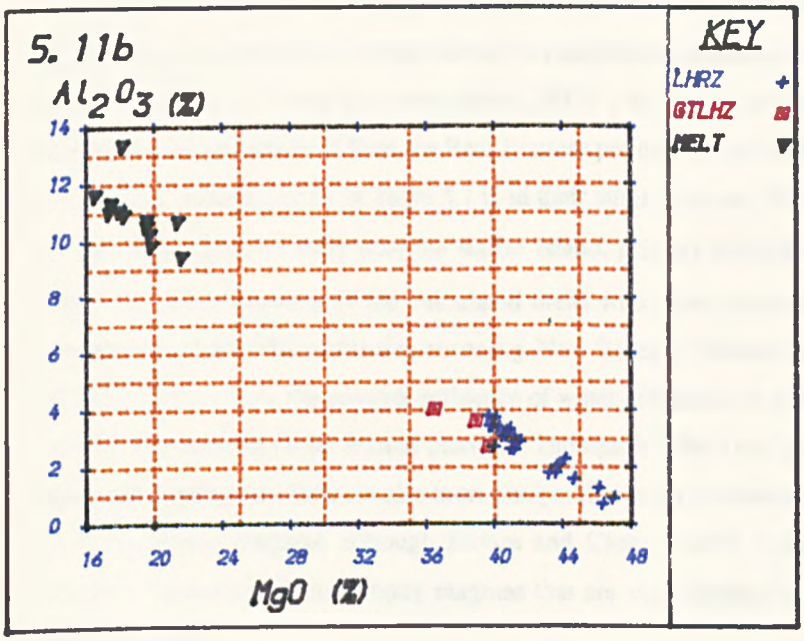
5. 11b
Al2O3 (%)
14
12
10
8
6
4
2
0
16
20
24
28
32
36
40
44
48
MgO (%)
KEY
LHRZ
GTLHZ
MELT

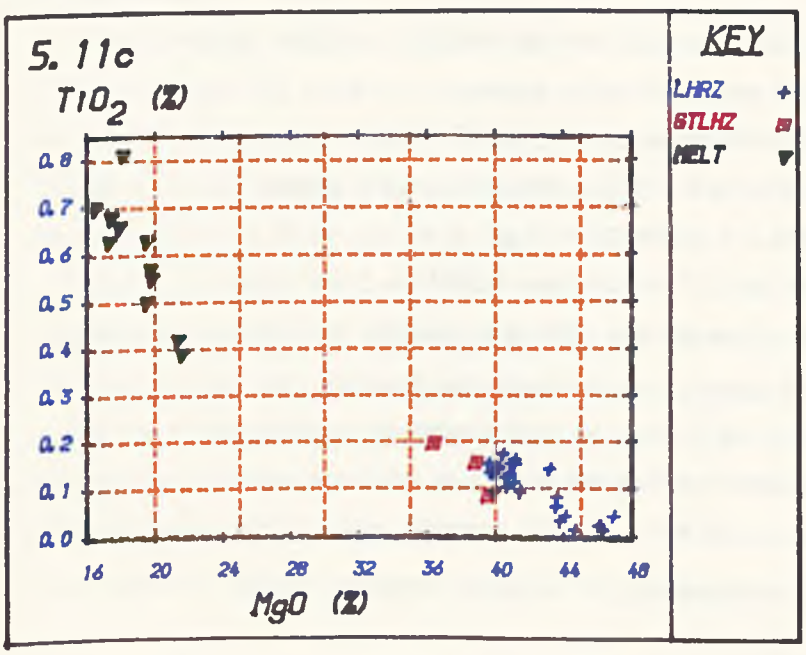
5. 11c
TiO2 (%)
0.8
0.7
0.6
0.5
0.4
0.3
0.2
0.1
0.0
16
20
24
28
32
36
40
44
48
MgO (%)
KEY
LHRZ
GTLHZ
MELT

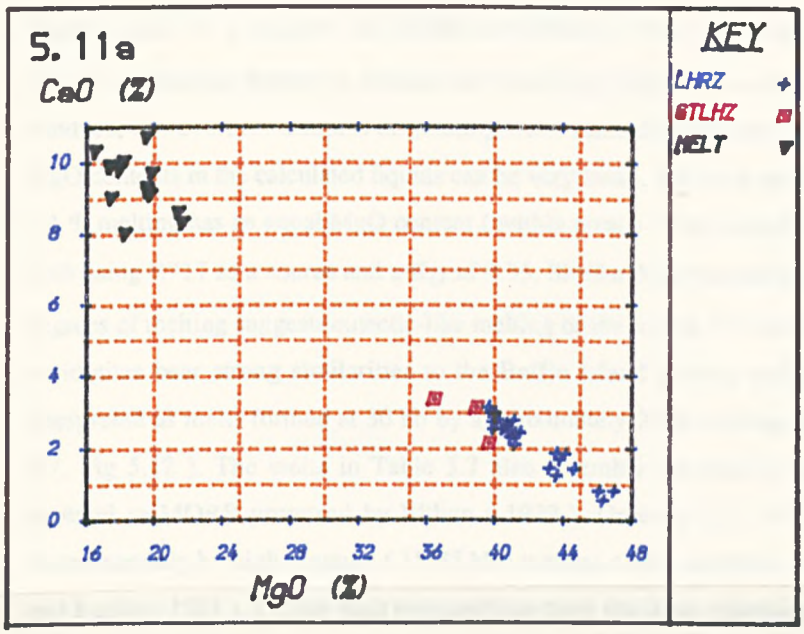
5. 11a
CaO (%)
10
8
6
4
2
0
16
20
24
28
32
36
40
44
48
MgO (%)
KEY
LHRZ
GTLHZ
MELT

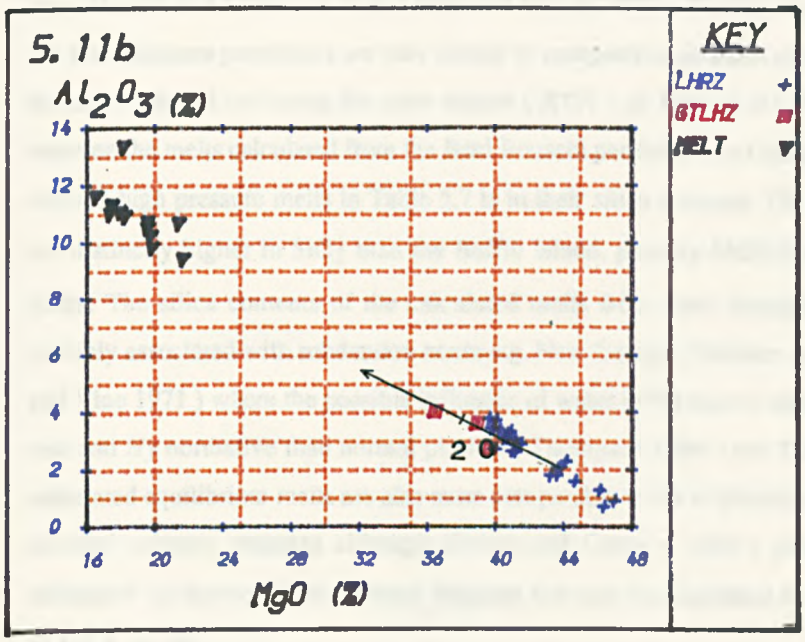
5. 11b
Al2O3 (%)
14
12
10
8
6
4
2
0
16
20
24
28
32
36
40
44
48
MgO (%)
2 0
KEY
LHRZ
GTLHZ
MELT

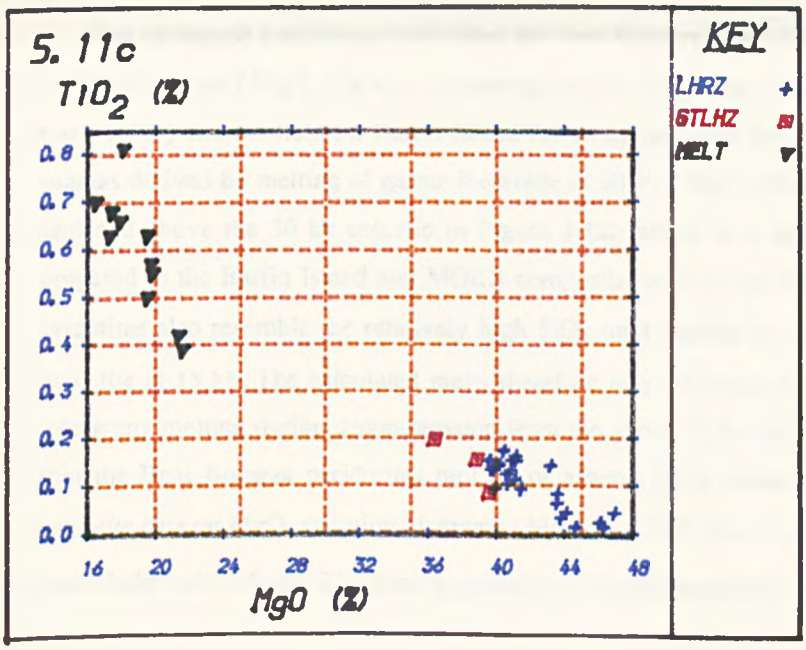
5. 11c
TiO2 (%)
0.8
0.7
0.6
0.5
0.4
0.3
0.2
0.1
0.0
16
20
24
28
32
36
40
44
48
MgO (%)
KEY
LHRZ
GTLHZ
MELT

Na_2O 0.3-3.2 %, (negative for GP220 and GP230); TiO_2 0.29-0.81 %. There is a general correlation between increasing degree of melting and increasing MgO in the calculated melt for the various selected, residues, however, for samples originating from markedly different degrees of melting the difference in MgO contents in the calculated liquids can be very small. The melt calculated from a GP13 residue of only 8.4 % melting has an equal MgO content (within error) to that calculated from 26.9 % melting of GP220, both using R717 as a source and a K_D of 0.35. Similar MgO contents of melts produced by very different degrees of melting suggests eutectic-like melting of the source. The calculated melts from the Beni Bousera peridotites bear strong similarities to the Baffin Island picrites analysed by Clarke (1970) which are interpreted as melts formed at 30 kb by approximately 20 % melting of a garnet lherzolite source (Table 5.7, Fig 5.12). The melts in Table 5.7 also resemble the picritic basalt compositions which may be parental to MORB proposed by Elthon (1979), Green et al (1979, Fig 5.11) and to melts derived experimentally by high pressure (15-35 kb) melting of dry peridotite (Jaques and Green 1970, Takahashi and Kushiro 1983). Similar melt compositions have also been calculated from lherzolite residual xenoliths from Hawaii and Kilbourne Hole (Reid and Woods 1978). Finally, the equilibrium melts calculated from the Beni Bousera peridotites are very similar in composition to those calculated for the Ronda peridotites by the same method and using the same source (R717) by Frey et al (1985). The only major discrepancy between the melts calculated from the Beni Bousera peridotites and the inferred primary and experimentally derived high pressure melts in Table 5.7 is in their silica contents. The Beni Bousera (and Ronda) melts are distinctly higher in SiO_2 than the Baffin Island, primary MORB and experimentally derived mantle melts. The silica contents of the calculated melts from Beni Bousera are more comparable to picrites possibly associated with subduction zones e.g. New Georgia (Stanton and Bell 1969) or Troodos (Moores and Vine 1971) where the possible influence of water in the source region causes melts to become more Si rich and *Hy* normative than normal picrites (Thompson 1984) see Table 5.6. The low Ti contents of the calculated equilibrium melts are also more comparable to the subduction related picrites than to MORB-like inferred primary magmas although Elthon and Casey (1985) proposed that many MORB's might ultimately be derived from primary magmas that are very depleted in Na_2O (0.6-1.50 wt %) and TiO_2 (0.1-0.5 wt %).

The calculated equilibrium melts from the Beni Bousera peridotites plot close to the 30 kb cotectic in the CMAS system (Fig 5.12 a + b), clustering around the primary MORB composition inferred by Green et al (1979) and the field for Baffin Island tholeiites, proposed by Clarke (1970) to represent primary magmas derived by melting of garnet lherzolite at 30 kb (Fig 5.12a). The calculated melts are slightly displaced above the 30 kb cotectic in Figure 5.12b which is a reflection of their higher Si contents compared to the Baffin Island and MORB compositions. The equilibrium melts from the Beni Bousera peridotites also resemble the relatively high SiO_2 melt derived by Jaques and Green (1980) from dry peridotite at 15 kb. The calculated melts therefore may represent the integrated product of a peridotite undergoing melting during decompression from the garnet to the spinel peridotite field. Melts calculated from the Beni Bousera peridotites plot on or around linear extrapolations through the Beni Bousera peridotite data on MgO variation diagrams (Fig.5.11). The linear trend on the Al_2O_3 vs MgO diagram is particularly well defined. The greater spread in TiO_2 compositions of the melts in Figure 5.11 may be a

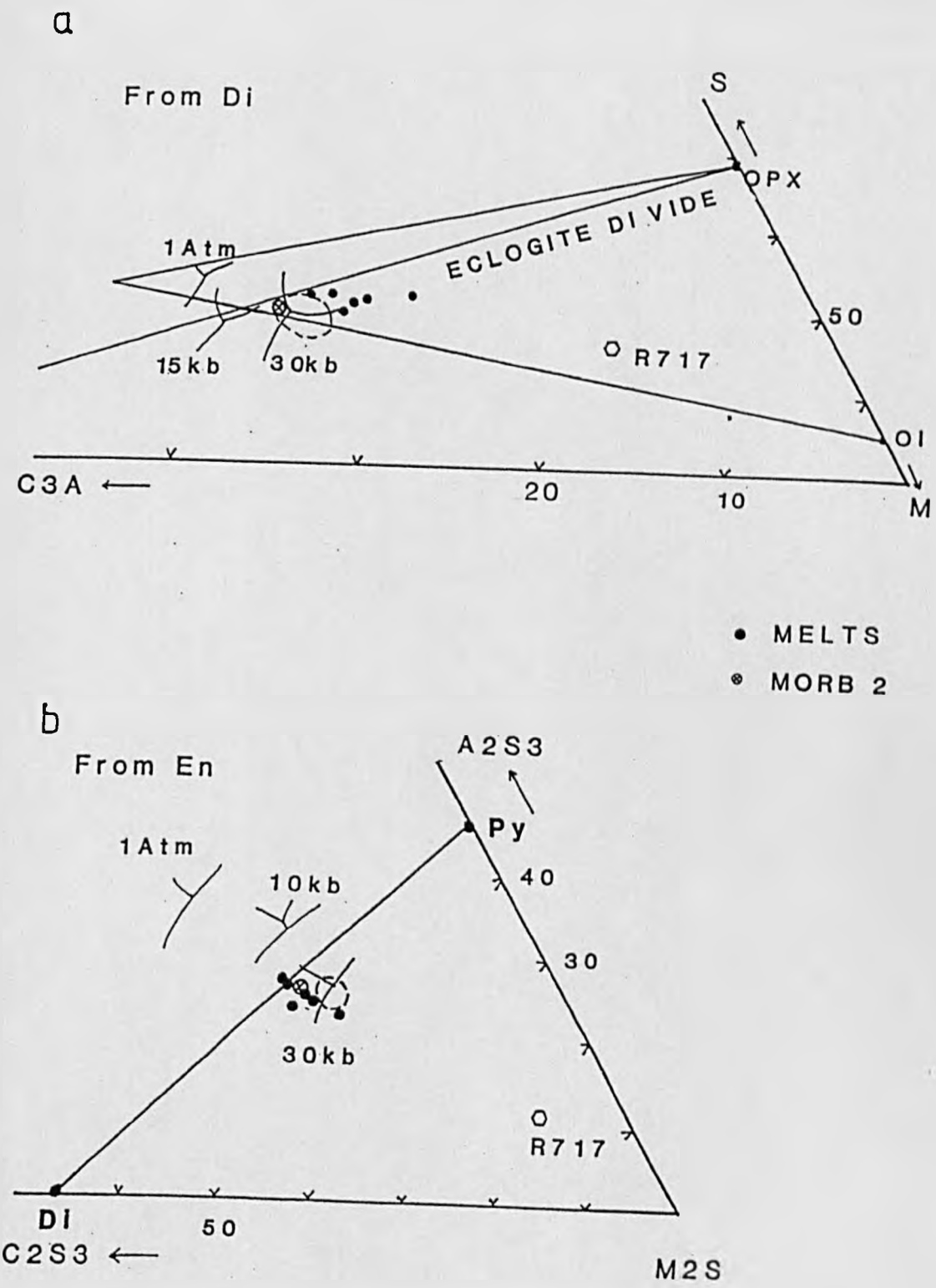

Figure 5.12a CMAS projection from *diopside* into C_3A, M, S (O'Hara 1968) showing calculated equlibrium melts from the peridotites (solid circles). Circle with cross = primary MORB composition of Green et al (1979), Table 5.7. Dashed field encloses Baffin Bay picrites of Clarke (1970). Cotectics from Clarke (1970).

Figure 5.12b CMAS projection from *enstatite* into C_2S_3, M_2S, A_2S_3. Dashed dield encloses Baffin Bay picrites. Cotectics from Clarke (1970). Solid line is GT-CPX thermal dévide at high pressure (O'Hara).

reflection of the lower degree of analytical precision for this element at relatively low abundances. The Baffin Island picrites, the proposed primary MORB composition of Green et al (1979), and the picrite from New Georgia (Table 5.6) all plot within the general field occu pied by the equlibrium melts from the Beni Bousera peridotites.

In conclusion, the major element compositionsof the Beni Bousera peridotites are consistent with an origin as residues of partial melting at pressures as high as 30kb which produced melts of picritic composition. There are two possible causes for the near-linear major element trends defined by the peridotite suite analysed. 1: The complete or incomplete extraction of a compositionally uniform melt. 2: Extraction of a compositionally variable, picritic melt formed due to varying degrees of melting. Major element data alone are not capable of distinguishing between these two alternatives. The calculated melts produced from the Beni Bousera peridotites by major element modelling techniques are similar to relatively Si-rich high pressure melts that occur in subduction related environments.

5:4 Garnet lherzolites

Petrographic and mineral chemistry data presented in Chapters 2 and 4 indicate that the garnet lherzolites originate due to shear-induced mixing of garnet clinopyroxenites and spinel lherzolites followed by high temperature bulk re-equilibration. This is consistent with the theory expounded by Obata (1980) who emphasised that whether the Ronda garnet lherzolites were primary or due to mixing they have totally equilibrated to garnet-bearing peridotites. Frey et al (1985) discarded mechanical mixing as a viable mechanism for producing the Ronda garnet lherzolite compositions on the basis of their lack of anomalously high Al_2O_3 contents which would be expected to result from mechanical addition of garnet. Frey et al (op. cit.) considered only the addition of garnet by mechanical mixing. Considering Beni Bousera, if a garnet clinopyroxenite whole rock composition is used as a mixing end member along with a spinel lherzolite from an area immediately adjacent, then mechanical mixing is a feasible means of producing garnet lherzolites. A least squares mixing calculation using the method of Wright and Doherty (1970) indicates that the major element composition (Si,Al,Ti,Fe,Mg,Ca,Na) of garnet lherzolite GP24 can be adequately generated by mixing of ~ 16 % garnet clinopyroxenite (GP20) and 84 % spinel lherzolite (GP224). The calculation yields very good residuals (0.11) if all elements are given equal weightings to eliminate undue weight being given to low concentration elements such as Na and K for which analytical error is greater at low concentrations. The calculation works equally well with various garnet clinopyroxenite and spinel peridotite end-members, only the proportions of the mixing end-members change. Like the Ronda garnet peridotites, those from Beni Bousera lie on the same compositional trend as their associated garnet free peridotites. This linearity is entirely consistent with addition of garnet clinopyroxenite which is virtually equivalent to re-fertilization of the peridotite with a basaltic component which in turn accounts for the generally more fertile, relatively low MgO compositions (Table 5.2) of the garnet peridotites compared with the spinel bearing peridotites.

5:5 Trace Elements.

5:5.1 Highly compatible trace elements: Nickel.

Nickel abundances in the peridotites show a positive correlation with MgO content (Fig 5.3), however, the correlation is not good at low MgO contents, where peridotites with MgO contents of approximately 40 wt % show a 150 ppm variation in Ni content. The total Ni variation is from 2008 to 2517 ppm (Table 5.1). This relatively narrow range in Ni concentration throughout the peridotite suite is consistent with derivation of the peridotites as residues of partial melting rather than as olivine rich cumulates from a basic/ultrabasic magma as postulated by Mikailov (1975). Olivine rich cumulates show a much greater range in Ni content over a given increment of F (the percentage of the rock which has crystallized). This principle is illustrated in Figure 5.13 a + b. In Figure 5.13a a "melting grid" and "crystallization grid" are defined by modelling partial melting and fractional crystallization of a source similar to R717 for variation in Ni compared with the relatively incompatible major element Al. Assuming solid/liquid partition coefficients of 10 for Ni and 0.1 for Al, which remains constant in the model but not in reality, the suite forms a relatively linear correlation on Figure 5.13a, with a shallow negative slope away from R717 indicative of derivation by partial melting. Most of the data plot close to equilibrium melting boundary line for between ~ 7 and > 30 % melting of a source equivalent to R717, a result similar to that obtained by modelling major elements only.

The narrow range of Ni contents in the Beni Bousera peridotites is also plotted on Figure 5.13b, taken from Frey et al (1985), to illustrate how Ni varies much more widely in an accumulating solid during fractional crystallization than in residues from partial melting. Examination of Figure 5.13b indicates that over the range of partial melting calculated for the Beni Bousera peridotites, the Ni content of the residual solid changes by only 33 % (for a range of K_Ds) whereas an equivalent range of crystallization (F=30%) using even the lowest Ni solid/liquid partition coefficients produces a factor of 4 variation in Ni concentration.

Figure 5.13c is a plot of MgO (mole %) in the residue versus Ni ppm for Beni Bousera peridotites. The two lines labelled are taken from Frey et al (1985) calculated using the approach of Hanson & Langmuir (1978), the upper line is calculated using the temperature dependent equation for partitioning of Ni between olivine and melt whilst the lower line is calculated using the composition dependent equation for $K_D{}^{ol/melt}{}_{Ni}$ of Hart and Davis (1978) $K_D{}^{ol/melt}{}_{Ni} = 124.13/MgO-0.897$. Both lines were calculated for temperatures of 1600 ^oC (isotherms taken from Fig 5.10). The Beni Bousera peridotites show a scattered distribution around the upper, temperature dependant line, the approximate values of F (degree of melting) along this line correspond fairly well to those estimated for the same samples using the major element approach. For example, GP189 is estimated to be a product of ~ 23 % melting of a source equivalent to R717 compared to the 22.9 to 21.1 % range in F calculated assuming differing values of the (Fe/Mg) olivine/melt exchange coefficient (K_D) in Table 5.7. Some samples however do plot close to the, composition dependant line in Figure 5.13c. Frey et al (1985) found that the Ronda peridotites more closely matched the trend calculated using the composition dependant equation of Hart and Davis (1978), however this equation would only simulate the trend of the majority of the Beni Bousera data at temperatures above 1600 ^oC.

Figure 5.13a Log-log plot of Ni vs Al (cation units) for anhydrous Beni Bousera peridotites. Horizontal field is calculated spectrum of residues produced by fractional (f) and equilibrium (e) partial melting (0-30 %) of a source equivalent to R717 assuming bulk solid/liquid partition coefficients for Ni of 10 and 0.1 for Al. Vertical field is calculated cumulate compositions obtained from a liquid in equilibrium with a harzburgite residue containing ~ 0.7 wt% Al_2O_3 and 2200 ppm Ni for 0-30% fractional (F) and equlibrium (E) crystallization.

Figure 5.13b Theoretical C^s/C^o (Ni in solid/bulk system) variation during fractional melting and fractional crystallization for various bulk solid / liquid partition coefficients (D). Horizontal axis (X) is percent completion of the process ie. 1=100% melting or crystallization. The model assumes constant D and is thus unrealistic, but illustrates the wide variation of Ni content of cumulates over a small range of X (solid lines) compared with the restricted range created by melting range indicated by Table 5.7. Modified after Frey et al (1985).

Figure 5.13c MgO (mole %) vs Ni ppm for Beni Bousera spinel peridotites. Upper diagonal line is calculated using the Hanson & Langmuir (1978) approach assuming R717 as the source and the Hart & Davis (1978) temperature dependent olivine/liquid Ni partition coefficients. Lower line is calculated using a compositionally dependent olivine/liquid partition coefficient (Hart & Davis 1978). Numbers next to curves are dgrees of melting as a fraction of 1 where 1 = 100 % melting. Modified from Frey et al (1965).

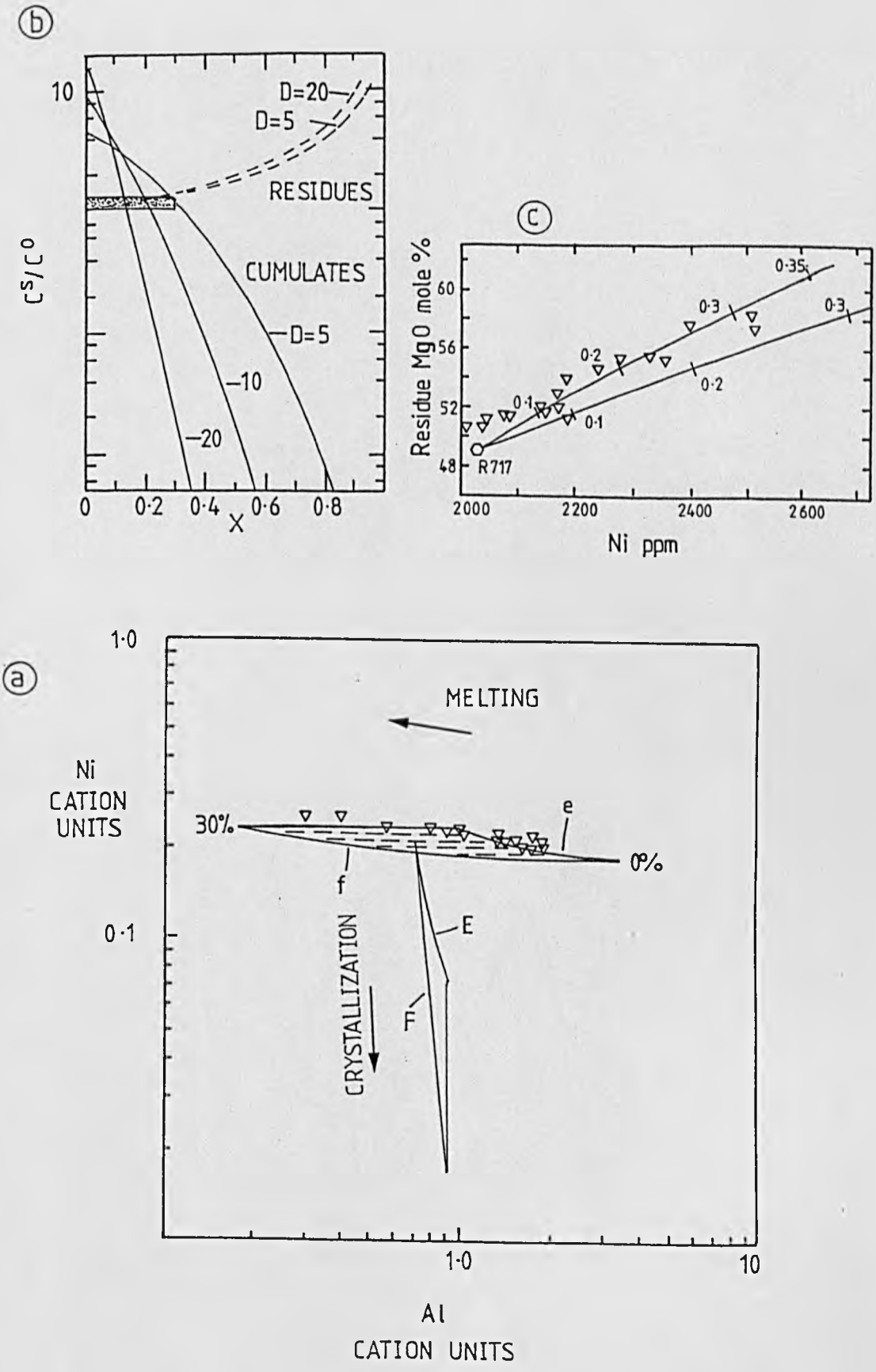
b
10
D=20
D=5
RESIDUES
CUMULATES
D=5
10
20
C^s/C^o
0
0·2
0·4
0·6
0·8
X
c
Residue MgO mole %
60
56
52
48
R717
0·35
0·3
0·3
0·2
0·2
0·1
0·1
2000
2200
2400
2600
Ni ppm
a
1·0
0·1
Ni
CATION
UNITS
MELTING
30%
e
0%
f
E
F
CRYSTALLIZATION
1·0
10
Al
CATION UNITS

The trend shown by MgO-Ni contents of the Beni Bousera peridotites is thus broadly consistent with either melting at ~ 1600 °C with $K_D^{ol/melt}{}_{Ni}$ being relatively insensitive to the MgO content of the equilibrium melt, or that the residues are sensitive to this parameter and underwent melting at ~ 1700 °C i.e. ~ 100 °C hotter than the Ronda peridotites. Melting at 1700 °C in the mantle is probably unrealistic considering the available high pressure experimental data (see reviews by Yoder 1976 and Takahashi and Kushiro 1983). Peridotite GP13 does not appear to correlate with either of these two models, having a lower Ni content (2008 ppm) than the proposed source R717 but being more residual in terms of Mg-Ca-Al concentrations (e.g. 50.74 mole % MgO). The generally increased scatter of NiO contents of samples with lower MgO contents of Figure 5.13 a + c may be evidence for original source heterogeneity in the Beni Bousera peridotites. It must be emphasised that the above calculations of F and equilibrium melt compositions are highly source dependant and hence subject to significant errors when the original source compositions are unknown. The calculations do, however provide valuable estimates of likely source-residue relationships.

Some of the scatter in Ni concentration at lower MgO contents in the Beni Bousera peridotites may be due to the effects of "cryptic" enrichment processes by melts passing through the peridotites, or due to serpentinization and mineralizing fluids passing through the rocks. The presence of Ni mineralized veins which cross cut the main foliation in the peridotites, containing various Ni sulphides and silicates (e.g. garnierite, see Chapter 2) suggest that Ni has been "leached" out of some areas of peridotite, possibly during serpentinization. Humphris and Thompson (1978) found that during hydrothermal alteration of oceanic basalts Ni and Co are redistributed to some extent within the altered rock but without significant modification to the bulk rock composition. However, many examples of residual Ni deposits are known, associated with variably serpentinized peridotites (see review by Coleman 1977) where the concentration of Ni within weathered horizons and veins is regulated by the breakdown of olivine and OPX during serpentinization.Some nickel may also be derived from breakdown of Ni sulphide accessory minerals in the peridotites. Ni and possibly platinum group elements may also be transported as carbonyl complexes during hydrothermal activity which circulates a reducing C-H-O bearing gas phase (Hopwood 1981). Thus Ni may become leached out of some peridotites and perhaps re-precipitated in others to yield secondary intergranular Cu-Fe-Ni sulphide assemblages. Fine grained, late-stage intergranular sulphide phases are not always visible during sample collection (Lorand 1985).

5:5.2 Compatible trace elements : chromium and cobalt.

Cr abundances in the Beni Bousera peridotites exhibit no systematic correlation with MgO content (Fig 5.3). For example, GP178 is the most refractory peridotite in terms of its major element chemistry but contains only 2200 ppm Cr compared to 2806 ppm Cr in GP230, the most fertile Beni Bousera sample. Frey et al (1985) attributed a similarly incoherent Cr-MgO relationship in the Ronda peridotites to heterogeneous Cr distribution (contained mainly in spinel) in the samples collected. The large sample sizes from which the Beni Bousera whole rocks were taken would act to minimize this effect. Maaloe and Aoki (1977) also found Cr to vary independantly of MgO content in 302 spinel peridotite nodules in continental basalts which suggests a bulk solid/melt Cr partition coefficient of approximately 1. Frey et al (1985) suggested that Cr may be incompatible during peridotite melting, the lower Cr contents of basaltic

liquids requiring a subsequent decrease in the Cr content of basalts by chromite fractionation. Frey et al (1985) also suggested that the early loss of Cr from a melt could also be the result of the segregation of the chromium pyroxenite layers from basaltic melt derived from the peridotites as suggested by Dickey (1970) and Obata (1980). Isotopic and trace element evidence presented in Chapter 6 and 7 does not permit the "segregation" of the Cr-Pyroxenites from the peridotites. There is no correlation between peridotite Cr abundance and proximity to pyroxenite layering.

Cobalt abundances in the Beni Bousera peridotites display a crude positive correlation with MgO (Figure 5.3). Co abundances range from ~ 105 to 130 ppm implying a bulk solid/melt partition coefficient for Co of greater than 1 but of lower magnitude than Ni. This is consistent with published estimates of Co solid/melt partition coefficients e.g. Clague and Frey (1982). The scatter in Co at lower MgO contents may represent original source heterogeneity or enrichment processes.

5:5.3 Sc-V-Cu

Scandium, vanadium and copper abundances show general inverse correlations with MgO content (Figure 5.3) implying bulk solid/melt partition coefficients of less than unity. This is consistent with published estimates of partition coefficients for these elements in olivine-pyroxene-melt systems. It is possible to infer the trace-element concentration of equilibrium melts from the peridotites using mass balance considerations. R717 was used as a source and the equilibrium trace element composition of a melt derived by 23 % melting to form the residue GP189 was calculated (Table 5.8). The elements used in the calculations were those for which good analytical precision were obtained by XRF (i.e. those above 10 ppm) for example, Ni, Cr, V, Sc, Co, Cu and Zn. From Table 5.8 it is obvious that the Cr and V contents of the calculated melt are much higher than typical MORB and Cr, Cu and Zn are more comparable to the concentrations recorded in Baffin Island picrites by Clarke (1970) and parental MORB magmas.

Bulk solid/melt partition coefficients for compatible and incompatible trace elements may be estimated from the mass balance equation:

$$C^s/C^o = D^{s/l}_x / D^{s/l}_x (1-F) + F)$$

where C^s and C^o are concentrations of elements in the liquid and solid phases respectively and $D^{s/l}x$ is the bulk solid/liquid partition coefficient for an element x.

By using R717 as the source and a residual solid composition of GP189 (or any other peridotites in Table 5.7) for which F has been calculated on the basis of major element considerations to be 0.23 the bulk solid/melt partition coefficients for an element can be calculated (Table 5.8). Cr, Sc, Co and Cu compare favourably with bulk D values inferred from the literature by Frey et al (1985) whereas V and Zn do not. The poor comparison of calculated and published bulk D values of V and Zn could reflect analytical errors or atypical values for these elements due to heterogeneous spinel distribution in the residue chosen for the calculation, ie. GP189. Despite discrepancies in the magnitude of the calculated bulk D values the relative order of decreasing bulk solid/melt partition coefficients presented in Table 5.8 is that expected for olivine rich solids i.e. Cr > Co > Zn > Sc > V > Cu. These data are consistent with a residual origin for the Beni Bousera peridotite suite, however the large degree of scatter of some of the correlations is not

TABLE 5.8 Calculated solid/melt ($D^{s/l}$) partition coefficients and equilibrium melt concentrations for Sc, V, Cr, Co, Cu and Zn for Beni Bousera spinel peridotites assuming sample GP189 was generated by 23% equilibrium melting of a source equivalent to R717.

	Calculated $D^{s/l}$ Beni Bousera	$D^{s/l}$ Published	Abundance in MORB	Abundance Baffin Is.	Abundance in B.B. Equilbm Melt
Sc	0.29	0.2-0.4	41		33
V	0.22	0.13	196		338
Cr	2.64	1.4	569	1850	1389
Co	1.48	1.4-2.6	50		85
Cu	0.04		87	109	101
Zn	0.49	0.8	122	58	86

MORB abundances taken from Frey et al (1985), Baffin Island picrite abundances from Clarke (1970).

consistent with their derivation from a compositionally homogeneous source during a single partial melting event.

5:5.4 Highly incompatible elements : Sr + Nd

The variation in highly incompatible trace element abundances in a suite of residual peridotites has the potential to distinguish between the various petrogenetic models proposed above for the Beni Bousera peridotites. Models involving variable degrees of melting of a source with complete extraction of melt will produce non-linear correlations between major elements and highly incompatible trace elements. Incomplete extraction of melt from peridotites undergoing a uniform degree of melting will lead to linear relationships between major and trace elements (Frey et al 1985). Due to the low concentrations of highly incompatible trace elements in the Beni Bousera peridotites, only Sr and the REE elements were analysed to a high degree of precision. The REE as a group of elements are considered separately in the next section; however Nd was selected as a highly incompatible element for petrogenetic modelling. La was not used as it was not successfully analysed in all the samples for which REE data were obtained. La analyses may also be subject to Ba interference during isotope dilution analysis. Ce was not successfully analysed on all samples run for REE (Table 5.5). Sr analyses were performed by XRF, and 5 non-leached whole rock samples were also analysed for Sr by isotope dilution (I.D.).The consistency of the results was found to be good, even for Sr abundances as low as 5 ppm, with maximum variations of 15 % between XRF and I.D. The I.D. data are reported in Table 5.1 in peference to the XRF analyses. Finely powdered whole-rock samples were not leached prior to Sr I.D. analyses because the generation of chlorides on the surfaces of the finely divided particles causes significant weighing errors.

Sr and Nd abundances are positively correlated with Al_2O_3 and inversely correlated with MgO content (Figure 5.14). In contrast to the major element relationships, the incompatible element trends are not linear and are more accurately described by curved trajectories, although the Nd vs Al_2O_3 or MgO trend relies heavily on the two low abundance points at 0.3 and 0.1 ppm respectively which could be subject to the largest analytical errors. Errors for Nd by I.D., even for low abundances (~0.1 ppm) are generally better than 1 % maximum (Thirlwall 1982, see Appendix 4). Models involving a uniform degree of melting of the source followed by incomplete and variable degrees of melt extraction would lead to linear relationships in Figure 5.14 (Frey et al 1985). The high degree of scatter at low Sr and Nd abundances preclude such a linear relationship and favours models requiring partial or complete extraction of compositionally variable melts formed over a wide range of melting. Melting of a compositionally heterogeneous source, in terms of major and trace elements, must also be considered as the trends for major and trace elements do not define perfect linear or curvilinear trajectories.

The scatter observed in incompatible element trends for the Beni Bousera peridotites may also be enhanced by other factors. Late-stage alteration and low-grade metamorphism during peridotite emplacement may substantially affect Sr abundances in the peridotites (and pyroxenites). These effects of secondary contamination of whole rock samples have been documented by leaching experiments on whole-rocks and CPX separates (Chapter 6, Zindler et al 1983 and Polve 1980). Possible variations in partition coefficients during melting and the possible presence of variable amounts of trapped melts in the residues may also generate deviations from ideal geochemical trends.

Figure 5.14 a & b. Sr and Nd (ppm) vs MgO (wt%) for Beni Bousera peridotites, c & d; Sr and Nd (ppm) vs Al_2O_3 (wt%).

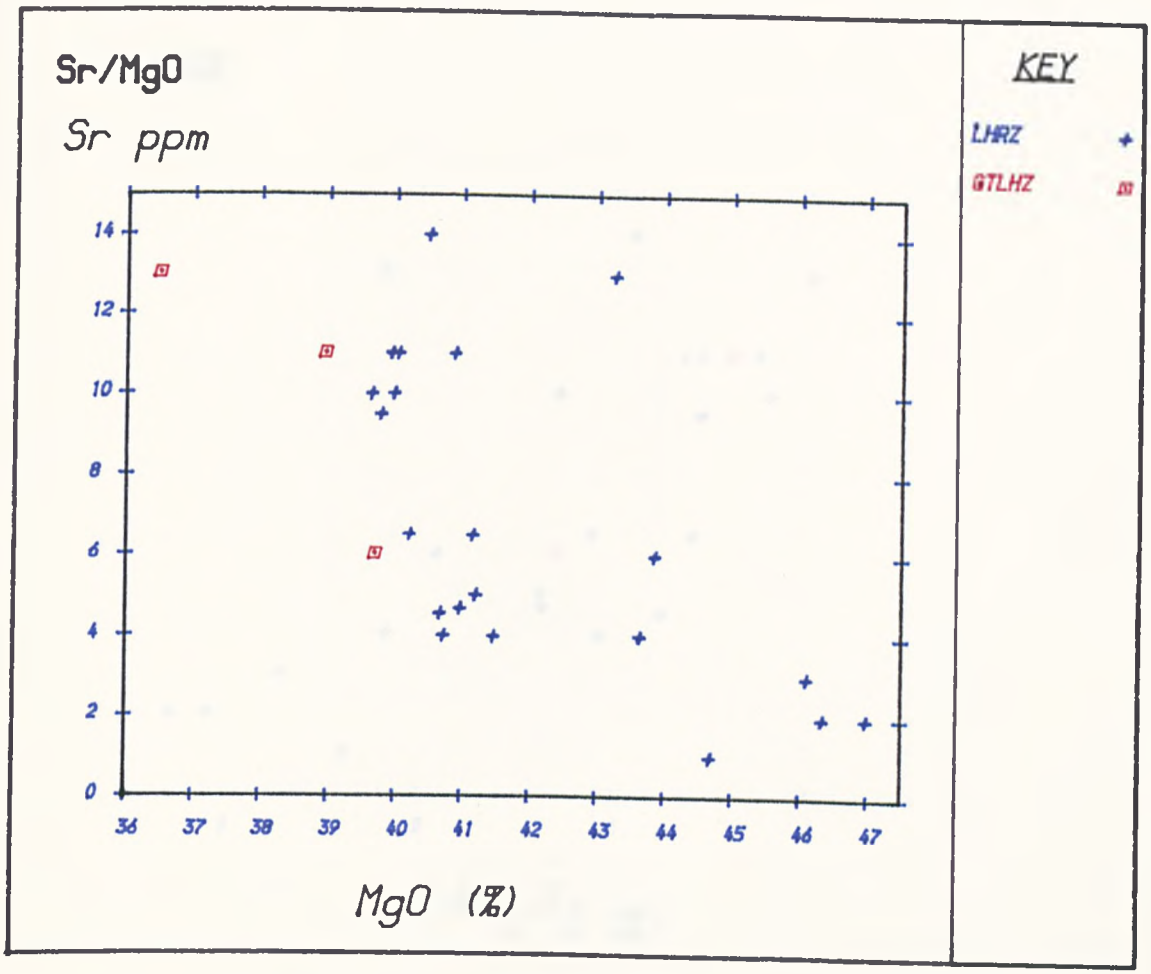
Sr/MgO
Sr ppm
14
12
10
8
6
4
2
0
36
37
38
39
40
41
42
43
44
45
46
47
MgO (%)
KEY
LHRZ
GTLHZ

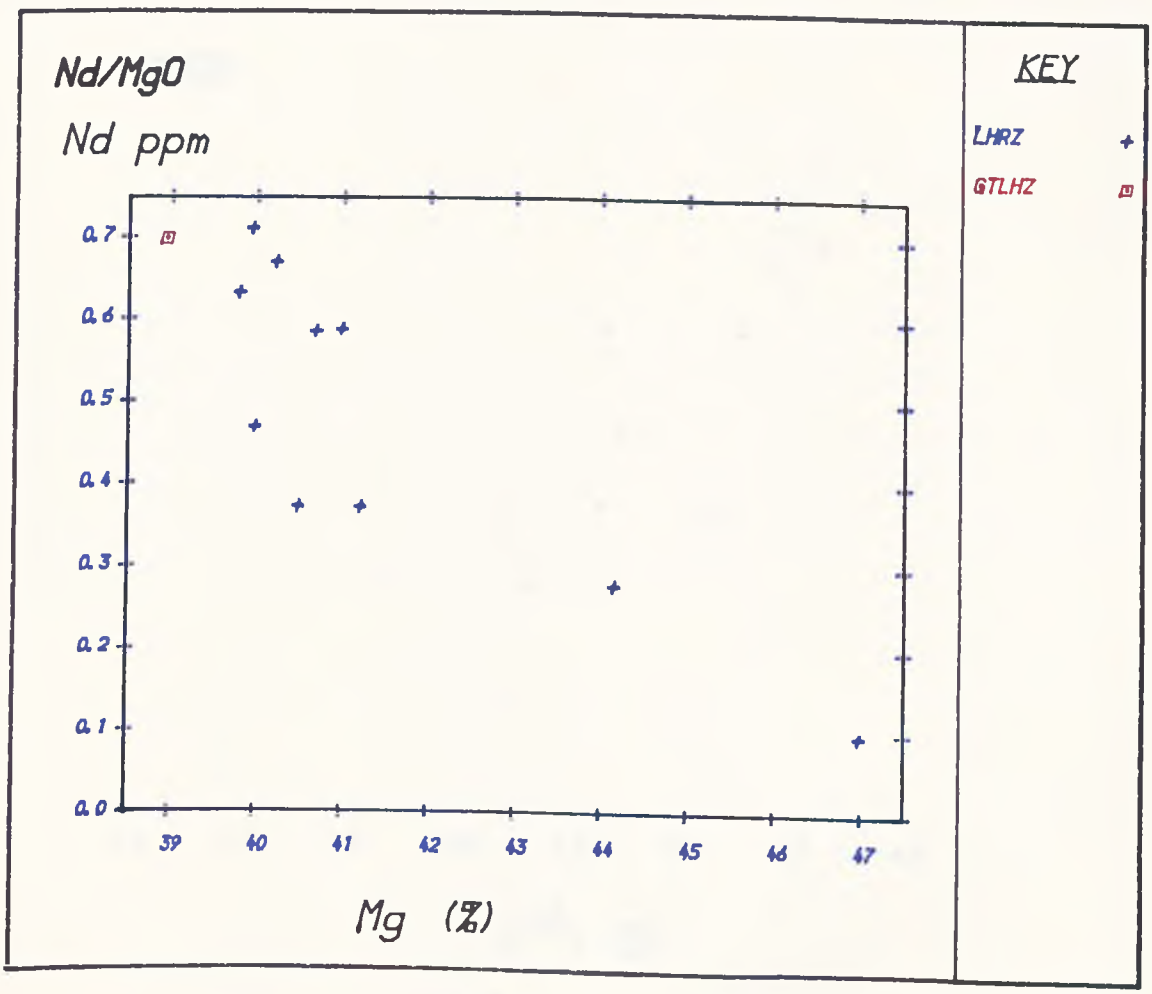
Nd/MgO
Nd ppm
0.7
0.6
0.5
0.4
0.3
0.2
0.1
0.0
39
40
41
42
43
44
45
46
47
Mg (%)
KEY
LHRZ
GTLHZ

Sr/Al203

Sr ppm

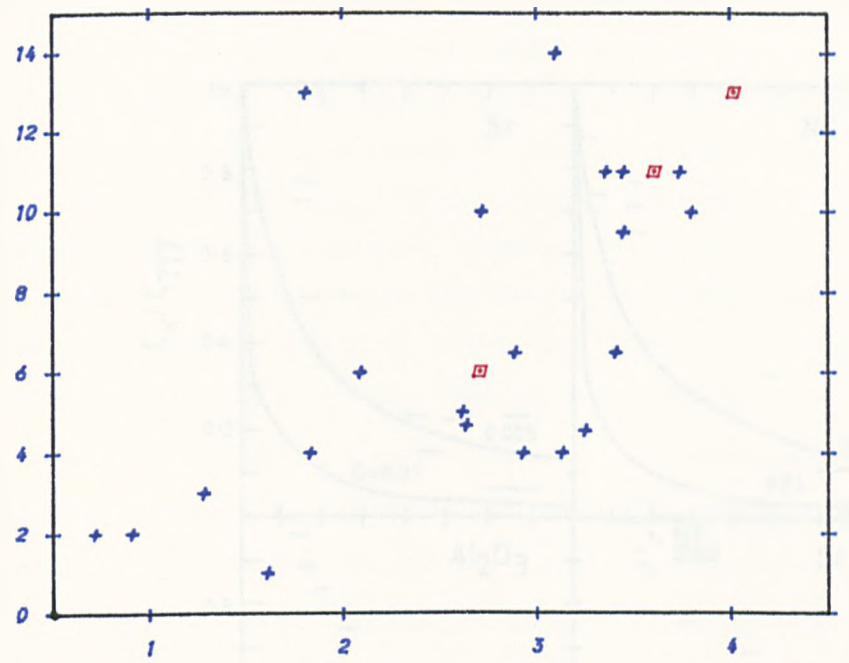

KEY

LHRZ +

STLHZ ⊡

Nd/Al203

Nd ppm

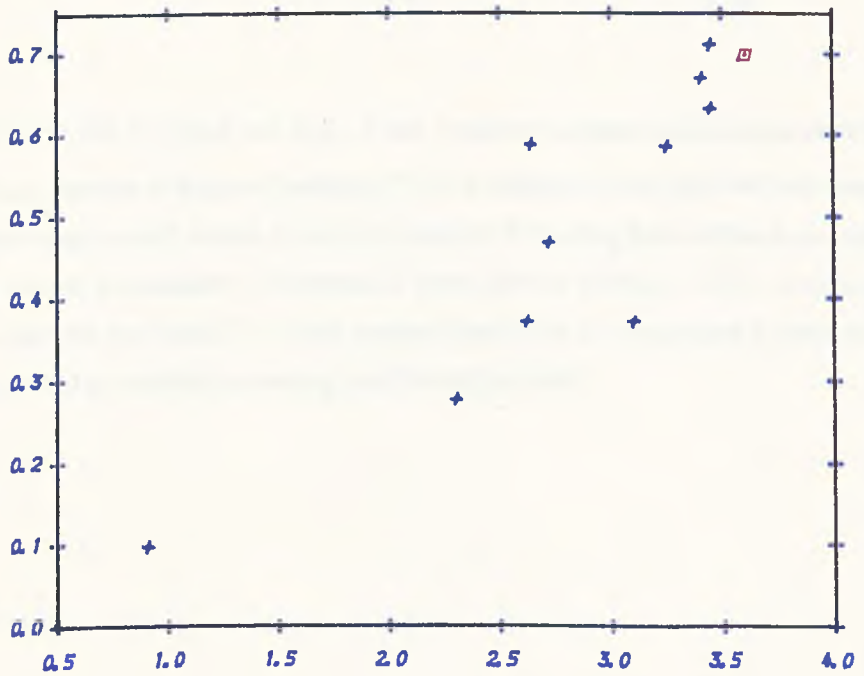

KEY

LHRZ +

STLHZ ⊡

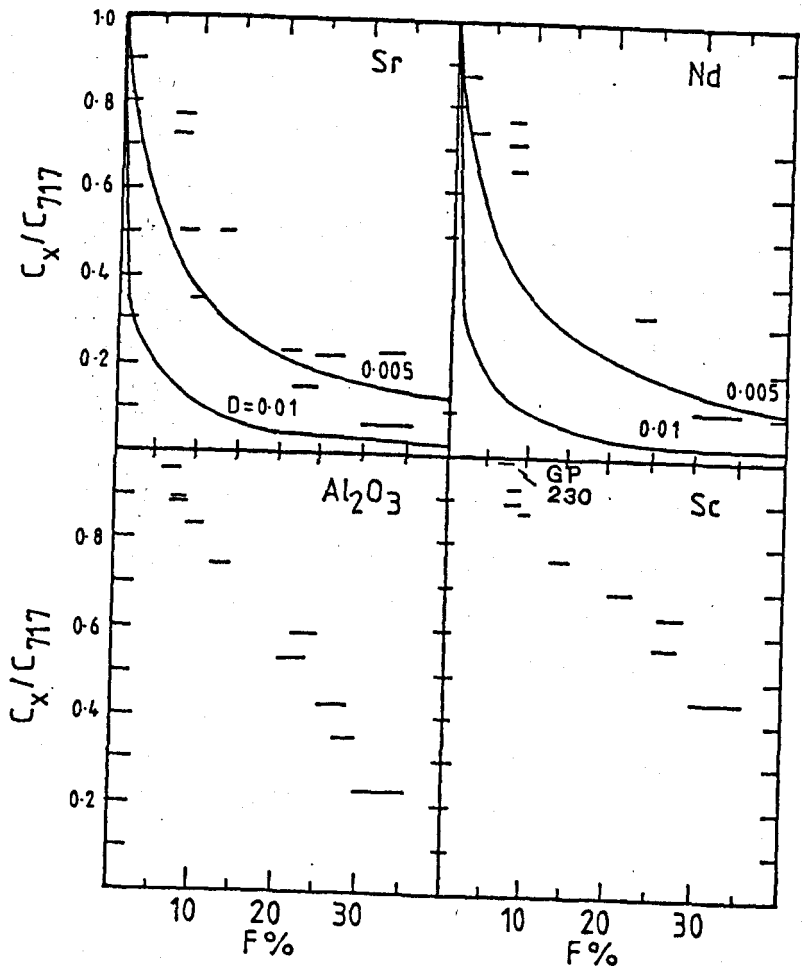

Figure 5.15. Sr, Nd, Sc (ppm) and Al_2O_3 (wt%) relative to concentration in sample R717 of Frey et al (1985) as a function of degree of melting (F) in % calculated from MgO-FeO relationships (see text). Horizontal range of each sample point is the range of F resulting from different assumptions about the residual olivine composition (Maximum F when olivine Fe/Mg = R717, minimum when Fe/Mg olivine = sample, see Table 5.7). Only samples from Table 5.7 are plotted. Curves are trajectories of residues formed by equilibrium melting with D= 0.05 and 0.01.

Residue/source concentrations of Sr, Nd, Sc and Al_2O_3 were calculated for 10 Beni Bousera peridotites assuming they are residual from a source similar in trace element composition to the Ronda peridotite R717 (Figure 5.15). Degrees of melting, F, were calculated using equation 5.2 and assuming a variety of residual olivine/melt K_Ds (resultant variation in F shown by horizontal lines in Figure 5.15). Considering the highly incompatible elements Sr and Nd, most of the samples define curved trajectories of rapidly decreasing Sr and Nd concentrations as F increases. The trajectories are similar to the $D_{Nd\text{-}Sr}$ = 0.05 curve in Figure 5.15. No samples lie significantly off this trend for both Sr and Nd, hence the 10 samples considered here can be interpreted as residues formed by variable degrees of equilibrium melting of a source similar to R717 where the melt produced was completely segregated from the residue. Retention of 0-50 % trapped melt in the residue during melting would create linear trajectories on Figure 5.15. The 10 samples in Figure 5.15 included 2 anomalously enriched in FeO. The high ΔFeO peridotite samples (ΔFeO> 0.25%) do not show any *consistent* variation in trace element geochemistry with respect to the other peridotites suggesting the samples have suffered only FeO enrichment or have been derived from a source significantly enriched in FeO. Although LREE are enriched in some high ΔFeO samples eg. GP132(3) CPX, the sample with the highest ΔFeO value , GP88, shows no significant LREE enrichment. It is considered unlikely that the Beni Bousera peridotite samples represent the product of low degrees of fractional melting because none of the samples analysed show the magnitude of depletion in incompatible elements required for even low degrees of fractional melting.

The curvilinear trends shown by Nd and Sr contrast sharply with the rectilinear trends shown by the moderately incompatible elements Al and Sc (Figure 5.15). Such rectilinear trends are expected in residues from < 30 % equilibrium melting.

Finally, the C^R/C_{717} value of unity for sample GP230 for Sc in Figure 5.15 is not expected for a sample of more residual major element character than R717 the model source. This further supports the possibility that the Beni Bousera peridotite suite was derived from a source that was slightly heterogeneous in terms of both major and trace elements.

5:5.5 Rare earth elements (REE).

All the samples except GP89 a have LREE/HREE ratios less than chondrites (Table 5.3, Figure 5.4 a and b). HREE (Dy-Lu) in the lherzolites range from ~ 0.75 to 1.7 x chondrite and are comparable to other orogenic lherzolites (see review by Frey 1984), suggesting that large portions of the upper mantle are slightly enriched in HREE relative to ordinary chondrites (Frey et al 1985). The harzburgite sample GP178 is significantly more depleted in HREE, $(Yb)_n$ = 0.13 and also shows evidence of LREE enrichment. Most of the lherzolites have a relatively restricted range in $(Ce/Yb)_n$ from 0.228 to 0.495, except that GP89a has $(Ce/Yb)_n$ = 1.84 whilst harzburgite GP178 has $(Ce/Yb)_n$ = 1.08. Significantly, both these samples have anomalous, high FeO contents with ΔFeO contents of 0.6 and 0.52 respectively (Table 5.5). However, the sample with by far the highest ΔFeO in Table 5.6 shows no indication of LREE enrichment ie $(Ce/Yb)_n$ = 0.495. The only garnet lherzolite analysed, GP24, is slightly more HREE

enriched than the spinel lherzolites and possesses a slight negative Eu anomaly. Eu anomalies are absent from the whole-rock spinel lherzolites. The negative Eu anomaly in GP24 is further support for the origin of the garnet lherzolites by mixing of spinel lherzolites and garnet pyroxenites which commonly have negative Eu anomalies.

LREE abundances for the non LREE enriched rocks (i.e. $(Ce/Yb)_n < 1$) vary from 0.6 to 0.25 x chondrite. This feature is consistent with the analysed peridotites representing residues from varying degrees of melting of a compositionally homogeneous source. This simple model is not supported by the complicated intersecting relationhips on Figure 5.4, or by the lack of correlation of $(Ce/Yb)_n$ with residual major element characteristics. The alternatives to explain the intersecting nature of the REE patterns in Figure 5.4 and the lack of $(Ce/Yb)_n$ correlation with degree of residual character are :

1) If peridotites are derived from a homogeneous source, the variations are due to analytical errors, alteration or possible REE partition coefficient variation during melting.

2) The peridotites are the residua of melting a compositionally heterogeneous source.

3) The peridotites originate from a compositionally homogeneous source but have experienced melting under different conditions i.e. under garnet and/or spinel facies conditions.

4) A combination of 2 and 3.

Alternative 1 seems unlikely in that the REE have been analysed by I.D. to a high level of reproducibility and the acid leached CPX from some of the same samples also show crossing REE patterns (Fig. %.3). Additionally, significant secondary alteration of orogenic peridotites produces negative Eu and Ce anomalies (Ottonello et al, 1979). A compositionally heterogeneous source is attractive in terms of explaining the irregularity of the observed REE trends and some of the scatter of the major and trace element correlations observed above. The lack of correlation of $(Ce/Yb)_n$ with residual major element characteristics such as Al_2O_3 content may also be explained by melting of a homogeneous peridotite to differing extents in the garnet stability field and then variable extents of melting in the spinel field. This theory was used by Loubet et al (1975) to explain the trends of the Beni Bousera (and Lanzo) peridotites on a $(Ce)_n$ vs $(Yb)_n$ diagram. Plots of $(Ce)_n$ vs $(Yb)_n$ (Figure 5.16a) are useful for attempting to estimate whether the melting event which depleted the peridotites occurred in the spinel or garnet stability field (Frey 1984, Davies 1984).

During partial melting of the upper mantle HREE may be only moderately incompatible with the residual solid e.g. $D^{S/L} \sim 0.1$ for spinel facies peridotites, or even slightly compatible e.g. $D^{S/L} \sim 1$ for garnet peridotites. Hence, variations in HREE abundances (e.g. Yb) in residual solids provide information about the mineralogy of the residue during the melting process. The Beni Bousera data form a relatively large spread on Figure 5.16a. The two LREE enriched samples plot about the $(Ce/Yb)_n = 1$ line and cannot be modelled as residues from any known melting process on the basis of REE alone. If we assume

Figure 5.16a. Chondrite normalized Ce vs Yb plot for Beni Bousera peridotites. Shaded field covers residues between 0-20% equilibrium and 0-4% fractional melting of a spinel peridotite source with 2 X chondritic REE abundance. Garnet peridotite field (clear) boundaries from 0-18% equilibrium melting and 0-2 % fractional melting. Model fields calculated using the following parameters:

Partition coefficients: set 2 of Frey et al (1978).
Initial mode, spinel peridotite: 55% Ol, 25% OPX, 20% CPX
garnet peridotite: 55% Ol, 25% OPX, 10% CPX, 10% GT.

Melting proportions; spinel peridotite: CPX:OPX:Ol = 0.6:0.2:0.2
garnet peridotite: CPX:GT:OPX:Ol = 0.4:0.4:0.1:0.1

Dashed line indicates equilibrium melting trajectory using REE partition coefficients of Loubet et al (1975) for spinel peridotite. (After Frey 1984).

Figure 5.16b. Chondritic normalized Nd vs Sm for Beni Bousera peridotites compared to other orogenic and ophiolitic peridotites and MORB glasses. Modified after Menzies (1984) . Fields marked "Beni Bouchera" are data from Menzies (1984) and Loubet and Allegre (1982).

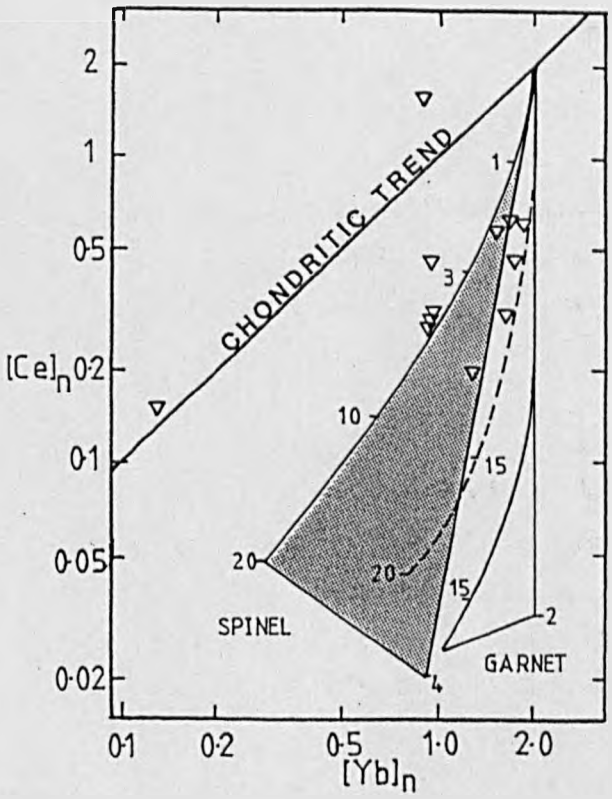
CHONDRITIC TREND
SPINEL
GARNET
[Ce]n
[Yb]n
2
1
0·5
0·2
0·1
0·05
0·02
0·1
0·2
0·5
1·0
2·0
1
3
10
15
20
20
15
2
4

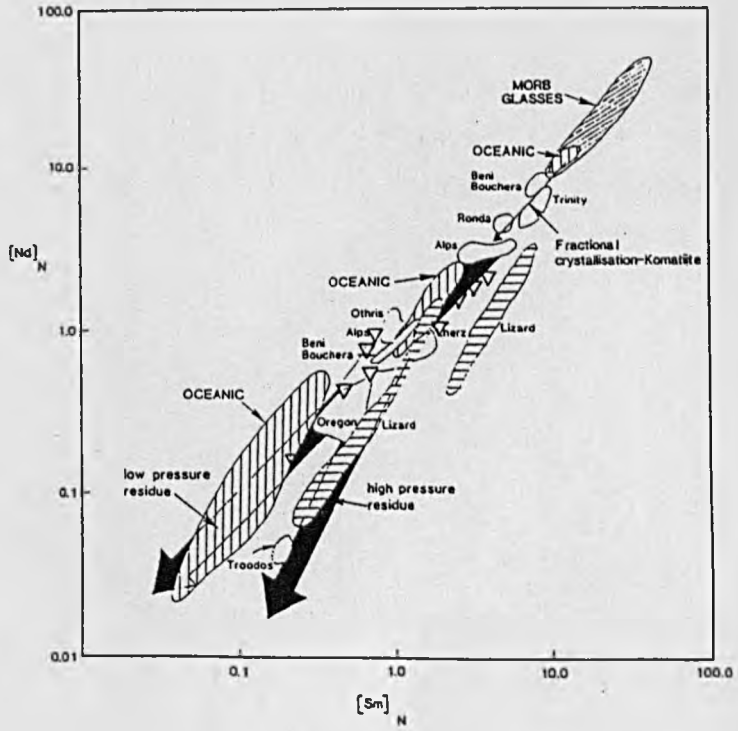
MORB GLASSES
OCEANIC
Beni Bouchera
Trinity
Ronda
Alps
Fractional crystallisation-Komatiite
OCEANIC
Othris
Alps
Beni Bouchera
Lherz
Lizard
OCEANIC
Oregon
Lizard
low pressure residue
high pressure residue
Troodos
[Nd]N
[Sm]N
100.0
10.0
1.0
0.1
0.01
0.1
1.0
10.0
100.0

that only LREE have undergone significant enrichment in sample GP178 we can use the Yb abundance to estimate melting conditions for this sample which is the most depleted in terms of major elements. Depending on the melting model and partition coefficients used, the very low Yb abundance in GP178 can only be generated by > 25 % batch melting of a *spinel* facies lherzolite. The degree of melting calculated for GP178 is reasonably consistent with the degree of melting inferred from major element considerations for this sample (29-36 %). Batch melting in the garnet stability field requires unrealistically high degrees of melting (> 50 %). Fractional melting would produce extremely rapid depletion of Ce and insufficient depletion of Yb. The LREE depleted samples show a large degree of variation in Yb_n on Figure 5.16a ranging from the edge of the batch melting line for garnet peridotites to outside the melting field for either batch or fractional melting using the assumption in the figure captions. The melting trends in Figure 5.16a are very model dependent and the low Yb_n samples do plot close to the batch melting trend defined using the melting parameters of Loubet et al (1975).

The salient conclusion from Figure 5.16a is that the large degree of variation shown by Ce and paticularly Yb in the spinel peridotites is difficult to explain in terms of single stage melting of a homogeneous source. The data permit a multistage melting model involving small degrees (> 5 %) of melting in the garnet peridotite stability field followed by varying degrees of melting in the spinel peridotite stability field. Samples GP12 and GP13 were taken from less than 50 m apart and show greatly differing $(Ce/Yb)_n$ ratios (0.228-0.433) due to their markedly different Ce contents (0.302 to 0.591 respectively). GP12 could be a product of ~ 8 % equilibrium melting of a spinel lherzolite using the partition coefficients of Loubet et al 1975. However, the greater Ce content of GP13 content requires it to be the product of ~ 5 % melting in the spinel stability field (Fig. 5.16a). Major element data suggest that these two peridotites are the products of very similar degrees of melting (8-9 %). The chondrite normalized REE plot of GP13 (Fig. 5.3) does not indicate that this sample has suffered any LREE enrichment, thus the original lherzolite source composition may have been heterogeneous in its REE content on the scale of tens of metres. Given the large effects of varying partition coefficients in Figure 5.16a it is not possible to assess whether the scatter in Yb contents is due to melting in two different environments or due to REE heterogeneity in the source. On a plot of $(Nd)_n$ vs $(Sm)_n$ (Fig. 5.16b) the Beni Bousera peridotite whole rock samples form an elongated trend parallel to the " low pressure residue trend " of Menzies (1984) which is indicative of varying degrees of melting in the spinel or plagioclase stability field. As none of the Beni Bousera peridotites contain significant Eu anomalies (except GP24) the melting is likely to have taken place in the spinel peridotite stability field from a source > 1 x chondritic REE abundance. The Beni Bousera data overlap the two fields marked for "oceanic peridotites" in Figure 5.16b and are distinctly different to the highly LREE depleted Lizard peridotites (Davies 1984). The data do not preclude melting from an originally heterogeneous source, nor do they rule out some degree of melting in the garnet peridotite stability field.

In summary, the REE data for the Beni Bousera peridotites indicate that the dominant melt extraction event which created the suite of residual peridotites occurred in the spinel peridotite stability field with some (prior ?) melt extraction possibly in the garnet stability field. Major element data presented previously suggested that the equilibrium melts extracted from the peridotite suite were similar to natural and experimental melts produced at a range of pressures (15-30 kb) by anhydrous partial melting of peridotite.

5:5.6 Summary of peridotite petrogenesis.

The major and trace element abundance trends defined by the Beni Bousera peridotites may result from the subtraction of a partial melt component of approximately constant composition. The residual compositions would move directly away from the extracted composition forming an extraction line. The linearity of this line is dependant on the constancy of the extracted melt composition and the compositional heterogeneity of the source. Melting of a four phase lherzolite produces a pseudo-invariant liquid composition (Yoder 1976). Therefore, if the peridotites from different parts of the massif were formed by varying degrees of melting, significant deviation from a linear extraction line should theoretically represent source heterogeneity. Incompatible trace element abundances and correlations suggest that batch melting was the dominant process which generated the observed major and trace-element trends in the peridotites. The calculated equilibrium melt compositions extracted from the peridotites assuming a source similar to PUM (Hart and Zindler 1986) is picritic. This equilibrium melt is similar to melts produced by natural and experimental melting of anhydrous peridotite from between 30-15 kb, with high SiO_2 contents resembling some picrites from subduction related environments. The results from major element modelling can be reconciled with REE data via a model involving generation of the residual peridotite suite by varying degrees (< 35 %) of partial melting in the garnet and/or spinel peridotite stability field during diapric ascent and decompression, the peridotites remaining close to the solidus during ascent from the garnet stability field. The source peridotite may have been compositionally heterogeneous in terms of major and trace-element composition however any source variation is difficult to quantitatively constrain due to the operation of second order processes such as alteration which act to disperse correlations.

Some peridotite samples, frequently those located close to pyroxenite layers, have suffered FeO and possibly synchronous LREE enrichment, however, GP88, the most FeO enriched sample shows no evidence of LREE enrichment. The FeO enrichment is could be related to the formation of the pyroxenite layers. The apparent lack of correlation between LREE and FeO enrichment is reconcilable with the observation that few of the liquids in equilibrium with CPX's from the pyroxenite layers are LREE enriched.

The range in partial melting experienced by different members of the Beni Bousera peridotite suite (~ 5 to > 30 %) is much higher than the range inferred by the REE data of Loubet et al (1975), Menzies and Murthy (1978), Polve and Allegre (1980) and Loubet and Allegre (1982), probably due to the small, non-representative sample sets studied by these authors. The range of melting inferred for the Beni Bousera samples is comparable to that calculated for the Ronda peridotites studied by Frey et al (1985). The Beni Bousera peridotite body is apparently composed of a greater proportion of residual, MgO-rich, Ca and Al-poor peridotites than Ronda.

5:6 PYROXENITES: Whole rock geochemistry.

5:6.1 Major element chemistry

Whole rock major and trace element data for pyroxenites from Beni Bousera are presented in Table 5.3 and REE data are presented in Table 5.9. REE data for pyroxenite mineral seperates are listed in Table 5.10. Whole rock fine powders were not leached prior to REE analyses due to the large weighing errors resulting from the build up of chloride/fluoride grain boundary layers. CPX and GT separates were leached according to the procedure given in Chapter 6.

The major element compositions of the pyroxenites superficially resemble those of picritic basalts. MgO contents of the GP layers vary from 11.8 to 19.5 wt % (mostly > 14 wt %) whereas the GGP layers range to slightly lower MgO contents, 10.8 (GP81) to 15 (GP147) wt %. The difference in MgO contents between the two GGP layers is reflected in their mineral chemistry. Garnets from the low MgO layer (GP81) have pyrope contents of ~ 39 to 42 % whereas those from GP147 have pyrope contents ranging up to 56 %. MgO contents of websterites range from ~ 15 % up to > 30 % for the samples richer in OPX (e.g. GP188). The major difference between the less MgO rich pyroxenite layers and picritic basalts is the low abundance of Na_2O and particularly K_2O, TiO_2 and P_2O_5 in the pyroxenites (compare with Baffin Island picrites in Table 5.7). The low abundance of total alkalis in the Beni Bousera pyroxenites is illustrated in Figure 5.17. An iron enrichment "fractionation" trend is also evident with the GGP generally plotting at the low Mg/Fe end of the trend but with no significant increase in total alkalis. On a MgO-CaO-Al_2O_3 diagram (Figure 5.18) the pyroxenites occupy a large field extending from highly magnesian compositions (OPXITES) to MORB like compositions. Most of the data fall within the fields defined by ultramafic and mafic cumulates from ophiolite sequences (Fig. 5.18). On the AFM diagram (Fig. 5.17) the GP and GGP plot to more Fe-rich compositions than ophiolitic rocks. The websterites form intermediate compositions between the garnetiferous pyroxenites and the orthopyroxenites. The coexisting marginal OPXITE and central GGP compositions are joined by a dashed line on Figure 5.8.The corundum bearing garnet pyroxenite analysed by Kornprobst et al (1982) is Si-poor and extremely enriched in Al_2O_3 compared to the other pyroxenites (Fig. 5.18).

The pyroxenites range from quartz normative compositions (32 % in GP188) to nepheline normative (maximum GP97, 9.3 % Ne), Figure 5.19. Few of the pyroxenites are picritic in terms of normative mineralogy, the samples plotting mainly in the olivine tholeiitte to alkali olivine basalt/basanite field. The websterite GP188 and the orthopyroxenite GP137 contain ~ 30 % normative quartz. Rocks from a single lithological group span a large range of normative compositional space in Figure 5.19; garnet bearing pyroxenites (GP +/- graphite) range from silica saturated (23 % *Hy* , GP147) to nepheline normative, silica undersaturated (6.3 % *Ne*, GP237), with some specimens plotting close to the critical plane of silica saturation. None of the GGP contain normative nepheline. The garnetiferous pyroxenites from Ronda, analysed by Suen and Frey (1987), are all silica saturated. Also plotted on Figure 5.19 are 3 samples from a composite pyroxenite layer analysed by Kornprobst (1969) which illustrate the change in crystallizing solid composition from the outer margin of the layer (OPXITE) to the layer centre (GP).

A CMAS projection (from Di) also illustrates the varying degree of silica saturation in the pyroxenite suite (Figure 5.7) with samples plotting to either side of both the hypersthene gabbro and

Figure 5.17. AFM plot of Beni Bousera pyroxenite suite. Fields for mafic and ultramafic cumulates from ophiolites shown. MAR = Mid Atlantic Ridge basalt composition. Symbols as in Chapter 4 and Figure 5.18. Additional data from Coleman (1977).

Figure 5.18. CaO, Al_2O_3, MgO ternary plot of Beni Bousera pyroxenite suite, major element variation from composite layer margin (OPXITE) to centre (GP) illustrated by dashed line. Overlay illustrates fields for mafic and ultramafic cumulates from ophiolites, the " average oceanic crust " composition of Elthon (1979) and the composition of likely fractionating phases during pyroxenite crystallization (GT, CPX, OPX).

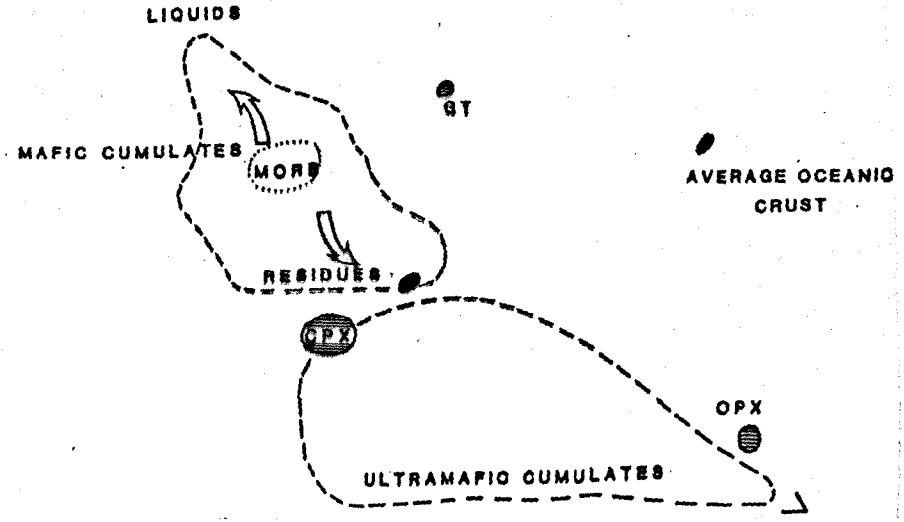
LIQUIDS
GT
MAFIC CUMULATES
MORB
AVERAGE OCEANIC
CRUST
RESIDUES
CPX
OPX
ULTRAMAFIC CUMULATES

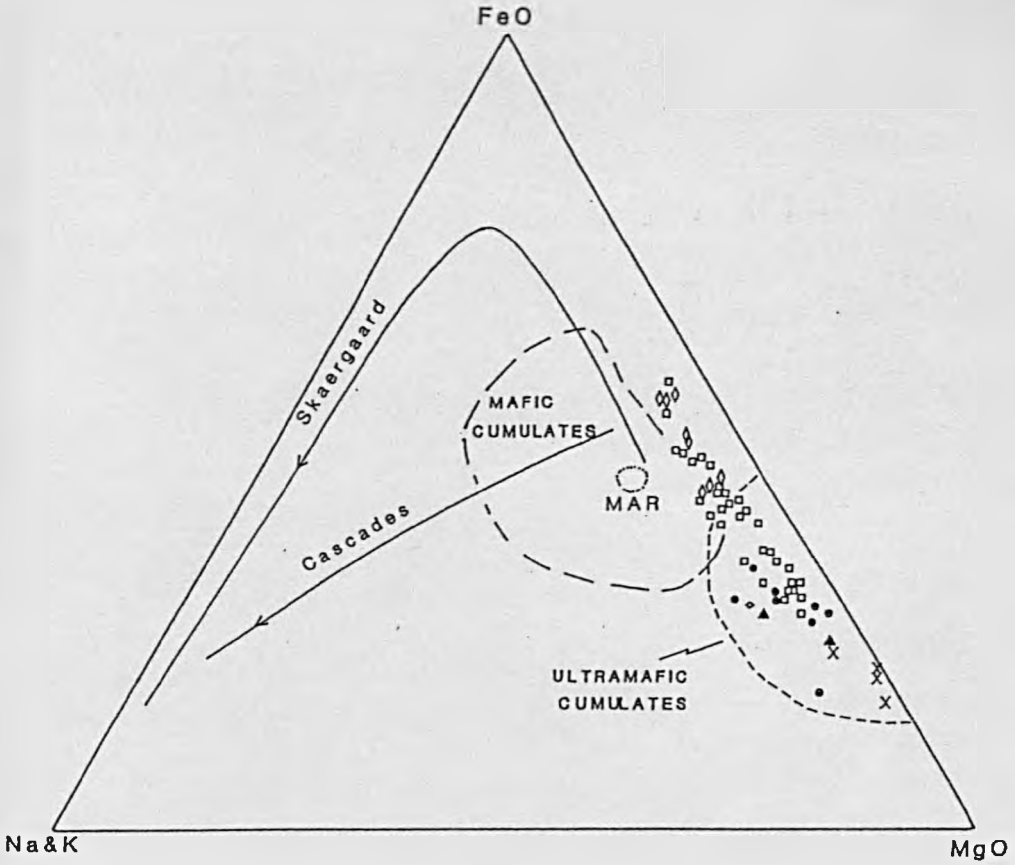
FeO
Skaergaard
MAFIC
CUMULATES
MAR
Cascades
ULTRAMAFIC
CUMULATES
Na&K
MgO

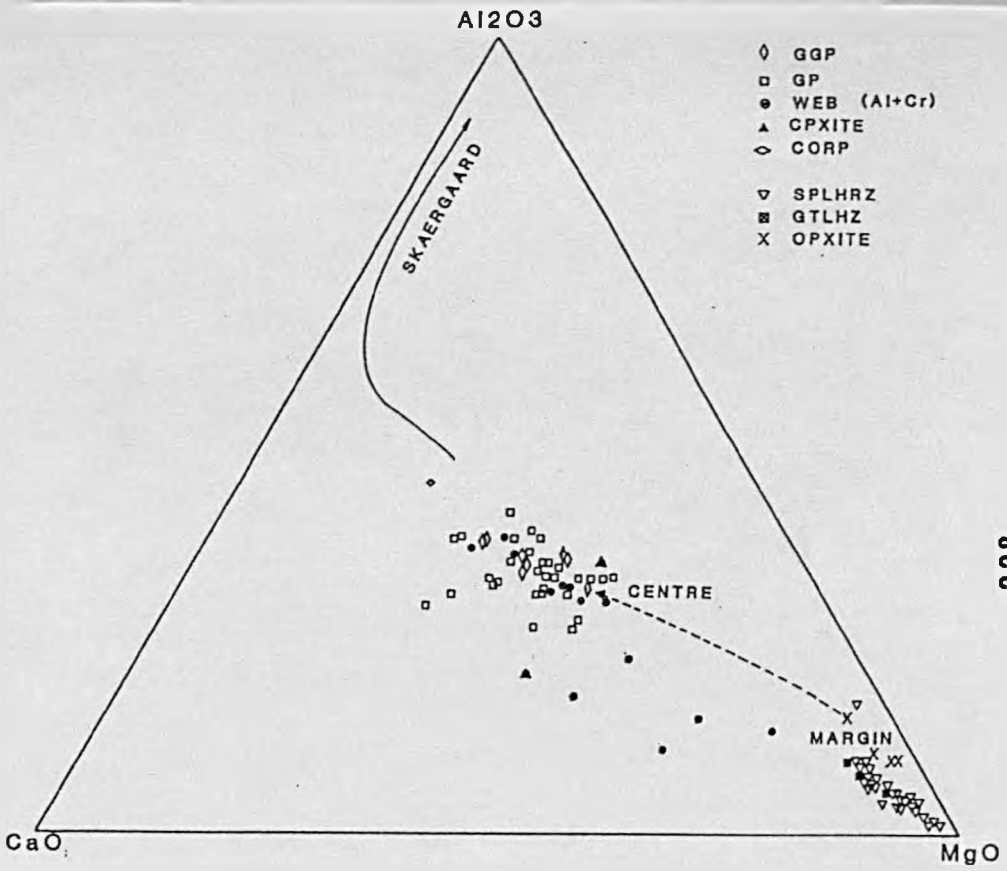
Al2O3
GGP
GP
WEB (Al+Cr)
CPXITE
CORP
SPLHRZ
GTLHZ
OPXITE
SKAERGAARD
CENTRE
MARGIN
CaO
MgO

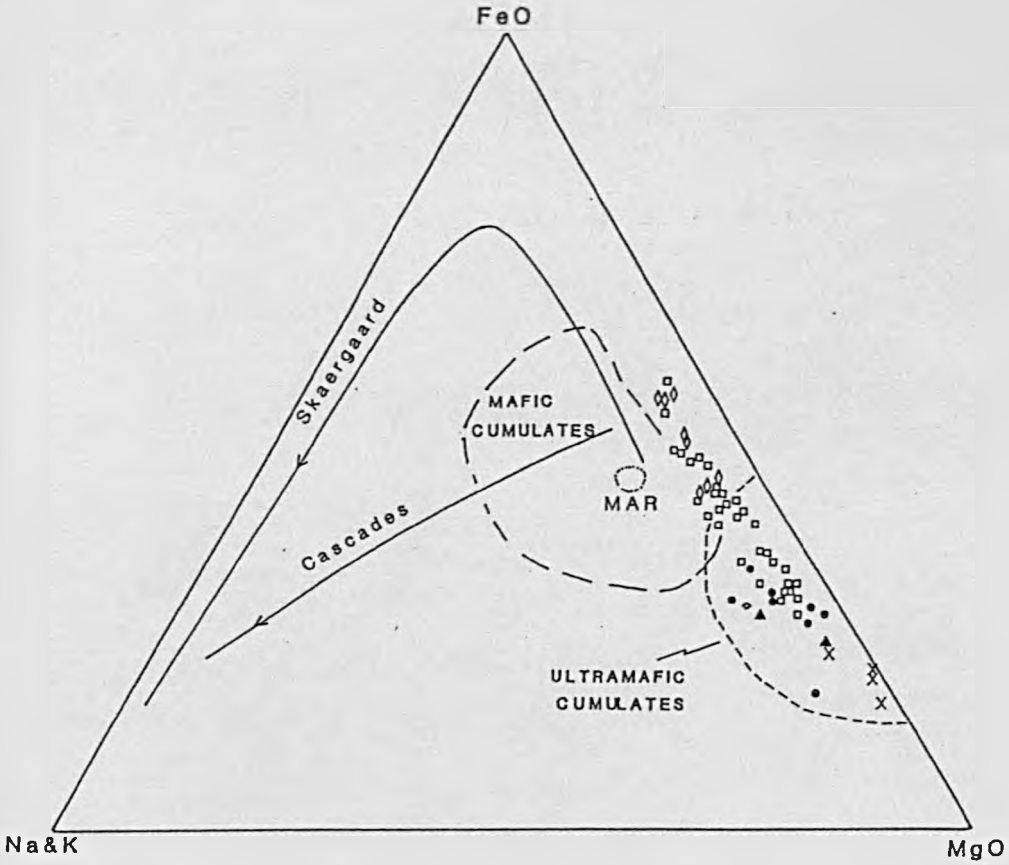
FeO
Skaergaard
MAFIC
CUMULATES
MAR
Cascades
ULTRAMAFIC
CUMULATES
Na&K
MgO

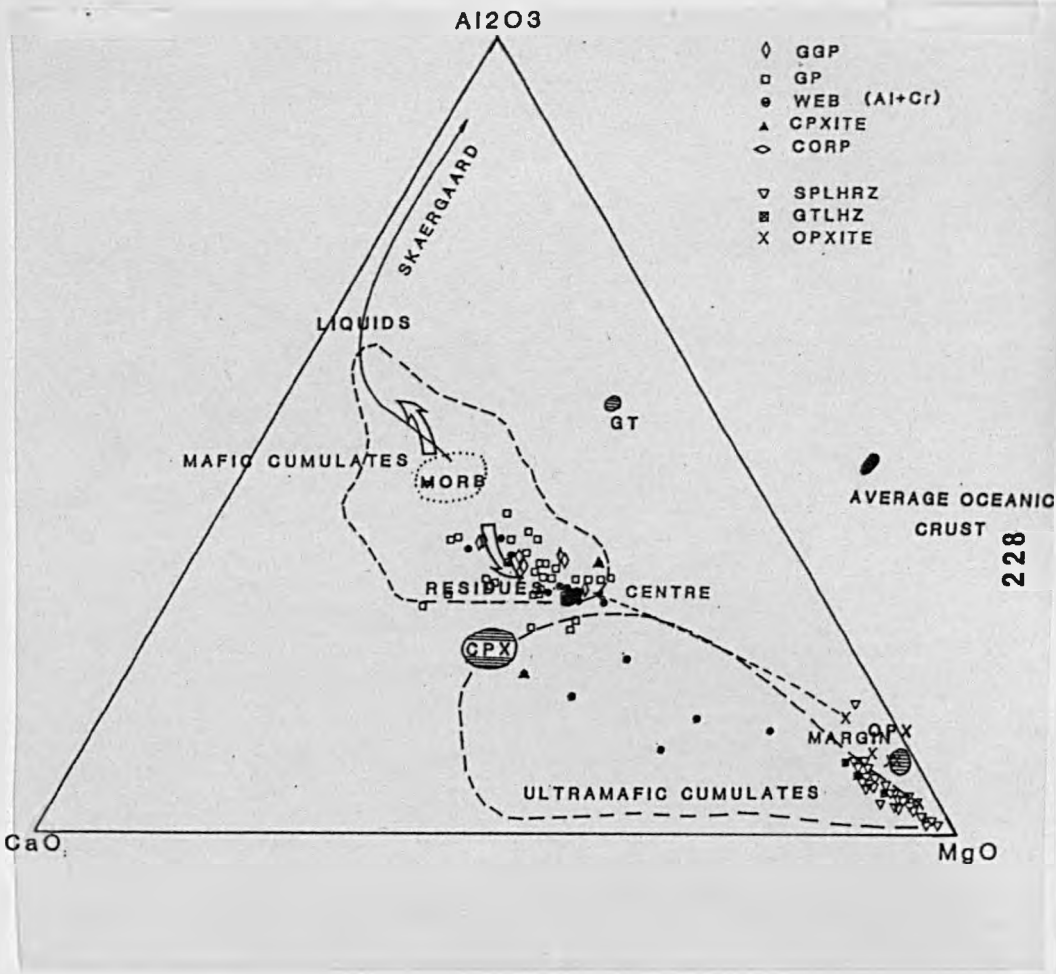
Al2O3
GGP
GP
WEB (Al+Cr)
CPXITE
CORP
SPLHRZ
GTLHZ
OPXITE
SKAERGAARD
LIQUIDS
GT
MAFIC CUMULATES
MORB
AVERAGE OCEANIC
CRUST
RESIDUE
CENTRE
CPX
CPX
MARGIN
ULTRAMAFIC CUMULATES
CaO
MgO

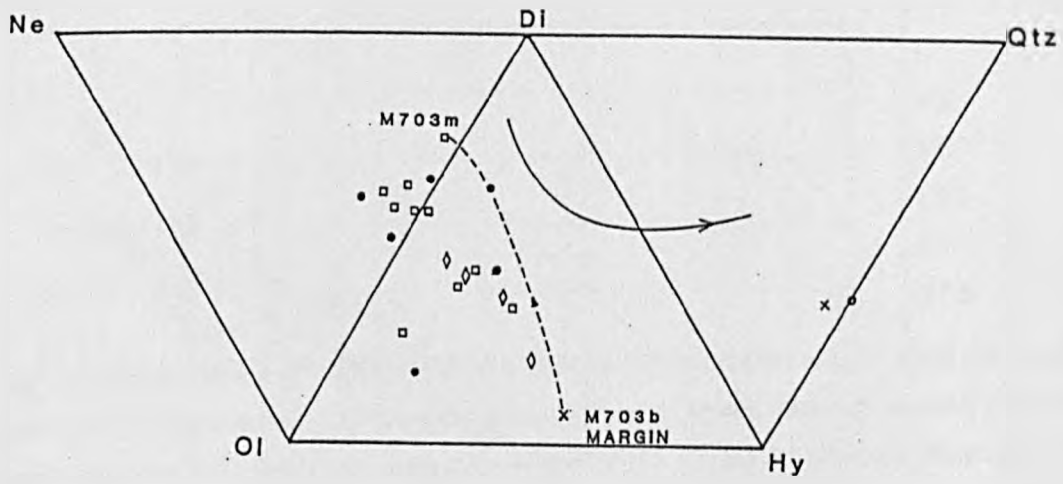

Figure 5.19. Normative basalt tetrahedron plot showing selected pyroxenites. Solid line is 1 atmosphere basalt cotectic of Thompson (1984). Dashed line shows evolution of a composite layer M703 (Komprobst 1969) from OPXITE through WEB to GP.

Figure 5.20a and b. CaO vs MgO and FeO vs MgO (wt %) variation for pyroxenites and peridotites from Beni Bousera. The solid line on the overlay is an " extract line " drawn between Ronda sample R717 and equilibrium melt 2 (Table 5.7) for Beni Bousera peridotite GP189. The line passes through an open field which encompasses the equilibrium melt compositions from Table 5.7 which use R717 as a source.

Figure 5.20c and d. SiO_2 vs MgO and Al_2O_3 vs MgO (wt %) variation for Beni Bousera pyroxenites and peridotites. Extraction line and melt fields as described above.

Figure 5.21. Ni and Cr (ppm) vs Mg No. for Beni Bousera pyroxenites.

Figure 5.22. Sc, V and Y (ppm) vs Mg No. pyroxenites.

Figure 5.23. Highly incompatible elements Sr, Rb and Zr vs Mg number pyroxenites.

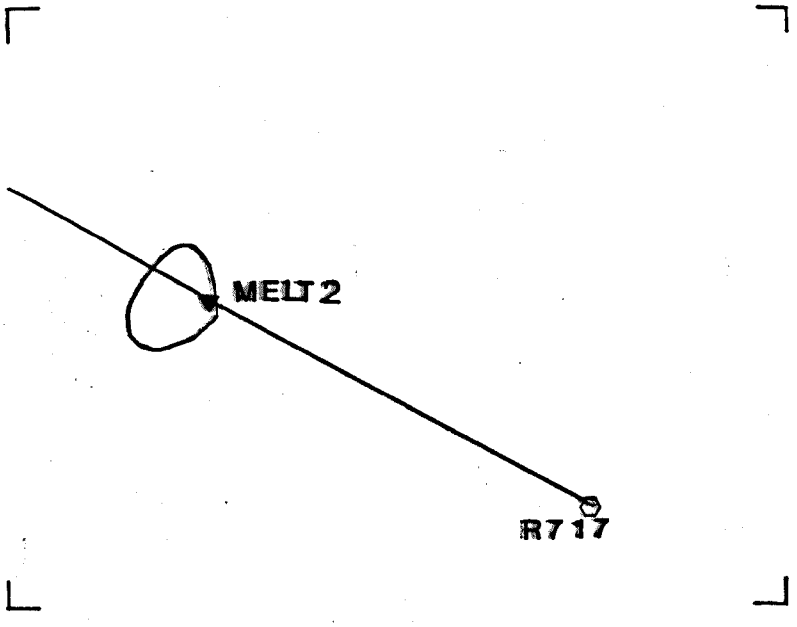
MELT2
R717

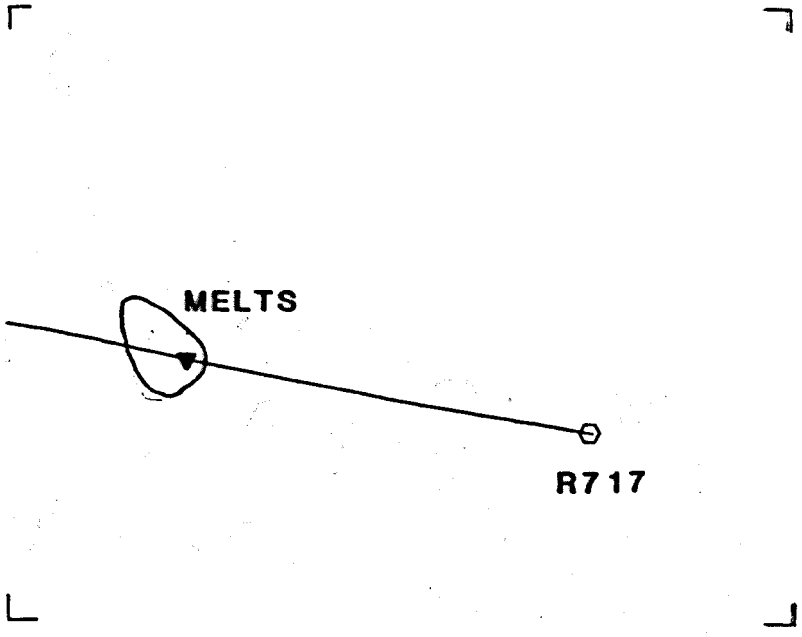
MELTS
R717

5. 20a

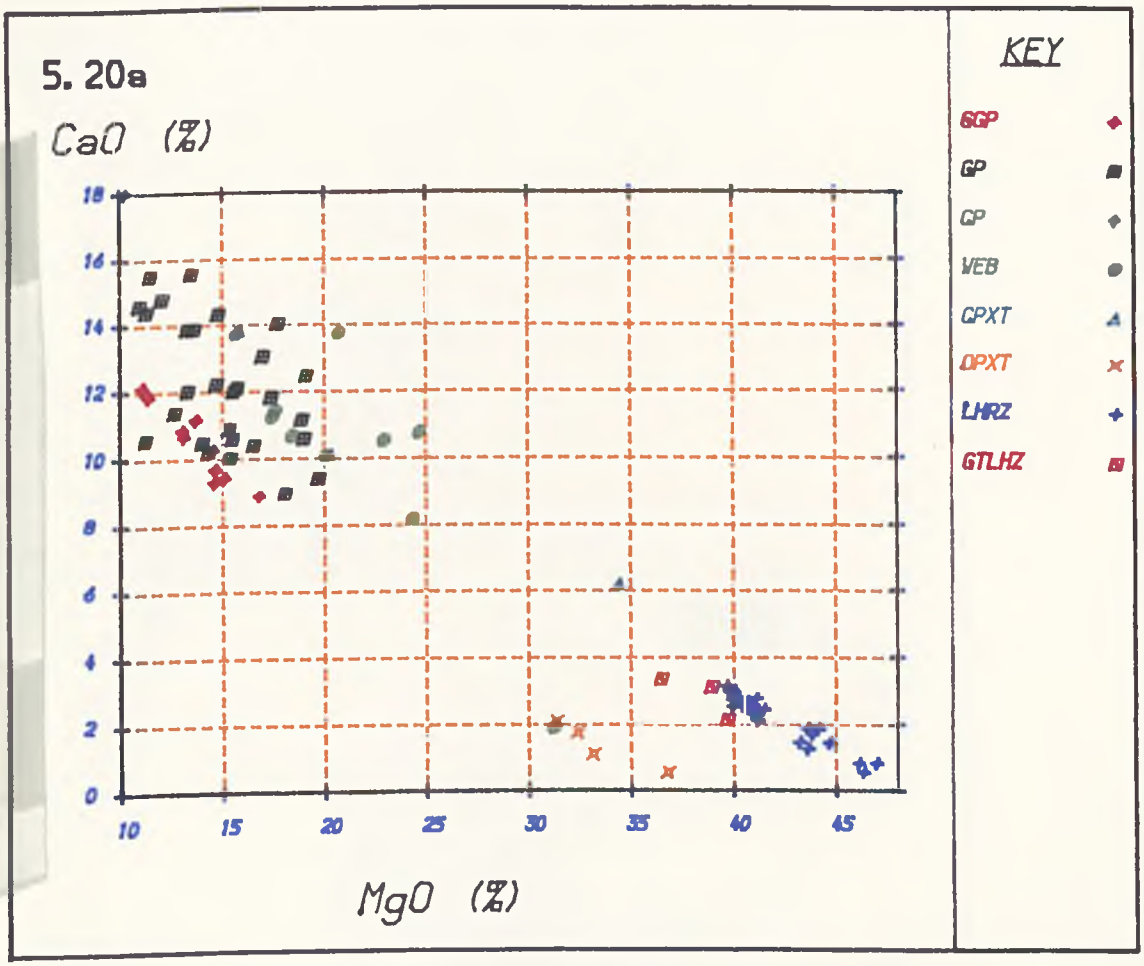
CaO (%)
18
16
14
12
10
8
6
4
2
0
10
15
20
25
30
35
40
45
MgO (%)
KEY
GGP
GP
CP
VEB
CPXT
OPXT
LHRZ
GTLHZ

5. 20b

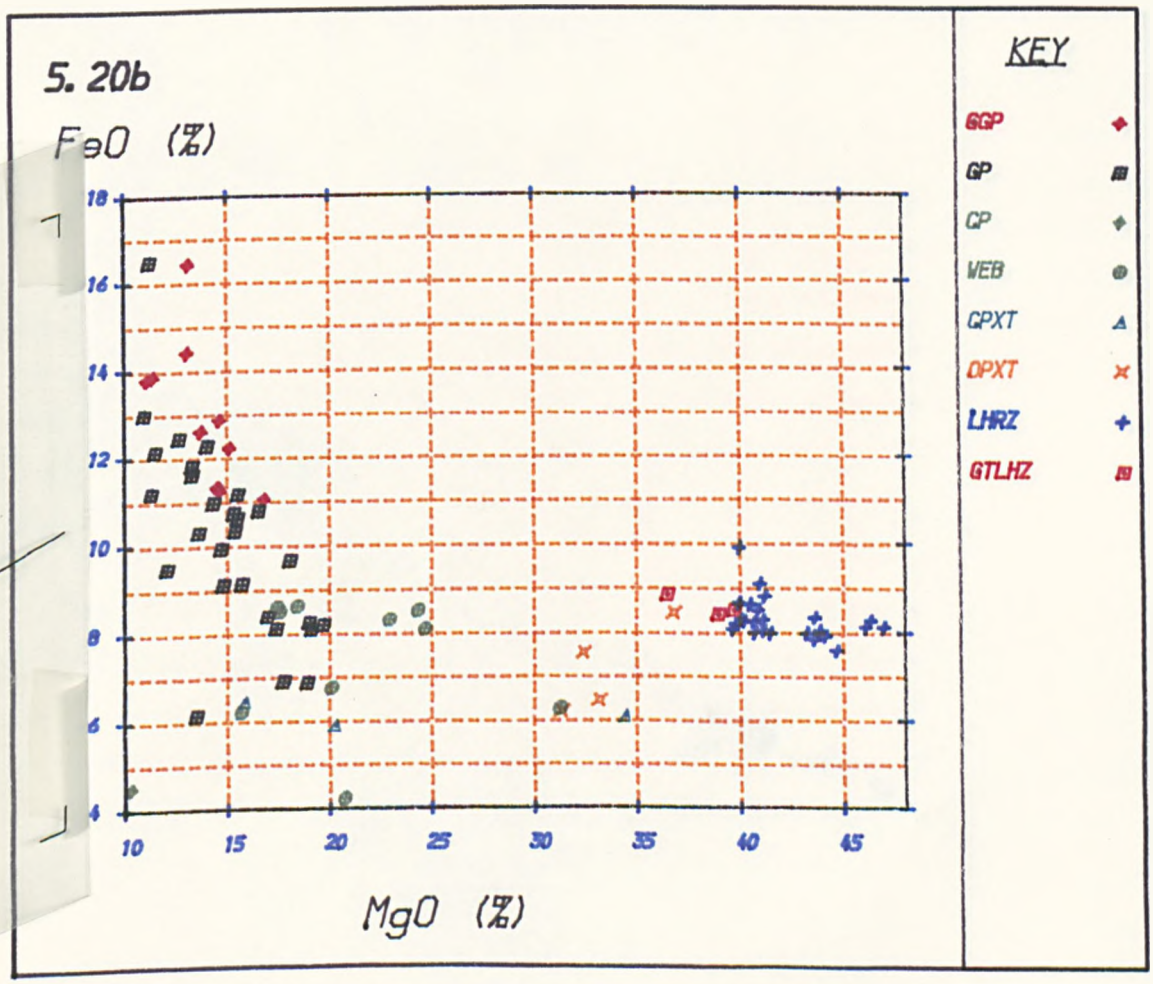
FeO (%)
18
16
14
12
10
8
6
4
10
15
20
25
30
35
40
45
MgO (%)
KEY
GGP
GP
CP
VEB
CPXT
OPXT
LHRZ
GTLHZ

5. 20a

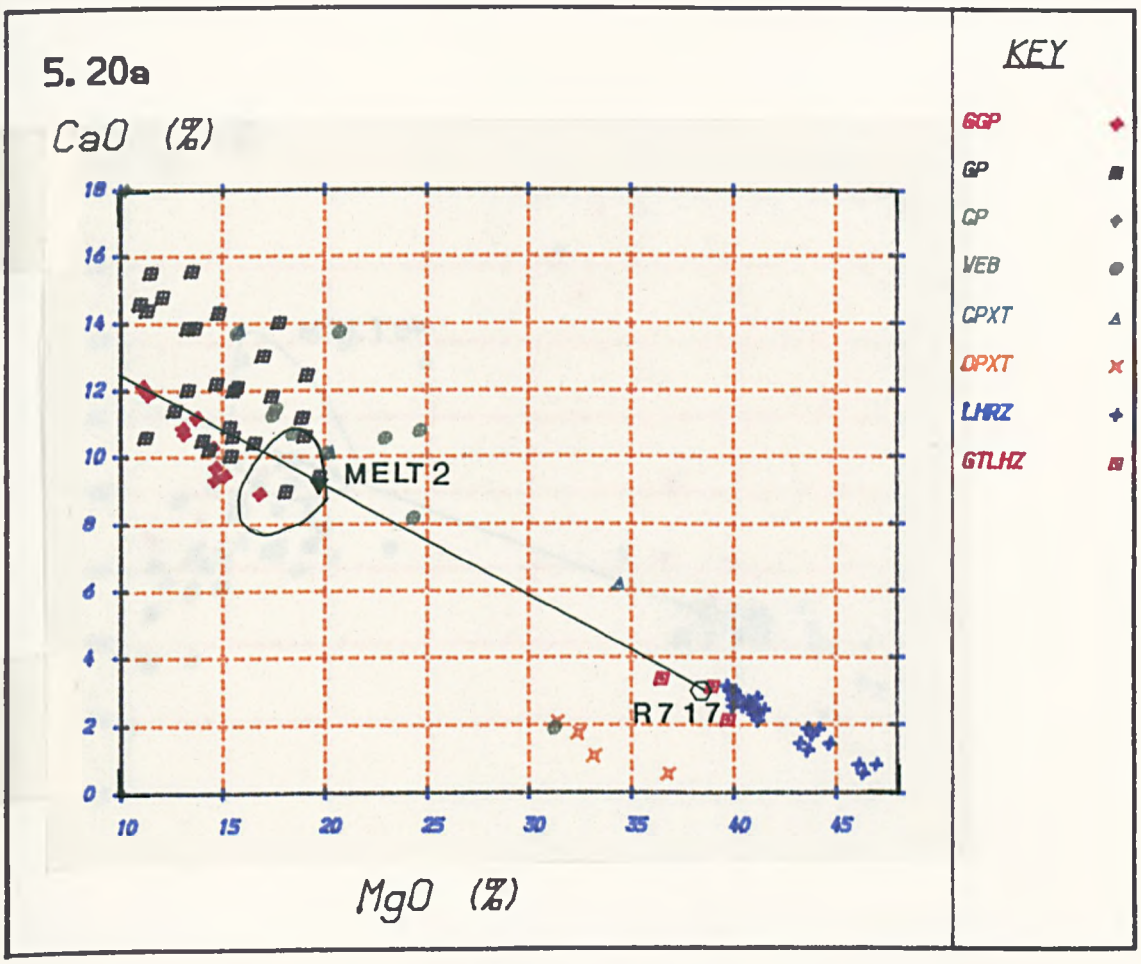
CaO (%)
MELT 2
R717
MgO (%)
KEY
GGP
GP
CP
VEB
CPXT
OPXT
LHRZ
GTLHZ

5. 20b

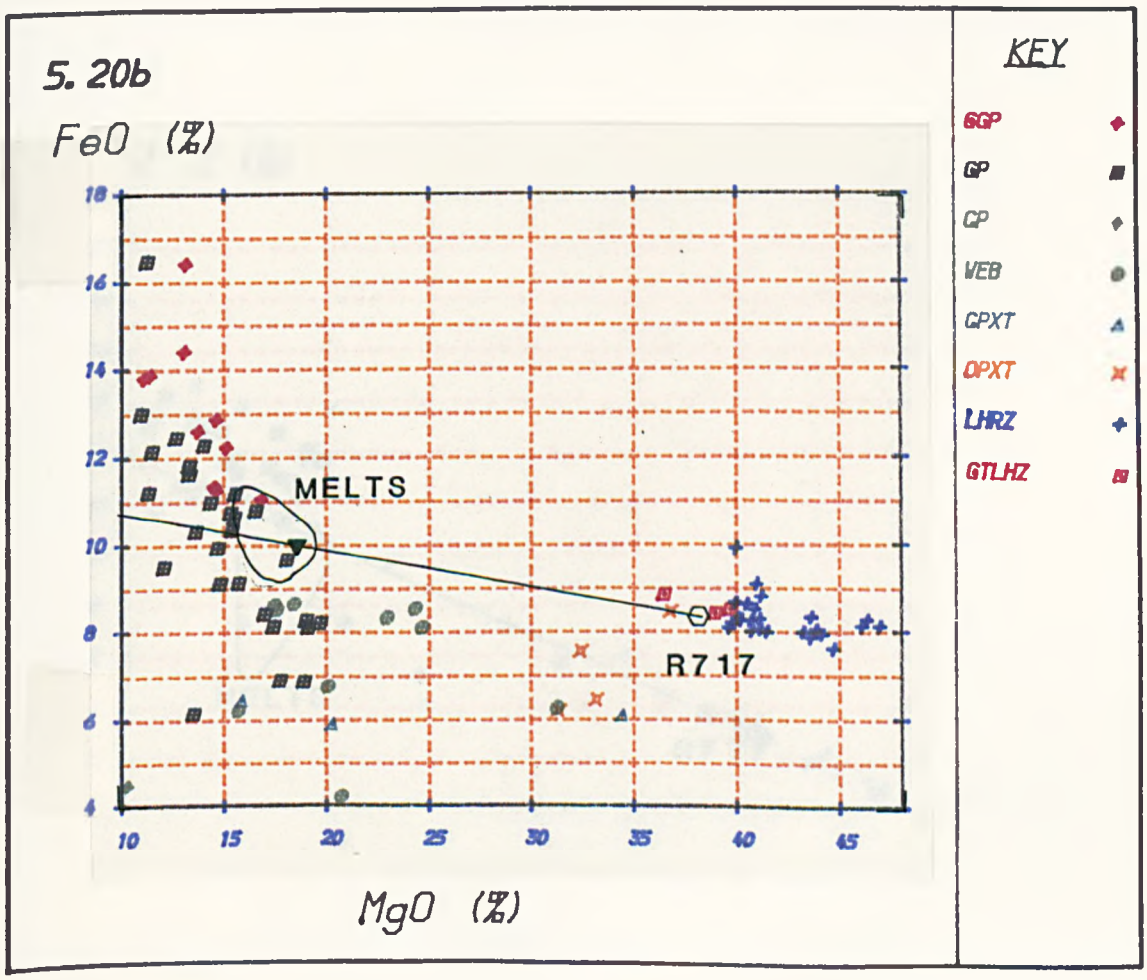
FeO (%)
MELTS
R717
MgO (%)
KEY
GGP
GP
CP
VEB
CPXT
OPXT
LHRZ
GTLHZ

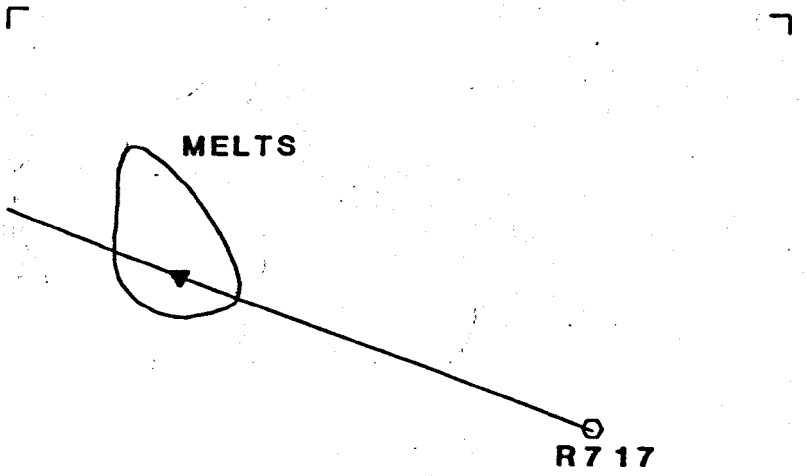
MELTS
R7 17

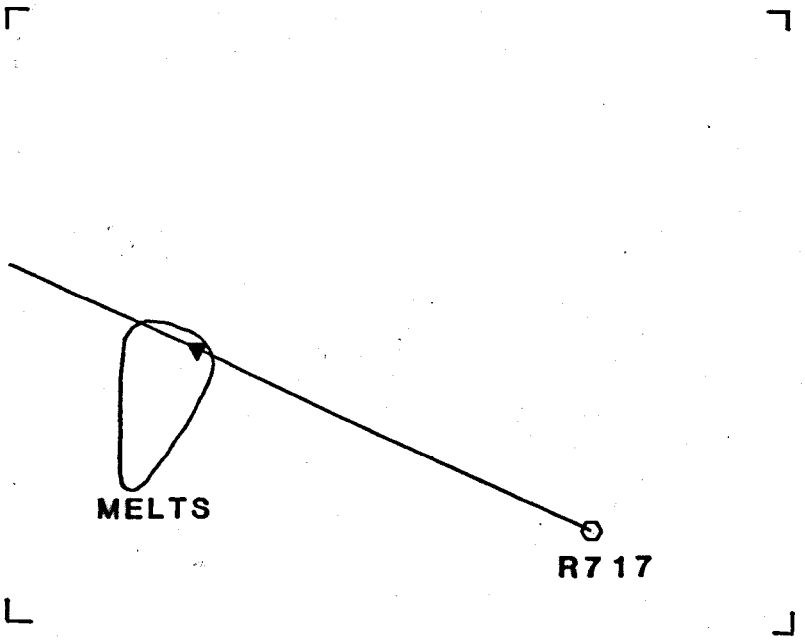
MELTS
R7 17

5. 20c

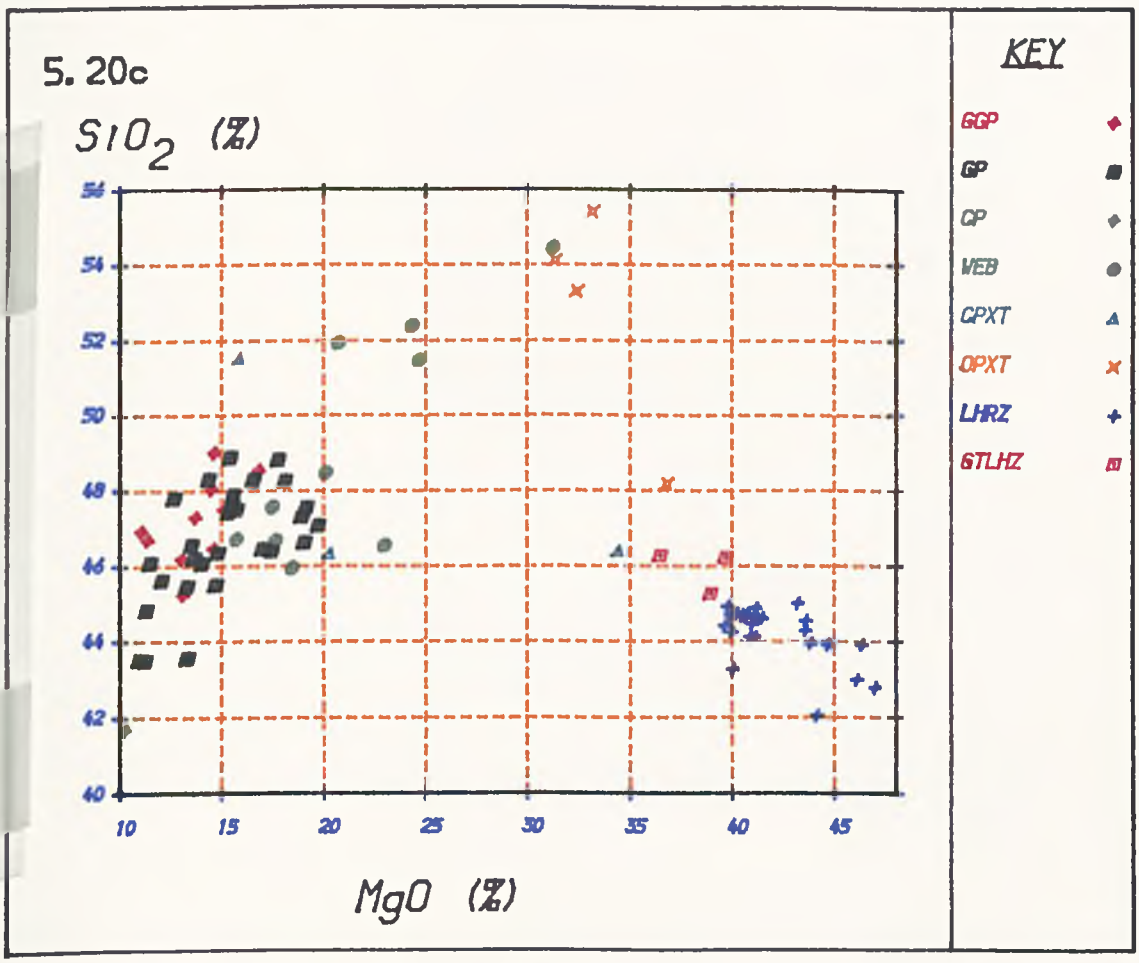
SiO2 (%)
56
54
52
50
48
46
44
42
40
10
15
20
25
30
35
40
45
MgO (%)
KEY
GGP
GP
CP
VEB
CPXT
OPXT
LHRZ
GTLHZ

5. 20d

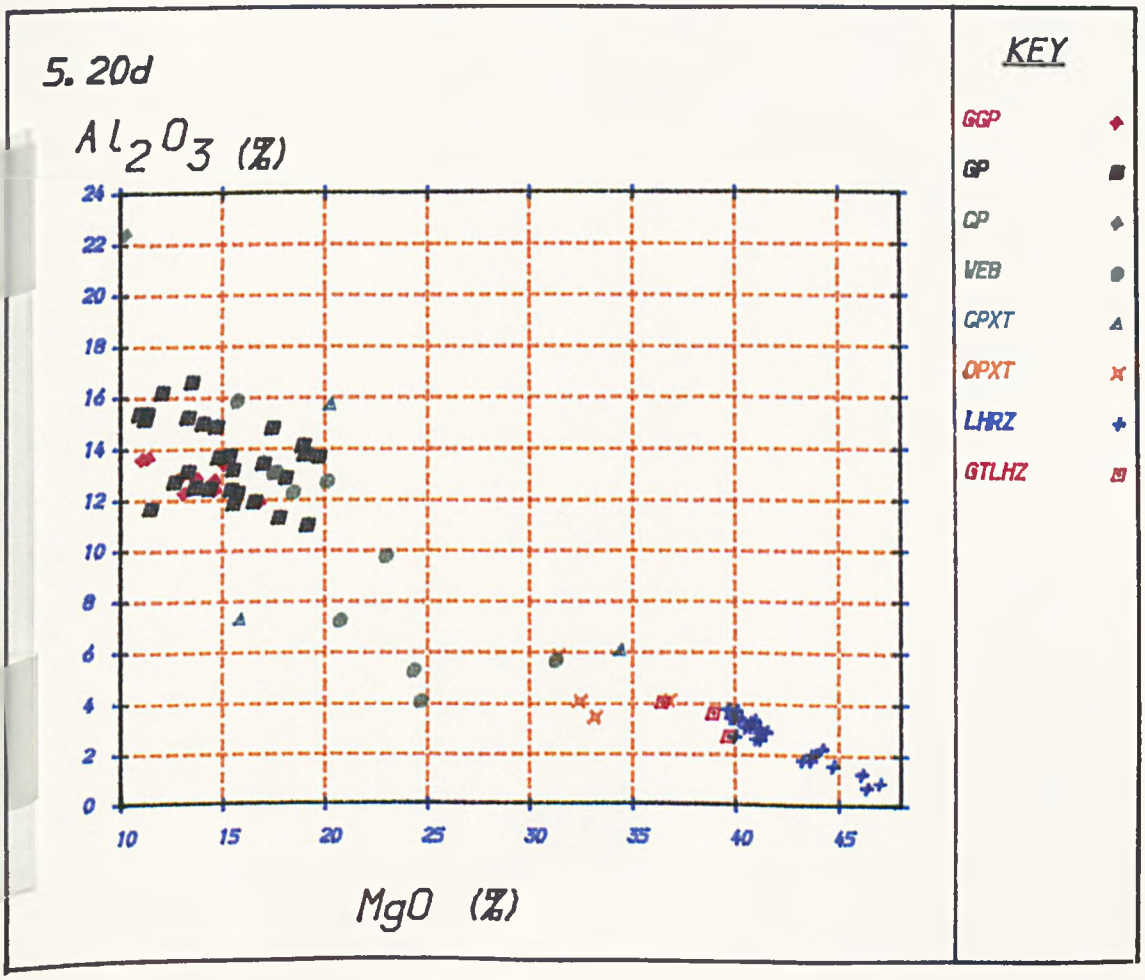
Al2O3 (%)
24
22
20
18
16
14
12
10
8
6
4
2
0
10
15
20
25
30
35
40
45
MgO (%)
KEY
GGP
GP
CP
VEB
CPXT
OPXT
LHRZ
GTLHZ

5. 20c

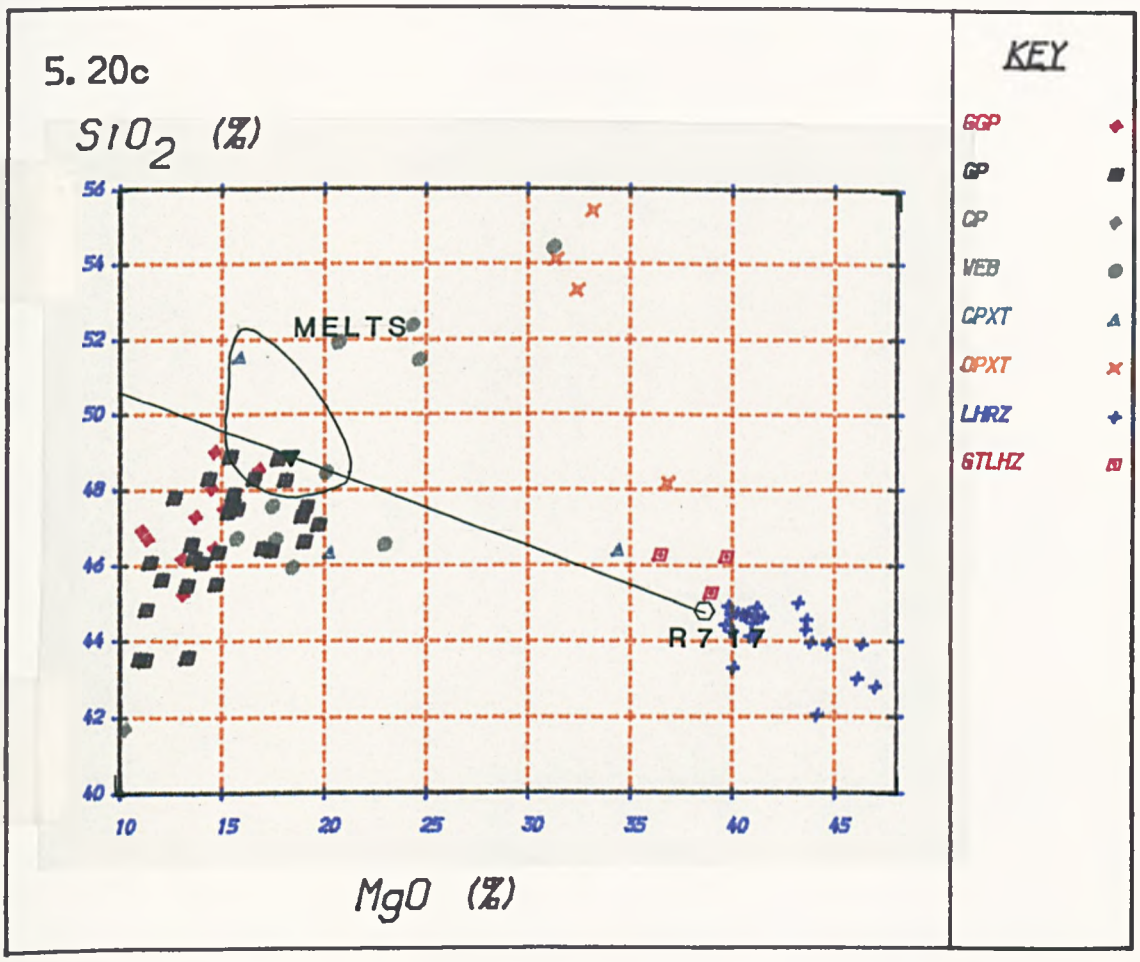
SiO_2 (%)
MELTS
R7 17
MgO (%)
KEY
GGP
GP
CP
WEB
CPXT
OPXT
LHRZ
GTLHZ

5. 20d

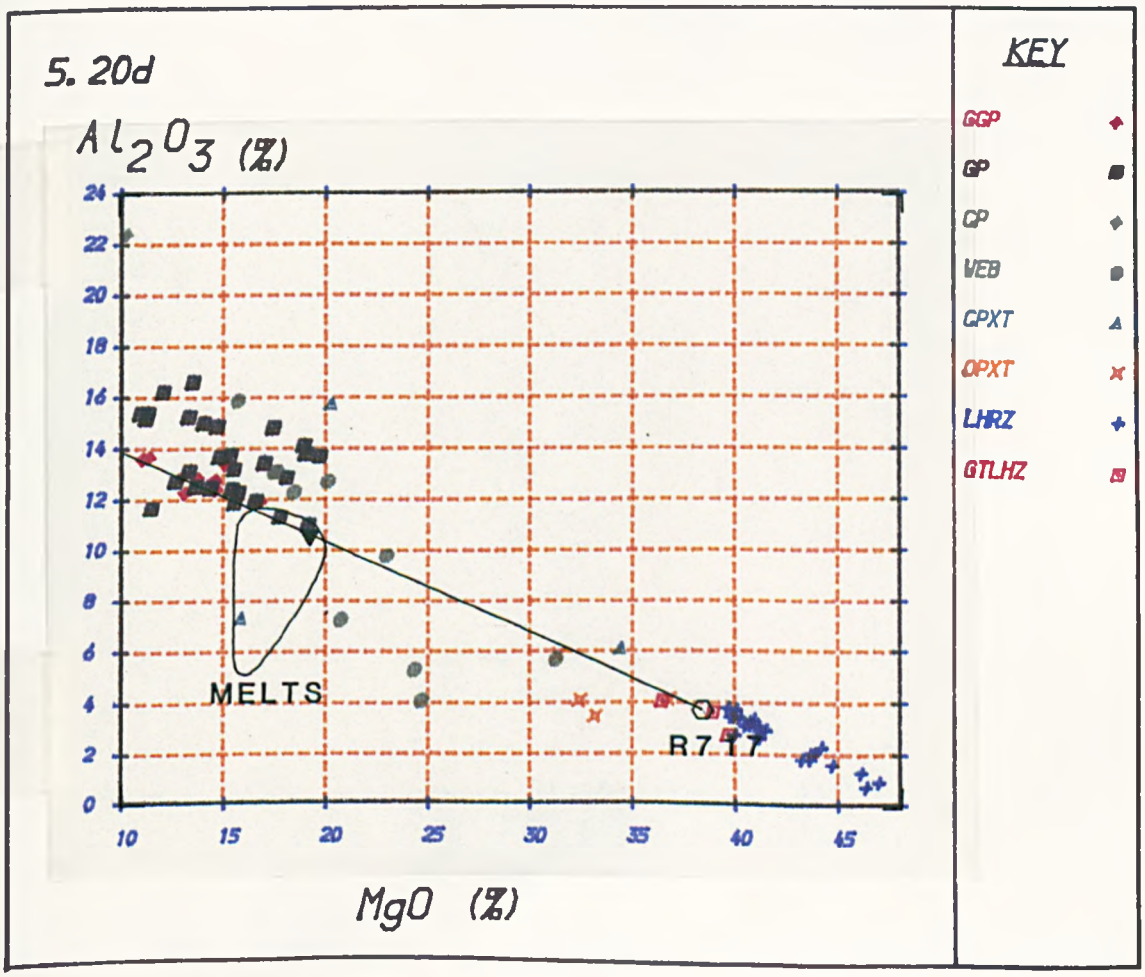
Al_2O_3 (%)
MELTS
R7 17
MgO (%)
KEY
GGP
GP
CP
WEB
CPXT
OPXT
LHRZ
GTLHZ

olivine gabbro planes. Most of the GP samples plot close to the 30 kb CMAS cotectic of Clarke (1970), comparable to the calculated equilibrium melts from the peridotites (Figure 5.12). When plotted against a fractionation index such as MgO (Figure 5.20) or Mg No. the whole rock major element data for the pyroxenites show moderate to considerable degrees of scatter, with Ca and Fe displaying poor negative correlations with MgO. The data also show a large degree of scatter around the linear " extract line " defined between the assumed source peridotites R717 and equilibrium melt number 2 from Table 5.7 . Rocks of the same lithology do not show much coherence in terms of major element variation e.g. Na_2O in the GGP almost doubles whilst MgO shows no consistent increase.

5:6.2 Trace elements: Ni and Cr

Compatible elements Ni and Cr in the pyroxenites show positive correlations with Mg No. (Figure 5.21) with the exception of GP132(1), a thin Cr-diopside websterite which locally contains over 5 % spinel and has almost 10,000 ppm Cr. The GGP and the, corundum-bearing pyroxenite specimen (Kornprobst et al 1982) contain the lowest Cr and Ni abundanc es (Figure 5.21). The Ni contents of the GGP form a poorly correlated trend of much shallower slope than the main trend in Figure 5.21. Some of the Ni concentrations in the GGP are very low given their relatively high MgO content. GP25 contains only 50 ppm Ni at 11 % MgO but these lower values are compatible with the lower Mg Nos. of the GGP (38-50). Other garnetiferous pyroxenite layers of similar or slightly higher MgO contents contain much higher Ni abundances (> 300ppm) Table 5.3. The only comparable GP layer in terms of Ni abundance to the GGP layers is sample GP139 which occurs 1 m up section from GGP sample GP147, (see Appendix 1). Ni and Cr abundances in samples from the margin of GP87, a garnet clinopyroxenite, are markedly more enriched than the centre of the layer and may indicate that the layer crystallised inwards

The moderately incompatible elements Sc, V and Y all show broad negative correlations with Mg No. (Figure 5.22). Abundances of these elements in the Beni Bousera pyroxenite suite are comparable to those in pyroxenites analysed from other orogenic peridotite massifs (e.g. Loubet and Allegre 1982, Bodinier et al 1987). Highly incompatible elements such as Zr, Rb and Sr show poor correlation with Mg No. (Figure 5.23). In the samples analysed by XRF, Rb was of such low abundances that it was either below detection limit or the data were subject to large error (concentrations < 2 ppm). Data plotted on Figure 5.23 were obtained on unleached whole rocks by isotope dilution (I.D.) and are given in Table 6.3. The highly mobile nature of Rb during secondary alteration probably accounts for some of the dispersion shown in Figure 5.23. However, Zr is particularly resistant to transport during alteration, hence the lack of correlation between Zr content and Mg No. is a primary feature of the whole rock geochemistry.

5:6.3 REE geochemistry

Chondrite normalized REE patterns for the whole rock pyroxenites (Figure 5.24 a, b and c) have extremely variable degrees of LREE/HREE depletion $(Ce/Yb)_n$ ranging from 2.33 in Cr-websterite GP101 to 0.0018 in the GGP sample GP25. GGP samples are all characterized by extreme LREE depletion, the least extreme of which is sample GP47 with $(Ce/Yb)_n \sim 0.09$. The garnetiferous pyroxenites are generally enriched in HREE, due to garnet's high partition coefficients for these elements, with Yb and Lu contents > 20 x chondritic. The HREE enrichment of some samples means that $(Ce/Yb)_n$ is not a useful parameter

5.21

Ni ppm

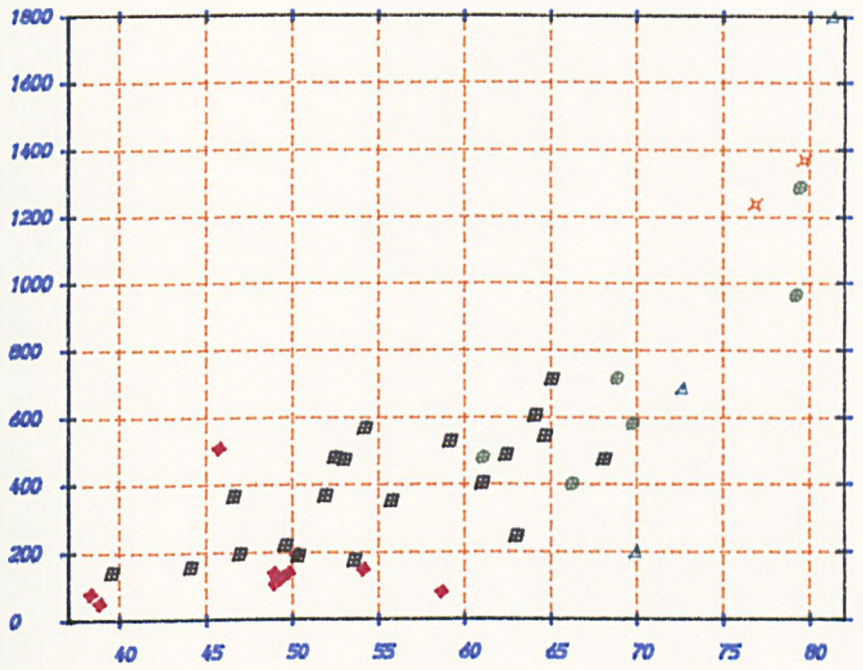

KEY

GGP

GP

VEB

CPXT

OPXT

5.21b

Cr ppm

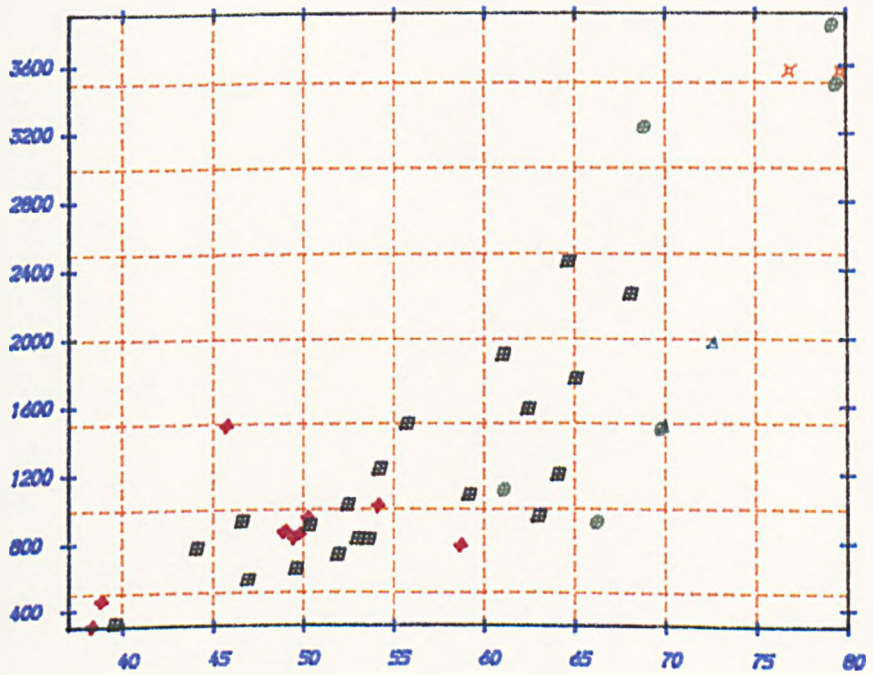

KEY

GGP

GP

VEB

CPXT

OPXT

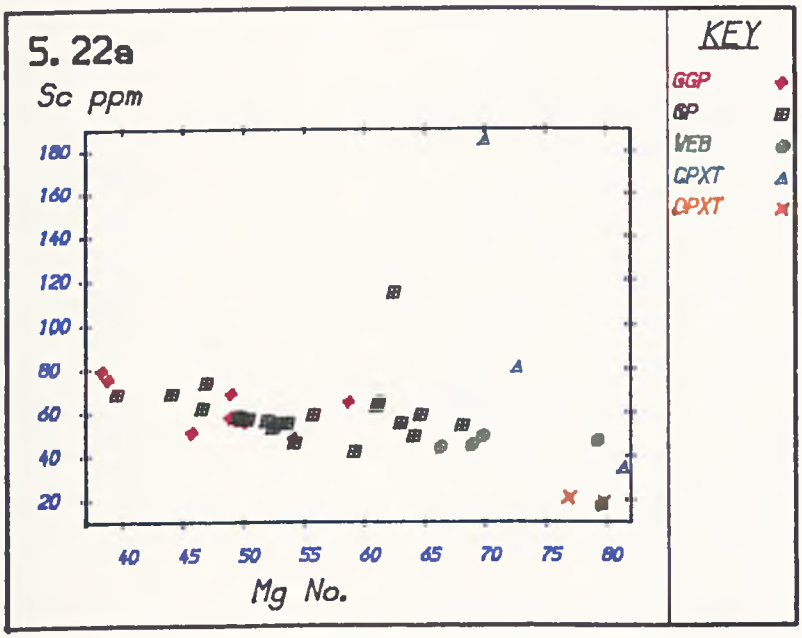
5. 22a
Sc ppm
180
160
140
120
100
80
60
40
20
40
45
50
55
60
65
70
75
80
Mg No.
KEY
GGP
GP
VEB
CPXT
OPXT

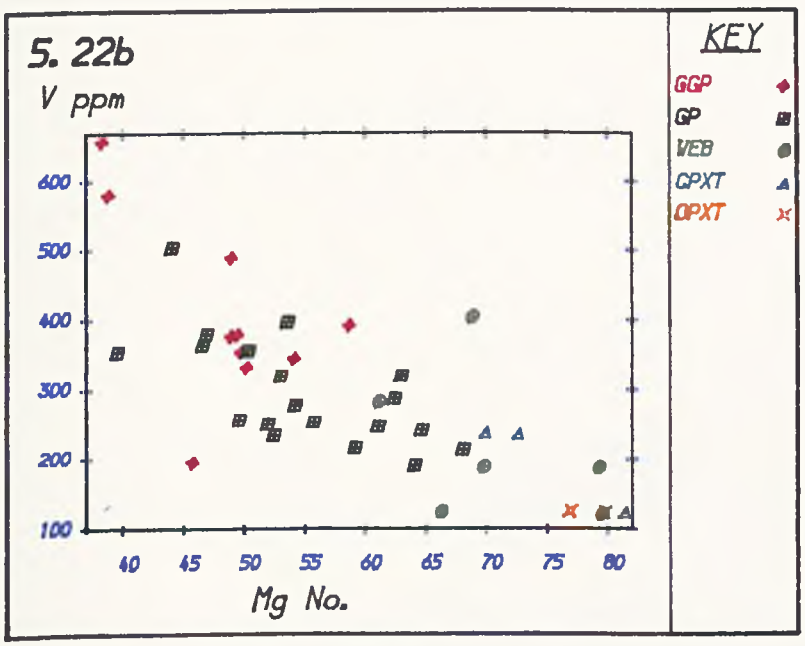
5. 22b
V ppm
600
500
400
300
200
100
40
45
50
55
60
65
70
75
80
Mg No.
KEY
GGP
GP
VEB
CPXT
OPXT

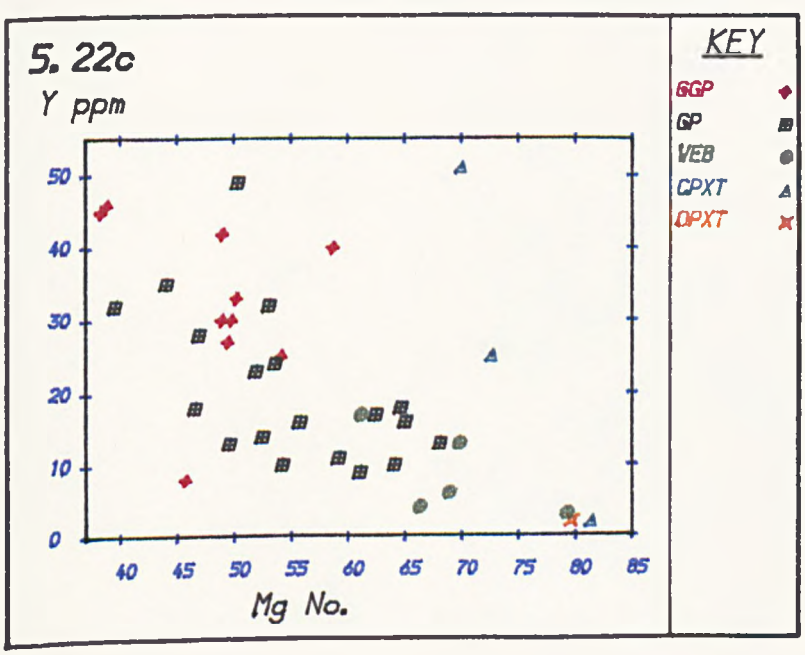
5. 22c
Y ppm
50
40
30
20
10
0
40
45
50
55
60
65
70
75
80
85
Mg No.
KEY
GGP
GP
VEB
CPXT
OPXT

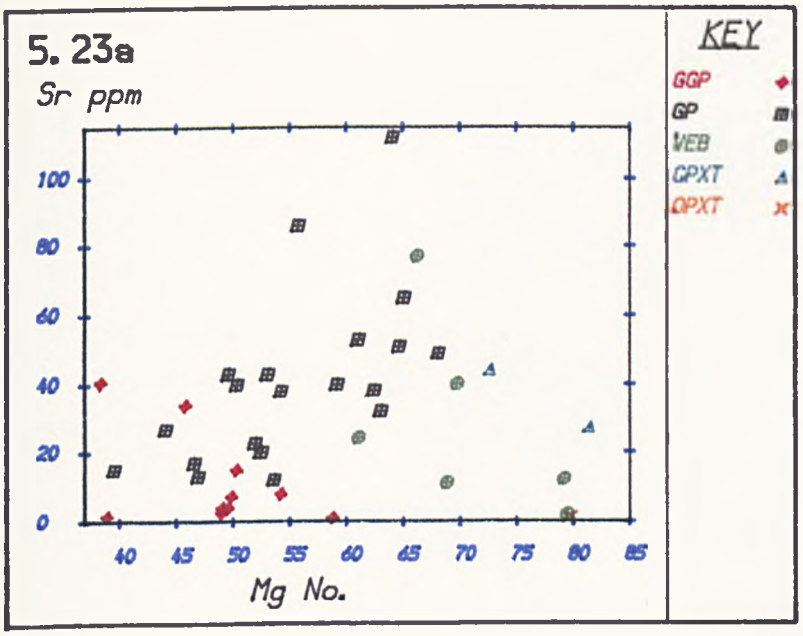
5. 23a
Sr ppm
100
80
60
40
20
0
40 45 50 55 60 65 70 75 80 85
Mg No.
KEY
GGP
GP
VEB
CPXT
OPXT

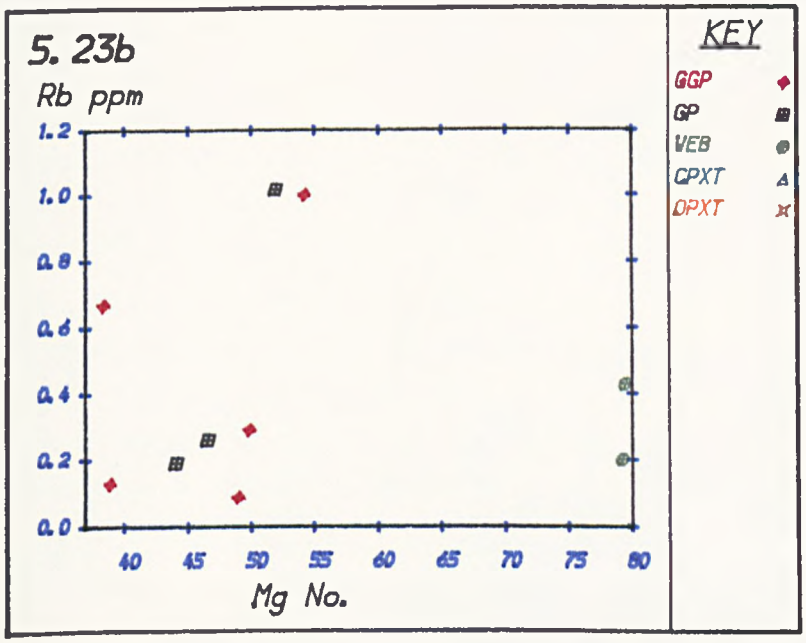
5. 23b
Rb ppm
1.2
1.0
0.8
0.6
0.4
0.2
0.0
40 45 50 55 60 65 70 75 80
Mg No.
KEY
GGP
GP
VEB
CPXT
OPXT

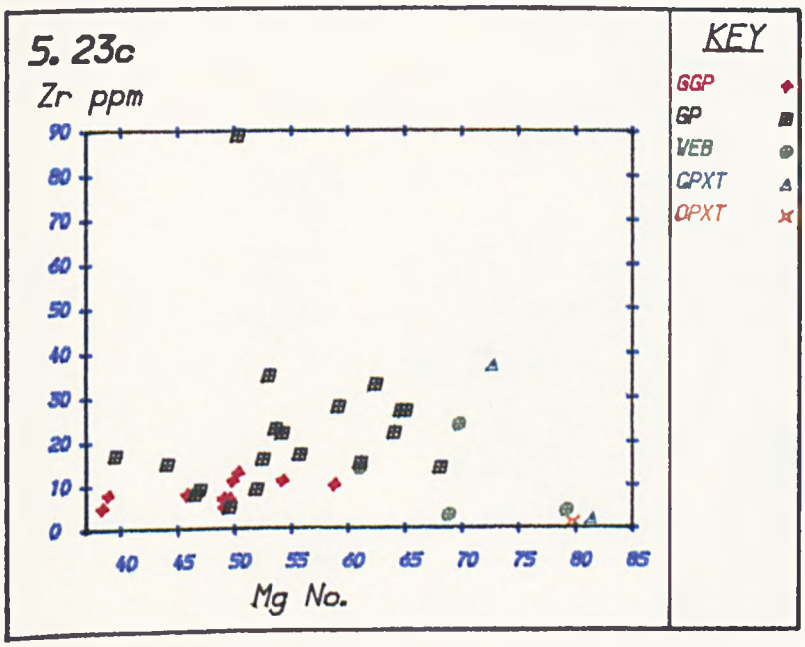
5. 23c
Zr ppm
90
80
70
60
50
40
30
20
10
0
40 45 50 55 60 65 70 75 80 85
Mg No.
KEY
GGP
GP
VEB
CPXT
OPXT

when comparing LREE fractionation of garnetiferous and non-garnetiferous samples. A more realistic measure of the LREE depletion which can be applied to all the pyroxenites is given by the (Ce/Sm)$_n$ ratio which varies from 0.91 (GP101) x to 0.016 (GP25), Table 5.9. Using this measure the GGP remain the most LREE depleted lithological group although GP139, a thick, garnetiferous layer which is isotopically similar to the GGP (Chapter 6), is the most LREE depleted sample. (Ce/Sm)$_n$ is preferable to the commonly used (La/Sm)$_n$ parameter because several of the samples, particularly the GGP's, exhibit anomalous La enrichment.

The marked "kinks" in the REE profiles between Nd and La in Figures 5.27a, b and c do not appear to be negative Ce anomalies comparable to those found by Hole et al (1984) in some Mariana basalts but are La enrichments. The La enrichment in some of the pyroxenites is indicative of some degree of LREE enrichment following extreme LREE depletion i.e. a complex magmatic evolution. Quantification of La enrichment is difficult to assess as there is no other LREE of lower atomic number to interpolate between from Ce. Lanthanum analyses by I.D. are potentially the most imprecise of the 10 REE measured due to interferences of $^{138}Ba^+$ and $^{138}Ce^+$ on the $^{138}La^+$ ion beam. Corrections are made for these interferences by monitoring $^{137}Ba^+$ and $^{140}Ce^+$ (Thirlwall 1982). La data presented in Table 5.9 were collected with $^{139}La^+$ ion beams of between > 1 x 10 $^{-11}$ A and ~ 3 x 10 $^{-12}$ A on the Faraday collector. Thirlwall (op.cit.) states that with $^{139}La^+$ beams of < 10 $^{-11}$ A on the Faraday, the high natural $^{138}Ba/^{137}Ba$ (~6.4) leads to imprecision in the ^{138}La correction but does not quantify its effect. A significant observation is that ^{139}La beams from the La enriched samples were of equivalent intensity to those obtained during analyses of samples which did not did not show any evidence of LREE enrichment. Precision of the La analysis is mainly a function of the intensity and stability of the Ba^+ ion beam. According to Thirlwall (1982) the correction for Ba interference appears accurate even with ^{138}Ba forming up to 90 % of the measured 138 ion beam. The samples analysed in this study did not have extreme natural Ba concentrations or Ba/La ratios (Chapter 6) which are somtimes problematical. No correlation is observed in the LREE enriched samples between Ce/Ce* and % Ba interference on ^{138}La.

The parameter (Ce/Ce*) gives a quantitative measure of La enrichment (in those samples without obvious Ce enrichment) as this parameter interpolates between Nd and La. If Ce is not anomalous then a Ce/Ce* ratio is less than 1 indicates La enrichment and the magnitude of this value is an indication of the degree of La enrichment. Ce/Ce* is defined as:

$$Ce/Ce^* = (Ce)_n \times [\{(Nd)_n/(La)_n\}^{-1/3}/(La)_n]]$$

The sample which had the lowest in run ^{138}Ba interference (GP25, 1.5 %) has the second largest Ce anomaly (Ce/Ce* = 0.37, Table 5.9). Conversely, GP101 has no significant Ce anomaly yet it had a ^{138}Ba interference of over 80 %. Hence the variable La enrichments in pyroxenites cannot be assigned to analytical error. Using Ce/Ce* as a measure of La enrichment (Table 5.9) indicates that the GGP's generally have the largest La enrichments (Ce/Ce * ~ 0.3 to 0.82). The Al-augite websterite, GP125 and the Cr-websterite GP188 also have (Ce/Ce*) values significantly below 1.0. However, in the case of GP188 there appears to be a true negative Ce anomaly rather than La enrichment due to the marked break in slope between Nd and Ce compared to Sm and Nd (Figure 5.27a), such a negative Ce anomaly in a mantle

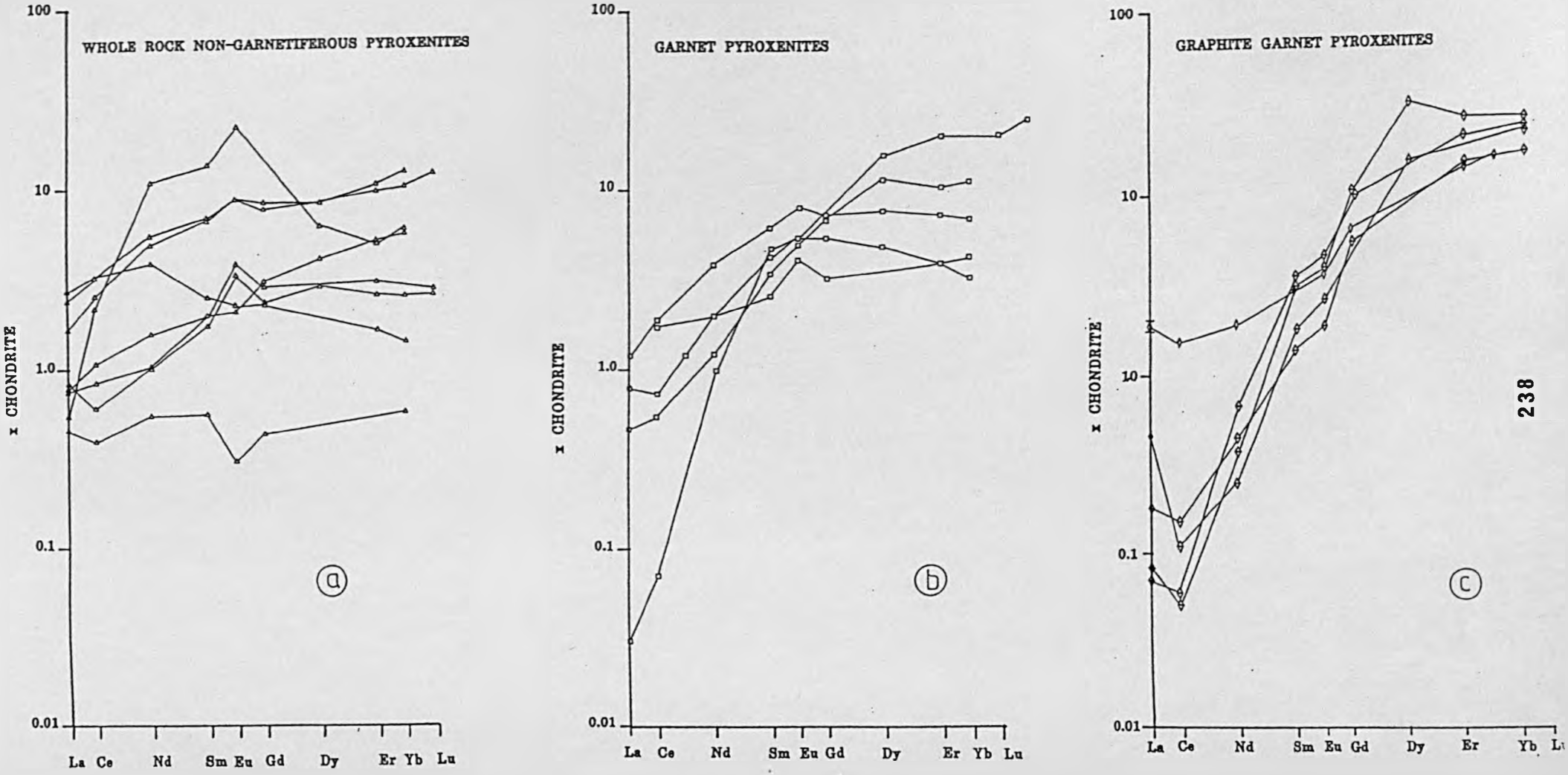

Figure 5.24. Chondrite normalized REE plots of a, whole rock non-garnetiferous pyroxenites, b, whole rock garnet clinopyroxenites, c, whole rock graphite garnet clinopyroxenites.

Table 5.9. PYROXENITE WHOLE ROCK REE

SAMPLE	GP19	GP20	GP25	GP28	GP33a	GP37	GP47	GP81	GP87m	GP97	GP101a	GP125	GP139	GP147	GP188	GP236	PHN5732	PHN5739	PHN5740	GP61
LITHOLOGY	GP	GP	GGP	WEB	WEB	GP	GGP	GGP	GP	WEB	WEB	WEB	GP	GGP	WEB	WEB	CPXITE	GP	GP	GRAN
La	0.112	0.178	0.028	0.780	0.542	0.262	0.624	0.022	0.393	0.249	0.873	0.270	0.008	0.060	0.147	0.252	0.164		0.152	2.028
Ce	0.469	0.476	0.045	2.817	2.183	0.636	1.370	0.052	1.696	0.718	2.866	0.523	0.062	0.132	0.325	0.922	1.899	1.514	0.098	5.846
Nd	1.025	0.761	0.241	3.442	3.072	1.275	1.260	0.422	2.458	0.688	2.448	0.665	0.615	0.288	0.313	0.994	6.814	1.292	0.160	5.733
Sm	0.850	0.710	0.678	1.381	1.341	0.865	0.616	0.764	1.265	0.396	0.743	0.348	0.941	0.299	0.107	0.403	2.673	0.528	0.396	2.144
Eu	0.449	0.391	0.321	0.673	0.659	0.417	0.289	0.373	0.624	0.298	0.187	0.257	0.414	0.151	0.023	0.161	1.707	0.323	0.216	0.073
Gd	1.609	1.938	3.072	2.320	2.115	1.491	1.921	2.962	2.036	0.775	0.614	0.645	5.360	1.567	0.119	0.833	0.842	0.915		3.110
Dy	4.106	4.082	11.879	2.910	2.979	1.690			2.668	1.175		0.950	5.418			1.375	2.230		5.600	4.117
Er	2.474	2.370	6.366	2.390	2.200	0.877	3.389	5.035	1.649	0.680	0.359	0.572	4.075	3.767		1.164	1.110	0.320		2.695
Yb	2.577	2.520	6.242	2.742	2.261	0.713	3.833	5.659	1.508	0.635	0.313	0.554	4.390	4.158	0.124	1.233	1.322	0.940	5.700	2.646
Lu	4.800	0.382	1.435		0.418	0.100		1.416		0.095		0.086	0.836	0.836		0.205				0.419
(Ce/Yb)n	0.046	0.048	0.0018	0.26	0.25	0.23	0.091	0.0023	0.28	0.29	2.33	0.24	0.0035	0.0079	0.67	0.19	0.37	0.409	0.0044	0.56
Eu/Eu*	1.18	1.02	0.68	1.15	1.204	1.129	0.815	0.758	1.195	1.66	0.784	1.67	0.536	0.828	0.62	0.85	1.11	2.4		1.04
Ce/Ce*	0.96	0.78	0.37	1.06	1.067	0.676	0.821	0.417	1.11	1.16	1.1	0.67	0.857	0.641	0.81	1.09	1.58		0.297	0.96
(Ce/Sm)n	0.13	0.16	0.016	0.489	0.382	0.175	0.374	0.016	0.314	0.422	0.91	0.349	0.015	0.102	0.713	0.539	0.167	0.671	0.0578	0.64

Table 5.10. PYROXENITES REE MINERAL SEPARATES

SAMPLE	GP30	GP33	GP37	GP81	GP87m	GP87m	GP147	GP188	GP194m	GP236	PHN5730	PHN5731	GP87M	GP147
MINERAL	CPX	CPX	CPX	CPX	CPX	GT	GT	CPX	CPX	CPX	CPX	CPX	GT	GT
LITHOLOGY	WEB	GP	GP	GGP	GP	GP	GGP	WEB	GP	WEB	GGP	GGP	GP	GGP
							0.011							
La	1.085	2.29	0.143	0.018	0.451	0.019	0.013	1.158	0.237	0.629	0.016	0.013	0.019	0.011
Ce	3.288	9.526	0.788	0.073	1.773	0.049	0.051	3.665	0.937	2.4	0.017	0.061	0.049	0.013
Nd	3.984	9.439	2.537	0.698	2.535	0.281	0.201	3.209	1.586	2.621	0.214	0.391	0.281	0.051
Sm	1.705	2.828	1.58	1.066	1.12	0.686	0.14	1.062	0.793	0.907	0.544	0.637	0.686	0.201
Eu	0.76	0.948	0.643	0.422	0.447	0.518	1.171	0.288	0.308	0.349	0.226	0.278	0.518	0.14
Gd		2.84	1.963	1.833	1.323	2.375		0.993	0.618	1.235	2.596	2.357	2.375	1.171
Dy		2.81	1.139	2.421	0.856		9.944	0.979			8.27	4.463		
Er		1.51	0.273	1.191	0.234	4.858	11.973	0.588	0.333		5.96	1.463	4.858	9.944
Yb	2.529	1.289	0.11	0.859	0.108	5.397		0.504	0.105	0.299	5.08	0.895	5.397	11.973
Lu			0.117		0.012									
Sm/Nd	0.346	0.3	0.623	1.527	0.35	2.44	3.941	0.331	0.5	0.346	2.455	1.641	2.44	3.941
Eu/Eu*		1.03	1.12	0.93	1.13	1.25	0.89	0.86	1.35	1.01	0.58	0.57	1.25	0.89
Ce/Ce*	0.93	1.23	0.99	0.57	1.04	0.49	0.33	1.06	0.99	1.12	0.21	0.71	0.49	0.33

SAMPLE	GP87b	GP101a	GP101a	GP132(1)	GP139	GP147
MINERAL	CPX	CPX	CPX	CPX	CPX	CPX
LITHOLOGY	GP	WEB	WEB	WEB	GP	GGP
La	0.953	2.171	0.028	1.803	0.014	0.015
Ce	3.693	3.135		4.006	0.126	0.085
Nd	4.726	4.251	0.0414	2.247	1.199	0.411
Sm	1.819	1.256	0.0166	0.867	2.494	0.374
Eu	0.68	0.33	0.01	0.455	0.521	0.159
Gd	1.899		0.065	1.572	2.963	0.951
Dy		0.962		1.92	2.974	1.378
Er	0.43	0.575		1.28	1.146	0.81
Yb	0.216	0.5	0.072	1.108	0.657	0.68
Lu						
Sm/Nd	0.385	0.295	0.401	0.386	1.335	0.91
Eu/Eu*	1.12			1.2	0.76	0.82
Ce/Ce*	1.07	0.94		0.98	0.96	0.88

derived rock was ascribed to sediment contamination of the mantle source by Hole et al (1984).

Samples from all lithologies have significant positive or negative Eu anomaties (Figure 5.24a, b and c) which are persistent in lithological groups and are not due to Ba intereference or poor analyses. The GGP samples consistently have markedly negative Eu anomalies, Eu/Eu^* varying from 0.68 to 0.83 (Table 5.9). This feature would appear much more pronounced on Figure 5.24c if the samples were not as HREE enriched. Sample GP139, the GP layer spatially associated with the in situ GGP also has a marked negative Eu anomaly (0.54). Other GP layers have positive Eu anaomlies, particularly GP87M ($Eu/Eu^* = 1.2$)and PHN 5739 ($Eu/Eu^* = 2.4$). Non-garnetiferous whole rocks show similar Eu anomalies, the two Cr-webserite samples GP101 and GP188 have negative Eu anomalies, $Eu/Eu^* = 0.78$ and 0.62 respectively , whereas the Al-augite websterites vary from markedly positive Eu anomalies e.g. GP97 $Eu/Eu^* = 1.66$, to slightly negative, GP236 $Eu/Eu^* = 0.85$. The clinopyroxenite sample PHN5732 would also have an Eu/Eu^* value of over 1.5 if its Gd content is inferred from the Sm and Dy analysis. The significance of Eu anomalies in the pyroxenites will be discussed below.

5:7 Pyroxenite petrogenesis

Major elements such as Al, Ca and Mg display relationships which may be mostly related to variations in modal abundancies of OPX, CPX, GT and spinel on Al_2O_3-SiO_2 and CaO-MgO trends (see Fig. 5.25) . The major element trends observed among the various pyroxenite layers can also be observed in composite pyroxenite layers. This suggests that the mono-lithological pyroxenite layers are cogenetic in the sense that they crystallized from compositionally similar liquids that were fractionating similar phases.

A variety of hypotheses have been advanced to explain the origin of the pyroxenite layers occuring in many orogenic peridotite massifs. The most simplistic model is that the pyroxenites are crystallized primary melts formed by partial melting of the host peridotite (Dickey 1970). Kornprobst (1969) proposed that the Beni Bousera pyroxenites represent the product of flow differentiation (i.e. crystallization as " cumulates ") of melts produced by melting of the host peridotite at high pressures. Other interpretations are that the layers formed as residues or liquids from selective remelting of previously existing pyroxenite layers (Dickey et al 1977, Loubet and Allegre, 1979 and 1982, Shervais 1978). Suen and Frey (1987) suggested that the Ronda pyroxenite suite originated by crystal/liquid fractionation at > 19 kb as melts migrated through magma conduits towards the cool, exterior portion of a diapir and implied that the melts were genetically related to the body as a whole. Polve and Allegre (1980), Polve (1983), Allegre and Turcotte (1986), Nixon et al (1986), Pearson et al (1987), and Hamelin and Allegre (1988) have suggested that the Beni Bousera pyroxenites are derived from protoliths of subducted, hydrothermally altered oceanic lithosphere. These alternatives can now be examined in the light of whole major and trace-element geochemistry.

5:7.1 Do the pyroxenite layers represent crystallized primary melts ?

The almost total lack of K_2O, and low Na_2O P_2O_5 and TiO_2 in all the pyroxenites renders them unlikely candidates for any known melt compositions. The large degree of major element variation shown by the pyroxenite suite, particularly in terms of FeO, CaO and Al_2O_3 vs MgO (Figure 5.23) is also

Figure 5.25a. SiO_2 vs Al_2O_3 (wt %) Beni Bousera pyroxenites. CPX , OPX and GT compositional fields are from pyroxenite mineral compositions given in Chapter 4 and Kornprobst (1969). Arrows point towards compositional fields of other minerals (Plag., Olivine and Spinel).

Figure 5.25b. CaO vs MgO (wt %) for Beni Bousera pyroxenites. Compositional fields of minerals taken from Chapter 4.

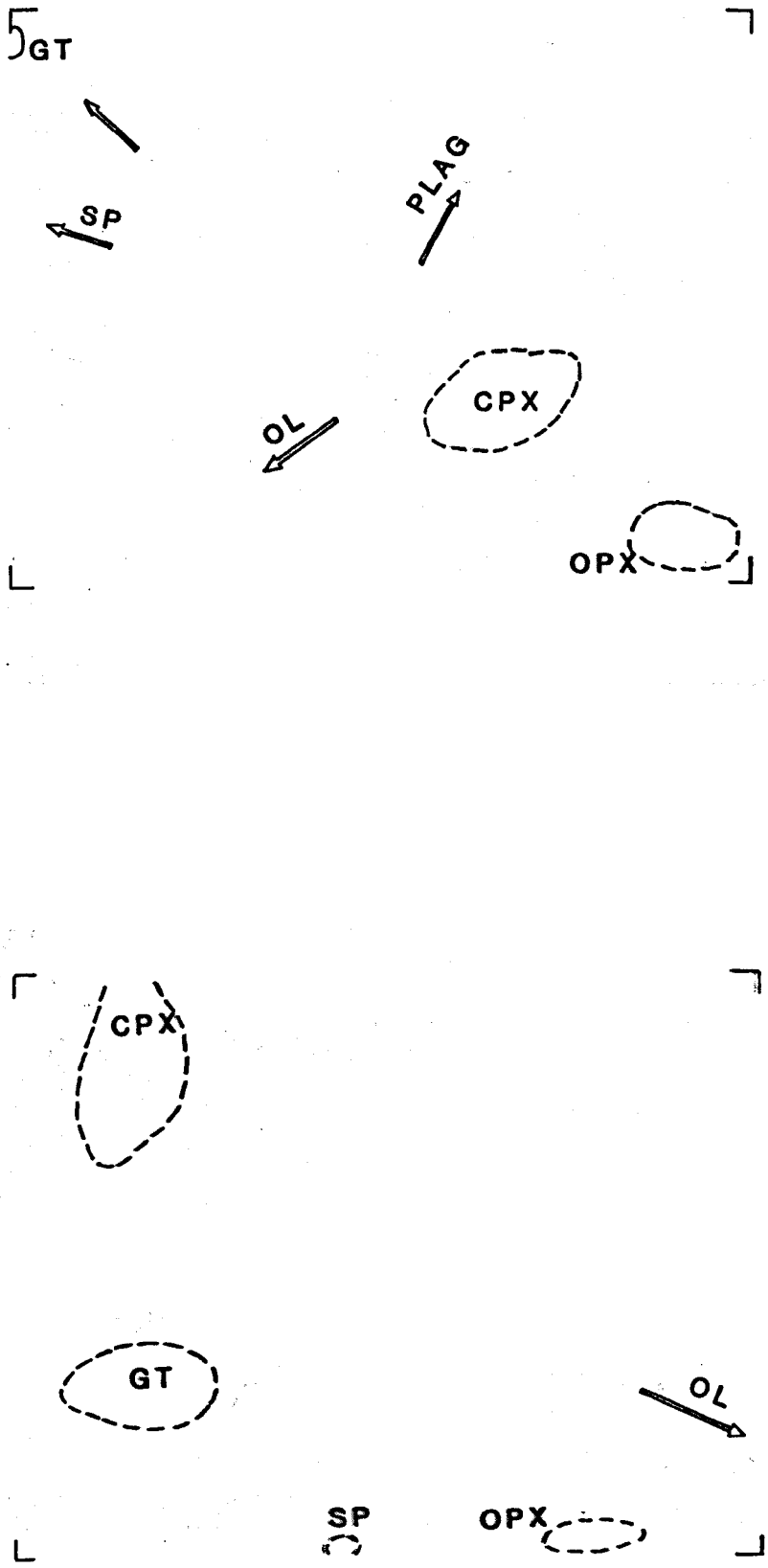
GT
SP
PLAG
CPX
OL
OPX
CPX
GT
OL
SP
OPX

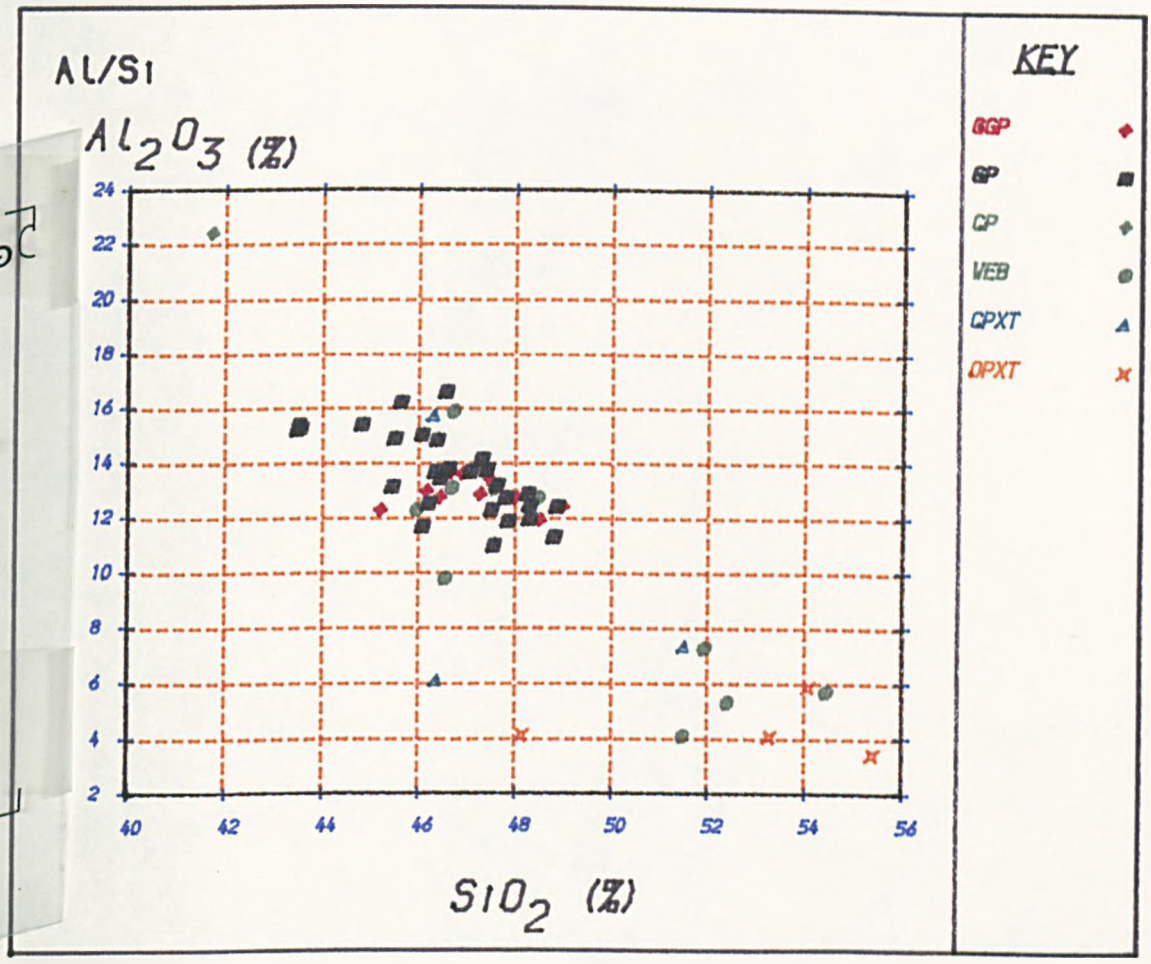
Al/Si
Al_2O_3 (%)
SiO_2 (%)
KEY
BGP
BP
CP
VEB
CPXT
OPXT

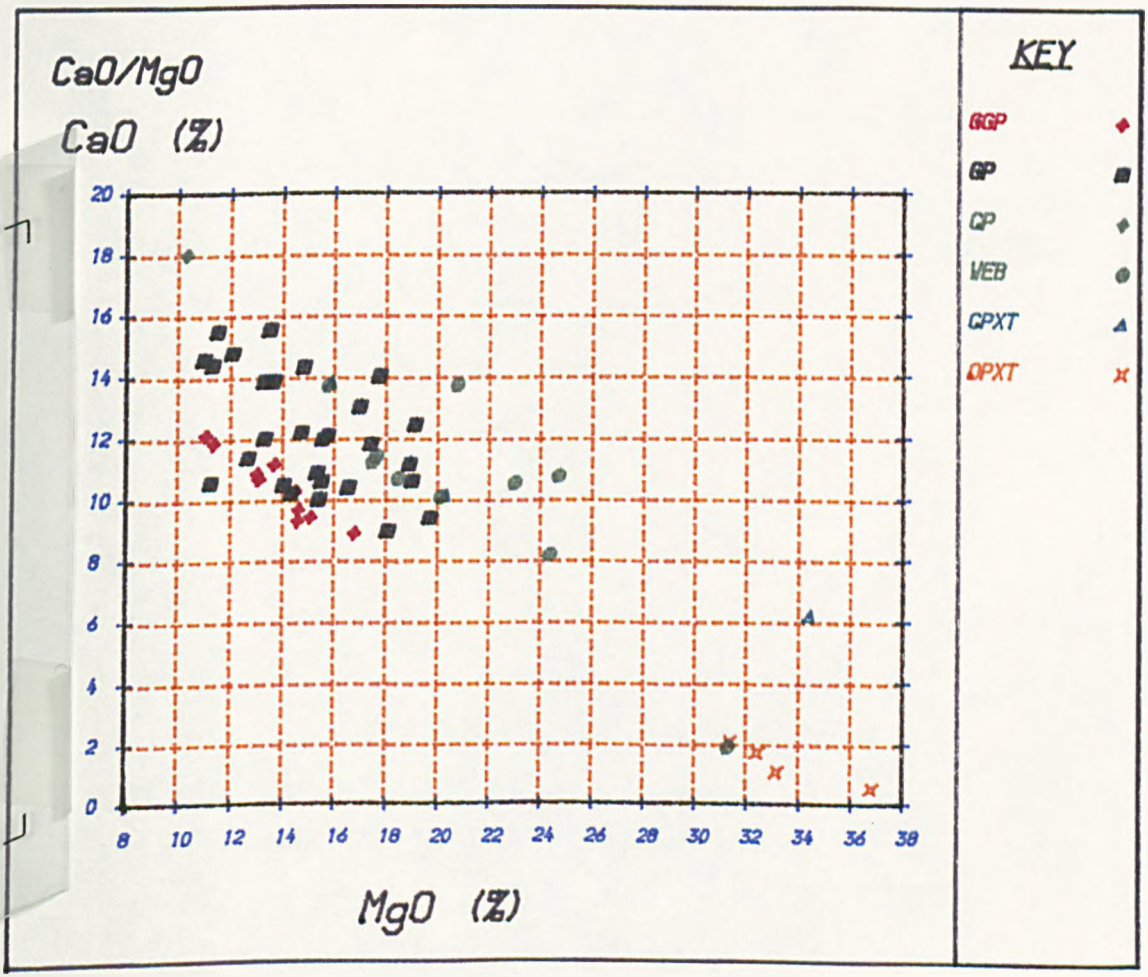
CaO/MgO
CaO (%)
MgO (%)
KEY
BGP
BP
CP
VEB
CPXT
OPXT

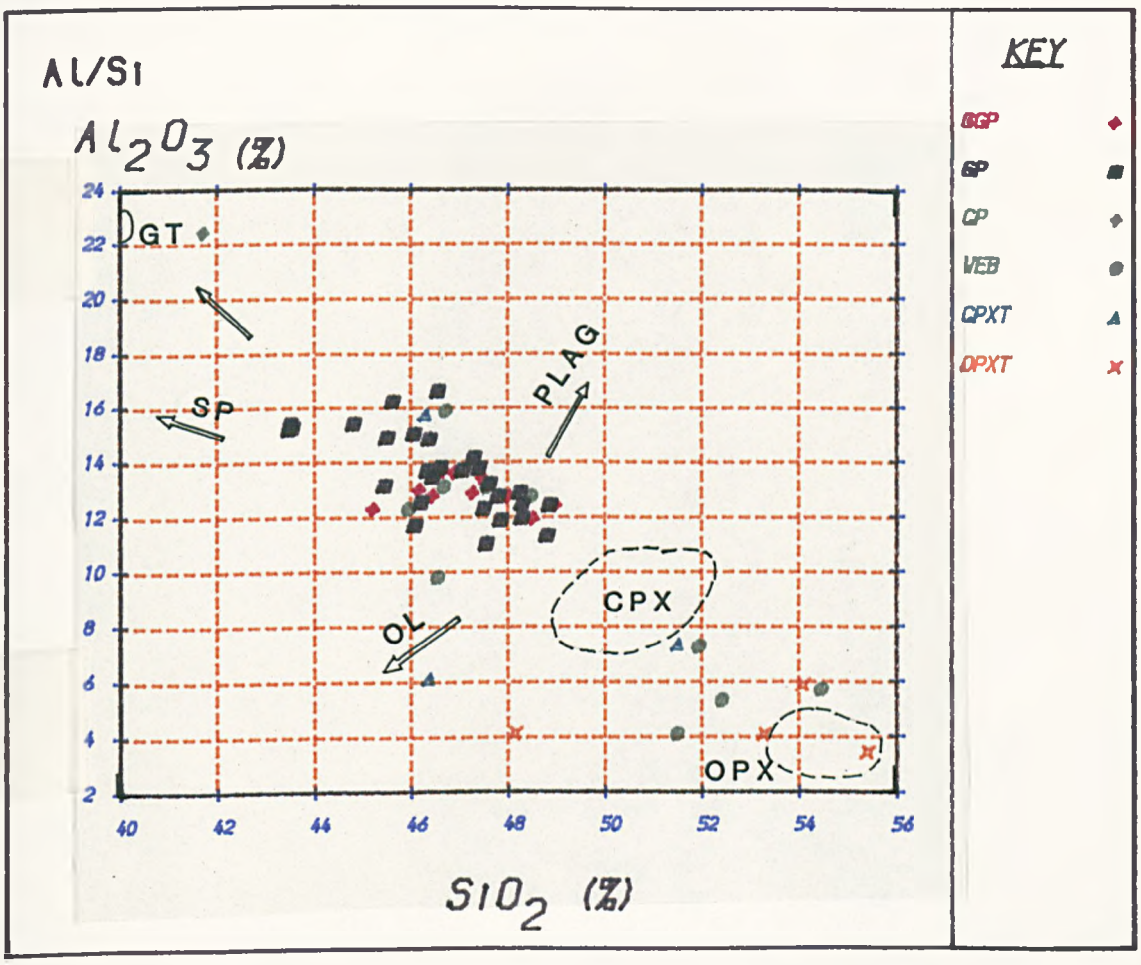
Al/Si
Al_2O_3 (%)
GT
SP
PLAG
OL
CPX
OPX
SiO_2 (%)
KEY
BGP
GP
CP
VEB
CPXT
OPXT

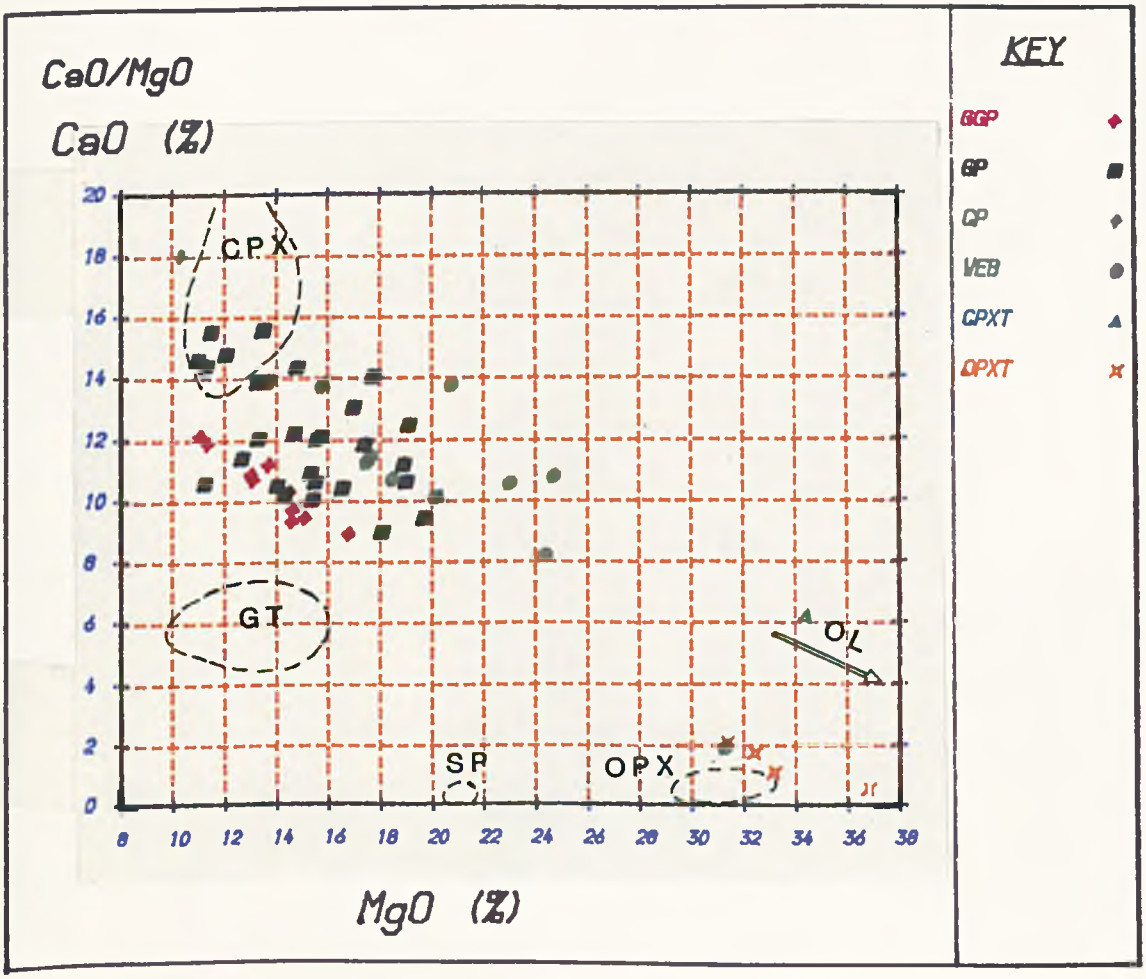
CaO/MgO
CaO (%)
CPX
GT
OL
SP
OPX
MgO (%)
KEY
BGP
GP
CP
VEB
CPXT
OPXT

incompatible with an origin as primary melts, most of the compositions plotting well outside the calculated equilibrium melt compositional fields (Figure 5.23) which also encloses the Baffin Island picrites. Compared to natural and experimentally derived primary mantle melts the pyroxenite samples range from more MgO depleted compositions (~ 11 wt %) to very MgO rich (> 36 wt %) rocks.

There is no apparent correlation between degree of silica saturation in the Beni Bousera pyroxenite layers and Mg No. with both high and low Mg No. websterites and garnet pyroxenites plotting in silica-under saturated and silica-saturated fields (Fig. 5.19). The breakdown of the garnet-pyroxene thermal divide at < 30 kb during melting of fertile lherzolite shifts the invariant melt composition into the silica saturated field (O'Hara 1968). The lack of correlation between increasing Mg No. and increasing degree of silica saturation is not consistent with the pyroxenite suite representing crystallized primary melts formed over a range of P and T during progressive melt extraction of an ascending diapir.

REE data provide the most convincing argument that the pyroxenite layers are not crystallized melts formed by partial melting of the host peridotites. All but one of the pyroxenites have LREE/HREE ratios less than chondrites. This LREE depletion is often extreme, eg (Ce/Yb)$_n$ 0.0023 for GP81, is not compatible with the calculated REE contents of melts formed in equilibrium with the Beni Bousera peridotites between 10 and 30 % melting (Figure 5.26). Layers with low Mg Nos. have lower LREE/HREE ratios than the host peridotites and there is no correlation between Mg No. and LREE/HREE fractionation. The pyroxenites are unlikely to represent late stage fractional melts in equilibrium with LREE depleted sources as there is no evidence of the abundant early LREE enriched melts that would have been formed. Late stage, LREE depleted fractional melts would also be expected to be the most refractory melts in terms of major elements; in fact the most LREE depleted pyroxenites, the GGPs, have the lowest MgO contents and Mg Nos. and among the highest CaO and Al_2O_3 contents. Furthermore, fractional melting is not considered as a common petrological process in the generation of basaltic magmas in general (Frey et al 1985). Many of the GP and GGP layers show considerable HREE enrichment (Yb)$_n$ ~ 10 to 50. Such high and variable HREE enrichment is not compatible with an origin as crystallized primary melts. Finally the presence of both positive and negative Eu anomalies in the pyroxenites, none of wihch contain any primary plagioclase is incompatible with their origin as melts from the host peridotite or any spinel or garnet facies peridotite source.

5:7.2 Do the pyroxenite layers represent fragments of subducted oceanic lithosphere ?

The possibility that the Beni Bousera pyroxenites represent subducted fragments of oceanic lithosphere which have simply been " stretched and thinned by the normal and shear strains in the convecting mantle " (Allegre and Turcotte 1986) can also be tested using whole-rock geochemical data. The major element compositions of many ultramafic cumulates from the lower sections of ophiolite massifs follow an iron enrichment trend that is not as extreme as that observed in the Beni Bousera pyroxenite suite. Ophiolitic rocks also follow a marked Al_2O_3 enrichment trend which is not as apparent in the Beni Bousera pyroxenites although the corundum bearing pyroxenite analysed by Kornprobst (1982) does plot on this trend (Fig.5.17). The moderate LREE depletions to slight LREE enrichments of the non-garnetiferous pyroxenite patterns together with their positive and negative Eu anomalies show close similarities to some of the varied REE patterns observed in sheeted dykes and gabbros from ophiolite massifs e.g. Pallister and

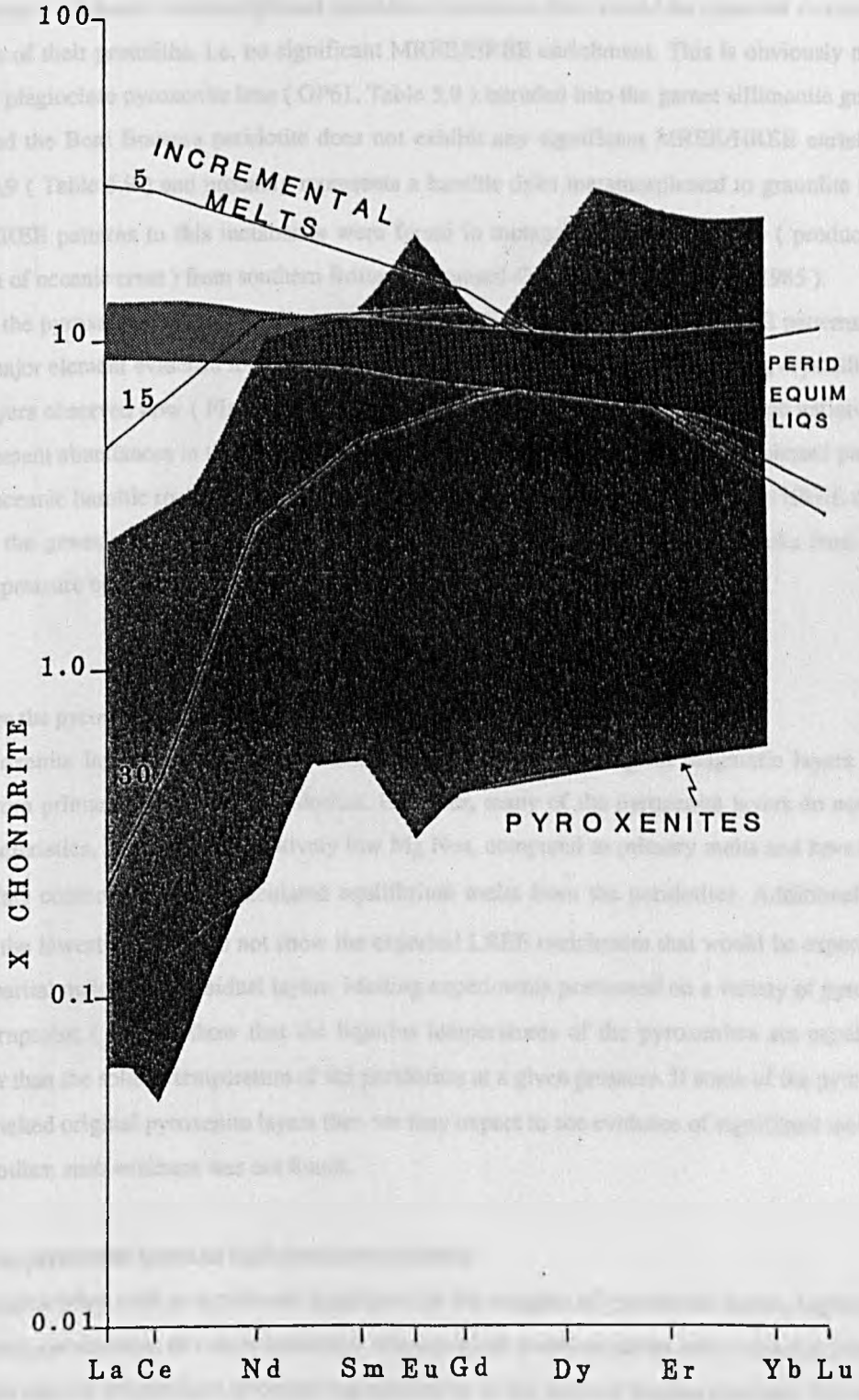

Figure 5.26. Chondrite normalized REE plot of equilibrium melts from Beni Bousera peridotites produced by 15-20 % melting (heavy stipple) compared to REE range shown by pyroxenites (lighter stipple). Solid lines are REE patterns for 5, 15 and 30 % incremental melting of a peridotite similar to R717.

Knight (1981), see Figure 5.27.

The marked HREE/MREE enrichment displayed by several of the Beni Bousera GP and GGP layers, $(Sm/Yb)_n$ down to 0.078, is not seen in any ophiolitic cumulates or magmas and can only be explained by invoking cumulate garnet crystallizing from a melt originating in the garnet stability field. No ophiolitic cumulates have been reported to contain garnet (e.g. Coleman 1977) thus if the Beni Bousera pyroxenites simply represented subducted metamorphosed ophiolitic cumulates they would be expected to retain the HREE profiles of their protoliths, i.e. no significant MREE/HREE enrichment. This is obviously not the case. A garnet plagioclase pyroxenite lens (GP61, Table 5.9) intruded into the garnet sillimanite gneisses that surrounded the Beni Bousera peridotite does not exhibit any significant MREE/HREE enrichment $(Sm/Yb)_n = 0.9$ (Table 5.9) and probably represents a basaltic dyke metamorphosed to granulite facies. Similar flat HREE patterns to this metabasite were found in metagabbros and eclogites (produced by metamorphism of oceanic crust) from southern Brittany (Bernard-Griffiths and Cornichet, 1985).

None of the pyroxenites displaying distinctive Eu anomalies in their whole-rock REE patterns show unequivocal major element evidence for the involvement of plagioclase fractionation during crystallization to form the layers observed now (Figure 5.25). The above evidence, coupled with the large variations in compatible element abundances in the pyroxenites preclude their origin as simple metamorphosed products of subducted oceanic basaltic rocks. The involvement of a highly aluminous phase with high HREE content i.e. garnet in the genesis of the GGP and GP layers further rules out many of the rocks from being relatively low pressure ophiolitic cumulates which have been metamorphosed by subduction.

5:7.3 Are the pyroxenites remelted primary melt layers ?

The pyroxenite layers may represent residues from, or melts of original magmatic layers which crystallized from primary melts of the peridotites. However, many of the pyroxenite layers do not show residual characteristics, i.e. they have relatively low Mg Nos. compared to primary melts and have higher Al_2O_3 and CaO contents than the calculated equilibrium melts from the peridotites. Additionally, the samples with the lowest Mg Nos. do not show the expected LREE enrichment that would be expected for the resultant partial melts of the residual layers. Melting experiments performed on a variety of pyroxenite layers by Kornprobst (1970) show that the liquidus temperatures of the pyroxenites are equal to, or slightly higher than the solidus temperature of the peridotites at a given pressure. If some of the pyroxenites represent re-melted original pyroxenite layers then we may expect to see evidence of significant melting of the host peridotites; such evidence was not found.

5:7.4 The pyroxenite layers as high pressure cumulates.

Field relationships such as occasional apophyses on the margins of pyroxenite layers, together with sharply bounded symmetrical or non-symmetrical mineralogical zonation across some layers indicate that the pyroxenites may be the products of crystal segregation on to the walls of magma conduits. This implies that the pyroxenite whole-rock compositions effectively represent a series of high pressure cumulates formed from liquids passing through the peridotites.

The extremely low K_2O and P_2O_5 contents of the pyroxenites and their low TiO_2 and Na_2O

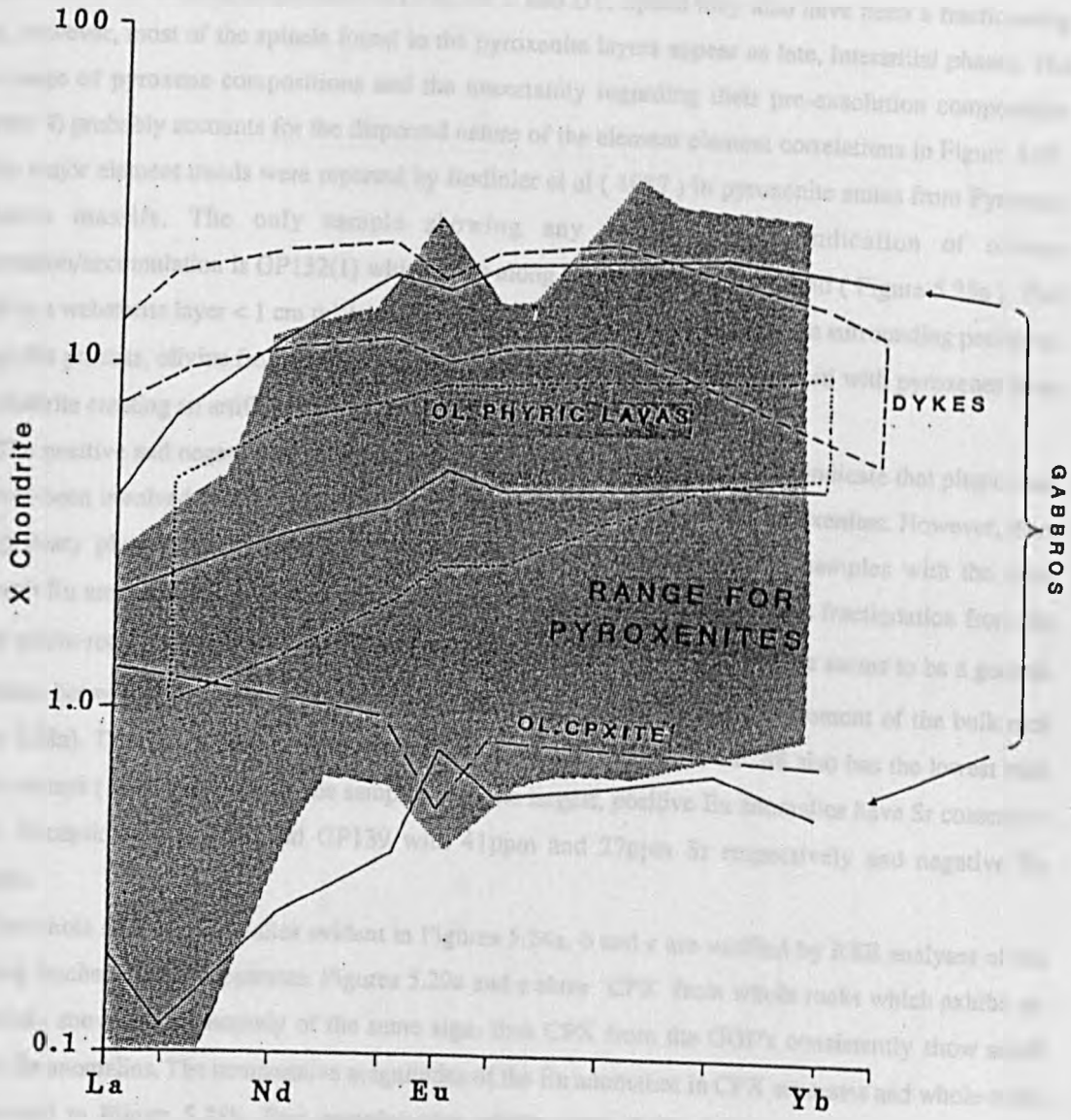

Figure 5.27. Chondrite normalized REE patterns for various units of ophiolites compared to the REE range observed in the Beni Bousera pyroxenites (light stipple).

abundances compared to basaltic liquids are compatible with the suite representing "cumulates" from basic/ultrabasic liquids. End-members of the major element trends shown by the pyroxenite suite are observed as discrete zones in multi-lithological (composite) layers. Zones from composite layers form very similar major element trends compared with the suite as a whole (Kornprobst 1969 and Fig. 5.18). This suggests that the composite and monominera lic layers were formed by the same crystal segregation process. Plots of Al_2O_3 vs SiO_2 and CaO vs MgO (Figure 5.25a and b) indicate that crystal fractionation was dominated by varying proportions of CPX, OPX and GT. Spinel may also have been a fractionating phase, however, most of the spinels found in the pyroxenite layers appear as late, interstitial phases. The large range of pyroxene compositions and the uncertainty regarding their pre-exsolution composition (Chapter 4) probably accounts for the dispersed nature of the element-element correlations in Figure 5.25. Similar major element trends were reported by Bodinier et al (1987) in pyroxenite suites from Pyrenean peridotite massifs. The only sample showing any major element indication of olivine fractionation/accumulation is GP132(1) which plots along the olivine addition trend (Figure 5.25a). This sample is a websterite layer < 1 cm thick which was mechanically extracted from the surrounding peridotite. During this process, olivine from the surrounding peridotite was mechanically mixed with pyroxenes from the websterite creating an artificial olivine accumulation trend.

The positive and negative Eu anomalies observed in bulk rock REE profiles indicate that plagioclase may have been involved at some stage during the petrogenesis of some of the pyroxenites. However, there is no primary plagioclase in any of the pyroxenites. In addition none of the samples with the most prominent Eu anomalies (positive or negative) give any indication of plagioclase fractionation from the present whole-rock major element compositions eg. low Al_2O_3. Interestingly, there seems to be a general correlation between magnitude of Eu anomaly, denoted by Eu/Eu^* and the Sr content of the bulk rock (Figure 5.28a). That is, the sample with the largest negative Eu anomaly, GP188 also has the lowest bulk rock Sr content (1.95 ppm) whilst the samples with the largest, positive Eu anomalies have Sr contents > 15ppm. Exceptions are GP81 and GP139 with 41ppm and 27ppm Sr respectively and negative Eu anomalies.

The whole rock Eu anomalies evident in Figures 5.24a, b and c are verified by REE analyses of the coexisting leached mineral separates. Figures 5.29a and c show CPX from whole rocks which exhibit an Eu anomaly show an Eu anomaly of the same sign, thus CPX from the GGP's consistently show small negative Eu anomalies. The comparative magnitudes of the Eu anomalies in CPX separates and whole-rocks is illustrated in Figure 5.28b. Few samples plot within error of the 1:1 line which indicates equal magnitude of Eu/Eu^* in whole-rock and mineral separate. Samples plot both above and below the line on Figure 5.28b, the discrepancies in Eu/Eu^* magnitude may in part be ascribed to Eu mobility during alteration/serpentinization (Jahn 1986). Another possibility is that other phases with an equal affinity for Eu have incorporated a significant proportion of the whole rock Eu budget. This is evident in the two samples for which both GT and CPX have been analysed (Table 5.10). Both garnets have higher Eu/Eu^* than their corresponding CPX and whole rocks. The GT from sample GP87M contains more Eu than the coexisting CPX. This is consistent with the overlapping ranges of mineral/liquid partition coefficients for Eu in CPX's (0.48 to 2.0) and GT (0.3 to 1.5), reported by Henderson (1982). The consistencey of negative Eu anomalies in the whole rock, CPX and garnet from GP147 together with the positive Eu

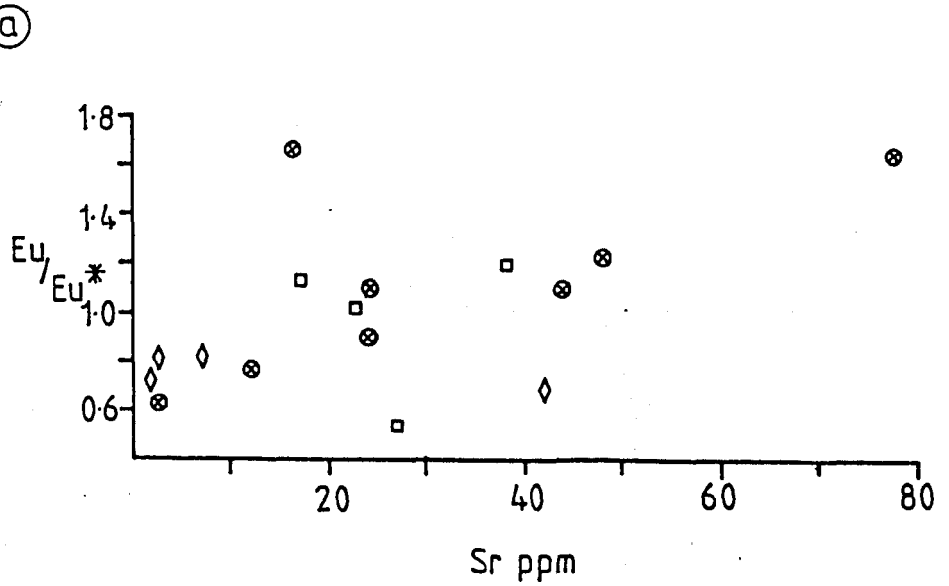

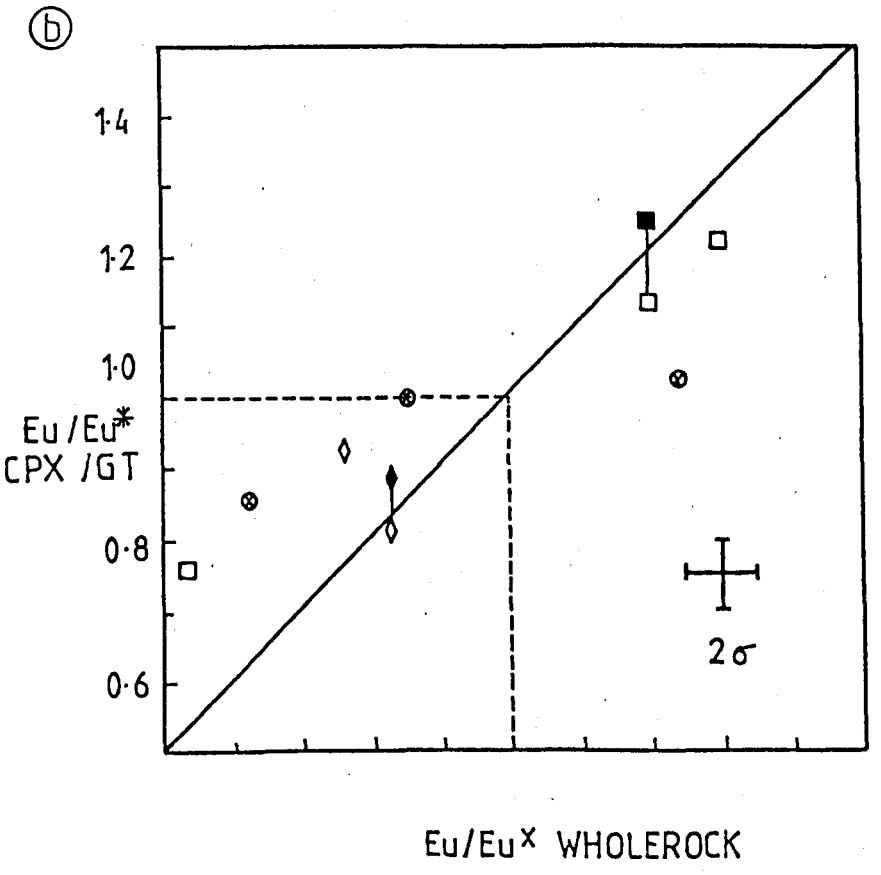

Figure 5.28a. Eu/Eu* vs Sr ppm in Beni Bousera whole rock pyroxenites. Symbols as in Figure 5.18.

Figure 5.28b. Eu/Eu* CPX or GT vs Eu/Eu* whole rock for Beni Bousera pyroxenites. Open symbols = CPX, closed symbols = GT. 2 sigma error bar based on duplicate analyses. Vertical lines join coexisting CPX and GT. Symbols as in Figure 5.18.

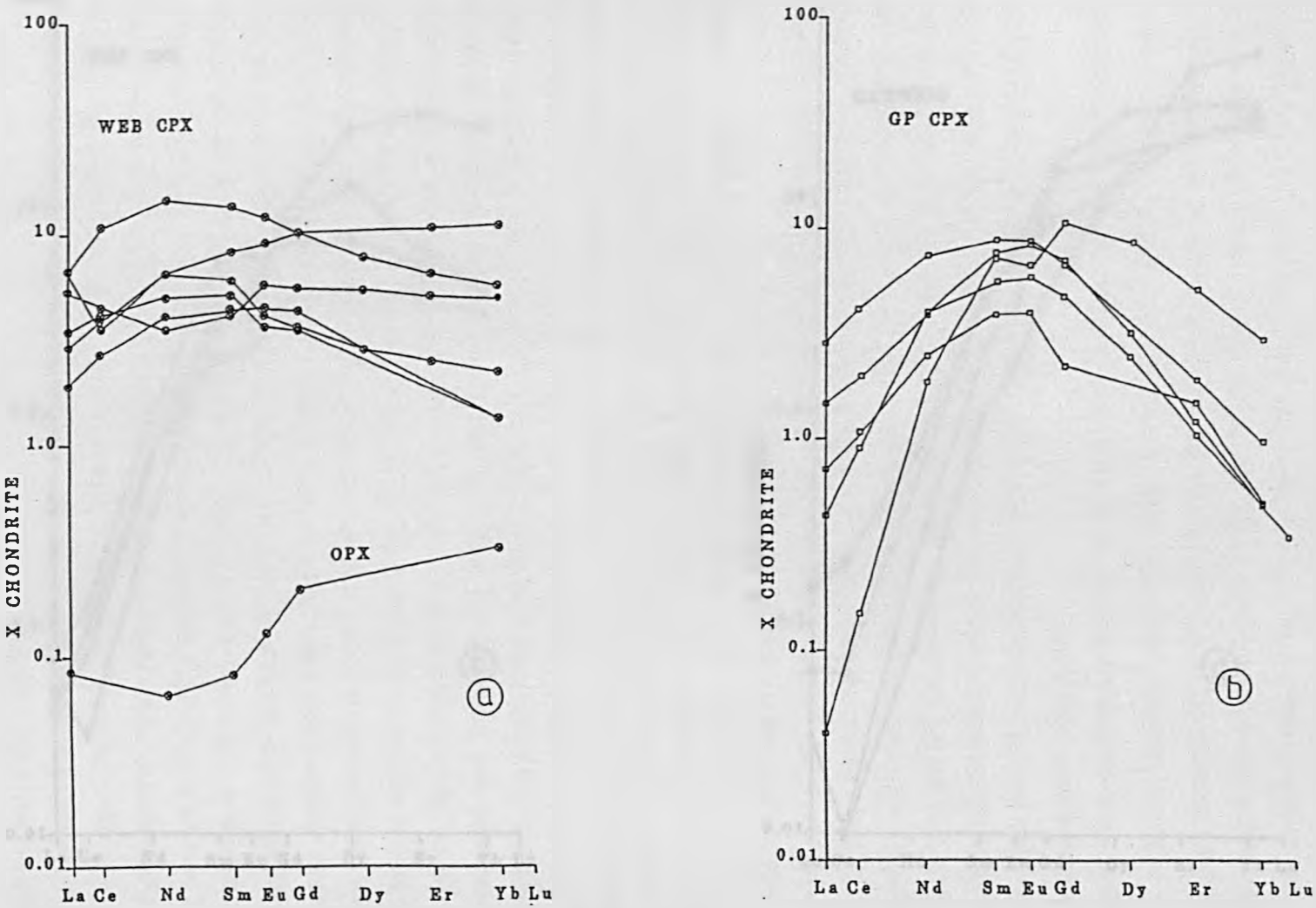

Figure 5.29. Chondrite normalized REE patterns for CPX (and one OPX) from a, websterites, b, garnet clinopyroxenites, c, graphite garnet clinopyroxenites and d, garnets from the pyroxenites and garnet lherzolite GP24 (square with cross).

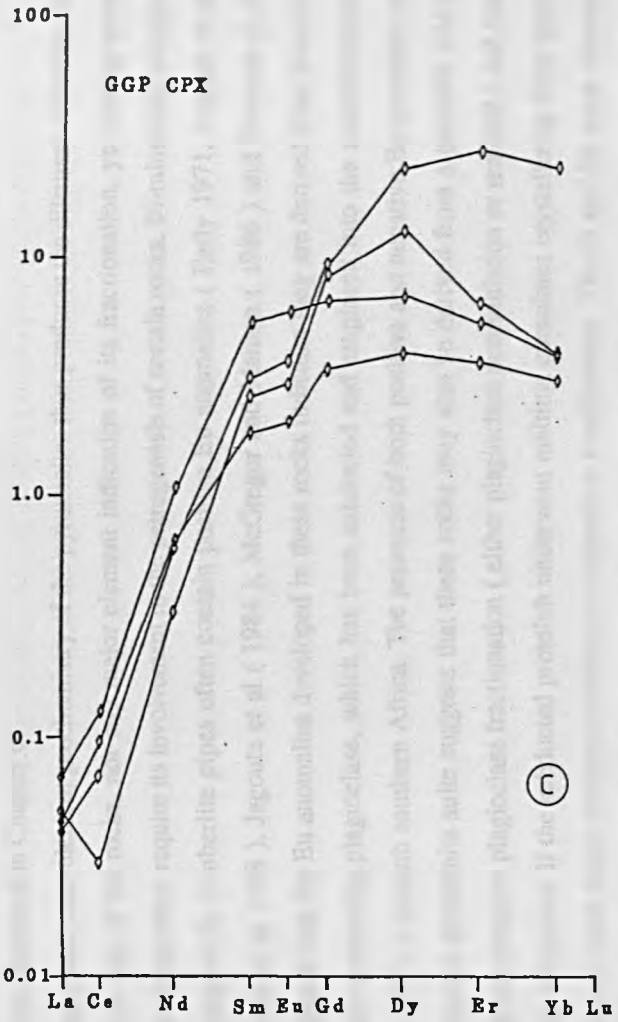
GGP CPX
100
10
1.0
0.1
0.01
La Ce Nd Sm Eu Gd Dy Er Yb Lu
C

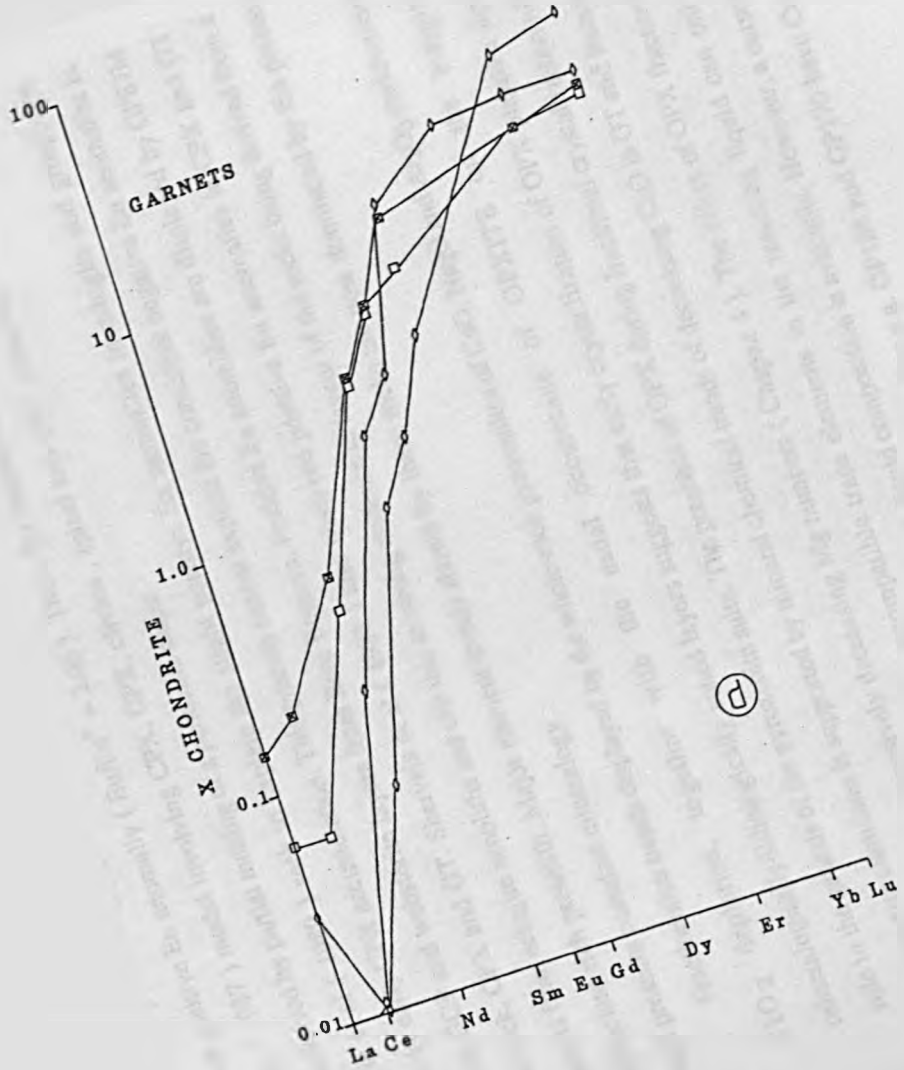
100
10
1.0
0.1
0.01
GARNETS
X CHONDRITE
La Ce
Nd
Sm Eu Gd
Dy
Er
Yb Lu
d

anomalies in the whole rock, CPX and garnet from GP87M is strong evidence in support of the effect of plagioclase fractionation at some stage during the petrogenic history of some of the pyroxenites. These presence of Eu anomalies in leached mineral separates does not favour the production of Eu anomalies in the whole rock pyroxenites by alteration/serpentinization. The possibility that the negative Eu anomalies observed in the GGP and some websterite samples originate via sediment incorporation into the parental magma will be examined in Chapter 6.

The major and trace element geochemistry of the pyroxenites thus produces the dilemma of having no plagioclase in any of the rocks, nor any major element indication of its fractionation, yet having trace element signatures which require its involvement in the petrogenesis of certain rocks. Bi-minera lic eclogite xenoliths sampled by kimberlite pipes often contain positive Eu anomalies (Early 1971, Jagoutz et al 1984, Shervais et al 1988). Jagoutz et al (1984), McGregor and Manton (1986) and Shervais et al (1988) suggested that the Eu anomalies developed in these rocks indicates they are derived from basaltic oceanic crust containing plagioclase, which has been subducted and emplaced into the subcontinental lithosphere (SCL) beneath southern Africa. The presence of both positive and negative Eu anomalies in the Beni Bousera pyroxenite suite suggests that these rocks may also be derived from a protolith which experienced low pressure plagioclase fractionation (either plagioclase accumulation or removal) and was subsequently subducted. If the subducted protolith underwent melting, cumulates crystallizing from these melts would not show major element evidence of plagioclase fractionation. The Sr and Eu trace element signatures may be retained and incorporated into CPX and GT during high pressure phase changes/crystallization. It is interesting to note that several of the Ronda " group E " pyroxenites studied by Suen and Frey (1987) show slight positive Eu anomalies whilst one sample in particular (R705A) has a very pronounced positive Eu anomally ($Eu/Eu^{*} = 2.06$). These Eu anomalies cannot be explained by the Suen and Frey (1987) model involving CPX, OPX, olivine , spinel and GT " cumulate " crystallization from liquids derived by partial melting of a peridotite diapir.

Smyth et al (1989) seek to explain the slight positive Eu anomalies in eclogite and grospydite xenoliths by early CPX accumulation. This process cannot explain the consistent negative Eu anomalies in CPX rich GGP and websterite layers from Beni Bousera. Positive Eu anomalies are displayed by GP87M whole rock, CPX and GT. Shervais et al (1988) also observed positive Eu anomalies in CPX and GT seperates from eclogite xenoliths and cite this as strong evidence in favour of the rocks being derived from a plagioclase rich protolith. Major element trends shown by these rocks are now dominated by the present high pressure cumulate mineralogy.

Fractionation trends displayed by the whole-rock pyroxenites of CaO, Na_2O and Al_2O_3 enrichment and SiO_2 depletion, together with the usual occurrence of OPXITE on the margins of mineralogically/lithologically zoned layers suggests that early crystallization of OPX played a significant role in the genesis of the pyroxenite suite. The presence of OPX during fractional crystallization of the early pyroxenite cumulates is supported by mineral chemical trends of decreasing CaO in GT and increasing Na_2O in CPX with progressively decreasing Mg numbers (Chapter 4). The effect of OPX fractionation on the compatible and moderately incompatible trace elements in the resulting liquid can only be assessed quantitatively if an undifferentiated source liquid composition is available. However, a cursory inspection of Table 5.3 reveals that some of the OPX-rich websterites e.g. GP188 and GP170 have Cr contents > 3500

ppm, i.e. greater than the concentrations observed in the peridotites. This observation and the very high, but very variable Cr/Ni ratios of the pyroxenites (up to 6.8) resemble values recorded in mafic and ultramafic cumulates. For example, Cr/Ni ratios for ophiolitic ultramafic cumulates typically range from ~ 2 to 8 (Lippard et al 1988). These high and variable Cr/Ni ratios preclude interpretations of the pyroxenites as pyroxene-rich end-members of the residual peridotite suite, or as crystallized melts.

Trace element modelling was used to asses the role of OPX fractionation in producing liquids from which the more evolved GGP and GP could crystallize as cumulates. A source " liquid " GP234 was chosen with relatively high MgO content and Mg No. and Cr and Ni contents of over 1000 and 400 ppm respectively, i.e. fulfilling the criteria suggested by Frey et al (1978) for the recognition of primary melts. GP234 is too low in K, P and Ti to realistically resemble a true primary mantle melt; except perhaps those proposed by Elthon and Casey (1985) to explain certain major element depleted MORB glass compositions. Accepting this, the compatible and moderately incompatible trace element abundances of GP234 are of similar magnitude to those except for primary melts, justifying its selection for trace element modelling. To create fractionated liquids from this source which are of similar Ni content to the fractionated GGPs (Mg Nos. < 60, Ni < 120 ppm) requires at least 30 % fractionation of OPX (Figure 5.30) from a source equivalent to GP234 using the more extreme $K_{D\ OPX/liquid}$ Ni values of 5 (Henderson 1982). Effects of varying the magnitude of the partition coefficients are modelled in Figure 5.30. Fractional crystallization of varying amounts of CPX and GT from this liquid produces a bulk cumulate more enriched in Ni than the liquid due to the high $K_D^{CPX/Liq}$ Ni of CPX (~ 3). More than 30 % OPX fractionation from the source liquid yields a fractionated liquid with < 7 wt % MgO which is too low for the GGP compositions. Fractionation of OPX cannot account for the increase in Y contents observed in the GGP and GP cumulates with low Mg Nos.. Addition of ~ 20 % CPX or GT to the fractionating assemblage (Fig. 5.30) only produces a trend intermediate between the two extreme $K_D^{OPX/Liq}$ Ni trends. Fractionation of CPX and GT from the source liquid would also rapidly deplete Sc. Sc is enriched relative to the GP234 in the more evolved Beni Bousera pyroxenites (up to 80 ppm in GP81). Addition of spinel to OPX in the fractionation scheme produces more rapid depletion in Ni for a given value of F (Figure 5.30), however, its effect on Y evolution is uncertain due to lack of published partition coefficients. In addition, fractionation of even small amounts (< 10 %) of spinel rapidly depletes the residua in V as the $K_D^{sp/liq}$ value for V is ~ 40 (Irving, 1978), and may cause slight depletion in Zr (see K_D ranges given by Nakamura et al , 1986).

The problem of producing the low and variable Ni abundances in cumulate products with relatively low Mg Nos. such as the GGP is alleviated if a source composition is selected with a lower Ni content. However, this does not explain the problem of how a GGP layer with a relatively high Mg No. such as GP147 (Mg no = 49) can have an Ni content a factor of > 2 lower than a GGP layer such as PHN5734 which has a lower Mg No. (46). PHN5734 also has 1.5 x higher Cr abundance than GP147. Such inconsistencies are common throughout the suite, particularly with respect to very incompatible elements such as Sr, Rb, Zr and LREE which show no correlation with Mg No. (Figure 5.23). The irregular trace element systematics of the pyroxenites cannot be reconciled with a simple model of the suite representing a series of high pressure cumulates from a single source.

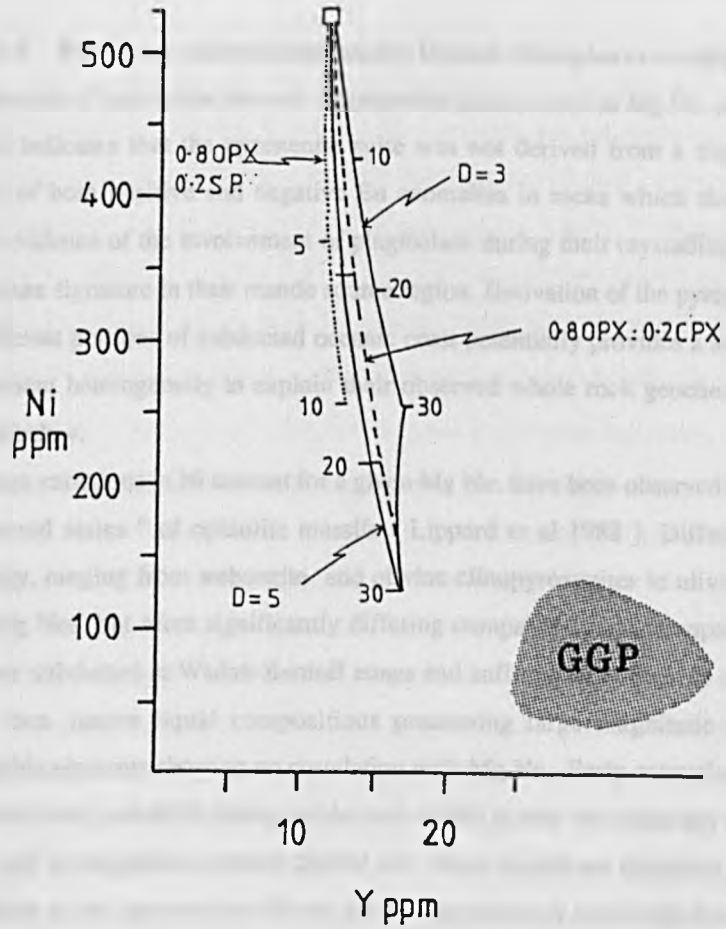

Figure 5.30. Ni (ppm) vs Y (ppm) for fractional crystallization from a source equivalent to GP234. Solid lines enclose field for fractional crystallization (0-30 %) of OPX with $K_D = 3$ and 5. Dashed line fractionating assemblage 80 % OPX, 20 % CPX. Dotted line 80 % OPX, 20 % spinel. Shaded area is field for GGP whole rocks. Partition coefficients from Frey et al (1978)and Henderson (1982).

5:7.5 Pyroxenite source heterogeneity: Oceanic lithosphere recycling ?

The lack of correlation between fractionation indices such as Mg No. and compatible and incompatible elements indicates that the pyroxenite suite was not derived from a single homogeneous source. The presence of both positive and negative Eu anomalies in rocks which show no petrographical or major element evidence of the involvement of plagioclase during their crystallization indicates the presence of a low pressure signature in their mantle source region. Derivation of the pyroxenite suite as melts or residues from different portions of subducted oceanic crust potentially provides a source with sufficient major and trace element heterogeneity to explain their observed whole rock geochemistry. This possibility will be evaluated below.

Large variations in Ni content for a given Mg No. have been observed in various cumulate rocks from the " layered series " of ophiolite massifs (Lippard et al 1988). Different cumulate units of varying mineralogy, ranging from websterite and olivine clinopyroxenites to olivine and pyroxene gabbros have similar Mg Nos. but often significantly differing compatible and incompatible element contents. If such rocks were subducted at Wadati-Benioff zones and suffered large degrees of melting, the resultant liquids would form source liquid compositions possessing large magnitude variations in compatible and incompatible elements showing no correlation with Mg No.. Early extraction of small degree (hydrous ?) melts from these protoliths during subduction would further decouple any original relationships between Mg No. and incompatible element content and cause significant depletion of LREE. If liquids similar in composition to the pyroxene or olivine gabbro cumulates or even high level boninites observed in many ophiolite sections acted as sources for the generation of the more evolved cumulates the amount of OPX fractionation required to produce the low Ni liquids from which the more " evolved " cumulates crystallized is significantly reduced. Ni contents of these rocks can vary from over 300 ppm to less than 120 ppm (Coleman 1977, Boudier and Coleman 1981, Lippard et al 1988), hence less than 15 % OPX fractionation is required to generate liquids with < 70 ppm Ni. This degree of OPX fractionation leaves residual liquids with > 11 % MgO. Interestingly the CaO-Al_2O_3-MgO major element compositions of " Mean Oceanic Crust " calculated by Elthon (1979) is located within the field defined by the Beni Bousera pyroxenites (Figure 5.18) from which the various pyroxenite varieties could be generated by varying degrees of accumulation of OPX, CPX and GT.

Derivation of the Beni Bousera pyroxenites by subduction of relatively low pressure, oceanic lithosperic cumulates is also attractive in terms of explaining their REE abundances. Subducted, protoliths which were subject to either plagioclase accumulation or loss would retain the particular Eu anomaly imparted on the rock by either of these processes when metamorphosed and even melted at high pressure. Figure 5.27 shows that members of the gabbro and pyroxenite layered sequences in ophiolites can have positive and negative Eu anomalies.The presence of Eu anomalies in the Beni Bousera pyroxenite precludes them representing cumulates crystallized from melts of the host peridotites (as does their highly variable compatible and incompatible trace element abundancies).

REE patterns of some moderately depleted garnetiferous and non-garnetiferous pyroxenites are comparable to those produced by incremental batch melting of a garnet peridotite (Figure 5.26). If these pyroxenites are incremental melts of the host peridotites, pyroxenites with the lowest $(Ce/Yb)_n$ values

would be expected to have the highest Mg numbers. This is not observed; the GGP have some of the lowest Mg Nos. (38-50) among the pyroxenite suite analysed and yet have the lowest (Ce/Yb)$_n$ values. Further evidence against batch melting as a mechanism for producing the observed depletions in LREE in the Beni Bousera pyroxenites is the lack of associated and complementary LREE enriched to moderately LREE enriched liquids produced over the first increments of melt " extraction ".

Calculation of the REE patterns of equilibrium liquids from pyroxenite CPX REE data reveals considerable variation (Figure 5.31). The GGP equilibrium liquids and that for GP139 are very LREE depleted (Ce/Sm)$_n$ = 0.03 to 0.24. GP layers (except GP139) vary from LREE enriched (Ce/Sm)$_n$ = ~ 1.7 to slightly depleted (Ce/Sm)$_n$ = 0.5 whereas equilibrium liquids calculated from websterite CPX are all LREE enriched (Ce/Sm)$_n$ = 2.75-3.6. Calculated equilibrium liquids for the GGP and GP CPX are similar to the range of liquids produced by incremental batch melting of a garnet lherzolite (Figure 5.26/5.30). However, the large variation in Ni abundances, lack of correlation between Mg No. and LREE depletion and the presence of both positive and negative Eu anomalies in the pyroxenite suite preclude the GGP and GP being cumulates from incremental melts of garnet peridotites. The Eu anomalies of liquids coexisting with the GP CPX from GP37 and GP87M are unavoidable even if varied partition coefficients are used. This suggests these liquids were derived from sources containing Eu anomalies. The LREE enriched equilibrium liquids from the websterite CPX are similar to early incremental melts from a garnet peridotite source (Fig. 5.26) but these rocks have the highest MgO contents and Mg Nos. and the lowest Al_2O_3 contents of the pyroxenite suite and are hence not likely to have crystallized from such melts.

Strontium abundances in the calculated equilibrium liquids for the GGP and GP139 range from 6.2 to 22.9, much lower than any known terrestial magma. In contrast, the calculated websterite equilibrium liquids contain between 126 and 588 ppm Sr. The observed range in LREE and Sr abundances in calculated equilibrium liquids for the pyroxenite suite is far too large for the liquids to be genetically related to each other by fractional crystallization (especially in the absence of primary plagioclase). This conclusion supports the theory that heterogeneous protoliths are required to generate the pyroxenite suite. Large ranges of Sr contents are displayed by different units within ophiolite sequences (olivine clinopyroxenites to gabbros and basic lavas vary from ~ 5 to > 200 ppm Sr , Lippard et al 1988, McCulloch et al 1980), although generally they are not as LREE enriched as the equilibrium liquids from the websterites shown in Figure 5.31.

5:7.6 Variable LREE enrichment of the pyroxenite suite.

Several of the whole-rock REE patterns illustrated in Figure 5.24 exhibit marked enrichments in La and smaller changes in pattern slope at Ce. This effect is particularly evident at low LREE concentrations, i.e. in the GGP whole-rock REE patterns where all of the samples display concave patterns between La and Nd. Certain garnetiferous and non-garnetiferous pyroxenites in Figures 5.24 also show this effect to a lesser degree.

The pronounced La and Ce enrichment could be due to analytical contamination of LREE enriched material into certain samples with the lowest LREE abundances. This possibility can be ruled out for several reasons:

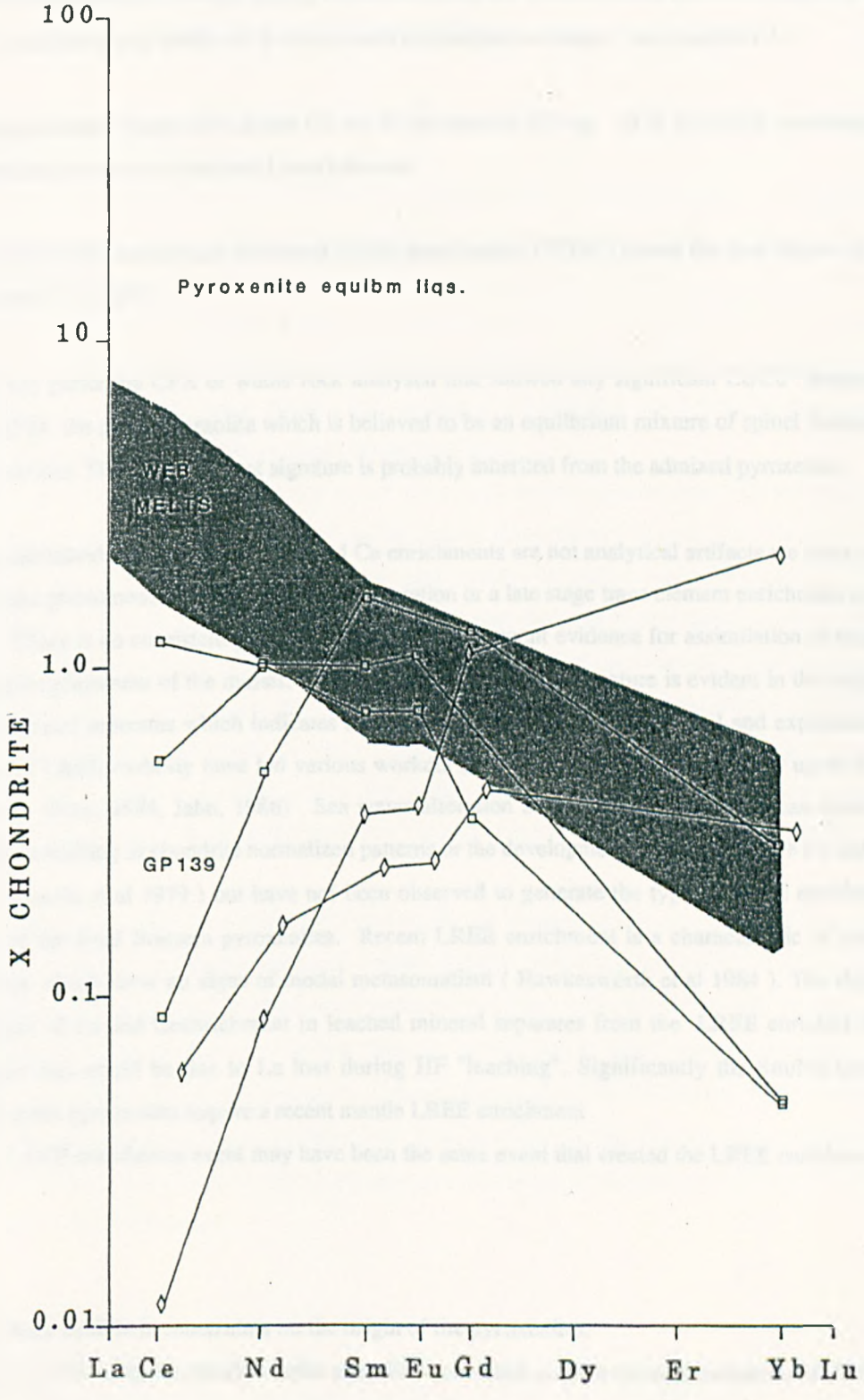

Figure 5.31. Chondrite normalized REE patterns of calculated equilibrium liquids for CPX analyses from Beni Bousera websterites (heavy stipple) and selected garnetiferous pyroxenites. Calculated using the partition coefficients of set 2 of Frey et al (1978).

1) The low Ce/Ce^* values observed in whole rock samples (from 1 to 0.3, table 5.9) are present in acid leached CPX and GT separates from the same sample (Tables 5.9 & 5.10).

2) GP147 was re-analysed using a $LiBO_2$ fusion technique and showed the an equivalent degree of La enrichment, La analysis being within 10 % of the bomb dissolution technique (see Appendix 4).

3) Total procedural blanks for La and Ce are of the order of 0.2 ng. 10 X this blank contribution would be required to produce the observed La enrichments.

4) The whole rock sample with the lowest LREE abundances (GP139) shows the least degree of La enrichment ($Ce/Ce^* = 0.857$).

5) The only peridotite CPX or whole rock analysed that showed any significant Ce/Ce^* deviation from unity is GP24, the garnet lherzolite which is believed to be an equilbrium mixture of spinel lherzolite and garnet pyroxenite. The La enrichment signature is probably inherited from the admixed pyroxenite.

Having established that the observed La and Ce enrichments are not analytical artifacts we must now assess whether the phenomenon is due to secondary alteration or a late stage trace element enrichment event in the mantle. There is no consistent physical, major or trace element evidence for assimilation of crustal material during emplacement of the massif. The La and Ce enrichment signature is evident in the leached CPX and GT mineral seperates which indicates a high temperature origin. Theoretical and experimental considerations of LREE mobility have led various workers (to consider LREE immobile for up to 30 % serpentinization (Frey, 1984, Jahn, 1986) . Sea water alteration and low-grade alteration can result in sub-parallel down-shifting of chondrite normalized patterns or the development of slight negative Ce and Eu anomalies (Ottonello et al 1979) but have not been observed to generate the type of LREE enrichment seen in some of the Beni Bousera pyroxenites. Recent LREE enrichment is a characteristic of certain mantle xenoliths which show no signs of modal metasomatism (Hawkesworth et al 1984). The slightly lower magnitude of La and Ceenrichment in leached mineral separates from the LREE enriched Beni Bousera pyroxenites could be due to La loss during HF "leaching". Significantly the Sm/Nd isotope systematics of some pyroxenites require a recent mantle LREE enrichment
This selective LREE enrichment event may have been the same event that created the LREE enrichment in the GGP.

5:7.7 Phase equilibria constraints on the origin of the pyroxenites.

Pyroxenites with graphite pseudomorphs after diamond which contain facetted inclusions of CPX and GT indicate that the pyroxenite suite originally crystallized in the diamond stability field i.e. >45 kb. The associated pyroxenites that do not contain graphite all show the same structural/deformation styles as the GGP, do not show crosscutting relationships and occur within ~ 6km of the GGP layers, thus they must

have originally crystallized under similar conditions to the GGP.

High pressure experimental studies of garnet peridotite melting behavior indicate that olivine is always a liquidus phase at >40 kb (Takahashi and Kushiro 1983). The Beni Bousera pyroxenites contain little evidence for primary olivine as a fractionating phase from the liquids which produced the cumulate pyroxenite layers. The absence of olivine indicates that either the liquids were derived from a garnet lherzolite which melted peritectically via the reaction relationship:

$$OPX = olivine + melt$$

or that the source rocks were olivine free. Kushiro and Yoder (1974) demonstrated that the olivine reaction relationship holds up to only 27 kb in the system CMAS. Experimental studies on natural systems suggest that the addition of Fe and minor components has limited effect on this relationship (known as the eclogite thermal devide, O'Hara 1968), possibly extending it to 35 kb (Takahashi and Kushiro 1983). The presence of graphitized diamonds in the GGP establishes minimum crystallization pressures at least 10 kb above this reaction relationship (~ 45kb), hence volatile free melting of peridotite is not a feasible process for generating the observed pyroxenite suite as they contain no olivine.

The major and trace element chemistry of the pyroxenite suite is compatible with an origin as cumulates from melts of different portions of subducted oceanic lithosphere. The melts may be derived by large degrees of melting of pyroxene rich cumulates and gabbros or mixtures of both that have either fractionated olivine, or did not contain enough olivine to saturate the melt and produce liquidus olivine. These protoliths produced basic to ultrabasic melts saturated in OPX which fractionated to form the variety of pyroxenites observed. It is unlikely that the bi-minerallic garnet clinopyroxenites are the metamorphosed products of basalts because either quartz or olivine would be formed from most compositions due to the stoichiometry of the reactions. The GP layers could also be cumulates from large degree melts of metamorphosed basaltic layers, these melts becoming trapped in the mantle to crystallize as biminera lic layers.

Hatton and Gurney (1987) favoured melting of subducted basaltic oceanic crust to produce Group 1 Roberts Victor eclogites. These authors favoured molten oceanic crust being transported in diapirs rising from a " megalith " of subducted residual harzburgite and basaltic crust similar to that envisaged by Ringwood (1982). If a high proportion of garnet lherzolite partial melt is mixed with the molten oceanic crust it becomes saturated in OPX. This sequence of events may explain the lithological division between OPX rich websterites and garnet clinopyroxenites in the Beni Bousera pyroxenite suite. Some of the thicker GP and GGP layers are the products of OPX fractionation as indicated by the presence of coarse OPXITE segregations on one or both margins.

5:8 Summary

Bulk-rock and mineral geochemistry indicates that the Beni Bousera pyroxenite suite is a series of cumulates formed at high pressure, within the diamond stability field. Extremely varied compatible and incompatible element abundances are best explained by the parental liquids to the cumulates being derived from heterogeneous protoliths, represented by subducted fragments of lithologically varied oceanic crust. Small degree partial melt extraction/dehydration of some of the protoliths, and subsequent large scale melting at high pressures and temperatures created some sources with extreme depletion of LREE/HREE. This multi stage, variable degree, partial melting caused decoupling of highly incompatible trace elements with Mg No.. Large scale melting of subducted oceanic crustal material (possibly admixed with pelagic sediment during subduction ?) followed by fractionation of OPX, CPX and GT may explain the large observed range in major and trace element compositions. The more MgO-rich websterite compositions may represent residues from the final melting process. Ater et al (1984) also invoked subduction related melting of oceanic crust to explain the broad compositional spectrum of mantle derived eclogites from the Colorado-Wyoming kimberlites, however these authors did not consider the effects of large scale trace-element compositional hererogeneity among the protoliths.

Subduction of lithologically varied magmatic cumulates followed by multiple melting, crystal fractionation and sub-solidus re-equilibration/interaction with the host peridotite imparts very complex, overlapping major and trace element geochemical effects on the final pyroxenite layer product. The multi stage nature of the above model combined with relatively poor constraints on the physical and chemical processes operating in subduction zones inhibits well constrained numerical simulation of the model

One means of searching for original protolith geochemical signitures is to employ radiogenic and stable isotopic analyses to the pyroxenites and peridotites. The results of this method of investigation are summarized in the following two chapters.

CHAPTER 6

RADIOGENIC ISOTOPE SYSTEMATICS

6:1 Introduction.

Data presented in Chapter 5 suggest that the Beni Bousera pyroxenite suite may have crystallized as a series of cumulates from liquids derived by melting various portions of subducted oceanic lithosphere. This hypothesis requires that the host peridotites are genetically unrelated to the pyroxenite layers which intrude them. In contrast to this conclusion, previous workers have proposed that pyroxenites in orogenic peridotites are derived in some way from liquids produced by melting the host peridotites (e.g. Kornprobst 1969, Dickey 1970, 1977, Conquere 1977, Bodinier et al 1987 and Suen and Frey 1987).

Sr, Nd and Pb radiogenic isotope data are presented which can be used to determine the relationship between the peridotites and pyroxenites and to constrain the formation ages of both rock groups. In addition this section will assess the isotopic heterogeneity of the peridotites over different scale lengths. Work on the nearby Ronda massif has demonstrated very large magnitude Sr and Nd isotopic heterogeneity in the peridotites (Reisburg and Zindler 1987). Previous isotopic data for the Beni Bousera pyroxenites and peridotites have been reported by : Menzies and Murthy(1978), Polve and Allegre (1980), Richard and Allegre (1980), Loubet et al (1980), Polve(1983), Menzies (1984), Reisburg and Zindler (1987) and Hamelin, Allegre (1988). These authors studied a limited number of samples whose locations were not always known or stated. Polve (1983) carried out the most extensive study of Beni Bousera but reported results from predominantely whole rock samples. At present, this study represents the most extensive compilation of Sr-Nd-Pb isotopic and trace-element data for both peridotites and pyroxenites from an orogenic peridotite massif.

6:2 Analytical methods:

6:2.1 Sample selection

Samples for isotopic analyses were selected to yield a spatially representative coverage of the massif and to span a variety of different lithologies. Locations of samples utilized for isotopic analyses are detailed in Figure 6.1. Peridotite samples were selected from areas both devoid and rich in pyroxenite layers. Lherzolite samples from both CPX-rich and CPX-poor lithologies were analysed to assess any correlation between degree of melt depletion and isotopic signature. Pyroxenite samples were selected primarily from the centre of layers to avoid any metasomatic/alteration effects at layer margins. The pyroxenite sample population is composed of layers of widely varying thickness (2.6m to < 1cm). A sequence of interlayered spinel peridotites and garnet pyroxenites was chosen from the Oued el Jouj river section to characterise the degree of trace element and isotopic exchange between pyroxenite layers and the surrounding peridotites.

6:2.2 Sample preparation

Fine powders were prepared using an agate swing mill (Chapter 5). Mineral separates were prepared from the excess rock chips after cone-and quartering. These chips were crushed with a stainless steel pestle and mortar reserved specifically for ultrabasic rocks. Mineral separation techniques are described in Appendix 3. Only garnets from the garnetiferous pyroxenites were separated using heavy liquids. Any trace element contamination introduced by the heavy liquids should have been removed by the extensive leaching procedure described below.

Whole rocks and mineral separates were analysed in order to assess the effect of late stage crustal contamination on trace element and isotope systematics. Many of the samples analysed in this study contained very low abundances of Sr, Nd and Pb. In order to obtain high precision isotopic analyses , sample sizes were larger than those for which the ion-exchange columns were calibrated. Unleached whole-rock specimens were analysed primarily to assess the effects of loading large sample volumes (>200mg) on various columns (Appendix 4).

6:2.3 Isotopic analyses

All whole rocks were dissolved in teflon bombs at 170°C in HF and HNO_3. Certain CPX separates that resisted dissolution in screw-top FEP beakers were also subjected to bomb dissolution. Whole rock Sr and Nd isotopes were generally separated from ~0.4 to 0.7g of powder. REE were analysed from separate dissolutions. Pb-Sr-Nd isotope compositions for CPX were obtained from a single dissolution which was also aliquoted for REE analysis. U/Pb, Ba, Rb and Sr spiking was performed prior to dissolution. Mineral separate sample weights all exceeded 150mg and were mostly >200mg. The large sample sizes reduced weighing errors, minimized sub-sampling problems and counteracted the effects of blanks on samples of low daughter isotope abundance. Details of analytical procedures, blanks and mass spectrometry are given in Appendix 4.

6:3 Assessing the role of secondary alteration on the isotope systematics of the peridotites and pyroxenites.

It has long been recognised that whole rock Sr and to a lesser extent Nd and Pb isotope systematics of orogenic peridotites are readily perturbed by late stage/secondary alteration processes at crustal levels (Menzies and Murthy 1978, Polve and Allegre 1980, Zindler et al 1983). Zindler et al (1983) found that even after leaching a Ronda pyroxenite in two aliquots of 2.5M HCL and a 5 % HF solution, the leached whole rock still retained Sr with high $^{87}Sr/^{86}Sr$ of crustal origin. These authors, together with Zindler and Jagoutz (1988) conclude that to obtain meaningful Sr isotopic data from orogenic or xenolithic peridotites and pyroxenites requires analysis of leached CPX mineral separates which contain the majority of the Sr, Nd and Pb budget of the rock. Zindler et al (1983) employed a leaching technique for mineral separates involving washing twice in hot 2.5 M HCL for twenty minutes and once in cold 5 % HF for ten minutes followed by grinding in cold 2.5 M HCL. Whilst it is important to remove the effects of secondary alteration/crustal contamination from mineral separates there is a need to be aware of the effect of the process on the indigenous trace-element content and isotopic composition of the specimen. Machado et al (1986) found that on leaching hand picked CPX separates, the degree of " extractability " of K, Rb, Sr, Ba and Nd and Sr is proportional to their respective Coulomb coefficients (Z/r^2). These

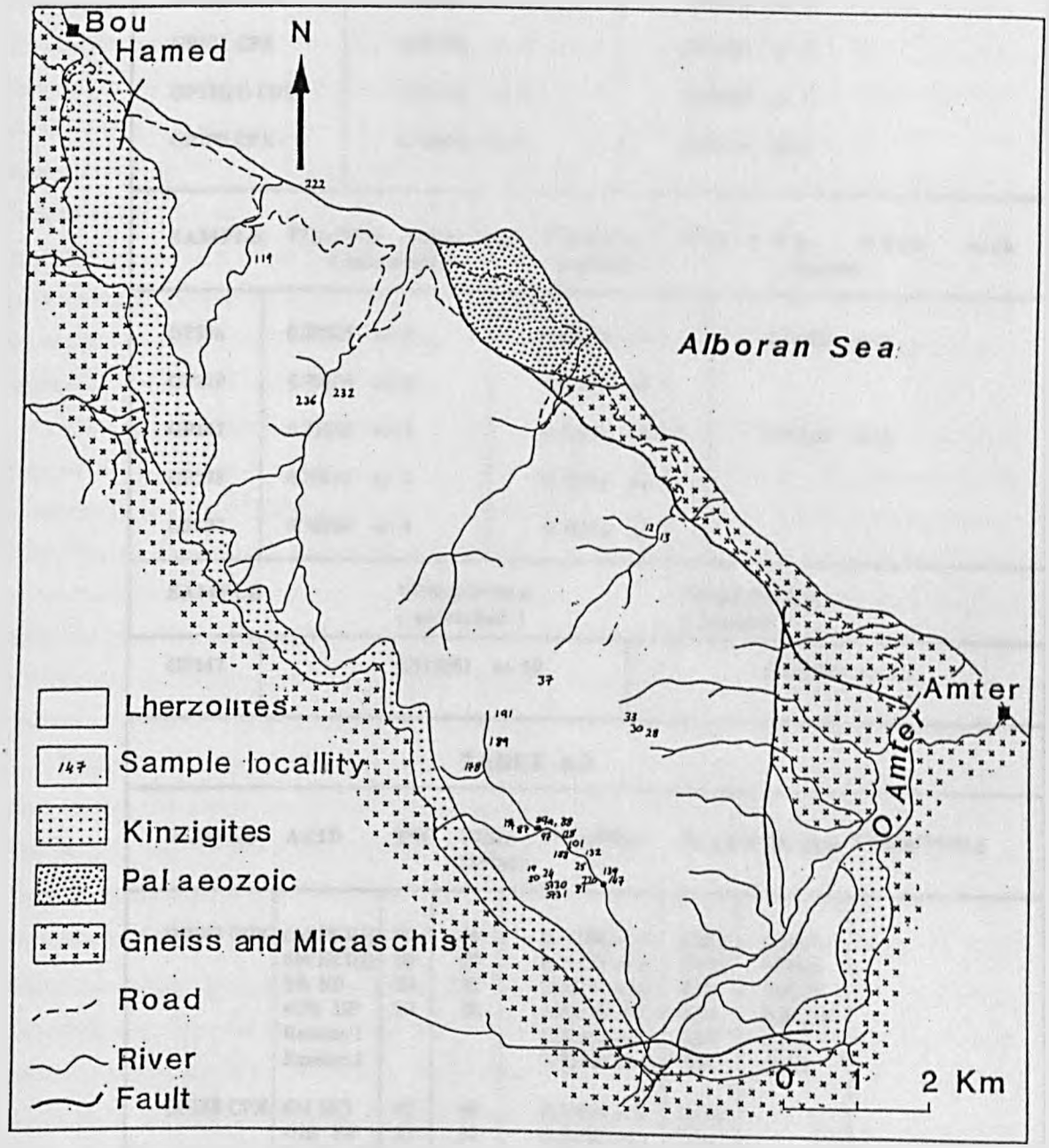

Figure 6.1. Locality map of samples analysed for Pb, Sr and Nd isotopes.

TABLE 6.1

SAMPLE	$^{87}Sr/^{86}Sr$ 6M HCl leachate	$^{87}Sr/^{86}Sr$ Residue
GP87M CPX	0.70809 +/- 7	0.70662 +/- 3
GP101 CPX	0.70879 +/- 5	0.70854 +/- 1
GP132(1) CPX	0.71413 +/- 4	0.70288 +/- 1
GP189 CPX	0.70452 +/- 2	0.70318 +/- 1

SAMPLE	$^{87}Sr/^{86}Sr$ Whole rock (unleached)	$^{87}Sr/^{86}Sr$ Leachate	$^{87}Sr/^{86}Sr$ Whole rock (leached)
GP89a	0.70329 +/- 1	0.70369 +/- 1	0.70303 +/- 1
GP119	0.70204 +/- 4	0.70296 +/- 4	
GP147	0.71355 +/- 3	0.71601 +/- 3	0.71118 +/- 5
GP178	0.70412 +/- 1	0.70381 +/- 3	
GP222	0.70204 +/- 4	0.70226 +/- 1	

SAMPLE	$^{143}Nd/^{144}Nd$ (unleached)	$^{143}Nd/^{144}Nd$ (leached)
GP147	0.513061 +/- 19	0.513080 +/- 18

TABLE 6.2

SAMPLE	ACID	T°C	TIME (Mins)	$^{87}Sr/^{86}Sr$	Sr ppm	Rb ppm	$^{143}Nd/^{144}Nd$
GP147 CPX	6M HCl(1)	80	60	0.71596 +/-5	0.028	0.0005	
	6M HCl(2)	80	60	0.71121 +/-6	0.008	0.0006	
	5% HF	20	30	0.70842 +/-6	0.02	0.0017	
	40% HF	20	30	0.70520 +/-6	0.04	0.00021	
	Residue 1			0.70511 +/-3	2.00	0.011	
	Residue 2			0.70509 +/-2	2.01	0.008	
GP188 CPX	6M HCl	80	60	0.70837 +/-2	0.002		
	40% HF	20	30	0.70786 +/-1	0.04		
	Residue 1			0.70781 +/-1	20.85		0.512234 +/-17
	Residue 2			0.70785 +/-2	20.91		0.512210 +/-20
GP194M CPX	6M HCl	80	60	0.70324 +/-4			
	5% HF	20	30	0.70318 +/-3			
	40% HF	20	30	0.70313 +/-2			
	Residue			0.70315 +/-1			

authors found that prolonged leaching of CPX separates with concentrated HCl at 100 °C caused significant fractionation of Sm from Nd but did not alter the $^{143}Nd/^{144}Nd$ ratios of the samples. K, Sr, Rb and Ba abundances are also significantly decreased during prolonged HCL treatment causing reduction of the Rb/Sr ratio. The $^{87}Sr/^{86}Sr$ ratio remained constant throughout the various degres of HCL treatment. Machado et al (1986) also investigated the detailed effects of HF treatment of CPX samples, finding that Sr and Ba abundances vary only slightly with increasing severity of HF treatment. However, Rb abundances were found to be dramatically lowered during progressive HF leaching causing a drastic decrease in the Rb/Sr ratio. Significantly, the $^{87}Sr/^{86}Sr$ ratios of the CPX separates showed marked decrease with increasing degree of partial dissolution by HF. Machado et al (op.cit.) proposed that the decrease in $^{87}Sr/^{86}Sr$ ratios with increasing intensity of HF treatment indicates that radiogenic Sr is located in the " Rb sites " of the CPX. Rb is not thought to occupy normal cation sites in CPX and probably resides in point or linear defects in the CPX lattice (Machado et al 1986). There is no preferential leaching of Sr as the "normal" Sr is incorporated into the M2 CPX site during crystal formation (Machado et al 1986). HF partial dissolution was not found to fractionate Sm from Nd, or to affect the $^{143}Nd/^{144}Nd$ ratio of the residue.

The evidence discussed above indicates that prolonged leaching in HF (leading to large degrees of dissolution) will begin to remove or "leach" the natural Rb and Sr from the mineral separate and will lower the indigenous $^{87}Sr/^{86}Sr$ ratio of the sample. It is crucial that the effects of crustal/secondary contamination are removed without significantly affecting the primary isotopic composition and trace element abundances of the sample. Reisburg and Zindler (1987) employed a mixed HCl-HF leaching technique involving washing in 2.5N HCl for one hour at 125 °C followed by fifteen minutes in cold 5% HF followed by a further thirty minutes in hot 2.5N HCl. These authors state that this leaching procedure "did not affect the CPX-hosted fractions of Sm, Nd and Sr" but did not present any evidence to prove this.

Preliminary leaching studies were carried out on several whole rock and mineral separate specimens from various lithologies that appeared to have suffered differing degrees of alteration/serpentinization. The samples were washed in sub-boiled-quartz distilled (SBQD) 6M HCl at 80 °C for one hour with frequent agitation periods in an ultrasonic bath. This leachate was decanted and the powders/mineral separates washed four times in SBQD H_2O which was decanted and added to the leachate. The CPX residues were then subjected to a further 6M HCl leach followed by thirty minutes in cold 40 % HF and then dried and dissolved for Sr isotope analyses. For whole rock samples an unleached sample was dissolved and analysed for Sr isotopes. Whole rocks were also dissolved after the 6M HCl step. The results of the 6M HCl leachings are presented in Table 6.1 The various peridotite and pyroxenite whole rock and mineral specimens analysed produced leachates of widely varying Sr isotopic composition and suggest that the samples contain varying degrees of secondary contamination. $^{87}Sr/^{86}Sr$ values of the 6M HCl leachate vary from 0.71601 (GGP) to 0.70296 (SP LHERZ). The pyroxenite whole rock and mineral separates appear to have been most affected by secondary alteration processes (despite being far less serpentinized than the peridotites), as they show the largest differences between $^{87}Sr/^{86}Sr$ of the leachate and residue respectively. The contaminating material in the pyroxenite samples also has the highest $^{87}Sr/^{86}Sr$ ratios (0.71601 to 0.70809). The greater susceptibility of the pyroxenites to secondary alteration effects may be due to the more Fe-rich nature of their constituent phases. However, one of the pyroxenite CPX samples, GP101 CPX, appears to be little affected by secondary

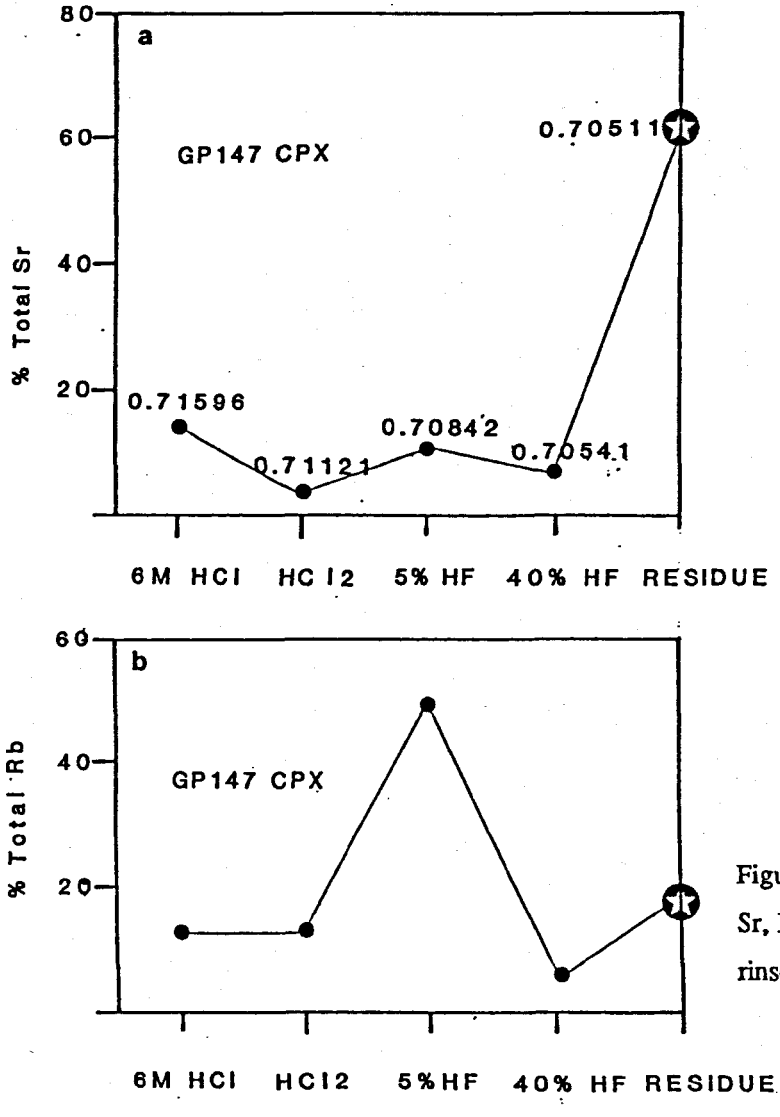

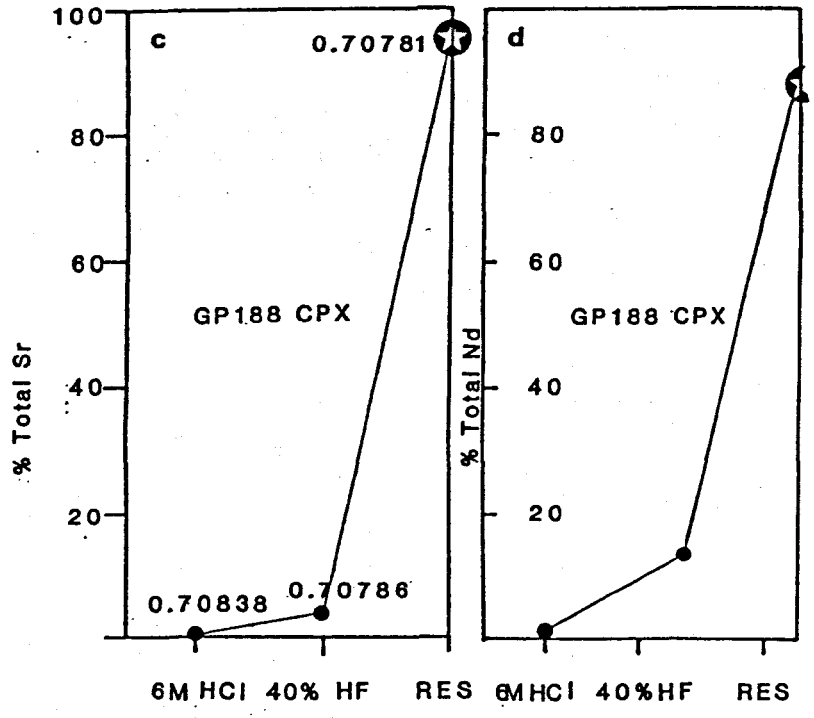

Figure 6.2. Leaching experiments on samples GP147 CPX and GP188 CPX. Graphs show % of tota Sr, Rb or Nd found in leachate and its Sr isotopic composition. HCl 2 refers to the second 6M HC rinse. Residue is the post leaching material remaining.

contamination, the fully leached residue having a similar $^{87}Sr/^{86}Sr$ ratio to the 6M HCl leachate (Table 6.1). The unleached peridotite whole rock samples are enriched in radiogenic Sr by significant amounts (Table 6.1), the largest difference being seen between GP178 leached residue and unleached whole rock. Significantly this sample is the most serpentinized of those analysed. Polve and Allegre (1980) used an ion microprobe to find intergranular high Rb phases in pyroxenites and peridotites. Such phases may cause enrichment in radiogenic Sr. The intergranular phases were characterized by variable K/Rb ratios (100 to 930). Polve and Allegre (op.cit.) also found that serpentine from a whole rock lherzolite sample had an $^{87}Sr/^{86}Sr$ ratio of 0.7076 and contained 6.5 ppm Sr and 0.6 ppm Rb. The presence of secondary serpentine in the whole rock lherzolite and pyroxenite samples and on the grain boundaries of mineral separates can thus significantly affect the Sr isotopic composition of the sample.

To quantitatively assess the most effective means of removing secondary phases and surface films on the CPX separates, a series of progressive leaching/dissolution experiments were conducted on two samples. A graphitic pyroxenite, GP147 CPX was first washed in 15mls of SBQD 6M HCl at 80 ^{o}C for one hour with periods of ultrasonic agitation. The 6M HCl solution was decanted, the grains rinsed in SBQD H_2O and a further 15mls of 6M HCl added for one hour at 80 ^{o}C. The HCl solution was again decanted, the sample washed ultrasonically in H_2O and 15mls of 5% HF added. The sample was then ultrasonically agitated for thirty minutes, the HF decanted and finally the CPX separate was subjected to 30 minutes in 40% HF at 20 ^{o}C in an ultrasonic bath. Each of the leachate solutions were spiked for Rb and Sr. The results of the leaching experiments are presented in and Table 6.2 and Figure 6.2. The $^{87}Sr/^{86}Sr$ ratio of the first 6M HCl wash is very similar to the whole rock leachate from GP147 (Table 6.1). Approximately 15% of the total Sr was leached in the first 6M HCl wash which was dominated by very radiogenic secondary Sr. The $^{87}Sr/^{86}Sr$ ratio of the leachate gradually decreases as the leaching process progresses towards the 40% HF stage. After the 40 % HF leaching approximately 20 % of the sample had dissolved, the $^{87}Sr/^{86}Sr$ ratio of this leachate is 0.70541, significantly above the 0.70511 obtained for the residual CPX which is presumably dominated by the indigenous/primary strontium. In order to prove that the progressive HCl-HF leaching had removed virtually all effects of secondary contamination, a second CPX separate from GP 147 was prepared and subjected to the same leaching routine. However, after the 40 % HF leach this separate was washed in another 15 mls of hot 80 ^{o}C 5 % HF for twenty minutes, resulting in an extra 12 % weight loss. The Sr isotopic composition of residue after this step was within error of the residue obtained from the first leaching procedure. Following Machado et al (1986) this is taken to indicate that virtually all the effects of secondary/crustal alteration effects had been removed from the CPX and the resultant residue yielded the $^{87}Sr/^{86}Sr$ isotopic composition of the original Sr trapped in the growing crystal. Furthermore, the Sr and Nd abundances in the two residues are very similar (within weighing errors). Rb concentrations are lower (~ 20 %) in the second residue indicating significant Rb loss during both HCl and HF leaching. Figure 6.2b shows that the largest portion of Rb from the CPX is lost during 5 % HF dissolution although significant proportions are also lost in the two HCl washings. This result concurs with the findings of Polve (1983), Zindler et al (1983) and Machado et al (1986) that large proportions of both secondary and indigenous Rb is lost during HCl and HF leaching, hence Rb/Sr ratios from HCL/HF leached mineral separates are probably lower than the "pristine" Rb/Sr ratios.

Cr-websterite sample GP188 CPX was leached in hot 6M HCl and then 40 % HF (Table 6.2).

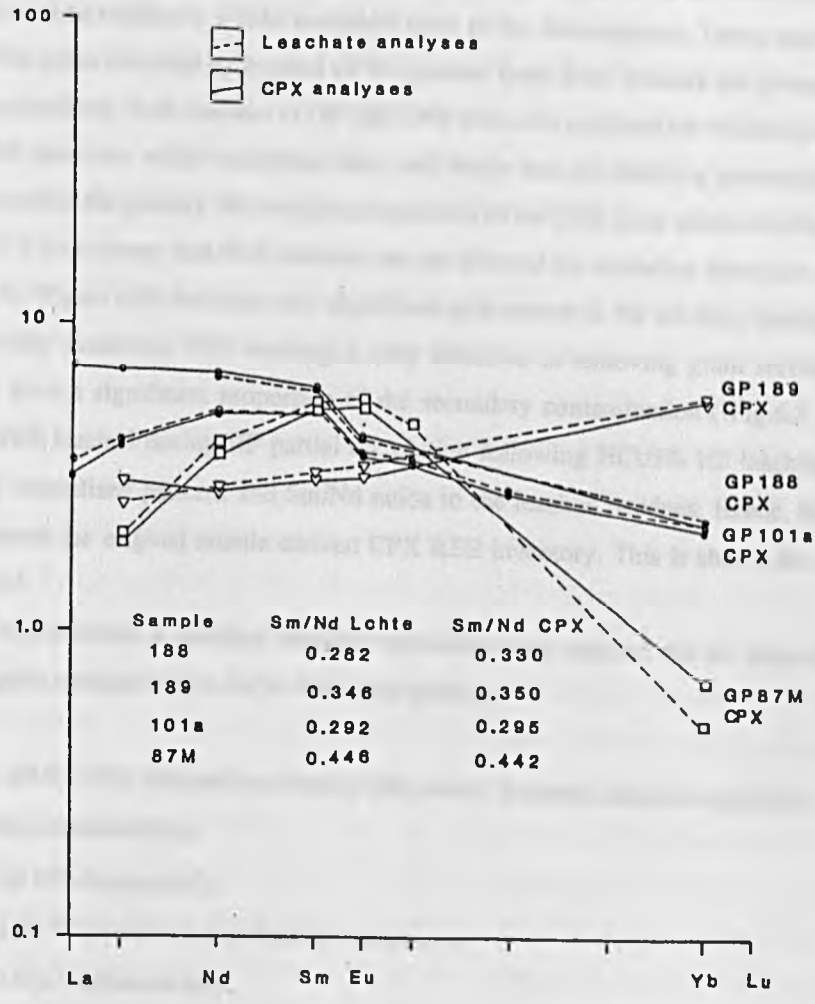

Figure 6.3. REE patterns of leachates and residue CPX from leaching experiments. All leachates are HF leachates apart from GP188 CPX leachate which is the first 6 M HCL leachate (see text). Note similarities in Sm/Nd fractions of leachate and residue CPX.

This sample apparently contains much less surface/defect related secondary contaminants than GP 147 CPX, in that a much lower percentage of Sr was removed during the initial 6M HCl wash and subsequent 40 % HF partial dissolution (Figure 6.2c). Additionally the $^{87}Sr/^{86}Sr$ composition of the 40 % HF leachate is within error of that obtained for the residue. A second CPX separate was also prepared from this sample and subjected to the additional hot 5 % HF partial dissolution after 40 % HF treatment. The $^{87}Sr/^{86}Sr$ ratio of this second residue is within analytical error of the first separate. These results verify that the high $^{87}Sr/^{86}Sr$ ratios recorded by leached CPX separates from Beni Bousera are primary features of their isotope geochemistry. Both residues of GP 188 CPX were also analysed for Nd isotopes. The resultant $^{143}Nd/^{144}Nd$ ratios are within analytical error and imply that the leaching procedures adopted are successful in revealing the primary Nd isotopic composition of the CPX. Less severe leaching methods (Zindler et al 1983) have shown that REE contents are not affected by secondary alteration to the same extent as Rb and Sr. Figure 6.2d indicates that significant proportions of Nd are only leached when the host CPX is partially dissolved. HCl washing is only effective in removing grain surface contamination which may form a significant proportion of the secondary contamination (Fig.6.2). Figure 6.3 shows that the REE leached during HF partial dissolution following HCl/5% HF leaching have very similar chondrite normalized patterns and Sm/Nd ratios to the leached residues. Hence, the leached REE fraction represents the original mantle derived CPX REE inventory. This is shown for 4 different samples in Figure 6.3.

Following the above experiments, a standard leaching procedure was adopted for all mineral separates analysed for radiogenic isotopes in this study: After final picking:

1) Ninety minutes 6 M HCl, 80 °C, HCl changed once during this period, frequent ultrasonic agitation.

2) Twice rinse with SBQD H_2O ultrasonically.

3) Thirty minutes 40 % HF 20 °C ultrasonically.

4) Thirty minutes 2.5 M HCl 80 °C to remove any fluoride complexes.

5) Rinse five times in SBQD H_2O, ultrasonically.

6) Rinse twice SBQD methanol, dry under filtered air.

Analyses of coexisting leached GT separates from some samples support the above conclusions that the leaching technique employed for CPX separates is sufficient to remove the effects of secondary contamination. GT is much more resistant to low temperature alteration than CPX. Data from leached GT separates presented in Table 6.4 show that their $^{87}Sr/^{86}Sr$ ratios are very close to their coexisting CPX (allowing for radiogenic decay since emplacement) suggesting that the CPX Sr isotope results are those of their primary, unaltered values. Furthermore, oxygen isotope equlibrium between GT and CPX pairs (Chapter 7) confirms that CPXs leached using the above procedure does not retain effects of isotopic exchange with crustal fluids.

The effect of this leaching procedure on Pb abundances and isotopic compositions was not evaluated. Hamelin and Allegre (1988) used a 0.5 N HBr or 0.5 N HBr/1 N HF leach prior to dissolution to convincingly remove the effects of secondary alteration. The procedure adopted in this study was even more severe and is considered to be at least as effective at removing secondary Pb. The effect on U and Pb abundances and the U/Pb ratio is not known. The effect of the leaching on Pb isotopic ratios is

usually to remove crustal Pb with generally higher $^{207}Pb/^{204}Pb$, which proved to be the case for the whole rocks leached by Hamelin and Allegre (1988). However, in the two samples they conducted leaching experiments on from Beni Bousera, the leachates had lower $^{207}Pb/^{204}Pb$ than the remaining residues.

6:4 Emplacement age of the massif and calculation of initial ratios:

Knowledge of the emplacement age of the peridotite massif allows the calculation of syn-emplacement, "initial" Sr, Nd and Pb isotopic ratios by removing the effects of *in situ* radioactive decay. The initial ratios thus calculated are the isotopic ratios inherited by the minerals or rocks from their mantle source regions, immediately prior to cooling past the closure temperature which prevents diffusion and isotopic equilibration.

Loomis (1975) obtained K-Ar mica ages of 20.7 and 20.2 +/- 0.6 Ma from a kinzigite and pegmatitic vein respectively from Beni Bousera area. The pegmatite vein cross cuts the peridotite massif. These ages are similar to the 19.5 to 18.5 Ma Rb-Sr biotite-whole rock and K-Ar biotite ages obtained by Priem et al (1979) from contact metamorphic rocks surrounding the Ronda massifs, S.Spain. Priem et al (op.cit.) interpreted these ages as the cooling ages produced when the contact metamorphic rocks had cooled past their Rb-Sr and K-Ar blocking temperatures, i.e. slightly post emplacement dates.

Polve (1983) obtained a "rough isochron" of 18.3 +/- 1 Ma (no MSWD given) from whole rock, post deformational aplite dikes which cross cut the Beni Bousera massif (Chapter 2). Sm-Nd mineral relationships obtained by Polve (1983) from the kinzigite gneisses surrounding Beni Bousera gave error-chrons of between 0 and 29 Ma. The small degree of Sm/Nd fractionation shown by the minerals and short time since closure conspire to produce large errors on the "ages" obtained. Polve (op.cit.) also obtained an Sm-Nd "isochron", (no stated MSWD) of 19.2 +/- 2.6 Ma from CPX-GT-whole rock analyses of a garnet pyroxenite within the peridotite massif. This "age" is within error of the 21.5 +/- 1.8 Ma (no MSWD given) Sm-Nd mineral isochron produced by Zindler et al (1983) from a plagioclase garnet pyroxenite layer from the Ronda massif. Zindler et al (op. cit.) interpreted this result as either dating the closure of inter-mineral diffusive equilibria of Nd isotopes during post metamorphic re-equilibration and cooling in crust or mantle or, as dating the age of formation of the pyroxenite layer.

In order to obtain more precise age information, in particular to rule out the possibility of slow cooling giving spuriously young emplacement ages, a variety of dating methods were applied to selected samples. A K-feldspar separate was obtained from a kinzigite specimen (GP5) collected within 50m of the peridotite contact. This rock contains sillimanite which is thought to be produced by high temperature metamorphism of original kyanite in the gneiss due to peridotite intrusion (Kornprobst 1974). A large book of muscovite crystals was extracted from a coarse aplitic pegmatite which cross cuts the deformational fabric of the massif (GP62). These two mineral separates were dated by the K-Ar method by D.C.Rex of Leeds University. The feldspar separate from GP5 gave an age of 25.7 Ma whilst the mica separate GP62 produced an "age" of 63.0 Ma. The feldspar cooling age is clearly older than K-Ar dates of 20.7 Ma obtained from a biotite separate from a Beni Bousera kinzigite by Loomis (1975). This sample may contain inherited excess ^{40}Ar. The mica sample gave a much older cooling age than expected and the presence of excess ^{40}Ar was suspected. This sample was analysed by the $^{40}Ar/^{39}Ar$ step heating technique to check for the presence of excess argon. An excellent plateau age of ~ 70 Ma was obtained

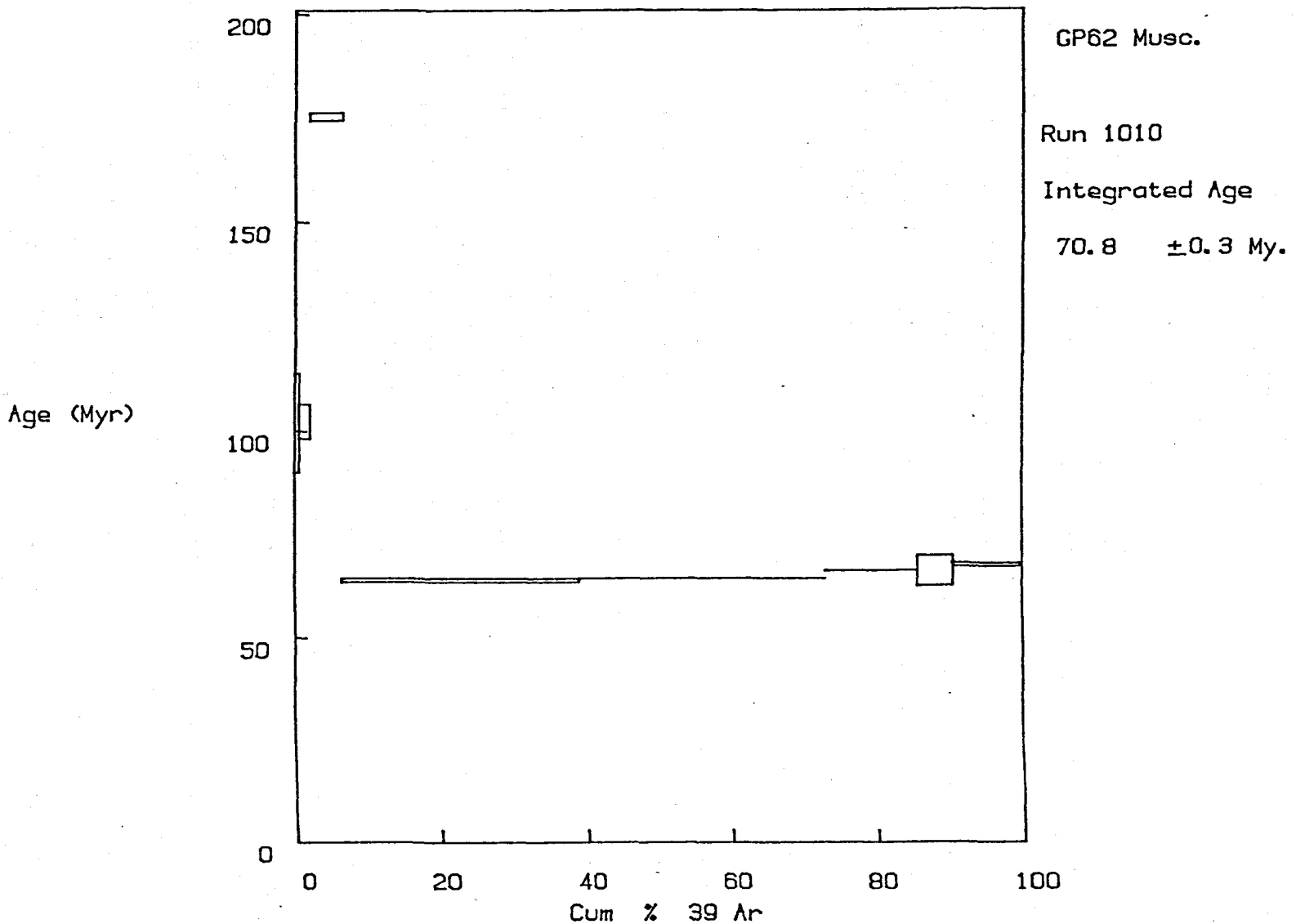

Figure 6.4. ^{39}Ar-^{40}Ar spectrum for white mica from pegmatite vein GP62 which cross cuts the peridotite. Raw data in Appendix 4.

(Figure 6.4) with little sign of the characteristic "saddle shaped" spectrum produced by excess ^{40}Ar. The relative consistency of the earlier published results leads to the conclusion that even this excellent plateau age is not reliable. The spurious spectrum and age may be due to excess ^{40}Ar. The excess argon in the mica may be due to the high volatile pressure of the pegmatite trapping crustal argon. Roddick et al (1980) and Foland (1983) have reported micas known to contain excess ^{40}Ar with analogous partial release spectra, i.e. with good plateaus that exceed the known geological ages of the rocks.

Nd isotopic analyses of garnet separates from a garnet pyroxenite (GP 87m) and a garnet peridotite (GP24) failed to achieve sufficient precision to be of use for isochron dating.

The coincidence of cooling ages obtained for the contact metamorphic effects of peridotite intrusion on the country-rock (19-25 Ma) and the Sm-Nd mineral isochron ages of 19.2 to 21.5 Ma, indicate that both sets of dates represent cooling ages as minerals ceased diffusive isotopic equilibrium after peridotite emplacement into the lower crust. This is supported by the intrusion of pegmatitic aplites shortly after peridotite emplacement ~ 19.6 to 18.3 Ma (Polve 1983), which may be the result of crustal anatexis due to peridotite intrusion (Priem et al 1979). Polve (1983) proposes that adiabatic uplift induced the melting which caused the formation of the pyroxenite layers at 19.2 Ma ago. Chapter 2 documents convincing evidence that the original diamonds in the GGP crystallized at the same time as the host mineralogy. To derive the GGP from ~ 150 km deep in the mantle after crystallization at 19.2 Ma requires an uplift rate of almost 8km per Ma which is clearly unrealistic. Hence the above dates are taken to represent approximately syn-emplacement cooling ages in this study. An emplacement age of 20.5 Ma is adopted here for the purpose of calculating initial isotopic ratios. This age complies with the 20.7 and 20.2 Ma K-Ar cooling ages obtained from metamorphosed crustal rocks by Loomis (1975) and is within error of the 19.2 Ma Sm-Nd mineral isochron obtained by Polve (1983).

6:5 Pb-Sr-Nd isotope data.

Whole rock and mineral separate isotope data are presented in Tables 6.3, 6.4 and 6.5; all quoted errors are within run 2 σ errors at the 95 % confidence level. Initial $^{87}Sr/^{86}Sr$ and $^{143}Nd/^{144}Nd$ ratios for mineral separates (calculated for the 20.5 Ma emplacement age assumed above) are shown in Table 6.3 and 6.5. The $^{87}Sr/^{86}Sr$ ratios generally do not change within the limits of analytical uncertainty due to their low $^{87}Rb/^{86}Sr$ ratios; accordingly, whole rock initial $^{87}Sr/^{86}Sr$ ratios have not been calculated in Table 6.3. Pb isotopes have not been age corrected due to lack of available Th data. However the relatively low $^{238}U/^{204}Pb$ ratios of many of the samples (Table 6.5) would not generate significant ^{206}Pb or ^{207}Pb in the last 20.5 Ma.

6:5.1 Peridotites.

In agreement with previous studies on Beni Bousera and other orogenic peridotites (Polve and Allegre 1980, Richard and Allegre 1980, Menzies 1984, Reisburg and Zindler 1987 and Hamelin and Allegre 1988) the Sr-Nd-Pb isotope geochemistry of the peridotites reveals extreme heterogeneity over comparitively small length scales. Leached whole rock peridotites show a large variation in $^{87}Sr/^{86}Sr$, from extremely unradiogenic ratios, 0.70198 (GP41) to radiogenic values, 0.70519 (GP220). This $^{87}Sr/^{86}Sr$ range is much larger than that reported from leached whole rock and mineral separates from the

TABLE 6.3 WR.DATA

SAMPLE	LITHOLOGY	Rb ppm	Sr ppm	87Sr/86Sr	+/-	Sm ppm	Nd ppm	143Nd/144Nd	+/-	147Sm/144Nd	143Nd/144Nd i	206Pb/204Pb	207Pb/204Pb	208Pb/204Pb
1 GP12	SPLHRZ	0.134	6.533	0.70257	5									
2 GP13	SPLHRZ	0.280	9.500	0.70414	4									
3 GP24 *	GTLHZ			0.70242	2	0.279	0.697	0.513278	10	0.242	0.513246			
4 GP41 *	SPLHRZ			0.70198	2	0.290	0.711	0.513327	16	0.408	0.513294			
5 GP88	SPLHRZ											17.971	15.570	37.803
6 GP89a *	SPLHRZ			0.70303	1	0.185	0.588	0.513041	30	0.190	0.513016	18.145	15.579	38.106
7 GP119	SPLHRZ	0.044	4.555	0.70204	4	0.234	0.585							
8 GP178 *	SPLHRZ			0.70381	3	0.043	0.097	0.512706	35	0.268	0.512670			
9 GP220 *	SPLHRZ			0.70519	2			0.512856	14					
10 GP222 *	SPLHRZ			0.70226	1			0.513234	20					
11 GP189 *	SPLHRZ			0.70397	1							18.556	15.457	37.906
12 GP230 *	SPLHRZ											18.064	15.457	37.906
13														
14 GP19	GP	0.778	4.200	0.71098	4	0.850	1.025	0.513178	15	0.502	0.513066			
15 GP20	GP	1.015	22.531	0.71292	1	0.710	0.761	0.513316	14	0.564	0.513240			
16 GP25	GGP	0.135	1.656	0.71281	2	0.678	0.241	0.512997	30	1.702	0.512769			
17 GP33a	WEB		48.528	0.70418	4									
18 GP37	GP	0.264	16.928	0.70541	3	0.865	1.275	0.513925	18	0.410	0.513825	17.474	15.515	37.334
19 GP47	GGP		7.240	0.71219	1	0.616	1.260	0.512968	24	0.295	0.512884			
20 GP81	GGP	0.670	41.000	0.71660	4	0.764	0.422					18.582	15.651	38.784
21 GP87M *	GP		38.100	0.70709	2	1.265	2.458	0.513136	24	0.311	0.513094	17.780	15.547	37.536
22 GP87B	GP	0.055	86.300	0.70480	1									
23 GP97	WEB		16.345	0.70917	1	0.363	0.634	0.513506	16	0.346	0.513459			
24 GP101	WEB	0.215	12.100	0.70866	3	0.743	2.449	0.512175	20	0.184	0.512150	18.523	15.668	39.115
25 GP139	GP	0.192	26.810	0.71012	3	0.941	0.615	0.513178	14	0.605	0.513097	18.038	15.597	38.030
26 GP147 *	GGP	0.088	2.543	0.71118	5	0.299	0.288	0.513080	18	0.627	0.512997	18.316	15.629	38.427
27								0.513061	19					
28 GP188	WEB	0.439	1.950	0.70932	5	0.107	0.313	0.512242	35	0.207	0.512214	18.647	15.752	39.802
29 GP232 *	WEB			0.70445	1			0.512674	28			18.104	15.444	38.277
30 GP236 *	WEB			0.70671	2	0.403	0.994	0.512765	14	0.245	0.512732	18.431	15.585	38.567
31 PHN5731	GGP		2.832	0.71051	3			0.512952	20					

TABLE 6.4 MINERAL DATA

SAMPLE	LITHOLOGY	Ba ppm	Rb ppm	Sr ppm	87Sr/86Sr	+/-	Sm ppm	Nd ppm	143Nd/144Nd	+/-	U ppm	Pb ppm	206Pb/204Pb	207Pb/204Pb	208Pb/204Pb
1 GP13 CPX	SPLHRZ	0.964	0.0310	70.670	0.70247	2	1.703	4.343	0.513101	12	0.0053	0.5760	17.600	15.526	37.488
2 GP24 CPX	GTLHZ		0.3340	249.970	0.70212	4	1.721	5.109	0.513157	28					
3 GP88 CPX	SPLHRZ	0.327	0.0868	73.010	0.70318	2	1.692	4.730	0.513173	16	0.0110	0.0619	17.554	15.495	37.041
4 GP89a CPX	SPLHRZ	0.374	0.0660	54.410	0.70319	4	1.709	3.924	0.513147	17	0.0626	0.2740	17.549	15.591	37.469
5 GP119 CPX	SPLHRZ	0.503	0.1510	66.570	0.70202	3	1.877	4.727	0.513306	17					
6 GP132(3) CPX	SPLHRZ		0.0678	87.680	0.70282	1	0.739	2.023	0.513334	12					
7 GP189 CPX	SPLHRZ	0.233	0.0353	42.540	0.70318	1	0.655	1.870	0.513128	18	0.0015	0.0990	17.559	15.554	37.437
8 GP191 CPX	SPLHRZ	0.743	0.0178	66.690	0.70209	2	1.460	3.460	0.513408	12	0.0220	0.9050	16.997	15.566	37.021
9 GP220 CPX	SPLHRZ	0.700	0.0224	35.920	0.70515	2	0.887	3.040	0.512801	10	0.0350	0.4330	17.568	15.611	37.759
10 GP222 CPX	SPLHRZ	0.374	0.1180	60.650	0.70222	1	1.617	3.438	0.513316	18	0.0350	0.3300	17.277	15.375	36.616
11															
12 GP30 CPX	CR-WEB		0.0510	60.270	0.70228	1	1.705	3.980	0.513473	14					
13 GP33 CPX	WEB		0.0852	46.350	0.70417	1	2.628	9.439	0.512614	10					
14 GP37 CPX	GP	0.780	0.2660	36.940	0.70245	4	1.580	2.537	0.513982	19	0.0012	0.2590	17.653	15.615	37.671
15 GP81 CPX	GGP	2.930	0.2610	3.770	0.71101	2	1.066	0.698	0.512661	24	0.0023	0.4160	17.404	15.547	37.305
16 GP87M CPX	GP	0.304	0.0297	28.750	0.70662	3	1.120	2.535	0.512902	12	0.0870	0.9630	17.722	15.536	37.491
17 GP87M GT	GP		0.0789	0.119	0.70676	10	0.686	0.281	0.513005	58					
18 GP87B CPX	GP/WEB	0.580	0.2720	72.400	0.70312	6	1.820	4.730			0.0076				
19 GP101a CPX	CR-WEB	0.349	0.0376	30.340	0.70854	1	1.256	4.251	0.512188	12	0.0920	0.3550	18.362	15.628	38.851
20 GP101a OPX	CR-WEB		0.1570	0.455	0.70737	14	0.017	0.041							
21 GP132(1) CPX	CR-WEB	0.841	0.0260	97.080	0.70281	1	0.867	2.247	0.513295	12	0.0520	0.4170	17.515	15.545	37.437
22 GP139 CPX	GP	0.489	0.1640	1.955	0.70501	6	1.494	1.119	0.513243	15					
23 GP147 CPX	GGP	0.440	0.0110	2.002	0.70511	3	0.374	0.411	0.513078	20		0.0780	17.445	15.569	37.386
24 GP147 GT	GGP		1.1740	0.065			0.201	0.051							
25 GP188 CPX	CR-WEB	0.327	0.0043	20.850	0.70781	1	1.062	3.209	0.512234	17	0.0047	0.3470	18.085	15.617	38.361
26 GP194M CPX	GP	0.650	0.0489	59.240	0.70315	1	0.793	1.586	0.512926	14	0.0190	0.3210	17.593	15.602	37.667
27 GP236M CPX	WEB		0.0204	35.240	0.70654	1	0.907	2.621	0.512727	21	0.0075	3.3600	17.969	15.612	37.823
28 PHN5730 CPX	GGP			1.016	0.70500	1	0.544	0.214	0.513117	26	0.0046	0.0485			
29 PHN5730 GT	GGP			0.024	0.70507	2									
30 PHN 5731 CPX	GGP			1.295	0.70507	1	0.637	0.391	0.513106	24	0.0066	0.0296			
31 PHN5731 GT	GGP			0.092	0.70513	2									
32 PHN5734 CPX	GGP			2.003	0.70590	1					0.0025	0.0296			
33 PHN5734 GT	GGP			0.097	0.70587	1									

TABLE 6.5 INITIAL RATIOS

SAMPLE	87Rb/86Sr	86Sr/86Sr i	147Sm/144Nd	143Nd/144Nd i	238U/204Pb	Δ 8/4
1 GP13 CPX	0.00130	0.70247	0.237	0.513069	0.57	58.3
2 GP24 CPX	0.00390	0.70212	0.204	0.513157		
3 GP88 CPX	0.00340	0.70318	0.217	0.513157	10.90	19.1
4 GP89a CPX	0.00350	0.70319	0.264	0.513112	14.10	62.5
5 GP119 CPX	0.00670	0.70202	0.240	0.513274		
6 GP132(3) CPX	0.00220	0.70282	0.221	0.513304		
7 GP189 CPX	0.00240	0.70318	0.267	0.513092	0.94	58.1
8 GP191 CPX	0.00078	0.70209	0.255	0.513374	1.50	84.5
9 GP220 CPX	0.00180	0.70515	0.176	0.512777	5.10	89.2
10 GP222 CPX	0.00560	0.70222	0.285	0.513278	6.50	10.1
11						
12 GP30 CPX	0.00250	0.70228	0.209	0.513470		
13 GP33 CPX	0.00530	0.70417	0.181	0.512590		
14 GP37 CPX	0.02080	0.70248	0.377	0.513931	0.29	70.1
15 GP81 CPX	0.20030	0.71095	0.923	0.512537	0.34	63.7
16 GP87M CPX	0.00290	0.70662	0.212	0.512874	5.60	43.8
17 GP87B CPX	0.01080	0.70387				
18 GP101a CPX	0.00360	0.70854	0.179	0.512164	16.40	102.4
19 GP132(1) CPX	0.00078	0.70281	0.233	0.513263	7.70	63.4
20 GP139 CPX	0.24470	0.70498	0.807	0.513141		
21 GP147 CPX	0.01590	0.70511	0.550	0.513004		65.0
22 GP188 CPX	0.00061	0.70781	0.200	0.512207	0.85	87.0
23 GP194M CPX	0.00240	0.70315	0.302	0.512886	3.70	77.0
24 GP236M CPX	0.00170	0.70654	0.209	0.512693	0.14	47.1
25 PHN5730 CPX						
26 PHN 5731 CPX						

Δ7/4	Sr/Nd	Ba/La	d18O	T CHUR Sr My	T CHUR Nd My
12.7	16.3	0.94		1389	1754
	48.9		6.1	1786	
10.1	42.7	0.36	6.0	729	1226
19.8	13.9	0.48		720	1157
	14.1	0.44		1962	2340
	43.3	0.22	5.8	1067	4318
16.0	22.7	0.22	5.3	718	1066
23.3	19.3	1.20		1738	2011
21.6	11.9	0.52	6.0		
1.1	17.6	0.24		1729	1170
	15.1			1596	10066
	4.9		5.4		214
21.0	14.6	5.50	4.9	1921	960*
16.9	5.4	162.80	5.2	3840	4*
12.4	11.3	0.67	7.3		353*
	39.8	0.61	7.4		
14.7	7.1	0.16	8.7		5234*
15.5	43.2	0.47	5.5	1056	2751
	1.7	34.50	5.7	451	226*
18.7	4.9	29.30	7.5		156*
16.6	6.5	0.28	9.3		
20.4	37.4	2.70	7.1	748	421
17.3	13.5		5.6		263*
					57
					90

Ronda peridotite (Reisburg and Zindler 1987). The variation in leached whole rock initial $^{143}Nd/^{144}Nd$ is equally as large, 0.513327 (GP41) to 0.512856 (GP220), exhibiting good anti-correlation on an Nd-Sr plot (Figure 6.5), i.e. the samples with the most depleted $^{143}Nd/^{144}Nd$ values (relative to Bulk Earth) have the least radiogenic $^{87}Sr/^{86}Sr$ ratios.

CPX from the lherzolites confirm the Nd-Sr isotope variation shown by the leached whole rocks and also show extreme Pb isotopic heterogeneity (Table 6.5). The CPX data support the general Nd-Sr isotope negative correlation (Figure 6.5), initial $^{87}Sr/^{86}Sr$ values ranging from 0.70202 to 0.70515 (ε Sr = -35.2 to + 9.2). Peridotite CPX initial $^{143}Nd/^{144}Nd$ ratios vary from 0.513374 to 0.512777 (ε Nd = +14.4 to +2.71). Although the leached CPX separates have similar initial $^{143}Nd/^{144}Nd$ ratios to their corresponding leached whole rocks, the differences are generally outside within run error. The $^{143}Nd/^{144}Nd$ ratios may be higher or lower than the whole rocks. This may be due to the presence of variably LREE enriched material at grain boundaries in the whole rocks (see Chapter 5 and Polve 1983) which was not fully removed by the leaching process, or, equally likely, small scale isotopic heterogeneity may exist in samples which was not effectively homogenized during extraction of the CPX concentrates. Jagoutz (1988) documented Nd isotopic heterogeneity in different magnetic fractions of garnet in a Tanzanian eclogite xenolith. Closer concurrence of $^{87}Sr/^{86}Sr$ ratios from leached whole rock peridotites and their corresponding CPX indicates that the whole rock leaching procedure is sufficient to effectively remove much of the effects of secondary crustal alteration from the peridotites. Furthermore, the whole rock and CPX analyses for the highly radiogenic Sr sample GP220 are virtually within error, confirming a primary mantle origin for this $^{87}Sr/^{86}Sr$ ratio.

The majority of the peridotite whole rock and CPX data in Figure 6.5 and 6.6 plot either in the present day MORB field defined by Zindler and Hart (1986), or diagonally to the upper left of this field, i.e. to more "depleted" Nd and Sr isotopic compositions relative to Bulk Earth. There is no correlation between proximity of peridotites to pyroxenites and extreme isotopic compositions. Two CPX separates (GP220 and one from Menzies, 1984) have both unradiogenic $^{143}Nd/^{144}Nd$ and $^{87}Sr/^{86}Sr$ which define a shallow negative trend from the MORB field to isotopic compositions similar to the Samoan and Society Island volcanics. In contrast, two whole rock peridotites, one from Richard and Allegre (1980) and harzburgite GP178, define a steeper negative trend away from present day MORB.

Peridotite CPX Rb/Sr and Sm/Nd ratios are not well correlated with MgO contents or Mg Nos. of the whole rock peridotites, even if only low Δ FeO samples are considered. CPX Rb/Sr and Sm/Nd ratios are also poorly correlated with measured $^{87}Sr/^{86}Sr$ and $^{143}Nd/^{144}Nd$ ratios respectively. The data define highly scattered positive to sub-horizontal trends and do not record isochronous relationships for either Rb/Sr or Sm/Nd systematics. Equally, neither the low ΔFeO or high ΔFeO samples record good isochrons e.g. 860 Ma +/- 785 Ma Sm/Nd errorchron for low ΔFeO spinel lherzolite samples. The reasons for the lack of isochronous relationships for Sm/Nd and Rb/Sr systematics in the peridotites will be discussed later.

Lherzolite CPX show the following variation in blank corrected Pb isotope compositions: $^{206}Pb/^{204}Pb$ = 16.997 to 17.712, $^{207}Pb/^{204}Pb$ = 15.375 to 15.611, $^{208}Pb/^{204}Pb$ = 36.616 - 37.803. These rocks are characterized by high $^{207}Pb/^{204}Pb$ ratios at relatively unradiogenic $^{206}Pb/^{204}Pb$ ratios. This observation was also made by Hamelin and Allegre (1988) who analysed leached whole rock and

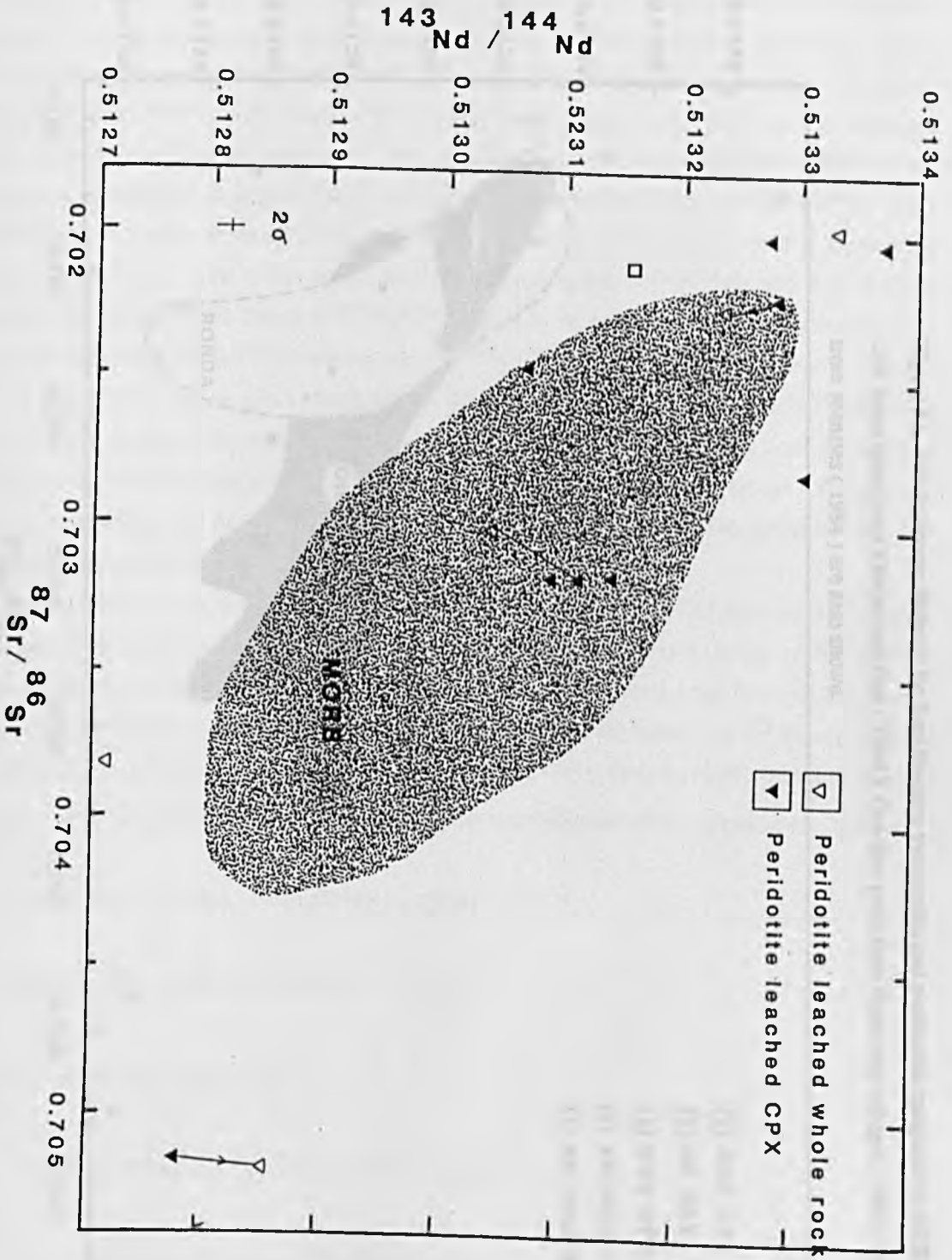

Figure 6.5. Nd-Sr isotope diagram of Beni Bousera leached whole rocks and CPX separates (analyses from same rock joined by line). Shaded field is present day present day MORB field from Zindler and Hart (1986).

Figure 6.6. Nd-Sr isotope diagram for Beni Bousera pyroxenites and peridotites compared to MORB and OIB fields taken from Zindler and Hart (1986). One data point from Polve and Allegre (1980) and one from Menzies (1984) are also shown.

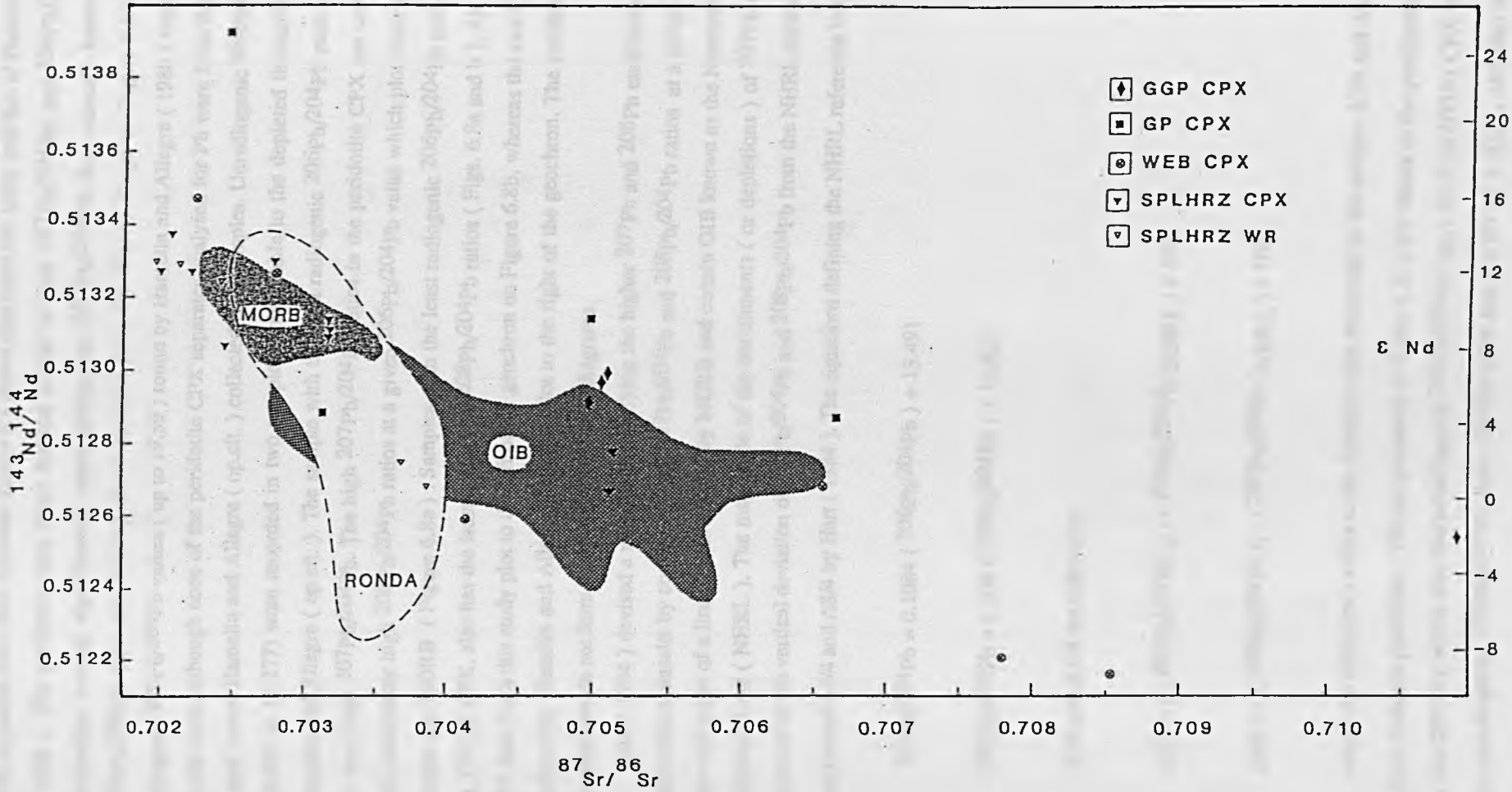

CPX separates from Beni Bousera. Figure 6.7 shows data from this study and that of Hamelin and Allegre (1988). The peridotite data show marked scatter in both $^{207}Pb/^{204}Pb$ and $^{206}Pb/^{204}Pb$, most peridotites having significantly more radiogenic $^{207}Pb/^{204}Pb$ than oceanic basalts at a given $^{206}Pb/^{204}Pb$ ratio and plotting above samples from the Walvis Ridge on Figure 6.8 b. The highly radiogenic $^{206}Pb/^{204}Pb$ values (up to 19.59) found by Hamelin and Allegre (1988) were not recorded in this study although none of the peridotite CPX separates analysed for Pb were from the North of the massif where Hamelin and Allegre (op.cit.) collected their samples. Unradiogenic $^{206}Pb/^{204}Pb$ values (16.997 to 17.277) were recorded in two samples, comparable to the depleted lherzolite analysed by Hamelin and Allegre (op.cit.). The sample with the least radiogenic $^{206}Pb/^{204}Pb$ ratio (GP191 CPX) has very high $^{207}Pb/^{204}Pb$. The high $^{207}Pb/^{204}Pb$ ratios in the peridotite CPX are accompanied by only moderately high $^{208}Pb/^{204}Pb$ ratios at a given $^{206}Pb/^{204}Pb$ value which plot close to the field of present day MORB (Figure 6.8a) . Samples with the least radiogenic $^{206}Pb/^{204}Pb$ and $^{207}Pb/^{204}Pb$ e.g. GP222 CPX, also has the least radiogenic $^{208}Pb/^{204}Pb$ ratios (Figs. 6.8a and b). All the peridotite CPX data from this study plot to the left of the geochron on Figure 6.8b, whereas the two CPX separates analysed by Hamelin and Allegre (op.cit.) plot to the right of the geochron. The peridotite CPX data reported here do not form linear arrays on Pb-Pb diagrams.

Hart (1984) devised a means of quantifying the higher ^{207}Pb and ^{208}Pb enrichments shown by some oceanic basalts by comparing their $^{207}Pb/^{204}Pb$ and $^{208}Pb/^{204}Pb$ ratios at a given $^{206}Pb/^{204}Pb$ ratio with those of a linear trend defined by MORB and certain OIB known as the Northern Hemisphere Reference Line (NHRL). The magnitude of the enrichments (or depletions) of ^{207}Pb and ^{208}Pb is expressed as the vertical deviation of $^{207}Pb/^{204}Pb$ and $^{208}Pb/^{204}Pb$ from the NHRL reference lines and were termed $\Delta 7/4$ and $\Delta 8/4$ by Hart (1984). The equations defining the NHRL reference lines are:

$$^{207}Pb/^{204}Pb = 0.1084 \, (^{206}Pb/^{204}Pb) + 13.491$$

$$^{208}Pb/^{204}Pb = 1.209 \, (^{206}Pb/^{204}Pb) + 15.627$$

$\Delta 7/4$ and $\Delta 8/4$ are defined by

$$\Delta 7/4 = [(^{207}Pb/^{204}Pb)_s - (^{207}Pb/^{204}Pb)_{NHRL}] \times 100$$

$$\Delta 8/4 = [(^{208}Pb/^{204}Pb)_s - (^{207}Pb/^{204}Pb)_{NHRL}] \times 100$$

where the subscript s refers to the isotopic ratio measured in the sample. $\Delta 7/4$ and $\Delta 8/4$ values for the Beni Bousera peridotite CPX are presented in Table 6.5. $\Delta 7/4$ values in the peridotites range from +1.1 for GP222 (which also has unradiogenic $^{206}Pb/^{204}Pb$) to + 23.3 for GP191 CPX which has the most unradiogenic $^{206}Pb/^{204}Pb$ ratio. GP220 CPX has a $\Delta 7/4$ of + 21.6 , and also has the most radiogenic Sr and unradiogenic Nd isotopic signatures. Except, for GP222 the $\Delta 7/4$ values for the peridotite CPX in Table 6.5 are of similar magnitude or higher than those recorded by the isotopically

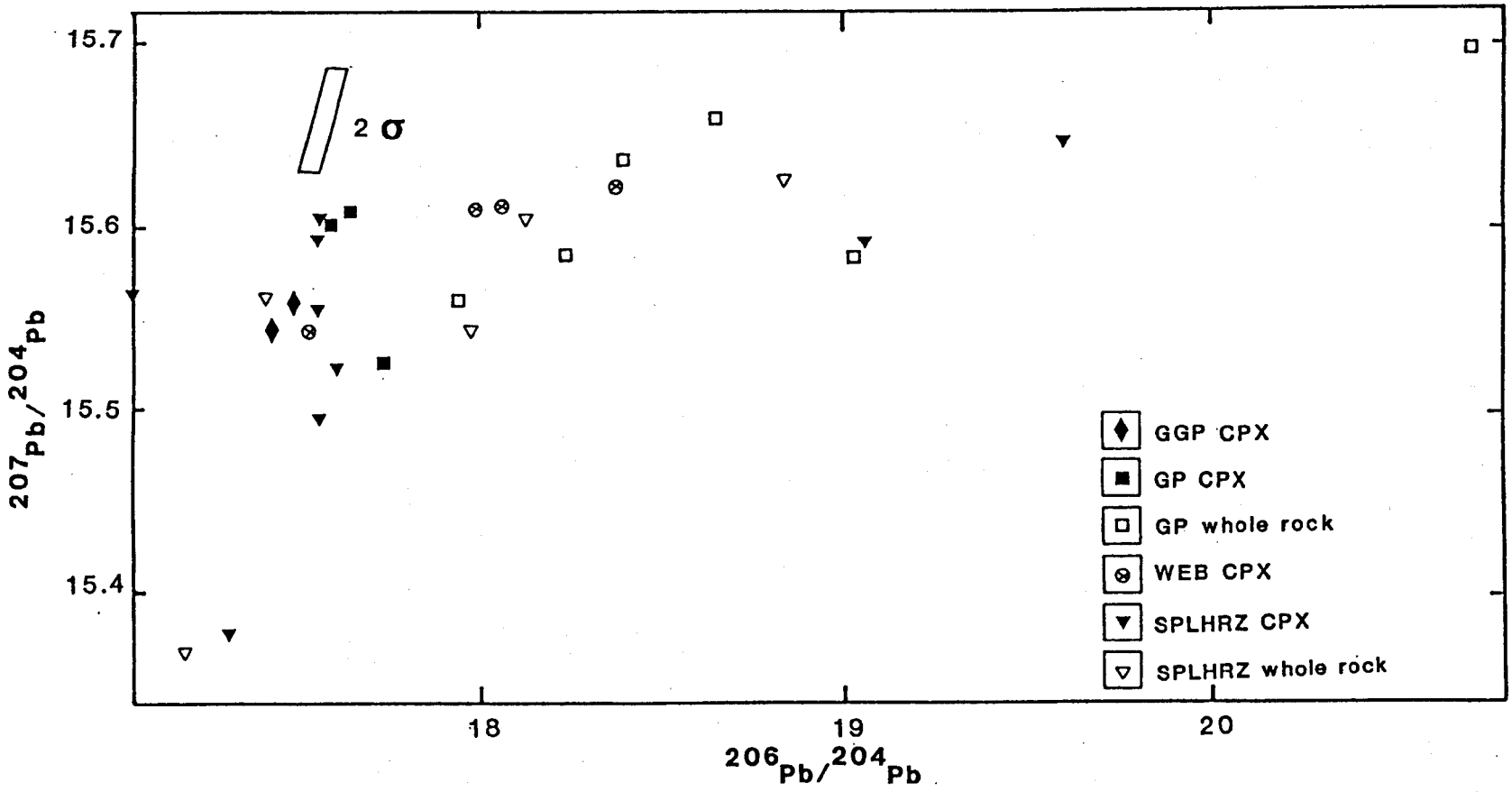

Figure 6.7. $^{207}Pb/^{204}Pb$ vs $^{206}Pb/^{204}Pb$ isotope plot of Beni Bousera pyroxenites and peridotites, including data from Hamelin and Allegre (1986). All whole rock data is from Hamelin and Allegre (op.cit.) and is for leached whole rocks (see text). Samples marked as whole rock garnet clinopyroxenites (GP) are described only as pyroxenites by the above authors.

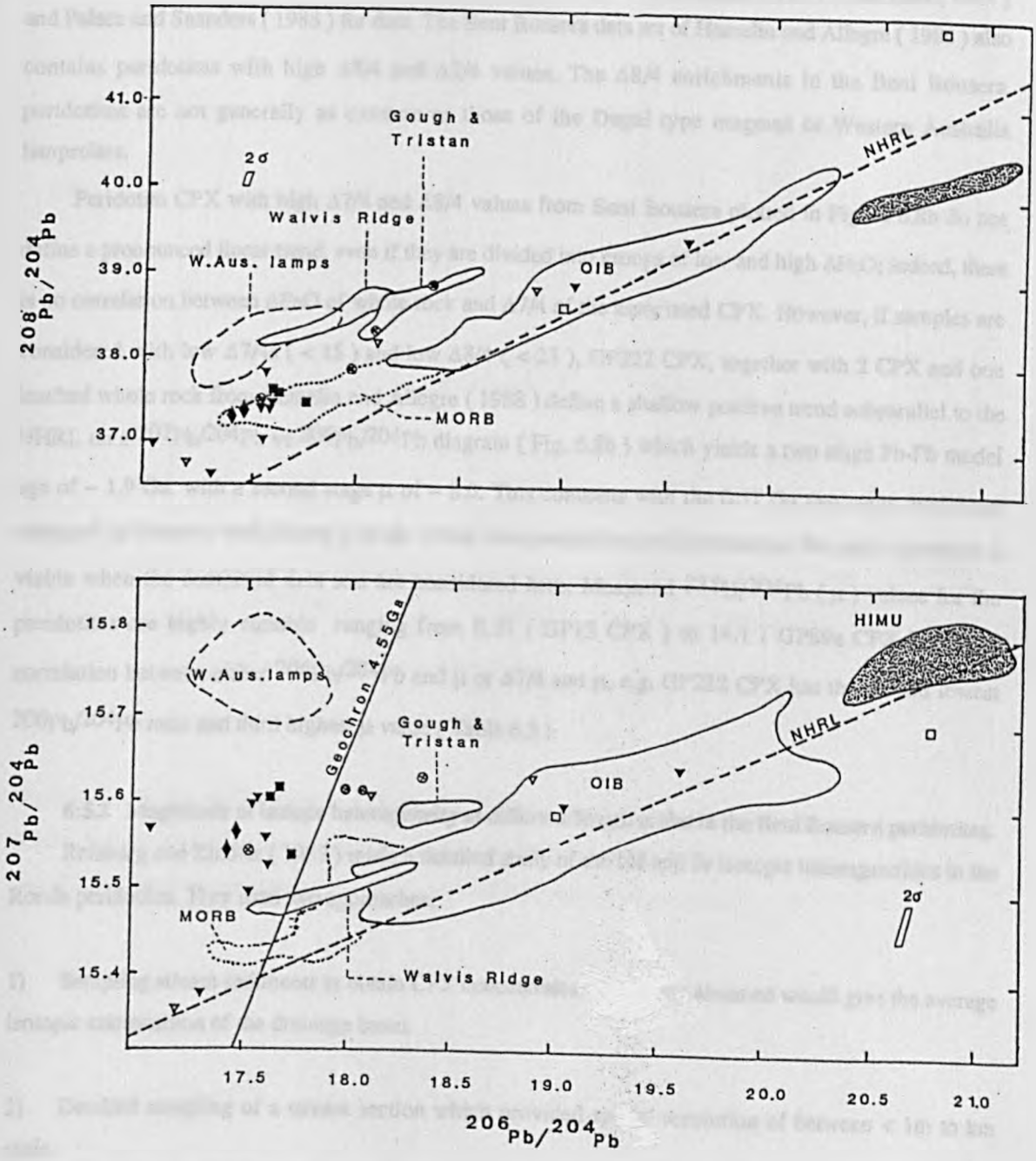

Figure 6.8a. $^{208}Pb/^{207}Pb$ and b, $^{207}Pb/^{204}Pb$ vs $^{206}Pb/^{204}Pb$ plot for Beni Bousera peridotites and pyroxenites, values are measured ratios. Symbols as in Figures 6.5 and 6.6. Open, empty symbols whole rocks, closed symbols are leached CPX analyses. Selected analyses from Hamelin and Allegre (1988) are also plotted. All whole rock data is from Hamelin and Allegre (1988). Selected high Δ7/4 OIB are shown separately from main OIB field. HIMU field (stippled) encloses St.Helena and Tubaii. Data from Zindler and Hart (1986) and Chaffey (1988). W.Australian Lamproite data from Nelson et al (1986).

anomalous Indian Ocean MORBs, OIBs and other volcanics which form the Southern Hemisphere "DUPAL" anomaly of Hart (1984). Although the Δ7/4 magnitudes are not as far displaced from NHRL as the W.Australian lamproites (see Nelson et al 1986) they define a general trend towards comparable $^{207}Pb/^{204}Pb$ values at low $^{206}Pb/^{204}Pb$ ratios (Figure 6.8b). Δ8/4 values are also high in the Beni Bousera CPX +10.1 to +89.2 in GP220 CPX, higher values only being found in DUPAL type oceanic volcanics such as Gough (100.2) Raratonga (117.5) and the Walvis Ridge (118.7), see Hart (1984) and Palacz and Suanders (1988) for data. The Beni Bousera data set of Hamelin and Allegre (1988) also contains peridotites with high Δ8/4 and Δ7/4 values. The Δ8/4 enrichments in the Beni Bousera peridotites are not generally as extreme as those of the Dupal type magmas or Western Australia lamproites.

Peridotite CPX with high Δ7/4 and Δ8/4 values from Beni Bousera plotted in Figure 6.8b do not define a pronounced linear trend, even if they are divided into groups of low and high ΔFeO; indeed, there is no correlation between ΔFeO of whole rock and Δ7/4 of the associated CPX. However, if samples are considered with low Δ7/4s (< 15) and low Δ8/4 (< 23), GP222 CPX, together with 2 CPX and one leached whole rock from Hamelin and Allegre (1988) define a shallow positive trend subparallel to the NHRL on a $^{207}Pb/^{204}Pb$ vs $^{206}Pb/^{204}Pb$ diagram (Fig. 6.8b) which yields a two stage Pb-Pb model age of ~ 1.9 Ga. with a second stage μ of ~ 8.0. This contrasts with the 0.57 Ga two stage model age obtained by Hamelin and Allegre (op.cit.) from both peridotites and pyroxenites. No such regression is viable when the combined data sets are considered here. Measured $^{238}U/^{204}Pb$ (μ) values for the peridotites are highly variable ranging from 0.57 (GP13 CPX) to 14.1 (GP89a CPX) with no correlation between either $^{206}Pb/^{204}Pb$ and μ or Δ7/4 and μ, e.g. GP222 CPX has the second lowest $^{206}Pb/^{204}Pb$ ratio and third highest μ value (Table 6.5).

6:5.2 Magnitude of isotope heterogeneity at different length scales in the Beni Bousera peridotites.

Reisburg and Zindler (1987) made a detailed study of the Nd and Sr isotopic heterogeneities in the Ronda peridotites. They used two approaches;

1) Sampling stream sediments to obtain CPX concentrates which they assumed would give the average isotopic composition of the drainage basin.

2) Detailed sampling of a stream section which provided spatial resolution of between < 1m to km scale.

In Chapter 2 it was noted that the Cr-pyroxenites contain green diopsidic CPX which is chemically and physically identical to the CPX in the peridotites. However, the Sr-Nd and Pb isotopic compositions of the CPX from the Cr-pyroxenites can be drastically different from the surrounding peridotites. Inclusion of CPX from Cr pyroxenites may thus seriously affect the average isotopic compositions of the "drainage basin". For this reason the *in situ* stream exposure sampling approach was adopted to investigate small and large scale isotopic heterogeneity in the Beni Bousera peridotites. The Oued el Jouj Wadi was selected for this purpose as it provides the most continuous, fresh exposure in the entire massif

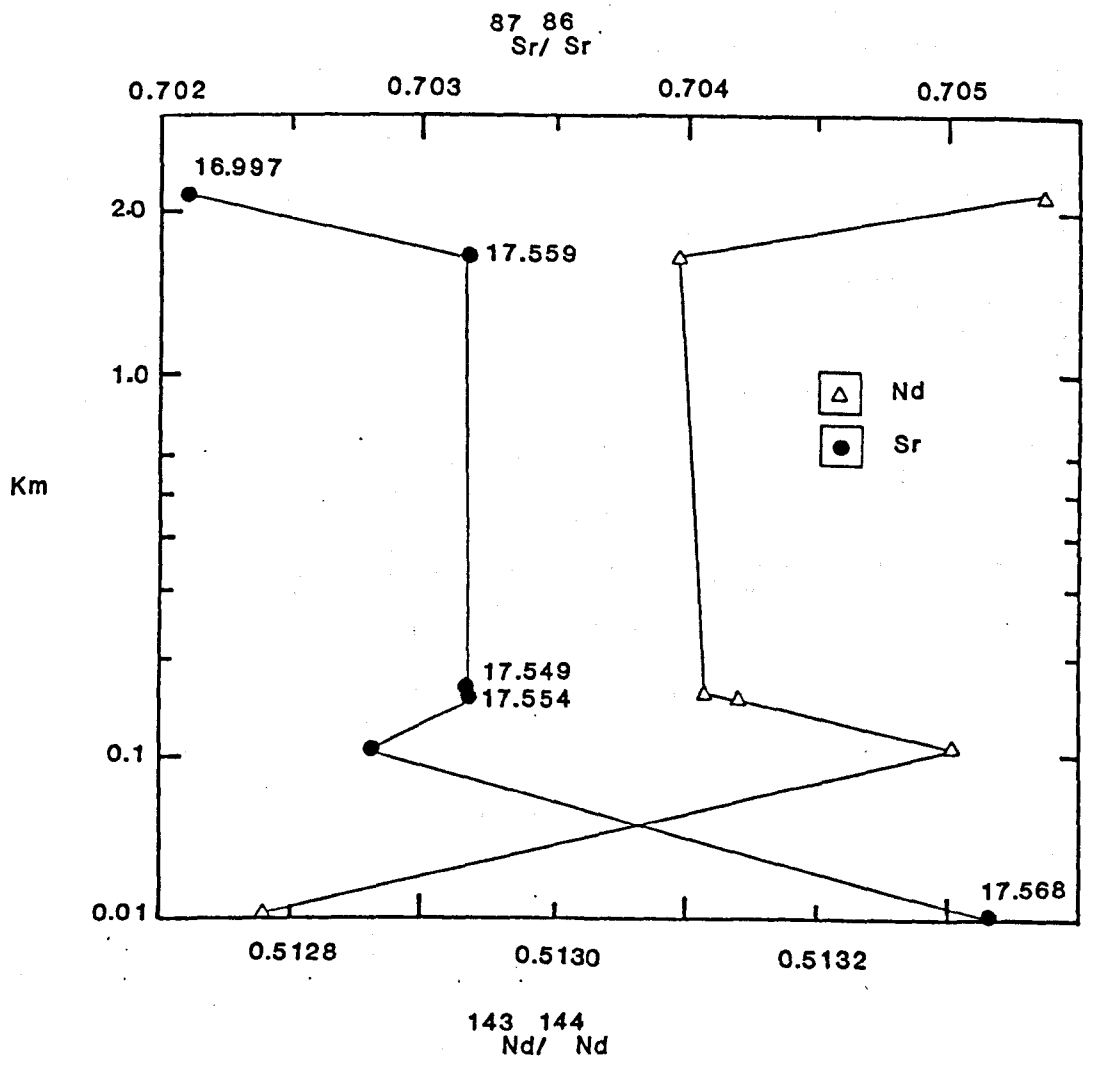

Figure 6.9. Sr, Nd and Pb isotope variations of CPX from peridotites collected along the Oued el Jouj stream section plotted against distance (in km) from the sample GP220. Note the distance scale is logarithmic. Numbers against solid circles are $^{206}Pb/^{204}Pb$ ratios (measured).

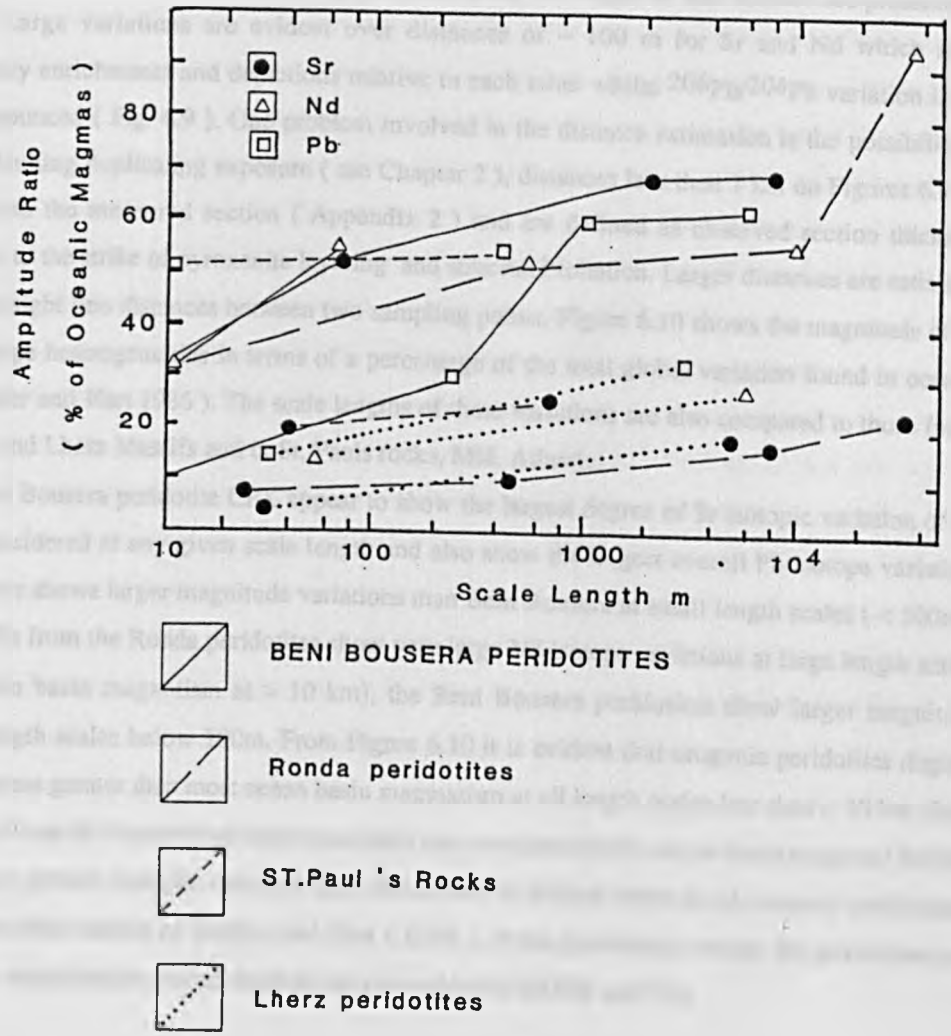

Figure 6.10. Isotopic heterogeneity vs scale length (meters) for Beni Bousera and other orogenic peridotites. Beni Bousera data are for leached CPX separates only. Isotopic heterogeneity (amplitiude ratio) is expressed as a percentage of the total isotopic range observed in all oceanic basalts (OIB and MORB). The two end points for each line represent the scale length of the maximum observed variation in each massif (right) and the largest variation observed at the smallest scale length (left); Data from Zindler and Hart (1986).

and was logged in detail along part of its length (see Appendix 2). Sr, Nd and Pb isotopic variations for six peridotite CPX samples taken at varying distances along the length of this traverse are presented in Figure 6.9. Large variations are evident over distances of ~ 100 m for Sr and Nd which show complementary enrichments and depletions relative to each other whilst $^{206}Pb/^{204}Pb$ variation is not quite as pronounced (Fig. 6.9). One problem involved in the distance estimation is the possibility of folding and faulting duplicating exposure (see Chapter 2), distances less than 1 km on Figures 6.9 are calculated from the measured section (Appendix 2) and are defined as observed section thickness perpendicular to the strike of pyroxenite layering and structural foliation. Larger distances are estimated in terms of straight line distances between two sampling points. Figure 6.10 shows the magnitude of the recorded isotope heterogeneities in terms of a percentage of the total global variation found in oceanic basalts (Zindler and Hart 1986). The scale lengths of these variations are also compared to those found in the Ronda and Lherz Massifs and in St. Pauls rocks, Mid. Atlantic.

The Beni Bousera peridotite CPX appear to show the largest degree of Sr isotopic variation of the peridotites considered at any given scale length and also show the largest overall Pb isotope variation. However, Lherz shows larger magnitude variations than Beni Bousera at small length scales (< 100m). Although CPXs from the Ronda peridotites show very large Nd isotope variations at large length scales (95 % of ocean basin magmatism at > 10 km), the Beni Bousera peridotites show larger magnitude variation at length scales below 100m. From Figure 6.10 it is evident that orogenic peridotites display isotopic variations greater than most ocean basin magmatism at all length scales less than ~ 30 km. Only when regions of mantle thousands of kilometers apart are considered do the ocean basin magmas (MORB and OIB) show greater isotopic variation than that shown in limited outcrops of orogenic peridotites, confirming the observations of Zindler and Hart (1986). If the pyroxenites within the peridotites are considered, the variations far exceed those shown by worldwide MORB and OIB.

6:5.3 Pyroxenites.

Analyses of whole rock pyroxenites were mainly undertaken whilst developing chemical separation techniques for low abundance samples. Rigorous leaching of these samples was not carried out. The consequences of not removing the imprint of secondary alteration/crustal interaction from the whole rock samples are evident by inspection of corresponding unleached whole rock and CPX data in Tables 6.3 and 6.4. Unleached whole rock samples possess significantly higher $^{87}Sr/^{86}Sr$ ratios than their corresponding CPXs, although some extremely fresh whole rock samples such as GP101 and GP33a show similar $^{87}Sr/^{86}Sr$ ratios (GP33a whole rock and CPX are within analytical error). Pb isotopic compositions of unleached whole rocks and leached CPXs also differ drastically. The unleached pyroxenite whole rock samples have generally higher $^{206}Pb/^{204}Pb$ and $^{208}Pb/^{204}Pb$ ratios than their corresponding CPXs and have both higher and lower $^{207}Pb/^{204}Pb$ ratios. Even whole rock samples which were leached for two hours in 80 °C 6M HCl show marked differences from their associated CPXs, having both lower and higher $^{207}Pb/^{204}Pb$ ratios. These variations between unleached whole rock and leached CPX separates contrast with the leaching experiments of Hamelin and Allegre (1988). The above authors recorded lower $^{206}Pb/^{204}Pb$ and $^{208}Pb/^{204}Pb$ ratios and high $^{207}Pb/^{204}Pb$ in leachates compared with residues, consistent with some degree of crustal fluid contamination. The variability of both the leached and unleached whole rock Pb isotope data presented in Table 6.3 suggests that the data are not representative

of mantle values and are consequently not considered further in this study. A similar stance is adopted for the whole rock Sr isotope data.

Nd isotopic compositions for CPX separates from the pyroxenites should theoretically be close to the whole rock Nd isotopic composition, depending on the proportions and Sm/Nd ratios of other phases present. Figure 6.11 presents the coexisting unleached whole rock and leached CPX separate $^{143}Nd/^{144}Nd$ ratios for Beni Bousera pyroxenites. If the whole rock contains garnet it would be expected to have a more radiogenic $^{143}Nd/^{144}Nd$ composition than the primary CPX. This relationship is only observed for one sample (GP87 CPX-WR) in Figure 6.11 where the $^{143}Nd/^{144}Nd$ ratio is significantly greater than the whole rock. This is consistent with the very high $^{147}Sm/^{144}Nd$ ratio recorded in the garnet for this rock. Unfortunately, the $^{143}Nd/^{144}Nd$ analysis of this garnet was not sufficiently accurate to permit comparison of calculated and observed modes. The unleached whole rocks of other garnetiferous samples are slightly, to substantially less radiogenic in terms of $^{143}Nd/^{144}Nd$ ratios than their leached CPXs. This is unexpected and could be interpreted in terms of a low Sm/Nd ratio secondary phase contaminating the whole rock. However, GP147 CPX and leached whole rock (6M HCl) have Nd isotope compositions within analytical uncertainty of the value measured for the unleached whole rock (Table 6.3). The presence of a large proportion of highly radiogenic, leachable Sr in this sample suggests it has suffered late stage crustal alteration which does *not* appear to have significantly affected the $^{143}Nd/^{144}Nd$ ratio of the whole rock. A similar conclusion was reached by Polve (1983) after analysing leached and unleached whole rocks. It would be unwise to assume that all the $^{143}Nd/^{144}Nd$ for the unleached whole rocks in Table 6.3 are totally unaffected by secondary alteration. Zindler et al (1984) reported differing Sm/Nd ratios between leached and unleached whole rocks. Despite this, it is apparent that the $^{143}Nd/^{144}Nd$ values of unleached whole rocks reported in Table 6.3 are a good indication of the $^{143}Nd/^{144}Nd$ ratio of the whole rock prior to emplacement.

6:5.4 Sr and Nd isotope systematics of the pyroxenites.

The pyroxenites show even greater heterogeneity than the peridotites in terms of their Sr and Nd isotopic compositions. Total initial Sr isotope variation is from 0.70228, ε Sr = - 31.5 (GP30 CPX) to 0.71095, ε Sr = + 92.4 (GP81 CPX). The high Rb/Sr ratio of GP81 CPX requires significant age correction. GP81 CPX has the highest Sr content of the GGP samples (>40 ppm) suggesting it is the least likely to be subject to Sr isotope disruption by secondary alteration processes. Total initial Nd isotope variation is from 0.512164, ε Nd = - 8.78 (GP101a CPX) to 0.513931, ε Nd = + 26.21 (GP37 CPX). The high $^{147}Sm/^{144}Nd$ of most pyroxenites requires significant correction to the measured $^{143}Nd/^{144}Nd$ ratios despite the long half life of ^{147}Sm. Both Sr and Nd isotope ranges are much greater than the total range observed for present day ocean basin volcanism. Cr-pyroxenite and Al-augite pyroxenite isotopic ranges show considerable overlap, but the Cr-pyroxenites extend to less radiogenic $^{143}Nd/^{144}Nd$ ratios whereas the Al-augite group have samples with more radiogenic $^{87}Sr/^{86}Sr$ and $^{143}Nd/^{144}Nd$. Whole rocks analysed for Nd isotopes all fall within the $^{143}Nd/^{144}Nd$ range shown by the CPX samples (Figure 6.11).

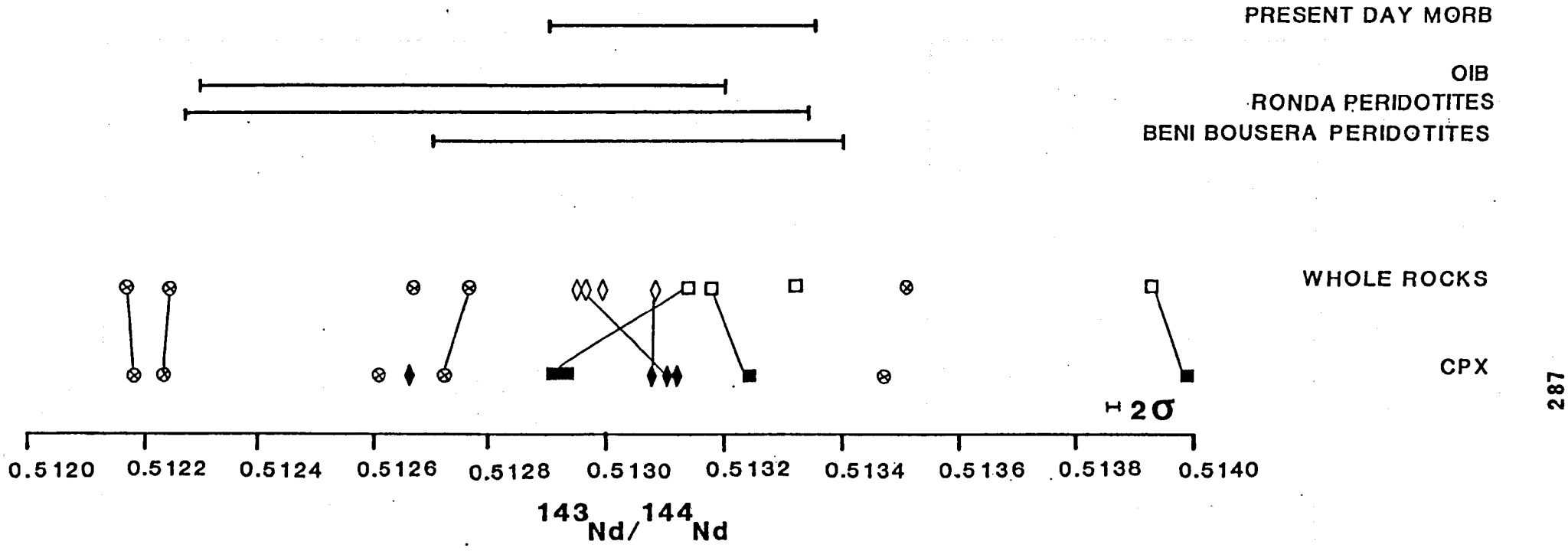

Figure 6.11. Initial Nd isotopic variation shown by Beni Bousera pyroxenites compared to host peridotites, Ronda peridotites, OIB and present day MORB lines join whole rock and CPX. Additional data from Reisburg and Zindler (1987) and Zindler and Hart (1986).

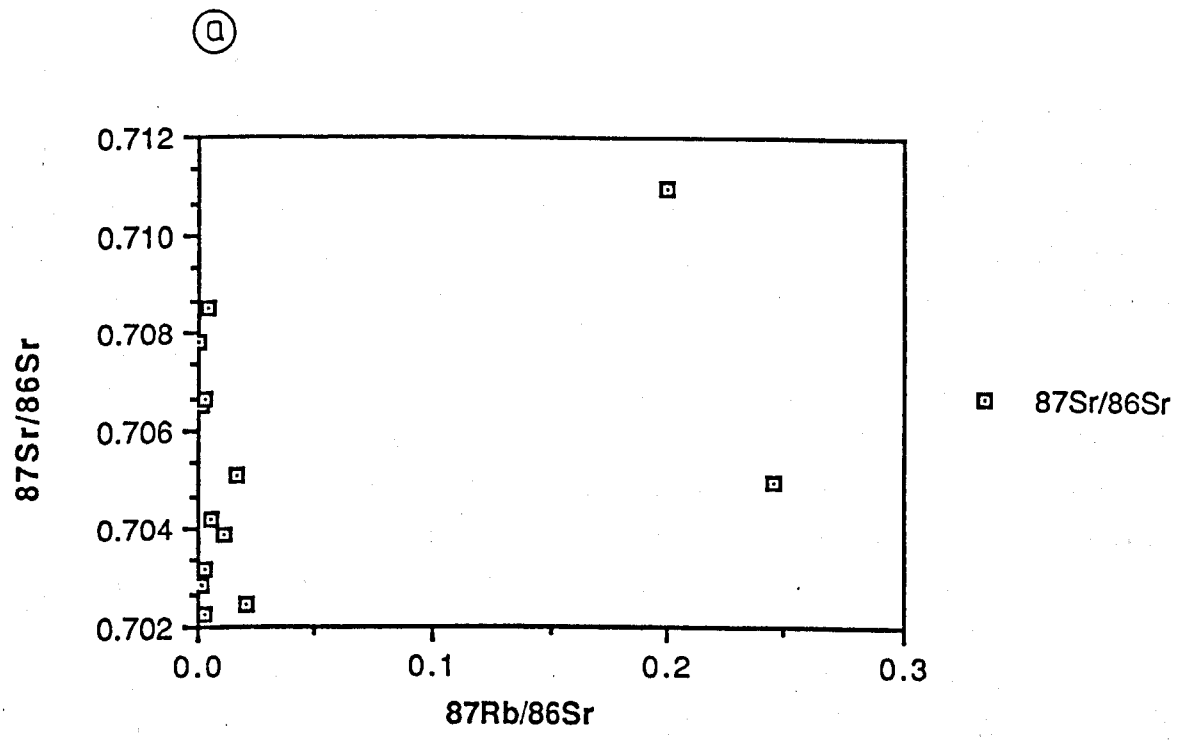

Figure 6.12a. $^{87}Sr/^{86}Sr$ vs $^{87}Rb/^{86}Sr$ for Beni Bousera pyroxenites, all samples plotted as squares.

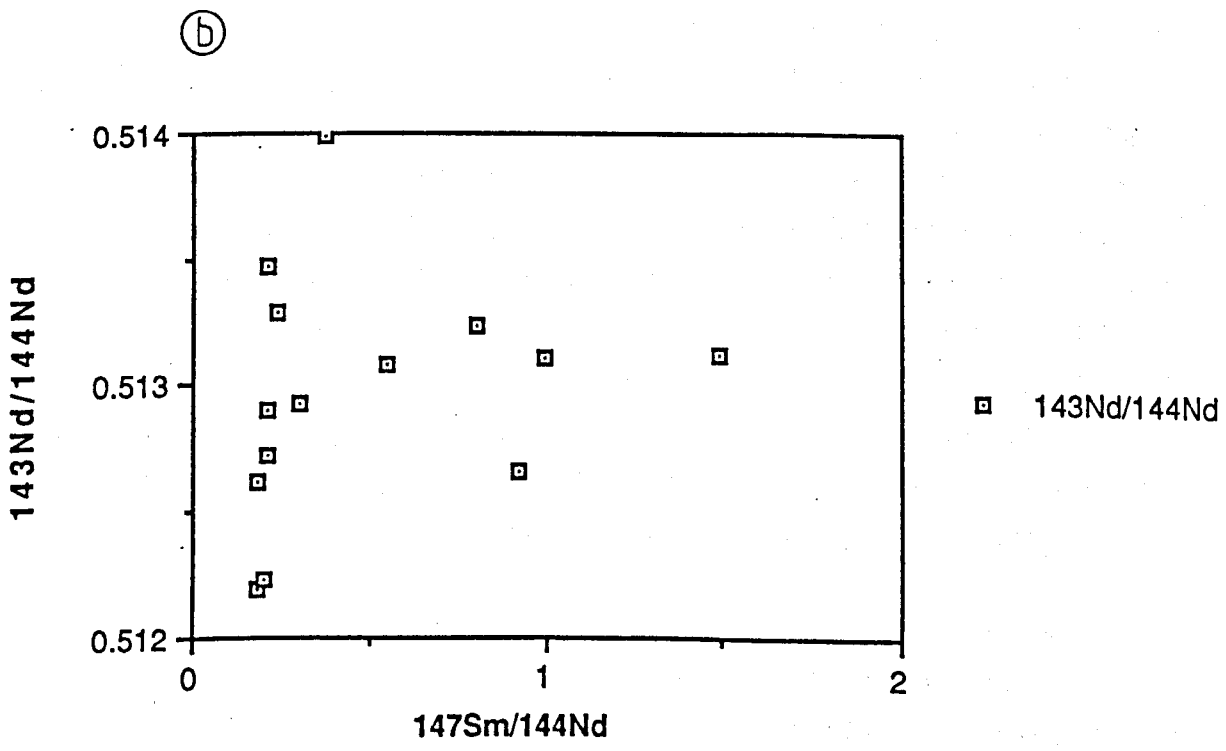

Figure 6.12b. $^{143}Nd/^{144}Nd$ vs $^{147}Sm/^{144}Nd$ for Beni Bousera pyroxenites, all samples plotted as squares.

The relationships of the pyroxenites to the Beni Bousera peridotites and present day ocean basin volcanism are shown in Figure 6.6. Several pyroxenites plot on a shallow negative trend from the MORB/depleted peridotite fields towards much more radiogenic $^{87}Sr/^{86}Sr$ ratios and gradually decreasing $^{143}Nd/^{144}Nd$ ratios. Three of the GGP samples plot close together, near the similarly LREE depleted GP139 CPX sample with high $^{87}Sr/^{86}Sr$ (~ 0.705) and relatively radiogenic $^{143}Nd/^{144}Nd$ ratios (~0.51320 to 0.51295). GGP sample GP81 has an extremely radiogenic initial $^{87}Sr/^{86}Sr$ value > 0.710 and less radiogenic initial $^{143}Nd/^{144}Nd$ (0.51254). No general trend is evident in Figure 6.6 for the pyroxenites as a group; few of the data points plot within the field of present day oceanic volcanism.

As observed for the peridotite CPX, no well defined isochronous relationships exist in the pyroxenites for Rb/Sr or Sm/Nd isotope systematics (Figs. 6.12 a and b). Omitting extremely LREE depleted samples (i.e. GGP and GP139 CPX) yields a steeply trending straight line relationship on an Sm/Nd isochron diagram whose best fit line yields an "age" of 2.75 Ga. The large MSWD (>5) preclude calling the line an isochron. The most salient point to be gathered from the isotope-parent/daughter-systematics of Figure 6.12 and Table 6.5 is that there seems to be complete decoupling of the parent/daughter ratio and isotopic composition. For instance, the Cr-pyroxenite samples GP101a CPX and GP188 CPX have some of the most radiogenic $^{87}Sr/^{86}Sr$ ratios (0.7078 - 0.7085) and yet have two of the lowest $^{87}Rb/^{86}Sr$ ratios (0.0036 - 0.00061). Similarly GGP sample PHN5730 CPX has the highest $^{147}Sm/^{144}Nd$ ratio and yet has a relatively unradiogenic $^{143}Nd/^{144}Nd$ ratio compared with other samples.

6:5.5 Pb Isotopes:

The Beni Bousera pyroxenites exhibit considerable Pb isotopic heterogeneity (Figure 6.7 and 6.8). CPX samples analysed in this study show the following variation: $^{206}Pb/^{204}Pb$: 17.404 - 18.362, $^{207}Pb/^{204}Pb$: 15.536 - 15.628, $^{208}Pb/^{204}Pb$: 37.305 - 38.851. Six out of nine samples plot to the left of the geochron of Figure 6.8b; all samples are considerably enriched in ^{207}Pb and to a lesser extent in ^{208}Pb compared to NHRL. $\Delta 7/4$ values vary from + 12.4 to +21 and $\Delta 8/4$ values vary from 43.8 to 102.4 (see Table 6.5). On a $^{207}Pb/^{204}Pb$ vs $^{206}Pb/^{204}Pb$ diagram the pyroxenites plot to the left of the geochron, above samples from the Walvis Ridge, towards the area defined by W.Australian lamproites (Fig. 6.8b). The data in this region do not define linear relationships and plot below Walvis Ridge samples on a ^{208}Pb vs ^{206}Pb plot (Figure 6.8a). Three websterite samples (one Al-augite type and two Cr-pyroxenites) plot to the right of the geochron on Figure 6.8b forming a shallow positive trend close to the areas defined by Gough and Kerguelen Islands. These samples have both high $\Delta 7/4$ and $\Delta 8/4$ and $^{87}Sr/^{86}Sr$ ratios and consequently have "DUPAL-like"signatures. The slope of this linear trend is too shallow to yield a sensible two stage isochron age. No coherent isochronous relationships are evident in the points to the left of the geochron.

Pyroxenites analysed in this study do not show equivalent ^{206}Pb variation to those analysed by Hamelin and Allegre (1988). Analytical Pb blanks obtained during this study were equal to or better than those obtained by Hamelin and Allegre (op.cit). These authors found some whole rock pyroxenites with $^{206}Pb/^{204}Pb$ ratios up to 20.8 with a large proportion over 18 (Figure 6.7). The samples show variable $\Delta 7/4$ and $\Delta 8/4$ values, as high as those found in this study. The sample with the most radiogenic

Figure 6.13. Δ7/4 and Δ8/4 vs initial $^{143}Nd/^{144}Nd$ and $^{87}Sr/^{86}Sr$ ratios for Beni Bousera pyroxenites.
All samples plotted as squares.

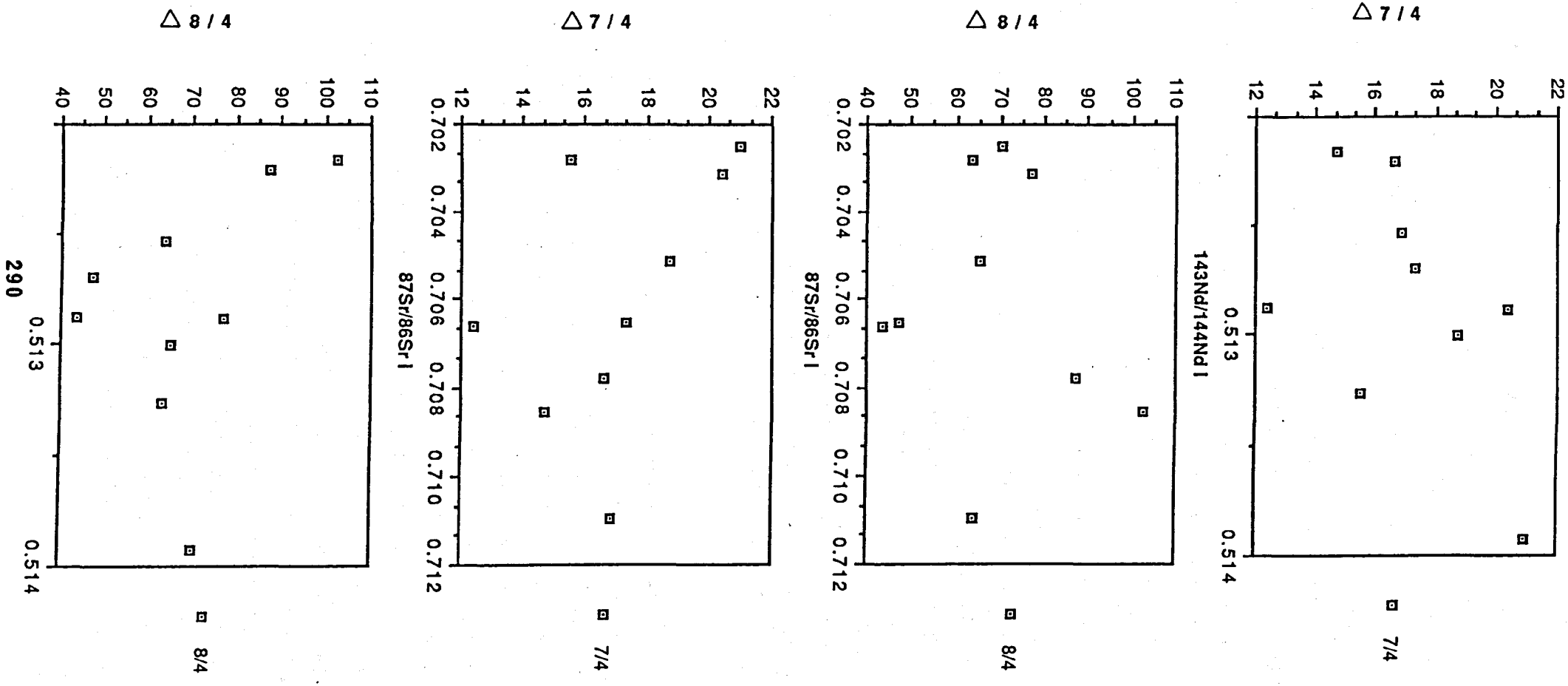

$^{206}Pb/^{204}Pb$ (M82-7) plots below the NHRL in terms of Δ7/4 and above NHRL interms of Δ8/4 (~42). When all the pyroxenite data are considered they show extreme Pb isotope heterogeneity. The pyroxenite Pb isotope data display a lack of parent/daughter isotope correlation similar to that observed for Rb/Sr and Sm/Nd isotope systematics. $^{238}U/^{204}Pb$ (μ) values vary from 0.14 to 16.4, although the highest μ value (16.4) is associated with the most radiogenic $^{206}Pb/^{204}Pb$ composition of 18.36 (GP101 CPX), the sample with the second highest $^{206}Pb/^{204}Pb$ value of 18.08 (GP188 CPX) has one of the lowest μ values (0.85). Thus there is little correlation between μ and $^{206}Pb/^{204}Pb$. The GGP sample with the most radiogenic $^{87}Sr/^{86}Sr$ ratio (GP81 CPX) has one of the lowest μ values (0.34) but does not have an especially unusual Pb isotope composition compared with the rest of the samples. Unfortunately, U analysis of the other GGP sample GP147 CPX was not successful, hence no μ value can be calculated.

No convincing correlations are apparent between Pb-Sr-Nd isotopes (Figure 6.13) although there is a trend towards samples with the least radiogenic $^{87}Sr/^{86}Sr$ having the highest Δ7/4 values. With the addition of the Pb isotope data differences between the Cr-pyroxenites and Al-augite pyroxenites can now be examined. The isotopic variation shown by the two groups is summarized in Table 6.6. Sample GP132(1) is not considered here as this Cr-pyroxenite probably includes some CPX from the host lherzolite. This sample will be discussed separately. The range of Sr-Nd-Pb isotope characteristics for these two rock groups largely overlap, however the Cr-pyroxenites have the lowest $^{87}Rb/^{86}Sr$ and $^{147}Sm/^{144}Nd$ ratios and the most radiogenic Pb isotope ratios. Given that the Cr pyroxenites have reasonably well correlated Sr-Nd isotope e.g. radiogenic Nd, unradiogenic Sr and vice-versa, the low Sm/Nd and Rb/Sr ratios of GP101 CPX and GP188 CPX are not compatible with normal mantle-melt fractionation relationships.

6:5.6 Isotopic heterogeneity of peridotites and pyroxenites: The scale of re-equlibration

Fine scale sampling was undertaken to investigate peridotite/pyroxenite isotopic interaction/equilibration within the mantle along the well exposed Oued el Jouj wadi. Pyroxenite samples from layers of varying thickness were chosen to investigate whether a cut-off thickness existed at which the pyroxenite and adjacent peridotite reached isotopic equilibrium. Two closely spaced garnet clinopyroxenite layers at the top of the logged section of the Oued el Jouj (Appendix 2) were chosen to study pyroxenite/peridotite interaction and the results are presented in Figure 6.16. CPX separates were obtained from the centre and margin of one layer, GP87, the centre only of the other, GP194, and the two adjacent spinel lherzolites, one of which (GP88) was situated between the two layers. Peridotite from immediately adjacent the pyroxenite/peridotite contact was not analysed as this material was highly weathered and deformed due to grain size reduction produced by layer parallel shearing (Chapter 2). The CPX separate obtained from the bottom edge of GP87; GP87B, consisted of a mixture of pink/grey Al-augite grains and various gradations of green Cr-diopsidic CPX (see Chapter 4). The green Cr-diopside grains came from nearest the pyroxenite-peridotite contact and were shown in Chapter 4 to be partially re-equilibrated in terms of major elements towards the peridotite composition. These CPX grains were not mechanically incorporated into the pyroxenite margin. Layer GP87 was 19cm thick and layer GP194 was 15cm thick. The two surrounding lherzolites, GP89a and GP88, appeared to be in Pb, Sr and

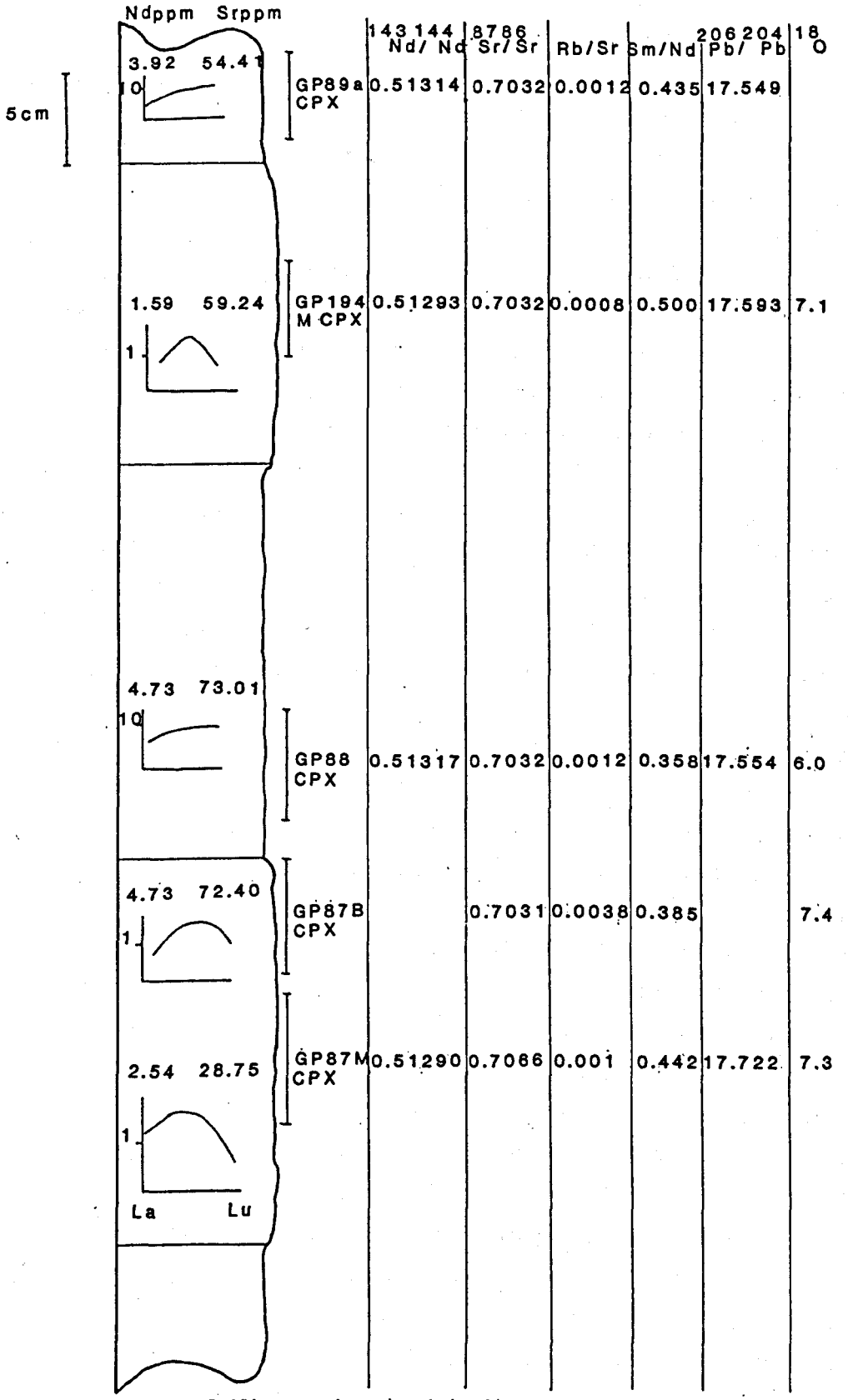

Figure 6.14 Pb-Sr-Nd-oxygen isotopic relationships in an interlayered sequence of two garnet clinopyroxenites and spinel lherzolites in the Oued el Jouj stream section. Bars on the right of the section indicate the portion of rock the CPX separates were extracted from. Isotopic ratios are initial values except Pb data.

Nd isotopic equlibriumwhich facilitated comparison of peridotite/pyroxenite re-equilibration between the two pyroxenite layers.

From Figure 6.14 it is evident that the edge of GP87 has undergone some Sr isotopic re-equilibration with the surrounding lherzolite. The centre of the layer has a more radiogenic $^{87}Sr/^{86}Sr$ ratio (0.70662) than the layer margin (0.70312) which is outside error of the adjacent peridotite CPX (0.70318). This interaction is also evident in terms of Nd and Sr concentrations (Fig. 6.16), the CPX separate from the centre of the layer having a factor of two lower concentration of Nd and Sr than the outer margin CPX separate whose Nd and Sr concentrations are extremely similar to those of the surrounding lherzolite CPX. This variation from layer centre to margin is virtually identical to that observed in the whole rock powders analysed from the same specimens (Table 6.3).

From these observations it appears that the layer margin of GP87 has re-equilibrated in terms of Sr isotopes and Sr concentration with the surrounding peridotite, whose higher Sr and Nd concentration appears to have "buffered" both the Nd and Sr content and Sr isotopic composition of the pyroxenite layer margin. This is in contrast to the effect observed on Pb isotopes by Hamelin and Allegre (1988) in a closely layered pyroxenite-peridotite sequence from the Lherz massif. In their study, higher Pb concentrations of the pyroxenites buffered the Pb contents and Pb isotopic compositions of the narrow volumes of inter-layered peridotites. From Figure 6.14 it would appear that the opposite would be expected for Nd isotopes as the peridotite GP88 CPX contains almost twice as much Nd as the centre of GP87, therefore the $^{143}Nd/^{144}Nd$ ratio of the layer margin would be expected to be closer to the adjacent peridotite $^{143}Nd/^{144}Nd$ ratio. Although the Nd concentrations of GP87B CPX and GP88 CPX are identical, their REE patterns remain different. The HREE content of GP87B is considerably higher than GP87M indicating that it has partially equilibrated with the surrounding lherzolites. The Sm/Nd ratio of the layer margin, GP87B, is lower than the centre, GP87M, comparable to the lherzolite, GP88. The centre of the slightly thinner layer, GP194 has a $^{143}Nd/^{144}Nd$ ratio which is closer to that of the surrounding lherzolite, but probably not in isotopic equilibrium as there is a factor of two concentration difference between the Nd content of the pyroxenite and peridotite. However, the Sr concentration and the $^{87}Sr/^{86}Sr$ ratio of GP194M CPX is very similar to GP89a CPX. It is difficult to assess to what extent this is due to isotopic re-equilibration without analysis of the layer margin, but it is interesting to note that in contrast to the $^{206}Pb/^{204}Pb$ ratio of the centre of the layer, GP194, is within error of the lherzolite GP89a (Fig. 6.14). The differing Nd concentrations between the layer centre and surrounding lherzolite suggest that the similarity of isotopic compositions between the pyroxenite layer and surrounding peridotite in this case may be coincidental and that equilibration due to diffusion has had little effect over a distance of ~ 8cm. Another point to note about Figure 6.14 is the higher Rb/Sr ratio of GP87B compared to the layer margin and the surrounding peridotite. This is not compatible with the Sr isotopic similarity between GP87B and GP88 nor the trend towards similar Sm/Nd ratios between the two. The result may be due to inclusions of a high Rb/Sr phase in GP87B CPX. Perhaps a more plausible explanation is that the margin of the pyroxenite layer interacted with melts from the peridotite which were created by pyroxenite intrusion.

Finally, despite some Sr isotope re-equilibration between layer edge and host peridotite there seems to be no oxygen isotope equilibration, the $\delta^{18}O$ value of the pyroxenite margin, GP87B CPX, is slightly heavier, but within analytical error of the CPX from the layer centre, GP87M. This aspect will

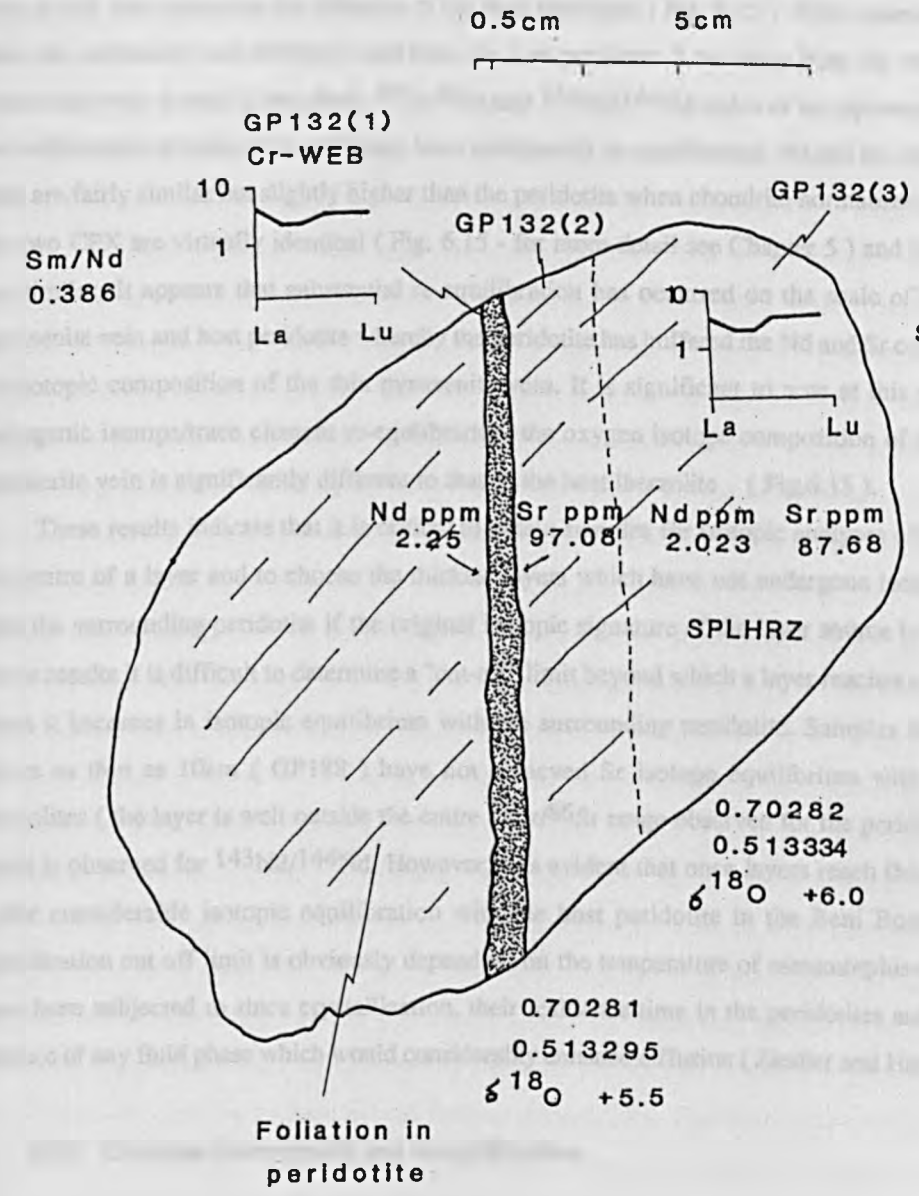

Figure 6.15. Sr, Nd and oxygen isotope interaction between a sub-cm websterite vein GP132(1) and the host spinel peridotite, GP132(3) recorded by leached CPX separates. Isotope ratios are initial values. Nd and Sr ppm are indicated for vein and host together with their Sm/Nd ratio. Chondrite normalised CPX total REE pattern also indicated. See Chapter 5 for more detailed REE patterns.

be discussed further in Chapter 7.

The second sample chosen to assess pyroxenite/peridotite interaction was the composite sample GP132. This sample is a spinel lherzolite block which is cut by a deep green Cr-diopside rich websterite vein which also cross-cuts the foliation of the host peridotite (Fig. 6.15). CPX separates were obtained from the websterite vein GP132(1) and from the host peridotite 2 cm away from the vein GP132(3). The pyroxenite vein is only 0.5cm thick. $^{87}Sr/^{86}Sr$ and $^{143}Nd/^{144}Nd$ ratios of the pyroxenite and peridotite are within error of each other and hence have isotopically re-equilibrated. Nd and Sr concentrations of the vein are fairly similar but slightly higher than the peridotite when chondrite normalized. REE patterns for the two CPX are virtually identical (Fig. 6.15 - for more detail see Chapter 5) and their Sm/Nd ratios are similar. It appears that substantial re-equilibration has occurred on the scale of 2cm between the pyroxenite vein and host peridotite whereby the peridotite has buffered the Nd and Sr contents and Nd and Sr isotopic composition of the thin pyroxenite vein. It is significant to note at this point that despite radiogenic isotope/trace element re-equlibration, the oxygen isotope composition of the CPX from the websterite vein is significantly different to that of the host lherzolite (Fig.6.15).

These results indicate that it is critical to obtain samples for isotopic analyses of pyroxenites from the centre of a layer and to choose the thickest layers which have not undergone isotopic equilibration with the surrounding peridotite if the original isotopic signature of the layer source is sought. From the above results it is difficult to determine a "cut-off" limit beyond which a layer reaches a certain thickness when it becomes in isotopic equilibrium with the surrounding peridotite. Samples from the centre of layers as thin as 10cm (GP188) have not achieved Sr isotope equilibrium with the surrounding lherzolites (the layer is well outside the entire $^{87}Sr/^{86}Sr$ range observed for the peridotites). A similar result is observed for $^{143}Nd/^{144}Nd$. However, it is evident that once layers reach the sub cm size they suffer considerable isotopic equilibration with the host peridotite in the Beni Bousera massif. The equilibration cut off limit is obviously dependent on the temperature of metamorphism the pyroxenites have been subjected to since crystallization, their residence time in the peridotites and the presence or absence of any fluid phase which would considerably enhance diffusion (Zindler and Hart 1986).

6:5.7 O-isotope heterogeneity and re-equilibration.

Large magnitude oxygen isotope heterogeneity on a fine scale is evident in the pyroxenite suite. Sample GP101 consists of a 30cm thick Cr-pyroxenite lens (GP101a CPX and OPX) cut by a 5cm thick Al-augite pyroxenite (GP101d CPX and OPX). The two pyroxenite CPX separates have $\delta^{18}O$ values of + 8.7 ‰ and + 6.4 ‰ respectively (Table 7.1) and are both in oxygen isotope equilibrium (within error) with their coexisting OPX (Figure 7.2b). Therefore large magnitude oxygen isotope heterogeneities exist on the sub 10cm scale. The persistence of large magnitude oxygen isotope heterogeneity on a small scale is confirmed by the lack of oxygen isotope re-equilibration between the margin of layer GP87 and the surrounding peridotite GP88.

The O-isotope composition of the CPX separate from the margin of the GP87 (GP87B CPX) is within error of the CPX from the centre of the layer (GP87M CPX), see Figure 6.14 and both CPXs are in oxygen isotopic equilibrium with their coexisting garnets (Table 7.1, Fig. 7.3). The lack of O-isotope re-equilibration with the surrounding perditotite is in marked contrast to Sr isotope data (Fig.

6.16). The sub-cm scale Cr-pyroxenite vein (GP132(1) CPX) which cross cuts the peridotite GP132(3) (Figure 6.15) is not in O-isotope equilibrium with the surrounding peridotite. Hence, sub-cm O-isotope heterogeneity exists in the pyroxenites which, in contrast to Sr and Nd isotopes, has survived high temperature re-equilibration with the surrounding peridotites.

6:5.8 Pyroxenite equilibration with the surrounding peridotites.

The Beni Bousera pyroxenite suite displays much greater Sr and Nd isotopic variation than the total field of OIB and MORB (Figure 6.) and Pb isotope heterogeneity of equivalent magnitude (Figure 6.8a and b). The large magnitude, small length scale isotopic variation of the pyroxenites is probably due to a combination of the ancient protolith histories, heterogeneous source and complex evolution. Some of the pyroxenite isotope (and trace element) heterogeneity shows signs of equilibration with the host peridotite at layer margins but there is no relationship between isotopic ratio and layer thickness. Over a distance of less than 5 cm some layer margins appear to have reached > 95% equilibration with the surrounding peridotites in terms of their $^{87}Sr/^{86}Sr$ ratios, Sr and Nd concentrations (Fig. 6.14). Knowledge of the appropriate diffusion coefficients can place constraints on the time scale required to achieve such equilibration. Sneeringer et al (1984) calculated that for two adjacent 1 cm thick layers initially out of equilibrium, the time required to reach 95% Sr concentration equilibrium is ~ 30 Ma at 1000 °C. This time increases to 90 Ma if a 1 cm thick intervening layer is present between the two layers considered that has the same diffusion coefficient as the layer. At 1250 °C the 95% equilibration times are reduced to below ~ 100,000 years. However, because equlibration times due to diffusion alone are proportional to distance squared (Hoffman and Hart 1978), it may take approximately 100 Ma to equilibrate Sr and Nd isotopes over distances of greater than 5 cm by diffusion alone. The outer 5 cm of GP87 is over 95% equilibrated with the surrounding lherzolite (Figure 6.16) indicating that diffusion has operated over at least this scale during the evolution of the Beni Bousera massif. In terms of dating absolute mantle residence ages of pyroxenite layers by measuring the extent to which they have chemically equilibrated with the surrounding lherzolite across their profile, it is necessary to know how long (relatively) the layers have existed in their present form. The conclusions of Chapter 2 were that the present pyroxenite layer orientations and thickness were largely controlled by pre-syn emplacement shearing and folding, much of which probably occured during the last 50 Ma. These conclusions arise from the structural similarities between the fabrics and folding in the crustally derived kinzigites and the peridotite body. The inference made by Allegre and Turcotte (1986) that the pyroxenites represent thinned crust of different ages, whose present state of boudinage and folding is due to "streamline mixing" in the asthemosphere is probably erroneous as the folding in the pyroxenites and crustal kinzigites is coaxial. Furthermore, similar fold structures and boudinage can be observed in pyroxenite veins cutting the "mantle sequences" in ophiolites which are also believed to be emplacement related (Lippard et al 1986).

Some of the pyroxenite bodies in Beni Bousera, which do not retain evidence of igneous emplacement such as zoning or apophyses at their margins, may once have existed as parts of much larger bodies that were disrupted by folding and shearing during diapiric upwelling and emplacement into the crust. This means that some of the layers may not have existed in their present physical form (thickness and shape) for very long relative to their whole history. Consequently, the degree to which the

layer has interacted with the surrounding peridotite throughout its thickness may only be a reflection on how long the layer has existed in its present physical form. Alternatively, the original pyroxenite sources may have been remelted relatively recently which led to crystallization of their present forms at 150 km or less during diapirism.

The apparent lack of O-isotope interaction between peridotites and pyroxenites and the survival of small scale, large magnitude O-isotope heterogeneity in the pyroxenites is consistent with available published diffusion data on dry mantle systems (Cole and Ohmoto 1986). The diffusion coefficient for oxygen in fosteritic olivine is significantly lower at ~ 1200°C (9.2 x 10^{-17} cm^2/sec) than the diffusion coefficient for Sr or Sm in diopside at 1200°C (~ 8 x 10^{-14} cm^2/sec , see compilation by Sneeringer et al 1984 and Cole and Ohmoto 1986). The lower diffusion coefficient of oxygen in silicates compared to trace elements probably results from strong Si-O bonding and favours preservation of O-isotope heterogeneities on a small scale at mantle temperatures (T.K. Kyser, pers. Comm.).

One further conclusion to be drawn from the study of peridotite/pyroxenite interaction is that if eclogite and pyroxenite xenoliths sampled by kimberlites originate by disruption of "layers" of eclogite/pyroxenite in the deep lithospheric mantle; at least some of their isotopic and chemical variation may be explained by sampling of material which resided at the margins of such layers. Xenoliths commonly do not provide the opportunity to determine peridotite/pyroxenite spatial relationships, this fact emphasises the importance of studying large ultrabasic massifs like Beni Bousera in order to understand mantle geodynamics.

6:6 PETROGENESIS

6:6.1 Introduction

This section will consider the petrogenesis of the Beni Bousera pyroxenites and peridotites with the aim of answering the following questions :

1) Are the peridotites and pyroxenites cogenetic and when did they form ?

2) Have both groups of rocks suffered single or multistage histories since separation from their source?

3) Do the peridotites and pyroxenites show any evidence of contamination by crustal rocks/sediments during their evolution ?

6:6.2 Sr-Nd isotope systematics of the peridotites and pyroxenites

The radiogenic $^{143}Nd/^{144}Nd$ and unradiogenic $^{87}Sr/^{86}Sr$ ratios of some of the peridotite CPX separates and leached whole rocks are comparable to present day MORB (Figure 6.6) and suggest long term depleted histories with respect to Bulk Earth. This conclusion is supported by the LREE depleted nature of these samples. Peridotite CPX and leached whole rocks with $^{87}Sr/^{86}Sr < 0.703$ have relatively radiogenic $^{143}Nd/^{144}Nd$ ratios with $CHUR_{Nd}$ model ages of between 1170 and 2340 Ma (Table 6.7). Nd model ages assuming a depleted mantle source vary from 260-1560 Ma. Sample GP132(3) has an unrealistically high $CHUR_{Nd}$ model age of 4318 Ma, probably due to a recent LREE enrichment (see

REE patterns, Chapter 5). The LREE enrichment event may have been associated with the Fe enrichment experienced by this sample. $CHUR_{Sr}$ model ages for the "depleted" peridotite CPX samples (1390-1960 Ma) are within the range of Nd model ages demonstrating coherent Rb/Sr and Sm/Nd isotope fractionation. Loubet et al (1980) reported comparable $CHUR_{Nd}$ model ages of 2300 +/- 200 Ma for leached whole rock peridotites from Beni Bousera. The CHUR model ages calculated above could date the last partial melting events experienced by the "depleted" peridotites if they originated from a chondritic source mantle. Both Sm/Nd and Rb/Sr systematics give consistently old ages for the "depleted" peridotites (generally > 1 Ga), suggesting that they have not experienced recent melting events or significant post emplacement alteration. A recent melting event would disrupt the Sm/Nd and Rb/Sr systematics such that Sr model ages would be older and Nd model ages younger than those calculated. The opposite effect is observed in Table 6.5 which is consistent with there being little disruption of the Rb/Sr and Sm/Nd systematics of the depleted peridotites samples since formation. Peridotites with "enriched" isotope characteristics relative to the present day MORB field e.g. GP220 CPX and GP178 WR record recent LREE enrichment, in terms of young model ages/decoupled Rb/Sr, Sm/Nd isotope systematics and having more LREE enriched REE patterns (Chapter 5).

Combined with the data of Polve (1983) and Menzies (1984), the peridotite samples with enriched Sr-Nd isotope systematics show two distinct trends, on Figure 6.6, a trend with steep negative slope and a trend with relatively shallow negative slope. These trends are similar to those shown by the pyroxenites (Fig. 6.6) and may be due to peridotite enrichment by components with differing Sr/Nd ratios. The pyroxenite trends are much more extreme than those of the peridotites, having more radiogenic Sr and more variable Nd isotopic signatures. The pyroxenite Sr-Nd isotope variations are almost a factor of two greater than that observed in all oceanic basin magmatism (Figure 6.6). Rb concentrations and Rb/Sr ratios are low but variable in the pyroxenites and uncorrelated with $^{87}Sr/^{86}Sr$, such that the most radiogenic Sr isotopic compositions could not have evolved from a common mantle/chondritic source even over protracted periods of time. For example the $^{87}Sr/^{86}Sr$ ratio of GP81 could only be produced with its present Rb/Sr ratio from a "chondritic" source over a period of almost 4 Ga (Table 6.5) whilst a depleted mantle source would require greater than the age of the Earth.

$CHUR_{Nd}$ ages in the pyroxenites also show extreme variation, from 4 Ma to 3.8 Ga. Depleted mantle model ages are unfeasible for pyroxenites with $^{143}Nd/^{144}Nd$ ratios less than present day MORB due to their high Sm/Nd ratios. (Table 6.5). Where possible, $CHUR_{Nd}$ model ages for the pyroxenites were calculated using the $^{143}Nd/^{144}Nd$ ratio of the leached separate and the $^{147}Sm/^{144}Nd$ ratio of the unleached whole rock. Ages calculated by this method are denoted with an asterisk in Table 6.5. Other $CHUR_{Nd}$ model ages are calculated from CPX data only. The effect of using the Sm/Nd ratio of the whole rock in the Nd model age calculation is generally to lower the model ages to a variable extent depending on the difference in Sm/Nd ratios between whole rock and CPX. For example, a $CHUR_{Nd}$ model age calculated using the $^{144}Nd/^{143}Nd$ ratio of GP147 CPX and the $^{147}Sm/^{144}Nd$ ratio of the whole rock gives 156 Ma compared to 191 Ma using only the CPX data.

The decoupling of Sm/Nd and Rb/Sr systematics in the pyroxenites indicates recent Sm/Nd and Rb/Sr fractionation has taken place (probably due to partial melting) and that the pyroxenite suite cannot be produced from a homogeneous source unless variable degrees of isotope/trace element

Figure 6.16. Nd isotope evolution of GGP and GP139. Reference lines are
CHUR: $^{143}Nd/^{144}Nd = 0.512638$, $^{147}Sm/^{144}Nd = 0.1967$
Depleted Mantle: $^{143}Nd/^{144}Nd = 0.51310$, $^{147}Sm/^{144}Nd = 0.2282$
North Atlantic Sediments: $^{143}Nd/^{144}Nd = 0.5120$, $^{147}Sm/^{144}Nd = 0.115$.
Evolution curves calculated using $^{143}Nd/^{144}Nd$ ratio of CPX and $^{147}Sm/^{144}Nd$ ratio of whole rock.

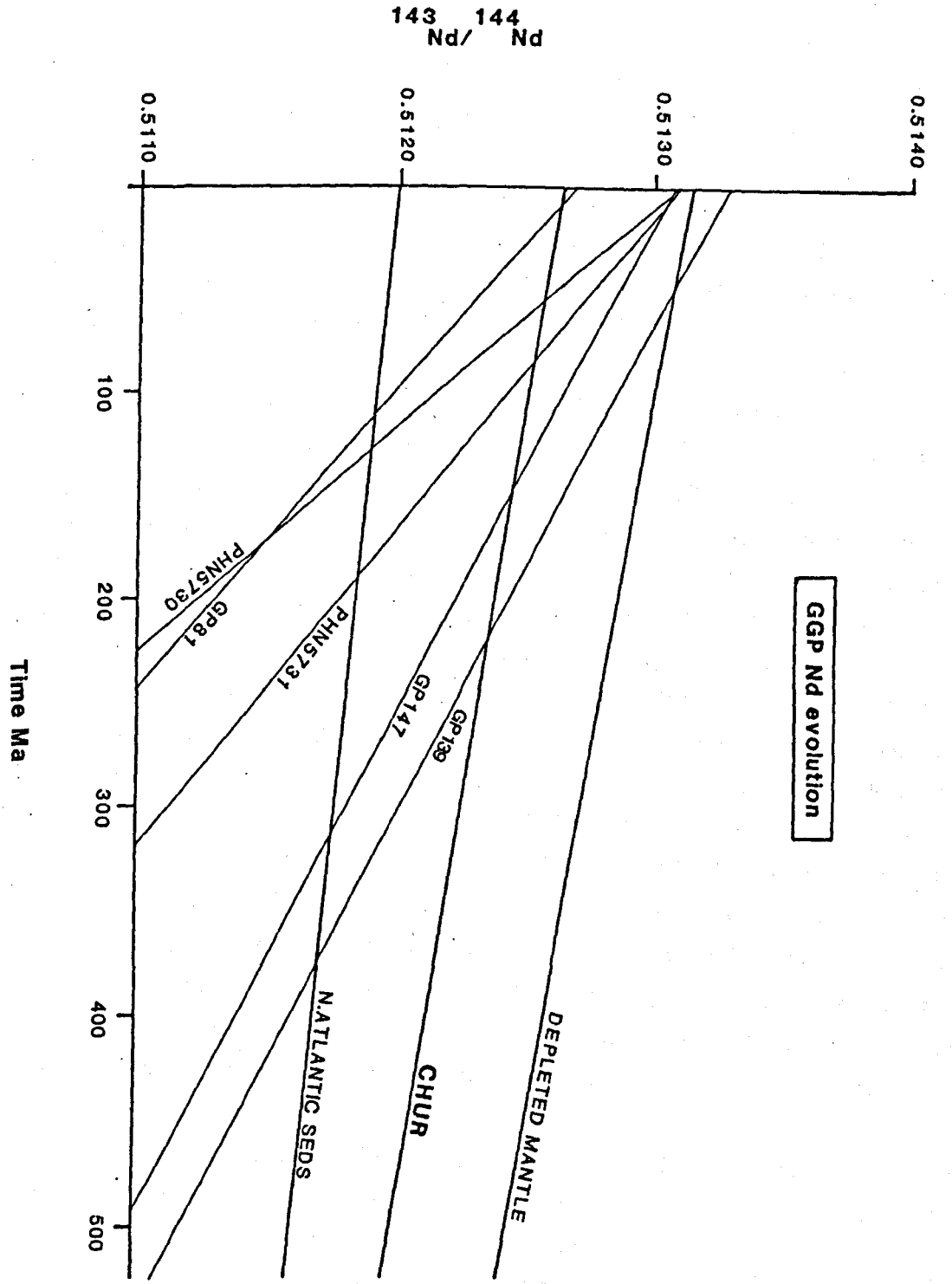

enrichments from isotopically distinct components took place.

Consideration of the Nd isotope evolution of the GGP (Figure 6.16) reveals several interesting conclusions that are relevant to the petrogenetic history of the pyroxenite suite as a whole.

1) The Nd isotope evolution curves of the GGP do not all converge at one point.

2) $CHUR_{Nd}$ model ages of the GGP show considerable variation (4 to 190 Ma), from pre- to post-emplacement times implying a single stage derivation from a chondritic source region is not adequate to explain the Nd isotope evolution of the GGP.

3) Significantly older one stage model ages for the GGP can only be obtained by assuming a much more unradiogenic source region than CHUR, e.g. similar to sediments. This still produces relatively young model ages but with a very large age range (120-340 Ma, Figure 6.16).

Nd isotope evolution with time indicates that the GGP cannot have been derived simultaneously from an isotopically homogeneous source with their present Sm/Nd ratios. The GGP could only have separated simultaneously from an isotopically heterogeneous source. If a single stage model is assumed, a separation time of > 200 Ma ago would require a source $^{143}Nd/^{144}Nd$ variation of > 25 epsilon units. This value is clearly unrealistic. A multistage evolution model for the GGP most adequately explains their Nd evolution trends, incorporating a very recent Sm/Nd and Rb/Sr fractionation event to explain the observed decoupling of Sr and Nd isotope systematics. The diverging nature of the Nd isotope evolution trends (Figure 6.16) require that the older the latest partial melting event the greater the Nd isotope variation is required prior to this event. A latest Sm/Nd fractionation age of ~ 50 Ma ago minimizes Nd isotope variation required prior to this melting event whilst being ~ 30 Ma older than the emplacement age of the massif. Melting at 50 Ma still requires significant Nd isotope variation to be generated. If a source of restricted isotopic composition is invoked, significant Sm/Nd differences in the GGP are required during genesis. The petrological and major/trace element similarity of the GGP do not favour widely varying Sm/Nd ratios during formation. Hence, some degree of Nd isotopic source heterogeneity and time to generate diverse Nd isotopic compositions is probably the optimal requirement for the GGP evolution. A long term, multistage evolution of the GGP from a slightly heterogeneous source is one way of producing the observed Nd isotope systematics of the GGP and the remainder of the pyroxenite suite.

An ion microprobe study of the GGP host rocks and CPX/GT inclusions in the graphite octahedra was undertaken to place constraints on trace element fractionation events affecting the GGP. Ion microprobe REE data from the host rock CPX and GT of two GGP samples studied were within error of the REE composition of the inclusions within the graphite octahedra (Figure 6.17). The similar inclusion/host chondrite normalized REE patterns may indicate that the last Sm/Nd fractionation event was synchronous with, or pre-diamond formation in the GGP. However, the ability of graphite to "insulate' mineral inclusions from physical processes is probably much less than that of diamond. Consequently, if melting of the GGP occurred post diamond graphitization, defects in the graphite surrounding included silicates or even cracks in the original diamond induced during graphitization could

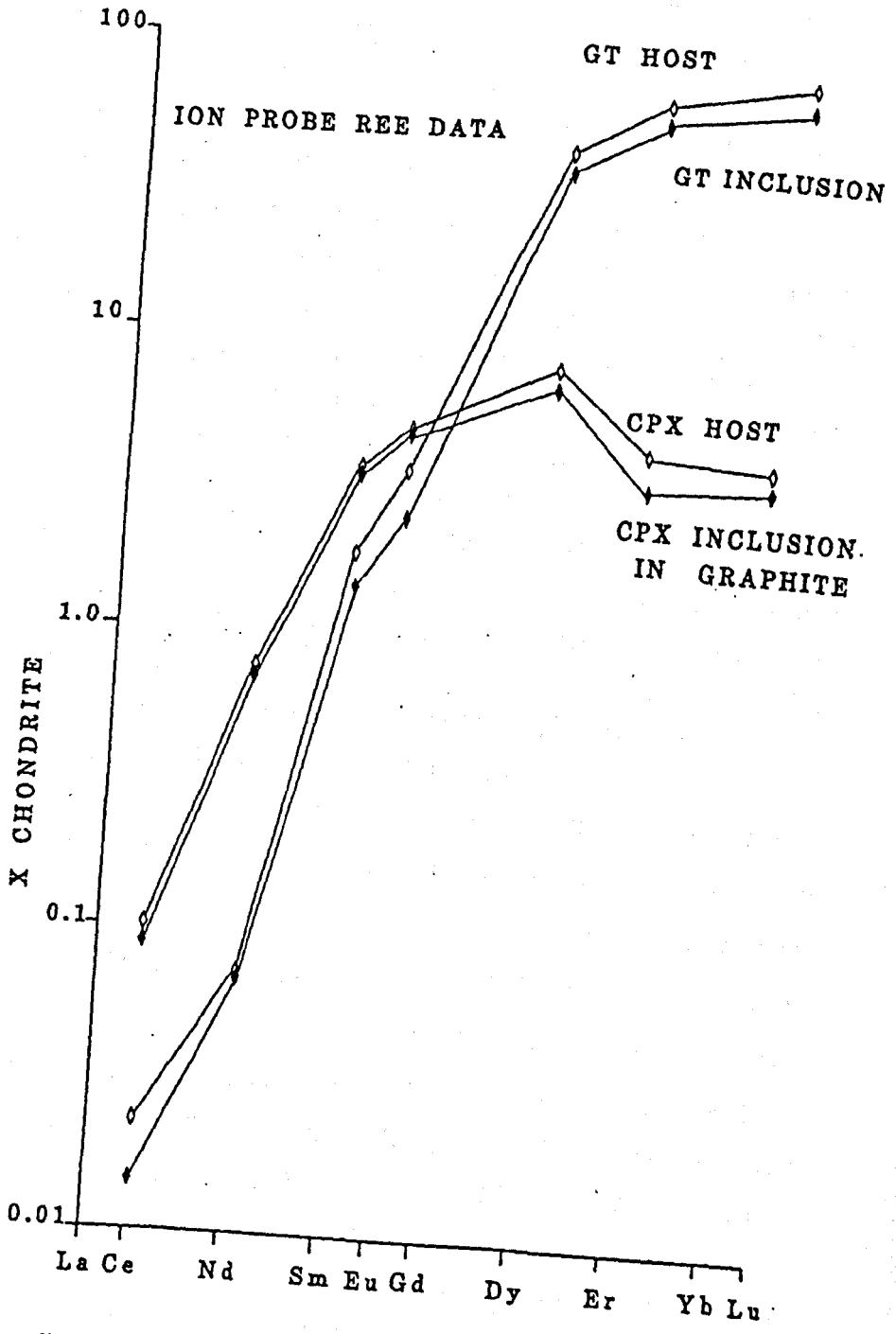

Figure 6.17. Chondrite normalized REE data for individual CPX and GT crystals from PHN 5731 analysed by ion microprobe (Appendix 4). Closed symbols are mineral inclusions within graphite octahedron, open symbols are minerals within host rock matrix.

have lead to a melt phase buffering the inclusion trace element geochemistry. The ion microprobe study therefore does not accurately constrain the relative age of the most recent melting event which influenced the GGP.

6:6.3 Pb isotope systematics.

The Pb isotope systematics of the "depleted" peridotites require a more complex petrogenetic history than that indicated by their Sr and Nd isotope relationships. The widely varying Pb isotope compositions of the peridotites requires U/Pb fractionation events occuring in the mantle long before the 20.5 Ma "emplacement age" of the massif. The peridotites with MORB/MORB-source like Sr-Nd isotope characteristics have a range in $^{207}Pb/^{204}Pb$ ratios that must have been generated over 1 Ga ago. These peridotite CPX separates have high Δ7/4 ratios (Table 6.5, except GP222). The exceptionally high Δ7/4 ratio of GP191 CPX is unusual in that it has the most unradiogenic $^{206}Pb/^{204}Pb$ ratio of the suite (16.997). Such unusual Pb isotope compositions from mantle derived rocks have only been recorded in certain ultrapotassic volcanics e.g. Fraser et al (1985). Nelson et al (1986). A possible explanation for the unusual Pb isotopic signature of GP191 CPX is that it could be influenced by a high blank contribution. The Pb isotopic composition of the blanks obtained during this study are characterised by unradiogenic $^{206}Pb/^{204}Pb$ but radiogenic $^{207}Pb/^{204}Pb$. The blank performed with this sample was relatively low, 0.3 ng total Pb, which would contribute less than 0.2 % of the total Pb, hence the isotopic composition appears to be real. When all the peridotite Pb data are considered, the samples analysed in this study form a steeply inclined, scattered trend on a $^{207}Pb/^{204}Pb$ vs $^{206}Pb/^{204}Pb$ diagram (Figure 6.7) which is too steep to represent a secondary isochron. Such a steep trend may be a result of mixing with a high $^{207}Pb/^{204}Pb$ component with a similar $^{206}Pb/^{204}Pb$ ratio. The data do not show any distinct mixing trends towards the blank composition (see Appendix 4).

Excepting GP191, it is interesting to note that the peridotite sample with the most depleted Sr and Nd isotopic signature, GP222, has the least radiogenic Pb isotopic compositions and the lowest Δ7/4 and Δ8/4 values (Table 6.5). This sample therefore seems distinct from the other samples in Table 6.5, and together with the low Δ7/4 and Δ8/4 peridotites analysed by Hamelin and Allegre (1988) form a 1.9 Ga secondary isochron. The low Δ7/4 peridotites represent mantle that has not mixed with an "enriched" component with high Δ7/4 values and "enriched" Sr and Nd isotope characteristics. The 1.9 Ga "separation age" is within the range of $CHUR_{Nd}$ and $CHUR_{Sr}$ model ages in Table 6.5 and is comparable to the two stage Pb/Pb model age of present day MORB of ~ 1.8 Ga (Chase 1981). The "depleted" Sr-Pb-Nd isotope signature of GP222 suggests it is equivalent to MORB source/residue.

All the pyroxenites analysed in Table 6.5 have high Δ7/4 values (>10) and plot both to the left and right of the geochron (Figure 6.8). The Pb isotope compositions of the Beni Bousera peridotites and pyroxenites indicate a history of U/Pb variation involving at least two stages; an early high U/Pb stage is required to generate the high $^{207}Pb/^{204}Pb$ ratios while there is sufficient ^{235}U available, followed by a low U/Pb stage to retard the generation of ^{206}Pb. Long histories are therefore required to generate the unusual Pb isotopic compositions. Subduction of sediments into the source of the pyroxenites and peridotites could create their observed Pb isotope compositions as hemipelagic/pelagic

TABLE 6.6

SAMPLE	GP5 WR	GP54 WR	GP57 WR	GP161 WR
La	13.218	30.030	16.160	24.992
Ce	52.039	118.391	72.517	90.629
Nd	30.906	67.736	45.806	50.613
Sm	8.504	13.010	8.687	10.132
Eu	1.382	1.550	1.176	1.596
Gd	11.562	11.304	7.239	9.097
Dy	15.727	10.498	6.806	8.410
Er	10.519	6.324	4.071	5.032
Yb	10.186	5.846	3.855	4.775
Lu	1.537	0.849	0.567	
Eu/Eu*	0.429	0.393	0.456	0.511
Ce/Ce*	1.401	1.420	1.498	1.354

	SAMPLE	Rb ppm	Sr ppm	87Sr/86Sr	+/-	143Nd/144Nd
1	GP5	60.130	60.130	0.72052	1	0.512016
2						
3	GP54	69.330	106.900	0.72232	1	0.512005
4						
5	GP57	63.960	91.790	0.72173	1	0.512030
6		63.410				0.512047
7						
8	GP161	73.900	149.550	0.71887	1	0.512070
9		74.020	150.120	0.71887	2	0.512067

sediments contain ancient continentally derived crustal material which results in high Δ7/4 values (White + Dupre 1986, Ben Othman et al 1989).

6:6.4 Evidence for a sediment derived component in the source of the Beni Bousera peridotites and pyroxenites.

The Pb, Sr and Nd isotope characteristics of the peridotites and pyroxenites may be explained by addition of a crustal component to their mantle source or alternatively via recent contamination by assimilation of locally derived kinzigite during emplacement. The low Sr/Nd ratios of the kinzigites (Table 6.6) means that on;y some of the pyroxenites would lie on kinzigite mixing trends. Of the samples lying on the kinzigite mixing trends, some require almost 10 % kinzigite to create their Sr and Nd isotope characteristics (Fig. 6.18). Contamination of the peridotites by melts of the kinzigites is unlikely due to the difficulty of separating viscous, high SiO_2 melts from the residue (Mckenzie 1984). Furthermore, the LREE enriched nature of the kinzigites (Fig. 6.19, Table 6.6) does not favour their recent incorporation into the LREE depleted pyroxenites and peridotites. Clearly the most plausible way to introduce a crustal component into the pyroxenites and peridotites is to subduct sediments into their source and subsequently decrease their LREE concentrations by a recent melting event as indicated by pyroxenite Sm/Nd systematics . The isotopic effects of sediment contamination will be most pronounced on the peridotites due to their lower daughter isotope concentrations. The influence of sediment subduction on the peridotite source may be evaluated in terms of the crust/mantle ratios of Pb, Sr and Nd. Using typical sediment and residual mantle abundancies (e.g. Ben Othman et al 1989, Frey et al 1985);

Pb CRUST/MANTLE = 30/0.1 = 300,
Sr CRUST/MANTLE = 100/10 = 10, and
Nd CRUST/MANTLE = 30/1 = 30.

From the above considerations, Sr isotopes should be the least altered by physically mixing sediment into the source and Pb isotopes should show the most profound effects of sediment mixing. The isotopic effects of recent mixing of kinzigite into the peridotites are similar to those of mixing sediments into the peridotites. Mixing calculations indicate that the Sr/Nd isotope systematics of the peridotites could be generated by mixing of less than 2 % of sediment with a peridotite source similar to GP222 CPX (which does not show any Pb or Sr-Nd evidence for sediment contamination). Applying similar mixing calculations to the pyroxenites and assuming their source was subducted oceanic crust indicates that:

a) Large amounts of sediment, or even sediment derived melt (> 2 %) are required to generate the unradiogenic $^{143}Nd/^{144}Nd$ and radiogenic $^{87}Sr/^{86}Sr$ ratios of some of the pyroxenites.

b) Sediment/mantle mixtures of widely varying Sr/Nd ratios are required to generate all the Sr-Nd isotope trends shown by the pyroxenites (Figure 6.18).

Hydrothermal alteration of the oceanic crust forming the pyroxenite source can shift the $^{87}Sr/^{86}Sr$ ratio

Figure 6.18. Nd vs Sr isotope diagram illustrating the effect of recent mixing of kinzigite and sediment on the Beni Bousera peridotites and pyroxenites. Main diagram shows mixing lines between peridotites/pyroxenites and kinzigites, the following end members are used in the calculation:

	$^{87}Sr/^{86}Sr$	Sr ppm	$^{143}Nd/^{144}Nd$	Nd ppm	Sr/Nd
Peridotite:	0.70272	5	0.513278	0.6	
Pyroxenite:	0.70228	40	0.51347	1	
Kinzigite (GP54)	0.72232	107	0.512005	68	1.6
Kinzigite (GP161)	0.71887	150	0.51207	51	3

overlay illustrates mixing between hydrothermally altered crust and sediment, end members are:

	$^{87}Sr/^{86}Sr$	Sr ppm	$^{143}Nd/^{144}Nd$	Nd ppm	Sr/Nd
Oceanic crust 1	0.703	60	0.5130	8	
Oceanic crust 2	0.706	60	0.5130	8	
Sediment V21/196	0.70859	325	0.512392	159	2
Sediment V26/341	0.709959	778	0.512162	17	46

Sediment compositions from Ben Othman et al (1989). End members chosen to illustrate the effect of mixing sediment with different Sr/Nd ratios. Numbers adjacent ticks represent percent sediment/ kinzigite added. Open stars = sediment compositions.

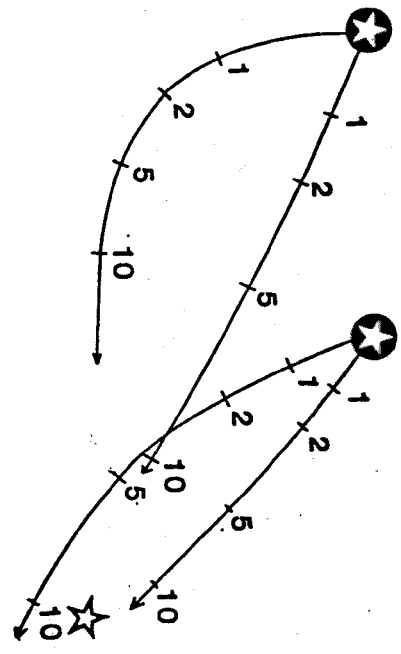
1
2
5
10
1
2
5
1
2
10
5
1
2
5
10
10

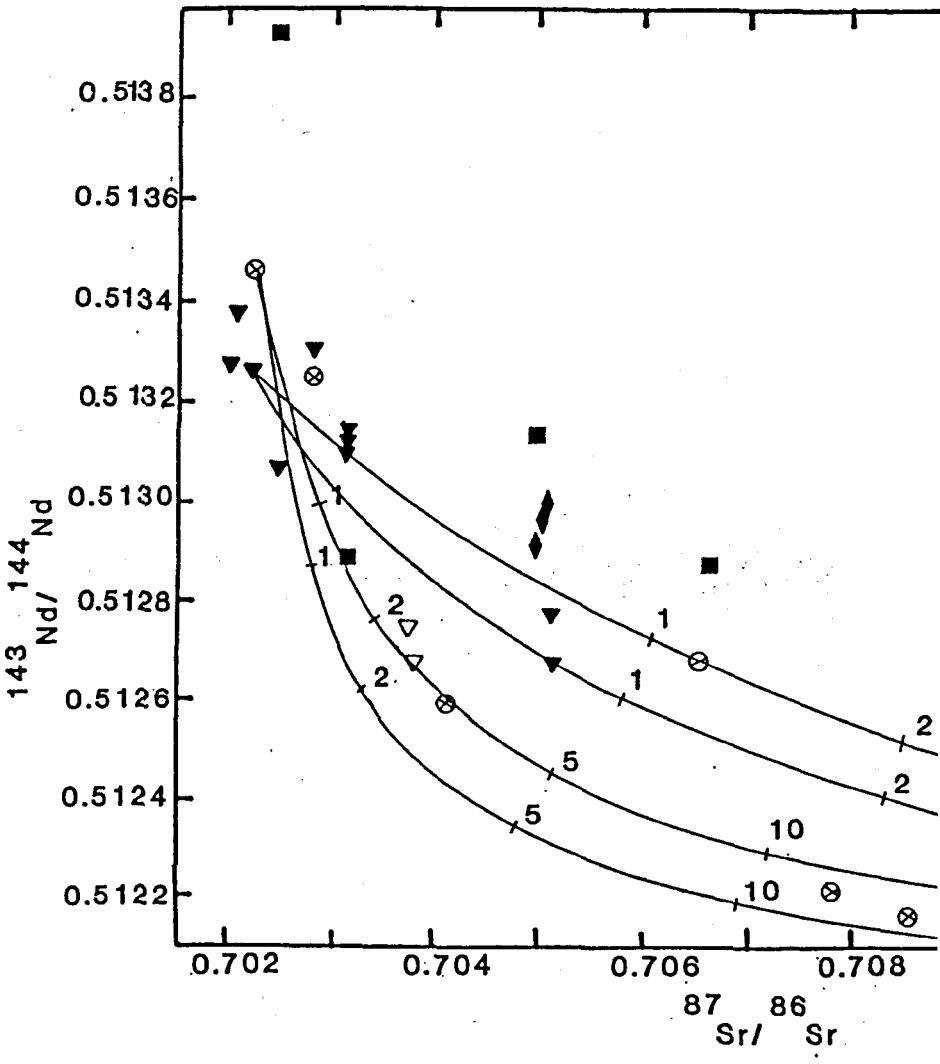
0.5138
0.5136
0.5134
0.5132
0.5130
0.5128
0.5126
0.5124
0.5122
143 Nd/ 144 Nd
0.702
0.704
0.706
0.708
87 Sr/ 86 Sr
1
1
1
2
2
2
5
5
10
10

5
5
0.710
0.712

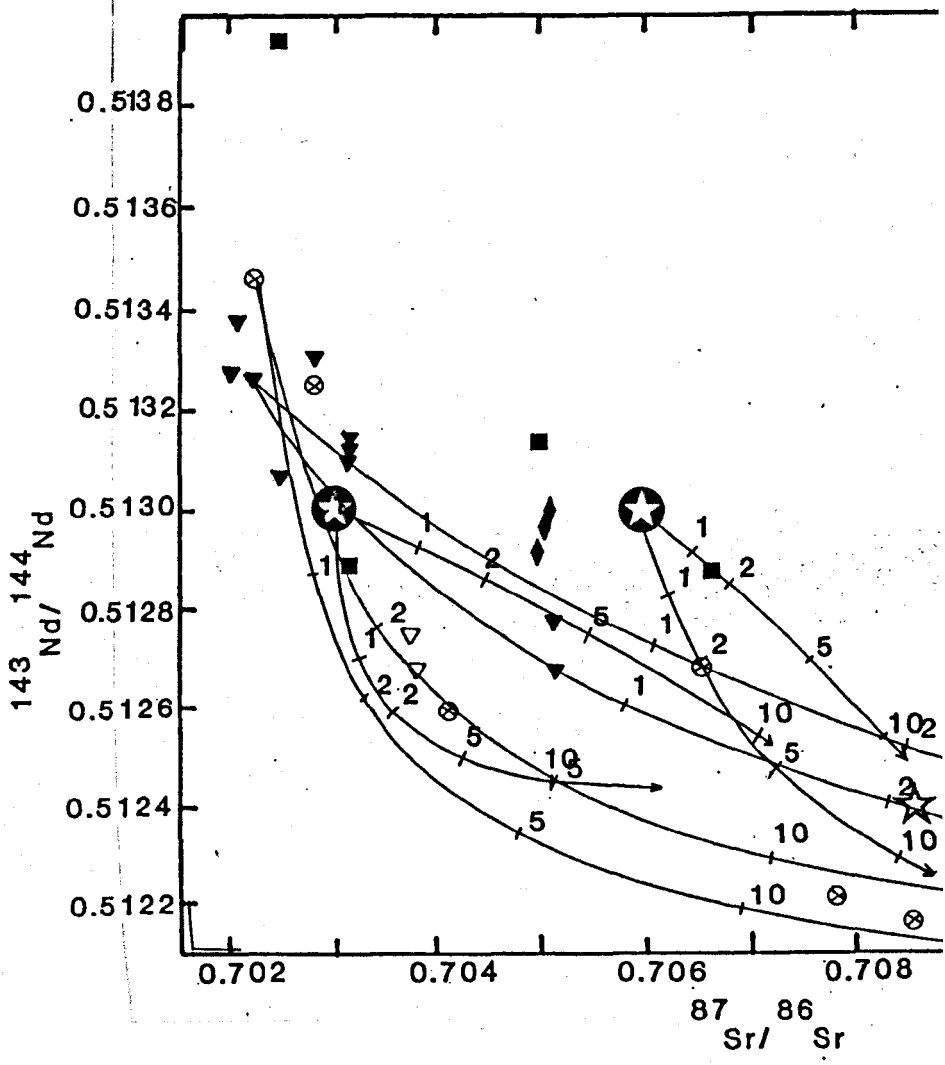
0.5138
0.5136
0.5134
0.5132
0.5130
0.5128
0.5126
0.5124
0.5122
143 144
Nd/ Nd
0.702
0.704
0.706
0.708
87 86
Sr/ Sr

5
5
0.712
0.710

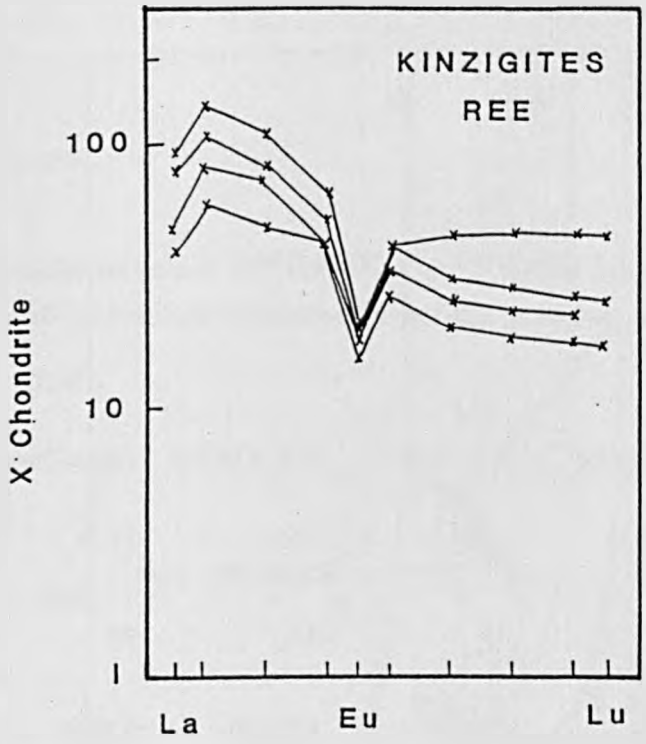

Figure 6.19. Chondrite normalized whole rock REE patterns for kinzigites.

Figure 6.20. $^{87}Sr/^{86}Sr$ and $^{143}Nd/^{144}Nd$ vs $^{206}Pb/^{204}Pb$ mixing relationships between depleted mantle, lower crust (L.C.) and marine sediments (Open stars). Mixing end members are:

	Depleted Mantle	Sed. V24/73	Sed. V28/343	Lower Crust
$^{206}Pb/^{204}Pb$	17.0	18.64	18.99	17.29
Pb ppm	0.02	31	33	20
$^{143}Nd/^{144}Nd$	0.5133	0.51235	0.51216	0.5120
Nd ppm	1	122	23	50
$^{87}Sr/^{86}Sr$	0.7025	0.7107	0.7168	0.7200
Sr ppm	5	252	119	100

Percent mixing ticks beside each curve. Sediment data from Ben Othman et al (1989), lower crust composition from Zartman & Doe (1981). Present day MORB and OIB indicated together with selected high Δ7/4 OIB are shown for comparison. Symbols as in Fig. 6.6.

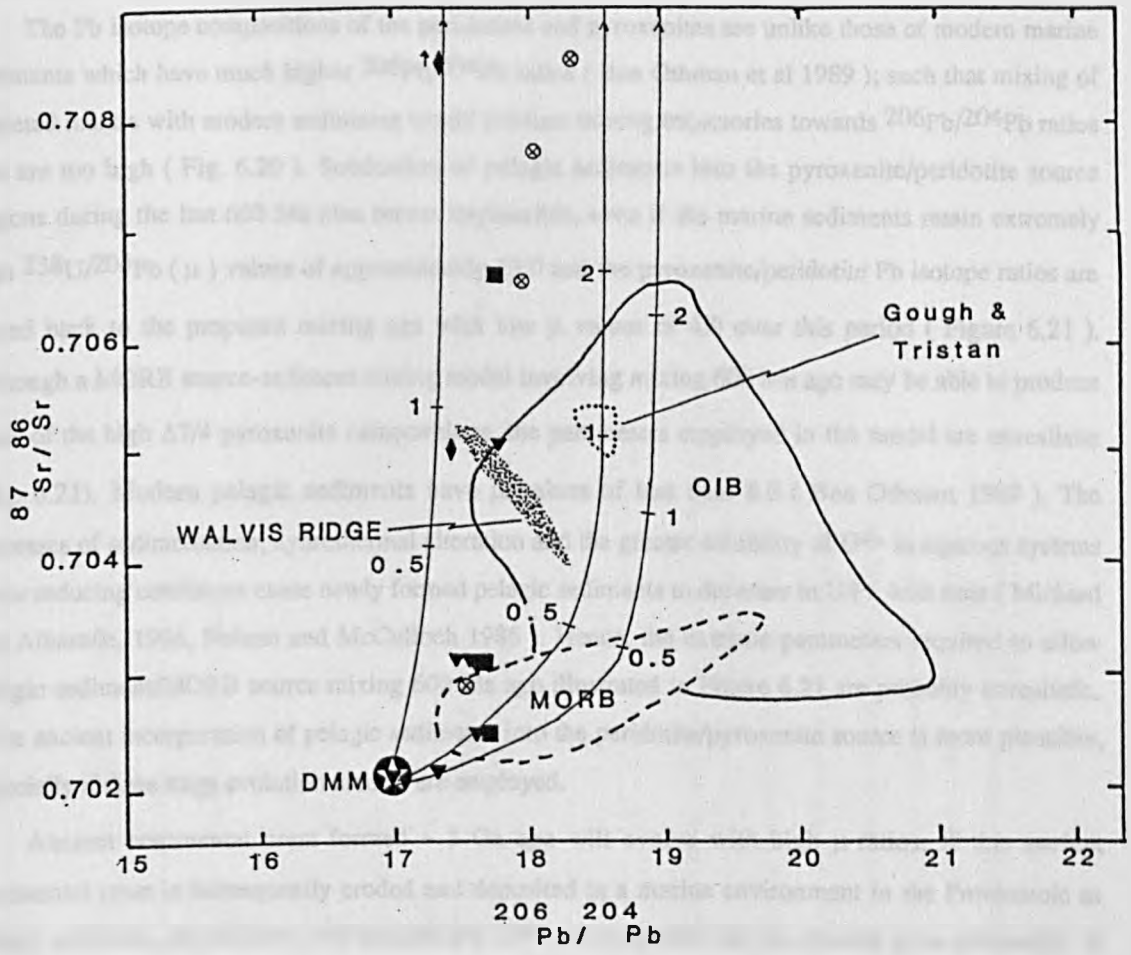
0.708
0.706
0.704
0.702
87 86 Sr/ Sr
15
16
17
18
19
20
21
22
206 204 Pb/ Pb
Gough & Tristan
OIB
WALVIS RIDGE
MORB
DMM
0.5
1
2

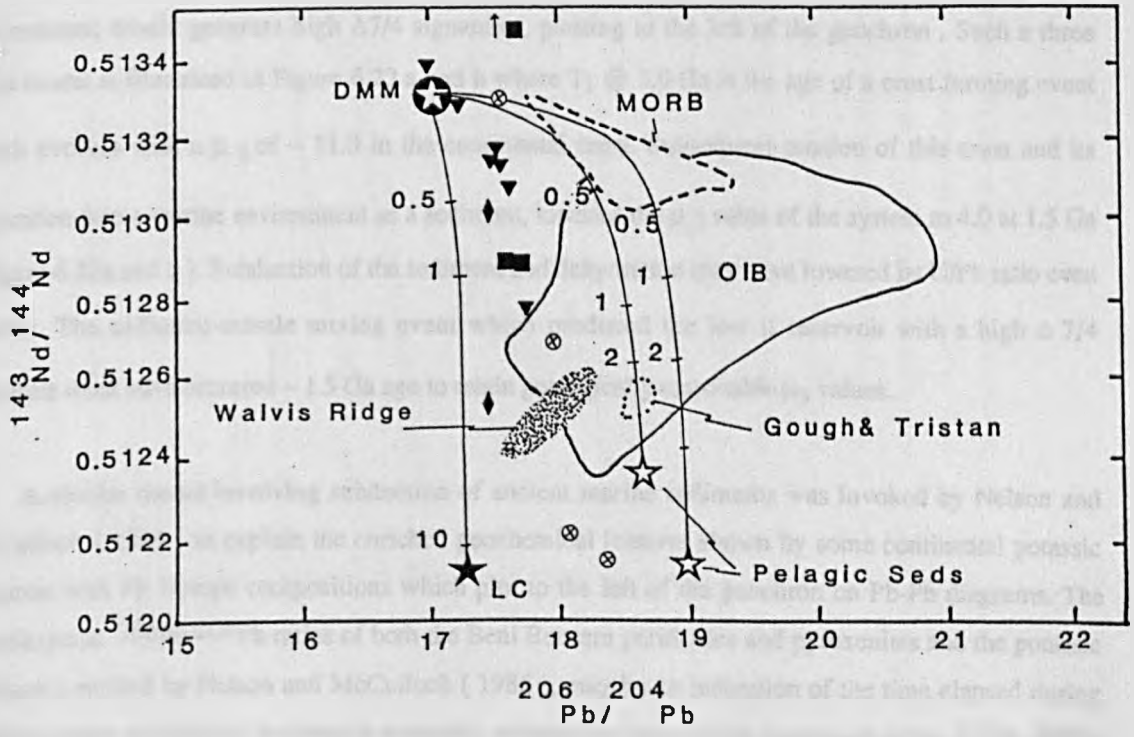
0.5134
0.5132
0.5130
0.5128
0.5126
0.5124
0.5122
0.5120
143 144 Nd/ Nd
15
16
17
18
19
20
21
22
206 204 Pb/ Pb
DMM
MORB
OIB
Walvis Ridge
Gough& Tristan
Pelagic Seds
LC
0.5
1
2
10

of the mixture significantly (Figure 6.18), but does not contribute towards the Nd budget.

The Pb isotope compositions of the peridotites and pyroxenites are unlike those of modern marine sediments which have much higher $^{206}Pb/^{204}Pb$ ratios (Ben Othman et al 1989); such that mixing of depleted mantle with modern sediments would produce mixing trajectories towards $^{206}Pb/^{204}Pb$ ratios that are too high (Fig. 6.20). Subduction of pelagic sediments into the pyroxenite/peridotite source regions during the last 600 Ma also seems implausible, even if the marine sediments retain extremely high $^{238}U/^{204}Pb$ (μ) values of approximately 13.0 and the pyroxenite/peridotite Pb isotope ratios are traced back to the proposed mixing age with low μ values of 4.0 over this period (Figure 6.21). Although a MORB source-sediment mixing model involving mixing 600 Ma ago may be able to produce *some* of the high $\Delta 7/4$ pyroxenite compositions, the parameters employed in the model are unrealistic (Fig. 6.21). Modern pelagic sediments have μ values of less than 8.0 (Ben Othman 1989). The processes of sedimentation, hydrothermal alteration and the greater solubility of U^{4+} in aqueous systems under reducing conditions cause newly formed pelagic sediments to decrease in U/Pb with time (Michard and Albarede, 1986, Nelson and McCulloch 1986). Hence, the extreme parameters required to allow pelagic sediment/MORB source mixing 600 Ma ago illustrated in Figure 6.21 are probably unrealistic. More ancient incorporation of pelagic sediments into the peridotite/pyroxenite source is more plausible, especially if three stage evolution models are employed.

Ancient continental crust formed ~ 3 Ga ago will evolve with high μ ratios. If this ancient continental crust is subsequently eroded and deposited in a marine environment in the Proterozoic as pelagic sediment, the sediment will acquire low U/Pb characteristics for the reasons given previously. If the pelagic sediment is subducted soon after deposition and mixed into a mantle source which aquires the U/Pb and Pb isotopic characteristics of the sediment, long term Pb isotope evolution in a low μ environment would generate high $\Delta 7/4$ signatures, plotting to the left of the geochron . Such a three stage model is illustrated in Figure 6.22 a and b where T_1 @ 3.0 Ga is the age of a crust forming event which evolves with a μ_2 of ~ 11.0 in the continental crust. Subsequent erosion of this crust and its deposition into a marine environment as a sediment, lowered the μ_3 value of the system to 4.0 at 1.5 Ga (Figure 6.22a and b). Subduction of the sediment and dehydration may have lowered its U/Pb ratio even further. The sediment-mantle mixing event which produced the low μ reservoir with a high Δ 7/4 signature must have occurred ~ 1.5 Ga ago to retain geologically reasonable μ_3 values.

A similar model involving subduction of ancient marine sediments was invoked by Nelson and McCulloch (1986) to explain the enriched geochemical features shown by some continental potassic magmas with Pb isotope compositions which plot to the left of the geochron on Pb-Pb diagrams. The unradiogenic $^{206}Pb/^{204}Pb$ ratios of both the Beni Bousera peridotites and pyroxenites and the potassic volcanics studied by Nelson and McCulloch (1986), may be an indication of the time elapsed during sedimentation and storage in a mantle reservoir, whereas variation in the magnitude of the $^{207}Pb/^{204}Pb$ ratio reflects the nature and age of the continental provenance (Nelson and McCulloch 1986). The multistage evolution of the Beni Bousera peridotites and pyroxenites together with the recent Sm/Nd

Figure6.21. Pb isotope mixing diagram showing trends produced by mixing of Pacific sediments with present day MORB glass compositions (~ equivalent to a depleted mantle source). Selected Beni Bousera pyroxenites clearly plot off the present day/recent mixing trend. Some pyroxenites plot on a mixing trend between the two reservoirs 600 Ma ago, but only if the pyroxenites are traced back with low μ values (4.0) and the sediment Pb isotopic compositions are traced back with unrealistically high μ values (13.0). 0.5 % sediment addition indicated. Data from Ben Othman et al (1989) and Cohen and O'Nions (1981).

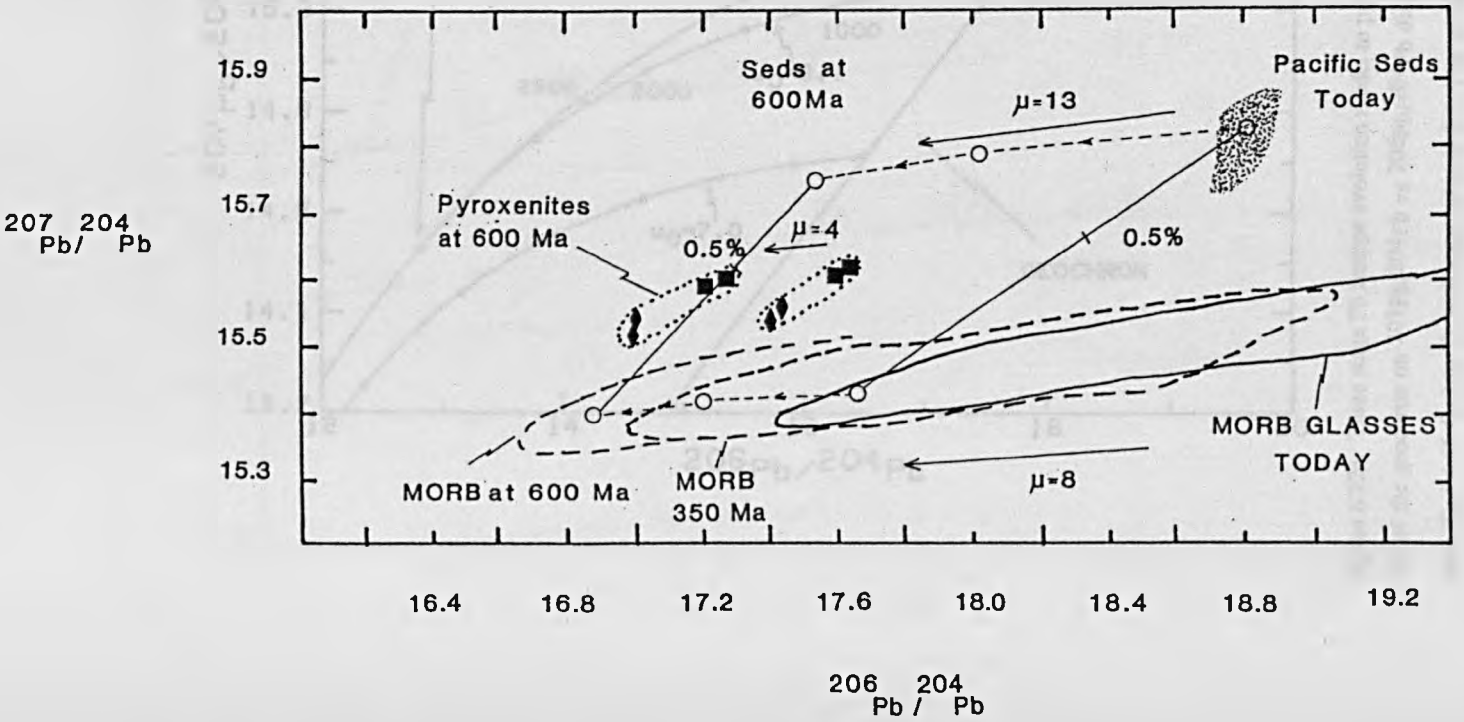

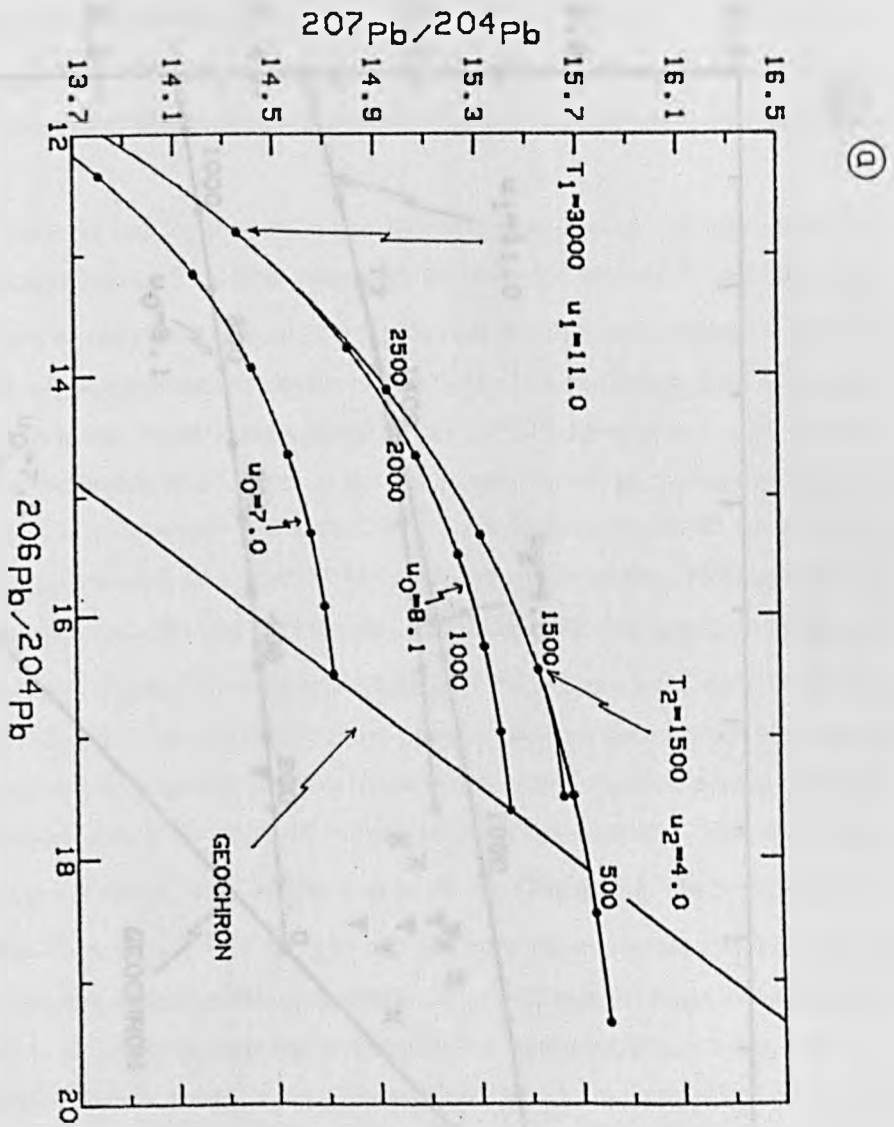

Figure 6.22a. Three stage Pb isotope evolution model to produce isotopic compositions plotting to the left of the geochron on $^{207}Pb/^{204}Pb$ vs $^{206}Pb/^{204}Pb$ diagrams (eg. Fig 6.8b). Reservoir evolves from T_0 (4.55 Ga) to T_1 with a μ_0 value of 8.1. The μ value of the reservoir is increased due to a crust formation event at T_1 (3 Ga ago). The crust evolves with high μ (11.0) until it is eroded into a marine environment where it undergoes a decrease in U/Pb ratio (and hence μ value) and is subducted into the mantle to form the isotopically dominant Pb component in a mixed sediment/mantle reservoir (see text). Post-subduction evolution with a low μ value (4.0) over a 1.5 Ga period leads to similar Pb isotope compositions to the Beni Bousera pyroxenites and peridotites ie. to the left of the geochron. All times on diagram ara in Ma.

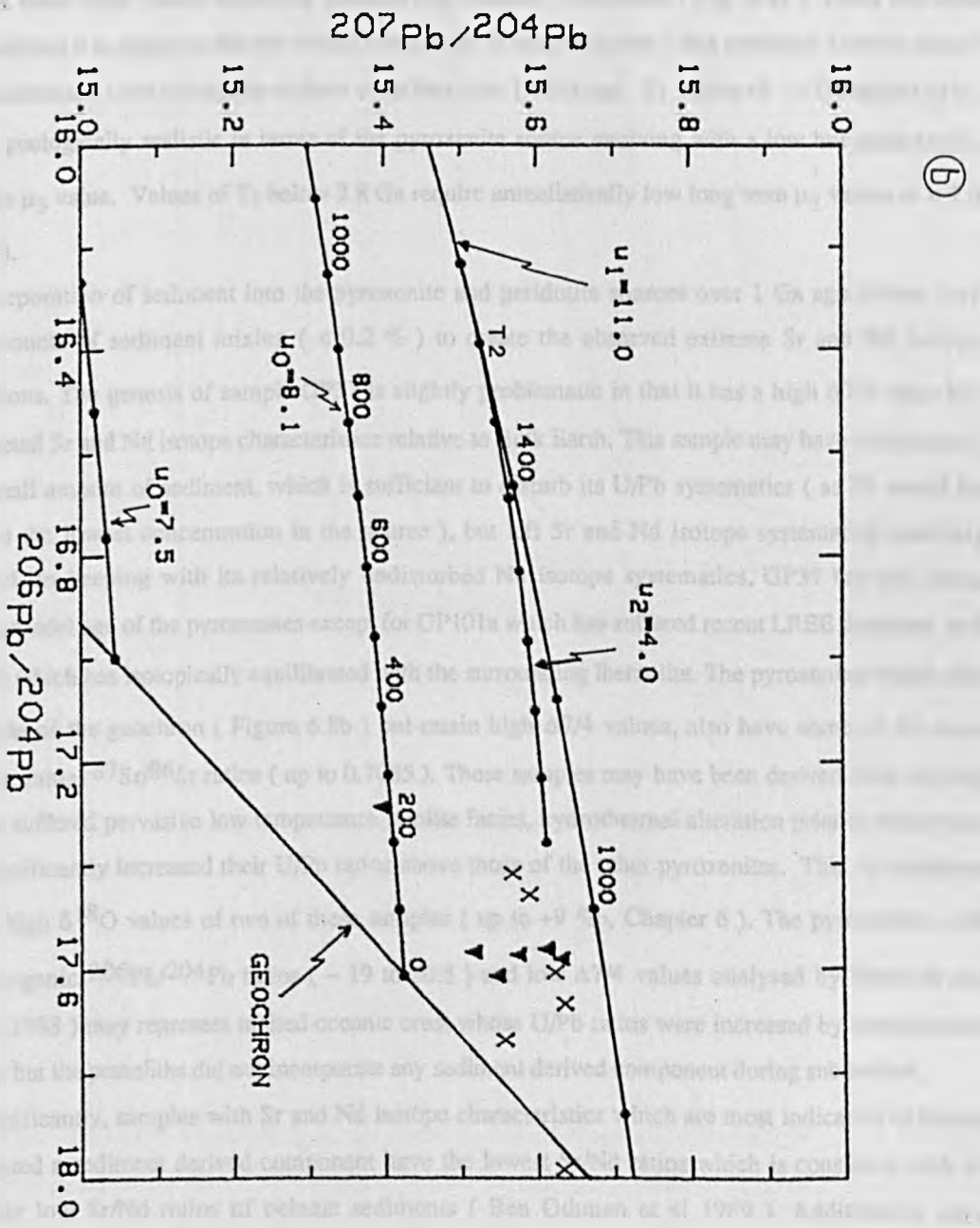

Figure 6.22b. Expanded view of three stage Pb isotope evolution model. Crosses are representative pyroxenite CPX compositions, inverted solid triangles are peridotite CPX.

fractionation/melting event which has affected the pyroxenites makes it difficult to constrain possible values of T_1 and T_2 in Figure 6.22 a and b. Minimum age constraints on the 3 stage evolution model are illustrated in Figure 6.23 which indicates the possible permutations of T_1, T_2, μ_2 and μ_3, necessary to produce the Pb isotopic composition of the GGP sample, GP81 CPX. Evidently (Fig. 6.23), younger values of T_1 require higher μ_2 and lower μ_3 values until T_1 becomes $< \sim 1.8$ Ga when the value of μ_3 becomes less than zero. It then becomes impossible to produce the Pb isotopic composition of GP81 CPX by a three stage model involving geologically realistic parameters (Fig. 6.23). From the three stage modelling it is apparent that the crustal component in the pyroxenite (and peridotite) source cannot have differentiated from the mantle to form crust less than 1.8 Ga ago. T_1 values of ~ 3 Ga appear to be the most geologically realistic in terms of the pyroxenite source evolving with a low but geologically reasonable μ_3 value. Values of T_1 below 2.8 Ga require unrealistically low long term μ_3 values of < 2.0 (Fig.6.23).

Incorporation of sediment into the pyroxenite and peridotite sources over 1 Ga ago allows very minor amounts of sediment mixing (< 0.2 %) to create the observed extreme Sr and Nd isotope compositions. The genesis of sample GP37 is slightly problematic in that it has a high Δ7/4 value but very depleted Sr and Nd isotope characteristics relative to Bulk Earth. This sample may have incorporated a very small amount of sediment, which is sufficient to disturb its U/Pb systematics (as Pb would be present in the lowest concentration in the source), but left Sr and Nd isotope systematics relatively unaffected. In keeping with its relatively undisturbed Nd isotope systematics, GP37 has the oldest $CHUR_{Nd}$ model age of the pyroxenites except for GP101a which has suffered recent LREE depletion, and GP132(1) which has isotopically equilibrated with the surrounding lherzolite. The pyroxenites which plot to the right of the geochron (Figure 6.8b) but retain high Δ7/4 values, also have some of the most radiogenic initial $^{87}Sr/^{86}Sr$ ratios (up to 0.7085). These samples may have been derived from oceanic crust that suffered pervasive low temperature, zeolite facies, hydrothermal alteration prior to subduction which significantly increased their U/Pb ratios above those of the other pyroxenites. This is consistent with the high $\delta^{18}O$ values of two of these samples (up to +9 ‰, Chapter 6). The pyroxenites with very radiogenic $^{206}Pb/^{204}Pb$ ratios (~ 19 to 20.5) and low Δ7/4 values analysed by Hamelin and Allegre (1988) may represent melted oceanic crust whose U/Pb ratios were increased by hydrothermal alteration but the protoliths did not incorporate any sediment derived component during subduction.

Significantly, samples with Sr and Nd isotope characteristics which are most indicative of having incorporated a sediment derived component have the lowest Sr/Nd ratios which is consistent with the commonly low Sr/Nd ratios of pelagic sediments (Ben Othman et al 1989). Additionally some pyroxenites possess high Ba/La ratios which are significantly greater than MORB (Table 6.5), eg. Ba/La= 160 in GGP sample GP81 CPX. Although some high Ba/La ratios in Table 6.5 may be due in part to LREE depletions of the pyroxenites, especially in the GGP, it is notable that GP81 CPX contains significantly more Ba than any other pyroxenite (3 ppm) and has the most radiogenic $^{87}Sr/^{86}Sr$ ratio. Finally, although the fractionation of plagioclase from an original oceanic lithosphere precursor may account for the negative Eu anomalies observed in some pyroxenite CPXs (especially the GGP), the incorporation of sediment may have contributed towards this feature. Sediments often display marked

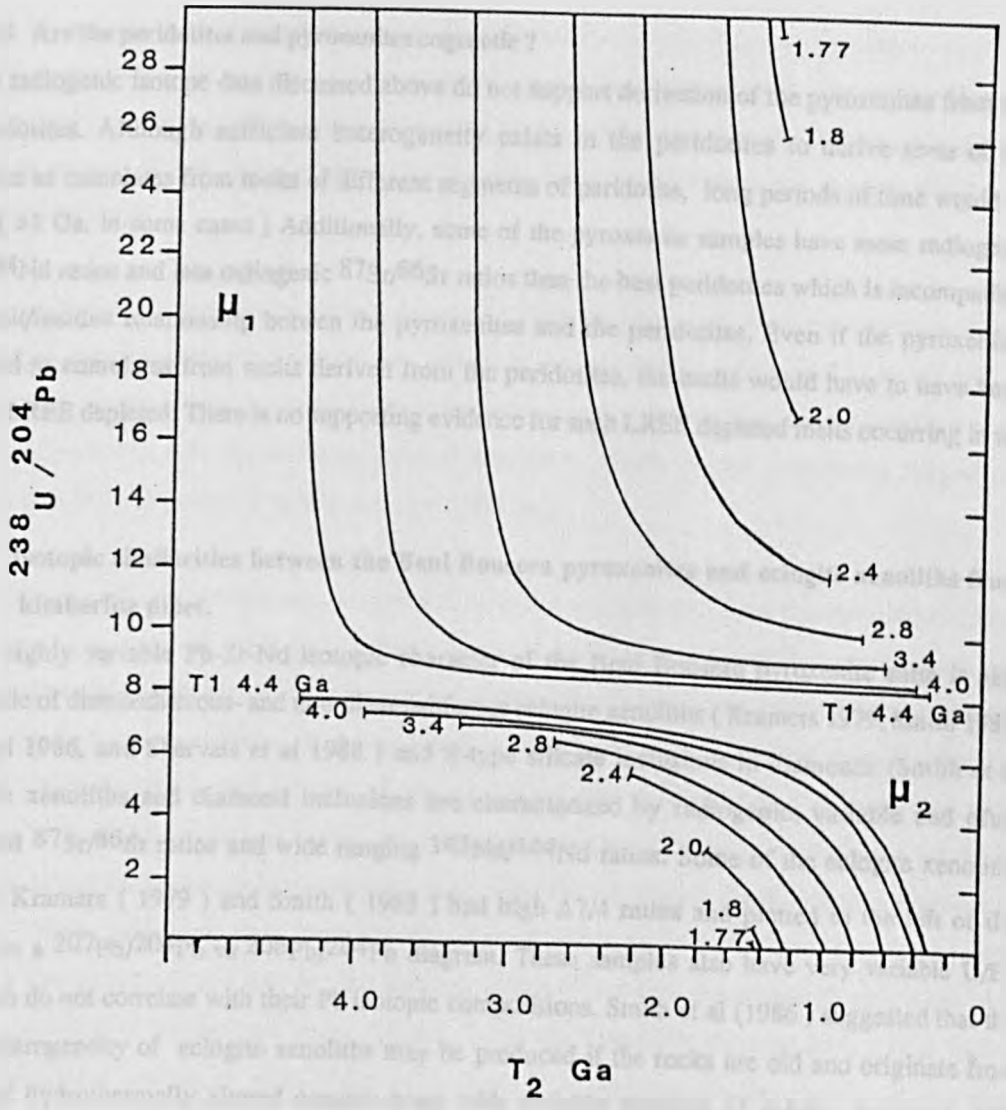

Figure 6.23. Quantitative modelling of the three stage Pb isotope evolution model outlined in Fig. 6.22 applied to match the $^{207}Pb/^{204}Pb$ and $^{206}Pb/^{204}Pb$ isotopic compositions of GGP sample GP81 CPX. Solutions are given for μ_1, upper curves, and μ_2 , lower curves for selected values of T_1 (Ga) plotted against T_2 (Ga) on the *x* axis. From the graph; younger values of T_1 (crust formation) require higher μ_1 and lower μ_2 until at $T_1 \sim 1.77$ Ga, μ_2 becomes negative. This means that in the three stage model proposed, the sediment/mantle mixing event, T_2, occurred no less than 1.4 Ga ago if μ_1 values of less than 30 are required. Pb evolution begins at T=4.55 Ga ago using the initial Pb isotope compositions given by Chen and Wasserburg (1983) with $\mu_0 = 8.1$. For details of calculation see Appendix 5.

negative Eu anomalies which often become more negative with increasing maturity (Bhatia 1985). *Mixing calculations suggest that ~ 2% of a sediment derived component in the source of the GGPs could* create negative Eu/Eu^* anomalies of ~ 0.9, similar to those observed. GP188 whole rock also has a prominant negative Eu anomaly (Chapter 5). The very unradiogenic $^{143}Nd/^{144}Nd$ of this sample together with its high Δ7/4 and high $^{87}Sr/^{86}Sr$ all indicate a significant crustal component in this rock.

6:6.5 Are the peridotites and pyroxenites cogenetic ?

The radiogenic isotope data discussed above do not support derivation of the pyroxenites from the host peridotites. Although sufficient heterogeneity exists in the peridotites to derive *some* of the pyroxenites as cumulates from melts of different segments of peridotite, long periods of time would be required (>1 Ga. in some cases) Additionally, some of the pyroxenite samples have more radiogenic $^{143}Nd/^{144}Nd$ ratios and less radiogenic $^{87}Sr/^{86}Sr$ ratios than the host peridotites which is incompatible with a melt/residue relationship betwen the pyroxenites and the peridotites. Even if the pyroxenites crystallized as cumulates from melts derived from the peridotites, the melts would have to have been extremely LREE depleted. There is no supporting evidence for such LREE depleted melts occurring in the mantle.

6:7 Isotopic similarities between the Beni Bousera pyroxenites and eclogite xenoliths from kimberlite pipes.

The highly variable Pb-Sr-Nd isotopic character of the Beni Bousera pyroxenite suite is also characteristic of diamondiferous- and non-diamondiferous eclogite xenoliths (Kramers 1979, Smith 1983, Smith et al 1986, and Shervais et al 1988) and E-type silicate inclusions in diamonds (Smith et al 1989). The xenoliths and diamond inclusions are characterized by radiogenic, variable and often unsupported $^{87}Sr/^{86}Sr$ ratios and wide ranging $^{143}Nd/^{144}Nd$ ratios. Some of the eclogite xenoliths studied by Kramers (1979) and Smith (1983) had high Δ7/4 ratios and plotted to the left of the geochron on a $^{207}Pb/^{204}Pb$ vs $^{206}Pb/^{204}Pb$ diagram. These samples also have very variable U/Pb ratios which do not correlate with their Pb isotopic compositions. Smith et al (1986) suggested that the isotopic heterogeneity of eclogite xenoliths may be produced if the rocks are old and originate from mixtures of hydrothermally altered oceanic crust with variable amounts of pelagic sediment. This suggestion is very similar to the model outlined above to explain the petrogenesis of the Beni Bousera pyroxenites.

The E-type diamond inclusions studied by Smith et al (1989) which had the most radiogenic $^{87}Sr/^{86}Sr$ ratios also had anomalously high MnO and FeO contents. Such geochemical peculiarities are also common to the GGP (this chapter and Chapter 4). Smith et al (1989) proposed that the radiogenic $^{87}Sr/^{86}Sr$ ratios and high MnO contents of the diamond inclusions could be the result of sea floor alteration processes. This theory could also account for analagous geochemical features seen in the GGP.

6:8 Summary

The Pb-Sr and Nd isotope geochemistry of peridotites and pyroxenites from the Beni Bousera massif permit the following conlusions to be drawn:

1) Both the peridotites and pyroxenites display considerable Pb-Sr and Nd isotopic heterogeneity that is equal to or greater than the variation observed in all MORB and OIB magmas. The parent-daughter isotope systematics of both peridotites and pyroxenites have been decoupled, probably by a melting event occurring in the past 50 Ma. Some of the peridotites may represent MORB source residues which were depleted upto 2 Ga ago.

2) The peridotites and pyroxenites record isotopic evidence for interaction with small amounts (<1%) of an enriched component which is isotopically similar to ancient pelagic sediment. The recent melting event indicated by Nd isotope systematics has destroyed most of the coupled trace element/isotopic evidence of interaction with the sediment derived component. Pb-Pb isotope systematics suggest that interaction with this component probably occurred >1Ga ago.

3) The isotope and trace element data are compatible with a model in which the pyroxenites are derived as cumulates from melts of subducted hydrothermally altered oceanic crust/lithosphere which have interacted with a component derived from pelagic sediments and may have been subducted simultaneously at >1 Ga ago. Later partial melting of the pyroxenites (and peridotites ?) during diapiric upwelling created the LREE depletions seen in many of the pyroxenites. The peridotites may represent part of the lower oceanic lithosphere, subducted with the pyroxenite protoliths. In the latter case, the subducted oceanic lithosphere and sediment may have descended to the 670 km seismic discontinuity as proposed by Ringwood (1982, 1986), where it thermally equilibrated over a period of 1Ga to later rise as small diapirs into the asthenospheric mantle. Diapiric upwelling of asthenospheric mantle seems the most plausible mechanism of emplacing a large (70Km^2) peridotite massif into the crust from at least 150Km deep. Recent partial melting of some of the pyroxenites and peridotites during diapiric emplacement would act to decouple their parent/daughter isotopic relationships.

6:9 Implications for mantle evolution.

The location of most present day MORB and ocean island volcanism to the right of the geochron (Figure 6.8b), indicates their sources have undergone progressive or episodic enrichment of U relative to Pb, e.g. O'Nions et al (1979), Chase (1981), Zartman and Doe (1981), Nelson and McCulloch (1986) and Zindler and Hart (1986). The existence of such a large high U/Pb reservoir requires the existence of a complementary reservoir with low U/Pb and unradiogenic Pb which lies to the left of the geochron. Recent OIB trace element data published by Newsome et al (1987) precludes Pb loss to the Earths core to form the high U/Pb mantle reservoir. Nelson and McCulloch (1986), Davies and Lloyd (1986) and Davies et al (1989) favour storage of unradiogenic Pb in the subcontinental lithosphere mantle (SCL). Incorporation of low U/Pb reservoirs within the SCL may be achieved by sediment

subduction processes involving the migration of subduction related H_2O-rich fluids and/or melts containing a sediment derived low U/Pb signature which with time result in radiogenic $^{206}Pb/^{204}Pb$ ratios (Davies and Lloyd 1986, Davies et al 1989). This Pb isotopic signature is recorded in samples which have originated from or interacted with the SCL in at least 3 different continents (Australia, USA and Africa) but its extent is unknown.

The strong DUPAL-like isotopic signature of the Beni Bousera pyroxenites and some of the peridotites is striking. A currently unresolved question is whether the DUPAL signature in some OIB (Hart 1984) is a consequence of direct sediment incorporation into their source regions, or whether their sources have incorporated ancient SCL which has been metasomatised by sediment derived fluids during subduction. An alternative to sediment subduction producing the DUPAL signature in the Beni Bousera pyroxenites and peridotites is the subduction of oceanic lithosphere whose base was heterogeneously veined by small degree partial melts carrying DUPAL signatures. Subsequent melting of this material in the subducting slab or during diapiric uprise could impart the DUPAL like signature to the pyroxenites and peridotites.

Evidence presented above indicates large bodies of mantle derived peridotite may contain km scale Pb isotope heterogeneities, including peridotites which plot both to the left and right of the geochron. These peridotites may originate from the convecting asthenospheric mantle and may be direct evidence in support of the "marble cake" mantle models currently advocated by Allegre and Turcotte (1986) and Prinzhofer et al (1989).

CHAPTER 7

STABLE ISOTOPE GEOCHEMISTRY

7.1: Introduction.

Low temperature processes occurring near the surface of the Earth produce extremely variable stable isotope compositions. The high temperatures prevailing in the mantle do not allow significant stable isotope fractionation between different phases during partial melting and crystallization, hence marked variations in the isotopic composition of mantle derived rocks suggest they may have interacted with a crustally-derived component. Heterogeneities in the stable isotope composition of mantle derived rocks can be used to place constraints on processes such as the extent of recycling of subducted sediments and hydrothermally altered oceanic lithosphere and the role of metasomatism. Oxygen isotopes are particularly useful in this respect due to the high abundance of oxygen in terrestial rocks and fluids and the substantial differences in $\delta^{18}O$ values of crustal and mantle reservoirs. Additionally, stable isotopes do not vary in abundance with time, hence in a closed system mantle, the isotopic composition of a rock is identical to that of its source.

Radiogenic isotope evidence presented in Chapter 6 indicates that:

a) Both the peridotites and pyroxenites may have a sediment derived component in their source.

b) The pyroxenite suite may be derived from melting of subducted, hydrothermally altered oceanic lithosphere.

Coupled Pb-Sr-Nd and oxygen isotope relationships may be able to further constrain the petrogenetic evolution of the pyroxenites. Carbon isotope analysis of the graphite within the GGP will provide information on the source of the carbon and will establish whether the graphite has undergone late stage carbon isotope exchange with crustally derived fluids.

7.2 Oxygen Isotope Geochemistry.

7.2.1 Sample selection and data representation and precision.

Samples were selected for oxygen isotope analysis to cover both a wide variety of lithological and radiogenic isotope variation and on the basis of their lack of alteration. Hand-picked, acid leached mineral separates were analysed to avoid the effects of late stage, post emplacement alteration processes. The leaching procedure is given in Chapter 6 and Appendix 4.9. The layer margin of GP87 was analysed to complement radiogenic isotope data documenting peridotite-pyroxenite interaction. Unless otherwise stated, all samples were obtained from *in situ* exposures, from the centre of the layers.

Oxygen isotope analyses are reported in the standard delta notation, in units of permil variation relative to the V-SMOW international standard.

$$\delta^{18}O(‰) = [(^{18}O/^{16}O_{SAMPLE} - ^{18}O/^{16}O_{STANDARD} / ^{18}O/^{16}O_{STANDARD}) - 1] * 1000$$

The permil fractionation value, Δ for small δ differences (< 10) is determined by

$$\Delta_{A-B} = \delta_A - \delta_B = 1000 \ln \alpha_{A-B}$$

Where a is the isotopic fractionation factor between two substances A and B. Note that for large values of Δ the formal mathematical derivation must be used.

Oxygen isotope analyses were performed at the NERC Isotope Geology Centre, British Geological Survey, London under the supervision of P.B.Greenwood (see Appendix 4.9 for analytical details). Analytical precision: All garnets were run in duplicate. The $\delta^{18}O$ value of GP87B GT is based on one result only, because one of the extractions gave an anomalously low yield. Based on replicate analyses, analytical precision averages for GT were better than 0.2 ‰ (0.17 2σ errors) but ranged from 0.4 to 0.0 (Table 7.1).

GP143 GT and GP87m GT were analysed in quadruplicate and gave replicate 2σ precisions of 0.2 and 0.1 permil respectively. Average CPX analytical precision based on duplicate analyses is better than 0.2 ‰ ranging from 0.5 ‰ to 0.0 ‰ (Table 7.1). OPX analyses were not as reproducible, despite comparable yields, the two samples analysed giving +/- 0.6 and +/- 0.0 ‰ duplicates. The olivine was similarly variable with 4 analyses of GP132(3) Ol giving 6.5 +/- 0.7 ‰. despite yields of close to 100%.

7.2.2 Oxygen Isotope Variations.

7:2.2a Peridotites:

5 CPXs and 1 olivine separate were analysed from the spinel facies peridotites and one CPX-GT pair were analysed from the garnet peridotite sample GP24 (Table 7.1). Of the five spinel facies CPX samples GP88 and GP132(3) have ΔFeO values significantly greater than 0.25 (0.95 and 0.45 respectively) and have therefore suffered Fe enrichment (Chapter 5).

All the spinel peridotite CPX values form a relatively tight cluster around the typical mantle value of $\delta^{18}O$ = 5.6 ‰ with a range of $\delta^{18}O$ + 5.3 to 6.0 which is within the "Mantle CPX" range derived from CPX from over 100 peridotite xenoliths (Fig. 7.1; data from Kyser et al 1981 and R.S.Harmon, pers.comm.). The peridotite CPX data are also within the $\delta^{18}O$ range of + 5.3 to + 6.1 ‰ for MORB glasses reported by Ito et al (1987). The peridotite CPX values are compatible with those found by Javoy (1980). There is no distinct difference in $\delta^{18}O$ values between the high and low ΔFeO peridotites. The garnet peridotite CPX has a slightly heavier oxygen isotope composition than the spinel peridotite CPX ($\delta^{18}O$= 6.1 ‰). Considering the wide variation in $\delta^{18}O$ for the pyroxenites (Fig. 7.1) this value does not strongly support or oppose the spinel lherzolite-garnet clinopyroxenite mixing origin proposed in Chapters 4 and 5.

SAMPLE	LITHOLOGY	$\delta^{18}O_{SMOW}$‰	+/-	Δ_{CPX-GT}
GP88 CPX	SP LHERZ	+6.0		
GP119 CPX	SP LHERZ	+5.8		
GP132(3) CPX	SP LHERZ	+6.0		
GP132(3) Ol		+6.5	0.7	
GP189 CPX	SP LHERZ	+5.3	0.1	
CP220 CPX	SP LHERZ	+6.0	0.0	
GP24 CPX	GT LHERZ	+6.1		
GP24 GT		+6.1	0.4	0.0
GP81 CPX	GGP	+5.2		
GP81 GT		+5.4	0.0	-0.2
GP143 GT	GGP	+7.5	0.2 (n=4)	
GP147 CPX	GGP	+7.5	0.1	
GP147 GT		+7.6	0.4	-0.1
GP37 CPX	GP	+4.9	0.1	
GP37 GT		+4.5	0.0	+0.4
GP87M CPX	GP	+7.3		
GP87M GT		+7.1	0.1 (n=4)	+0.2
GP87B CPX	GP	+7.4		
GP87B GT		+7.5		-0.1
GP139 CPX	GP	+5.7	0.2	0.0
GP139 GT		+5.7	0.1	
GP194M CPX	GP	+7.1	0.1	
				$\Delta_{CPX-OPX}$
GP33 CPX	WEB	+5.4	0.1	
GP101a CPX	WEB	+8.7		
GP101a OPX		+9.4	0.0	-0.7
GP101d CPX	WEB	+6.4		
GP101d OPX		+6.3		+0.1
GP132(1) CPX	WEB	+5.5	0.2	
GP188 CPX	WEB	+9.3	0.5	
GP188 OPX		+8.8	1.1	+0.5
GP236 CPX	WEB	+5.6		

TABLE 7.1 Oxygen isotope analyses of Beni Bousera silicate phases from peridotites and pyroxenites.

SP LHERZ= Spinel lherzolite, GT LHERZ= Garnet lherzolite, GGP= Graphite garnet clinopyroxenite, GP=Garnet clinopyroxenite, WEB= Websterite. Errors are 2σ for duplicate analyses unless otherwise stated.

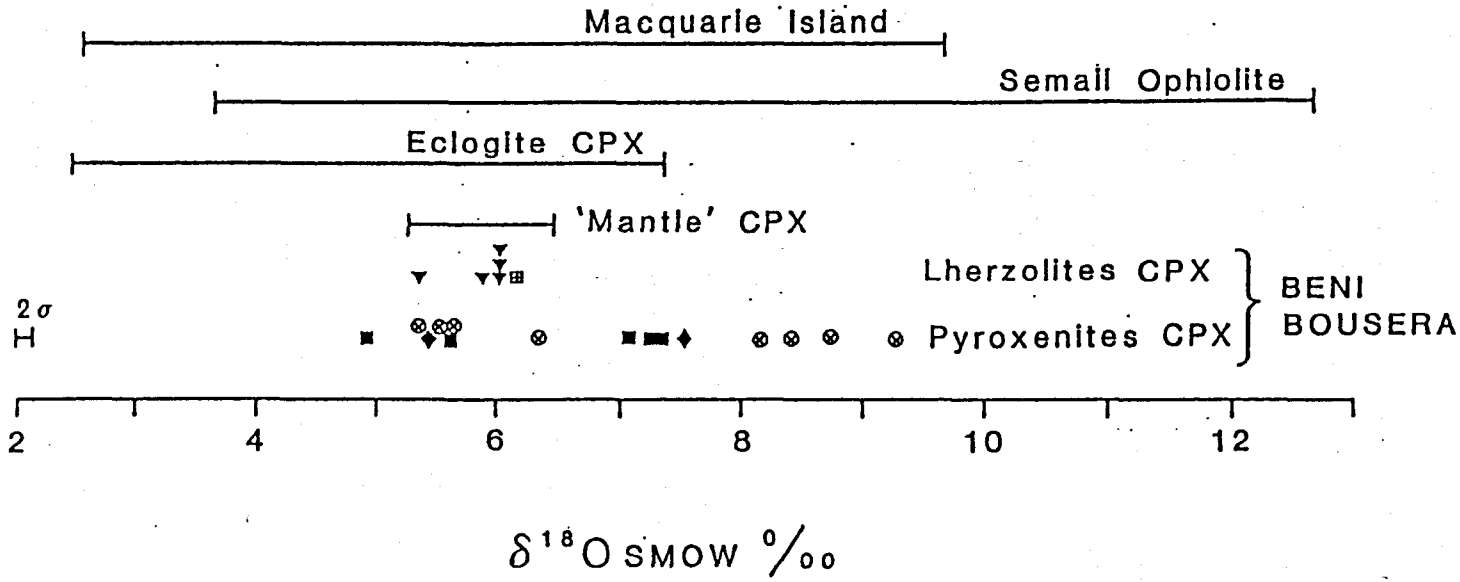

Figure 7.1. Oxygen isotope composition of CPX from Beni Bousera peridotites and pyroxenites compared with CPX from mantle peridotite xenoliths and eclogite xenoliths. Range for Semail ophiolite and Macquarie Island also shown. Data from Kyser et al (1981), R.S.Harmon (pers.comm.), MacGregor and Manton (1986), Shervais et al (1988), Cocker et al (1981) and McCulloch et al (1981). Inverted triangles = SPLHRZ, box with cross = GTLHRZ, diamond = GGP, solid square = GP, circle with cross = WEB.

The olivine coexisting with GP132(3) CPX has a heavier $\delta^{18}O$ value (+ 6.5 ‰) than the CPX (+ 6.0 ‰). However, the large error on this determination (despite obtaining ~ 100 % yields for four separate analyses) makes interpretation of the significance of this single analysis speculative. The coupled CPX-Ol data plot off the equilibrium $\Delta = 0$ fractionation line in Figure 7.2a, in contrast to the 3 points obtained by Javoy (1980). The CPX-Ol point from GP132(3) plots within the field for spinel peridotite xenoliths defined by data from Kyser et al (1982). Without a more comprehensive Ol-CPX study it is not possible to determine whether disequilibrium oxygen isotope relationships similar to those found in xenoliths by Gregory and Taylor (1986) and Kempton et al (1987) exist in the Beni Bousera peridotites.

7:2.2b O-Pb-Sr-Nd isotope relationships.

There is no correlation between $\delta^{18}O$ and degree of LREE depletion in the peridotite CPX analysed. No correlations are evident between $\delta^{18}O$ and Pb-Sr and Nd isotopes in this relatively limited sample set. GP132(3) CPX has MORB-source like Sr and Nd isotopic composition and has the same $\delta^{18}O$ value (+ 6.0 ‰) as GP220 CPX which has much more radiogenic $^{87}Sr/^{86}Sr$ and unradiogenic $^{143}Nd/^{144}Nd$ ratios.

7:2.2c Pyroxenites.

The pyroxenite CPX show a much greater range of oxygen isotope compositions than the peridotites (Fig. 7.1) with $\delta^{18}O$ values ranging from + 4.9 to + 9.3‰ (Table 7.1). The small magnitude of CPX-melt, GT-melt fractionation factors at mantle temperatures (Kyser et al 1981, Kyser 1986) preclude the pyroxenites being derived by melting of peridotites, even if substantial (> 50%) crystal fractionation took place. The $\delta^{18}O$ values of the 2 GGP samples (GP81 and GP147) are significantly different (+ 5.2 and + 7.5 ‰ respectively). Their similarity in mineral and bulk rock chemistry rule out such large O isotope variations being the product of crystal fractionation of a phase enriched or depleted in ^{18}O. A large range in $\delta^{18}O$ is also evident for websterites and garnet clinopyroxenites (Fig. 7.1) with the two Cr-diopside websterites having the heaviest $\delta^{18}O$ compositions (up to + 9.3 ‰). Such isotopically heavy values were also recorded from CPX in a websterite and an orthopyroxenite ($\delta^{18}O$ = 8.4 and 8.2 ‰ respectively) by Javoy (1980). To determine to what extent these $\delta^{18}O$ variations are due to post emplacement or recent alteration effects, or whether the variation is a primary mantle signature, coexisting GT and CPX were analysed.

7:2.2d Mineral-mineral equilibria.

Relatively small amounts of material are required for oxygen isotope analysis (< 50 mg) hence it is possible to guarantee that the samples are 100% pure and free of any visible signs of alteration/inclusions. The fresh nature of the minerals analysed coupled with HCl and HF leaching/partial dissolution eliminates surface films of low temperature origin contributing to the $\delta^{18}O$ value of the sample. Furthermore, coexisting GT-CPX pairs are in oxygen isotopic equilibrium, plotting close to or on the $\Delta_{GT\text{-}CPX} = 0$ ‰ line in Figure 7.3. The magnitude of $\Delta_{GT\text{-}CPX}$ in the pyroxenites analysed is within the range of Δ values obtained for similar high temperature mantle derived eclogites and pyroxenites by other workers (Garlick et al 1971, McGregor and Manton 1986, Ongley et al 1987 and Shervais et al 1988). The GT-CPX pair from

Figure 7.2a. $\delta^{18}O$ olivine vs $\delta^{18}O$ CPX for Beni Bousera spinel lherzolites. Three data points plotting close to $\Delta = 0$ line are from Javoy (1980). Dashed field is for spinel lherzolite xenoliths from Kyser (1986).

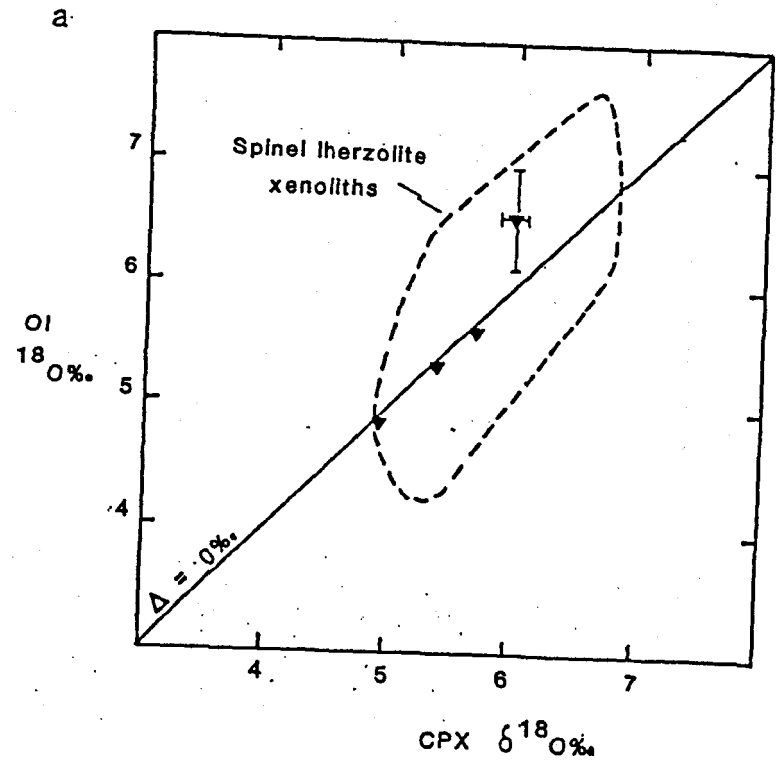

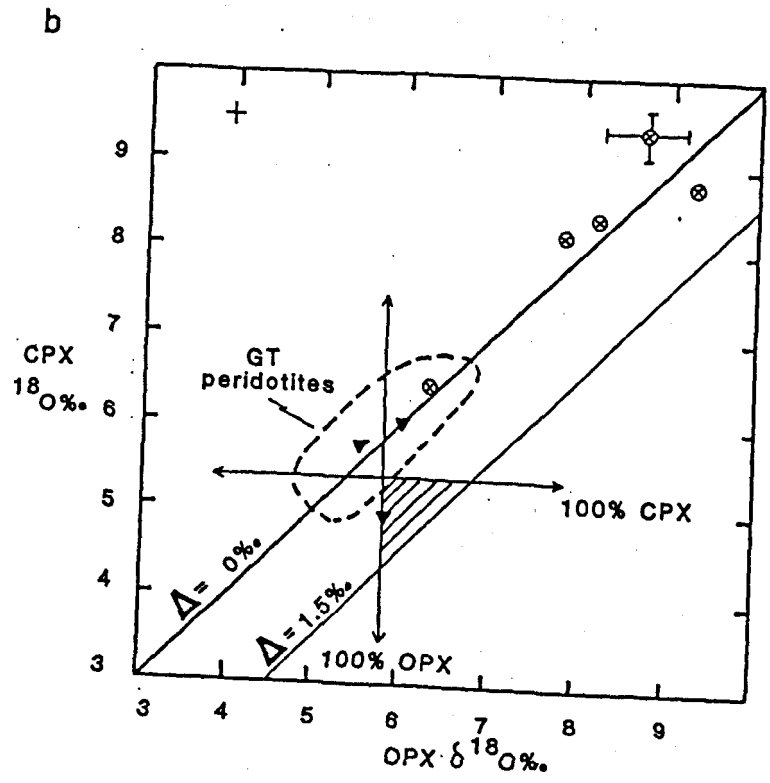

Figure 7.2b. $\delta^{18}O$ CPX vs $\delta^{18}O$ OPX for Beni Bousera spinel peridotites (closed triangles) and websterites (circles with crosses). Typical two sigma error bar is shown along with individual error bar for one sample. Vectors mark effect of closed system fractionation of 100 % CPX or OPX from a bulk mantle $\delta^{18}O$ composition of + 5.5 ‰. Garnet peridotite xenolith field is from Kyser (1986).

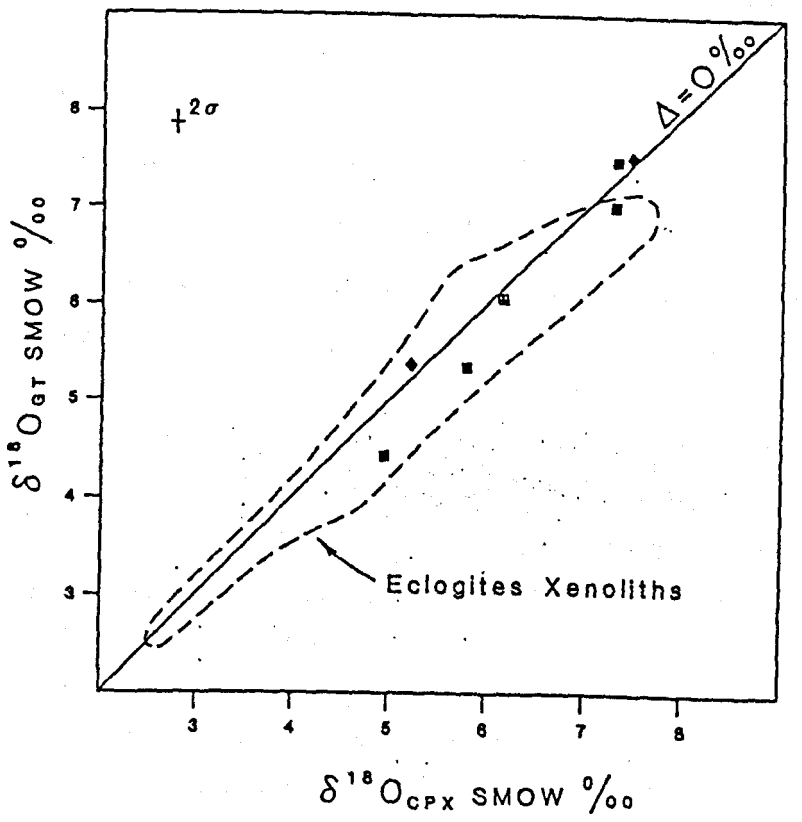

Figure 7.3 $\delta^{18}O$ values of coexisting garnet and CPX from Beni Bousera pyroxenites and garnet peridotite. Symbols as in Fig. 7.1. Field for GT-CPX pairs from eclogite xenoliths from kimberlite also shown.

the Beni Bousera garnet peridotite are also in oxygen isotopic equilibrium, implying that the rock equlibrated as a garnet lherzolite at high temperature. CPX-OPX pairs from the isotopically extreme websterites (including those of Javoy 1980) do not plot as close to the $\Delta = 0$ line (Fig. 7.2b) as the GT-CPXpairs. This may be a result of the poorer reproducibility of both OPX and CPX from some of these samples (see error bars).

GT-CPX pairs from the Beni Bousera GGP and GP samples show a diagonal spread on a $\delta^{18}O_{GT}$ vs $\delta^{18}O_{CPX}$ diagram (Fig. 7.3) parallel to the 45° $\Delta = 0$ ‰ line. Among mantle derived rocks the Beni Bousera range is only exceeded by eclogite xenoliths which plot to lower and higher $\delta^{18}O$ values than the typical mantle value of 5.6 to 5.8 ‰ (Figs. 7.1 and 7.3). The $\delta^{18}O$ range shown by the Beni Bousera pyroxenite CPX (Fig. 7.1) is far greater than that shown by CPX from Al-augite and Cr-diopside pyroxenite xenoliths from alkali basalts which vary from + 5.4 ‰ to + 6.5 ‰ (Wilshire et al 1988).

Pyroxenite-peridotite interaction does not appear to have had much, if any, effect on the oxygen isotopes of the layer margin of the pyroxenite layer GP87 (see Chapter 6). The $\delta^{18}O$ value of GP87B CPX is within error of the layer centre, GP87M and coexisting GT-CPX pairs from centre and edge are in isotopic equilibrium in Figure 7.3 (see Chapter 6 for discussion).

7:2.2 e O-Pb-Sr-Nd isotope relationships in the pyroxenites.

Combined O-Pb-Sr-Nd data are given in Table 6.5. The decoupled parent-daughter isotopic relationships in the pyroxenites do not produce coherent trends between either Rb/Sr or $^{87}Sr/^{86}Sr$ ratios and $\delta^{18}O$ (eg. Fig. 7.4a). Although Sm/Nd ratios do not show any coherent correlation with $\delta^{18}O$ the two samples with the lowest Sm/Nd ratios (GP101a and GP188) also have the highest $\delta^{18}O$ values. Similarly, $^{143}Nd/^{144}Nd$ does not correlate with $\delta^{18}O$ (Fig. 7.4b) although the high $\delta^{18}O$ samples also have the most unradiogenic $^{143}Nd/^{144}Nd$ ratios. U/Pb ratios and $\Delta 7/4$ Pb values (Fig. 7.5) are uncorrelated with $\delta^{18}O$, however, $^{206}Pb/^{204}Pb$ ratios show a poor positive correlation with $\delta^{18}O$ in that GP188 and GP101 have the highest $^{206}Pb/^{204}Pb$ ratios and $\delta^{18}O$ values. The limited geothermometric data available in Chapter 4 is not precise enough to resolve any $\delta^{18}O$ vs equilibration temperature relationships.

In summary, the two significant points about the Pb-Sr-Nd versus O-isotope relationships in the pyroxenites are:

1) Pyroxenites with the most unradiogenic $^{143}Nd/^{144}Nd$ ratios and most radiogenic $^{87}Sr/^{86}Sr$ and $^{206}Pb/^{204}Pb$ ratios have the highest $\delta^{18}O$ values.

2) Pyroxenites with less extreme $^{143}Nd/^{144}Nd$ ratios but variable $^{87}Sr/^{86}Sr$ ratios have very variable $\delta^{18}O$ values.

Figure 7.4a. $^{87}Sr/^{86}Sr$ vs $\delta^{18}O$ for pyroxenite CPX. Mixing lines are shown between mantle compositions and two different sediment end members. The two mantle compositions have a $\delta^{18}O$ of + 5.8 ‰ and $^{87}Sr/^{86}Sr$ ratios of 0.7022 and 0.7040. The latter value was chosen as a composition of hydrothermally altered oceanic crust. The diagram indicates that even using the altered oceanic crust end member, the extreme $\delta^{18}O$ values and $^{87}Sr/^{86}Sr$ ratios of some of the data can only be explained if ~ 30 % of sediment is added to the mantle source. Vectors showing the effect of hydrothermal alteration and radioactive decay of the parent isotope are also shown. Sediment compositions (open stars) are : $\delta^{18}O$ = + 17.0 ‰ (for both) $^{87}Sr/^{86}Sr$ = 0.70859 at 60 ppm Sr and $^{87}Sr/^{86}Sr$ = 0.71887 at 150 ppm Sr. Mantle compositions: $^{87}S/^{86}Sr$ = 0.70228 at 40 ppm Sr and $^{87}Sr/^{86}Sr$ = 0.704 at 60 ppm respectively.

Figure 7.4b. $^{143}Nd/^{144}Nd$ vs $\delta^{18}O$ for pyroxenite CPX. Mixing lines are shown between typical mantle composition and sediments. Mantle $^{143}Nd/^{144}Nd$ = 0.5130 at 8 ppm Nd, $\delta^{18}O$ = + 5.6 ‰. Sediment compositions; $^{143}Nd/^{144}Nd$ = 0.512392 at 159 ppm Nd, and $^{143}Nd/^{144}Nd$ = 0.511962 at 32 ppm Nd. Both sediments have $\delta^{18}O$ = + 17 ‰. Symbols as in Figure 7.1.

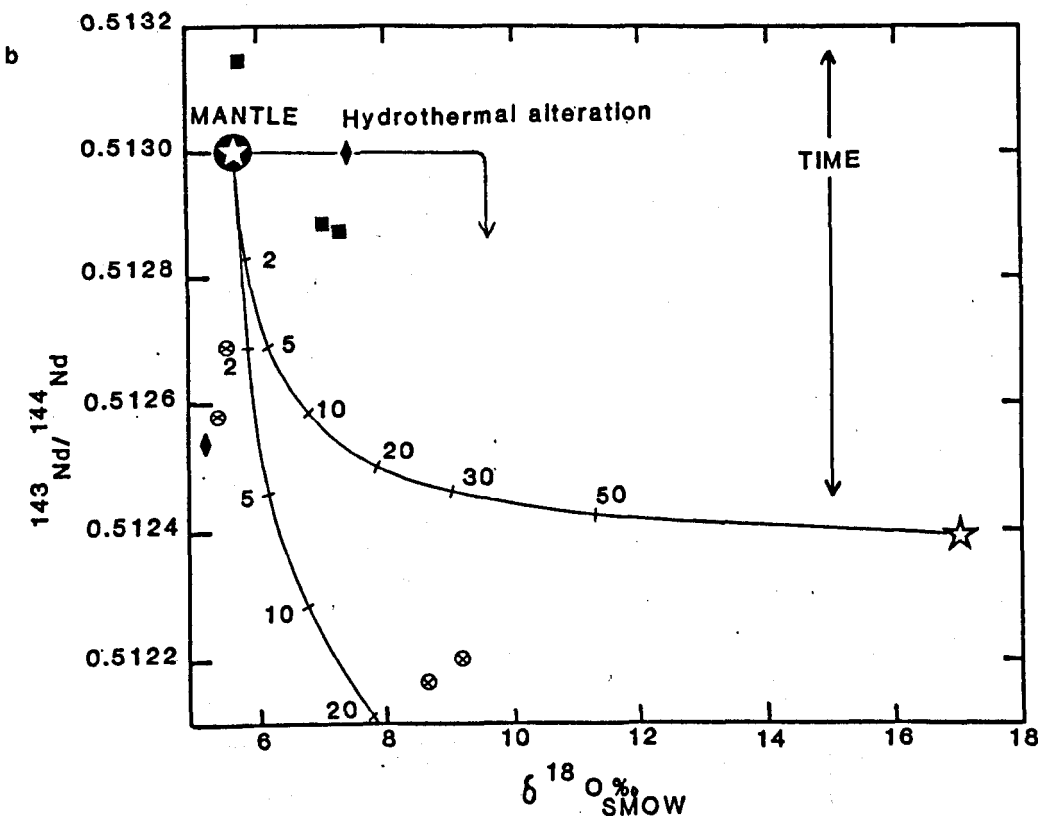
b
MANTLE
Hydrothermal alteration
TIME
0.5132
0.5130
0.5128
0.5126
0.5124
0.5122
$^{143}Nd/^{144}Nd$
2
5
10
20
30
50
6
8
10
12
14
16
18
$\delta^{18}O_{SMOW}$

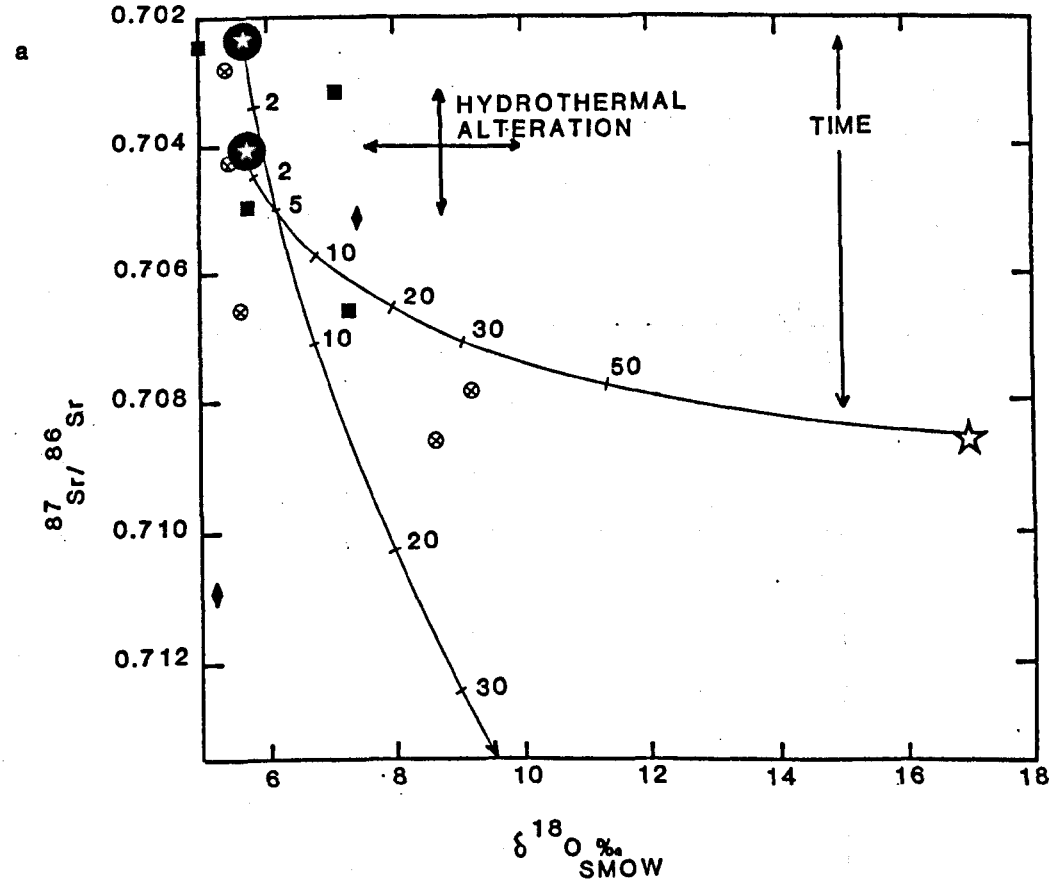
a
HYDROTHERMAL ALTERATION
TIME
0.702
0.704
0.706
0.708
0.710
0.712
$^{87}Sr/^{86}Sr$
2
5
10
20
30
50
6
8
10
12
14
16
18
$\delta^{18}O_{SMOW}$

Figure 7.5. Δ8/4, Δ7/4 and Ba/La vs $\delta^{18}O$ for Beni Bousera pyroxenites, all samples shown as squares.

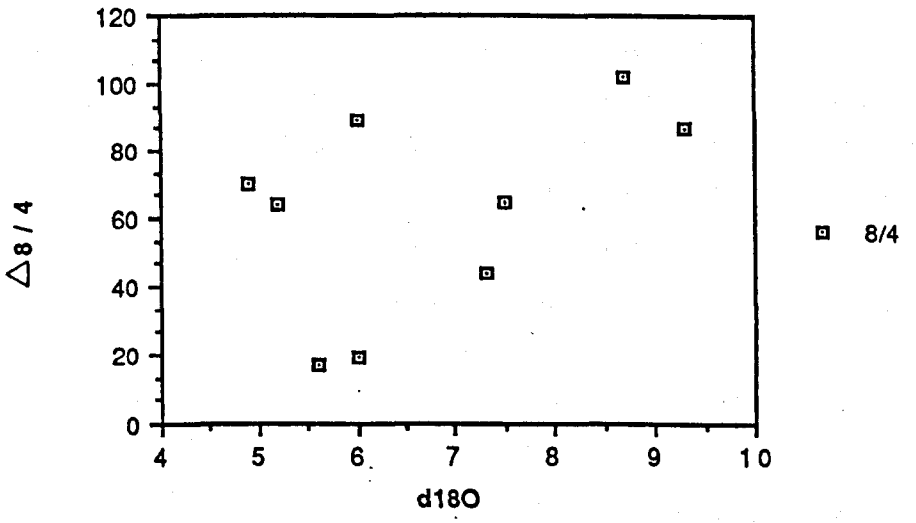

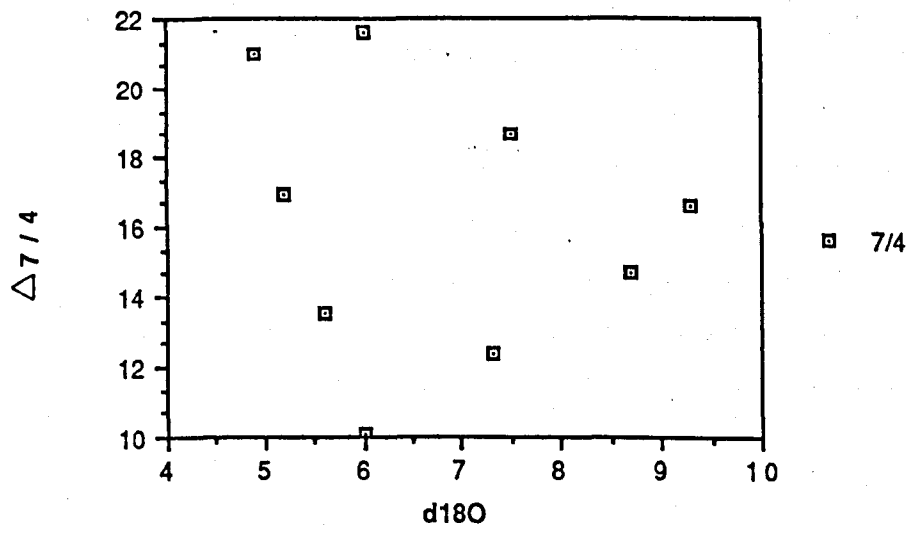

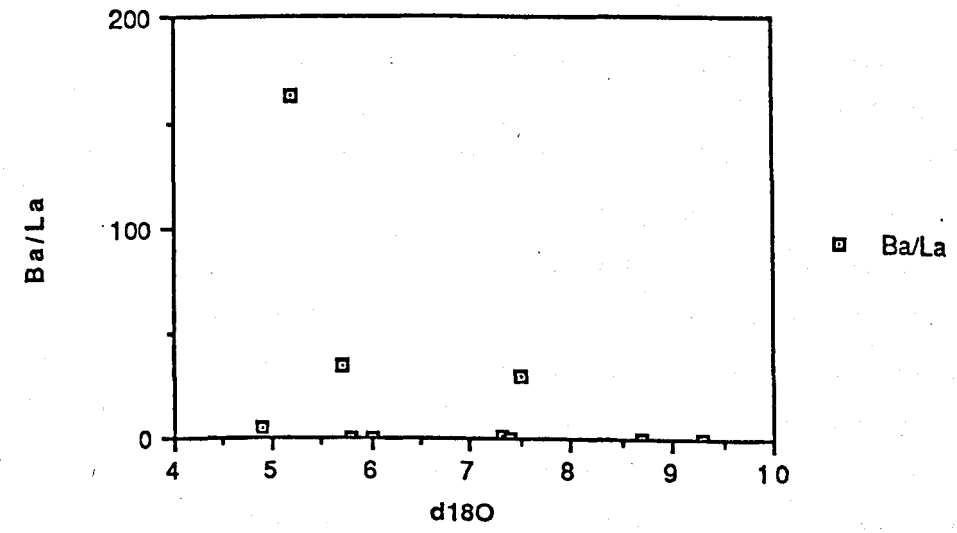

7:2.3 Discussion: The bearing of oxygen isotope data on the petrogenesis of the Beni Bousera peridotites and pyroxenites.

7:2.3 a Peridotites:

At 1200°C, fractionation between mantle phases and melts is very small hence large degrees of melting (> 90%) are necessary to affect the oxygen isotope composition of any phase (Kyser et al 1982). Such large degrees of melting are physically unlikely and not consistent with major and trace element data for the Beni Bousera peridotites (Chapter 5). Furthermore, no correlation exists between degree of LREE depletion and $\delta^{18}O$. The general lack of correlation between $\delta^{18}O$ and radiogenic isotope ratios in the peridotites indicates that $\delta^{18}O$ variations may be unrelated to incompatible element enrichments and depletions in the source. The conclusion is difficult to confirm due to the limited data set available and the complex incompatible element history experienced by the peridotites (Chapter 6). The observed radiogenic isotope - $\delta^{18}O$ decoupling in the Beni Bousera peridotites is similar to the general lack of Pb-Sr-Nd isotope - $\delta^{18}O$ correlation shown by most MORB glasses (Ito et al 1987). Despite possible 2nd order processes causing some variation, Ito et al (op.cit.) conclude that significant $\delta^{18}O$ variations must exist in the MORB source mantle but cannot constrain their origin.

The oxygen isotope data for the Beni Bousera peridotite CPX place no constraints on the petrogenetic model advocated in Chapter 6, which involves small amounts of ancient subducted sediment (< 1 %) interacting with the peridotite source. If 1 % sediment with a $\delta^{18}O$ value of + 20 ‰ is mixed with a peridotite source of + 5.6 ‰ the resultant mixture would only have $\delta^{18}O$ of + 5.9 ‰ (assuming approximately equal oxygen concentrations of the end members). The small $\delta^{18}O$ variations produced by small scale sediment mixing are probably not resolvable unless a much larger sample set is available. GP220 CPX, the sample with the largest potential sediment component has the same $\delta^{18}O$ value (within error) as GP132(3) whose Sr and Nd isotope systematics do not appear to be affected by a sediment derived component.

7:2.3b Pyroxenites:

The total $\delta^{18}O$ range of CPX in the pyroxenites (+ 4.9 ‰ to + 9.3 ‰) is much greater than that observed in CPX from mantle peridotite and pyroxenite xenoliths and the host Beni Bousera perdiotite CPXs. The pyroxenites are thus unlikely to have been derived from the host peridotites, a conclusion in agreement with trace element and isotopic data (Chapters 5 and 6). Equilibrium CPX-GT and CPX-OPX relationships (Figs. 7.3 and 7.2b) are unlikely to be the result of open system "metasomatic" effects. This is corroborated by the lack of the expected $\delta^{18}O$ - radiogenic isotope or trace element enrichment relationships (e.g. Kempton et al 1987). Other explanations for the O-isotope variation must be sought.

The effects of pressure on isotope fractionation: Garlick et al (1971) sought to explain the large range of $\delta^{18}O$ in eclogite xenoliths by crystal fractionation due to increased mineral melt fractionations at high pressure. As the change in molar volumes of solids on isotopic substitution is small it is generally now believed that the effect of pressure on isotopic fractionation between minerals is negligible. Pressure effects may be expected for mineral-gas or melt-gas systems because the isotopic proportions of the gas may change drastically with the large density changes while those of the minerals and melts would be

relatively unaffected (O'Neil 1986). Clayton et al (1975) observed negligible oxygen isotope fractionation effects in a study of $CaCO_3$ and H_2O at 500 °C from 1 atmosphere up to 20 kb and sugested that the effect of pressure on oxygen isotope fractionation in the mantle would be < 0.2% for tens of kb. A review of experimental and theoretical aspects of isotope fractionation by O'Neil (1986) also indicates that pressure plays a minor role during oxygen isotope fractionation in the mantle and indicates the conclusions of Garlick et al (1971) to be unfounded.

Considering the effects of closed-system exchange on a 2-phase mixture of CPX and GT with a bulk starting $\delta^{18}O$ of + 5.5 ‰, (Fig. 7.6), all products of closed-system exchange will lie within the quadrants bounded by the CPX and GT vectors (diagonal lined area in Figure 7.6, Gregory and Taylor 1986, Gregory and Criss, 1986). Similar O-isotope exchange vectors can be drawn on the CPX-OPX diagram from a similar starting composition (Fig. 7.2 b). Closed-system isothermal processes involving uniform reservoirs of $\delta^{18}O$ cannot account for the observed variability of the pyroxenites (Fig. 7.2b and 7.6). Furthermore, the observed variations are unlikely to be the result of either closed or open system processes operating solely within the mantle because:

1) Only some of the bulk rock pyroxenite $\delta^{18}O$ values are within close proximity of an appropriate average mantle $\delta^{18}O$ value.

2) The positions of the data points on Figure 7.2b and 7.6 indicate that if a metasomatic event caused the $\delta^{18}O$ enrichments, typical mantle of ~ $\delta^{18}O$ ~ 5.5 ‰ is not an acceptable starting material for the fluid/melt. Spinel lherzolites showing marked Fe and REE enrichment do not have anomalous $\delta^{18}O$ values.

Similar conclusions to those presented above were reached by Gregory and Taylor (1986) and Gregory and Criss (1986) regarding the genesis of the highly variable $\delta^{18}O$ range in eclogite xenoliths and "crustal" eclogites from Alpine massifs (Fig. 7.6) which show similar O isotopic variations to the Beni Bousera pyroxenites.

The subduction and incorporation of sediment into the pyroxenite source was proposed as a mechanism of creating radiogenic isotope heterogeneity in Chapter 6. The results of modelling mixing of sediments which tend to have high but variable $\delta^{18}O$ ratios with a mantle source is shown in Figure 7.4 a and b. Using various mantle and sediment compositions it is apparent that to achieve the high $\delta^{18}O$ values of some of the websterites by sediment mixing requires between 20 and 30 % sediment of $\delta^{18}O$ + 17 ‰ in the source. Additionally, very variable sediment Sr/Nd ratios are needed to explain some of the trends in Figure 7.4, whilst $\delta^{18}O$ values of <6 ‰ cannot be explained in terms of sediment mixing. The lack of K in the pyroxenites together with their relatively high Mg Nos. rule out addition of more than a few % (max. ~5 %) sediment. Larger amounts of sediment incorporation would be evident from major element considerations. Additionally, the websterites with the highest $\delta^{18}O$ and most unradiogenic $^{143}Nd/^{144}Nd$ ratios are among the most unfractionated pyroxenites in terms of major and trace element chemistry. Major and trace element constraints together with the lack of coherent isotope/trace element versus $\delta^{18}O$ correlations rule out sediment incorporation into the pyroxenite source as the major cause of O-isotope

Figure 7.6. $\delta^{18}O$ garnet vs $\delta^{18}O$ CPX plot indicating the effects of closed system isotopic exchange on a 2-phase mixture of CPX and GT with a bulk $\delta^{18}O$ starting composition of + 5.5 %. All products of closed system exchange lie in the diagonal lined fields.

Figure 7.7. $^{87}Sr/^{86}Sr$ vs $\delta^{18}O$ variation produced by closed system hydrothermal alteration of oceanic crust with a $\delta^{18}O$ of + 5.8 ‰. $^{87}Sr/^{86}Sr$ of the unaltered oceanic crust = 0.702 at 160 ppm Sr. $^{87}Sr/^{86}Sr$ of present day seawater = 0.709 at 8 ppm Sr and has a $\delta^{18}O$ of 0‰ i.e. = SMOW. Mixing hyperbolae were calculated after McCulloch et al (1981). Δ = the temperature dependant oxygen isotope fractionation factor between water and rock. Δ = 10 is approximately equivalent to zeolite facies alteration, Δ = 6 to greenschist facies and Δ = 0 to upper amphibolite facies water-rock interaction. The curves indicate that in a complex, closed system, hydrothermal alteration regime involving water/rock isotopic exchange at different temperatures, any $\delta^{18}O/Sr$ isotope composition can be expected that lies between the Δ = 0 and Δ = 10 curves.

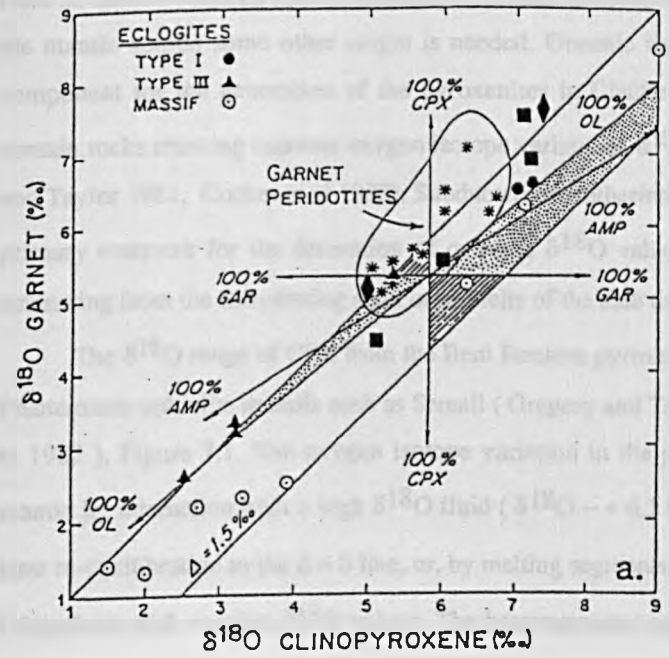
ECLOGITES
TYPE I
TYPE III
MASSIF
GARNET PERIDOTITES
100% CPX
100% OL
100% AMP
100% GAR
100% GAR
100% AMP
100% OL
100% CPX
Δ = 1.5 ‰
a.
δ18O GARNET (‰)
δ18O CLINOPYROXENE (‰)

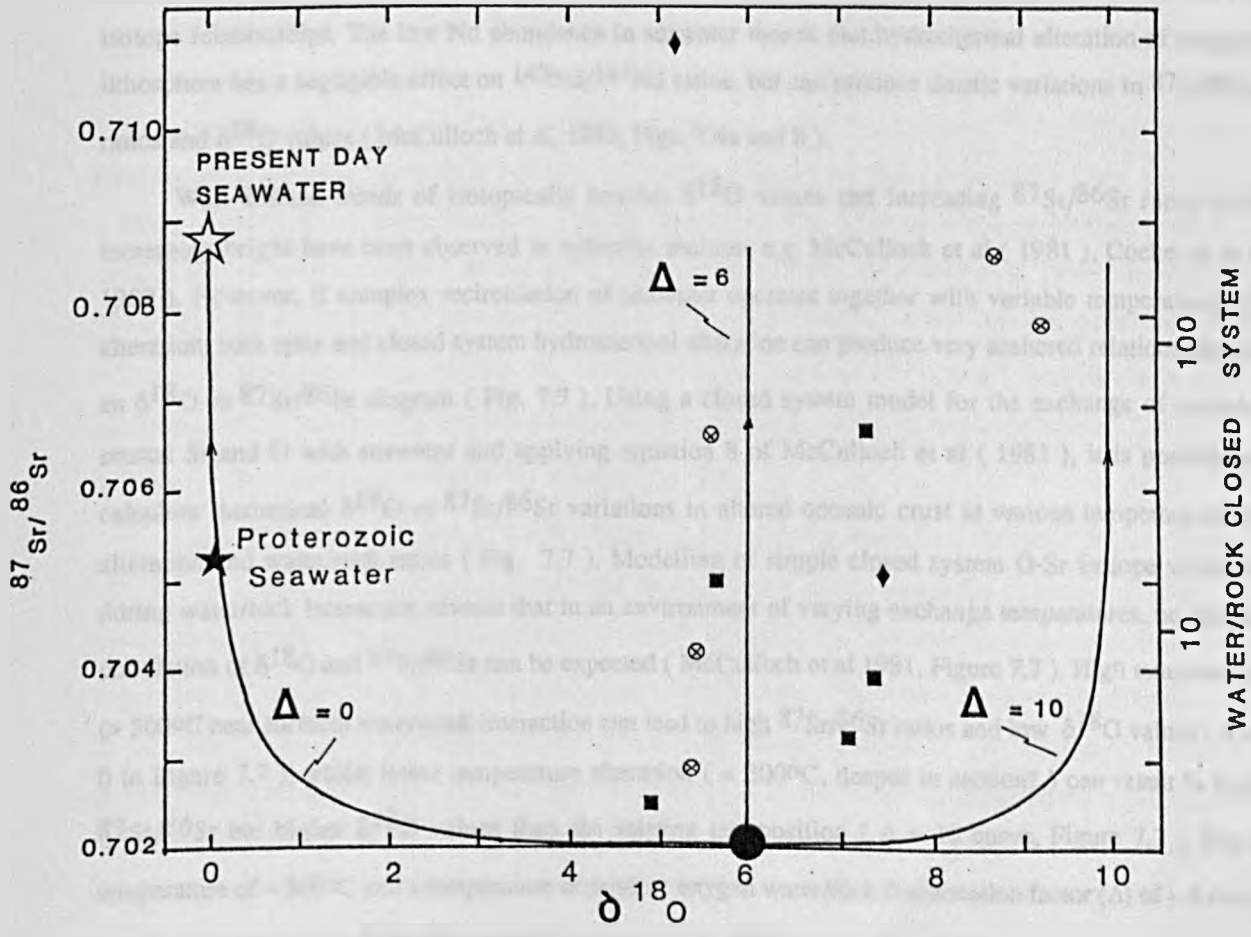
PRESENT DAY SEAWATER
Proterozoic Seawater
Δ = 0
Δ = 6
Δ = 10
100
10
WATER/ROCK CLOSED SYSTEM
87Sr/86Sr
δ18O

heterogeneity.

If the oxygen isotope heterogeneity in the Beni Bousera pyroxenites is unlikely to have originated from an uncontaminated mantle reservoir by partial melting/fractionation or by sediment contamination of the mantle source some other origin is needed. Oceanic lithosphere is implicated as the major source component for the generation of the pyroxenites in Chapter 5 and 6. Oceanic lithosphere is known to contain rocks showing extreme oxygen isotope variations, $\delta^{18}O$ varying from + 2 < to ~ +20 ‰ (Gregory and Taylor 1981, Cocker et al 1982). Subducted hydrothermally altered oceanic lithosphere forms an ideal primary reservoir for the derivation of extreme $\delta^{18}O$ values in the mantle either in the form of fluids emanating from the dehydrating slab, or as melts of the slab during subduction.

The $\delta^{18}O$ range of CPX from the Beni Bousera pyroxenites is well within the $\delta^{18}O$ range shown by Phanerozoic ophiolite massifs such as Semail (Gregory and Taylor 1981) and Macquarie Island (Cocker et al 1982), Figure 7.1. The oxygen isotope variation in the pyroxenites could either be generated in the mantle by interaction with a high $\delta^{18}O$ fluid ($\delta^{18}O$ ~ + 6.5 ‰ for 50 % fluid/rock ratios), followed by later re-equilibration to the $\Delta = 0$ line, or, by melting segments of subducted, hydrothermally altered oceanic lithosphere with varying $\delta^{18}O$ values. The heterogeneous major and trace element characteristics of the pyroxenite suite indicate that the pyroxenites were generated by melting of oceanic lithosphere. Typically, oceanic lithosphere is hydrothermally altered to varying extents; this would contribute to the major and trace element heterogeneity observed in the pyroxenites and also explain much of the decoupled $\delta^{18}O$ - Sr and Nd isotope relationships. The low Nd abundance in seawater means that hydrothermal alteration of oceanic lithosphere has a negligible effect on $^{143}Nd/^{144}Nd$ ratios, but can produce drastic variations in $^{87}Sr/^{86}Sr$ ratios and $\delta^{18}O$ values (McCulloch et al, 1981, Figs. 7.4a and b).

Well defined trends of isotopically heavier $\delta^{18}O$ values and increasing $^{87}Sr/^{86}Sr$ ratios with increasing height have been observed in ophiolite sections e.g. McCulloch et al (1981), Cocker et al (1982). However, if complex recirculation of seawater operates together with variable temperatures of alteration, both open and closed system hydrothermal alteration can produce very scattered relationships on an $\delta^{18}O$ vs $^{87}Sr/^{86}Sr$ diagram (Fig. 7.7). Using a closed system model for the exchange of oceanic crustal Sr and O with seawater and applying equation 8 of McCulloch et al (1981), it is possible to calculate theoretical $\delta^{18}O$ vs $^{87}Sr/^{86}Sr$ variations in altered oceanic crust at various temperatures of alteration and water/rock ratios (Fig. 7.7). Modelling of simple closed system O-Sr isotope variation during water/rock interaction reveals that in an environment of varying exchange temperatures, no simple correlation of $\delta^{18}O$ and $^{87}Sr/^{86}Sr$ can be expected (McCulloch et al 1981, Figure 7.7). High temperature (> 500°C near surface) water-rock interaction can lead to high $^{87}Sr/^{86}Sr$ ratios and low $\delta^{18}O$ values (Δ = 0 in Figure 7.7), whilst lower temperature alteration (< 300°C, deeper in section?) can result in high $^{87}Sr/^{86}Sr$ but higher $\delta^{18}O$ values than the starting composition (Δ = 10 curve, Figure 7.7). For a temperature of ~ 300°C and a temperature dependent oxygen water/rock fractionation factor (Δ) of ~ 6 there can be large changes in $^{87}Sr/^{86}Sr$ without any change in $\delta^{18}O$ value (Fig. 7.7).

More geologically realistic models of Sr-O isotope variation probably lead to even more complex variations, especially if the effect of re-circulation of ^{18}O depleted waters from deep within the convective cycle is taken into account (Gregory and Taylor 1981). Deep level fracturing and repeated stoping of

hydrothermally altered roof rocks also act to destroy depth/O-isotope correlations (Stakes et al 1984). This means that a rock with a high $\delta^{18}O$ value and high $^{87}Sr/^{86}Sr$ ratio need not necessarily originate from the upper levels of the ophiolite section, although it is most likely. The $\delta^{18}O$ ranges shown by the Beni Bousera pyroxenite suite are most common in the upper-gabbros, sheeted dykes and pillow lavas of Phanerozoic ophiolites. The upper oceanic lithosphere also contains rocks of varied MgO contents, including very MgO rich boninites (eg. Lippard et al 1988) which could be the sources of the high $\delta^{18}O$, MgO rich Cr-pyroxenites.

The decoupling of Sr isotopes with $\delta^{18}O$ seen in Figure 7.7 is expected if the Beni Bousera pyroxenite suite is derived from melted oceanic lithosphere. Hydrothermal alteration also acts to decouple Sr from Nd isotopes, producing horizontal trends on Sr versus Nd isotope diagrams (Chapter 6). As this process is capable of producing large $\delta^{18}O$ variations at constant $^{143}Nd/^{144}Nd$ ratios, oxygen and Nd isotopes become similarly decoupled. Clearly, hydrothermal alteration is able to produce the decoupled O-Sr-Nd isotopic relationships observed in the Beni Bousera pyroxenite suite.

The seawater-rock $\delta^{18}O$ vs $^{87}Sr/^{86}Sr$ interaction curves plotted in Figure 7.7 are for modern day seawater. U/Pb and Sm/Nd systematics of the pyroxenites (Chapter 6) require an ancient origin, probably older than 1 Ga. $^{87}Sr/^{86}Sr$ ratios of Proterozoic carbonates indicates that the Sr isotopic composition of seawater was less radiogenic than the present day, (Veizer et al 1982) but still considerably more radiogenic than the contemporaneous mantle. The $^{87}Sr/^{86}Sr$ ratio of seawater between 1.0 and 2.0 Ga. ago varied from ~0.707 to 0.704 (Faure 1986). Hence, although hydrothermal alteration of oceanic crust would not have produced such marked increases in $^{87}Sr/^{86}Sr$ as shown in Figure 7.7 the rocks would still have been isotopically shifted to much more radiogenic Sr isotope ratios. The increased $^{87}Sr/^{86}Sr$ ratios would then evolve to even more radiogenic values (comparable to those seen in the pyroxenites) over a period of > 1Ga.. Hydrothermally altered Archean greenstones indicate that the oxygen isotope composition of the ancient oceans were essentially similar to those of the present day (Hoffman et al 1986, Muelenbachs 1986). Melting of various horizons of hydrothermally altered oceanic crustal sections generated in the Proterozoic would therefore produce the observed scatter between $\delta^{18}O$ and $^{87}Sr/^{86}Sr$ ratios in the pyroxenite suite. Incorporation of small amounts of sediment (< 1%) or sediment derived fluid would contribute only minor increases in $\delta^{18}O$ values (Fig. 7.4).

The high $\delta^{18}O$ values and $^{87}Sr/^{86}Sr$ ratios of the two Cr-pyroxenites, GP101a CPX and GP188 CPX are consistent with these two samples being derived from a source containing oceanic crust which has been altered at relatively low temperatures (< 300°C, Figure 7.7). The uppermost sections of ophiloite sequences (dikes and pillow lavas) frequently record the highest $\delta^{18}O$ values in the section (Gregory and Taylor, 1981, and Cocker et al 1982) due to pervasive zeolite facies alteration. The most likely part of the oceanic crustal section incorporated into the source of GP101a and GP188 is therefore the upper section consisting of sheeted dykes or pillow lavas. This is compatible with the more radiogenic Pb isotopic composition of GP101a CPX and GP188 CPX (Table 6.5) which plot to the right of the geochron on Pb isotope diagrams. The upper portions of oceanic crust generally acquire increased U/Pb ratios during hydrothermal alteration by seawater (Michard and Alberade 1986). If GP188 CPX and GP101 CPX maintained higher U/Pb ratios than the rest of the pyroxenite suite over long periods of time, their Pb isotopic compositions would evolve to the right of the geochron but would retain high $\Delta 7/4$ values.

Recent petrogenetic models of the origin of eclogite xenoliths also require that they are either melts or, the metamorphosed products of ancient, hydrothermally altered oceanic crust (Jagoutz et al 1979, Gregory and Taylor 1986, MacGregor and Manton 1986, Kyser 1986, and Ongley et al 1987). The oxygen isotopic similarity of the Beni Bousera pyroxenites to eclogite xenoliths complements their similarities in major element and radiogenic isotope geochemistry and provides a strong case for long term recycling of oceanic lithosphere back into the mantle.

7:2.4 Oxygen isotope conclusions.

1) CPXs from Beni Bousera peridotites show a relatively restricted range of O-isotope compositions, within the range shown by present day MORB and CPXs from mantle peridotite xenoliths.

2) The peridotite O-isotope variation does not correlate with radiogenic isotopes, LREE depletion/enrichment or ΔFeO enrichment. The present data set does not conflict with petrogenetic models established in previous chapters but provides no further constraints on their genesis.

3) The pyroxenite suite displays large magnitude, fine scale O-isotope heterogeneity, $\delta^{18}O$ values ranging from slightly lower than the peridotites (+ 4.9 ‰) to much higher values (+ 9.3 ‰). This range in $\delta^{18}O$ values is inconsistent with models involving derivation of the pyroxenites from the host peridotites.

4) The large range in pyroxenite O-isotope compositions cannot result from petrogenetic processes involving only depleted mantle-type reservoirs. The pyroxenite O-isotope diversity is compatible with their derivation by melting subducted oceanic lithosphere which has suffered varying degrees of hydrothermal alteration. This petrogenetic model is consistent with the major, trace element and radiogenic isotope geochemistry of the pyroxenites.

5) The O-isotope variation in the pyroxenite suite is similar to that seen in some eclogite xenoliths and reinforces geochemical and petrological similarities of the 2 rock groups. The oxygen and radiogenic isotope geochemistry of eclogite xenoliths also indicate derivation from a subducted, hydrothermally altered oceanic crustal source (McGregor and Manton 1986 and Shervais et al 1988) and imply close genetic links between the Beni Bousera pyroxenites and eclogite xenoliths from kimberlite pipes.

7:3 Carbon Isotope Geochemistry.

7:3.1 Sample selection, data representation and precision.

Bulk carbon isotope compositions (Table 7.2) were measured on graphite flakes from the Beni Bousera graphitic garnet clinopyroxenites (GGP), 33 analyses, 4 graphitic kinzigite gneisses which surround the peridotites and 2 graphites associated with Ca-Ni-Fe mineralized veins which cross-cut the emplacement fabric of the peridotites. In addition, graphite from 4 graphitic peridotites and 2 lower crustal gneiss xenoliths from kimberlite pipes were analysed for comparitive purposes (Table 7.2). Graphites were

hand picked from the host rocks and washed ultrasonically in 10 % HNO_3 for 30 minutes prior to analysis (see Appendix 4.10).

Carbon isotope analyses are reported in Delta notation, in units of permil relative to the V-PDB standard.

$$\delta^{13}C \text{ ‰} = [(^{13}C/^{12}C_{SAMPLE} - ^{13}C/^{12}C_{STANDARD} / ^{13}C/^{12}C_{STANDARD}) - 1] * 1000$$

Analytical precision was assessed by replicate analyses of samples and an Open University internal diamond standard and found to be typically +/- 0.1 ‰.

7:3.2 Carbon isotope variations.

7:3.2a Graphitic pyroxenites:

The carbon isotope composition of graphite in the GGP varies from $\delta^{13}C$ = - 16.4 ‰ to - 27.6 ‰ with a mode at ~ - 21 ‰ slightly skewed towards isotopically lighter compositions (Fig. 7.8). This range extends to isotopically lighter values than those recorded by Slodkevich and Lubkov (1983). Graphite extracted from aggregates with more regular, cubic symmetry (see Chapter 3) have a much narrower and isotopically lighter range in carbon isotope compsition than graphite from aggregates with no obvious symmetry (Fig. 7.9). Graphite from cores of aggregates with cubic symmetry and their irregular graphite coats show a wide variation in $\delta^{13}C$ ($\delta^{13}C$ = - 18.5 ‰ to - 27.6 ‰) including the most isotopically light value (Figure 7.9). In Chapter 3 it was tentatively proposed that the irregular "fibrous" coat graphite surrounding cores of regular cubic symmetry, including macles, could be graphitized coated diamonds. Coated diamonds are characterized by having cores of diamond with cubic symmetry which may have widely varying $\delta^{13}C$ values, approximately -8 to -20 ‰ (Boyd et al 1988 and S.R.Boyd pers.comm.). The $\delta^{13}C$ value of their rounded, fibrous coat always plots in a restricted range of $\delta^{13}C$ from ~ - 8 ‰ to - 6 ‰ (Fig. 7.10). $\delta^{13}C$ values of coat-core pairs from the Beni Bousera coated graphite octahedra have very similar, sometimes identical, $\delta^{13}C$ values to those of their coats (Fig. 7.10).

Significant $\delta^{13}C$ variation also exists in graphite from different regions of a GGP layer, graphite in the 2.5m thick GGP layer in the Oued el Jouj varying from - 18.2 ‰ to - 21.7 ‰ (Fig. 7.11). From the limited data set there does not appear to be any correlation between amount of graphite present and its carbon isotopic composition in the GGP.

The only other comparably light $\delta^{13}C$ depleted values of primary igneous graphite were recorded by Pineau et al (1987) in ultramafic xenoliths from Eggere, Algeria. Primary graphite in harzburgite and lherzolite xenoliths from kimberlites give "typical mantle" $\delta^{13}C$ values of - 4.8 to - 7.9 ‰ (Table 7.2).

7:3.2.b Kinzigites:

Five analyses of graphite from kinzigites were performed on four rocks, the data are combined with that presented by Slodkevich and Lobkov (1983) in Figure 7.8. The kinzigite $\delta^{13}C$ values vary from - 17.5 ‰ to - 22.5 ‰ (Table 7.2) with a mode at - 20 ‰, very close to the mode of the GGP graphite. The carbon isotope composition of graphite from the kinzigites is mostly within the range found in just 2

TABLE 7.2

Carbon isotope analyses of graphite from Beni Bousera pyroxenites, kinzigites and Cu-Ni mineralised veins. Graphites from peridotite and crustal xenoliths in kimberlite also reported.Data reported in units of permil (‰) relative to the V-SMOW standard.

SAMPLE	$\delta^{13}C$ ‰
PYROXENITES	
CORE/COAT PAIRS	
GP75 CORE	-24.6
GP75 COAT	-21.9
GP75b CORE	-27.5
GP75b COAT	-27.6
GP146 CORE	-19.5
GP146 COAT	-18.6
GP147a CORE	-20.6
GP147a COAT	-22.3
PHN5734 CORE	-22.1
PHN5734 COAT	-22.1
REGULAR (CUBIC) SYMMETRY	
GP25 CORE	-25.2
GP48	-21.1
GP81	-20.5
GP144	-21.3
GP146 OCTA	-20.1
GP146 CORE	-20.4
GP147b	-21.7
GP147d CORE	-20.7
GP209a	-20.0
GP209b	-20.9
GP211 OCTA CORE	-21.5
IRREGULAR SYMMETRY	
GP25	-16.4
GP25 I	-25.2
GP25 II	-25.0
GP80	-19.6
GP84	-24.5
GP143	-19.4
GP146/2	-17.7
GP147b	-19.9
GP147 IR	-20.5
GP148	-18.2
GP149a	-20.6
GP211b	-21.0
	-21.1

SAMPLE	$\delta^{13}C$ ‰
KINZIGITES	
GP5a	-17.5
GP5b	-20.3
GP54	-20.0
GP57	-21.0
GP161	-22.5
	-22.4
	-22.5
VEIN GRAPHITE	
GP9	-16.1
GP202	-15.9
PERIDOTITE XENOLITHS	
PHN5633a	-6.9
	-6.5
PHN5633c	-6.3
PHN5633d	-7.9
PHN2492	-5.8
SEH500/1	-5.4
SEH500/2	-4.8
FRB888/1	-5.0
LOWER CRUSTAL XENOLITHS	
PHN1922	-14.4
PHN4250a	-21.3

graphites recorded in this study from Southern African lower crustal xenoliths in kimberlites. Graphite from sample GP5 shows a $\delta^{13}C$ variation of almost 3 permil (- 17.5 to - 20.3 ‰).

7:3.2c Vein graphite:

Only 2 samples of vein graphite were analysed for carbon isotopes; these data are combined with 5 analyses from Slodkevich and Lobkov (1983) and Slodkevich (pers.comm.) in Figure 7.8. The vein graphite $\delta^{13}C$ values range from - 13.8 ‰ to - 17.6 ‰ with no well defined mode.

7:3.3a Discussion: The genesis and relationship of graphite parageneses at Beni Bousera.

The carbon isotope composition of all three graphite parageneses overlap to some extent (Fig. 7.9), which raises the possibility that all three varieties originated from the same source. Convincing evidence is presented in Chapter 3 that the graphite in the GGP represent graphitized diamonds. The morphology of the GGP graphite aggregates and the mineral chemistry and facetted nature of their silicate inclusions indicate the original diamonds grew in the diamond stability field. Hence, the carbon that formed the original diamonds in the GGP cannot be the same as that which precipitated the graphite in the kinzigite gneisses or the graphite mineralized veins in the peridotite. The carbon isotope similarity between the GGP graphite and the kinzigite and vein graphite could be a secondary effect, produced by carbon isotope buffering of the GGP graphite by large scale interaction with a crustally derived carbonaceous fluid phase. This possibility will be examined after the genesis of the kinzigite and vein graphite has been discussed.

7:3.3b Kinzigites

Graphite flakes in the kinzigites are parallel to the metamorphic foliation and are affected by the same episode of folding which deformed the host rock, hence this graphite was generated either pre- or syn-deformation. The origin of the graphite by precipitation from a non-pervasive CO_2 gas phase streaming from the mantle (e.g. Newton et al 1980) is not supported by the isotopically light composition of the graphite. Such extreme $\delta^{13}C$ values could only be produced by extreme (> 90 %) Rayleigh fractionation of a mantle carbon reservoir of $\delta^{13}C = -7$ ‰. Valley (1986) states that there is no clear mantle carbon signature in granulite facies ortho- and para- gneisses containing small amounts of graphite. Analyses of CO_2 from fluid inclusions in incipient charnockites from S.India by Jackson et al (1988) do provide some evidence for CO_2 of mantle origin being involved in the genesis of granulite facies rocks. The ultimate source of the isotopically light graphite in the Beni Bousera kinzigites may have been carbonaceous organic matter contained in the original pelitic assemblage. Volatilization of this graphite as CO_2 may have induced partial melting and migmatization of the kinzigites close to the peridotite contact. This is supported by the graphite poor nature of the migmatitic kinzigites. Graphite in the kinzigites may therefore originate as the metamorphic product of organic carbonaceous material present in the original pelitic assemblage, or by precipitation when a CO_2 rich fluid (derived from oxidation of such carbonaceous matter) infiltrates low fO_2 rocks under granulite conditions (eg. Glassley 1982, Lamb and Valley 1984). Graphite of pre-metamorphic, biogenic origin is often preserved in granulites (Lamb and Valley, 1984). A biogenic origin for the kinzigite graphite is consistent with its isotopically light carbon isotope signature.

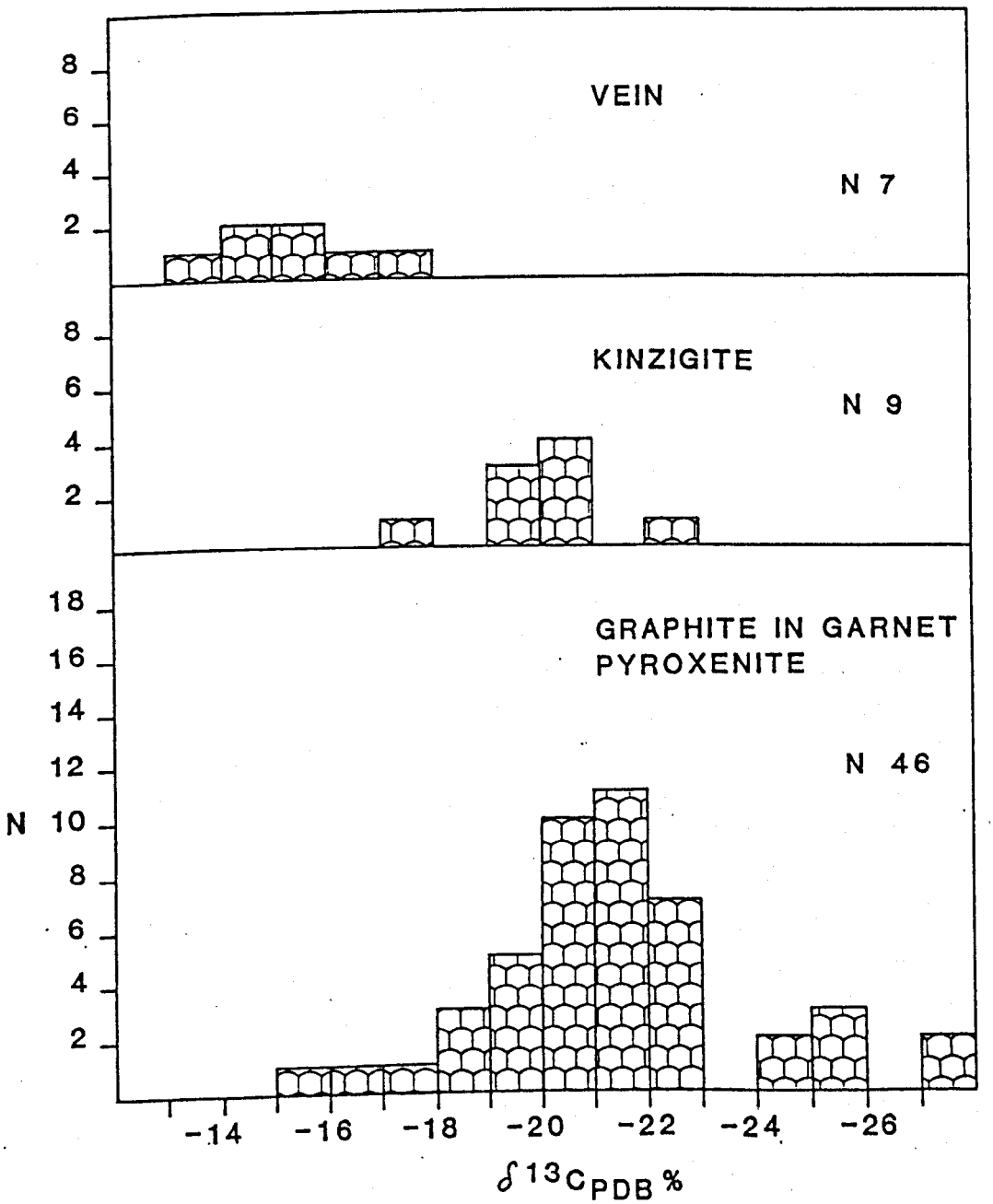

Figure 7.8. Carbon isotopic composition of graphite from the Beni Bousera GGP, kinzigites and Cu, Ni minera lised veins. N = number of samples analysed. Data includes analyses from Slodkevich and Lobkov (1983) and Slodkevich (pers.comm.).

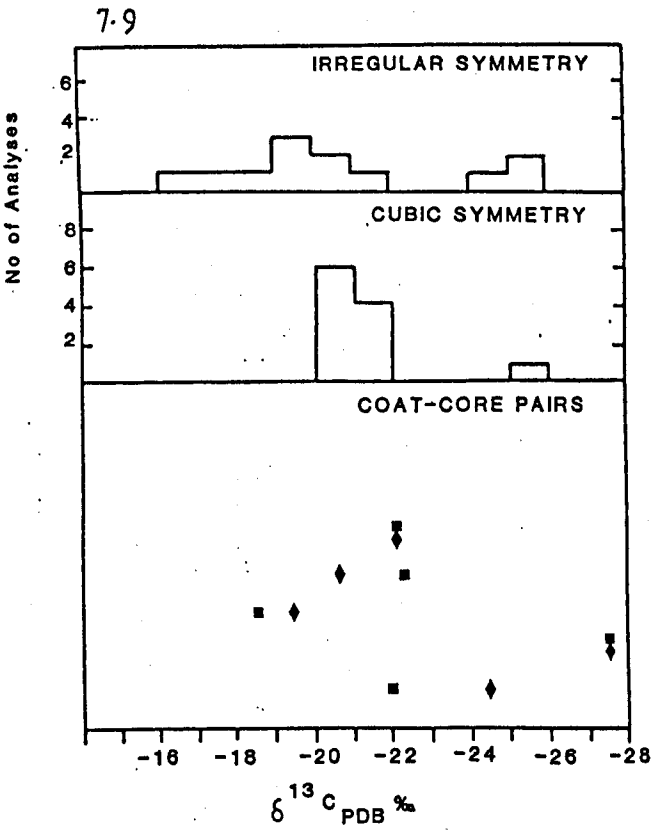

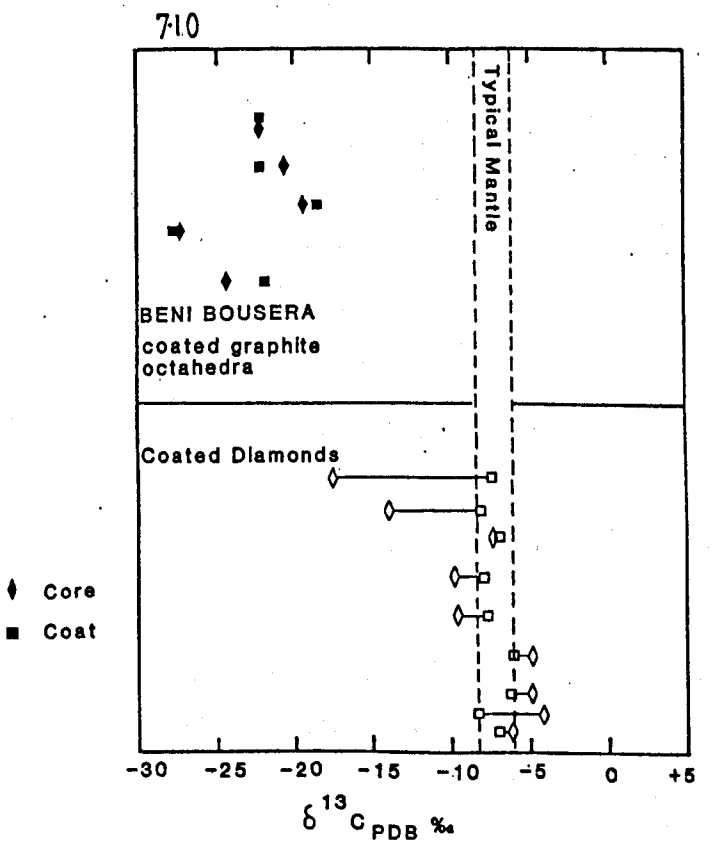

Figure 7.9. Carbon isotopic composition of GGP graphite of irregular symmetry compared to aggregates possessing regular, cubic symmetry and core-coat pairs.

Figure 7.10. Carbon isotopic variation between coat and core of Beni Bousera GGP coated graphite aggregates compared to that displayed by coated diamonds. Diamond data from Boyd et al (1987).

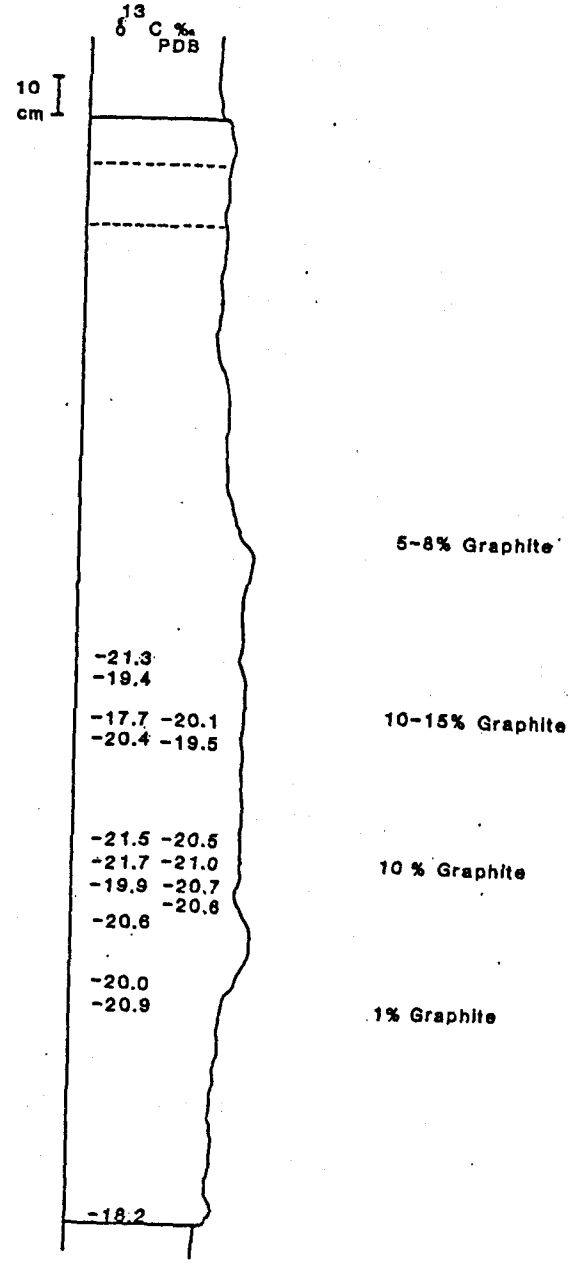

Figure 7.11. Carbon isotopic composition (values in $\delta^{13}C$ per mil.) of graphite aggregates sampled at varying heights in the GGP layer outcropping in the Oued el Jouj (Chapter 2).

7:3.3c Vein graphite:

The majority of global economic graphite vein deposits are formed at high temperature under upper amphibolite to granulite facies conditions (Frost 1979). Mixed C-H-O volatile equilibria calculations (Frost op.cit.) show that high temperature graphite veins can form by reduction of a CO_2 bearing fluid phase, carbon being transported in the fluid phase from a graphitic gneiss into a graphite vein. The stability field of graphite plus fluid in the C-H-O system expands with falling temperature at the expense of the fluid-only field. A hot fluid, almost saturated with graphite (derived via melting of the kinzigites ?) will precipitate graphite as it cools and flows through a fracture (Frost 1979), thus producing graphite mineralized veins.

This mechanism for generating graphitic veins can be applied to the vein paragenesis graphite from Beni Bousera. Raman spectroscopy indicates that the vein graphite is of high temperature origin (~ amphiholite - granulite grade, Chapter 3) and hence compatible with the following model:

A) Peridotite emplacement into the kinzigites at a mid to lower crustal level induces local migmatization with a CO_2 rich fluid phase being evolved as the graphite is oxidized. The evolution of a CO_2 rich fluid phase may actually promote migmatization (Newton et al 1980).

B) The CO_2 bearing fluid, almost saturated with carbon, infiltrates the peridotite which is undergoing serpentinization.

C) The lower fO_2 environment of the peridotite and serpentinizing fluids causes reduction of the CO_2 vapour and precipitation of graphite.

Several observations support this hypothesis:

1) Although the carbon isotope compositions of the kinzigite and vein graphite overlap, the vein graphite is generally more ^{13}C enriched than the kinzigite graphite. This isotopic shift is compatible with the CO_2 bearing fluid being evolved from the kinzigites by gaseous fractionation as the CO_2 should be isotopically heavier than its source (Bottinga 1969).

2) fO_2 conditions in peridotites undergoing serpentinization are known to be highly reducing (Moody 1976) as indicated by the presence of secondary native metals and awaruite in the Beni Bousera peridotites (Chapter 2 and Lorand 1985). A highly reducing environment is ideal for the reduction of CO_2 bearing fluids to graphite.

3) Most of the graphite veins are close to, or on the peridotite/kinzigite contact indicating rapid reduction of the CO_2 bearing fluids on entering the peridotites along fractures.

4) The Cr - Cu -Ni - Fe mineralized nature of the graphitic veins is compatible with the CO_2 bearing phase from the kinzigites mixing with reducing, serpentinizing fluids which were transporting Cr, Ni and

Fe, perhaps in the form of carbonyl complexes.

It is significant that a combination of graphite and CO_2 in the presence of pyrrhotite (a common secondary mineral in the peridotites) is thought to generate carbonyls of Ni, Cr, Co and platinum group elements (Hopwood 1981). High temperature carbonyls are stabilized at high pressure i.e. mid to lower crust (Hopwood, op.cit.) and reducing conditions. The presence of carbonyl complexes in the serpentinizing fluid / CO_2 phase mixture could account for the high PGE contents recorded by Lorand and Zdenek (1986) in the Beni Bousera Cr - Ni - Cu - Fe mineralized graphite veins.

7:3.3d Graphite in the GGP:

The similarity in modes of the carbon isotope distribution of the GGP graphite and the kinzigite graphite (Figs. 7.8 & 7.12) raises the possibility that the GGP graphite has been buffered by a carbonaceous fluid phase derived from the kinzigites. This fluid phase cannot be the same as that which created the graphite veins in the peridotites as the vein graphite is isotopically heavier than the kinzigite graphite, whereas the GGP graphite is more isotopically light.

The following evidence argues against a late stage origin for the GGP graphite: The lack of graphite intersecting the margins of the GGP, the restriction of graphite to 2 out of the hundreds of pyroxenite layers in the massif, the presence of faceted silicate inclusions in the octahedral graphite and most importantly, the presence of cubic graphite inclusions within primary CPX (Slodkevich 1980b). The only plausible way to alter the primary carbon isotopic composition of the GGP graphite is by buffering due to large scale interaction with a carbonaceous fluid phase with $\delta^{13}C$ value of at least - 27 ‰. Leaching experiments performed on CPX separates from the GGP prior to radiogenic isotope analyses (Chapter 6) indicate that the GGP have suffered interaction with a secondary, crustal derived fluid, syn or post emplacement. Microthermometry demonstrates that the Kinzigites contain pure CO_2 bearing fluid inclusions in their silicates. CO_2 bearing fluids derived from the crustal graphitic gneisses (kinzigites), would be characterized by $\delta^{13}C$ values equal to or heavier than their carbonaceous source. Assuming that the original $\delta^{13}C$ value of the GGP graphite had typical diamond values of ~ - 6 ‰, a fluid $\delta^{13}C$ value of at least -27.5 ‰ would be required to buffer the carbon isotopic composition of the graphite aggregates to their present composition. Such a fluid would only be produced by mobilization of graphite remaining in the kinzigites after at least 70 % Rayleigh fractionation of the original graphite, i.e. less than 30 percent remaining at relatively low T (<700°C). This residual graphite would then need to be remobilized.

Several observations argue against this fluid buffering hypothesis:

1) There is no isotopic gradient in graphite aggregates of large radius e.g. GP75b, ~ 7mm of graphite separates the areas where the coat and core specimens were taken from but their carbon isotopic compositions are identical (within error). Assuming the carbon isotopic composition of the original graphite was a typical mantle value ($\delta^{13}C$ - 6 ‰) at least some isotopic gradient would be expected in the graphite over 7 mm in radius at temperatures below 700 °C.

2) Evidence of pervasive infiltration of high temperature carbonaceous fluid phase would be expected in more than just 2 pyroxenite layers.

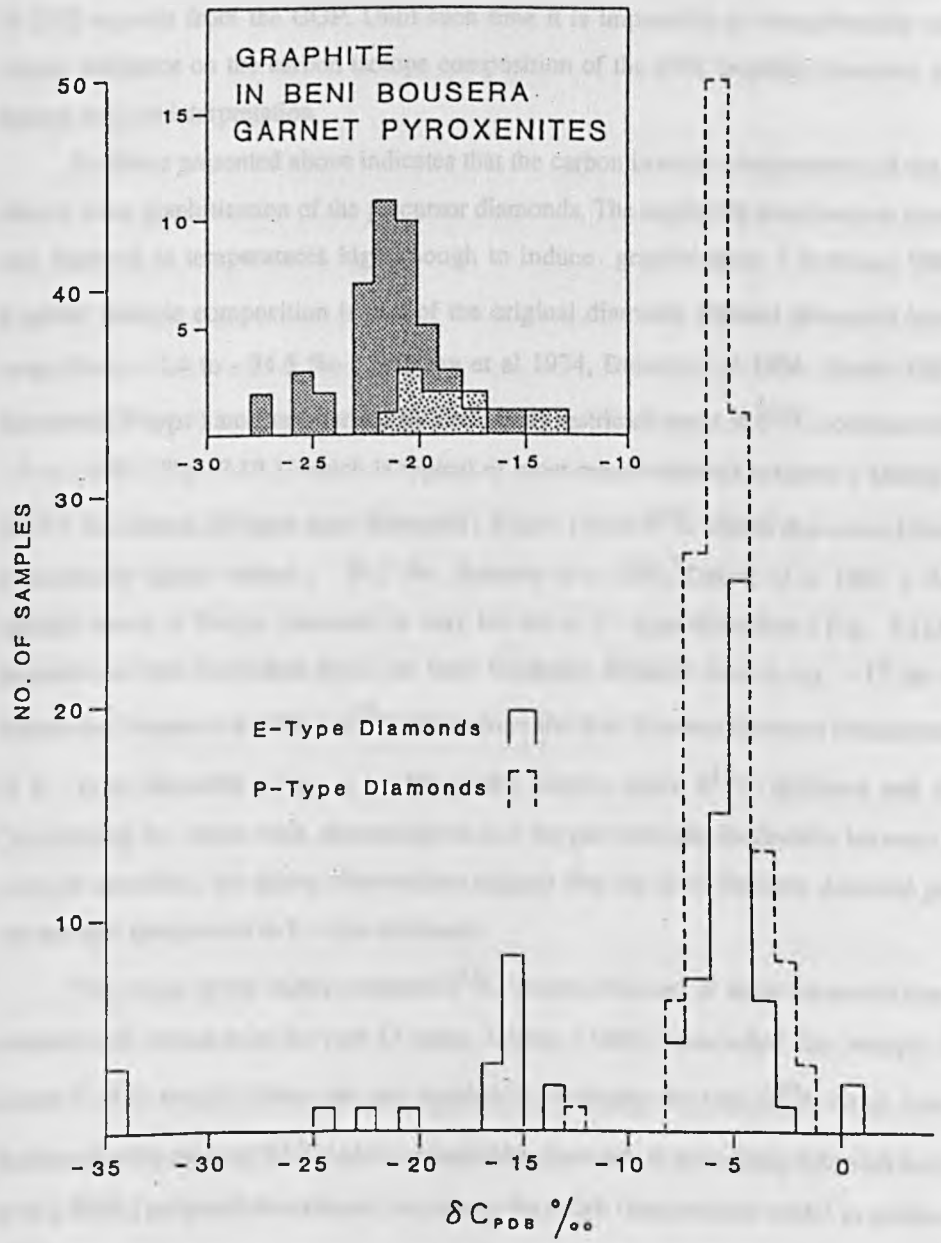

Figure 7.12. Carbon isotopic composition of the GGP graphite (heavy stipple) and Kinzigite graphite (light stipple) compared to the range shown by P and E-type diamonds. Diamond data from Sobolev et al (1979) and Deines et al (1987).

3) Although methane bearing fluids from the kinzigites could produce lighter $\delta^{13}C$ values in the fluid phase than the residual graphite, there is no evidence for such fluids, whilst the isotopic composition of the vein graphite is shifted in the wrong direction (i.e. to higher $\delta^{13}C$ values).

4) Oxygen isotope equilibrium relationships exhibited by coexisting GT and CPX phases in the GGP do not suggest extensive infiltration of relatively high temperature crustal fluids.

The problem of whether the GGP graphites record the carbon composition of their diamond precursors will only be resolved by analysing the carbon isotope composition of cubic graphite inclusions in CPX crystals from the GGP. Until such time it is impossible to unequivocally rule out a late stage, crustal influence on the carbon isotope composition of the GGP graphite, however, available data argue against such an interpretation.

Evidence presented above indicates that the carbon isotopic compositions of the GGP have not been altered since graphitization of the precursor diamonds. The negligible fractionation factor between graphite and diamond at temperatures high enough to induce graphitization (Bottinga 1968) means that the graphite isotopic composition is that of the original diamond. Natural diamonds have $\delta^{13}C$ values that range from + 2.4 to - 34.5 ‰ (Sobolev et al 1974, Deines et al 1984, Harris 1987) Peridotite suite diamonds (P-type) are characterized by a relatively restricted range in $\delta^{13}C$ contents with a marked mode ~ - 5 to - 6 % (Fig. 7.12), which is typical of most mantle derived magmas (Mattey et al 1984, Mattey 1987). In contrast, Eclogite suite diamonds (E-type) have $\delta^{13}C$ values that extend from heavier (+0.5‰) to markedly lighter values (- 34.5 ‰, Sobolev et al 1979, Deines et al 1984). Although the carbon isotopic mode of E-type diamonds is very similar to P - type diamonds (Fig. 7.12), E - type diamond populations from individual pipes can have markedly different modes, e.g. ~ 12 ‰ for Argyle E - type diamonds (Jaques et al 1986). $\delta^{13}C$ values from the Beni Bousera diamond pseudomorphs lie in the range of E - type diamonds (Fig. 7.1) but to the scarcer, more $\delta^{13}C$ depleted end of the distribution. Considering the whole rock, mineralogical and oxygen isotopic similarities between the GGP and some eclogite xenoliths, the above observations suggest that the Beni Bousera diamond pseudomorphs are of comparable paragenesis to E - type diamonds.

The origin of the highly depleted $\delta^{13}C$ values observed in some diamonds has been the subject of considerable debate over the past 15 years. Deines (1980) concluded that isotopic fractionation from a mixed C-H-O volatile phase was not capable of producing the total $\delta^{13}C$ range seen in diamonds. This implies that the range of $\delta^{13}C$ values recorded by diamonds is essentially inherited from their source. Javoy et al (1986) proposed an extreme, multistage Rayleigh fractionation model to produce the large range of $\delta^{13}C$ observed in diamonds but did not specify the nature of this process, eg compositions of gas phase etc.

One explanation of the origin of the large $\delta^{13}C$ range recorded by diamonds is to assume that it is inherited from heterogeneities created during the accretion of the Earth (Deines 1989). Another alternative is that the diamond $\delta^{13}C$ range is produced by subduction of a mixture of kerogenous carbon ($\delta^{13}C$ approx. - 20 ‰ to - 35 ‰) and marine carbonates ($\delta^{13}C \sim 0$ ‰), (Sobolev et al 1979, Milledge et al 1983). Subduction of carbonaceous sediments has been advocated by Jaques et al (1986) to explain the

dominantly $\delta^{13}C$ depleted signatures of the Argyle E - type diamonds ($\delta^{13}C$ mostly - 9 to - 12 ‰). Stable isotope studies of back arc basin glasses (Mattey et al 1984, Exley et al 1986) and mantle derived diopsides (Mattey et al 1986) provide compelling evidence for the subduction of marine sediments into relatively deep mantle source regions (~ 100 km). Whether subducted, carbonaceous marine sediments can survive subduction to be incorporated into the deep lithospheric mantle or the asthenosphere remains controversial (see Mattey 1987 for discussion). The varied, predominantly heavy $\delta^{18}O$ values of the Beni Bousera pyroxenites (GGP $\delta^{18}O$ CPX + 5.2 ‰ to + 7.5 ‰), together with their Pb - Sr - Nd isotopic systematics support a near surface, oceanic crustal origin with incorporation of varying amounts of sediment (<1 %). Subducted kerogenous oceanic sediments, perhaps protected in grabens on the sea floor, are a possible source for the isotopically light carbon in the GGP diamond pseudomorphs. The association of isotopically light carbon in the GGP with highly radiogenic initial $^{87}Sr/^{86}Sr$ ratios (0.7051 to 0.7109) and relatively unradiogenic $^{143}Nd/^{144}Nd$ ratios (0.51300 to 0.51254) is similar to the $\delta^{13}C$ - Sr - Nd isotope relationships observed by Mattey et al (1986) in both anhydrous and hydrous suites of Bullenmerri (Australia) diopsides and in diopsides from the Foster Crater (Antarctica) and Bulfontein (S.Africa). The combined stable and radiogenic isotope signatures of the Beni Bousera GGP and the mantle diopsides studied by Mattey et al (1986) may be evidence for the recycling of an organic carbon component from subducted oceanic sediments deep into the mantle. The subducted sediment/oceanic crust isotopic signature may be stored in the deep continental lithosphere or on the asthenosphere/mesosphere boundary until reactivated by diapirism or magmatism (Hofmann and White 1982, Allegre and Turcotte 1985).

Finally if the rounded to irregular graphite "coats" on octahedral cores of the GGP graphite aggregates represent coated diamonds the typical carbon isotope relationship between core and coat diamond (e.g. Boyd et al 1988) is not evident (Fig. 7.10). In the Beni Bousera case this may be due to carbon isotopic equilibration between coat and core, due to the very high temperatures required to completely graphitize diamonds on a geologically reasonable time scale (i.e. less than the age of the Earth).

7:4 Conclusions from carbon isotope geochemistry.

The main conclusions from carbon isototpe analyses of the different Beni Bousera graphite occurrences are:

1) The GGP contain graphite that is very isotopically depleted ($\delta^{13}C$ - 16.4 to - 27.6 ‰) relative to normal mantle values.

2) The $\delta^{13}C$ range of the GGP graphite overlaps that of the graphitic kinzigites which surround the ultramafic massif. Isotopic interaction between these two carbon reservoirs is impossible to rule out with the present data set but seems unlikely.

3) If the $\delta^{13}C$ values recorded by the GGP graphite are those of the original diamonds, the carbon may have originated from kerogenous material present in sediment subducted into the source of the GGP.

4) If some of the GGP graphite aggregates were originally coated diamonds with contrasting coat/core isotopic compositions, this isotopic heterogeneity has been destroyed by high temperature graphitization.

CHAPTER 8

SUMMARY

8:1 Origin of the graphite aggregates in the GGP.

Morphological and X-ray crystallographic observations and the presence of cubo-octahedral faceted GT and CPX inclusions in the graphite aggregates from the GGP provide convincing evidence that they represent graphitized diamonds (Slodkevich 1980 a and b, Pearson et al 1989). Some of the precursor diamonds may have been coated stones (Chapter 3). Detectable quantities of Na in GT inclusions in octahedral graphites and in the GGP host rocks independantly suggest that the GGP originated from within the diamond stability field.

8:2 The stability of diamond in the upper mantle.

The thermodynamically metastable existence of diamond at the surface of the Earth is mainly a result of the high activation energy required to initiate its inversion to the low pressure allotrope of carbon, graphite. Experimental studies of graphitization at various temperatures (Evans 1976) indicate that the rate of diamond inversion to graphite increases exponentially as the temperature is raised. Retardation of the rate of graphitization due to increasing pressure indicates that the rate controlling step during graphitization is the detachment of single carbon atoms from the diamond surface (Evans 1976). Consequently, the activation energy for graphitization of { 111 } faces is higher than that for { 110 } faces due to the fewer C-C bonds to be broken. The rate of graphitization of a particular face is proportional to:

$$e(- E/kT) \qquad (8.1)$$

where E = the activation energy for that face, k = Boltzmann's constant, T = Absolute temperature

The rate of graphitization per unit time can be expressed as;

$$dx/dt = Ce^{-(\Delta E + P\Delta V)/RT} \qquad (8.2) \quad \text{(Evans 1979)}$$

where C is a constant related to the density of active sites, R = the gas constant, ΔV = the activation volume, P = pressure.

The $P\Delta V$ term accounts for the decrease in graphitization rate with increasing pressure. Using values for the parameters in equation 8.2 given in Davies and Evans (1972), Eggler (1986) produced a graph of weight of diamond graphitized vs time. This indicated that 1 carat (0.2 g) diamonds would take less than 1 Ma to graphitize at 1200 ^{o}C and 20 kb along { 110 } faces. If the same parameters are used to calculate graphitization rates along the slower { 111 } direction (E = 1066 kJ mol $^{-1}$ compared to 730 KJ mol $^{-1}$ for { 110 }) a 1 carat (0.2 g) diamond would take less than 20 Ma to completely graphitize at

1300 °C and 40 kb (pressure has a relatively small effect on the graphitization rate). Diamond bearing peridotite xenoliths are probably at least 1 Ga old (Nixon et al 1987), whilst inclusions within P-type diamonds suggest the diamonds are probably nearer 3.5 Ga old (Richardson et al 1984). Shee et al (1982) suggest equilibration temperatures of at least 1150 °C for 2 diamondiferous lherzolite xenoliths from South Africa whereas diamondiferous eclogite xenoliths record temperatures of up to 1300 °C and $CHUR_{Nd}$ model ages of > 1 Ga (Smith et al 1986). The above data suggest that both E-type and P-type diamonds have been held at ambient upper mantle temperatures (~ 1200 °C) for hundreds of millions of years, yet none of the diamonds from the xenoliths studied above show any significant signs of graphitization. This suggests that the available experimental data are not adequate to quantitatively assess rates of diamond graphitization.

Clearly from the above discussion, increasing temperatures above "normal" mantle conditions (1100 - 1300 °C) will significantly increase graphitization rates due to the exponential form of equation 8.2. Complete graphitization of the original diamonds in the Beni Bousera garnet clinopyroxenites, (GGP) upto 7mm in radius implies that the GGP have been subjected to enhanced temperatures of probably greater than 1300 °C to produce graphitization of such large diamonds over a time scale shorter than the age of the Earth. This conclusion is consistent with the high temperatures, over 1400 °C, estimated from recombining exsolved CPX from the GGP (Chapter 4). Similar, pre-exsolution equilibration temperatures have been estimated for garnet pyroxenite layers from other orogenic peridotites in the Pyrenees (Conquere 1977) and are consistent with the Beni Bousera massif being emplaced into the crust diapiric processes.

8:3 Implications for the origin of anomalous diamond occurrences:

Diamonds are found in several areas of the world where their commonly accepted source, kimberlite-lamproite volcanism is unknown (see reviews by Kaminski et al 1981 and Nixon et al 1986). Furthermore, some of these occurrences occur away from the cratonic regions where diamondiferous volcanics commonly occur. Some of the alluvial or placer diamond sources have recognised or probable distant cratonic sources and are associated with typical diamond indicator minerals such as low Ca chrome-pyrope garnets (e.g. Namibia, Figure 8.1). Other diamond occurrences are not obviously kimberlite-related but occur in, or near collision zones which have emplaced orogenic and ophiolitic peridotite massifs into the crust (Figure 8.1). Diamond has been reported in low concentrations in orogenic peridotites, but the certainty of these finds is debatable (see Kaminski et al 1981). Diamonds have rarely been reported from the primary source rock but occurr in adjacent alluvial deposits. Orogenic peridotites are generally considered to originate from depths well above the diamond stability field e.g. Nicolas (1986), where graphite is the stable form of carbon. The discovery and confirmation of graphite pseudomorphs after diamond in the Beni Bousera massif indicates that this massif, at least, originated from within the diamond stability field. The Beni Bousera occurrence lends support to the theory that diamond occurrences close to or within orogenic belts could originate from orogenic peridotite massifs (Kaminski et al 1981, Dawson 1983, Nixon et al 1986, Pearson et al 1989).

Recently it has been proved that tectonically emplaced peridotite massifs can transport diamond into the crust without it suffering graphitization. Fang and Bai (1981) and in communication to P.H.Nixon, have reported diamonds occurring within a chromite-harzburgite massif in Tibet which also forms the source of alluvial diamondiferous gravels. In the Tibetan example, evidence of garnet in the peridotites is

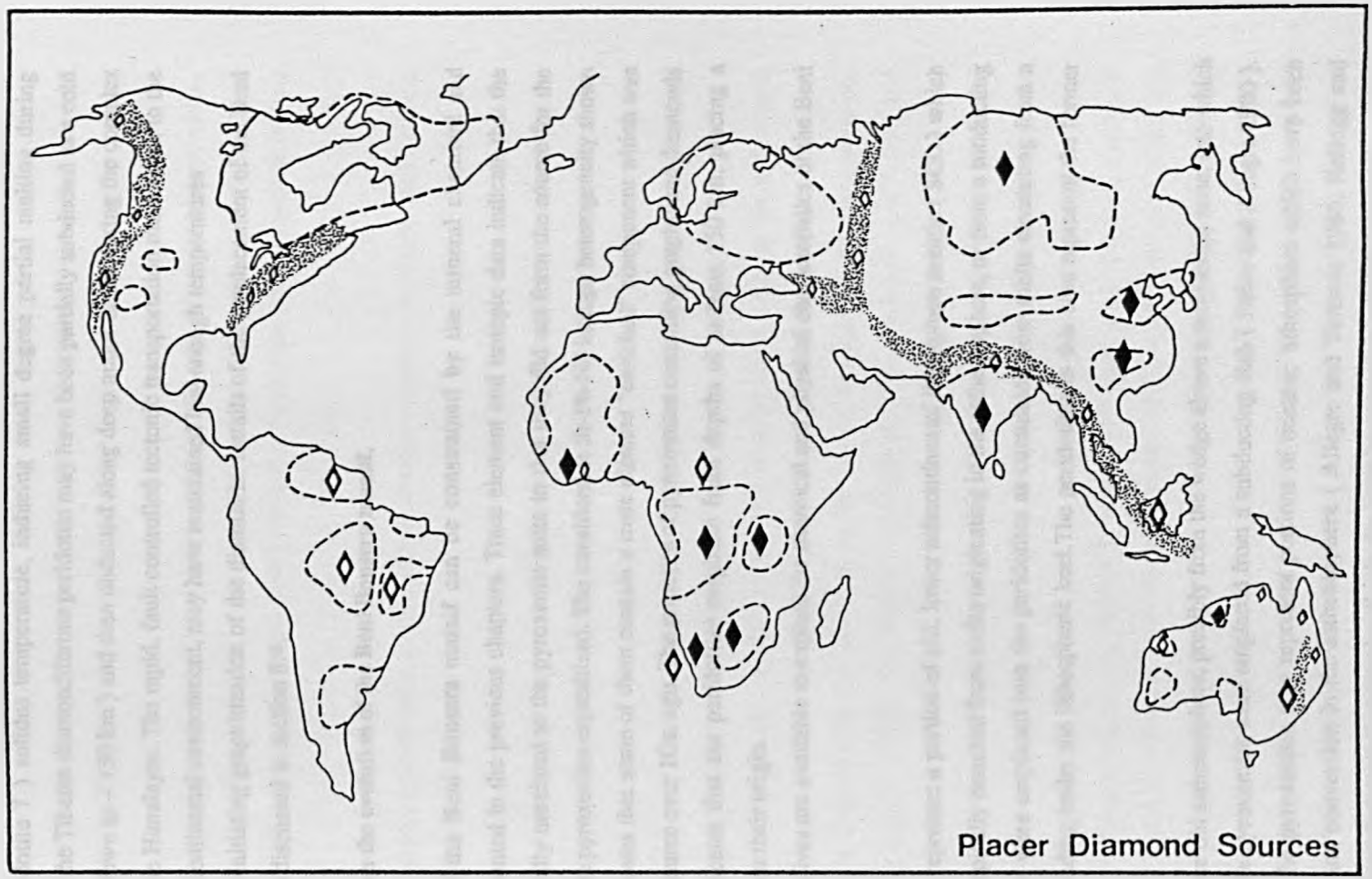

Figure 8.1. World map of secondary/placer diamond deposits, size of diamond relative to size of deposit, showing cratonic areas (dashed lines) and adjacent tectonic collision zones. Placer deposits of known source are represented by closed diamonds, those of unknown sources are open symbols. Note the proximity of placer diamonds of unknown source to collision zones which contain peridotite massifs. Fold belts/ collision zones not associated with diamond deposits are not shown for clarity. Data from Gurney (1986) and P.H.Nixon (pers.comm.).

lacking and no evidence of graphitization of the diamond is reported (P.H.Nixon pers.comm.). The diamond concentrations in the Tibetan ophiolitic peridotite are much lower than the pseudomorph concentrations found in the Beni Bousera GGP but are made economical by alluvial concentration processes. The fundamental reason for the survival of diamond here must be related to the relative emplacement temperatures and hence emplacement mechanisms of the two massifs. The Beni Bousera massif probably originated from the deep mantle as part of a hot diapiric body that was close to the pyroxenite (and peridotite ?) solidus temperature, inducing small degree partial melting during upwelling. In contrast, the Tibetan diamondiferous peridotite may have been partially subducted as a cold slab into the mantle (down to ~ 150 km) and then obducted along deep major faults during the complex collisional history of the Himalayas. The rapid, fault controlled tectonic transportation mechanism in the Tibetan case, within a continental environment, may have maintained low enough temperatures (< 1200 °C) to avoid initiating graphitization of the diamonds. Details of the emplacement of the Beni Bousera massif will be discussed in section 8:4.

8:4 Constraints on the evolution of the Beni Bousera massif.

The evolution of the Beni Bousera massif can be constrained by the mineral chemical and geochemical data presented in the previous chapters. Trace element and isotopic data indicate that the peridotites are genetically unrelated to the pyroxenite suite in that they did not form the source for the magmas from which the pyroxenites crystallized. The considerable Sr-Pb-Nd isotope heterogeneity shown by the peridotites indicates that some of them contain a trace element "enriched" component which was incorporated into the source over 1Ga. ago. The presence of pyroxenites containing graphitized diamonds in the peridotites indicates that the peridotites originate from depths of at least 150 km, placing a significant constraint on their origin.

Several alternatives are available to explain the chemical and physical characteristics of the Beni Bousera massif:

1) The massif could represent a portion of old, lower subcontinental lithosphere mantle (SCL) which has been variably isotopically enriched from melts originating in the asthenosphere, or from a subducting plate. The pyroxenites were emplaced into the peridotites as cumulates from melts emanating from a subducting slab descending under the lithospheric keel.The peridotites in this case represent the former SCL "keel".

2a) The peridotites are old asthenosphere, possibly from the wedge above a subduction zone, into which the source melts for the pyroxenites were emplaced from a subducting slab (Polve and Allegre 1980). Alternatively (2b), the pyroxenites may represent portions of oceanic lithosphere which have been thinned by diffusion and convection in the asthenosphere (Allegre and Turcotte 1986, Kellogg and Turcotte 1987). Asthenosphere was then emplaced into the crust by extension related upwelling.

3) The peridotites may be derived from a diapir originating from a thermally buoyant "megalith" of subducted oceanic crust lithosphere which ponded at the 670 km seismic discontinuity e.g. Ringwood (1982). The pyroxenites are thus melts or residues from subducted oceanic crust which formed part of the megalith. The peridotites formed the lower portion of the subducted oceanic lithosphere.

4) The peridotites may be derived from delamination of the lower SCL either into the asthenosphere or down to the 670 km discontinuity to be later reactivated by diapirism.

The validity of the above models can now be examined using constraints imposed by the pyroxenites which are summarised briefly below:

a) Major and trace element geochemistry requires the pyroxenites to be derived from a low pressure (plagioclase-bearing) heterogeneous reservoir such as subducted oceanic crust/lithosphere.

b) Large magnitude Pb-Sr-Nd isotope variations and their lack of correlation with trace element ratios, indicate old (> 1 Ga.) derivation involving subducted oceanic crust plus source enrichment from sediments. Magma extraction during subduction zone processing fractionates parent-daughter isotope relationships.

c) Oxygen isotope analysis of coexisting silicate phases strongly supports a hydrothermally altered subducted oceanic crustal source for the pyroxenites.

d) The decoupling of trace-element-isotope relationships indicates the pyroxenites have suffered recent melting and/or enrichment events, possibly during diapiric ascent from within the diamond stability field.

Field, petrological and geochemical constraints favour the pyroxenites crystallizing as cumulates from melts derived from subducted oceanic crust plus a very small amount of sediment (probably < 1 %) or sediment derived fluid. This cumulate origin from melts is contrary to an origin as thinned oceanic crust as proposed by Allegre and Turcotte (1986) and Kellogg and Turcotte (1987). Structural observations presented in Chapter 2 further refute the theory that the structures in the pyroxenites are dominantly imposed by mantle "stream line mixing" (Allegre and Turcotte op.cit. and Kellog and Turcotte op.cit.). The folding and boudinage of the pyroxenites appears to have taken place during tectonic emplacement of a rising diapir into the lower crust. This theory is supported by the parallel hinges of the folds in the pyroxenites and crustal kinzigites and the parallel kinzigite/peridotite fabric at the peridotite margins (Chapter 2).

Emplacement of the pyroxenites into the basal SCL in the Proterozoic is an attractive concept, in terms of isolating them in a relatively cool, non-convecting environment where they could reside long enough to generate the observed extreme isotopic diversity . The establishment of thick (150 to 200 km) SCL early in Earths history is confirmed by Archean model ages for P-type diamond inclusions (Richardson 1984, Boyd et al 1985). The Beni Bousera peridotites could have formed part of the basal SCL into which the pyroxenites were intruded (Alternative 1). The Kaapvaal SCL is known to contain compositionally variable peridotites (Boyd and Mertzman 1987) which may be relatively fertile or very depleted. Tectonic constraints do not favour the existance of an ancient, deep SCL "root" beneath N.Morocco (Doblas and Oyarzun 1989). However, Platt (1989) postulates the temporary existence of a 150 km thick lithospheric root beneath the western Mediteranean during late Cretaceous times. The Beni Bousera (and Ronda) peridotites and pyroxenites may be part of the old SCL which was rapidly thickened by collision in the Platt (1989) model but no suitable mechanism is apparent for emplacing

the root of a cool, non-convecting SCL into the base of the crust. Indeed, Platt's (1989) model involves removal of the SCL root which induces later extension. Emplacement tectonics therefore do not favour the origin of the Beni Bousera massif as a portion of the basal SCL.

The steep gravity gradients at the edges of both the Beni Bousera and Ronda massifs favour their origin as diapirs of asthenospheric mantle impinging into the crust (Bonini 1973, Loomis 1975, Doblas and Oyarzun 1989). Diapirs of peridotite containing layers or "blobs" of pyroxenites of oceanic crustal origin may be present in the asthenosphere, ultimately being derived from thermally unstable megaliths of subducted oceanic crust plus lithosphere residing on either the 670 km seismic discontinuity (Ringwood 1982) or the core-mantle boundary (Hoffman and White 1982).

8:5 Petrogenesis of the peridotite/pyroxenite massif.

The model summarized below is proposed to explain the petrological evolution of the Beni Bousera massif and is believed to be the most consistent with the available geochemical data. The evolutionary sequence (summarised diagramatically in Figure 8.2) draws heavily on the mantle evolution model proposed by Ringwood (1982 and 1986).

1) Oceanic crust is generated at an oceanic spreading centre.

2) The oceanic crust is subjected to hydrothermal alteration of differing intensity depending on height in the oceanic pile, presence and density of fracturing and the ability of isotopically altered seawater to recirculated back up the pile. *Geochemical effects:* Increase in $^{87}Sr/^{86}Sr$ (varies according to the age alteration took place) which may or may not be accompanied by increasing $\delta^{18}O$. U sequestered from ocean water and sediments during hydrothermal alteration, results in increasing U/Pb in upper oceanic crust.

3) Cooling of oceanic crust away from spreading centre, low temperature seawater alteration. Radiogenic Pb-Sr and Nd increase with time.

4) Subduction of oceanic crust plus hemipelagic sediment which has accumulated on top of crust. Dehydration of sediments, some reduction of U/Pb and Rb/Sr, but if subducting plate deforms, hydrous fluids may "autometasomatize" fragments of the plate stacked above by thrusting.

5) The cool residual oceanic crust plus remaining sediments descend into asthenosphere together with the lower, harzburgite portion of the slab. Between 650 - 680 km the former basaltic oceanic crust and harzburgite became ~ 0.08 gcm^{-3} less dense than the surrounding pyrolitic asthenosphere (Ringwood 1986). The relative buoyancy of the slab and its resultant inhomogeneous stress distribution cause it to buckle at this depth and form a "megalith" of former oceanic crust and harzburgite lithosphere. The megalith spreads out and builds up due to sucessive subduction, becoming gravitationally stable and joins a globally continuous layer of former oceanic lithosphere "ponded" at the 670 km discontinuity (Figure 8.3a, Ringwood 1982, 1986). Minor amounts of residual sediments may also be incorporated into this layer creating a trace element and isotopically heterogeneous reservoir. The relatively constant Ce/Pb and Nb/U ratios of MORB and OIB (Hoffman et al 1986) together with their Lu/Hf isotope systematics

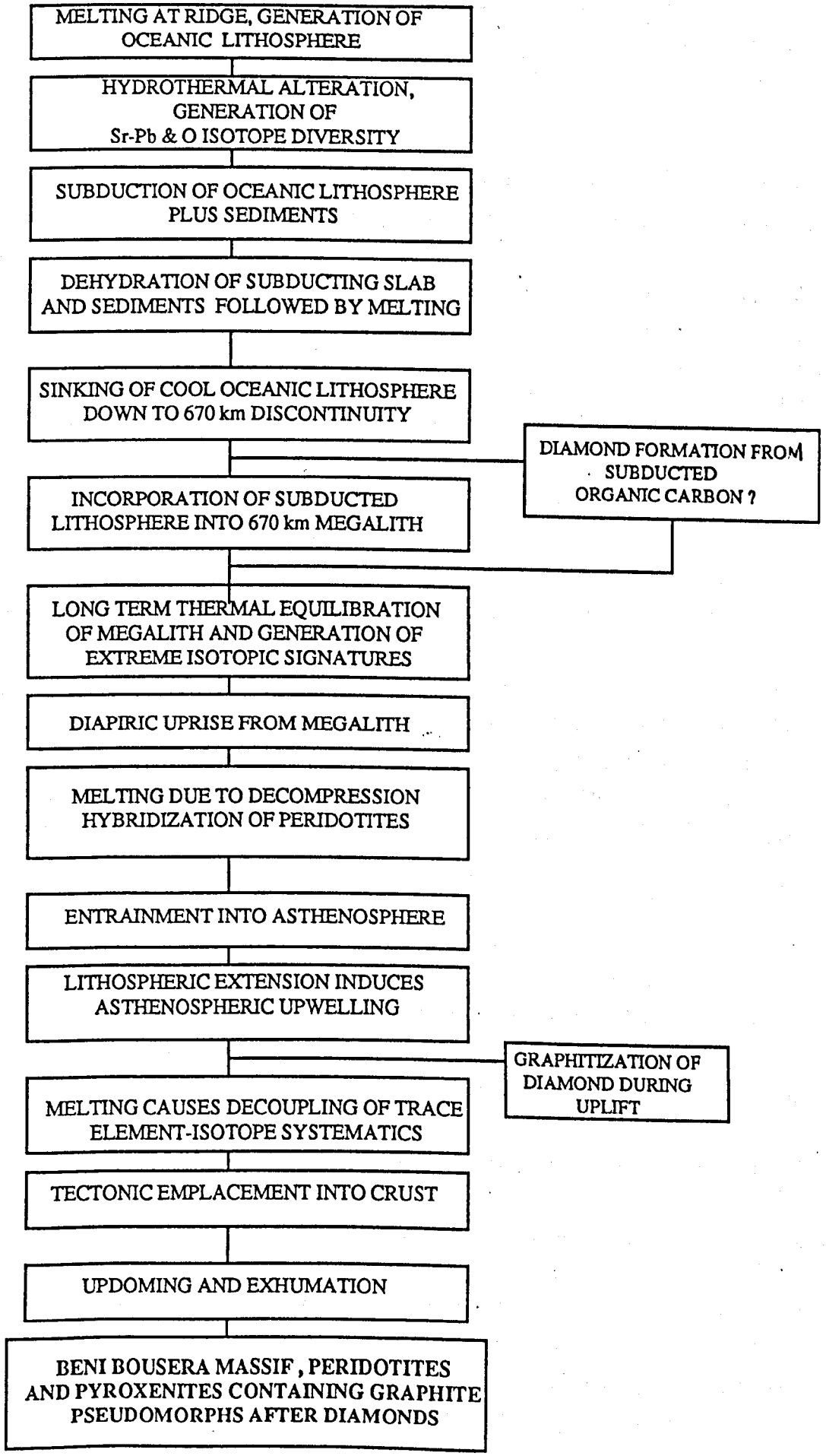

Figure 8.2. Box model of the petrogenetic evolution of the Beni Bousera massif.

(Patchett et al 1984), limit the amount of sediment subducted into the upper mantle to < 1 %. Ancient incorporation of such small amounts of sediment or sediment derived fluid into the pyroxenite source region and its subsequent long term isolation permit acquisition of the isotopically extreme source characteristics observed.

6) Thermal equilibration of the megalith with the surrounding asthenosphere over a period of ~1 Ga. induces localised partial melting of the former oceanic crust component of the megalith (Ringwood 1982, 1986). The resultant partial melts contaminate regions of former harzburgite rendering them more fertile with respect to their capacity to produce basaltic magmas (Figure 8.3b). Very small degree partial melts may impart the isotopic signature of oceanic crust plus subducted sediment on the surrounding harzburgite without significantly refertilizing the peridotite. This process leads to the generation of "hybridized" peridotite bodies of widely varying isotopic major element characteristics, which may not show the expected geochemical melt extraction trends. Such heterogeneity is observed in the Beni Bousera peridotite body. The long time scales required for thermal re-equilibration of the megalith allow extreme isotopic signitures to develop in this layer without subsequent destruction.

7) After extended residence times in the megalith layer (~1 Ga.) diapirs of fertilised former harzburgite and small amounts of residual and melted oceanic crust (pyroxenites) form due to convective boundary layer instability (Figure 8.3b, Ringwood 1982, 1986). The uprise of these diapirs may induce decompression partial melting in the former oceanic crust, now existing as bodies of cumulate pyroxenites, due to their lower solidus temperatures compared to the peridotites. Partial melting reduces Rb/Sr and U/Pb ratios and increases Sm/Nd ratios further complicating the parent-daughter isotope relationships of the pyroxenites/pyroxenite sources. The decrease in U/Pb ratios of many of the pyroxenites (and peridotites ?) at this stage arrests the development of radiogenic ^{207} and ^{206}Pb leading to their evolution to the left of the geochron on Pb isotope diagrams.

Small diapirs rising from the convectively unstable megalith may suffer "thermal death" and become entrained in the asthenospheric convective cycle for substantial periods, creating geochemically enriched local source regions for isotopically diverse oceanic magmatism (Ringwood 1982, 1986). Bodies of isotopically heterogeneous peridotites and pyroxenites may exist in the asthenosphere as isolated bodies for considerable time periods without becoming destroyed by convective and solid state diffusive mixing (Allegre and Turcotte 1986, Kellogg and Turcotte 1987). Such a portion of pyroxenite veined asthenosphere or a small diapir direct from the megalith boundary layer could form the present Beni Bousera massif.

An asthenosphere diapir origin for the massif is consistent with the emplacement model of Doblas and Oyarzan (1989). These authors invoke a major Neogene extensional event in the western Meditteranean to initiate asthenospheric upwelling, followed by the development of a lower crustal detachment zone to emplace the Ronda and Beni Bousera massifs into the crust (Figure 8.4a). Alternatively, extension could be a consequence of diapirism (asthenospheric upwelling). Upward arching due to isotatic rebound is then assumed to have triggered tectonic denudation of the ultramafic bodies (Figure 8.4b). Partial melting during final diapiric emplacement into the crust very recently (<50 Ma) would produce further incompatible element depletions (and enrichments ?) in both peridotites and pyroxenites which would totally decouple parent-daughter isotope relationships, as

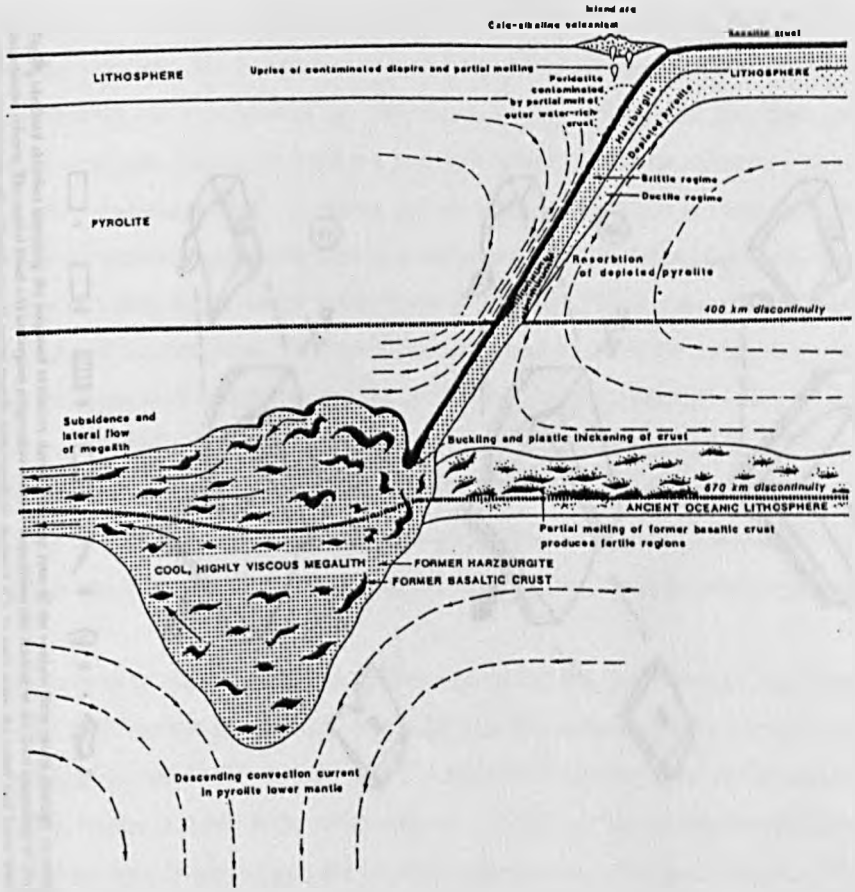

Fig. 8-3 a Subduction of differentiated oceanic lithosphere. Lower ductile layer of depleted pyrolite becomes resorbed into upper mantle convective circulation above the 670 km discontinuity. At this depth, the former oceanic crust and harzburgite layers plastically thicken and buckle to form a large melange (megalith) situated mainly below the seismic discontinuity. The lower region of the megalith provides a heat-sink which initiates a descending convection current in the lower mantle. Ultimately, the convection current entrains the lower part of the megalith and mixes it into the lower mantle.

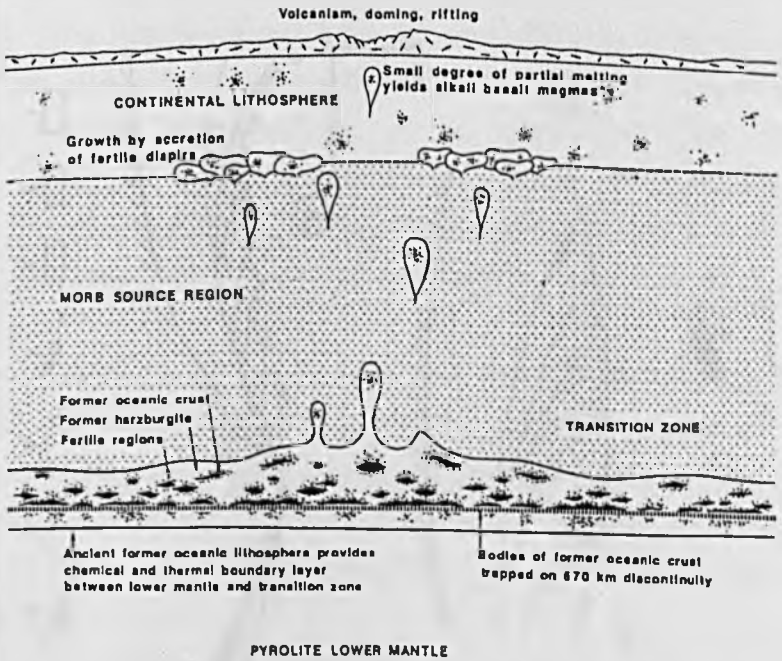

Fig. 8-3 b After the cessation of subduction, the upper regions of the megalith slowly contract towards the 670 km discontinuity and spread horizontally to form a lens-shaped body comprised of mixed domains of former basaltic crust and former harzburgite. With further heating, melts from former oceanic crust hybridize neighbouring regions of harzburgite. Ultimately, buoyant plumes of former harzburgite containing fertile regions ascend into upper mantle where they may cause intraplate volcanism or become incorporated into the subcontinental lithosphere. After Ringwood 1986

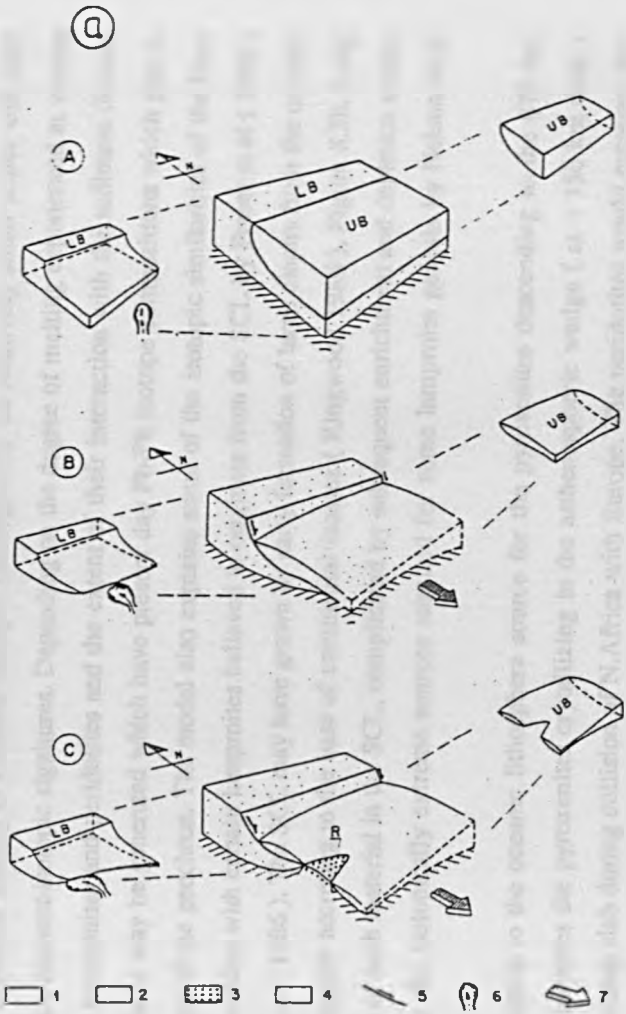

Fig. 8. Idealized sketches depicting the proposed evolution during Neogene time of the western Betic realm through an extensional detachment scheme. The initial block (A) undergoes progressive tectonic denudation (B), leading to the final unroofing of the Ronda peridotite in the form of a diapiric rise of upper mantle asthenospheric material (C). In each stage the upper and lower blocks (*UB* and *LB* respectively) have been additionally represented as separate units in order to show the uprise of asthenospheric mantle material, which has been progressively laterally drawn toward its final emplacement in the western thinner part of the wedge-shaped lower crustal block (upper block structural features such as high-angle normal faults not represented). Legend: *1* = crustal upper block; *2* = crustal lower block; *3* = peridotite; *4* = uppermost mantle; *5* = detachment surface; *6* = upper mantle asthenospheric diapir; *7* = movement of the upper block. *R* = Ronda.

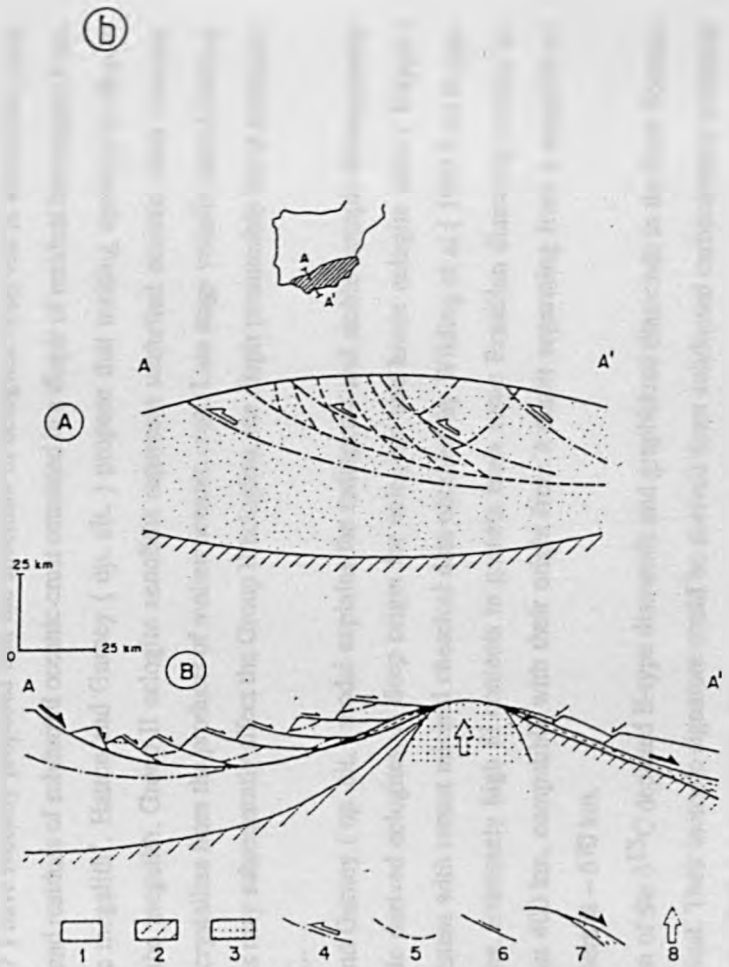

Fig. 8. Idealized sketches depicting the evolution of the Betic Cordilleras through extensional detachment tectonics, leading to the Neogene emplacement of the Ronda peridotite. A: Previous compressional scheme. B: Neogene extensional scheme. Legend: *1* = continental crust; *2* = uppermost mantle; *3* = peridotite; *4* = compressional nappe surfaces; *5* = future extensional structures; *6* = normal faults on the upper block; *7* = detachment surface; *8* = upward arching of the lithosphere.

After Dobles & Oyarzun (1984)

observed. The P/T evolution of the final part of the evolution of the massif is summarized in Figure 8.5.

The model proposed above explains most of the physical and geochemical characteristics of the Beni Bousera peridotites and pyroxenites i.e. their deep origin, at least 150 km, their ancient, multistage, multiprocess evolution leading to extreme isotopic heterogeneity on relatively small scales and their decoupled trace element-isotopic signitures. Depending on the degree of melting experienced at various stages by the pyroxenites and peridotites and the extent of their interaction with the sediment derived component, rocks may be generated which have present day Pb-Pb isotope compositions which plot to the left or right of the geochron. The model also explains some of the isotopic similarities of the Beni Bousera pyroxenites with certain lamproites believed to originate from the SCL by Fraser et al (1985) and Nelson et al (1986). The SCL may have grown by early formation of large diapirs from the oceanic lithosperic megalith accreting to the base of continental masses (Ringwood 1986), Figure 8.3b. Long term isolation of such material in the SCL, complicated by subsequent enrichment and depletion events could produce the isotopically extreme sources required for some lamproite genesis by Nelson et al (1986).

An alternative to the oceanic lithosphere source for the pyroxenites descending to the 670 km discontinuity involves the pyroxenites crytallizing in the asthenospheric wedge (at ~ 150 km deep) above a subducting slab during collision of N.Africa with Europe. The peridotites would represent the asthenospheric wedge into which the peridotites were emplaced. The pyroxenite veined asthenosphere thus formed would be later emplaced into the crust by diapirism as in the model above. This model requires a relatively recent origin for the pyroxenites and is not compatible with their Pb isotope geochemistry.

8:6 Mantle eclogites and diamond genesis.

Striking geochemical similarities between the Beni Bousera pyroxenite suite and mantle derived eclogite xenoliths and eclogite suite inclusions in diamonds indicate some generic connections. Hatton and Gurney (1987) have recently proposed that the spectrum of eclogites observed in kimberlite pipes originate as melts and residues of subducted oceanic crust entrained in a diapir of residual harzburgite from a "Ringwood type megalith". Hatton and Gurney (op. cit.) propose that melting operates in diapirs originating from the megalith, Group II eclogite xenoliths represent unmelted oceanic crust whereas Group I eclogites crystallize from the products of molten oceanic crust. Late stage volatile partial melting and AFC processes may subsequently affect the Group II eclogites, the diapir presumably being emplaced into the basal SCL.

The Hatton and Gurney (op. cit.) model explains the radiogenic and stable isotopic heterogeneity observed in mantle derived eclogites. A deep origin for eclogites and hence eclogite suite (E-type) diamonds is consistent with recent mineral chemical data obtained by Wilding et al (1989) on E-type diamond inclusions. Extremely high Si contents in garnets from some Brazilian diamonds require an origin from at least 400 km, compatible with their origin from a diapir separating from a megalith of subducted lithosphere at ~ 670 km.

The generation of the $\delta^{13}C$ depleted E-type diamonds and graphitized diamonds in the Beni Bousera GGP is problematical. Their isotopic signature could be derived from subducted carbonaceous sediment incorporated into the 670 km megalith. However, the small volumes of sediment in the deep mantle suggested by trace element and isotopic geochemistry (Sun and McDonough 1989, Davies et al 1989) and the redox conditions prevailing at subduction zones (Haggerty 1989), may preclude subduction of

sufficient biogenic carbonaceous material into the deep mantle. Alternatively, E-type diamonds (and those once present in the GGP) may have crystallized during melting in the megalith perhaps as a consequence of infiltration by an isotopically variable C-H-O "fluid" phase from the lower mantle. Present data are not adequate to further constrain the origin of the original GGP diamonds or E-type diamonds.

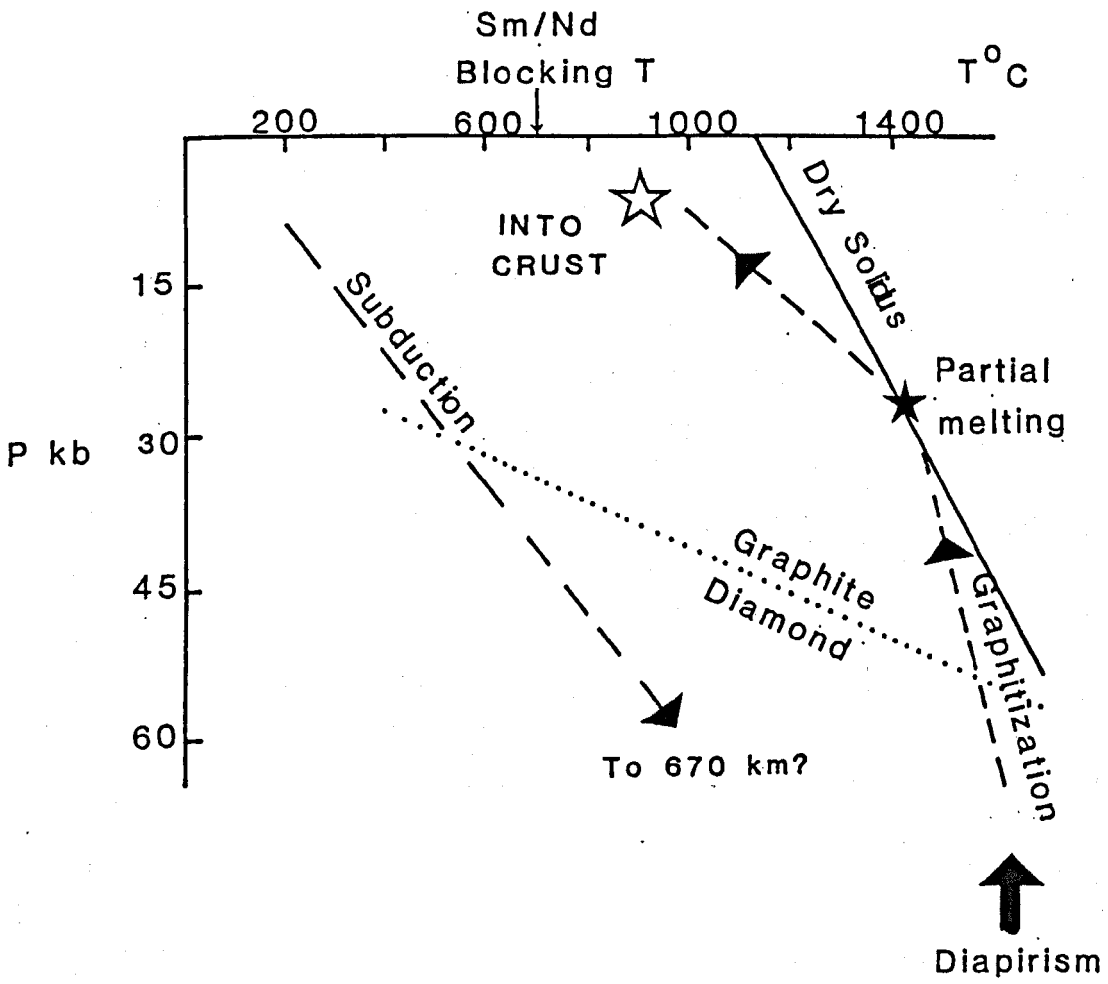

Figure 8.5. Schematic P/T path (dashed line) of Beni Bousera peridotites and pyroxenites.

REFERENCES

Ahrens,L.H., vons Michaelis,H., Erlank, A.T. & Willis, J.P. 1969 Fractionation of some abundant lithophile elements in chondrites. In "Meteorite Research" (ed. P.M. Millman) D.Reidel. Dordrecht 166-167.

Albarde,F. & Michard,A. 1986 Transfer of continental Mg,S,O & U to the mantle through hydrothermal alteration of the oceanic crust. Chem. Geol. 57: 1-15

Allegre, C.J. 1982 Chemical geodynamics. Tectonophysics 81 :109-132

Allegre,C.J. , Hamelin,B., Provost,A & Dupre,B. 1987 Topology in isotopic multispace and origin of mantle chemical heterogeneties. Earth. Planet. Sci. Lett. 81: 319-337

Allegre,C.J. , Staudaucher,T. & Sarda,P. 1986/7 Rare gas systematic: formation of the atmosphere, evolution and structure of the earth' s mantle. Earth. Planet. Sci. Lett: 81. 127-150

Allegre,C.J. & Turcotte,D.L. 1986 Implications of a two component marble-cake mantle. Nature, London. 323: 123-126

Anderson,D.L. 1985 Hot spot magmas can form by fractionation and contamination of mid ocean ridge balalis. Nature, London. 318: 145-149

Aoki,K. & Kushiro,I. 1968 Some clinopyroxenes from ultramafic inclusions in Dreiser Weiher,Eifel. Contrib. Mineral. Petrol. 18: 326-337.

Arculus,R.J. 1985 Oxidation status of the mantle past and present. Ann. Rev. Earth. Planet.Sci 13: 75-95.

Ater,P.C., Eggler,D.H. & McCallum,M.E. 1984 Petrology of mantle eclogite xenoliths from Colorado-Wyoming kimberlites recycled oceanic crust ? In "Kimberlites II .The Mantle and Crust-Mantle Relationships." (ed) J.Komprobst. Elsevier. Amsterdam 309-318.

Auge, T. A. & Roberts, S. 1982 Petrology and geochemistry of some chromiferous bodies within the Oman ophiolite. Ofioliti, 7:133-154.

Bakumenko,I.T., & Sobolev,N.V. 1984 Faceted inclusions in diamond crystals. Doklady Acedemii Nauk SSSR. 278: 1461-1465.

Balhaus,C.G. & Stumpel,E.F. 1985 Occurance and petrological significance of graphite in the upper critical zone,W. Busheld complex South Africa. Earth. Planet. Sci. Lett. 74: 58-68.

Barton,M.D. 1983 Calculation of C-O-H-S equilibria at constant bulk composition: some petrologic implications. Carnegie Institution Year Book Geophysical Lab. 1983 51-53.

Beeson,M.H. & Jackson,E.D. 1970 Origin of the garnet pyroxenite xenoliths at Salt Lake Crater, Oahu. Min. Soc. Am. Spec. Paper 3: 95-112.

Ben Othman, D., White, W.M. & Patchett, J. 1989 The geochemistry of marine sediments, island arc magma genesis, and crust-mantle recycling. Earth. Planet. Sci. Lett. 14: 1-21.

Bermon,R. 1965 "Physical Propeerties of Diamond." Oxford University Press.

Bernard-Griffiths, J. & Cornichet, J. 1985 Origin of eclogites from South Brittany, France: A Sm-Nd isotopic and REE study. Chem. Geol. 52: 185-201.

Bertrand,P.,Sotin,C.,Mercier,J.C.C. & Takahashi,E. 1986 From the simplest chemical system to the natural one:garnet peridotite barometry. Contrib. Mineral. Petrol. 93: 168-178.

Bertrand,P. & Mercier,J.-C.C. 1986 The mutual solubility of coexisting ortho and clinopyroxene: towards an absolute geothermometer for the natural system? Earth. Planet. Sci. Lett. 76: 109-122.

Bhatia, M.R. 1985 Rare earth element geochemistry of Australian palaeozoic greywacks and mudrocks: provenance and tectonic control. Sedimentary Geology 45: 97-113.

Bishop,F.C., Smith, J.V. & Dawson,J.B. 1978 Na,K, and Ti in garnet, pyroxene and olivine from periotite and eclogite xenoliths from African kimberlites. Lithos 11: 155-173.

Bodinier, J.L., Guiraud, M., Fabries, J., Dostol, J. & Dupuy, C. 1987 Petrogenesis of layered pyroxenites from the Lherz, Freychnede and Prades ultramafic bodies. (Ariege, French Pyrenees) Geochim. Cosmochim. Acta. 51: 279-290.

Bonatti,E., Ottonello,G. & Hamlyn,P.R. 1986 Peridotites from the Island of Zabargad (St.John), Red Sea : petrology and geochemistry. J. Geophys .Res: 91 599-631.

Bonini, W.E., Loomis, T.P., & Robertson,J.D. 1973 Gravity anomalies, ultramafic intrusions and the tectonics of the region around the Strait of Gibralter. Jour. Geophys. Res. 78: 1372-1382.

Bottinga,Y. 1969 Carbon isotope fractionation between graphite, diamond and carbon dioxide. Earth. Planet. Sci. Lett. 5: 301-307.

Boyd,F.R 1973 A pyroxene geotherm. Geochim. Cosmochim. Acta.. 37. 2533-2546.

Boyd,F.R. & Finnerty,A.A. 1980 Conditions of origin of natural diamond of peridotite affinity. Jour. Geophys. Research 85: 6911-6918.

Boyd,F.R., Gurney,J.J. & Richardson. S.H. 1985 Evidence for a 150-200km thick Archean lithosphere from diamond inclusion thermobarometry. Nature. 315: 387-389.

Boyd,F.R. & Gurney,J.J. 1986 Diamonds and the African lithosphere. Science. 232: 472-477.

Boyd, F.R. & Mertzman, S.A. 1987 Composition and structure of the Kaapvaal lithosphere, southern Africa. in " Magmatic Processes: Physicochemical principles " ed B.O. Mysen. Spec. Pub. No 1. Geochem Soc. Univ. Park. P.A. 13-24

Boyd, S.R., Mattey, D.P., Pillinger, C.T., Milledge, H.J., Mendelssohn, M. & Seal, M. 1987 Multiple growth events during diamond genesis: An integrated study of carbon and nitrogen isotopes and nitrogen aggregation state in coated stones. Earth. Planet. Sci. Lett 86: 341-353.

Bourrouilh, R. & Gorsline, D.S. 1979 Pre-Triassic fit and alpine tectonics of continental blocks in the western Mediterranean. Bull. Geol. Soc. Am. 90: 1074-1083.

Brett,R. & Higgins,G.T. 1969 Clifonite: a proposed origin and its bearing on the origin of diamonds in meteorites. Geochem. Cosmochimica 33: 1473-1484.

Brown,E.H. & Forbes,R.B. 1986 Phase petrology of eclogite rocks in the Fairbanks district of Alaska. Spec. Pub. Geol. Soc. Am. 164: 155-167.

Brown,L., Klein,J. , Middleton,R., Selwyn-Jacks., &Tera.,F. 1982 Be in island arc volcanoes and implications for subduction. Nature, London. 299: 718-720

Bundy,F.P. 1980 The P,T phase and reaction diagram for elemental carbon,1979. Jour. Geophys. Res .85: 6930-6936.

Carswell,D.A. 1986 The metamorphic evolution of Mg-Cr type Norwegian garnet peridiotites. Lithos 19. 279-297.

Carswell,D.A. & Gibb.I.G.F. 1987 Garnet lherzolite xenoliths in the kimberlites of northern Lesotho : revised P-T equilibrium conditions and upper mantle palaeogeotherm. Contrib. Mineral. Petrol. 97: 473-487.

Carswell,D.A. & Gibb.I.G.F. 1986 Evaluation of mineral thermometers and barometers applicable to garnet litherzolite assemblages. Contrib. Mineral. Petrol. 94: 403-416

Carswell,D.A., Dawson,J.B., &Gibb,F.G.F. 1981 Equilibration conditions of upper-mantle eclogites:implications for Kyanite-bearing and diamondiferous varieties. Min. Mag:44. 79-89.

Cawthorne,G.R. & Collerson,K.D. 1974 The recalculation of pyroxene end member parameters and the estimation of ferrous and ferric iron contents from electron microbe analyses. American Mineralogist 59: 1203-1208.

Chaffey, D.J. 1988 Characterization of oceanic island basalt sources: St.Helena. Unpub. PhD Thesis. Univ. Leeds.

C ampness,P.E. & Lorimer,G.W. 1973 Precipitation (exosolution) in an orthopyroxene. J. Mat. Sci. 8: 467-474.

Chase.C.G. 1981 Oceanic island Pb: two stage histories and mantle evolution. Earth. Planet. Sci. Lett. 52: 277-284.

Chen, J.H. & Wasserburg, G.J. 1983 The least radiogenic Pb in iron meteorites. Fourteenth lunar and planetary science conference. Abstracts. Pt 1. L.P.I. Houston. 103-104.

Clague,D.A. & Frey,F.A. 1982 Petrology and trace element geochemistry of the Honolulu volcanics, Oahu: implications for the oceanic mantle below Hawaii. Jour. Petrology 23: 447-504.

Clarke, D.B. 1970 Tertiary basalts of Baffin Bay: possible primary magma from the mantle Contrib. Mineral. Petrol. 25: 203-224.

Clayton,R.N, Goldsmith,J.R., Karel,K.J., Mayeda,T.K. & Newton,R.C. 1975 Limits on the effect of pressure on isotopic fractionation. Geochim. Cosmochim. Acta. 39: 1197-1202.

Clayton,R.N. & Mayeda,T.K. 1963 The use of bromine pentafluoride in the extraction of oxygen from oxides and silicates for isotopic analysis. Geochim. Cosmochim. Acta. 27: 43-52.

Cocker, J.D., Griffin, B.J. & Muehlenbachs, K. 1982 Oxygen and carbon isotope evidence for seawater hydrothermal alteration of the Macquarie Island ophiolite. Earth. Planet. Sci. Lett. 61: 112-122.

Cohen,R.S. & O'Nions,R.K. 1982 The lead, neodymium and strontium isotopic structure of oceanic ridge basalts. Jour. Petrology 23: 299-324.

Cole, D.R. & Ohmoto, H. 1986 Kinetics of isotopic exchange at elevated temperatures and pressures. In " Stable Isotopes in High Temperature Geological Processes" eds. J.W.Valley, H.P.Taylor & J.R.O'Neil. Reviews in Mineralogy vol 16 Min.Soc.Am. 41-87.

Coleman,R.G., Lee,D.E., Beatty,L.B. & Brannock,W.W. 1965 Eclogites and eclogites: their differences and similarities. Geol. Soc. Am. Bull. 76: 483-508.

Conquere,F. 1977 Petrologie des pyroxenites litees dans les complexes ultramafiques de L' Ariege (France) et autres gisements de lherzolite a spinelle.I compositions mineralogiques et chemiques, evolution des conditions d' equilibre des pyroxenites. Bull. Soc. Fr. Mineral. Cristallogr.

Craig.H. 1957 Isotopic standards for carbon and oxygen and correction factors for mass spectrometric analysis of carbon dioxide. Geochim. Cosmochim. Acta. 12: 133-149.

Cumming, G.L., Koppel, V. & Ferrario, A. 1987 A lead isotope study of the North Eastern Ivrea zone and the adjoining Ceneri zone (N.Italy): Evidence for a contaminated subcontinental mantle. Contrib. Mineral. Petrol. 97: 19-30.

Custers,J.F.H. 1955 On the nature of the opal-like outer coat on coated diamonds. Am. Mineral. 35: 51-58.

Davies,G. & Evans,T. 1972 Graphitization of diamond at zero pressure and high temperature. Prceedings Royal Society London. 328: 413-427.

Davies,G.R. 1984 The isotopic evolution of the lizrad complex. J. Geol .Soc .Lond. 141: 3-12.

Davies, G.R. & Lloyd, F.F. 1986 Pb-Sr-Nd isotope and trace element data bearing on the origin of the potassic subcontinental lithosphere beneath S.W.Uganda. In "Kimberlites and Related Rocks" Vol 2. Geol. Soc. Aus. Spec Publication No.14 ed.J.Ross et al. 784-794.

Davies, G.R. , Norry, M.J., Gerlach, D.C. & Cliff, R.A. 1989 A combined chemical and Pb-Sr-Nd isotope study of the Azores and Cape Verde hot spots: the geodynamic implications. In Saunders, A.D. and Norry, M.J. (eds). "Magmatism in the Ocean Basins" Geol. Soc. Spec. Publication No 42: 231-255.

Dawson,J.B. 1983 New developments in diamond geology . Naturwissenschaften 70: 586-593.

Dawson,J.B. & Smith,J.V. 1986 Relations between ecologites and certain megacrystals from the Jagersfotein kimberlite S. Africa. Lithos 19: 325-330.

DePaulo,D.J. 1981 Trace element and isotopic effects of combined wallrock assimilation and fractional crystallization. Earth. Planet. Sci. Lett. 53: 189-202.

Deines,P. 1980 The carbon isotopic composition of diamonds: relationship to diamond shape,color,occurance and vapour composition. Geochim. Cosmochim. Acta. 44: 943-961.

Deines,P. 1989 Regularities in the C and nitrogen content of the mantle revealed through studies of diamonds and the chemistry of their inclusions. Extended Abstracts. Diamond symposium. 28 th I.G.C. Washington. 18-21.

Deines,P.,Gurney,J.J. &Harris,J.W. 1984 Associated chemical and carbon isotopic composition variations in diamonds from Finsch and premier kimberlite , South Africa. Geochim. Cosmochim. Acta. 48: 325-342.

Dick,H.J.B. & Fisher,R.L. 1984. Mineralogic studies of the residues of mantle melting:abyssal and alpine-type peridotites. In Kornprobst,J. (ed) "Kimberlites II the Mantle and Crust Mantle Relations." Elsevier. 295-308.

Dick,H.J.B. & Sinton,J.M. 1979 Compositional layering in Alpine peridotites: evidence for pressure solution creep in the mantle. J. of Geology 87: 403-416.

Dickey,J.S. 1970 Partial fusion products in Alpine peridotites:Serrania De La Ronda and other examples.Min .Soc.Am.Pap. No. 3: 33-49.

Dickey,J.S. 1977 Partial fusion versus fractional crystallization hypothesis for the differentiation of the Ronda ultramaffic massif S.Spain. Min.Soc.Am.Spec.PAP. 3: 79-90.

Dickey,J.S.,Basset,W.A., Bird,J.M. & Weathers,M.S. 1983 Liquid carbon in the lower mantle. Geology 7: 219-220.

Dickey,J.S. & Obata,M. 1974 Graphitic hornfels dikes in the Ronda high temperature peeridotite massif. Am.Min. 59: 1183-1189.

Doblas, M. & Oyarzun, R. 1989 " Mantle core complexes " and Neogene extentional detatchment tectonics in the western Betic Cordilleras, Spain: an alternative model for the emplacement of the Ronda peridotite. Earth. Planet. Sci. Lett. 93: 76-84

Duke,E.F. & Rumble,D. 1986 Textural and isotopic variations in graphite from plutonic rocks,South-central New Hampshire. Contrib. Mineral. Petrol. 93: 409-419.

Duncan, R.A. & Green, D.H. 1987 The genesis of refractory melts in the formation of oceanic crust. Contrib. Mineral. Petrol. 96: 326-342.

Dupre,B. & Allegre,C.J. 1983 Pb-Sr isotope variation in Indian Ocean basalts and mixing phenomena. Nature, London. 303: 142-146.

Dupuy,C., Dosial,J., Dautria,J.M. & Girod,M. 1986 Geochemistry of spinel peridotite inclusions in basalts from Hoggar,Algeria. J. African Earth Sciences 5: 209-215.

Early, T.O. 1971 Rare Earths in eclogites from the Roberts Victor Kimberlite, South Africa. Contrib. 2144, Publ. Div. Geol and Planet. Sci., Calif. Inst. of Technol. Pasadena.

Eggler. D.H. 1986 Kimberlites: How do they form ? In: "Kimberlites and Related Rocks " Vol.2 ed. J. Ross et al G.S.A. Spec. Pub. No. 14. 489-504

Eggler,D.H. & Baker,D.R. 1982 Reduced volatiles in the system C-O-H: implications for mantle melting ,fluid formation and diamond genesis. In " High Pressure Research in Geophysics" (eds.) S. Akimoto and M.H. Manghani. Centre for Academic Publications, Tokyo. 301-315.

Ellis,D.J. 1986 Garnet-liquid Fe -Mg equilibria and implications for the beginning of melting in the crust and subduction zones. American Journal of Science: 286: 765-791.

Ellis,D.J. & Green,D.H. 1979 An experimental study of the effect of Ca upon garnet-clinopyroxene Fe-Mg exchange equilibria. Contrib. Mineral. Petrol. 71: 13-22.

Elthon, D. 1979 High magnesia liquids as the parental magma for ocean floor basalts. Nature, London. 278: 514-518.

Ernst,W.G. 1978 Petrochemical study of lherzolitic rocks from the W.Alps. Jour. Petrology 19: 341-353.

Essene,E.J. & Fyfe,W.S. 1967 Omphacite in Californian metamorphic rocks.Contrib. Mineral. Petrol. 15. 1-23.

Evans,T. 1976 Diamonds. Contemporary Physics 17: 45-70.

Evans,T. 1979 Changes produced by high temperature treatment of diamond. In Properties of Diamond (ed) J. E. Field. Academic Press 403-424.

Evans,T. & James,P.F. 1964 Experimental graphitization of diamond. Proc. R. Soc. Lond. A277,260.

Exley,R.A., Boyd,S.R., Mattey,D.P. & Pillinger,C.T. 1986/7 Nitrogen isotope geochemistry of basaltic glasses:implications for mantle degassing and structure? Earth. Planet. Sci. Lett. 81: 163-174.

Exley,R.A.,Mattey,D.P.,Pillinger,C.T. & Sintom, J.M. 1986 Carbon isotope geochemistry od basalt glasses from the Lau and North Fiji marginal basins. Terra Cog. 6: 324.

Exley,R.A.,Smith,J.V. & Dawson,J.B. 1983 Alkremite,garneite and eclogite xenoliths from Bellsbank and Jagersfontein,S.Africa. Am.Min 68: 512-516.

Fabries, J. 1979. Spinel-olivine geothermometry in peridotites from ultramafic complexes. Contrib. Mineral. & Petrology 69. 329-336

Fang, Chingson and Bai Wenji 1981 The discovery of Alpine-type diamond bearing ultrabasic intrusion in Xizang (Tibet). Int.Geol.Rev. 27: 455-457 (in Chinese).

Faure, G. 1986 "Principles of Isotope Geology." J. Wiley. New York.

Field,J.E. 1979 "Properties of diamond". Academic Press.

Finnerty,A.A. & Boyd,F.R. 1986 Thermobarometry for garnet peridotite xenoliths:a basis for upper mantle straigraphy. Nixon,P.H. (ed) Mantle Xenoliths. Wiley.

Finnerty,A.A. & Boyd,F.R. 1984 Evaluation of thermobarometers for garnet peridotites. Geochim. Cosmochim. Acta. 48: 15-27.

Fitton,J.G. & Dunlop,H.M. 1985 The Cameroon line,W.Africa and its bearing on the origin of

oceanic and continental alkali basalt. Earth Planet Sci.Lett. 23: 150-177

Folond, K. A. 1983 $^{40}Ar/^{39}Ar$ incremental heating plateaus for biotites with excess argon. Isotope Geosci. 1: 3-21.

Francis, D. 1987. Mantle- melt interaction recorded in spinel lherzolite xenoliths from the Alligator Lake volcanic complex, Yukon, Canada. Jour. Petrology 28: 569-597.

Fraser, K.J., Hawkesworth, C.J., Erlank, A.J., Mitchell, R.H. & Scott-Smith, B.H. 1985 Sr, Nd and Pb isotope and minor element geochemistry of lamproites and kimberlites. Earth. Planet. Sci. Lett. 76: 57-70.

French,B.M. 1966 Some geological implications of equilibrium between graphite and a C-H-O gas phase at high temperatures and pressures. Reviews of Geophysics 4: 223-253.

Frey,F.A., Suen, & Stockman,W. 1985 The Ronda high temperature peridotite: geochemistry and petrogenesis. Geochim. Cosmochim. Acta. 49: 2469-2491.

Frey,F.A. & Prinz,M. 1978 Ultramafic inclusions from San Carlos,Arizona: petrologic and geochemical data bearing on their petrogenesis.Earth. Planet. Sci. Lett.38: 129-176.

Frey,F.A.,Green,D.H. & Roy,S.D. 1978 Integrated models of basalt petrogenesis: a study of quartz tholeities to olivine melilities from S.E. Australia utilising geochemical and experimental petrological data.Jour. Petrology 19: 463-513.

Friedel,G. & Ribaud,G. 1924 Graphitization of diamond. Bull. Soc. Franc. Miner. 47: 94.

Frost, B.R. 1979 Mineral equilibria involving mixed-volatiles in a C-O-H fluid phase: The stabilities of graphite and siderite. Am. J. Sci 279: 1033-1059.

Galer,S.J.G. & O'Nions,R.K. 1985 Residence time of thorium and lead in the mantle with implications for mantle convection. Nature.London 316: 778-780

Galimov,E.M.,Kaminskiy,F.V. & Ivanovskaya,I.N. 1978 Carbon-isotope composition of diamonds from the Urals,Timan,Sayan, The Ukraine and elsewhere. Geochemistry International 15: 11-16.

Galimov,E.M. 1978 Problem of the origin of diamonds in the light of new data on the carbon isotopic composition of diamonds. Nat Symp. Isotope Geochem. Moscow. 13.

Garlick,G.D.,Macgregor,I.D. & Vogel,D.E. 1972 Oxygen isotope ratios in eclogites from kimberlites. Science 172: 1025-1026.

Gast,P.W. 1968 Trace element fractionation and the origin of tholeiitic and alkaline magmas.Geochim. Cosmochim. Acta. 32: 1057-1086.

Gerlach, D.C., Cliff, R.A., Davies, G.R., Norry, M.J. & Hodgson, N. 1988 Magma sources of the Cape Verdes Archipelago: Isotopic and trace element constraints. Geochim. Cosmochim. Acta: 52: 2979-2992.

Giardini,A.A. & Melton,C.E. 1976 Significance of gases released from natural diamonds by crushing and graphitzation. International Geological Congress.25: 807.

Giardini,A.A. & Tydings,J.E. 1962 Diamond synthesis: Observations on the mechanism of formation. Am.Mineral. 47: 1393-1421.

Glassley,W. 1982 Fluid evolution and graphite genesis in the deep continental crust. Nature.London 295: 229-231.

Goodrich,C.A. and Bird,J.M. 1985. Formation of iron-carbon alloys in basaltic magma at Uivfaq, Disko Island: The role of carbon in mafic magmas. Jour. Geology 79: 102-116.

Green, D.H. 1967 High temperature peridotite intrusions. In " Ultramafic and Related Rocks" (ed) P.J.Wyllie, Wiley, New York. 212-222.

Gregory,R.G. & Taylor,H.P. 1981 An oxygen isotope profile in a section of cretaleous oceanic crust,Samail ophiolite,Oman:evidence for $\delta^{18}O$ buffering of oceans by deep (> 5km) seawater hydrothermal alteration at mid ocean ridges.J Geophys. Res. 86: 2737-2755.

Gregory, R.T. & Taylor, H.P. 1986 Possible non-equilibrium oxygen isotope effects in mantle nodules, an alternative to the Kyser-O'Neil-Carmichael $^{18}O/^{16}O$ geothermometer. Contrib. Mineral. Petrol. 93: 114-119.

Gregory, R.T. & Taylor, H.P. 1986 Non-equilibrium, metasomatic $^{18}O/^{16}O$ effects in upper mantle mineral assemblages. Contrib. Mineral. Petrol. 93: 124-135.

Gregory, R.T. & Criss, R.E. 1986 Isotopic exchange in open and closed systems. In, " Stable Isotopes in High Temperature Geological Processes " Reviews in mineralogy, Vol 16.(eds) J.W.Valley, H.P.Taylor & J.R.O'Neil. Min. Soc. Am. 91-126

Grenville-Wells,H.J. 1952 The graphitization of diamond and the nature of cliftonite. Min .Mag. 24: 803-817.

Grew,E.S 1973 Carbonaceous material in some metamorphic rocks of New England and other areas.J. Geology. 82: 50-73.

Grew,E.S. & Day,H.W. 1972 Staurolite, kyanite and sillimantle from the Narragansett Basin of Rhode Island. US.Geol.Survey. Prof.Paper. 800-D 151-157.

Griffin,W.L. & Bruckner, H.K. 1984 Sm-Nd, Rb-Sr and REE patterns in Norwegian eclogites. Proc. 1st Int. Eclogite Conf. (ed. D. Smith) Elsevier.

Griffin,W.L. & O'Reilly,S.Y. 1986 Mantle-derived sappharine. Min. Mag. 50: 635-640.

Gurney,J.J. 1986 Diamonds. In 'Kimberlites and Related Rocks" Vol. 2 Spec. Pub. G.S.A. No. 14 935-965.

Haggerty,S.E. 1986 Diamond genesis in a multiply constrained model. Nature.London 320: 34-36

Haggerty,S.E. & Tompkins,L.A. 1983 Redox state of earth's upper mantle from kimberlitic ilmenites.Nature.London 303: 295-298

Haggerty,S.E.,Erlank,A.J. & Grey,I.E. 1986 Metasomatic mineral titanate comlexing in the upper mantle. Nature.London 319: 761.

Hahn-Weinheimer,P. & Hirner,A. 1981 Isotopic evidence for the origin of graphite.Geochemical Journal.15: 9-15

Haidinger,W.K.V. & Partsch,P. 1846 Pseumomorph nach schwefelkies. Ann.Phys. 67. 437-439.

Hamelin, B., & Allegre, C. 1988 Lead isotope study of orogenic lherzolite massifs. Earth. Planet. Sci. Lett. 91: 112-131.

Harley, S.H. 1984. Comparison of the garnet orthopyroxene geobarometer with recent experimental studies and applications to natural assemblages. Jour. Petrol. 25: 697-712.

Harris,J.W. 1979 Physical and chemical constraints on the formation of natural diamond in the upper mantle. Diamond Research 2-6.

Harris, J.W. 1987 Recent physical, chemical and isotopic research of diamond. In " Mantle Xenoliths" (ed) P.H.Nixon. Wiley.England. 477-500

Harris,J.W. & Gurney,J.J. 1979 Inclusions in diamond. In " Properties of Diamond" (ed) J.E.Field. Academic Press 555-594.

Hart,S.R. 1984 A large scale isotope anomaly in the southern hemisphere mantle.Nature.London 309: 753-757.

Harte,B. 1982 Metasomatic events recorded in mantle nodules. In "Continental Basalts and Mantle Xenoliths" (ed) Hawksworth C.J. and Norry M.J. Shiva UK. 46-91.

Harte,B. & Hawksworth,C.J. 1986 Mantle and crustal xenoliths and the nature of the lower crust and upper mantle. Extended Abstracts Proc.4th Int.Kimb. Conf. Perth.224-227.

Hatton,C.J. & Gurney,J.J. 1987 Roberts Victor eclogites and their relation to the mantle. In "Mantle Xenoliths", P.H.Nixon (ed) 453-463. Wiley.

Hawksworth,C.J.,Rogers,N.W., Van Calsteren,P.W.C. & Menzies,M.A. 1984 Mantle enrichment processes.Nature.London 311: 331-334.

Henderson, P. 1982 "Inorganic Geochemistry." Pergamon Press, London .

Hervig,R.L., Smith,J.V., Steele,I.M., Gurney,J.J., Meyer,H.O.A. & Harris,J.W. 1980 Diamonds:minor elements in silicate inclusions:pressure-temperature implications. Journal of Geophysical Research 85. 6919-6929.

Herzberg,C.T. 1978 The bearing of phase equilibria in simple and complex sytems on the origin and evolution of some well-documented garnet-websterites. Contrib.Mineral.Petrol. 66: 375-382.

Hickey,R.L. & Frey,F.A. 1982 Geochemical charachteristics of boninite series volcanics:implications for their source.Geochim. Cosmochim. Acta.46: 2099-2115.

Hickey,R.L. & Frey,F.A. & Gerlach,D.C. 1986 Multiple sources for basaltic arc rocks from the southern volcanic zone of the Andes(34-41 S) trace element and isotopic evidence for contributions from subducted oceanic crust mantle and continental crust. Jour. Geophys. Res.86: 5963-5983.

Hofmann,A.W. & White,W.M. 1982 Mantle plumes from ancient oceanic crust. Earth. Planet. Sci. Lett. 57: 421.

Hofmann,A.W., Jochum,K.P., Seufert,M. & White,W.M. 1986 Nb and Pb in oceanic basalts on mantle evolution. Earth. Planet. Sci. Lett.79: 33-45.

Hoffman, S.E., Wilson, M. & Stakes, D.S. 1986 Inferred oxygen isotope profile of Archean oceanic crust, Onverwacht Group, South Africa. Nature.London 321: 55-58.

Hopwood,T. 1981 The significance of pyritic black shales in the genesis of archean nickel sulphide deposits. In "Handbook of Stratiform and Stratabound Ore Deposits".(ed) K.H.Wolf,Vol 9. Elsever,Amsterdam.412-465

Hooker, P.J., O'Nions, R.K. & Parkhurst, R.J. 1975 Determination of rare earth elements in U.S.G.S. standard rocks by mixed solvent ion exchange and mass spectrometric isotope dilution. Chem. Geol. 16: 189-196.

Howes,V. 1962 The graphitization of diamond. Proc. Phy. Soc. 80: 648-662.

Hulvin,P. & Permingeat,F. 1980 Graphite Ch.9 Notes et Memoires du Service Geologique du Maroc No. 276. 246-256.

Irving, A.J. 1978 A review of experimental studies of crystal/liquid trace element partitioning. Geochim. Cosmochim. Acta. 42: 743-770.

Irving, A.J. 1980. Petrlogy and geochemistry of composite ultramafic xenoliths in alkalic basalts and implications for magmatic processes in the mantle. Am. Jour. Science 280a: 389-426.

Ito, E., White, W.M. & Gopel, C. 1987 The O, Sr, Nd and Pb isotope geochemistry of MORB. Chemical Geology 62: 177-189.

Jackson, D.H., Mattey, D.P. & Harris, N.B.W. 1988 Carbon isotope compositions of fluid inclusions in charnokites from Southern India. Nature.London 333: 167-169.

Jacobsen, S.B., Quick, J.E. & Wasserburg, G.J. 1984 A Nd-Sr isotopic study of the Trinity peridotite; implications for mantle evolution. Earth. Planet. Sci. Lett. 68: 361-378.

Jagoutz, E. 1988 Nd and Sr systematics in an eclogite xenolith from Tanzania: evidence for frozen mineral equilibria in the continental lithsphere. Geochim. Cosmochim. Acta. 52: 1285-1293.

Jagoutz, E. Dawson, J.B., Hornes, S., Spettel, B. & Wanke, H. 1984 Anorthositic oceanic crust in the Archean. Lunar. Planet. Sci. 15: 395-396.

Jahn, B.M. 1986 Mid ocean ridge or marginal basin origin for the East Taiwan ophiolite: chemical and isotopic evidence. Contrib. Mineral. Petrol. 92: 194-206.

Jaques, A.L., Hall, A.E., Sheraton, J.W., Smith, C.B., Sun, S.S., Drew, R.M., Foudoulis, C. & Ellingsen, K. 1986 Composition of crystalline inclusions and C-isotopic composition of Argyle and Ellendale diamonds. In "Kimberlites and Related Rocks Vol 12. ed. J.Ross et al G.S.A. Spec.Pub. 14. Blackwell.Aus.966-990.

Javoy,M. 1980 $^{18}O/^{16}O$ and D/H ratios in high temperature peridotites. Colloq.Int. C.N.R.S. 272: 279-287.

Javoy,M.,Pineau,F. & Delorme, 1986 Carbon and nitrogen isotopes in the mantle. Chemical Geology 57: 41-62.

Javoy,M.,Pineau,F. & Iiyama,I. 1978 Experimental determination of the isotopic fractionation between genesis CO_2 and carbon dissolved in a tholeritic magma.Contrib. Mineral. Petrol. 67: 35-39.

Jenkins,G.M. 1973 Deformation mechanisms in carbons.In Physics and chem. 11 .189-242.

Jeyenes, C. 1978. Natural polycrystalline diamond. Industrial Diamond Review. Jan. 14-23

Kaminski,F.V., Patoka,M.G. & Sheymovich,V.S. 1980 The authority and regularity of occurances of dimonds in alkaline basaltoid and ultrabasic (other than kimberlite) rocks. Zapis.Vses.Min.Obsh. 4: 488-493 (in Russian).

Kamiya, Y. & Lang,A.R. 1965. On the structure of coated diamonds. Phil. Mag. 11 ser 7. 347-356

Kato, T. 1986 Stability relations os (Mg,Fe)SiO_3 garnets, major constituents of the Earth's interior. Eart. Planet. Sci. Lett. 77: 399-405.

Kellogg,A.H. &Turcotte,D.L. 1986 Homogenization of the mantle by convective mixing and diffusion. Earth. Planet. Sci. Lett. 81: 371-378.

Kempton, P.D., Harmon, R.S., Stosch, H.G., Hoefs, J. & Hawkesworth, C.J. 1988 Open-system-O-isotopic behavoir and trace element enrichment in the sub-Eifel mantle. Earth. Planet. Sci. Lett. 89: 273-287.

Koons, P.O. 1984 Implications to garnet clinopyroxene geothermometry of non-ideal solid solution in jadeitic pyroxenes. Contrib. Mineral. Petrol. 88: 340-347.

Kornprobst, J, 1969 Le massif ultrabasique des Beni Bouchera (Rif Interne, Maroc) Contrib. Mineral. Petrol. 23: 283-322.

Kornprobst, J, 1970 Les peridotites et les pyroxenolites du massif ultrabasique des Beni Bouchera: une etude experimentale entre 1100 et 1550 C sous 15 a 30kb de pression seche. Contrib. Mineral. Petrol. 29:

290-309.

Kornprobst,J, 1974 Contribution a l'etude petrographique et strucurale de la zone interne du Rif (Maroc Septentrional) Notes. Serv. Geol. Maroc. T 251. 256pp.

Kornprobst, J. 1976 Existence d'un affleurment de Websterite a spinelle d;origine mantelique dans le trias d'une unite du teil meridonac au voisinage de mendes.C.R.Acad.Sc.Paris. 283.

Kornprobst,J, 1977 Garnet zoning and orthopyroxene+plagioclase coronitization Contrib. Mineral. Petrol. 38: 290-301.

Kornprobst,J. Piboule, M. & Roux, L. 1982. Corundum bearing garnet pyroxenites at Beni Bousera (Morocco): An exceptionally Al-rich clinopyroxene from grospydites associated with ultramafic rocks. Terra Cgnita 2. 257-259.

Kornprobst, J. &Vielzeuf,D. 1984 Transcurrent crustal thinning: a mechanism for the upper lift of deep continental crust/ upper mantle associations. In "Kimberlites II : The Mantle and Crust-Mantle Relations " Elsevier, Amsterdam. 347-355.

Kornprobst,J. Piboule, M. & Roden, M.F. 1987 Corundum bearing garnet pyroxenite from Beni Bousera, Morocco. EOS 68, No.16: 437.

Kramers, J.D. 1979 Lead, uranium, strontium, potassium and rubidium in inclusion-bearing diamonds and mantle derived xenoliths from Southern Africa. Earth. Planet. Sci. Lett. 42: 58-70.

Krogh, E.J. 1988 The garnet clinopyroxene Fe-Mg geothrmometer- a reinterpretation of existing experimental data. Contrib. Mineral. Petrol. 99: 44-48

Kyser,T.K. 1986 Stable isotope variations in the mantle. In "Stable Isotopes in High Temperature Geological Processes" Reviews in Mineralogy. Vol.16. (ed) J.W.Valley, H.P.Taylor & J.R.O'Neil. Min. Soc. Am. 141-164.

Kyser,T.K.,O;Neil,J.R. &Carmichael,I.S.E. 1981 Oxygen isotope thermometry of basic lavas and mantle nodules. Contrib. Mineral. Petrol. 77: 11-23.

Kyser,T.K., Cameron, W.E. & Nisbet, E.G. 1986 Boninite perogenesis and acteration history: constraints from stable isotope compositions of boninites from Cape Vogel, New Caledonia and Cyprus. Contrib. Mineral. Petrol. 93: 222-226.

Kyser,T.K.,O'Neil,J.R. &Carmichael,I.S.E. 1982 Genetic relations among basic lavas and ultramafic nodules: evidence from oxygen isotope compositions.Contrib. Mineral. Petrol. 81: 88-102.

Lamb, W. & Valley, J.W. 1984 Metamorphism of reduced granulites in low- CO_2 vapour-free environment. Nature.London 312: 56-58.

Lang, A.R. 1974 . Glimpses into the growth history of natural diamonds Jour. Crystal Growth 24/25. 108-115.

Langmuir,C.H., Vocke,R.D. & Hanson,G.N. 1978 A general mixing equation with applications to Icelandic basalts. Earth. Planet. Sci. Lett. 37: 380-392.

Lansier, B. 1971 Les peridotites and pyroxenolites a grenat du Boid des Feuilles Contrib. Mineral. Petrol. Contrib. Mineral. Petrol. 34: 29-42

Lardeaux,J.M., Caron,J.M., Pequignot,G. &Boudeulle,M. 1986 Microstructural criteria for reliable thermometry in low temperature eclogites.Lithos 19. 187-203.

Leblanc,M. 1986 Co-Ni arsenide deposits, with accessory gold, in ultramafic rocks from Morocco. Canadian Mineralogist.23. 1592-1602.

Leblanc,M.& Zdenek,J. 1986 Un nouveau type de mineralisation plantinifere: exemple des filons a arseniures de nickel et chromite du massif lherzolitique des Beni Bousera (Maroc). C.R.Acad.Sci .Paris. T

303 Ser II No.2: 163-166.

Lespade,P., Al-Jishi,R. & Dresselhaus,M.S. 1982 Model for Raman scattering from incompletely graphitized carbons. Carbon 20: 427-431.

Lindsley, D.H. & Anderson, D.J. 1983 A two pyroxene thermometer. Proc. 13th Lunar & Planetary Science Conference. Part2. A887-A906

Lippard,S.J., Skelton,R.W & Gass,I.G. 1988 The ophiolite of Northern Oman. Blackwell, London.

Lonsdale,K. & Milledge,H.J. 1964 X-ray diffraction studies on diamonds. In " The Physical Properties of Diamond".R.Berman (ed). Oxford Univ. Press. 12-64.

Loomis, T.P. 1972 Diapiric emplacement of the Ronda high temperature intrusion, southern Spain. Geol. Soc. Am. Bull. 83. 24-75

Loomis,T.P. 1975 Teritary mantle diapirism, orogeny and plate tectonics east of the Strait of Gibralter. AmJ.Sci 275: 1-30.

Lorand,J.P. 1985 The behavoir of thr upper sulphide component during the incipient alteration of 'Alpine'-type peridotites as illustrated by the Beni Bousera (N.Morocco) and Ronda (S.Spain) ultramafic bodies.Tschermaks Min.Petr.Mitt 34, 183-209.

Loubet,M., Polve,M., Richard,P. & Allegre,C. 1980 Geochemical studies in orogenic lherzolites: evidence about multiple magmatic events. Colloq.Int.CNRS. 272: 269-277.

Ludwig,K. 1986 Isoplot 200. A plotting and regression program for isotope geochemists, for use with HP series 200 computers. U.S. Geological Survey, open file report 85: 51.

Luth, R.W., Virgo, D., Boyd, F.R. & Wood, B.J. 1989 Iron in mantle derived garnets. EUG abstracts p136.

MacGregor,I.D. 1974 The system MgO-Al2O3-SiO2: solubility of Al2O3 in enstatite for spinel and garnet peridotite compositions Am. Mineral. 59. 110-119.

MacGregor,I.D. & Manton,W.I. 1986 Roberts victor eclogites : ancient oceanic crust. Jour. Geophys. Research.91: 14063-14079.

Machado,N., Brooks,C. & Hart,S.R. 1986 Determination of initial $^{87}Sr/^{86}Sr$ and $^{143}Nd/^{144}Nd$ in primary minerals from mafic and ultramafic rocks: Experimental procedure and implications for the isotopic characteristics of the Archean mantle under the Abitibi greenstone belt, Canada. Geochim. Cosmochim. Acta. 50: 2335-2348.

Machado, W.G., Moore, M. & Woods, G.S. 1985 On the Dodecahedral growth of coated diamonds Jour. Crystal Growth 71. 718-727

Malpas,J. 1978 Magma generation in the upper mantle, field evidence from opholite suites and application to the generation of oceanic lithosphere. Phil.Trans.R.Soc.Lond. A 288: 527-546.

Mattey,D.P. 1987 Carbon isotopes in the mantle. Terra Cognita, 7: 31-37.

Mattey,D.P., Carr,R.H., Wright,I.P. & Pillinger,C.T. 1984 Carbon isotopes in submarine basalts. Earth. Planet. Sci. Lett. 70: 196-206.

Mattey,D.P., Exley,R.A., Pillinger,C.T., Menzies,M.A., Porcelli,D.R., Galer,S. & O'Nions,R.K. 1986 Relationships between C, He, Sr and Nd isotopes in mantle diopsides. In "Kimberlites and Realted Rocks" Vol 2 ed.J.Ross et al. Spec.Pub. No.14. 913-921. Blackwell, Australia.

McCullough,M.T., Gregory,R.T., Wasserburg,G.J. & Taylor,H.P. 1980 A neodymium,strontium and oxygen isotopic study of the Cretaceous Samail ophiolite and implications for the petrogenisis and seawater-hydrothermal alteration of oceanic crust.Earth. Planet. Sci. Lett. 46: 201-211.

McCulloch,M.T., Jaques,A.C., Nelson,D.R. & Lewis,J.D. 1983 Nd and Sr isotopes in kimberlites and lamproites from Western Australia: an enriched mantle origin. Nature 302: 400-403.

McDonough,W.F. & McCulloch,M.T. 1987 The South East Australia lithospheric mantle: Isotopic and geochemical constraints on its growth and evolution. Earth. Planet. Sci. Lett. 86: 327-340.

McKenzie,D. 1986 Mantle mixing still a mystery. Nature 323: 297.

Menzies,M.A., Halliday,A.N., Palacz,Z., Hunter,R.H., Upton,B.G.T., Aspen,P. & Hawkesworth,C.J. 1987 Evidence from mantle xenoliths for an enriched lithospheric keel under the Outer Hebrides.Nature.London 325: 44-47.

Mercier, J.C. (1985) Olivines and pyroxenes In " Preferred Orientation in Deformed Metals and Rocks" (ed) H.R. Wenk Academic Press 407-423

Mercier, J.C., Benoit, V., & Girardeau, J. 1984 Equlibrium state od diopside bearing harzburgites from ophiolites: Geobarometric and geodynamic implications. Contrib. Mineral. & Petrology 85. 391-403.

Meyer,H.O.A. 1982 Mineral inclusions in natural diamond.International Geological Proceedings: Gemological institute of America,Los Angeles. 447-465.

Mikailov, N.P. 1975 Donnees nouvelles sur la petrologie et la structure interne du massif ultramfique des Beni Bousera (Rif paleozoique, Maroc du Nord) Mines et Geologie No. 38. Rabat.

Milledge,H.J., Hendelssohn,M.J., Seal,M., Rouse,J.E., Swart,P.K., & Pillinger,C.T. 1983 Carbon isotopic variation in spectral type II diamonds. Nature 303: 791-792.

Miller,C. & Richter,W. 1982 Solid and fluid phases in lherzolite and pyroxenite inclusions from the Hoggar,Central Sahara. Geochemical Journal 16. 263-277.

Milliard, Y. 1959 Les massifs metamorphiques et ultrabasiques de la zone Paleozoique Interne du Rif. Notes. Serv. Geol. Maroc. T.18: 125-160.

Moody, J.B. 1976 Serpentinization: A review Lithos 5: 125-138.

Moore,R.O. & Gurney,J.J. 1985 Pyroxene solid solution in garnets incuded in diamond.Nature.London 318: 553-555

Moore,M. 1979 Optical studies of diamonds and their surfaces: a review of the late Professor Tolansky's work.J.E.Field (ed) Properties of Diamond 245-278. Aced. Press.

Moore,M. & Lang,A.R. 1974 On the origin of the rounded dodecahedral habit of natural diamond.J. Crystal Growth.26. 133-139.

Morgan,J.W. 1986 Ulramafic xenoliths : clues to Earth's late accretionary history.Jour. Geophys. Research. 91: No.B12. 12375-12387.

Morimoto, N. and sub. comittee, 1988 Nomenclature of pyroxenes Am. Min. 73: 1123-1133.

Morten,L., Brunfelt,A.O. & Mottana,A. 1979 Rare earth abundences in superferrian eclogites from the Voltri group. Lithos 12: 25-32.

Mottana,A. 1986 Crystal-chemical evaluation of garnet and omphalite microprobe analysis: its bearing on the classification of eclogites. Lithos 19: 171-186.

Muehlenbachs,K. 1986 Alteration of the oceanic crust and the ^{18}O history of seawater. In "Stable Isotopes in High Temperature Geological Processes". (eds) Valley,J.W., Taylor,H.P.& O'Neil,J.R. Reviews in Mineralogy, Vol 16.Min.Soc.Am.

Munke,G. 1979 Physics of diamond growth. In "Properties of Diamond" (ed) J.E.Field Academic.Press. 473-499.

Mutsukazu,K, Sato,Y. Matsumoto,S. & Setaka,N. 1983 Diamond synthesis from gas in microwave plasma.J. Crystal Growth. 62: 642-644.

Nakahura,Y., Fujimaki,H., Nakamura,N. & Tatsumoto,M. 1986 Hf, Zr and REE partition coefficients between ilmenite and liquid: Implications for Lunar petrogenesis. Jour. Geophys. Res. 91.84: D239-D250.

Nelson,D.R. & McCulloch,M.T. 1986 Enriched mantle components and recycling of sediments. Ch.6. In: "Kimberlites and Related Rocks, Vol 1. Geol.Soc.Aus.Spec.Pub. No 14 ed J.Ross et al Blackwell Aus. 560-570.

Nelson,D.R. & McCulloch,M.T. & Sun,S.S. 1986 The origins of ultrapotassic rocks as inferred from Sr, Nd and Pb isotopes. Geochim. Cosmochim. Acta. 50: 231-245.

Nemanich,R.J. & Solin,S.A. 1979 First and second order Raman scattering from finite size crystals of graphite. Physical Review B, 20: 392-401.

Newsome,H.E., White,W.M., Jochum,K.P. & Hofmann,A.W. 1986 Siderphile and chalcophile element abundances in oceanic basalts,Pb isotope evolution and growth of the earth's core. Earth. Planet. Sci. Lett. 80: 299-313.

Newton,R.C. 1986 Metamorphic temperatures and pressures of group B and C eclogites. Spec. Pub. Geol. Soc. Am. 164 :17-25.

Newton,R.C., Smith,J.V. & Windley,B.F. 1980 Carbonic metamorphism, granulites and crustal growth. Nature 288: 45-50.

Nickel,K.G. & Green,D.H. 1985 Empirical geothermobarometry for garnet periodites and implications for the nature of the lithosphere, kimberlites and diamond. Earth. Planet. Sci. Lett. 81: 158-170

Nicolas,A. 1986a Stucture and petrology of peridotites clues to their geodynamic environment. Reviews of Geophysics. 24. No.4 875-895.

Nicolas,A. 1986b A melt extraction model based on structural studies in mantle peridotites Jour. Petrology 27: 999-1022.

Nicolas,A. & Jackson, M. 1982 High temperature dikes in peridotite: Origin by hydraulic fracturing. Jour. Petrology 23: 568-582.

Nixon, P.H. 1973 (ed) "Lesthoto Kimberlites" Maseru National Development Board. Lesotho.

Nixon,P.H., von Calsteren,P., Boyd,F.R. & Hawkesworth,C.J. 1987 Harzburgites with garnets of diamond facies from Southern Africa. In "Mantle Xenoliths" ed P.H.Nixon. Wiley.U.K. 523-533.

Nixon,P.H. & Davies,G.R. 1986 Mantle xenoliths: perspectives. In: P.H.Nixon (ed) Mantle Xenoliths.

Obata,M. 1980 The Ronda peridotite : garnet,spinel and plagioclase lherzolite facies and the P-T trajectories of a high temperature mantle intrusion. Jour. Petrology 21. 533.

Oen,I.S., Burke,E.A.J., Kieft,C. & Westerhof,A.B. 1971 Ni-arsenides,Ni-rich loellingite and (Fe-Co)-rich gersdorffite in Cr-Ni ores from Malaga Province,Spain.Neues.Jahrbuchfeur Mineralogie, Abhandlungen 115: 123-139.

Oen,I.S., & Kieft,C. 1974 Nickeline with pyrrhotite and cubanite exsolutions Ni-Co-rich loellingite and Au-Cu alloy in Cr-Ni ores from Beni Bousera,Morocco. Neues. Jahrbuch Feur Mineralogie, Abhandlungen 119: 1-8.

O'Hara,M.J. 1967 The bearing of phase equilibria studies in synthetic and natural systems on the origin and evolution of basic and ultrabasic rocks. Earth Sci. rev. 4: 69-133.

O'Hara,M.J. 1985 Importance of the 'shape' of the melting regime during partial melting of the

mantle. Nature.London 314: 58-62.

Ohmoto,H. & Krerrick,D. 1977 Devolatization equlibria in graphitic systems Am. J. Sci. 277: 1013-1044.

Okada,A. & Shima,M. 1972 Crystallographic study of cliftonite: A new internal structure found in the inclusion of the Campo Del Cielo meteorite. Journal Japan. Assoc. Min. Petr. Econ. Geol 67: 45-49.

O'Neil,J.R. 1986 Theroretical and experimental aspects of isotopic fractionation. In "Stable Isotopes in High Temperature Geological Processes" (eds)J.W.Valley, H.P.Taylor and J.R.O'Neil. Reviews in Minerlogy. Vol 16. Min.Soc. Am. 1-37.

O'Neill,H.St.C. 1981 "The transition between spinel lherzolite and garnet lherzolite and its use as a geobarometer" Contrib. Mineral. Petrol. 77: 185-194.

O'Nions,R.K., Evensen,N.M. & Hamilton,P.J. 1979 Geochemical modelling of mantle differentiation and crustal growth. J.Geophys.Res. 84: 6091-6101.

Ongley,J.S., Basu,A.R. & Kyser,T.K. 1987 Oxygen isotopes in coexisting garnets, clinopyroxenes and phlogopites of Roberts Victor eclogites: implications for petrogenesis and mantle metasomatism. Eart. Planet. Sci. Lett. 83: 80-84.

Orlov,Yu. 1973 "The Mineralogy of the Diamond." Wiley, New York.

Ottenello,G., Joron,J.L., & Piccardo,G.B. 1984 Rare earth and 3d transition element geochemistry of peridotitic rocks: II Ligurian peridotites & associated basalts. Jour. Petrol. 25: 373-393.

Ottenello,G., Piccardo,G. & Ernst,W.G. 1979 Petrogenesis of some ligurian peridotites,II rare earth element chemistry. Geochim. et Cosmoch. acta. 43: 1273-1281

Ozawa, K. 1983 Evaluation of olivine -spinel geothermometry as an indicator of thermal history for peridotites. Contrib. Mineral. & Petrology 82. 52-65.

Ozima,M., Zashu,S. &Nitoh,O. 1983 $^{3}He/^{4}He$ ratio,noble gas abundance and K-Ar dating of diamonds- an attempt to search for the records of early terrestrial history. Geochim. Cosmochim. Acta. 47: 2217-2224.

Palacz,Z.A. & Saunders,A.D. 1986 Coupled trace element and isotopic ecrichment in the Cook-Austral-Samoa Islands, South West Pacific. Earth. Planet. Sci. Lett. 79: 270-280.

Pallister,J.S. & Knight, R.J. 1981 Rare-earth element geochemistry of the Samail ophiolite near Ibra, Oman. Jour. Geophys. Res. 86: 2673-2697.

Pasteris,J.D. 1981 Occurrence of graphite in serpentinized olivines in kimberlite Geology 9: 356-359.

Pasteris,J.D. 1987 Fluid inclusions in mantle xenoliths. In "Mantle Xenoliths".(ed) P.H.Nixon. Wiley. New York.

Patchett,P.J., White,W.M., Feldmann,H., Kielinczuk,S. & Hofmann,A.W. 1984 Hafnium/rare earth element fractionation in the sedimentary system and crustal recycling into the earth's mantle. Earth. Planet. Sci. Lett. 69: 365.

Pattison, D.R.M. & Newton, R.C. 1987 Garnet-clinopyroxene Kd (Fe-Mg) variations due to X^{GT}_{Ca} and pressure. Abstract. EOS. Trans. AGU. 68: 461.

Pauly, H. 1969 White cast iron from cohenite, schreibersite and sulphides from Tertiary basalts on Disko Island, Greenland. Medd. Dansk. Foren. 19: 8-26.

Pearson, D.G., Davies, G.R., Nixon, P.H. & Milledge, H.J. 1989 Graphitized diamonds from a peridotite massif in Morocco and implications for anomalous diamond occurrences. Nature 338, 60-62.

Pearson, D.G., Davies, G.R. & Nixon, P.H. 1989 Graphite-bearing pyroxenites from Morocco: evidence of recycled oceanic lithosphere and the origin of E-type diamonds. Extended abstracts: Workshop on Diamonds 28 th I.G.L. 83-86.

Philpotts,J.A., Schnetzler,C.C. & Thomas,H.H. 1972 Petrogenic implications of some new geochemical data on eclogite and ultrabasic inclusions. Geochim. Cosmochim. Acta 36: 1131-1166.

Pineau,F. & Javoy,M. 1983 Carbon isotopes and concentrations in mid-oceanic ridge basalts. Earth. Planet. Sci. Lett. 62: 239-257.

Pineau,F. & Javoy,M. & Kornprobst,J. 1987 Primary igneous graphite in ultramafic xenoliths: II Isotopic composition of the carbonaceous phases.Present in xenoliths and host lava at Tissemt, (Eggere, Algerian Sahara). Jour. Petrology 28: 313-322.

Platt,J.P. 1989 Extensional collpase of thickened continental lithosphere: A working hypothesis for the Alboran Sea and Gibralter arc. Geology. vol 17: 540-543.

Polve,M. 1983 Les isotopes du Nd et du sr dans les lherzolites orogeniques: contribution a la determination de la structure et de la dynamique du manteau superieur. Unpub. PhD thesis. Paris 7.

Polve,M. & Allegre,C.J. 1980 Orogenic lherzolite complexes studied by ^{87}Rb-^{87}Sr. A clue to understanding mantle convection processes? Earth. Planet. Sci. Lett. 51: 71-81.

Powell, R. 1985 Regression diagnostics and robust regression in geothermometer/geobarometer calibration: The garnet clinopyroxene geothermometer revisited. Jour. Metamorphic Geol. 3. 231-243.

Priem,H.N.A., Bolerrijk,N. Hebeda,E., Oen,I.S., Verdurmen,E. & Verschure,R.H. 1979 Isotopic dating of the emplacement of the ultramafic masses in the Sierra De La Ronda, southern Spain. Contrib. Mineral. Petrol. 70: 103-109.

Prinzhofer,A. & Allegre,C.J. 1985 Residual peridotites and the mechanisms of partial melting . Earth. Planet. Sci. Lett. 74 : 251-265.

Prinzhofer,A., Lewin,E. & Allegre,C.J. 1989 Stochastic melting of the marble cake mantle: evidence from local study on the East Pacific Rise at 12°50' N. Earth. Planet. Sci. Lett. 92: 189-206.

Raheim,A. & Green,D.H. 1975 P.T. paths of natural eclogites during metamorphism, a record of subduction.Lithos 8. 317-328.

Reid, A.M. & Dawson, J.B. 1970 Olivine -garnet reaction in peridotites from Tanzania Lithos 5/; 115-124

Reid,A.M.,Brown,R.W.,Dawson,J.B.,Whitfield,G.G. & Seiebert,J.C. 1976 Garnet and pyroxene compositions in some diamondiferous eclogites. Contrib. Mineral. Petrol. 58: 203-220.

Reid, J.B. & Woods, G.A. 1978 Oceanic mantle beneath the southern Rio Grande rift. Earth Planet. Sci. Lett. 41: 303-341.

Reisberg,L. & Zindler,A. 1987 Extreme isotopic variations in the upper mantle: evidence from Ronda. Earth. Planet. Sci. Lett..81: 29-45.

Reuber,I.,Michard,A., Chalcouan,A. Juteau,T. & Jermoumi,B. 1982 Structure and emplacement of the Alpine type periodites from Beni Bousera, Rif Morocco: a polyphase tectonic interpretation.Techtonophysics. 82: 231-251.

Reynolds. 1968 "Physical Properties of Graphite". Elselvier.

Richard,P. & Allegre,C.J. 1980 Neodymium and strontium isotope study of ophiolite and orogenic lherlite petrogenesis. Earth. Planet. Sci. Lett.47: 65-76

Richardson,S.H., Erlank,A.J. & Hart,S.R. 1985 Kimberlite-borne garnet peridotite xenoliths from old

enriched subcontinental lithosphere. Earth. Planet. Sci. Lett. 75: 116-128.

Richardson,S.H., Gurney,J.J, Erlank,A.J. & Harris,J.W. 1984 Origin of diamonds in old enriched mantle. Nature.London 310: 198-201.

Richardson,S.H. 1986 Latter-day origin of diamonds of eclogite paragenesis. Nature.London 322: 623-625.

Richter,F.M. 1986 Simple models for trace element fractionation during melt segregation. Earth. Planet. Sci. Lett. 77: 333-344.

Ricou, L.E. Dercourt. J., Geyssant, J., Grandjacquet, C., Lepvrier, C. & Biju-Duval, B. 1986 Geological consrtaints on the Alpine evolution of the Mediterranean Tethys. Tectonophys. 123: 83-122.

Ringwood,A.E. 1982 Phase transformations and differentiation in subducted lithosphere: implications for mantle crustal evolution. J. Geology. 90: 611-629.

Ringwood, A.E. 1986 . Constitution and evolution of the mantle. In " Kimberlites and Related Rocks" Vol.2 G.S.A. Spec. Pub. Blackwell Aus. 457-485.

Robinson,D.N 1978 A review of the characteristics of natural diamond and their interpretation. Min. Sci. Eng. 10: 55-72.

Robinson,D.N., Gurney,J.J. & Shee,S.R. 1984 Diamond eclogite and graphite eclogite xenoliths from Orapa Botswana. In " Kimberlites II, The Mantle and Crust-Mantle Realtions " (ed) J. Kornprost, Elsevier, Amsterdam. 11-24.

Robinson,D.N. 1979 Diamond and graphite in eclogite xenoliths from kimberlite. In "The Mantle Sample" (eds) Boyd,F.R. & Meyer,H.O.A. A.G.U. Press Washington. 50-58

Roddick,J.C., Cliff,R.A. & Rex,D.C. 1980 The evolution of excess argon in Alpine biotites - A $^{40}Ar/^{39}Ar$ analysis. Earth. Planet. Sci. Lett. 48: 185-208.

Roden,M.F. & Rama-Murthy,V. 1985 Mantle metasomatism.Ann.Rev. Earth. Planet Sci. 1985 13: 269-297.

Roden,M.K., Frey,F.A. & Melson,W.G. 1984 Sr, Nd and Pb isotopic and REE geochemistry of St. Paul's Rock : the metamorphic and metasomatic development of an alkali basalt source. Contrib. Mineral. Petrol. 85: 376-390.

Roeder, P.L., Campbell, I.H. & Jamieson, H.E. 1979 A re-evaluation of the olivine-spinel geothermometer. Contrib. Mineral. & Petrology 68. 325-334.

Rubie,D.C. 1983 Reaction-enhanced ductility : the role of solid-solid univariant reactions in deformation of the crust and mantle. Tectonophysics. 96: 331-352.

Rumble,D. & Hoering,T.C. 1986 Carbon isotope geochemistry of graphite vein deposits from New Hampshire,U.S.A. Geochim. Cosmochim. Acta 50: 1239-1247.

Schidlowski,M. 1988 A 3,800 - million- year isotopic record of life from carbon in sedimentary rocks. Nature. 333: 313-318.

Schweitzer,E.L., Papike,J.J. & Bence,A.E. 1979 Statistical analysis of clinopyroxenes from deep sea basalts . Am. Min. 64. 501-513.

Seal,.M. 1958 Graphitization and plastic deformation of diamond .Nature.London 182: 1264-1266.

Sekine,T., Irifune,T., Ringwood,A.E. & Hibberson,W.O. 1986 High pressure transformation of eclogite to garnite in subducted oceanic crust. Nature.London 319: 584-586.

Shaw,H.F., Chen,J.H., Saleeby,J.B. & Wasserburg,G.J. 1987 Nd-Sr-Pb systematics and age of the Kings River ophiolite, California: implications for depleted mantle evolution. 96: 281-290.

Shee,S.R., Gurney,J.J. & Robinson,D.N. 1982 Two diamond-bearing peridotite xenoliths from the Finsch kimberlite, South Africa. Contrib. Mineral. Petrol. 81: 79-87.

Shervais,J.W.,Taylor,L.A., Lugmair,G.W., Clayton,R.N., Mayeda,T.K. & Kordiev,R.L. 1988 Early proerozoic oceanic crust and the evolution of subcontinental mantle: eclogites and related rocks from Southern Africa. Bull. Geol. Soc. Am 100: 411-423.

Shimizu,H. 1980 Experimental study on rare earth element partitioning in minerals formed at 20 and 30 kb for basaltic systems. Geochem. J. 14: 185-202.

Shimizu,N 1975 Rare earth elements in garnets and clinopyroxenes from garnet lherzolite nodules in kimberlite. Contrib. Mineral. Petrol. 25: 26-32.

Shimizu,N. & Richardson,S.H. 1987 Trace element abundance patters of garnet inclusions in periotite suite diamonds. Geochim. Cocmochim. Acta. 51: 755-758.

Shimizu,N. & Le Roux,A.P. 1986 The chemical zoning of augite phenocrysis in alkaline basalts from Gough Island ,South Atlantic. Jour. Volcanology and Geothermal Research 29: 159-188.

Simakov,S.K. 1982 Formation and crystalization of diamond from fluid in mantle melts. Doklady Academi Nauk SSSR 266. No.2: 470-473

Simakov,S.K. 1984 Possible production of metastable diamond from fluids in the crust.Doklady Akademii Nauk SSSR 278. No.4: 953-957.

Sleep, N.H. 1988 Trapping of melt by veins and dikes. Jour. Geophys. Res. 93: 10255-10272.

Slodkevich,V.V. 1980a Polycrystalline aggregates of octahedral graphite.Doklady.253. No.3: 697-700.

Slodkevich,V.V. 1980b Graphite paramorphs after diamond .Internat. Geol. Rev 25 .No.5

Slodkevich,V.V. & Lobkov,V.A. 1983 Isotopic composition of graphite from the mafic-ultramafic pluton at Beni Bousera, Morocco (in Russian). Doklad. Akad. Nauk. SSSR 272: 698-701.

Smith,C.B. 1983 Rubidium, Strontium, Uranium-Lead and samarium-neodymium isotopic studies of kimberlite and related mantle derived xenoliths. Unpub. PhD thesis. Univ. Witwatersrand. South Africa.

Smith,C.B., Gurney,J.J., Harris,J.W., Otter,M.L., Kirkley,M.B. & Jagoutz,E. 1989 Sr and Nd isotope systematics of large eclogite and lherzolite paragenesis single diamonds, Finsch and Kimberley Pool. Extended Abstracts, Workshop on diamonds 28 th I.G.C. 102-104.

Smith,C.B., Gurney,J.J., Harris,J.W., Robinson,D.N., Shee,S.R. & Jagoutz,E. 1986 Sr and Nd isotopic systematics of diamond-bearing eclogite xenoliths and eclogite inclusions in diamonds from Southern Africa. Ch 17 In: "Kimberlites and Related Rocks" Vol 2 Geol. Soc. Aus. Special Publication No 14 ed. J.Ross et al Blackwell. 853-863.

Smyth,J.R., Caporuscio,F.A. & McCormick,T. 1989 Mantle eclogites: evidence of igneous fractionation in the mantle. Earth. Planet. Sci. Lett. 93: 133-141.

Sneeringer,M., Hart,S.R. & Shimizu,N. 1984 Strontium and samarium diffusion in diopside. Geochem. Cosmochim. Acta. 48: 1589-1608.

Sobolev, N.V 1979 "The Problem of the Constitution of the Earth's Upper Mantle" AGU press Washington (Translated from Russian).

Sobolev, N.V. & Lavrent'ev, Ju.G. 1971 Isomorphic sodium admixture in garnets formed at high pressures. Contrib. Mineral. Petrol. 31: 1-12.

Sobolev,N.V., Galimov,E.M., Ivanovskaya,I.N. & Yefimova,E.S. 1979 Isotopic composition of carbon of diamonds containing crystalline inclusions. (In Russian). Docklady. Ak. Nauk. SSSR 249:

1217-1220.

Song,Y. & Frey,F.A. 1989 Geochemistry of peridotite xenoliths in basaltic form Hannuoba, Eastern China: Implications for subcontinental mantle heterogeneity. Geochem. Cosmochim. Acta. 53: 97-113.

Stakes,D.S.,Taylor,H.P. & Fisher,R.L. 1984 Oxygen-isotope and geochemical characterization of hydrothermal alteration in ophiolite complexes and modern oceanic crust. In Ophiolites and Oceanic Lithosphere, eds. Lippard,S. Gass,I.G. and Skelton,R.W. Spec.publ. Geol. Soc. Cond. 199-214.

Steiger,R.H. & Jager,E. 1977 Subcommission on geochronology: convention on the use of decay constants in geo-and cosmochronology. Earth. Planet. Sci. Lett. 36: 359-362.

Stosch,H.G. & Lugmair,G.W. 1986 Trace element and Sr and Nd isotope geochemistry of periodite xenoliths from the Eifel, (West Germany) and their bearing on the evolution of the subcontinental lithosphere. Earth. Planet. Sci. Lett. 80. 281-298.

Suen,C.J. & Frey,F.A. 1987 Origins of the mafic and ultramafic rocks in the Ronda peridotite. Earth. Planet. Sci. Lett. 85: 183-202.

Sun,S.S. & McDonough,W.F. 1989 Chemical and isotopic systematics of oceanic basalts: implications for mantle composition and processes. In "Magmatism in the Ocean Basins" eds. M.J.Norry and A.D.Saunders. Geol. Soc. Spec. Pub 42: 313-345.

Sun,S.S. & Nesbitt,R.W. 1979 Geochemical charcteristics of mid-ocean-ridge basalts.Earth. Planet. Sci. Lett. 44.119.

Sun,S.S 1980 Lead isotopic study of young volcanic rocks from mid-ocean ridges, ocean islands and island arcs. Phil. Trans. R. Soc. Land. 409-445.

Sunagawa,I. 1977 Journal of crystal growth . 42. 214-223.

Sunagawa,I. 1984a Morphology of natural and synthetic diamond crystals. In Sunagawa,I., ed., Materials Science of the Earth's Interior. 303-330. Terra Scientific, Tokyo.

Sunagawa,I. 1984b Growth of crystals in nature. In Sunagawa,I., ed., Materials Science of the Earth's Interior, 63-105. Terra Scientific, Tokyo.

Suzuki,S. & Lang,A.R. 1976 Internal structures of natural diamonds revealing mixed growth habit.Diamond Research 1976 39-47 Supplement to Industrial Diamond Review, London.

Swart,P.K., Pillinger,C.T., Milledge,H.J. & Seal,M. 1983 Carbon isotopic variation within individual diamonds. Nature.London 303: 693-695.

Tatsumoto,M. 1978 Isotopic composition of lead inoceanic basalts and its implications for mantle evolution.Earth. Planet. Sci. Lett. 38. 63-87.

Taylor,H.P. 1980 The effects of assimilation of country rocks by magmas on $^{18}O/^{16}O$ and $^{87}Sr/^{86}Sr$ systematics in igneous rocks. Earth. Planet. Sci. Lett. 47: 243-254.

Taylor,H.P. & Margaritz,M. 1976 Oxygen, hydrogen and carbon isotope studies of the Franciscan formation, Coast Ranges, California. Geochem. Cosmochim. Acta 40: 215-234.

Thayer,T.P. 1960 Some critical differences between alpine-type and stratiform peridotite-gabhro complexes. Inter. Geol. Congr. 21st Sess. Copenhagen. 13: 247-259.

Thompson,R.N. 1974 Some high pressure pyroxenes. Min. Mag.39: 768-787.

Thompson,R.N. 1975 Is upper mantle phosphorous contained in sodic garnet ? Earth. Planet. Sci. Lett. 26: 417-424.

Thompson,R.N. 1984 Dispatches from the basalt front .I experiments. Proc .Geol. Assn. 249.

Thompson,R.N., Morrison,M.A., Hendry,G.L. & Parry,S.J. 1984 An assessment of the relative roles of crust and mantle in magma genesis; an elemental approach.Phil. Trans.R. Soc. Land. 310: 549-561.

Tolansky,S. 1964 Graphitized natural diamond .Diamond Research 1976 8-10. Supp. to Ind. diamond review, London.

Torres-Rodlan, R.L. 1979 The tectonic subdivision of the Betic zone (Betic Cordilleras, Southern Spain): Its significance and one possible geotectonic scenario for the westernmost Alpine belt. Am. J. Sci. 279: 19-51.

Trofimov,V.S. 1983 Diamond concentration in crustal structures. Doklady Akedemi Nauk. SSSR 273 No.4: 949-953.

Tsai,H., Sheih,Y. & Meyer,H.O.A. 1979 Mineralogy and $^{34}S/^{32}S$ ratios of sulphides associated with kimberlite, xenoliths and diamonds. In "The Mantle Sample" ed. F.R.Boyd & O.A.Meyer AGU Press. 87-103.

Tuinstra,P. & Koenig,J.L. 1970 Raman spectrum of graphite. J. Chem. Phys. 53: 1126-1130.

Urey,H.C. 1956 Diamonds, meteorites and the origin of the solar system. Astrophysical Journal. 124. 623-637.

Valley,J.W. 1986 Stable isotope geochemistry of metamorphic rocks. In "Stable isotopes in high temperature Geological processes" eds. J.W.Valley, H.P.Taylor and J.R.O'Neil, Reviews in Mineralogy vol 16. Min. Soc. Am. 445-489.

Veizer,J., Compston,W., Clauer,N. & Schidlowski,M. 1983 $^{87}Sr/^{86}Sr$ in late Proterozoic carbonates: Evidence for a mantle event at ~900 Ma ago. Geochim. Cosmochim. Act. 47: 295-302.

Vinogradov,A.P., Kropotova,O.I., Orlov,Y.U.L. & Grineko,V.A. 1966 Isotopic composition of diamond and carbonado crystals. Geochemistry International 3: 1123-1125.

Voshage,H., Hunziker,J.C., Hoffmann,A.W. & Zingg,A. 1987 A Nd and Sr isotopic study of the Ivrea zone, Southern Alps, N.Italy. Conrib. Miner. Petrol. 97: 31-42.

Wagner,L.R. & Brown,G.M. 1968 Layered Igneous Rocks. Oliver & Boyd, Edinburgh: 588p

Wagner,P.A. 1914 The diamond fields of Southern Africa. Struik Pty Ltd, Capetown (1971 reprinted).

Weaver,B.L., Wood,D.A., Tarney,J. & Jordon,J.L. 1986 Role of subducted sediment in the genesis of ocean-island basalts: geochemical evidence from S. Atlantic ocean islands .Geology.14: 275-278.

Wells,P.R.A. 1977 Pyroxene thermometry in simple and complex systems. Contrib. Mineral. Petrol. 62: 129-139.

Wenk, H.R. (ed) 1985 "Preferred Orientation in Deformed Metals and Rocks" Academic Press

White,W.M. 1985 Sources of oceanic basalts : radiogenic isotopic evidence.Geology 13. 115-118.

White,W.M. & Dupre,B. 1986 "Sediment subduction and magma genesis in the lesser Antilles: Isotopic and trace element contraints. Jour. Geophys. Res. 91: No 86. 5927-5941.

White,W.M. , Hofmann,A.W. & Puchelt,H. 1987 Isotope geochemistry of Pacific Morb. Jour. Geophys Res.

White,W.M. & Hofmann,A.W. 1982 Sr and Nd isotope geochemistry of oceanic basalts and mantle evolution.Nature.London 296: 821-823.

Wilding,M.C., Harte,B. & Harris,J.W. 1989 Evidence of asthenospheric source for diamonds from Brazil. Abstracts vol 3. 28th Int Geol Congress Washington D.C. 3-359.

Wilkinson,J.F.G. 1973 Garnet clinopyroxenite inclusions from diatremes in the Gloucester area, New South Wales. Contrib. Mineral. Petrol. 46: 275-299

Wilkinson,J.F.G. 1976 Some subcallic clinopyroxenes from Salt Lake Crater ,Oahu, and their petrological significance. Contrib. Mineral. Petrol. 58: 181-202.

Williams,A.F. 1932 The genesis of the diamond. 2 Vols. E. Benn Ltd, London.

Wilshire,H.G. Meyer,C.E., Nakata,J.K., Calk,L.C., Shervais,J.W., Nielson,J.E. & Schwarzman,E.C. 1989 Mafic and ultramafic xenoliths from volcanic rocks of the Western United States. U.S. Geol. Survey. Prof. Paper.

Wilshire,H.G. & Jackson,E.D. 1975 Problems in determining mantle geotherms from pyroxene compositions of ultramafic rocks. J. Geology. 83: 313-329.

Woodhead,J. & McCulloch,M.T. 1989 Ancient seafloor signals in Pitcairn Island lavas and evidence for large amplitude, small length-scale mantle heterogeneities. Earth. Planet Sci. Lett. 94: 257-273.

Wopenka,B. & Pasteris,J.D. (in press) Graphites in geological samples: Raman spectroscopic M13 fits ? Micro beam Analysis.

Wright,E. & White,W.M. 1986/7 The origin of Samoa: new evidence from Sr, Nd and Pb isotopes .Earth. Planet. Sci. Lett. 81. 151-162.

Vocke,R.D., Hanson,G.N. & Grunenfelder,M. 1987 Rare earth element mobility in the Roffna Gneiss, Switzerland. Contrib. Mineral. Petrol. 95: 145-154.

Yoder,H.S. & Tilley,C.E. 1962 Origin of basaltic magmas: an experimental study of natural and synthetic rock systems. Jour. Petrology 3: 342-532.

Zartman,R.E. & Doe,B.R. 1981 Plumbo tectonics- The Model. Tectonophysics. 75: 135-162.

Zindler,A. & Hart,S.R. 1986 Chemical geodynamics. Ann.Rev. Earth Planet. Sci. 14 493-571.

Zindler,A. & Jagoutz,E 1988 Mantle cryptology. Geochim. Cosmochim. Acta. 52: 319-333.

Zindler,A., Staudigel,H. & Batiza,R. 1984 Isotope and trace element geochemistry of young Pacific seamounts : implications for the scale of upper mantle heterogeneity. 70.175-195.

Zindler, A., Straudigel,H., Hart,S.R., Endres,R. & Golstein,S. 1983 Nd and Sr isotopic study of a mafic layer from Ronda ultramafic complex. Nature.London 304 : 226-230.

ADDITIONAL REFERENCES

Bonatti, E., Ottonello, G. and Hamlyn, P.R. (1986) Peridotites from the island of Zabargad (St. John), Red Sea: petrology and geochemistry. Jour. Geophys. Res. 91: 5989-631.

Bottinga, Y. (1968) Carbon isotope fractionation between graphite, diamond and carbon dioxide. Earth Planet. Sci. Lett. 5: 301-307.

Boudier, F. and Coleman, R.G. Cross section through the peridotite in the Semail Ophiolite, southeastern Oman Mountains. Jour. Geophys. Res. 86: 2573-2592.

Coleman, R.G. (1977) " Ophiolites " Springer Verlag, Berlin 229pp.

Deines, P., Gurney, J.J. and Harris, J.W. (1987) Carbon isotopic composition, nitrogen content and inclusion composition of diamonds from Roberts Victor Kimberlite, South Africa. Evidence for ^{13}C depletion in the mantle. Geochim. Cosmochim. Acta 51: 1227-1243.

Dick, H.J.B. and Sinton, J.M. (1979) Compositional layering in Alpine peridotites: evidence for pressure solution creep in the mantle. Jour. Geology 87: 403-416.

Dickey, J.S. (1977) Partial fusion versus fractional crystallization hypotheses for the differentiation of the Ronda ultramafic massif, S. Spain. Min. Soc. Am. Spec. Pap. 3: 79.

Eggler, D.H. (1983) Upper mantle oxidation state: evidence from olivine-orthopyroxene-ilmenite assemblages. Geophys. Res. Lett. 10: 365-368

Fleet, M.E., MacRae, N.D. and Herzberg, C.T. (1977) Partition of nickel between olivine and sulphide: A test for immiscible sulphide liquids. Contrib. Mineral. Petrol. 65: 191-198.

Ganguly, J. (1979) Garnet and clinopyroxene solid solutions and geothermometry based on Fe-Mg distribution coefficient. Geochim. Cosmochim. Acta 43: 1021-1029.

Green,D.H. 1964 The petrogenesis of the high temperature intrusion in the Lizard area, Cornwall. J.Petrology 5, 134-188.

Green, D.H., Hibberson, W.O. & Jaques, A.L. 1979 Petrogenesis of mid-ocean ridge basalts. In : The Earth: Its origin, structure and evolution (ed W.M. McElhinny) pp 265-299. Acedemic press.

Grover, J.E., Lindsley, D.H. & Bence. A.E. 1980 Experimental phase relations of olivine vitrophyres from breccia 14321: The temperature and pressure dependence of Fe-Mg partitioning for olivine and liquid in a highlands melt-rock. Proc. Lunar Planet. Sci Conf 11th. 179-196.

Hanson, G.N. and Langmuir, C.H. (1978) Modelling of major elements in mantle-melt systems using trace element abundancies. Geochim. Cosmochim. Acta 42: 725-741.

Hart, S.R. and Zindler, A. (1986) In search of a bulk Earth composition. Chemical Geology 57: 247-267.

Hart, S.R. and Davis, K.E. (1978) Nickel partitioning between olivine and silicate melt. Earth Planet. Sci. Lett. 40: 203-219.

Harte, B. (1977) Rock nomenclature with particular relation to deformation and recrystallization textures in olivine-bearing xenoliths. J. Geol 85: 279-288.

Hofmann, A.W. and Hart, S.R. (1978) An assessment of local and regional isotopic equilibrium in the mantle. Eart Planet. Sci. Lett. 38: 44-62.

Hole, M.J., Saunders, A.D., Marriner, G.F. and Tarney, J. (1984) Subduction of pelagic sediments: Implications for the origin of Ce anomalous basalts from the Marianas Islands. Jour. Geol. Soc. Lond. 141: 453-472.

Humphries, S.E. and Thompson, G. (1978) Hydrothermal alteration of oceanic basalts by seawater. Geochim. Cosmochim. Acta 42: 107-125.

Jaques, A.L. and Green, D.H. (1980) Anhydrous melting of peridotite at 0-15kb pressure and the genesis of tholeiitic basalts. Contrib. Mineral. Petrol. 73: 287-310.

Kushiro. I. and Yoder, H.S. Jr. (1974) Formation of eclogite from garnet lherzolite, liquidus relations in a portion of the system $MgSiO_3$-$CaSiO_3$-Al_2O_3 at high pressures. Carnegie Inst. Yearbk. 73, 266-269.

Loubet, M. and Allegre, C.J. (1979) Trace element studies in the Alpine type peridotite of Beni Bouchera (Morocco). Geochem. Journal 13: 69-75.

Loubet, M. and Allegre, C.J. (1982) Trace elements in ororgenic lherzolites reveal the complex history of the upper mantle. Nature 298: 809-811.

Maaloe, S. and Aoki, K. (1977) The major element composition of the upper mantle estimated from the compositions of lherzolites. Contrib. Mineral. Petrol. 63: 161-173.

Matsumoto, S., Sato, Y., Tsutumi, M. and Setaka, N. (1982) Growth of diamond particles from methane-hydrogen gas. Journal Material Sci. 17: 3106-3012.

Menzies, M. (1984) Chemical and isotopic heterogeneities in orogenic and ophiolitic peridotites. In "Ophiolites and Oceanic Lithosphere" eds. I.G. Gass, S.J. Lippard, amd R.W. Skelton Blackwell, London, 231-240.

Menzies, M. and Murthy, V.R. (1978) Strontium isotope geochemistry of alpine tectonite lherzolites; data compatible with a mantle origin. Earth Planet. Sci. Lett. 38: 346-354.

Meyer, H.O.A. (1987) Inclusions in diamond. In "Mantle Xenoliths" ed. P.H. Nixon, Wiley, London. 502-522.

Meyer, H.O.A. and Tsai, H.M. (1976) Mineral inclusions in diamond: temperature and pressure of equilibration. Science, 191: 849-851.

Michard, A. and Albarede, F. (1985) Hydrothermal uranium uptake at ridge crests. Nature 317: 244-246.

Moores, E.M. and Vine, F.J. (1971) The Troodos Massif, Cyprus and other ophiolites as oceanic crust: evaluation and implications. Phil. Trans. R. Soc. Lond. A268: 443-466.

Mori, T. (1977) Geothermometry of spinel lherzolites. Contrib. Mineral. Petrol. 59: 261-279.

Nixon, P.H., Davies, G.R., Slodkevich, V.V. and Bergman, S.C. (1986) Graphite pseudomorphs after diamond in the eclogite peridotite massif of Beni Bousera, Morocco and a review of anomalous diamond occurrences. Fourth Int. Kimberlite Conf. Perth, Extended Abst. Geol. Soc. Aust. No. 16 412-414.

Obata, M. and Nagahara, N. (1987) Layering of Alpine- type peridotite and the segregation of partial melt in the upper mantle. Jour. Geophys. Res. 92: 3467-3474.

Obata, M. (1976) The solubility of Al_2O_3 in orthopyroxene in spinel and plagioclase peridotites and spinel pyroxenites. Extended abstracts, Internetional Conf. on Geothermometry and Geobarometry, Penn. State Univ. (unpaged).

O'Hara, M.J., Saunders, M.J., and Mercy, E.L.P. (1975) Garnet peridotite, primary ultrabasic magma and eclogite; interpretation of upper mantle processes in kimberlite. Phys. Chem. Earth vol 9/; 571-604.

Ozawa, K. (1989) Stress induced Al-Cr zoning of spinel in deformed peridotite. Nature 338: 141-144.

Palme, H. and Nickel, K.G. (1985) Ca/Al ratio and composition of the Earths upper mantle. Geochim. Cosmochim. Acta. 49: 2123-2132.

Pearson, D.G., Davies, G.R. and Nixon, P.H. (1987) Diamond facies garnet pyroxenites of Beni Bousera, Morocco: Recycled Oceanic Lithosphere. Terra Cognita 7: 618.

Pineau, F., Javoy, M. and Kornprobst, J. (1987). Primary igneous graphite in ultramafic xenoliths: II. Isotopic composition of the carbonaceous phases present in xenoliths and host lavas at Tissemt (Eggre, Algerian Sahara). J. Petrol. 28: 313-322.

Pineau, F. (1988) Is carbon in high temperature peridotites a possible reference for mantle carbon. EOS 69: 1466.

Presnall, D.C. (1976) Alumina content of enstsatite as a geobarometer for spinel lherzolites. Extended abstracts, Internetional Conf. on Geothermometry and Geobarometry, Penn. State Univ. (unpaged).

Quick, J.E. (1981) The origin and significance of large tabular dunite bodies in the Trinity peridotite, northern California. Contrib. Mineral. Petrol. 78: 413-422.

Ringwood, A.E. (1975) "Composition and Petrology of the Earth's Mantle" McGraw-Hill, New York, 618pp.

Stanton, R.L. and Bell, J.D. (1969) Volcanic rocks of the New Georgia Islands. Overseas Geol. Miner. Resour. 10: 113-145.

Streckeisen, A. (1976) To each plutonic rock its proper name. Earth. Sci. Rev. 12: 1-33.

Sun, S.S. (1987) Chemical composition of Archean komatiites: implications for the early history of the Earth and mantle evolution. Jour. Volcanol. & Geoth. Res. 32: 67-82.

Takahashi, E. and Kushiro, I. (1983) Melting of dry peridotite at high pressures and basalt magma genesis. Am. Min. 68: 859-879.

Thirlwall, M.F. (1982) A triple filament method for rapid and precise analysis of rare earth elements by isotope dilution. Chem. Geol. 35: 155-166

Veizer, J., Compston, W., Clauer, N. and Schidlowski, M. (1983) $^{87}Sr/^{86}Sr$ in late Proterozoic carbonates: Evidence for a "mantle" event at ~ 900 Ma ago. Geochim. Cosmochim. Acta 47: 295-302.

Wicks, F.J. and Whittaker, E.J.W. (1977) Serpentine textures and serpentinization. Can. Min. 15: 459-488.

Wilshire, H.G. and Shervais, J.W. (1975) Al-augite and Cr-diopside ultramafic xenoliths in basalt host rocks from the western United States. Phys. Chem. Earth 9: 257-272.

Wright, T.L. and Doherty, P.C. (1970) A linear programming and least squares computer method for solving petrological mixing problems. Bull. Geol. Soc. Am. 81: 1995-2008.

Yoder, H.S. (1976) "The generation of basaltic magma" National Academy of Sciences, Washington D.C. 265pp.

Appendix 1. Sample list and locations

The following list compiles samples collected by the author during two field excursions in 1987 and 1988 and by Dr. P.H. Nixon in 1985. These specimens (or the remainder after analysis) are kept in the Department of Earth Sciences, The University of Leeds. More precise sample locations can be obtained either from the measured section in Appendix 2 or from the sample locallity maps in Chapter 5.

Abbreviations used in the list are defined below:

OeJ = Oued el Jouj

JK = Jbel Karabos summit area.

Amas = Amasihene beach

O.Sidi Y = Oued Sidi Yahia Aarab

Sidi Y = Sidi Yahia Aarab

Comp = Composite layer or specimen

GGP = Graphite garnet clinopyroxenite

GP = Garnet clinopyroxenite

WEB = Al- augite websterite

Cr-WEB = Cr-diopside websterite

OPXITE = orthopyroxenite

SAMPLE	LITHOLOGY	LOCATION	TS/PTS
GP1	Andalusite vein	Beach, Amter	
GP2	Qtz. vein	Beach, Amter	
GP3	Amphibolite	Beach, Amter	
GP4	Amphibolite	Beach Amter	7699
GP5	Kinzigite	Tazemourte	7702
GP6	Vermic. Vein	Tazemourte	
GP7	Comp. WEB/GP	Tazemourte	7655 a-f
GP8	GGP	Float, OeJ.	
GP9	Graphite vein	OeJ.	
GP10	Cr-WEB	Float, OeJ.	7661
GP11	Qtz. tourm. vein	Tazemourte	
GP12	SPLHRZ	Aarkob	
GP13	SPLHRZ	Aarkob	
GP14	SPLHRZ	Float, Aarkob	
GP15	PERID	Contact, Aarkob	
GP16	Dolerite dyke	Aarkob	
GP17M	GP	Tazemourte	
GP18B	GP base of 17	Tazemourte	
GP19T	GP top of 20	Tazemourte	
GP20M	GP middle	Tazemourte	
GP21B	GP base	Tazemourte	
GP22	GP	Tazemourte	
GP23	GP	Tazemourte	
GP24	GTLHZ	Tazemourte	7889,7658,49888a-c
GP25	GGP	Float, Tazemourte	7623
GP26	GGP	Float, OeJ.	
GP27	GP	Tazemourte	7613
GP28	OPXITE	Taza ridge	
GP29	OPXITE	Taza ridge	
GP30	Cr-WEB	Taza ridge	
GP31	Comp.OPXITE/WEB	Taza ridge	7643,7644,7701
GP32	SPLHRZ	Taza ridge	
GP33a	WEB	Taza ridge	
GP33b	WEB	Taza ridge	
GP34a	WEB	Taza ridge	
GP34b	WEB	Taza ridge	
GP35	Comp. WEB	Taza ridge	7704
GP36	GP	Taza ridge	
GP37	GP	JK	7887
GP38	Comp. GP	JK	49776 a-d
GP39	GP	JK	
GP40B	GP base	JK	
GP41	SPLHRZ	JK	7619
GP42	GP	JK	
GP43	GP	JK	
GP44	GP	OeJ	
GP45	Amphibole vein	OeJ	
GP46	GP	OeJ	
GP47	GGP	Float. Tazemourte	
GP48T	GGP top	Tazemourte track	
GP49	GGP	Float. Tazemourte	
GP50	GGP	Float. Tazemourte	
GP51	GGP middle	Tazemourte track	
GP52	GGP middle	Tazemourte track	
GP53	Kinzigite	O.Amter	
GP54	Kinzigite	O.Amter	
GP55	Kinzigite	O.Amter	
GP56	GP in SPLHRZ	O.Amter	
GP57	KINZ at perid contact	O.Amter	
GP58	Plag. rich breccia ?	O.Amter	
GP59	KINZ 15m contact	O.Amter	
GP60	GRAN in KINZ	O.Amter	
GP61	GRAN in KINZ	O.Amter	
GP62	Mica pegmatite	O.Amter	

GP63	GP	0.Amter	
GP64	SPLHRZ	O.Amter	
GP65	WEB	O.Amter	
GP66	SPLHRZ	Tazemourte track	
GP67	GP	Tazemourte track	
GP68	GP	Tazemourte track	
GP69	SPLHRZ	Tazemourte track	
GP70	Pegmatite vein	Tazemourte track	
GP71	GTWEB	Tazemourte track	
GP72	HARZ	Tazemourte track	
GP73	SPLHRZ next GP74	Tazemourte track	
GP74	GGP top	Tazemourte track	
GP75	GGP upper	Tazemourte track	
GP76	GGP base	Tazemourte track	7625
GP77	SPLHRZ	Tazemourte track	
GP78	Felsic dyke in GP	Tazemourte track	
GP79	GGP 20cm from top	Tazemourte track	
GP80	GGP middle	Tazemourte track	7635
GP81	GGP 1m from top	Tazemourte track	49889
GP82	GGP 30cm from base	Tazemourte track	
GP83	GGP	Tazemourte track	7626
GP84	GGP	Float Tazemourte	
GP85	Ni-GRAPH vein	OeJ valley	
GP86	Ni-GRAPH vein	OeJ valley	
GP87T	GP top of layer	OeJ valley	7651A
GP87M	GP middle	OeJ valley	7651C
GP87B	GP base of layer	OeJ valley	7651E
GP88	SPLHRZ	OeJ valley	
GP89	SPLHRZ	OeJ valley	7621
GP90	GP	OeJ valley	
GP91	SPLHRZ	OeJ valley	
GP92	SPLHRZ	OeJ valley	
GP93	Comp CPXITE	OeJ valley	49844
GP94	Comp OPXITE/WEB	OeJ valley	7653
GP95	Comp WEB	OeJ valley	
GP96	Comp WEB	OeJ valley	
GP97	Comp OPXITE/WEB	OeJ valley	7888
GP98	Comp WEB	OeJ valley	
GP99	WEB	OeJ valley	7636
GP100	OPXITE/WEB sheared	OeJ valley	7645-7647
GP101a	Cr-WEB	OeJ valley	7627-33
GP101d	WEB intruded into	OeJ valley	7630
GP102	Comp WEB	OeJ valley	7657 A-E
GP103	GGP top of layer	OeJ valley	7624
GP104	GGP	OeJ valley	
GP105	GT in SPLHRZ	OeJ valley	
GP106	GGP OeJ layer	OeJ valley	
GP107	GGP OeJ layer	OeJ valley	
GP108	SPLHRZ	Amas Beach	
GP109	SPLHRZ	Amas Beach	
GP110	SPLHRZ	Amas Beach	
GP111	OPXITE/WEB	Amas Beach	
GP112	WEB	AmasBeach	
GP113	SPLHRZ adjacent	Amas Beach	
GP114	WEB top	Amas Beach	
GP115	WEB middle	Amas Beach	
GP116	GP	Amas Beach	
GP117	OPXITE	Amas Beach	
GP118	SPLHRZ	Stream N. of Sidi Y.	
GP119	SPLHRZ	Stream N. of Sidi Y.	
GP120	WEB	Stream N. of Sidi Y.	
GP121	SPLHRZ	N. of Sidi Y.	
GP122	GP	Float N. of Sidi Y.	
GP123	WEB	OeJ valley	
GP124	Comp OPXITE/WEB	OeJ valley	7648-50

GP125	WEB	OeJ valley	50286
GP126	WEB	OeJ valley	
GP127	SPLHRZ	OeJ valley	
GP128	SPLHRZ	OeJ valley	
GP129	WEB/CPXITE	OeJ valley	
GP130	Cr-WEB	OeJ valley	7766
GP131	Cr-WEB	OeJ valley	7656A-C
GP132(1)	Cr-WEB	OeJ valley	7660
GP132(2)	SPLHRZ	OeJ valley	
GP132(3)	SPLHRZ	OeJ valley	
GP133	GT WEB	OeJ valley	
GP134	WEB	OeJ valley	7641,7642
GP135	GP layers in OPXITE	OeJ valley	7638-40
GP136	GP	OeJ valley	
GP137	OPXITE @ top of GP	OeJ valley	7652
GP138	GP base of layer	OeJ valley	
GP139	GP middle of layer	OeJ valley	7767
GP140	GP top of layer	OeJ valley	7768
GP141	WEB base of GGP layer	OeJ valley	
GP142	GGP base of GGP layer	OeJ valley	
GP143	GGP middle	OeJ valley	49887
GP144	GGP middle	OeJ valley	7614
GP145	GGP middle	OeJ valley	
GP146	GGP middle	OeJ valley	7615
GP147a	GGP ~ 1m from top	OeJ valley	7618
GP148	GGP	OeJ valley	7622
GP149	GGP near top	OeJ valley	
GP150	GT WEB	OeJ valley	7634
GP151	GP lens in SPLHRZ	OeJ valley	
GP152	GP	OeJ valley	
GP157	GP	Float OeJ valley	
GP158	GP	Float OeJ valley	
GP159	Tourmaline qtz vein	Inouline	
GP160	KINZ	Inouline	
GP161	KINZ	Inouline	
GP162	KINZ	Inouline	
GP163	SPLHRZ	Inouline	
GP164	GRAN in KINZ	Inouline	
GP165	Coarse KINZ GT	Inouline	
GP166	KINZ	Inouline	
GP168	SPLHRZ	O.Amter	
GP169	OPXITE	O.Amter	
GP170	Cr-WEB	O.Amter	50287
GP171	GP	OeJ valley	
GP172	SPLHRZ	OeJ valley	
GP173	OPXITE	OeJ valley	
GP174	SPLHRZ	OeJ valley	
GP175	SPLHRZ	OeJ valley	
GP176	WEB	OeJ valley	
GP177	GP in SPLHRZ	Float OeJ valley	49843A-D
GP178	SPLHRZ	OeJ valley	502090
GP179	GP	Float OeJ valley	
GP180	GP	Float OeJ valley	
GP181	GP	Float OeJ valley	
GP182	CPXITE/WEB	Taza ridge	
GP183	CPXITE	Taza ridge	
GP184	WEB	Taza ridge	
GP185	GP	Taza ridge	
GP186	SPLHRZ	J.K.	49841
GP187	SPLHRZ	Taza ridge	
GP188	Cr-WEB	OeJ valley	50289
GP189	SPLHRZ	OeJ valley	
GP190	GP	Float OeJ valley	
GP191	SPLHRZ	OeJ valley	
GP192	GP	Float OeJ valley	

GP193	GP	Float OeJ valley	
GP194T	GP	OeJ valley	
GP194M	GP	OeJ valley	
GP194B	GP	OeJ valley	
GP195	GP	OeJ valley	
GP196	GP	OeJ valley	
GP197	Perid./WEB cont.	OeJ valley	
GP198	SPLHRZ + GP	O.Amter	
GP199	GP	O.Amter	
GP200	GP	O.Amter	
GP201	GP	O.Amter	
GP202	GRAPH vein	O.Amter	
GP203	GRAPH-Ni vein	O.Amter	
GP204	GP 2m from vein	O.Amter	50288
GP205	Comp WEB/GP	O.Amter	
GP206	CPXITE/WEB	O.Amter	
GP207	GP	O.Amter	
GP208	GGP ~0.2m from top	OeJ valley	
GP209	GGP ~0.6m from top	OeJ valley	
GP210	GGP ~ 1m from top	OeJ valley	
GP211	GGP 1.1m from top	OeJ valley	
GP212	SPLHRZ adjacent GGP	OeJ valley	
GP213	SPLHRZ	OeJ valley	
GP214	GGP ~0.5m from base	OeJ valley	
GP215	OPXITE base of GGP	OeJ valley	
GP216	GGP ~0.3cm from base	OeJ valley	
GP217	GGP ~1.1m from base	OeJ valley	
GP218	GGP	Float OeJ valley	
GP219	GP next to GGP	OeJ valley	
GP220	SPLHRZ 4m from GGP	OeJ valley	50997
GP221	Qtz/feld vein	OeJ valley	
GP222	SPLHRZ	Amas. Beach	
GP223	Dunite pod.	Amas.Beach	49842
GP224	SPLHRZ	Amas.Beach	
GP225	GT WEB	Amas.Beach	
GP226	WEB	Amas.Beach	
GP227	WEB + PERID	Amas.Beach	
GP228	WEB	Amas.Beach	
GP229	SPLHRZ	Amas.Beach	
GP230	SPLHRZ	O Sidi Y.	
GP231	GP	Float OeJ valley	
GP232	WEB	O Sidi Y.	
GP233	SPLHRZ	O Sidi Y.	
GP234	GP	Float OeJ valley	
GP235	WEB folded	Float OeJ valley	
GP236	WEB	Float OeJ valley	
GP237	GP	Float O Sidi Y.	
GP238	SPLHRZ	Float O Sidi Y.	
GP239	Garnetite layering	Float O Sidi Y.	49839
GP240	SPLHRZ	O.Amas	
GP241	GP	O.Amas	
GP242	GP	O.Amas	
GP243	SPLHRZ + GP	O.Amas	
GP244	GP	O.Amas	
GP245	GTLHRZ	O.Amas	
GP246	GP	O.Amas	
GP247	GTLHRZ	O.Amas	
GP248	GTLHRZ	O.Amas	
GP249	GP	O.Amas	
GP250	GTLHRZ	O.Amas	498401-12
GP251	GP	O.Amas	
GP252	Comp WEB/GP	O.Amas	
GP253	GP	O.Amas	
GP254	GP	O.Amas	
GP256	Ni-graphite vein	Aarkob	

APPENDIX 2

Measured section of the Oued el Jouj stream outcrop ending at the contact between the peridotites and kinzigites at the confluence of the Oued el Jouj and the Oued Amter. Only sections showing significant lithological variation are represented in detail.

START 04508/35124 TO 04509/35131

KEY

GGP

GP

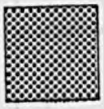

WEB

CPXITE

OPXITE/WEB

SPLHRZ

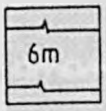

Section of rel. homogeneous lithology

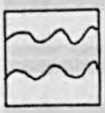

No significant exposure

Dip and strike of pyroxenite layer orientation or foliation.

Plunge of fold hinge

Sharp lithological contact

Gradational lithological contact

Section measured going down stream, south, towards Oued Amter.

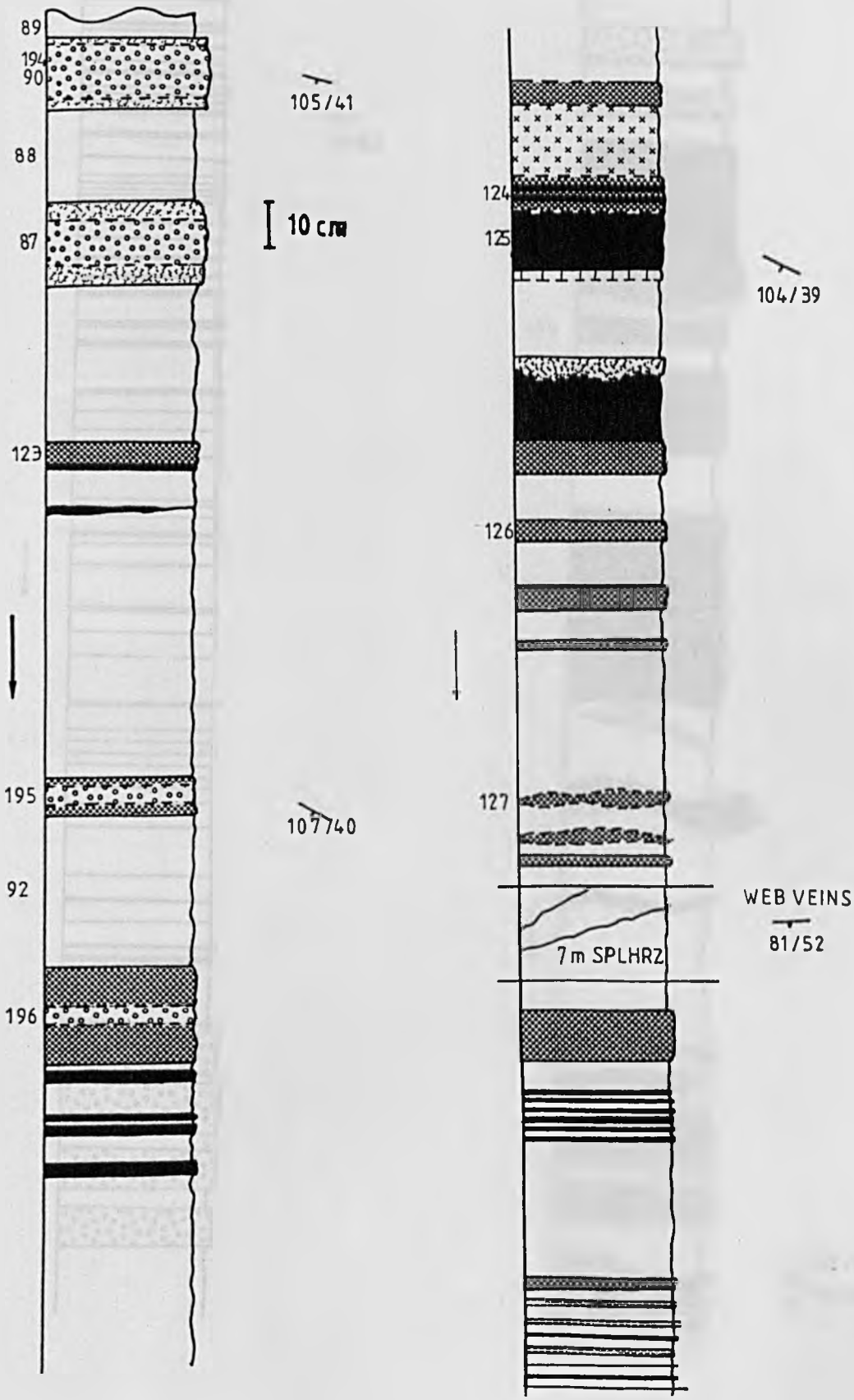
89
194
90
88
87
123
195
92
196
105/41
10 cm
107/40
124
125
104/39
126
127
WEB VEINS
81/52
7m SPLHRZ

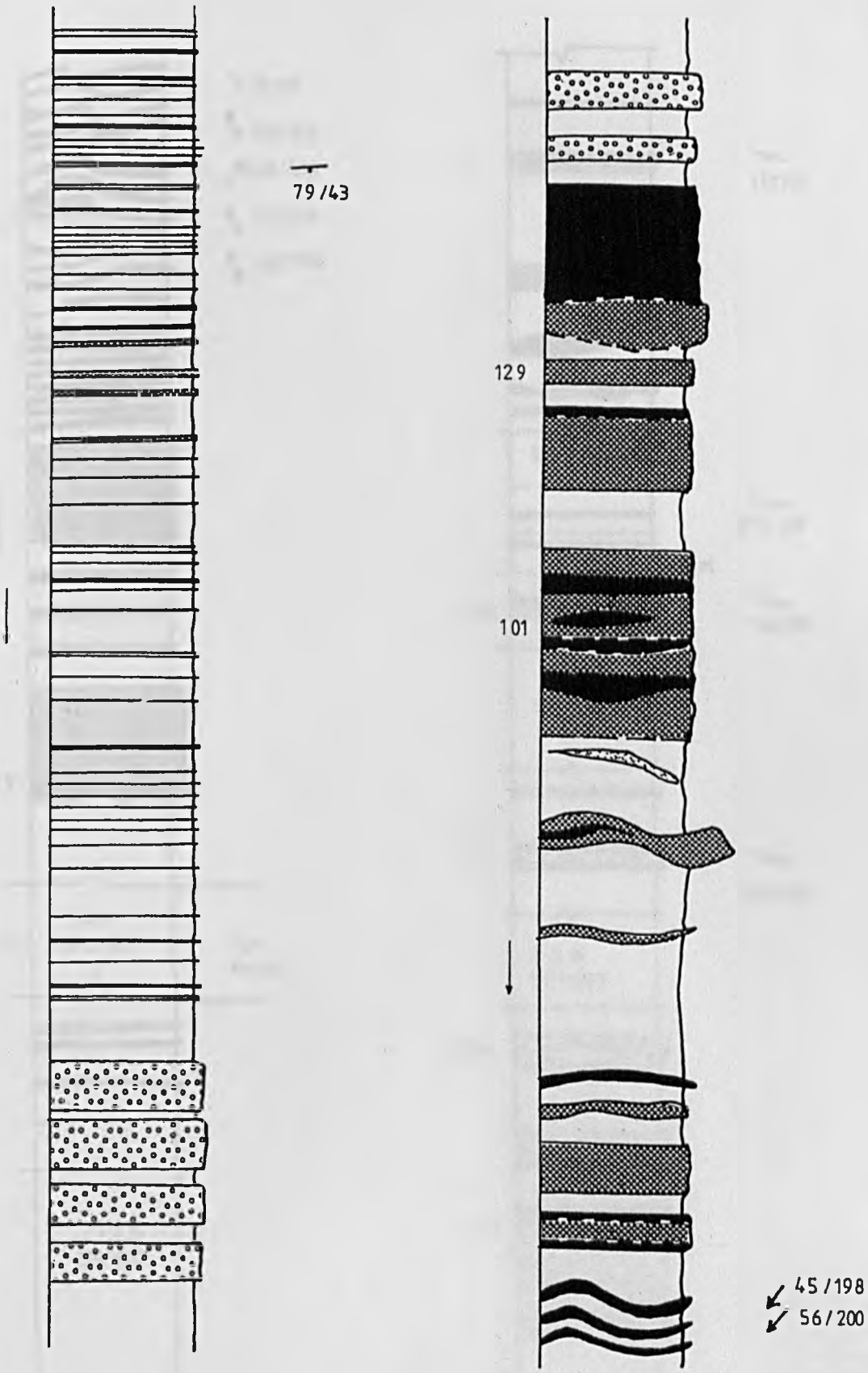
79/43
129
101
45/198
56/200

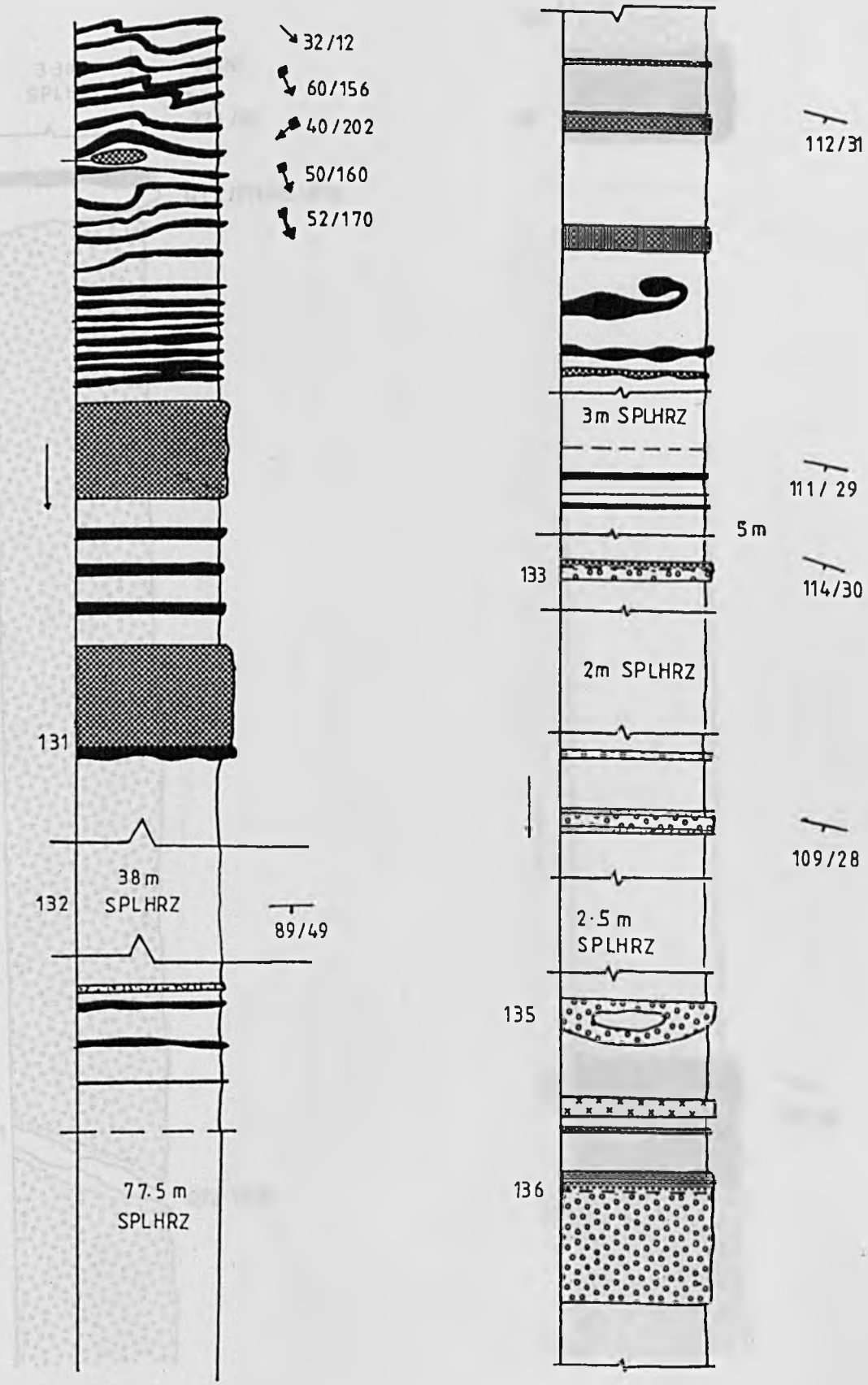
32/12
60/156
40/202
50/160
52/170
131
38m
SPLHRZ
132
89/49
77.5 m
SPLHRZ
112/31
3m SPLHRZ
111/29
5m
133
114/30
2m SPLHRZ
109/28
2·5 m
SPLHRZ
135
136

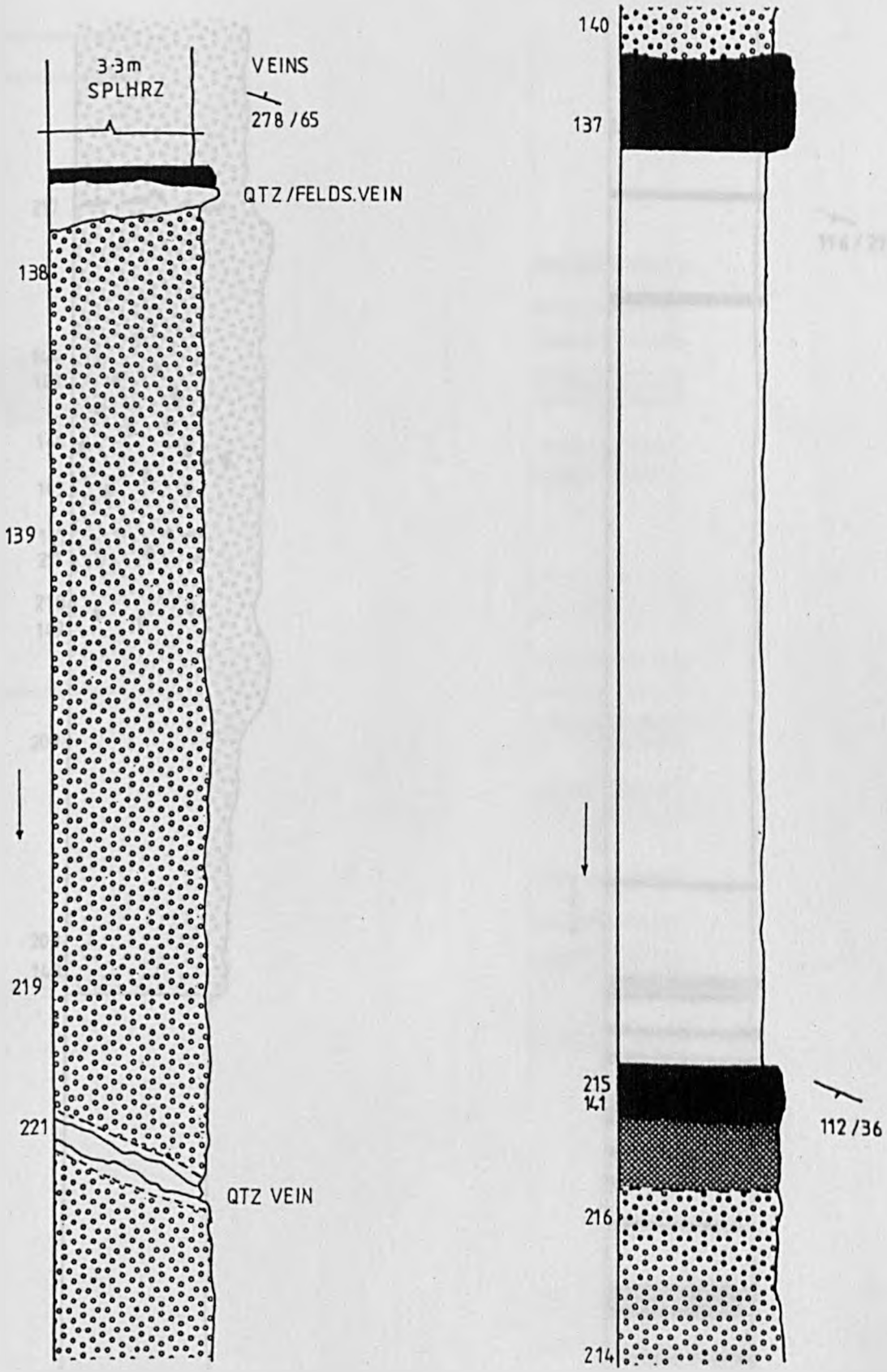
3·3m
SPLHRZ
VEINS
278 /65
QTZ /FELDS.VEIN
138
139
219
221
QTZ VEIN
140
137
215
14.1
112 /36
216
214

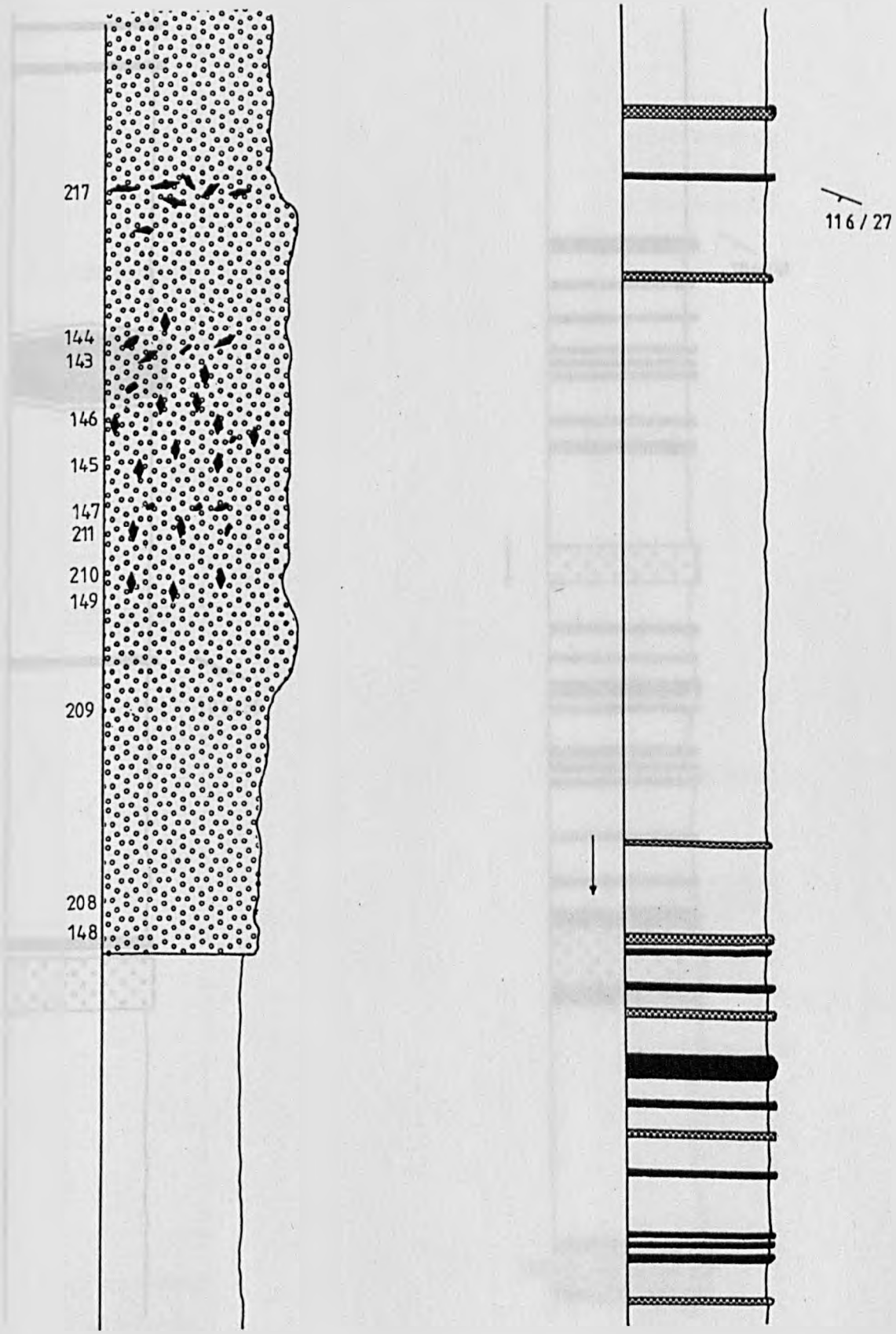
217
144
143
146
145
147
211
210
149
209
208
148
116 / 27

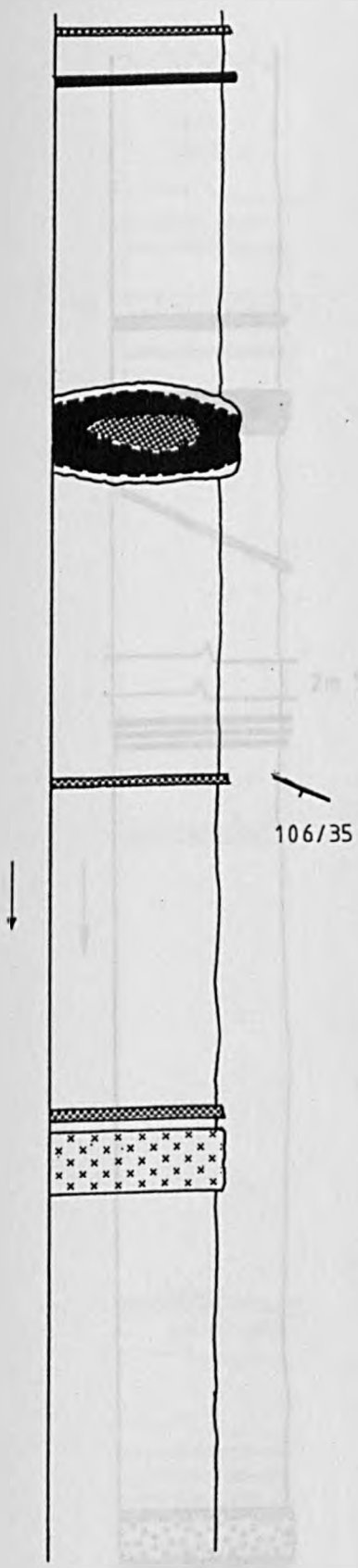
106/35

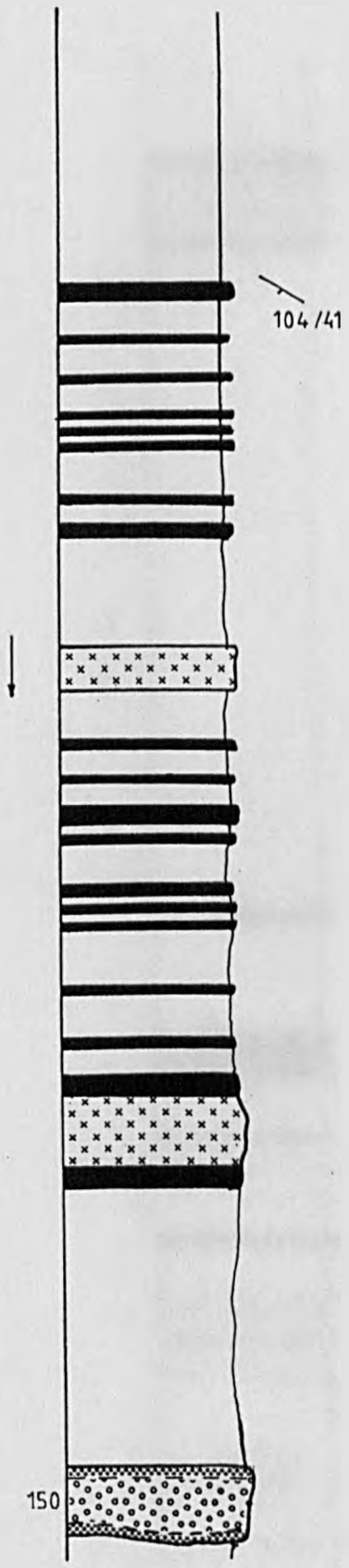
104/41
150

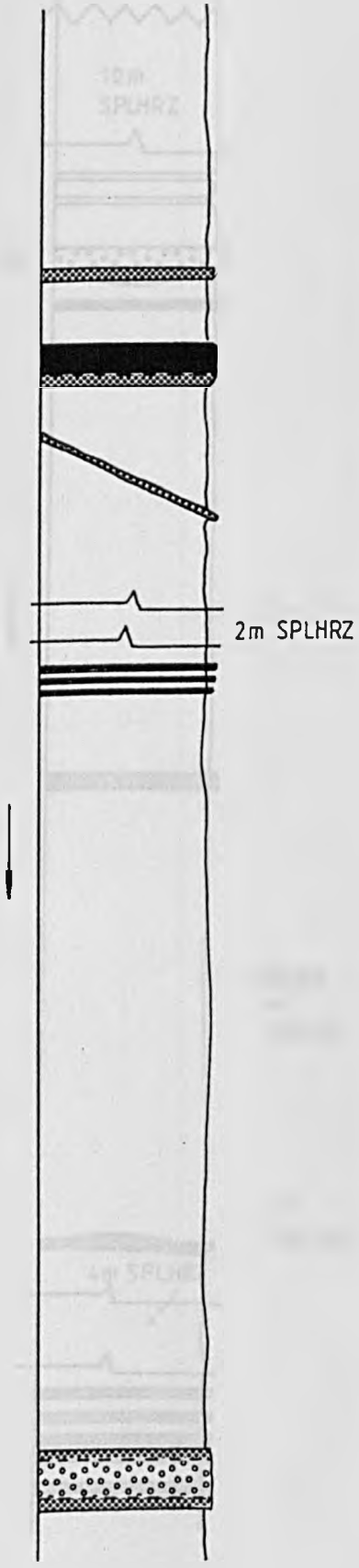
2m SPLHRZ

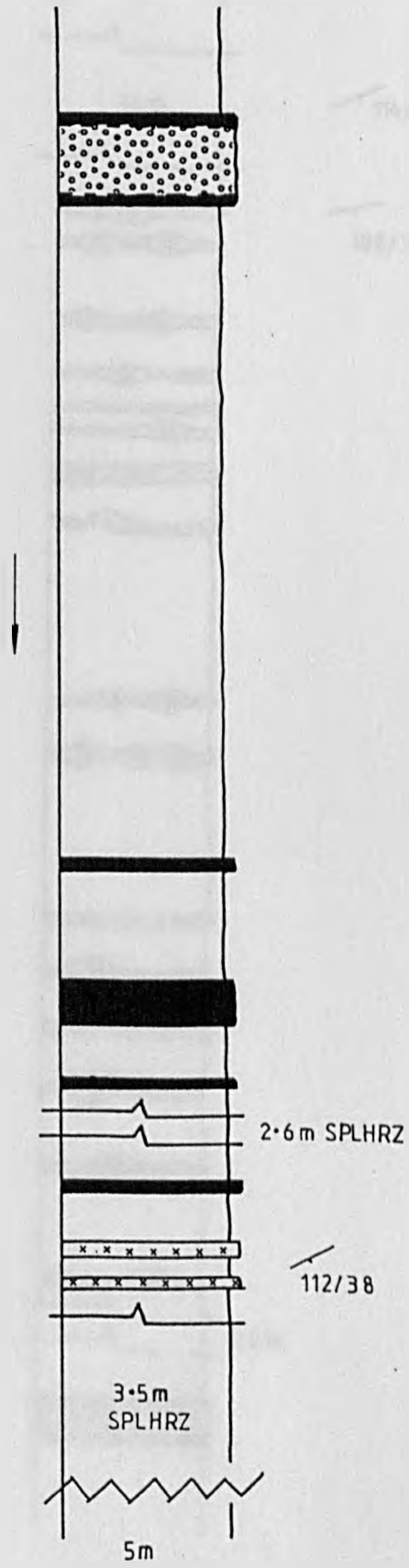
2·6m SPLHRZ
112/38
3·5m
SPLHRZ
5m

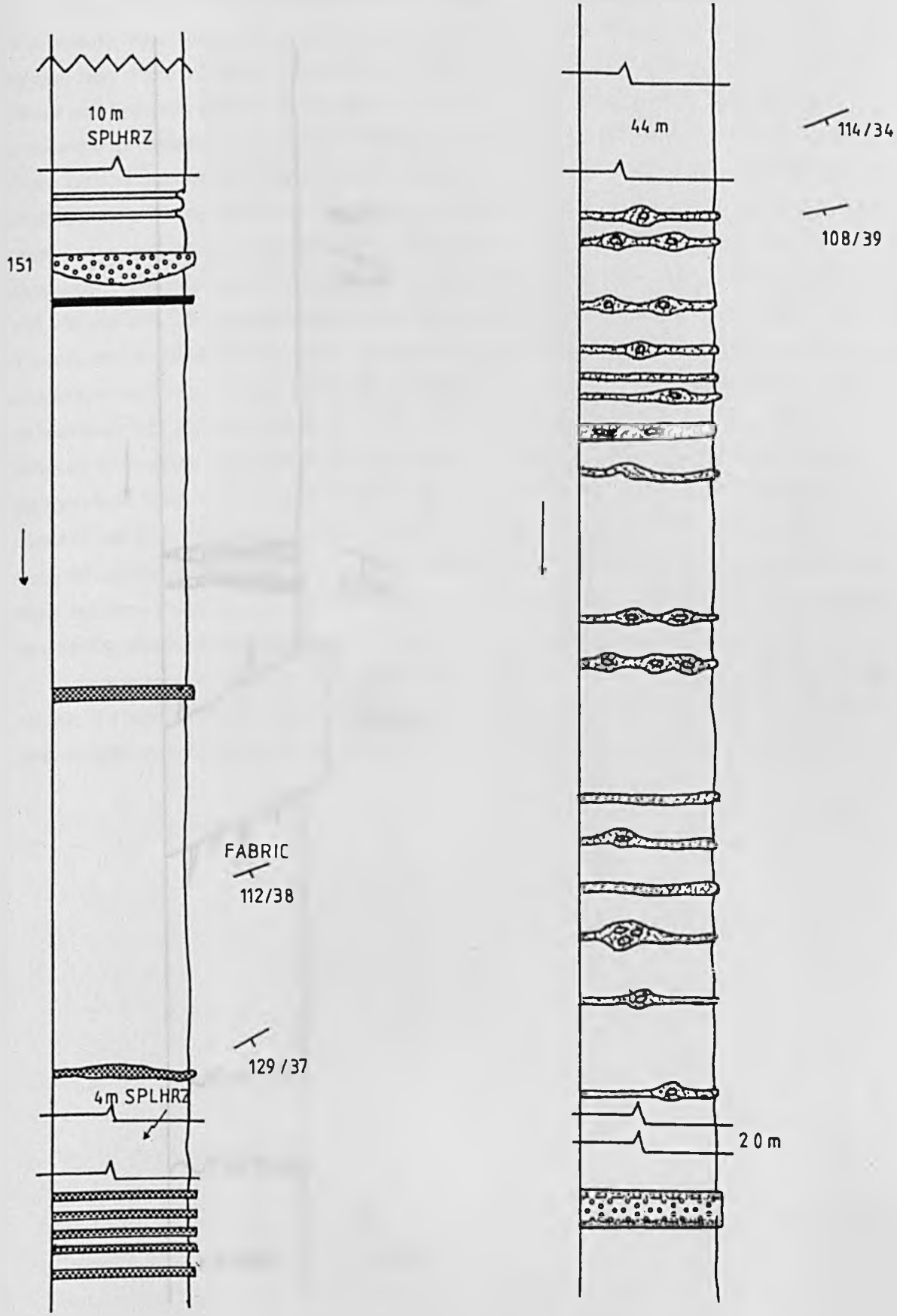
10 m
SPLHRZ
151
FABRIC
112/38
129/37
4m SPLHRZ
44 m
114/34
108/39
20 m

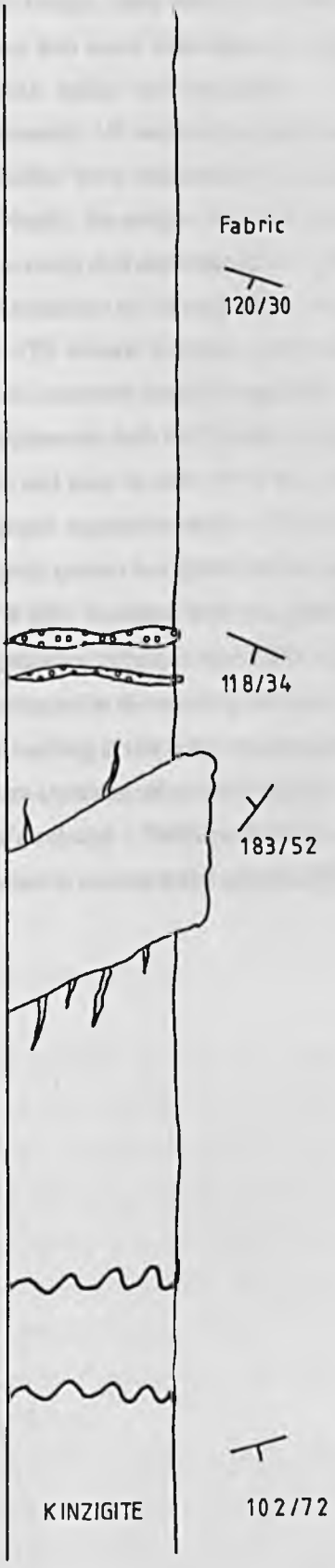
Fabric
120/30
118/34
183/52
KINZIGITE
102/72

Appendix 3. Sample Preparation.

Whole rock powders and mineral separates: All samples weighed at least 1kg unless from a thin vein or pyroxenite layer margin, many samples, including the GGP were prepared from samples > 2kg. The samples were rinsed with warm water and then distilled water to clean their surfaces. Samples were then placed in a hydraulic splitter and reduced to ~ 2 cm cubes. Any cubes showing signs of veining or alteration were discarded. All weathered surfaces were removed from samples. The resulting cubes were rinsed again in distilled water and crushed in a stainless steel pestle and mortar reserved specifically for ultrabasic rocks. Finally, the sample was cone-and-quartered and 90g of chips < 2mm in diameter were crushed in an agate swing mill and reduced to < 250 mesh. The tema barrel was rigourously cleaned after each sample. The remainder of the rock chips were crushed further and periodically sieved to obtain -30 +60, -60 +90 and -120 mineral fractions which were used in mineral separation. The -60 +90 or -30 +60 fractions were most commonly used for separation. Separates were first "deslimed" using a small amount of detergent in an ultrasonic bath for 15 mins. Separates were then washed repeatedly in distilled water in an ultrasonic bath and once in cold 10 % HCl ultrasonically for ~ 20 mins. All CPX separates were obtained by magnetic separation using a Franz-type magnetic separator. After initial concentration separates were lightly ground in a pestle and mortar to open any incipient cracks in any of the grains and rinsed in cold 10 % HCl. Separates were then picked under sub-boiled quartz distilled (SBQD) methanol using the side illumination technique described by Zindler and Jagoutz (1988). Separates were hand picked twice and then subjected to the leaching procedure described in Chapter 6. Separates were given a final examination after leaching to check for contamination.

Garnets were separated using heavy liquids, mainly methyl iodide, however GP147 GT necessitated the use of Clerici's solution (Thallium malnoate). After heavy liquid treatment garnet separates were ultrasonically washed in acetone and 2 aliquots of SBQD methanol in an ultrasonic bath for 30 minutes.

Appendix 4: Analytical Techniques:

A4:1 Electron microprobe analysis.

Mineral analyses were determined using a Joel JXA-50A electron microprobe at Leeds. The microprobe is fitted with an energy dispersive Link 860 series 2 analysing system operating at a beam current of 1 nA and an accelerating voltage of 20kv. Count times were always 100 seconds and individual mineral analyses tabulated in this thesis are the average of at least 3, usually 5, points in a particular area. Element calibration standards are as follows:

Si : Wollastonite
Ti : Rutile (synthetic)
Al : Corundum
Fe : Fe metal
Mn : Rhodonite
Mg : Periclase
Na : Jadeite
K : Orthoclase
Cr : Pure Cr metal
Ni : Pure Ni metal
Ca : Wollastonite

ZAF corrections are done "on-line". Only totals > 99.0 or < 100.9 % were accepted for single analyses. An average of 10 analyses of the core of an olivive from the peridotite GP89a gave the following 2σ errors of the total value: SiO_2 = 0.8%, FeO = 1.5%, MgO = 0.5%. For elements less than 1% abundance, errors are commonly 25% of the total value. Repeat analyses of CPX indicate the error on Na determinations above 0.5 % abundance are of the order of 5% of the total value.

A4:2 X-Ray Fluorescence analysis (XRF).

A4:2.1 Sample preparation.

Major elements: Major elements were determined on 46mm diameter fusion beads. 0.400 g of dried whole rock powder were weighed into a Pt/Au alloy crucible, 4.000 g of lithium tetraborate flux (Johnson Matthey spectroflux 110) were added to the rock powder and mixed thoroughly together. The Pt/Au crucible was covered and placed in a furnace for 1 hour. After cooling the flux/powder mixture was re-weighed to determine water loss from the hygroscopic flux, any loss was supplemented by addition of more flux. The mixture was remelted, homogenized by "swirlling" the hot crucible and cast into a copper ring. Cast fusion beads were stored in sealed plastic bags. Quantification of non-structurally bound water and other volatiles in each sample was determined by simple loss on ignition (LOI) at 1000 ^{o}C for 2 hours on ~ 1 g of sample.

Trace elements: 46 mm diameter powder briquettes consisting of 15 g of rock and 4 ml of Moviol P.V.A. were created in a polished steel hydraulic press at 10 tons pressure. Powder and Moviol were thoroughly mixed in clean, throw-away containers prior to formation. Briquettes were dried at 110 ^{o}C for at least 1 hour and placed in a vacuum dessicator prior to analysis.

Table A 4:3:1 Operating conditions for the PW 1400 XRF Spectrometer.

Measuring program 1. Rhodium target with power set at 40 kV by 60 mA

Element	line	Collimator	Detector	Crystal	2-theta	offsets +	offsets -	time (secs)
Na	Ka	Coarse	Flow	PX 1	23.65	1.6	1.6	160
Mg	Ka	Coarse	Flow	PX 1	28.60	1.2	1.2	80
Al	Ka	Coarse	Flow	PET	144.90	---	---	30
Si	Ka	Coarse	Flow	InSb	144.56	---	---	20
P	Ka	Coarse	Flow	Ge	141.03	---	---	20
K	Ka	Fine	Flow	LiF 200	136.69	---	---	8
Ca	Ka	Fine	Flow	LiF 200	113.09	---	---	8
Ti	Ka	Fine	Flow	LiF 200	86.14	---	---	8
Mn	Ka	Fine	Flow	LiF 200	62.97	---	---	8
Fe	Ka	Fine	Flow	LiF 200	57.52	---	---	4

Measuring program 2. Rhodium target with power set at 80 kV by 30 mA

Element	line	Collimator	Detector	Crystal	2-theta	offsets +	offsets -	time (secs)
Cr	Ka	Fine	Flow	LiF 200	69.38	1.0	1.0	80
Co	Ka	Fine	Flow	Lif 220	77.89	0.5	---	80
Ni	Ka	Fine	Flow	LiF 200	48.67	1.0	---	80
Cu	Ka	Fine	Flow	LiF 200	45.03	0.6	1.0	80
Zn	Ka	Fine	Scint	LiF 200	41.76	1.0	---	80
Rb	Ka	Fine	Scint	LiF 200	26.62	0.5	0.8	80
Sr	Ka	Fine	Scint	LiF 200	25.15	0.6	0.6	80
Y	Ka	Fine	Scint	LiF 200	23.80	0.8	0.8	80
Zr	Ka	Fine	Scint	LiF 200	22.55	0.4	0.8	80
Nb	Ka	Fine	Scint	LiF 220	30.39	0.6	0.6	80
Ba	Ka	Fine	Scint	LiF 220	15.54	0.5	0.3	80
Pb	Lb	Fine	Scint	LiF 200	28.26	0.5	1.0	80

Measuring program 3. Rhodium target with power set at 80 kV by 30 mA

Element	line	Collimator	Detector	Crystal	2-theta	offsets +	offsets -	time (secs)
Th	La	Fine	Scint	LiF 220	39.19	0.9	0.5	400
U	La	Fine	Scint	LiF 200	26.11	1.0	0.4	400

Measuring program 4. Rhodium target with power set at 50 kV by 50 mA

Element	line	Collimator	Detector	Crystal	2-theta	offsets +	offsets -	time (secs)
Sc	Ka	Fine	Flow	LiF 200	97.73	0.6	0.6	400
V	Ka	Fine	Flow	Lif 220	123.12	---	1.1	160

1 SAMPLE	GP130	GP130	GP188	GP188	GP170	GP170
2						
3 SiO2	53.73	54.08	53.86	54.14	52.36	51.69
4 TiO2	0.05	0.06	0.06	0.06	0.25	0.24
5 Al2O3	5.84	5.88	5.87	5.65	5.29	5.30
6 Fe TOTAL	6.85	6.97	6.90	6.93	9.48	9.44
7 MnO	0.13	0.13	0.13	0.13	0.19	0.19
8 MgO	31.23	31.44	31.87	31.11	24.32	24.09
9 CaO	2.19	2.15	1.92	1.90	8.15	8.10
10 Na2O	0.21	0.26	0.18	0.21	0.81	0.89
11 K20	0.01	0.00	0.00	0.00	0.02	0.01
12 P2O5	0.01	0.01	0.01	0.01	0.01	0.02
13 L.O.I.	0.08	0.07				
14						
15						
16 STANDARD	PCC-1 LEEDS	PCC-1 LEEDS	PCC-1 LEEDS	PCC-1 USGS ACCEPTED	MRG-1 LEEDS	MRG-1 LEEDS
17						
18 SiO2	41.76	41.99	41.94	42.15	38.95	38.98
19 TiO2	0.02	0.01	0.01	0.01	3.81	3.86
20 Al2O3	0.63	0.63	0.65	0.73	8.44	8.49
21 Fe TOTAL	8.41	8.41	8.38	8.28	17.32	17.56
22 MnO	0.13	0.13	0.13	0.12	0.18	0.18
23 MgO	43.57	43.16	43.51	43.63	13.67	13.61
24 CaO	0.50	0.54	0.51	0.53	14.87	14.78
25 Na2O	0.02	0.02	0.02	0.01	1.11	1.05
26 K20	-				0.21	0.20
27 P2O5	-				0.07	0.07
28 L.O.I.	-					
29						
30 Cr	2958	2991	2974	3000	417	418
31 Co	80	75	78		76	79
32 Ni	2515	2509	2512	2500	197	198
33 Cu	2	2	2		131	131
34 Zn	46	46	47		190	191
35 Rb	0	0	0	0.06	5	6
36 Sr	0	0	0	0.4	266	264
37 Y	0	0	0		19	20
38 Ba	2	2	2			
39 V	31	30	31	31	523	524
40 Sc	9	10	10	9	47	48

GP178	GP178	+/-
41.53	41.25	0.11
0.05	0.05	0.03
0.88	0.90	0.060
8.77	8.80	0.24
0.13	0.13	0.02
45.61	45.60	0.10
0.81	0.83	0.04
0.15	0.16	0.05
0.00	0.01	0.01
0.01	0.01	0.008

MRG-1 USGS ACCEPTED
39.24
3.75
8.56
17.80
0.17
13.51
14.72
0.71

420
87
200
135
185
8
260
20
520
48

A4:2.2 Analysis.

XRF analyses were performed on a Phillips PW1400 XRF at Leeds. Machine operating conditions are given in Table A4:3.1. Machine drift is corrected by reference to internal laboratory standards which are always included in a run whilst two cycles of measurements were made. Off-line data processing accounted for mass absorbtion and matrix effects. Reproducibility of the major element analyses can be assessed from Table A4:3.2. Duplicate analyses are presented for rocks spanning the range of compositions observed in this study, with variable loss on ignitions. For element oxides in excess of 5% the reproducibility is generally better than 1 % of the quoted value, elements present at levels of between 0.5 and 5% are reproducible to within 1 to 2% of the quoted value. Elements that constitute between 0.1 and 0.5 % of the rock are reproducible to within 5 % whereas < 0.1 % of an element can only be reproduced at the 20 % level. The +/- column at the end of the last analysis of GP178 in Table A4:3.2 is the population standard deviation on the mean measurement quoted at the end of a typical oxide analysis which covers 19 cycles of measurement. Of the common rock forming oxides, potassium and phosphorous are present in abundances equal to the precision achievable on the measurements and are hence not discussed in the text. Two U.S.G.S. external standards were analysed periodically over the period the sample analyses were made. The two standards, a peridotite and gabbro are comparable to the compositional range observed in the suite analysed from Beni Bousera.

Appendix 4.3: Ion microprobe analytical procedures.

A4:3.1 Analysis of REE and trace elements.

In situ trace and rare earth element analyses of CPX and GT inclusions within graphite octahedra together with CPX and GT mineral grains in the host rock were performed on 2 samples by Dr.N. Shimizu at M.I.T. The analytical data were obtained with the MIT-Brown-Harvard Cameca IMS 3f ion microprobe, details of the procedures are given in Shimizu and Le Roux (1986). A primary O^- ion beam was used with a net energy of 12.61 kev and an ion current of the order of 0.1nA. The REE analysis were carried out with moderate energy filtering (35-40-volt offset) with a 50 μm spatial resolution. Sc, Ti and Zr data were obtained with a beam of 5-8 μm diameter with 90-volt offset energy filtering. REE concentrations were calculated from empirical relationships between intensity ratios against Si and concentrations (i.e. working curves) determined from well documented pyrope standards. Accuracy and precision for REE are approximately 15 % even at sub ppm levels (N.Shimizu, pers.comm.) and within 10 % for the other elements. Comparison of a CPX separate analysed for REE by Isotope dilution and by ion microprobe is made in Figure 4:3.1. The two methods are comparable in accuracy in that their Sm/Nd ratios reproduce to within 1%.

A4:3.2 Garnet-CPX REE partitioning

Partitioning of Sm between CPX and GT ranges from Sm^{CPX}/Sm^{GT} = 1.63 to 2.34 for the garnet-CPX pairs studied (Chapter 6). These high values are within the range recorded in high temperature garnet lherzolite xenoliths from kimberlites (2.5 to 1.0) which are in isotopic equilibrium (Jagoutz 1988). The lower temperature, coarse granular lherzolites tend to have more Sm in GT than in CPX Sm^{CPX}/Sm^{GT} = 1.0 - 0.833 (Jagoutz 1988)

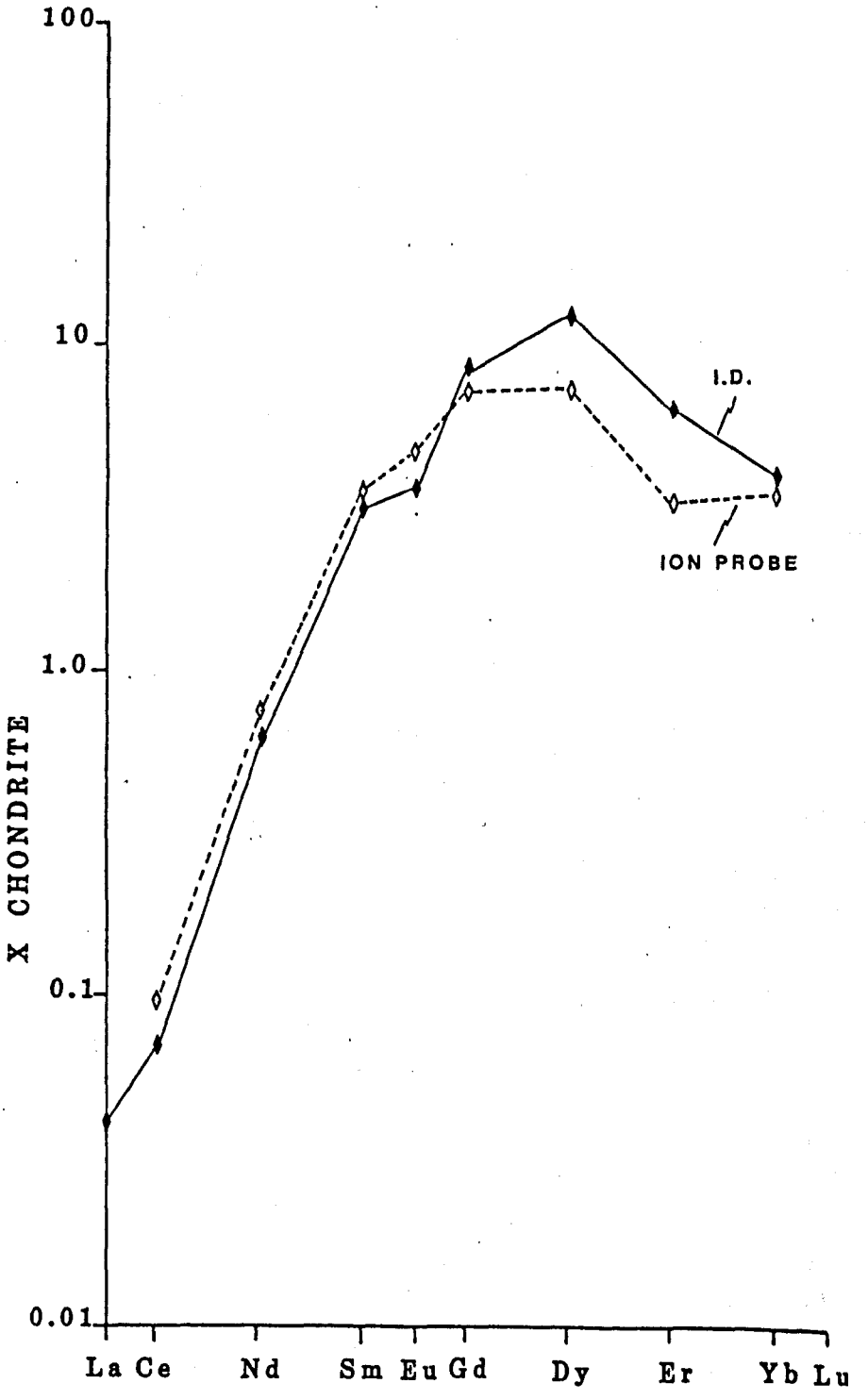
100
10
1.0
0.1
0.01
X CHONDRITE
I.D.
ION PROBE
La Ce Nd Sm Eu Gd Dy Er Yb Lu

FIG A 4:31

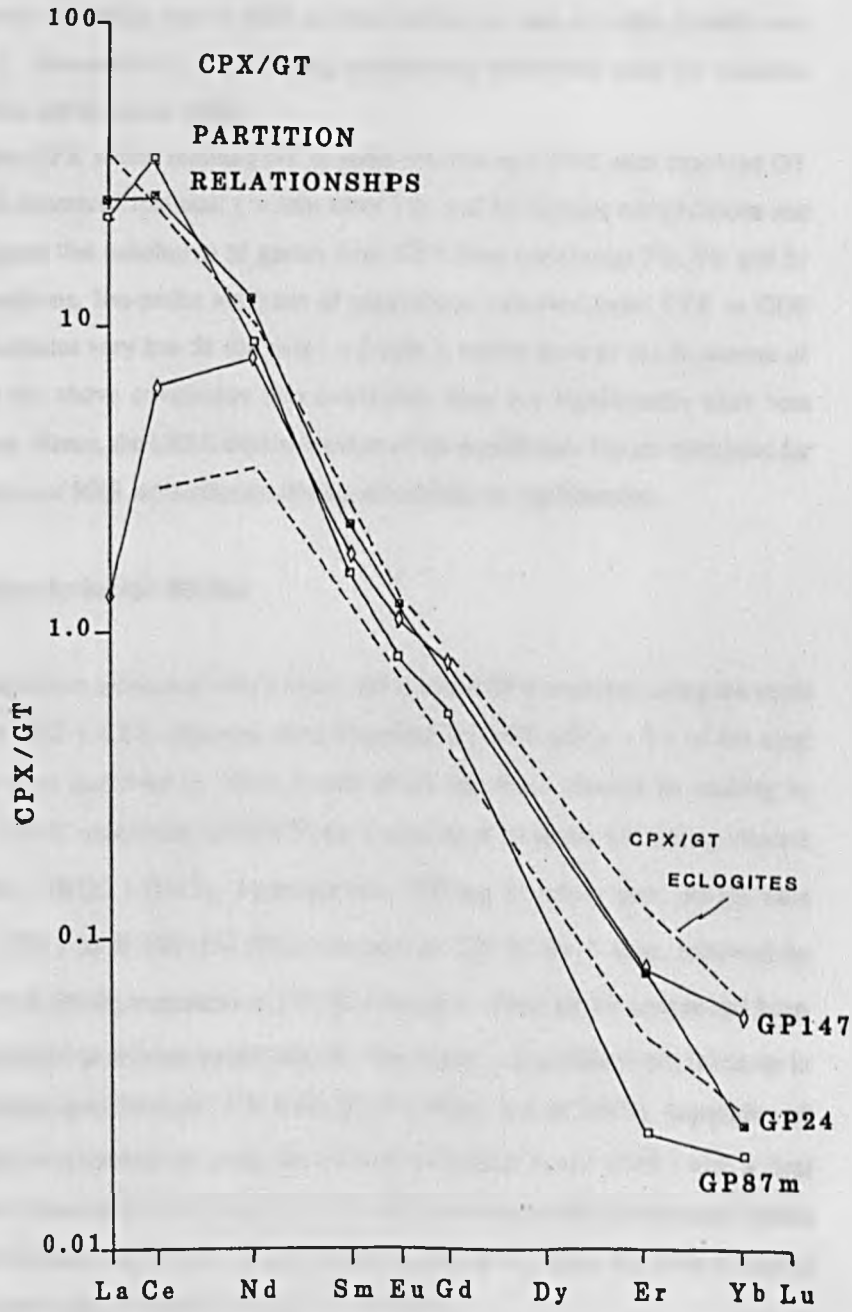
100
CPX/GT
PARTITION
RELATIONSHPS
10
1.0
CPX/GT
0.1
0.01
CPX/GT
ECLOGITES
GP147
GP24
GP87m
La Ce
Nd
Sm Eu Gd
Dy
Er
Yb Lu

FIG A 4·2

All available experimental Sm-Nd partitioning data for CPX and GT were obtained on crystal-liquid systems and therefore may not be directly applicable to the pyroxenite mineralogy studied here which has undergone sub-solidus equilibration. Experimental crystal-liquid partitioning studies by Nicholls and Harris (1980) show that the Sm/Nd ratios of garnets are higher by a factor of 1.8 than the Sm/Nd ratio in CPX crystallizing from the same liquid. The observed difference in Sm/Nd ratio between GT and CPX from the Beni Bousera GGP, GP and garnet peridotite lithologies ranges from a factor of 4.33 to 5.45. These values are similar to the differences in Sm/Nd ratio between GT and CPX in eclogites found by Jagoutz (1988), see Figure A4.3.2. The discrepancy between experimental and observed CPX/GT partitioning may be a function of mineral compositional variability due to solid solution behaviour and variation in bulk-rock composition (Jagoutz 1988). Alternatively the differing partitioning behaviour may be variable equilibration temperatures (Griffen and Bruckner 1984).

Jagoutz (1988) found that CPX which retained GT in solid solution and CPX with exsolved GT from the same eclogite xenolith possessed identical (within error) Sr and Nd isotope compositions and Sm/Nd, Sr/Nd ratios. This suggests that exsolution of garnet from CPX does not change Nd, Sm and Sr abundances or isotopic compositions. Ion-probe analyses of plagioclase exsolved from CPX in GGP samples PHN 5731 and 5734 indicates very low Sr contents (~ 2 ppm), within error of the Sr content of the host CPX . This supports the above conclusion that exsolution does not significantly alter host mineral trace-element abundances. Hence, the LREE depleted nature of the equilibrium liquids calculated for the GGP is probably not a function of REE redistribution during sub-solidus re-equilibration.

Appendix 4:4 REE analyses by isotope dilution

REE analyses were obtained from unleached whole rocks and leached CPX separates using the triple filament method of Thirlwall (1982). CPX separates were aliquoted for REE using ~ 1/4 of the total solution. Whole rock samples were dissolved in teflon bombs which had been cleaned by soaking in aqua-regia for 1 week, held at 170 ^{o}C containing HF/HNO_3 for 2 periods of 24 hours and finally cleaned with sub-boiled-quartz-distilled (SBQD) HNO_3. Approximately 300 mg of whole rock sample were dissolved in a triple distilled (TD) 60 % HF/15M HNO_3 mixture at 170 ^{o}C for 7 days, followed by alternate SBQD 6 M HCl and 10 % HNO_3 treatments at 170 ^{o}C overnight. When all the sample had been taken into solution, it was evaporated to dryness under laminar flow hoods using filtered air, taken up in conc. HNO_3, dried down and taken up in 5 mls of 75 % 8 M CH_3COOH/25 % 5 M HNO_3. Separation of REE from the bulk rock solution was carried out using the method of Hooker et al (1975) with a final stage "clean up" column pass to further reduce the presence of Ba and other impurities. Samples are loaded as nitrate, in water on to triple filament beads with Ta side filaments and a Re centre filament and dried down at 1 A in air. Beads were previously outgassed at 5 A for 5 minutes.

REE concentrations were determined on a VG-Isomass 54E mass spectrometer. Analytical reproducibility and precision were assessed on international standards by Thirlwall (1982). During this study Sm/Nd ratios were reproducible to ~ 0.3 % or better, (0.1% for non-aliquotted samples) and Ce/Yb ratios to ~ 0.6%. Absolute Nd and Sm concentrations were found to be reproducible to better than 1 %, down to 0.4 % on whole rock samples.

The Leeds dilute L5REE spike was used throughout this study. This spike is approximately 10 fold diluted compared to the "normal" L5REE spike and is used for low abundance samples where overspiking

is a danger. The larger volumes of dilute spike also reduce weighing errors. The "enriched" isotopes in the L5REE spike are: ^{153}Eu, ^{171}Yb, ^{149}Sm, ^{142}Ce, ^{145}Nd, ^{138}La, ^{155}Gd, ^{167}Er, ^{161}Dy and ^{175}Lu. The spike was prepared from pure metal ingots. Spike calibration was periodically checked by analysis of an internal "flat pattern" 25 X chondrite REE standard. Analysis of this standard by the author reproduced its gravimetrically determined Sm/Nd ratio to within 0.1 %. Absolute Sm and Nd abundances reproduced to better than 0.7%. La, Gd and Dy were the most aberrant elements, giving 2σ reproducibilities of 1.2, 1.4, and 1.4% respectively. The precision of the spike calibration for other REE can be assessed by the deviation of the analyses from a flat, chondrite normalised REE pattern with a slope of 1.000. For the spike calibration check carried out, the following values were obtained: Ce/Ce*=1.008, Nd/Nd*=1.004, Eu/Eu*=1.009. Typical analytical total procedural REE blanks were as follows:

La = 0.09 to 0.19 ng, Ce = 0.11 to 0.23 ng, Nd = 0.07 to 0.17 ng, Sm = 0.02 to 0.09 ng, Eu = 0.004 to 0.007 ng, Gd = 0.29 ng, Dy = 0.24 to 0.31 ng, Er = 0.06 to 0.12 ng, Yb = 0.02 to 0.1 ng.

Blank corrections were trivial except for the low La and Ce abundances in the highly LREE depleted GGP. As little as 3 ng of La or Ce could be present in the GGP, La and Ce values were therefore blank corrected for these samples, the correction was usually <5%.

Appendix 4:5 Radiogenic isotope analyses.

A4:5.1 Lead isotope analyses.

The standard leaching procedure applied to mineral separates is described in Chapter 6. Mineral separates were finely powdered using an agate ball mill shaker reserved specifically for low abundance samples. CPX separates were dissolved in screw-top P.F.A capsules in a mixture of TD 60% HF and 15M HNO_3. Pb, Rb/Sr and Ba spikes were added prior to dissolution.

The dissolved sample was evaporated to dryness and the residue converted to bromide by drying down in 3 mls of triple distilled 1 M HBr. The sample was redissolved in 1 ml of 1 M HBr and left overnight. Samples were centrifuged and the supernatent liquid added to minature columns containing ~ 0.2 mls of AG 1 X 8 anion exchange resin which had been pre-treated with 1 M HBr. Major elements, Sr, Nd and U were eluted with 3 mls of 1 M HBr and Pb was collected in 2 mls of triple distilled 6 M HCl. CPX samples were passed through the column a further time to ensure complete separation of Pb from major elements. The Pb collected after the second pass was dried down in the presence of 1 drop of TD 10 M HNO_3 and 1 drop of phosphoric acid until a very small drop remained in the beaker. This drop was loaded onto a single Re filament after a Si-gel ionization inhibitor was added to the filament.

Pb isotopic measurements were made on a VG MM 30 single collector mass spectrometer at temperatures between 1150 and 1300 ^{o}C. Peaks were switched between masses 204, 206, 207 and 208. 203.5 was measured as a background and 207.5 as the "tail". Mass fractionation was corrected for by repeated analyses of SRM 981. Although some of the samples analysed contained over 100 ng of Pb, relatively poor column yields and poor separation of the Pb from major elements resulted in Pb isotope data for most of the samples presented in Chapter 6 being analysed on the top scale of the Daly detector. The remaining samples were analysed using the Faraday collector. The mass fractionation corrections relative to SRM 981 are different for the two respective collectors. Nineteen measurements of SRM 981

on the Faraday collector gave a mass fractionation correction factor of 0.13 % per atomic mass unit (A.M.U.). In order to calculate mass fractionation correction for analyses run using the Daly collector, SRM 981 samples were run at equivalent beam intensities and temperatures using the Daly collector. In practice this proved difficult to achieve due to very small amounts of standard which needed to be loaded onto the filament. A dilute 40 ppm solution of the SRM 981 standard was used, 8 high precision runs of this standard at beam intensities which were gradually decreasing on the top scale of the Daly and between 1170 and 1300 ^{o}C gave the following mass fractionation factors; errors are 2σ:

208/204 = 0.5895 +/- 0.008 %, per A.M.U.

207/204 = 0.5185 +/- 0.022 %, per A.M.U.

206/204 = 0.5930 +/- 0.007 %, per A.M.U.

The significant difference between the 207/204 correction factor and the 208/204 and 206/204 factors may be partly due to uncertainty in the accepted $^{207}Pb/^{204}Pb$ ratio of SRM 981 (R.Cliff pers.comm.). In-run errors for Pb isotope analyses were usually better than 0.08 % for $^{208}Pb/^{204}Pb$ and $^{206}Pb/^{204}Pb$ and better than 0.1 % for $^{207}Pb/^{204}Pb$. Pb and U abundances were determined by spiking for ^{205}Pb and ^{236}U respectively. U was separated on cation exchange columns containing 2 ml of resin using 8M HNO_3 as an elutant, U was collected in 6M HCl. Uraniums were run on single Ta filaments with an "aqua-dag" inhibitor.

Pb blanks varied between 0.4 ng and 0.21 ng total Pb. All Pb isotope ratios are blank corrected, the correction being well within total analytical error except for GP147 CPX which was run with only 39 ng of Pb present. The blank in this case contributed 0.77 % of the total Pb. The average Pb isotopic composition of the blanks obtained during the period of this study in $^{208}Pb/^{204}Pb$ = 37.03 +/- 0.2, $^{207}Pb/^{204}Pb$ = 15.39 +/- 0.1, $^{206}Pb/^{204}Pb$ = 17.52 +/- 0.1. The high $^{207}Pb/^{204}Pb$ ratios of many of the samples analysed in this study are thus unlikely to be the result of blank contamination. Uranium blanks were typically less than 10 pg, all analyses were blank corrected.

A4:5.2 Neodymium isotope analyses

The HBr elutions collected from the U separations and were aliquotted for REE in 25 to 30 mls of dilute SBQD,TD HNO_3. Approximately 20-25% of the solution was used for REE analysis. The remainder was used for Nd and Sr isotopic analysis. Nd was extracted from the solution first as column yield experiments revealed that passing the solution through the Sr columns first gave poor Nd yields and allowed potential contamination by REE spike. The aliquotted HNO_3 solution was dried down and taken up in 5 mls of 75% 8M CH_3COOH / 25% 5M HNO_3 solution. A teflon beaker for the collection of the Sr fraction was placed under the column before loading the sample on to Bio-Rad AG 1x8 resin which was pre-conditioned in 90% 8M CH_3COOH / 10% 5M HNO_3 solution (90/10). Samples were washed in with 2x 90/10 solution and then eluted with 35 mls of 90/10. The first 30 mls of the elution were collected. Column calibration experiments showed that this volume of the elution contained over 99% of the total Sr. The REE fraction was collected in 10 mls of SBQD 0.05M HNO_3 taken to dryness and redissolved in 4

mls of SBQD 6M HCl, dried down and taken up in ~ 0.25 mls of SBQD 0.125M HCl. The sample was then loaded onto P.T.F.E. based cloumns containing di-(2-ethylhexyl)-orthophosphoric acid. The columns were eluted with a fixed volume (~ 30 mls) of 0.125M HCl and Nd was collected in SBQD 0.25M HCl. The separation of Nd from other REE is critically temperature/flowrate dependant and was always carried out under relatively fixed temperature conditions (usually ~20°C +/- 1°C). The separated Nd was not passed through a cation "clean up" column as this was found to decrease Nd yields. If the above separation procedure is followed rigourously, Ba intereferences approach levels which are easily "burned off" during sample warm up in the mass spectrometer. Nd was loaded as chloride on to the Ta side filaments of a triple filament bead with a Re centre filament. Beads were outgassed at 5 amps for 5 minutes prior to loading. Nd was run as Nd^+, oxide beams being negligable.

Until 1989, Nd isotopic determinations were made on a single collector VG MM30 mass spectrometer employing a peak swithching procedure. Masses 143, 144, 146 and 148 were measured along with the Sm interference monitored by measuring mass 147, background was 146.5. The 147 peak and background were eliminated from the mass scan when the Sm interference on 144 was < 0.02 % but the Sm interference and background were monitored every 8-10 sets. Between 800 and 1000 mass scans were commonly measured. The $^{143}Nd/^{144}Nd$ ratio was corrected for mass fractionation assuming $^{146}Nd/^{144}Nd$ of BCR-1 = 0.7219. Samples were run until the in-run error was +/- 20 ppm or until the Nd beam became < 10^{-11} A. External pecision was determined by repeated analyses of the La Jolla international standard which gave $^{143}Nd/^{144}Nd$ = 0.5119049 +/- 42 on 32 determinations over the period of data acquisition. Data were normalised with respect to the accepted value for the La Jolla standard.

After 1988, Nd isotopic determinations were made automatically on a VG 54E double collector mass spectrometer employing simultaneous measurement of 143 and 144 peaks. 145 and 146 peaks were also measured in the mass scan, each peak was measured for 5 seconds. Background and 147 peaks were measured for 30 seconds each outside the mass scan before collection of each data block. Between 100 and 200 mass scans were commonly measured. The $^{143}Nd/^{144}Nd$ ratios were normalised with respect to 2 different sets of La Jolla analyses. Prior to replacement of the "high mass" bucket, 36 determinations of the La Jolla Nd standard gave 0.511790 +/- 50 whilst after replacement of the collector, La Jolla gave 0.511850 +/- 50 on 40 determinations. Three La Jolla standards were commonly included in each sample turret containing 13 Nd samples in the 54E. Blanks during Nd isotopic analysis ranged between 0.056 and 0.15 ng. Blank corrections would produce correction factors well within the typical 20 ppm 2σ in run error of all samples hence analyses presented in Chapter 6 are not blank corrected.

A4:5.3 Strontium isotope analysis.

Strontium was collected from the first 30 mls of acetic/nitric acid elution during REE separation as described above. Sr fractions from whole rocks were passed through anion exchange columns containing Biorad AG50W - 1X8 resin 3 times and CPX separates were passed through twice. The Sr columns used were reserved for low abundance Sr work only and total procedural Sr blanks of 0.5 ng or less were obtained. Only SBQD HCl was used on these columns. Samples were loaded onto the columns in 1ml of 2.5 M HCl and washed in with 2 further additions of 2.5 M HCl. 2.5 M HCl was used as a fixed volume elutant, Rb being collected ~ 1/2 way through the elution. The Sr fraction was collected in ~ 12 mls of Sr, dried down, redissolved and the procedure repeated to remove any remaining Rb. After the first Sr pass, Ba was obtained by eluting 40 mls of SBQD 2 M HNO_3 and collecting in 20 mls of the same acid.

Sr samples were loaded onto Ta filaments, previously outgassed at 5 A (@ < 10^{-6} Torr), prior to loading the Sr (as chloride) one drop of phosphoric acid was added to the filament to promote stable ion emission. Sr isotopic analysis and Sr abundance determinations were made in the same run on the VG 54E double collector mass spectrometer. Masses 88, 87 and 86 were measured along with Rb interference at mass 85. The ^{86}Sr tail was monitored at mass 87.3 and background was 84.5. Upto 200 mass scans were commonly measured using 5 second peak counting times and a 2 second delay. $^{87}Sr/^{86}Sr$ is corrected for mass fractionation assuming the fractionation is linearly correlated with mass and is normalised to $^{86}Sr/^{84}Sr = 0.1194$. $^{87}Sr/^{86}Sr$ is normalised to the NBS 987 international standard ($^{87}Sr/^{86}Sr$ = 0.71023). 52 analyses of NBS 987 over the period of this study gave 0.710275 +/- 41. In run Sr errors were typically 0.002%. Precision of Sr abundances was found to vary from 0.4 to 1 % whilst $^{87}Rb/^{86}Sr$ ratios were reproducible to within 2 % on none leached samples and within 4 % on HF leached samples. Rb samples were run on triple Ta filaments so that mass fractionation could be monitored. Ba was loaded as nitrate after the addition of phosphoric acid to a Ta sinble filament.

The "low-blank" Sr columns used for Sr extraction gave total procedural Sr blanks of 0.3 to 0.8 ng which is insignificant for all the samples analysed. Rb blanks were commonly below 0.25 ng (highest 0.22) over the period of this study, the range for these columns being 0.15 to 0.33 ng (R. Green pers. comm.). All Rb analyses were blank corrected. Ba blanks were <0.2 ng which is negligable for all samples considered. Sr blanks using the "normal" Sr columns were found to be of the order of 1.8 to 2.5 ng.

Appendix 4:5.4 Sr and Nd isotopic analyses by flux dissolution.

Spec. pure lithium metaborate was purified using the method described by Vocke et al (1987). Flux to sample ratios of at least 3:1 were mixed in Pt crucibles which had been previously cleaned by soaking in HF, reagent grade conc. HNO_3 and 2 M SBQD HNO_3 for periods of 2 days each and placed in a muffle furnace at 1100 ^{o}C for 2 hours. Samples were taken out of the furnace and cooled rapidly in damp sand or on a piece of iron metal to prevent devitrification of the glass. The fused mixture was dissolved overnight in SBQD 2 M HNO_3, being stirred continuously by Teflon coated magnetic bars. Approximately 20- 30 mls of HNO_3 were used to dissolve the samples. During dissolution the solution was not allowed to become warm since this encourages the formation of insoluble Si-hydrate complexes. The clear solution was checked for solids by centrifuging and then aliquotted for REE. The larger aliquot was spiked for Rb/Sr and the smaller for REE. The solutions were then diluted to approximately 0.5M HNO_3 using SBQD H_2O and stirred for 2 hours to ensure spike equilibration. Samples were loaded onto anion exchange columns containing bio-rad AG50W-X8 resin which had been preconditioned in 30 mls of 0.5 M HNO_3. Samples were eluted with a further 40 mls of 0.5 M HNO_3 and collected in 20 mls of SBQD 6 M HCl. This solution was dried down and treated via the normal post dissolution Sr-Nd-REE chemistry starting at the acetic acid columns. 0.5 M HNO_3 is used to load the samples and as an elutant because stronger acid is not as efficient at eluting borates which then persist to create borate complexes which significantly interfere with HREE analyses, particularly Yb, during isotope dilution mass spectrometry.

Nd blanks using this method varied between 0.15 and 1.8 ng with an average value of ~ 0.7 ng. Therefore only the crustal kinzigite samples were analysed for Nd and Sr isotopes using flux dissolution. Other total REE blanks were: La = 0.6 to 1.0 ng, Ce = 0.4 to o.6 ng, Sm = 0.04 to 0.1 ng, and Yb = 0.4

to 0.64 ng. Sr blanks varied between 2 and 5 ng and Rb blanks were 2 ng. These blank levels are negligable at the Nd, Sr and Rb abundances present in the kinzigite whole rocks. Sm/Nd ratios are reproducible to better than 1% whilst the Sm/Nd ratios of analyses performed by both bomb and flux dissolution methods agreed to ~ 1% for sub ppm levels of Sm and Nd. Flux dissolutions of garnetiferous pyroxenite samples analysed previously by bomb dissolution gave ~1 to 1.5 % agreement in their HREE contents suggesting that the bomb disslution procedure is efficient at dissolving all the garnet and also indicating the absence of any HF insoluble phases in the pyroxenites.

Appendix 4:6 Stable isotope analyses

A4:6.1 Oxygen isotope analysis.

Mineral separates used for oxygen isotope analyses were taken from the same mineral concentrate used for radiogenic isotope analyses. The final separates underwent the same 6 M HCl, 40 % HF leaching procedure outlined in Chapter 6 for the radiogenic isotope samples. Samples were crushed in steel shakers. Procedures and control experiments are described in B.G.S. Isotope Geology Unit internal report No.104 (1983) which follows the method of Clayton and Mayeda (1963). 5 mg of powder were loaded in aluminium foil (in an atmosphere of flowing, dry N_2) into nickel reaction vessels. The line was evacuated to better than 10^{-5} Torr. and samples were outgassed at 250 ^{o}C overnight. Samples were prefluorinated at room temperature for 2 hours in distilled BrF_5. Samples were reacted for 16 hours at 600 ^{o}C, extracted using a series of liquid N_2 cold traps and converted to CO_2 using heated graphite rods. The CO_2 yield was measures using a capacitance manometer and could be directly related to the expected O_2 yield using chemical analysis of the reacting phases. The CO_2 was analysed on a VG MM 903 triple collector mass spectrometer. The isotopic ratios were compared to reference gas MCS-10. $\delta\,^{18}O$ values are reported relative to the V- SMOW international standard (see Chapter 7). Isobaric interferences were corrected using the method of Craig (1957).

Garnets were always run in duplicate and 9 out of 19 CPX separates were also run in duplicate. CPX yields were 100 % +/- 1.0 %. Preliminary experiments on the Beni Bousera garnets produced poor yields which were found to get worse if the fluorination temperature was increased to 660 ^{o}C due to some reaction of BrF_5 with the Ni vessel. Greatly improved garnet yields were obtained by grinding the garnets to an extremely fine powder (< - 300 mesh) and fluorinating at 600 ^{o}C for 16 hours. Garnets gave yields which averaged above 95 %, the only sample yielding below 90 % was GP 87B GT which gave a yield of 79 %. However, the ΔCPX-GT value of - 0.1 ‰ for this mineral pair is well within the range of CPX -GT fractionations obtained from other sample pairs giving better oxygen yields for the garnets (Chapter 7). Oxygen isotope analyses of garnets commonly reproduced to better than 0.2 % (2σ) and CPX < 0.1 % (Table 7.1, Chapter 7).

Four analyses of the international standard NBS-28 gave + 9.6 +/- 0.2 ‰ over the period of this study. Duplicate analysis of an internal BGS Glass Sand sSandard (LAGS) were made in alternate batches of samples as an internal control. 9 analyses of LAGS over the period of this study gave $\delta\,^{18}O$ = + 10.9 +/- 0.2 ‰ compared to the accepted value of +10.9 ‰. In run precision was always better than 0.1 ‰.

Appendix 4:6.2 Carbon isotope analyses

A4:6.2a Extraction Procedure.

Carbon isotope analyses were carried out in the stable isotope laboratory of the Planetary Sciences Unit, Open University, Milton Keynes. Samples were weighed out in a "clean room" into a quartz bucket which had been previously baked out at 1000 °C for 8 hours. Samples were handled with tweezers which were cleaned in an ultra-sonic bath of Toluene and methanol (50:50) after each sample handling. Approximately 20 mg of spectrographically pure Johnson-Mattey JMC - 40 copper II oxide was added to the sample to act as an oxidant. Batches of 6 samples were pre-combusted at 600 °C for 1 hour in a muffle furnace to burn off any surficial organic contamination and then sealed under vacuum into quartz ampoules. The sealed ampoules were then combusted at 1000 °C for 8 hours in a muffle furnace and allowed to stand for 1 hour at 600 °C to allow the copper II oxide to resorb any excess oxygen produced.

After cooling the sealed ampoules were cracked under vacuum of better than 10^{-5} Torr passed through a molecular sieve and platinum furnace at 600 °C to be trapped in a "cold finger" containing liquid nitrogen. The CO_2 was cryogenically separated from water using a methanol/liquid nitrogen (if no significant SO_2 was thought to be present) or n-pentane/liquid nitrogen "slurry" and the combustion yield measured in a capacitance manometer (MKS Baratron Ltd). The supposedly pure CO_2 was re-trapped in liquid nitrogen to a take off vessel which was transfered to the mass spectrometer. Typical combustion yields were > 99% except for some graphite vein and graphitic gneisses samples which contained slight silicate impuities.

A4:6.2b Mass Spectrometry.

Carbon was analysed as CO_2 on a VG SIRA-24 9 cm actual radius triple collector mass spectrometer. This instrument has a cold finger on the inlet system which allows analysis of as little as ~ 2-3 µg carbon samples. Samples and reference CO_2 are admitted to the mass spectrometer via a dual inlet system of stainless steel capillary leaks to a solenoid operated change over valve. As one gas is analysed the other is bled to waste at the same rate ensuring that both sample and reference gas pressure decay simultaneously. The reference gas used throughout this study was CO_2-7 dry ice which routinely gave $\delta^{13}C$ = -24.425 ‰ +/- 0.660 vs PDB. An aliquot of reference gas was run at the begining and end of each batch of samples. The pressures of each gas was balanced by means of two variable values, one on each side of the inlet.

The ion beams (M/Z 44, 45, 46) were collected simultaneously in 3 Faraday buckets and converted by three separate 1MHZ voltage- to - frequeny converters into the computer. The ratio of ^{13}C to ^{12}C in carbon dioxide was calculated by measuring ion beam currents at M/Z = 45 ($^{13}C^{16}O^{16}O^+$) and M/Z = 44 ($^{12}C^{16}O^{16}O^+$) . The contribution to M/Z = 45 from ^{17}O was corrected using the method of Craig (1957) by measurement of the ion beam current at M/Z = 46. Sample reproducibility is commonly +/- 0.1 %. Five analyses of the O.U. internal standard diamond powder gave -9.7‰ +/- 0.2 ‰. Blank levels of 1 µg ($\delta^{13}C$ = ~ -27 ‰) were negligable for the sample sizes used, hence analyses were not blank corrected. Sample sizes of between 0.1 and 0.01 mg of C allow isotopic individual analyses to be determined to an internal precision of better than 0.01‰.

GP62 Musc., run 1010, weight =0.02274 gms. J value

Temp	39K	37Ca	38Cl	Ca/K	*40/39K	%Atm 40
	{ Vol. *10-9 cc }					
600	0.446	0.000	0.003	0.000	13.202	78.0
650	0.857	0.009	0.004	0.020	13.302	75.1
735	2.797	0.020	0.006	0.014	23.226	60.6
800	19.656	0.002	0.041	0.000	8.216	61.3
855	20.473	0.000	0.043	0.000	8.207	24.0
925	7.684	0.017	0.016	0.004	8.503	41.0
1000	2.800	0.020	0.007	0.014	8.510	59.5
1350	5.653	0.379	0.016	0.133	8.678	43.7

Integrated values,	analytic	& J errors(2 sigma)
Age (My) 70.80	0.26	4.17
*40/39K 9.111	0.37 %	

Wt %K = 8.619 ,*40 = 241.85 x 10-7 cc/gm

=0.004393 +/- 3.0 %

Age	Err	%39
101.71	11.92	0.7
102.46	4.22	1.4
175.28	0.61	4.6
63.96	0.24	32.6
63.90	0.29	33.9
66.16	0.18	12.7
66.21	3.54	4.6
67.50	0.42	9.4

APPENDIX 5

THREE STAGE Pb ISOTOPE EVOLUTION

The Pb isotope evolution of a reservoir which has been subjected to three different U/Pb fractionation events can be modelled in terms of $^{206}Pb/^{204}Pb$ and $^{207}Pb/^{204}Pb$ ratios using the following equations:

$$(^{206}Pb/^{204}Pb)_m = (^{206}Pb/^{204}Pb)_i + (^{238}U/^{204}Pb)_1 [e^{\lambda 1 T} - e^{\lambda 1 t1}] + (^{238}U/^{204}Pb)_2 [e^{\lambda 1 t1} - e^{\lambda 2 t2}] + (^{238}U/^{204}Pb)_3 [e^{\lambda 1 t2} - 1] \quad (1)$$

and

$$(^{207}Pb/^{204}Pb)_m = (^{207}Pb/^{204}Pb)_i + 1/137.88\ (^{238}U/^{204}Pb)_1 [e^{\lambda 2 T} - e^{\lambda 2 t1}] + 1/137.88\ (^{238}U/^{204}Pb)_2 [e^{\lambda 2 t1} - e^{\lambda 2 t2}] + 1/137.88\ (^{238}U/^{204}Pb)_3 [e^{\lambda 2 t2} - 1] \quad (2)$$

where the subscript i refers to the initial Pb isotopic ratio of the Earth 4.55 Ga ago and m is the Pb isotope ratio measured now. Following Chen and Wasserburg (1981), For T = 4.55 Ga:

$(^{206}Pb/^{204}Pb)_i = 9.307$ and $(^{207}Pb/^{204}Pb)_i = 10.294$.

The decay constants; ^{238}U ($\lambda 1$) = 1.55125 * 10-11
and ^{235}U ($\lambda 2$) = 9.8485 * 10-10 (Steiger and Jaeger 1977).

To model three stage Pb isotope evolution of sample GP81 CPX

$(^{206}Pb/^{204}Pb)_m = 17.404$ and $(^{207}Pb/^{204}Pb)_m = 15.547$

Solutions of t2 and $(^{238}U/^{204}Pb)_3$ are required over a range of t1 and $(\ ^{238}U/^{204}Pb\ )_2$ values.

Redefining the terms as;

$(^{206}Pb/^{204}Pb)_m = P_{6m}$, $(^{207}Pb/^{204}Pb)_m = P_{7m}$, $(^{206}Pb/^{204}Pb)_i = P_{6i}$,

$(^{207}Pb/^{204}Pb)_i = P_{7i}$ and $(\ ^{238}U/^{204}Pb\ )_{1,2,3} = \mu_{1,2,3}$

equations (1) and (2) become

$$P_{6m} = P_{6i} + \mu_1 [\ e^{\lambda 1T} - e^{\lambda 1t1}\ ] + \mu_2 [\ e^{\lambda 1t1} - e^{\lambda 1t2}\ ] + \mu_3 [\ e^{\lambda 1t2} - 1\ ] \qquad (3)$$

and

$$P_{7m} = P_{7i} + \mu_1/137.88 [\ e^{\lambda 2T} - e^{\lambda 2t1}\ ] + \mu_2/137.88 [\ e^{\lambda 2t1} - e^{\lambda 2t2}\ ] + \mu_3/137.88 [\ e^{\lambda 2t2} - 1\ ] \quad (4)$$

Rearranging equation (3), μ_3 is obtained in the form

$$\mu_3 = 1/[\ e^{\lambda 1t2} - 1\ ] \{\ P_{6m} - P_{6i} - \mu_1 [\ e^{\lambda 1T} - e^{\lambda 1t1}\ ] - \mu_2 [\ e^{\lambda 1t1} - e^{\lambda 1t2}\ ]\ \} \quad (5)$$

Substituting equation (5) into equation (4) gives, after some manipulation,

$$t2 = 1/\lambda 2 \ln [\ 1/\mu_2 [\ 137.88 (\ P_{7i} - P_{7m} + X\ ] + e^{\lambda 2t1}\ ], \qquad (6)$$

where

$$X = \mu_1 [\ e^{\lambda 2T} - e^{\lambda 2t1}\ ] + [\ e^{\lambda 2t2} - 1\ ] / [\ e^{\lambda 1t2} - 1\ ] \{\ P_{6m} - P_{6i} - \mu_1 [\ e^{\lambda 1T} - e^{\lambda 1t1}\ ] - \mu_2 [\ e^{\lambda 1t1} - e^{\lambda 1t2}\ ]\ \} + e^{\lambda 2t2} . \quad (7)$$

It is not possible to obtain t2 explicitly. Equation (6) provides an implicit relationship for t2 which can be solved by a simple iteration technique.

APPENDIX 6

Radiogenic isotope data presentation:

The ε notation refered to in the text is an expression of Nd or Sr isotopes in a reservoir formed at a time t relative to the chondritic uniform reservoir (CHUR) or bulk earth uniform reservoir (UR) at that time. Thus:

$$\varepsilon Nd = [({}^{143}Nd/{}^{144}Nd)_{s(t)} / ({}^{143}Nd/{}^{144}Nd)_{CHUR(t)} -1] \times 10^4$$

$$\varepsilon Sr = [({}^{87}Sr/{}^{86}Sr)_{s(t)} / ({}^{87}Sr/{}^{86}Sr)_{UR(t)} -1] \times 10^4$$

where the subscript s refers to the isotopic composition of the sample at time t.

$CHUR_{Nd}$ model ages are calculated from the following equation:

$$T\,CHUR_{Nd} = 1/\lambda \ln [({}^{143}Nd/{}^{144}Nd)_s - ({}^{143}Nd/{}^{144}Nd)_{CHUR} / ({}^{147}Sm/{}^{144}Nd)_s - ({}^{147}Sm/{}^{144}Nd)_{CHUR} +1]$$

An analagous equation may written for $T\,UR_{Sr}$ model ages:

$$T\,UR_{Sr} = 1/\lambda \ln [({}^{87}Sr/{}^{86}Sr)_s - ({}^{87}Sr/{}^{86}Sr)_{UR} / ({}^{87}Rb/{}^{86}Sr)_s - ({}^{87}Rb/{}^{86}Sr)_{UR} +1].$$

where:

$\lambda\,{}^{147}Sm = 6.54 \times 10^{-12} y^{-1}$

$({}^{143}Nd/{}^{144}Nd)_{CHUR} = 0.512638$

$({}^{147}Sm/{}^{144}Nd)_{CHUR} = 0.1967$

$\lambda\,{}^{87}Sr = 1.42 \times 10^{-11} y^{-1}$

$({}^{87}Sr/{}^{86}Sr)_{UR} = 0.7047$

$({}^{87}Rb/{}^{86}Sr)_{UR} = 0.0847$,

also,

$\lambda\,{}^{238}U = 1.55125 \times 10^{-10} y^{-1}$

$\lambda\,{}^{235}U = 9.8485 \times 10^{-10} y^{-1}$

$\lambda\,{}^{232}Th = 4.948 \times 10^{-11} y^{-1}$

(After Steiger & Jaeger, 1977 and Faure, 1986).

$$({}^{147}Sm/{}^{144}Nd)_s = Sm/Nd (0.142556 \times ({}^{143}Nd/{}^{144}Nd)_s + 0.531628)$$

and,

$$({}^{87}Rb/{}^{86}Sr)_s = Rb/Sr [0.283 \times ({}^{87}Sr/{}^{86}Sr)_s + 2.6927]$$